**Promotors** **Prof. dr. ir. Marc Van Meirvenne**
Department of Environment
Faculty of Bioscience Engenering
Ghent University

**dr. Birger Stichelbaut**
Department of Archaeology
Faculty of Arts and Philosophy
Gent University

**Dean** **Prof. dr. ir. Marc Van Meirvenne**
**Rector** **Prof. dr. ir. Rik Van de Walle**

Nicolas Note

# Prospecting World War One conflict landscapes with non-invasive soil sensing techniques

Geophysical exploration of the former Western Front in Belgium

Thesis submitted in fulfilment of the requirements
for the degree of Doctor (PhD) in Applied Biological Sciences

**Dutch translation of the title:**
De prospectie van Wereldoorlog 1 conflictlandschappen door middel van niet-invasieve bodemsensoren: geofysische verkenning van het voormalige Westelijke Front in België

**Illustration on the cover:**
Magnetometer survey at Hill 80 near the centre of Wijschate (Heuvelland).

**Illustration on the back:**
Electrical conductivity data layer of an electromagnetic induction survey, performed at Hill 62 near Zillebeke. Orthophoto: copyright Agentschap Informatie Vlaanderen

**Citation of this thesis:**
Note, N. (2019). Prospecting World War One conflict landscapes with non-invasive soil sensing techniques: Geophysical exploration of the former Western Front in Belgium. Doctoral dissertation. Ghent University, Ghent, Belgium.

**ISBN-number**: 978-94-6357-169-2

**Notice of rights:**
The author and promoters give the authorisation to consult and to copy parts of this work for personal use only. Every other use is subject to the copyright laws. Permission to reproduce any material contained in this work should be obtained from the author.

# Dankwoord

**(dutch)**

In de eerste plaats wil ik mijn promotor Marc Van Meirvenne bedanken voor de kans die hij mij gegeven heeft om onderzoek uit te voeren op het UGent BOF GOA project 'Niet-invasieve landschapsarcheologie van de Groote Oorlog'. Als geograaf-landmeter was het voor mij een leerrijke ervaring om deel uit te maken van dit interdisciplinaire project en team waarbij naast de toegepaste geofysische metingen, aspecten uit de bodemkunde en archeologie aan bod kwamen. Het interdisciplinair karakter van het onderzoek heeft mijn kennis verbreed. Graag druk ik ook mijn waardering uit voor projectpromotoren Jean Bourgeois en Veerle Van Eetvelde die mede met mijn thesispromotor het project in goede banen hebben geleid. Tijdens mijn doctoraatsonderzoek kon ik telkens rekenen op de steun van collega-projectmedewerkers Wouter Gheyle, Hanne Van den Berghe, Timothy Saey en Birger Stichelbaut (co-promotor) voor het kritisch nalezen van papers, om inspiratie op te doen tijdens brainstormsessies en het coördineren van data-integratie. Hun medewerking was een van de belangrijkste pijlers gedurende mijn vier jaar onderzoek. Daarnaast genoot ik ook de volle steun van mijn collega's van de onderzoeksgroep ORBit. Hier gaat een speciaal woordje van dank uit naar Valentijn Van Parys die als all-round medewerker mij de kneepjes van het terreinwerk bijbracht en die samen met Timothy Saey en mezelf heel wat dagen spendeerde om de geofysische metingen uit te voeren. Daarnaast kon Philippe De Smedt met z'n kritische blik en ervaring in archeologische prospectie, mij in de juiste richting bijsturen. Hij zette mij ook aan om het MATLAB programmeren onder de knie te krijgen, wat een grote meerwaarde bleek te zijn voor de dataverwerking van verschillende bodemsensoren. Indien ik met vragen zat tijdens het programmeren was Samuel Delefortrie ook zeker een referentie om op terug te vallen. Tot slot wens ik ook mijn ouders, vriendin, familie en vrienden te bedanken voor hun blijvend vertrouwen en onvoorwaardelijke steun. Ik vermoed dat ik nog een aantal personen vergeten ben. Voor hen ook alvast een teken van waardering!

Nicolas Note

Gent, 31 Januari 2019

# Table of contents


**Dankwoord (Dutch)** **V**

**Table of contents** **VII**

**List of abbreviations and acronyms** **XIII**

**Summary** **XVII**

**Samenvatting (Dutch)** **XIX**

**Chapter 1: Introduction** **21**

**1.1 The unique situation of the former Western Front in Belgium** **22**

**1.2 World War One archaeology in the Flanders region** **22**

**1.3 Research objectives** **28**

**1.4 Structure of the thesis** **30**

**Chapter 2: Geophysical prospection techniques and supporting databases: elements for an integrated method** **33**

**2.1 Introduction** **34**

**2.2 Geophysical Soil Sensing** **35**

2.2.1 Basic principles of electromagnetic, electric and magnetic methods 36

2.2.2 Electric and magnetic properties of soil 39

2.2.3 Frequency domain electromagnetic induction 41

2.2.4 Time domain electromagnetic induction 46

2.2.5 Ground penetrating radar 49

2.2.6 Electrical resistivity 53

2.2.7 Fluxgate gradiometer magnetometry 57

**2.3 Other non-invasive techniques** **62**

2.3.1 Aerial photography 62

2.3.2 LIDAR 64

**2.4 WW1 battle phases and study area** **67**

2.4.1 Battle phases on the Western Front during the war in Belgium 67

2.4.2 Study area 68

**Chapter 3: Optimising fluxgate magnetometer survey data 71**

**3.1 Introduction 72**

**3.2 Basic post processing 74**

3.2.1 Datasets 74

3.2.2 Zero-median levelling 74

3.2.3 Removal of overlapping and too close recorded data 79

**3.3 Tilt noise filtering 81**

3.3.1 Test sites 82

3.3.2 Noise identification 84

3.3.3 Wavelet-based filtering procedure 86

*3.3.3.1 1D wavelet analysis* 86

*3.3.3.2 Isolating tilt noise* 87

*3.3.3.3 Result evaluation* 91

*3.3.3.4 Other applications* 94

**3.4 Conclusions 96**

**Chapter 4: Evaluation of soil sensing techniques to characterise buried features in WW1 conflict areas 99**

**4.1 Introduction 100**

**4.2 FD-EMI / FGM evaluation 101**

4.2.1 Study area 101

4.2.2 Feature type identification 103

*4.2.2.1 Trenches* 103

*4.2.2.2 Communication cables* 106

*4.2.2.3 Destroyed buildings* 107

*4.2.2.4 Shell holes and mine craters* 107

*4.2.2.5 Case 1: Characterisation of a British-Australian barrack camp* 109

*4.2.2.6 Case 2: Localisation of a horse mass grave* 111

4.2.3 Feature detection: quantitative evaluation 113

4.2.4 Metal objects 114

*4.2.4.1 Filtering* 115

*4.2.4.2 2D precision* 115

**4.3 GPR 117**

**4.4 ER 120**

4.4.1 Limitations 120

4.4.2 Error codes 121

4.4.3 Survey examples and tests 122

4.4.4 Processing 127

4.4.5 Suitability on WW1 sites 127

**4.5 TD-EMI 128**

**4.6 Conclusions 131**

**Chapter 5: Identification and validation of geophysical anomalies in WW1 battlefields 133**

**5.1 Introduction 134**

**5.2 Metal debris and shell craters: direct indicators of warfare 135**

5.2.1 Metal identification 135

5.2.2 Shell craters 138

**5.3 GSS-scan vs. surface covering excavation results 141**

5.3.1 Introduction 141

5.3.2 Site description 141

5.3.3 Results 142

**5.4 Validation of military structures 147**

5.4.1 Dugout 147

*5.4.1.1 Introduction* 147

*5.4.1.2 Study area – Tor Top* 148

*5.4.1.3 Results DUALEM 421S scan* 150

*5.4.1.4 Augering validation* 152

5.4.2 Tanks 158

*5.4.2.1 Historical background* 158

*5.4.2.2 Localisation at the front* 158

*5.4.2.3 GSS validation sites* 159

5.4.3 Military barracks 164

*5.4.3.1 Introduction and non-invasive research* 164

*5.4.3.2 Validation by test-trenching* 166
5.4.4 Horse mass grave 170
*5.4.4.1 Geophysical scans* 170
*5.4.4.2 Augering validation* 171
**5.5 Conclusions** **174**

**Chapter 6: Shell holes: A proxy for destruction intensity and buried iron clutter** **177**
**6.1 Introduction** **178**
**6.2 Prior attempts in France and Belgium** **179**
**6.3 New approach: Shelling as proxy** **182**
6.3.1 Method and study area 182
6.3.2 Class division and validation 186
**6.4 Geophysical integration** **188**
6.4.1 Metal filtering and parameters 189
6.4.2 Metal parameter description 190
**6.5 Conclusions and discussion** **192**

**Chapter 7: Preservation of WW1 features in the soil on a regional scale** **195**
**7.1 Introduction** **196**
**7.2 Soil conditions at the former Western Front in Belgium** **198**
7.2.1 Soil, warfare and trench construction 198
7.2.2 Degradation of WW1 construction materials vs. soil conditions 207
7.2.3 Anthropogenic effects of the post war period 210
7.2.4 Summary soil influencing parameters 211
**7.3 Field research: large-scale geophysical investigation** **213**
7.3.1 Transect 1: The polders 213
*7.3.1.1 Chien Marin and Jokveld, fortified farms near the Belgian frontline (ID 1 & 2)* 215
*7.3.1.2 Advanced posts in the inundated area near the front: sites near Oosthof (ID 3) and Roedesterkte farm (ID 5)* 219

7.3.1.3 *Scanned area between Rycken Hoek, Violette and Ter Stille farm (ID 5 & 9)* 223
*7.3.1.4 Absence of identifiable traces in the soil: Farm B (ID 4) / Railway (ID 6) and Near Yser site (ID 8)* 224
*7.3.1.5 Hinterland site: German Aerodrome near Gistel (ID 10)* 226
*7.3.1.6 An overview of the Polder results* 228
7.3.2 Transect 2: A section through the Ypres Salient 231
*7.3.2.1 Hinterland site: Vlamertinge (ID 1)* 232
*7.3.2.2 Bellewaarde Ridge (ID 4-9)* 234
*7.3.2.3 Hill 62: a heavily contested site (ID 10)* 240
*7.3.2.4 Black Watch Corner, on top of the Westrozebeke ridge (ID 13)* 241
*7.3.2.5 Other sites: Palingbeek, Sint-Juliaan and Clapham Junction* 243
*7.3.2.6 Summary of the 2nd transect results* 243
7.3.3 Transect 3: A section through the Messines Ridge 247
*7.3.3.1 Sites near Loker: from Allied hinterland to 1918 frontline (ID 1-2-3)* 247
*7.3.3.2 Kemmel sites: a well-targeted lookout hill and Allied 1915-17 hinterland (ID 4-5)* 251
*7.3.3.3 The 1915-1917 frontline sites: complex area's (ID 7 - 18, 23 & 29)* 254
*7.3.3.4 Near frontline sites after the 3rd battle of Ypres (ID 20-21-22, 26-27)* 266
*7.3.3.5 German hinterland site (ID 28)* 269
*7.3.3.6 Other sites (ID 18 - 19 - 24 - 25 - 30 - 31)* 269
*7.3.3.7 An overview of the 3rd transect results* 271
**7.4 Conclusions** **276**

**Chapter 8: Conclusions and future perspectives** **281**

**Appendices** **289**
Chapter 2 290
Chapter 3 295
Chapter 5 299
Chapter 6 301
Chapter 7 305

**References** **311**

**Curriculum Vitae** **325**

# List of abbreviations and acronyms

| | |
|---|---|
| 2D | two-dimensional |
| 3D | three-dimensional |
| AIV | Agentschap Informatie Vlaanderen |
| ALS | airborne laser scanning |
| AUV | unmanned aerial vehicle |
| ATV | all-terrain vehicle |
| AWM | Australian War Memorial |
| BH | Bayerisches Hauptstaatsarchiv |
| BW | black and white |
| CHAL | Centre for Historical and Archaeological Aerial Photography |
| DEM | digital elevation model |
| DIC | depth investigation characteristic |
| DMHV I/II | digital height model Vlaanderen I/II |
| DO | dissolved oxygen |
| DOE | depth of exploration |
| DOV | databank ondergrond Vlaanderen |
| DR | detection rate |
| DTM | digital terrain model |
| EC | electrical conductivity |
| $EC_a$ | apparent electrical conductivity |
| $EC_{sh}$ | shallow electrical conductivity |
| $EC_d$ | deep electrical conductivity |
| EM | electromagnetic |
| EMI | electromagnetic induction |
| ER | electrical resistivity |

| | |
|---|---|
| FDEM | frequency domain electromagnetics |
| FD-EMI | frequency domain electromagnetic induction |
| FEMP | fused electromagnetic metal predictor |
| FGM | fluxgate gradiometer magnetometry |
| GIS | geographic information system |
| GOA | geconcentreerde onderzoeksactie |
| GNSS | global navigation satellite system |
| GPR | ground penetrating radar |
| GPS | global positioning system |
| GSS | geophysical soil sensing |
| HCP | horizontal coplanar |
| HDPE | high-density polyethylene |
| IFFM | In Flanders Fields Museum |
| IGN | Institut Géographique National |
| IWM | Imperial War Museum |
| KLM-MRA | Royal Museum of Armed Forces and Military History |
| LF | linear feature |
| LIDAR | light detection and ranging |
| MHS | multi hill shading |
| MOH | metal object hotspots |
| MS | magnetic susceptibility |
| $MS_a$ | apparent magnetic susceptibility |
| MSP | metal shrapnel pollution |
| NCAP | national collection of aerial photography |
| ORD | Office des Régions Dévastées |
| PA | precision agriculture |
| PDA | personal digital assistant |

| | |
|---|---|
| PF | point feature |
| ppt | parts per thousand |
| PRP | perpendicular |
| RGB | red – green – blue (colour) |
| RSA | remote sensing archaeology |
| RTK | real time kinematic |
| Rx | receiver unit |
| SGRS | Service Général du Renseignement et de la Sécurité |
| SVF | sky view factor |
| TAW | tweede algemene waterpassing |
| TD1/2 | time domain one/two |
| TDEM | time domain electromagnetics |
| TD-EMI | time domain electromagnetic induction |
| Tx | transmitter unit |
| UXO | unexploded ordnance |
| VCP | vertical coplanar |
| VHF | very high frequency |
| WW1 | World War One |
| WW2 | World War Two |

# Summary

World War One (1914-18) was a global conflict that took place on various fronts in Europe, Asia, the Middle East and Africa, and this for the first time on an industrialised scale. This warfare had an enormous impact on the environment of which the remains are still visible today. During this war, military tactics underwent a strong evolution: from massive attacks with infantry and cavalry in 1914 to the use of new techniques such as poison gas, deep mines, aircrafts, submarines and tanks. More than a hundred years after the start of this conflict, numerous initiatives are being taken to keep the memory of this war in all its aspects alive. This also happened on a scientific level. One of the initiatives is Ghent University's '*Non-invasive landscape archaeology of the Great War*'-project (2014-18; BOF research fund: grant number 01G00214) whereby non-invasive techniques were used to study the remnants of the First World War both above and below the ground surface at the former Western Front in Belgium. The applied techniques to conduct this study were: aerial photography, airborne laser scanning and geophysical soil sensing. The use of this latter is tackled in this thesis whereby the potential of geophysical techniques are investigated to uncover World War One remains and how these can contribute to the modern conflict archaeology in Flanders and by extend to other similar historical conflict areas.

Concretely, the popular geophysical prospecting techniques of magnetometry, resistivity, electromagnetic induction and ground penetrating radar were tested with regard to the capabilities in a comparative study to characterise the war heritage in the subsoil. This was tested on plots with buried military World War One remains. Because the soil conditions have a large influence on the detection properties of these sensors, this was also taken into account. To take the detection of these war remains to a higher level, frequency domain electromagnetic induction was deployed to scan more than 240 hectares spread over 55 sites in the study area. This provides an insight into what might still be encountered in the contemporary soil archive by looking further than the local level.

Some specific anomalies from the detection results were subjected to ground truthing in order to characterise the phenomena that made the detection of military structures possible. This is necessary to calibrate the scans. Next, a classification technique for metal and shell craters was defined.

In addition, a search was made for a method that combines non-invasive techniques to display the destruction of the soil at the former Western Front on a map. A spatial sampling technique that characterises the density of shell craters on historic aerial photographs forms the basic source for this destruction mapping. Properties of detected metal from geophysical scans could be linked to these crater densities. This successful destruction mapping is a useful tool in different domains. It ensures that the representation of the Western Front not only can be visualised by a line but also by a zonal map with intensity variations. These destruction intensities indicate parts of the soil archive that were destroyed whereby potential older archaeology could be affected or discoveries of World War 1 remains (military infrastructure, missing soldiers, UXO) could have a higher frequency.

Finally, a filtering procedure based on wavelets was devised for the magnetometer technique. This was developed to remove sensor-tilt induced noise from the data in order to better analyse the scans for archaeological purposes within this study. This filter technique in its one-dimensional form has not yet been used for magnetometer prospecting in archaeology and is therefore innovative. This development deviates from the original objective of this thesis, but was necessary to deliver qualitative datasets.

# Samenvatting

De Eerste Wereld Oorlog (1914-18) was een intens globaal conflict dat zich op verschillende fronten in Europa, Azië, Midden-Oosten en Afrika afspeelde en dit voor het eerst op een geïndustrialiseerde schaal. Deze oorlogsvoering had een enorme impact op de directe omgeving waarvan de restanten tot op vandaag nog zichtbaar zijn. Tijdens deze oorlog kenden de militaire tactieken een sterke evolutie: van massale aanvallen met infanterie en cavalerie in 1914, naar het gebruik van nieuwe technieken zoals gifgas, dieptemijnen, vliegtuigen, onderzeeërs en tanks. Meer dan honderd jaar na de aanvang van dit conflict worden tal van initiatieven genomen om de gedachte aan deze oorlog in al haar facetten levende te houden. Dit gebeurde ook op wetenschappelijk vlak. Een van deze initiatieven is het '*Niet-invasieve landschapsarcheologie van de Groote Oorlog*'-project van de UGent (BOF onderzoeksfonds: toekenningsnummer 01G00214) dat gedurende de periode 2014-18 niet-invasieve technieken gebruikte om de restanten van de Eerste Wereldoorlog zowel boven als ondergronds te bestuderen aan het voormalige Westelijke Front in België. De ingezette technieken om deze studie uit te voeren waren: luchtfotografie, laserscanning (vanuit de lucht) en geofysische bodemsensoren. Het gebruik van deze laatste techniek wordt in deze doctoraatsthesis behandeld. Hierbij wordt er getoetst naar de mogelijkheden van deze sensoren om de ondergrond te karakteriseren: Wat kunnen deze technieken van de oorlog blootleggen in de voormalige conflict regio en hoe kunnen deze bijdragen tot de moderne conflict archeologie in Vlaanderen en bij uitbreiding gelijkaardige historische conflictgebieden?

Meer concreet worden de populaire geofysische prospectietechnieken magnetometrie, resistiviteit, elektromagnetische inductie en grondradar in een vergelijkende studie afgetoetst met betrekking tot de hoedanigheid dat deze het oorlogserfgoed in de ondergrond kunnen karakteriseren. Dit werd uitgetest op percelen met begraven Wereldoorlog 1 restanten. Doordat de bodem een grote invloed uitoefent op de detectie-eigenschappen van deze sensoren, werd ook rekening gehouden met de samenstelling ervan.

Om de detectie van deze oorlogsrestanten naar een hoger niveau te tillen werd frequentiedomein elektromagnetische inductie ingezet om ruim 240 ha, verspreid over 55 sites in het studiegebied, op te meten. Dit geeft een inkijk wat er mogelijks nog kan aangetroffen worden in het hedendaagse bodemarchief waarbij het lokale perseelniveau wordt overstegen.

Enkele specifieke anomalieën uit de detectieresultaten werden onderworpen aan (invasieve) validatie om te kunnen achterhalen welk fenomeen de detecteerbaarheid mogelijk maakte van deze militaire structuur. Dit is nodig om de scans te kunnen ijken. Ook werd een classificatietechniek voor metaal en bomkraters gedefinieerd.

Daarnaast werd er op zoek gegaan naar een methode die niet-invasieve technieken combineert om de vernieling van de bodem rondom het front op een kaart voor te stellen. Een ruimtelijke staalnametechniek die de densiteit van bomkraters karakteriseert op historische luchtfoto's, vormt hierbij de basisbron voor deze vernielingskartering. Eigenschappen van gedetecteerd metaal uit geofysische scans konden gekoppeld worden aan deze kraterdensiteiten. Deze succesvolle vernielingskartering is een nuttig instrument voor verschillende domeinen. Het zorgt ervoor dat de visualisatie van het Westelijke Front niet enkel door een lijn kan gebeuren maar ook door een zonale kaart met intensiteitsvariaties. Deze vernielingsintensiteiten geven aan welke delen van het bodemarchief werden aangetast waarbij potentiële oudere archeologie kan vernield zijn of vondsten van Wereldoorlog 1 (militaire infrastructuur, vermiste soldaten, UXO) een hoge frequentie kunnen hebben.

Tot slot werd voor de magnetometertechniek een filterprocedure bedacht gebaseerd op wavelets. Dit werd ontwikkeld om door sensor-tilt veroorzaakt ruis uit de data te halen om de scans beter te kunnen analyseren voor archeologische doeleinden binnen dit onderzoek. De filtertechniek in z'n eendimensionale vorm werd nog niet gebruikt voor archeologische magnetometerprospectie en is daarom vernieuwend. Deze ontwikkeling vormt een afwijking van de oorspronkelijke doelstelling van deze thesis, maar was noodzakelijk om bruikbare datasets af te leveren.

# Chapter 1

Introduction

## 1.1 The unique situation of the former Western Front in Belgium

World War One (WW1) left an enormous impact onto its conflict areas, especially at the Western Front (France and Belgium) where for four years the involved parties entrenched themselves and fought on an industrialised scale (Pearson et al., 2010). After the war, action was taken to make the destroyed front region inhabitable again (Debaeke, 2013; Dendooven, 2007). This created in Belgium (province of West-Flanders) a hazardous situation: the front was not well-cleaned (removal of military remains, structures, UXO, bodies…) and citizens quickly returned to the war affected region to rebuild their homes and lives. In France, similar post-war conditions were found but the most affected areas were restricted for housing and land cultivation by the government (Guicherd and Maîtrot, 1921). This was not the case in Belgium (Debaeke 2013; Dendooven, 2007). After the reconstruction phase in the 1920's, the front clean up in Flanders came to a standstill and war remains became covered up under the rebuilding. As a result, the current state of this enormous historical conflict area is not well defined. This unique situation feeds the need to characterise the remains in the subsoil in this region (former Western Front in Belgium). Therefore, several archaeological techniques are well suited whereof new developments in the last two decades are making this regional scale investigation possible without large-scale invasive ground truthing (Stichelbaut, 2009; Saey et al., 2013; Sittler and Hauger, 2007). Exploring the application of these techniques at the former Western Front in Belgium to characterise the military remains, would contribute to the study of this extensive conflict archaeological site.

## 1.2 World War One archaeology in the Flanders region

The development of World War One archaeology in Flanders towards a professional discipline, is a process that started in the year 2002 (Dewilde et al., 2004). Prior to this, WW1 archaeology

was mainly explored by amateur-archaeologists, who despite their respect and enthusiasm in researching the war heritage, were lacking the professional background to record the archaeological remains in the best way possible. In 2002, the Institute for Archaeological Patrimony was imposed by the government to undertake detailed archaeological research of WW1 remains (Dewilde, 2010; ministerial policy Paul Van Grembergen, 2003-2004). The first project was an investigation of the planned extension of the A19 highway (between Ypres and the Belgian coast). This project can be seen as a milestone for this discipline. From that moment on, the change was made between the ad hoc registration of WW1 remains as features which were then considered as 'disturbing the older archaeology' and the full study of those remains. Because of that, the WW1 archaeological branch has to be (re)defined: reports, studies and international experts were consulted (Dewilde, 2010). UK-experts had a large influence on this because in that country, battlefield archaeology is a full-grown discipline (Ferguson et al., 2012; Foard and Morris, 2012; Scott and McFeaters, 2011). In France, WW1 archaeology was included in the reporting since the end of the 1980's (Defossés, 1998; Defossés et al., 2008). That is why the proliferation of amateur archaeological associations was not possible like it was in Belgium. In the 20$^{th}$ century, battlefield archaeology in Flanders was mainly a site-oriented study. This evolved at the beginning of the 21$^{st}$ century into an interdisciplinary research of WW1 heritage (Van Hollebeeke, 2012), which encouraged the use of techniques, imported from other research domains. This evolution can be considered as 'Modern Conflict Archaeology' as defined by Nicholas Saunders (2012). To contribute to the development of Modern Conflict Archaeology concerning WW1, several research projects were written in the last decade to investigate the application of new combinations of techniques. International examples are:

- GARP (2006-14): Great Arab Revolt Project: Project to investigate WW1 archaeology in Jordan and develop new heritage sites for visitors (www.jordan1914-18archaeology.org, 2018).
- JHAS (2010-14): Joint Archaeological-Historical Survey: Project to study the 1915 Gallipoli conflict battlefield in Turkey by using archival, archaeological and cartographic sources. The purpose of this project was to set the Gallipoli campaign in a broader cultural and historical context (Büyüksaraç et al., 2014). This research was supported by the Australian, New Zealand and Turkish Governments.

- IMPACT 14-18 (2015-18): Combining trench maps, LIDAR and GIS to study the impact of the war in the Champagne-Ardenne region in France (Taborelli et al., 2017) and the effect of geography, geology and geomorphology on the spatial organisation of the front (Devos et al., 2015).

Another initiative – focussed on the Flanders region - is Ghent University's special research fund GOA project '*Non-invasive landscape archaeology of the Great War*' (2014-18), which investigates the use of non-invasive techniques to study the war remains on a regional scale at the Western Front in Belgium. Within this multi-disciplinary research project, aerial photography, geophysical scans and airborne laser scanning are combined to explore the complementary advantages to examine the war-landscape above and below the ground surface. The main benefit of the applied techniques is that research could be performed without excavations, which are expensive, dangerous, time-consuming and mostly unwanted by the landowners. These techniques have also the potential to be implemented during preliminary archaeological investigations without invasive ground truthing. Because the techniques are complementary and important building blocks of the joint project, a short overview of these non-invasive techniques for WW1 archaeology will be covered and linked to the Flanders region.

**Historical aerial photography**

Historical research as preliminary investigation (desktop assessment) of WW1 sites, is performed by consulting historical sources (army documents, war records, trench maps, aerial and terrestrial photography…). The photographic technology and the pioneering development of aircraft at that time, made it for the armies possible to photograph the enemy infrastructure in extent from the air. These aerial photographic recordings (Cowley & Stichelbaut, 2012; Stichelbaut, 2015a) are a source of great value to study the evolution of war landscapes (before, during and after the war). These historical photographs cover almost the entire Western Front in Belgium and France. Not only the evolution of the military landscape but also possible preserved war heritage can be studied prior to archaeological research or development works. By inventorying and digitising this information into a spatial database, an overview of the military infrastructure can be established (Stichelbaut, 2011a; Stichelbaut et al., 2017). This digital spatial database allows the study of the accumulation of war features

with their time dimension at one location instead of looking at it in time slices. Stichelbaut performed research on aerial WW1 photographs of Belgium and France since 2002. The gathered georeferenced library of photographs during this research led in 2014 to the creation of the Centre for Historical and Archaeological Aerial Photography (CHAL), which is a collaboration between Ghent University, the In Flanders Fields Museum and the Province of West-Flanders. The establishment of this institute is an important contribution to the professional WW1 archaeology in Belgium. Nowadays, the consultancy of CHAL during archaeological preliminary investigations of former WW1 conflict areas is often implemented. Aerial photographic research can investigate as no other sources the military infrastructure of the former battlefields. Trench maps as derived schematic representations from these photographs can provide similar info but their spatial precision is often inferior (scale reduction) and no further interpretation can be done (still possible with the original photographs). If photographs are absent, trench maps can be added to the investigation. However, these sources give only indication of what might possibly be preserved, not the current presence of the buried military infrastructure. To tackle this question without destructive archaeological research, a different additional/complementary approach is needed.

**Geophysical research**

The use of geophysical scans to verify the presence of buried WW1 archaeological structures, is a first complementary non-destructive method (Masters and Stichelbaut, 2009) that is finding its way into multiple disciplines. The main known technique is the popular applied metal detector (= time domain electromagnetic induction technique), which makes it possible to localise metallic objects at shallow depth. The use of other geophysical techniques is less common for archaeological purposes. In Flanders, the rare use of geophysics for non-scientific archaeological purposes stagnated for the last decade (Meylemans and De Smedt, 2018). The Agency for Cultural Heritage added geophysics as preliminary investigation technique to their code of good practice in 2017 (Agentschap Onroerend Erfgoed, 2017) which should stimulate the implementation of geophysics in archaeology. In the field of UXO clearance, these geophysical scans are regularly carried out.

In Flanders, geophysics was for the first time applied on WW1 sites for the A19 highway project. For this investigation, geophysical research was executed by performing magnetometer scanning to localise buried trench structures (Van Hollebeeke, 2012; www.a-

w-a.be, 2018). Another mentioning of the application of geophysics for WW1 in the region can be found in Osgood & Brown (2009): a multinational team led by No Man's Land – The European Group for Great War Archaeology, excavated in 2007-08 a series of trenches near the hamlet of Saint Yvon (Ploegsteert, Wallonia, Belgium). To assist these ground works, magnetometer scans were carried out. Masters and Stichelbaut (2009) described the success of the geophysical survey and aerial photography marriage as complementary for a non-destructive approach in this project. This combination led to a more comprehensive understanding of the Great War battlefields and allowed the No Man's Land team to excavate WW1 infrastructure with higher precision. In 2008, the Vampire dugout (located between Ypres and Passchendaele) was investigate by a British-Belgian team, led by Peter Barton, Tony Pollard and Johan Vandewalle. Geophysical surveys (ground penetrating radar and magnetometry) were carried out to localise the entrance of the dugout near its approximate known location (Jacobs and Pollard, 2008).

At the Western Front in France, a first notification of applied geophysics on WW1 sites for archaeology was made in 2000 at the Somme region where fluxgate magnetometry was applied to characterise the remains of several archaeological periods (from Roman to WW1) (Bossuet et al, 2001). In 2003, ground radar was deployed to assist an archaeological investigation (Price, 2005). This survey was performed in the context of the creation of a visitors centre near the Thiepval military cemetery. For a project in 2006 nearby Arras (Givenchy-Lez-La Bassée) (Pollard and Banks, 2007), ground penetrating radar and electrical resistivity (Banks, 2014) were deployed to survey mine crates, trench systems and tunnels. In 2010, magnetometer and resistivity surveys were executed near the village of Mametz (Picardy) in function of the Livens Gallery Flame Projector investigation (Banks and Pollard, 2014). In 2011, the technique of magnetometry was used for the 'La Boiselle' project (La Boiselle, France) (www.laboiselleproject.com, 2019) to assist the site clearance.

The use of frequency domain electromagnetic induction as fourth scanning technique was for the first time applied at the Western Front in 2008: a survey was executed on a site in Geluveld (Belgium) by Ghent University's department of Soil Management (Stichelbaut et al., 2011; Saey, 2011). Their research group ORBit also scanned in 2008-09 the terrain for the newly developing golf course 'Golf Ter Hille' at Oostduinkerke (Belgium) whereby hinterland WW1 military structures were encountered (De Smedt et al., 2013). In these projects, the complementarity of both geophysics and aerial photography were confirmed as in Masters and

Stichelbaut (2009). In 2011, the same research group scanned an area located near Kemmel hill and two sites near the village of Loker (Belgium) to verify the soil for WW1 archaeological traces. In 2012, a third Loker site (near 'Groot Lokerhof Farm') was covered as part of an official archaeological investigation. The applied electromagnetic induction sensor in combination with their own developed data processing, delivered satisfying results to verify the subsoil for WW1 traces (Saey et al., 2013). In all cases, aerial photography was included to assist the scan result identification. In 2013-14, the village of Comines-Warneton gave the order to carry out a study that covered its complete territory to inventory the possible finds of WW1 infrastructure. This inventory was based on historical aerial photography. Within this successful study, three fields were scanned with electromagnetic induction to find out what still could be encountered in the subsoil. The experience gathered by applying these multidisciplinary studies between 2008 and 2014, led to the research proposal of the '*Non-invasive landscape archaeology of the Great War*'-project (2014-18).

**Airborne laser scanning**

Between 2000 and 2004, the Flanders Agency for Geographical Information gave the assignment for the execution of an airborne laser scanning campaign to obtain a digital terrain model for the Flemish region (DHMV I) (https://overheid.vlaanderen.be, 2018). In this model, the accurately measured small differences in height were useful to identify archaeological remains in the landscape's micro topography. The advantage of this technique is that vegetation could be filtered out which makes it suitable to look through woodland where geophysics and aerial photography have their limitations. In 2003, LIDAR was for the first time utilised in the 'Baden forest' in Germany to execute a large-scale archaeological investigation (Sittler and Hauger, 2007). Similar research was performed to study land use and archaeological traces in the Haye forest near Nancy (France) by Georges-Leroy et al. (2011). In Belgium, LIDAR was used to study the archaeological landscape in the 'Kempen'-region to search for Celtic fields (Paesen et al., 2010). In the province of Antwerp (Belgium), Gheyle et al. (2014) used LIDAR data (DHMV I) to detect WW1 archaeology in areas where no aerial photography was available.

In the period of 2013-15, the Flanders Agency for Geographic Information carried out a new laser scanning campaign with a higher spatial resolution, which makes the suitability of this new digital terrain model (DHMV II) even better to identify (WW1) archaeological traces. The

potential of this third non-invasive source is highly regarded. Since the disclosure of this new model, there has been a lot of interest from the archaeological world but also from other disciplines.

Although historical sources are frequently consulted during the preliminary investigation of WW1 archaeological sites, the potential of geophysical soil sensing and airborne laser scanning were in 2015 (start of this PhD) rarely explored. There is a need to gain more insight in these non-invasive techniques exists to fully exploit their potential to investigate the former Western Front in Belgium.

## 1.3 Research objectives

The focus of this thesis is set on the exploration of the potential of geophysical soil sensors to characterise the subsoil for WW1 archaeology at the former Western Front in Belgium. Important research questions are: (a) How do different geophysical techniques relate to each other when applied in this conflict region? (b) How do these surveys compare to the remote sensing techniques? (c) What features can be detected? (d) What can be revealed of buried military features and the historical destruction on a regional scale by integrating geophysics with other non-invasive techniques? etc… The research in this thesis will be performed on both site-oriented cases and the level of a regional scale. The five selected main objectives are listed below. The investigation of these objectives will provide contributing information to the non-invasive exploration of WW1 conflict landscapes.

**Objective 1**: *The evaluation of different geophysical soil sensing techniques for the prospection of WW1 conflict landscapes*.

When the option for a geophysical scanning technique in an archaeological investigation is included, the selection of the most suited technique has to be made. In some cases, the full coverage of the buried military infrastructure is desired. In others, the characterisation of a specific feature or phenomenon has to be made. Evaluating the suitability of a set of popular geophysical prospection techniques to detect and map buried WW1 archaeology, is the first objective in this thesis.

**Objective 2**: *The improvement of fluxgate magnetometer data by developing a focussed approach to reduce interfering noise sources.*

This secondary objective resulted from the undertaking of geophysical scans for objective 1. By carrying out fluxgate magnetometry scans (geophysical technique), a number of disruptive effects were experienced in the data visualisation. There was a need to address these errors before going any further. In these datasets, interfering data and wave patterns appeared. The challenge for this objective was set to find a focussed technique to address these noise sources and to tackle them before data interpolation. A solution for this problem was needed to establish noise-reduced magnetometer data for this thesis.

**Objective 3**: *The identification and validation of geophysical anomalies.*

Soil sensors can detect anomalies related to buried WW1 features. The question remains: what is actually measured? When a signature and the location of an anomaly correspond to the information derived from historical aerial photographs, a clear link between both can be made. Still, it is unclear what is measured: remains of the structure, an indirect effect, filled up cavities etc… The third objective is focussed on a limited range of cases to validate different types of features. Based on these cases, insights can be gathered in what is actually detected with feedback to the geophysical research.

**Objective 4**: *The development of a non-invasive method to characterise the destruction of the war on a regional scale.*

A map that localises the destruction caused by WW1 is not available for the former Western Front in Belgium. Only a map based on the classification for repair payments exists but does not meet these detailed requirements. The need for such a detailed destruction map is real because it can provide more accurate information of the WW1 impact onto the soil (and impact onto older archaeology). This map can be a useful tool for risk assessment during government related administrative procedures (building permits, UXO detection…). In the toolbox of non-invasive techniques, aerial photography offers the possibility of visualising the destruction of the past while geophysical scans and airborne laser scanning can characterise the current state of the former war landscape. Defining a method with non-invasive techniques to construct

such a destruction map for multi-purposes to study the impact of WW1 on a regional scale, is the fourth objective of this thesis.

**Objective 5**: *Mapping buried war traces on a regional scale to characterise the current state of the subsoil of the former Western Front in Belgium.*

What is still hidden in the soil of WW1 structures? This is a question that arises for many residents but also archaeologists and local authorities in Belgium. More than 100 years after the start of WW1, there are still daily finds of ammunition, debris, utensils, construction materials, war infrastructure, missing soldiers, etc. The ongoing confrontation in this >1000 $km^2$ conflict archaeological site, feeds the need to characterise the subsoil of this open agricultural landscape. By performing large-scale geophysical research, this objective can be investigated in a non-invasive way.

## 1.4 Structure of the thesis

Chapter 2 describes (i) the range of applied geophysical techniques for this research and their principles, (ii) other non-invasive techniques that support the geophysical investigation of WW1 conflict landscapes and (iii) the demarcation of the thesis's study area. The research objectives which are covered in the other chapters, can be classified in three categories: geophysical sensor evaluation for site and feature investigation (objective 1 & 3), integration of geophysical soil sensing for spatial investigation on a regional scale (objective 4 & 5) and processing of sensor data (objective 2). The schematic division of the research objectives over the chapters is given in figure 1.1.

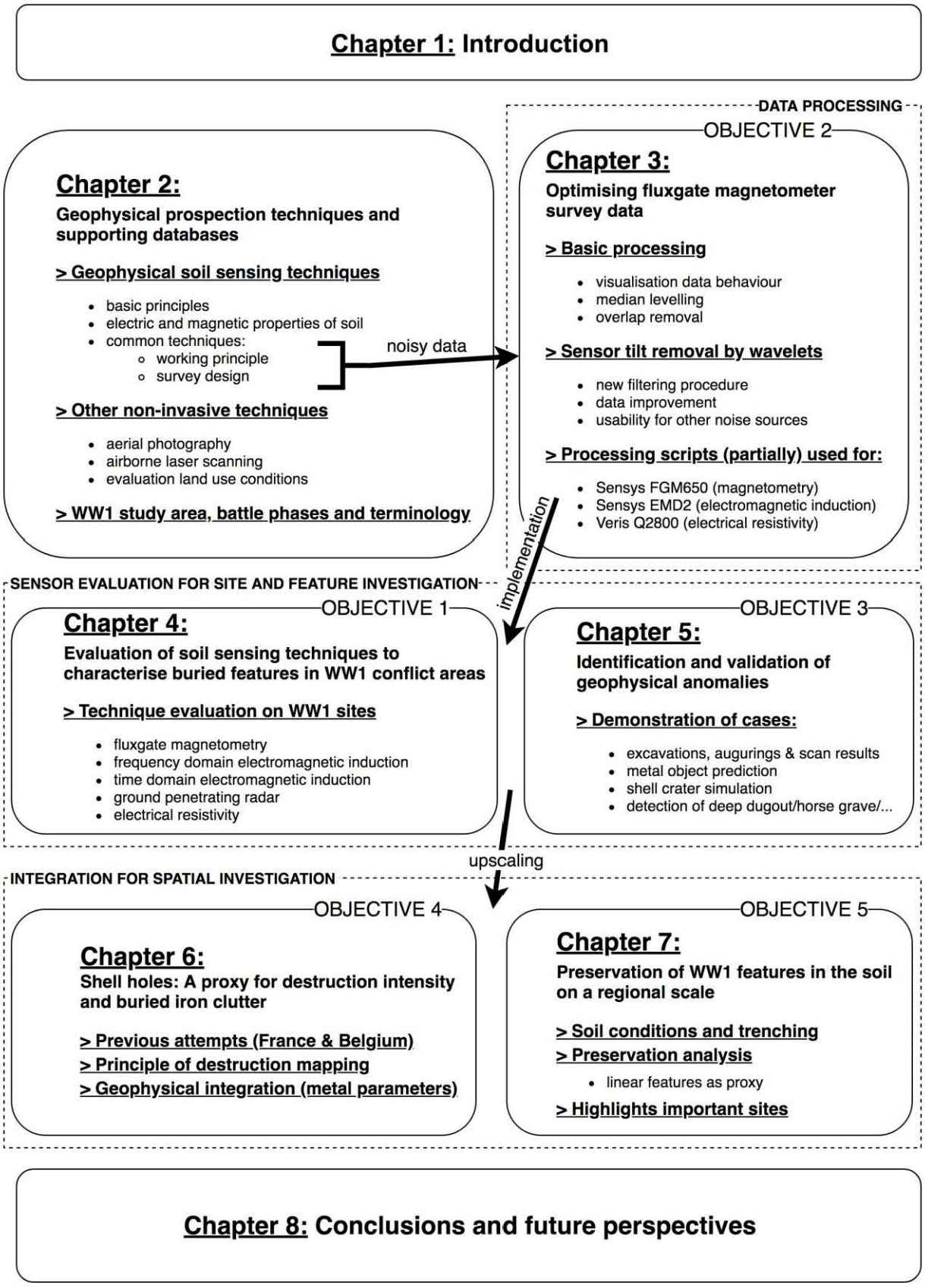



**Figure 1.1:** Schematic overview of the thesis structure.

# Chapter 2

## Geophysical prospection techniques and supporting databases: elements for an integrated method

## 2.1 Introduction

Geophysical soil sensors are able to measure directly or indirectly physical soil properties and by detecting contrasts in these, WW1 traces can non-destructively be studied. The identification of war features is a process of survey experience combined with additional data sources to verify the scan results. The best option for verification is the use of wartime aerial photographs combined with expert interpretation of visible and detected military infrastructure. This method is called Remote Sensing Archaeology (RSA). Trench maps can be a good addition to this but photographs (= original source) provides more information than a derived schematic state of the military structures. Matching locations and signatures of features in both aerial photography and geophysical surveys, can lead to the identification of military structures. Not only the war related photographs have to be considered but also time series of more recent remote sensing sources. By collecting those photographs (or other mapping information), more recent related disturbances can be excluded from the scan results. Also the study of land use changes has an important role in the equation to study the current state of a field in a former conflict region. The stability or the follow-up of land use changes will have an effect on the near-surface buried features. This whole process of integrating several data sources creates a standard approach to analyse geophysical scans to verify the current state of buried military features in the former conflict areas. When the exploration of conflict landscapes with geophysical techniques increases (= building up experience), a database of typical signatures from validated features can help the identification of war structures. A third source which more recently came into use is the application of Airborne Laser Scanning (ALS) to map the topography of a landscape in three dimensional point clouds. The derivatives of these scans are useful to identify micro topographies. WW1 features identified by ALS can be used together with aerial photography (both RSA methods) as primary (desktop) assessment to characterise the conditions of a certain field to encounter preserved war features. In this materials and methods chapter, the basic principles of geophysical soil sensing and remote sensing (aerial

photography and ALS) will briefly be explained. These elements are the backbone of this thesis with focus on geophysical soil scanning techniques. The latter will be used to investigate the WW1 conflict areas on the former Western Front in Belgium. The location of the study area together with some background information about WW1 infrastructure and important battle movements, will be given in the final section of this chapter.

## 2.2 Geophysical Soil Sensing

Geophysical soil sensing (GSS) as a non-invasive prospecting technique for archaeology has been under development since the 1940s-50s, and pioneered in Great Britain (Atkinson, 1953; Gaffney and Gater, 2010). Since the introduction of GNSS-receivers with cm-precision in the 2000's, the implementation of GSS techniques in archaeology increased to cover large areas with high planar precision in a relative short period. These techniques can be classified based on several aspects such as 'active' or 'passive' systems (using a transmitted signal), frequency range, the need for ground contact etc. In this thesis, the applied techniques will be divided in three main classes: electrical (1), electromagnetic (2) and magnetic (3) methods.

Electrical methods (Milsom, 2002) are based on the transmission of electrical currents into a medium (soil) whereby the resistance of the flow is measured. Such systems are identified as electrical resistivity systems (ER). Abnormal variations in soil electrical resistivity make it possible to detect archaeological features. The second group uses electromagnetic signals (Nabighian, 1987). Signal frequencies in the range of 10 MHz - 1.5 GHz are transmitted by ground penetrating radar (GPR) systems to measure contrasts in reflection of soil layers and other buried features. The lower EM frequency ranges (10 Hz – 100 kHz) are used by electromagnetic induction sensors (EMI) to induce a magnetic field into a medium (soil) by generating an electrical current. By measuring the response of the secondary magnetic field, magnetic and electrical conductivity soil properties can be mapped. Electromagnetic induction methods can be divided in two subclasses: time-domain (TD-EMI) and frequency-domain (FD-EMI) systems. TD uses the received response in function of time while FD uses this response in function of the transmitted signal frequency. The third method is the magnetic method (Telford et al., 1990). Magnetometry is the most applied magnetic technique for archaeological purposes. These systems are able to measure very small magnetic changes in a medium, including magnetic properties of archaeological features. In the following sub-paragraphs,

basic principles of electromagnetic waves in combination with electric and magnetic properties of soils will be defined. In addition, working principles and mobile survey configurations for archaeological prospection will be described for the above listed geophysical techniques. A classification overview of the methods can be found in figure 2.1.

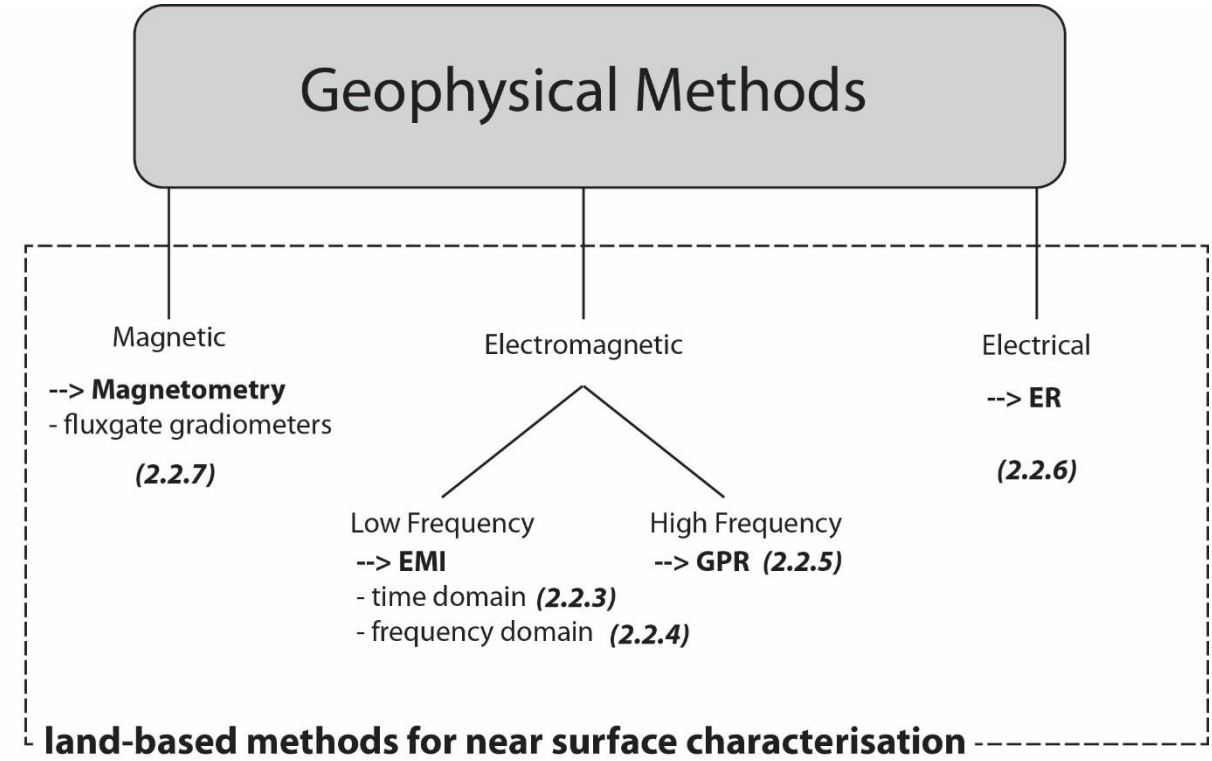



**Figure 2.1:** Classification of the tested geophysical methods and techniques for near surface characterisation of archaeological features with reference to their section in this chapter.

### 2.2.1 Basic principles of electromagnetic, electric and magnetic methods

Electromagnetic (EM) waves, used by EM-methods, consist out of two orthogonal vector components in a plane perpendicular to the direction of travel. These components are identified as a magnetic and an electrical field (figure 2.2). These fields can be described by field intensity vectors $\mathrm{E}$ (V/m) and $\mathrm{H}$ (A/m) or as flux density vectors $\mathrm{D}$ (C/m$^2$) and $\mathrm{B}$ (Wb/m$^2$). Behaviour of EM waves are expressed by the Maxwell equations. These differential equations in macro form (considering matter) and the relationships according to the physical material properties are given by equations 2.1-2.8. By detecting contrasts in these properties, features of interest can be found by geophysical methods.

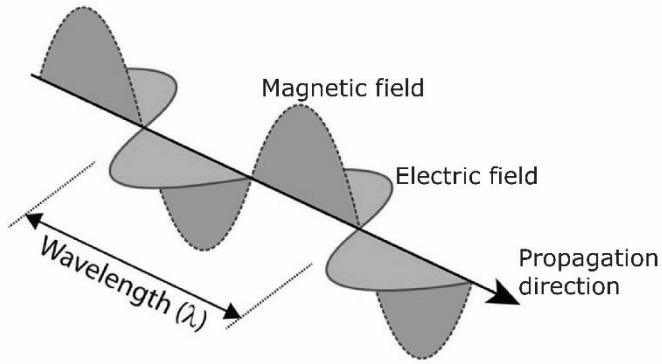



**Figure 2.2:** Schematic visualisation of an electromagnetic wave with indication of electric ($\mathrm{E}$) and magnetic ($\mathrm{H}$) vector components (Verhoeven, 2017).

**Maxwell equation 1 & 2: Gauss's law**

The electric flux through a closed surface is proportional to the charge inside an enclosed volume:

$$\nabla \cdot \mathrm{D} = \rho \qquad (2.1)$$

with $\mathrm{D}$ (C/m$^2$) = displacement field, $\rho$ (C) = electric charge

The magnetic flux through a closed surface is equal to zero:

$$\nabla \cdot \mathrm{B} = 0 \qquad (2.2)$$

with $\mathrm{B}$ (Wb/m$^2$) = magnetic flux density

**Maxwell equation 3: Maxwell-Faraday equation**

A magnetic flux varying in time generates an electrical field:

$$\nabla \cdot \mathrm{E} = \frac{\delta \mathrm{B}}{\delta \mathrm{t}} \qquad (2.3)$$

with $\mathrm{E}$ (V/m) = electric field intensity

**Maxwell equation 4: Ampère's circuital law with Maxwell's addition**

When a magnetic field is induced around a closed loop, this field is proportional to both the electric current and the displacement current trough an enclosed surface. This displacement current is proportional to the rate of change of electric flux. $\mathrm{J}$ is the total current density (A/m$^2$).

$$\nabla \times H = J + \frac{\delta D}{\delta t} \qquad (2.4)$$

with $H$ (A/m) = magnetising field / $J$ (A/m$^2$) = current density / $D$ (C/m$^2$) = displacement field

**Parameters describing the material response in function of the transmitted EM-field**

The electrical conductivity ($\sigma$) describes the ability of a material to pass free electric charges under the influence of a transmitted EM-field. Electrical conductivity is expressed in Siemens per metre (S/m) and defined by Ohm's law:

$$\sigma = \frac{J}{E} \qquad (2.5)$$

with $E$ (V/m) = electric field intensity / $J$ (A/m$^2$) = current density

The dielectric permittivity ($\varepsilon$) describes the ability of a material to restrict the flow of free electric charges or the degree of electric polarisation under the influence of an applied EM field. Dielectric permittivity is expressed in Farad per metre (F/m).

$$\varepsilon = \frac{D}{E} \qquad (2.6)$$

with $D$ (C/m$^2$) = displacement field /$E$ (V/m) = electric field intensity

The magnetic permittivity ($\mu$) describes the ability of a material to support the formation of a magnetic field within itself, due to intrinsic atomic and molecular magnetic moments. $\mu$ is expressed Henrys per metre (H/m).

$$\mu = \frac{B}{H} \qquad (2.7)$$

with $B$ (Wb/m$^2$) = magnetic flux density / $H$ (A/m) = magnetising field

The magnetic susceptibility ($\kappa$) describes the degree of magnetisation of a medium as a response to a transmitted magnetic field. $\kappa$ is dimensionless because $M$ and $H$ have the same units.

$$\kappa = \frac{M}{H} \qquad (2.8)$$

with $M$ (A/m) = magnetic polarisation vector / $H$ (A/m) = magnetising field

## 2.2.2 Electric and magnetic properties of soil

Measurable parameters related to physical soil properties are used by geophysical techniques to detect archaeological features. In relation to the soil, parameters that are measurable or influencing the measurements, will briefly be discussed.

### Soil electrical conductivity ($\sigma_s$)

The electrical conductivity in soils is often low and the EM-currents are mostly transported by electrolytes within the pores (McNeill, 1980). Mineral soil components have a low conductivity as well. Because of these properties, soil texture, bulk density, organic matter, soil moisture and the amount of dissolved ions in soil moisture are the main determining parameters of soil electrical conductivity. In non-saline environments, soil texture has the largest influence on the conductivity. From all soil texture types, clay has the largest influence on the increase of soil electrical conductivity because its property to attract ions benefits to the flow of currents. Furthermore, the size of the soil pores (related to the soil texture) and moisture retention influence the soil conductivity as well. On both properties, clay holds the best option to achieve a high soil conductivity. Reference values for different types of soil texture are given in table 2.1

### Soil magnetic susceptibility ($\kappa_s$)

Soil magnetic susceptibility defines the degree of soil magnetisation by an external field $H$ such an induced field or $H_{earth}$. Magnetisation can be classified into paramagnetic, ferromagnetic and diamagnetic materials. Paramagnetic materials obtain a weak magnetisation when exposed to an external field $H$. These materials can even have a slightly negative magnetisation. When this external field disappears, the magnetisation in the material is lost. For example, some clay minerals are paramagnetic. Ferromagnetic materials have the highest magnetic susceptibility and are rarely found in natural conditions in the soil. An example of a ferromagnetic material is iron (Fe). Ferrimagnetic materials as subcategory is the most important magnetisation in soil studies. This category includes particles such as magnetite and maghaemite. Antiferromagnetic materials have a weaker magnetisation than ferro but slightly stronger than paramagnetic materials. This category includes iron oxides such as haematite. Diamagnetic materials have a weak magnetic susceptibility when placed into a magnetic field $H$. These

materials are considered as non-magnetic. Examples are quartz, calcium carbonate and organic matter. More information about soil magnetic properties can be found in Schwertmann and Taylor (1977).

### Soil dielectric permittivity ($\varepsilon_s$)

Dielectric properties of materials are generally expressed by the relative permittivity $\varepsilon_r$. The relative permittivity defines the dielectric properties of a material ($\varepsilon_m$ in F/m) relative to that of free-space ($\varepsilon_0 = 8.8542 \cdot 10^{-12}$ F/m). $\varepsilon_r$ is expressed as:

$$\varepsilon_r = \frac{\varepsilon_m}{\varepsilon_0} \qquad (2.9)$$

This value is the first parameter to be considered when applying GPR-surveys because it influences the penetration depth of the transmitted signals. Elements that influence the dielectric permittivity of soils are soil texture, bulk density, soil moisture and ion concentration in soil moisture, which are similar to the influences on soil electrical conductivity. An increase of moisture and ions will decrease the penetration depth of the EM-signal together with the decrease of the pore size of soil texture. Reference values for $\varepsilon_r$ can be found in table 2.1.

**Table 2.1**: Reference values for dielectric permittivity and electrical conductivity of soils (Bevan, 1983; Cassidy, 2009; Cihlar and Ulaby, 1975).

| Soil | σ or EC (mS/m) | $\varepsilon_r$ |
|---|---|---|
| Sand - dry | 0.1-1 | 3 - 6 |
| Sand - wet | 1 - 10 | 10 - 30 |
| Gravel | 0.1-1 | 4 - 6 |
| Silty sand | 1 - 5 | 5 - 20 |
| Loam | 5 - 25 | 5 - 25 |
| Silt | 12.5 - 25 | 5 - 30 |
| Clay | 25 - 100 | 15 - 40 |

### 2.2.3 Frequency domain electromagnetic induction

#### Principle and characteristics

A frequency domain electromagnetic induction sensor can map the apparent electrical conductivity ($EC_a$, in mS/m units) and apparent magnetic susceptibility ($MS_a$, in ppt units) of the soil. The transmitter coil Tx in these sensors generates a fluctuating electrical current. This current creates a magnetic field (according to the Maxwell equations) which is transmitted into the soil and generates eddy currents within this medium. In turn, these currents produce a secondary magnetic field which, together with the primary magnetic field, are recorded by the sensor receiver coil(s) Rx. The ratio between the secondary and primary magnetic field is measured as both the in-phase and out-of-phase output of the EMI instrument. In low conductive environments (most soils), the out-of-phase response can be interpreted as the apparent electrical conductivity. $EC_a$ is mainly sensitive to differences in the soil's textural composition, organic matter content and moisture, while the $MS_a$, related to the in-phase response, depicts disturbances in the magnetic topsoil or plough layer in agricultural fields and infillings of the non-magnetic subsoil with magnetic topsoil. Moreover, fireplaces and brick-stone concentrations can cause substantial $MS_a$ deviations. At the former Western Front, both signals are uncorrelated, except in locations where metal objects are buried within the subsoil. These signals deliver complementary information about WW1 features, such as trenches, shell holes, bunkers, etc. (Gheyle et al., 2016; Saey et al., 2016 a & b).

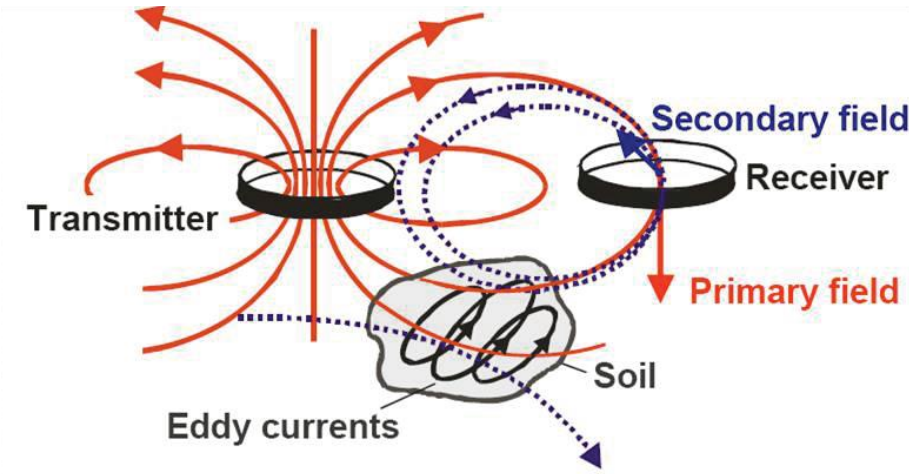



**Figure 2.3:** The working principle of electromagnetic induction (Saey, 2011).

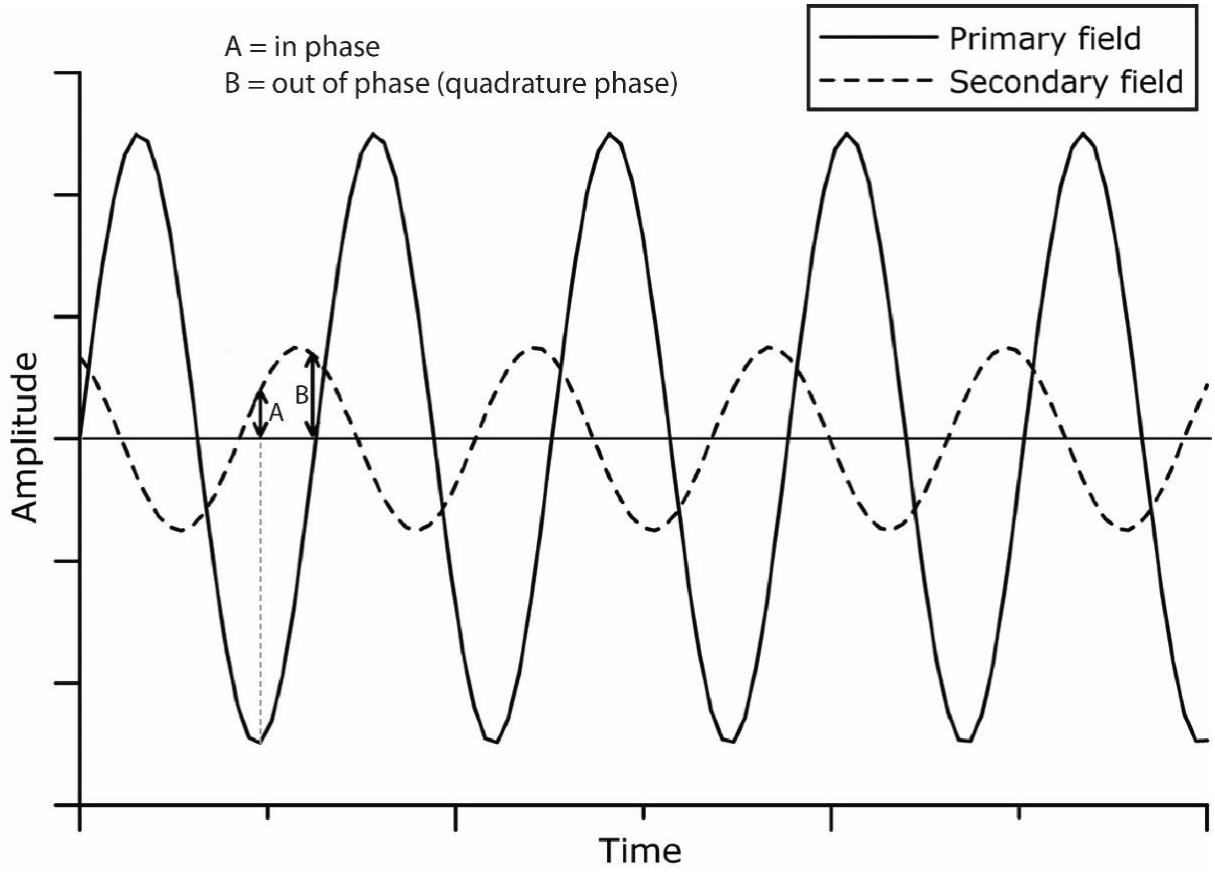



**Figure 2.4:** Amplitude of the primary and secondary field oscillating in time (Saey, 2011).

### Sensor setup

A DUALEM-421S and DUALEM-21HS sensor (Dualem Inc., Milton, Canada) were used to prospect the WW1 sites. These multi receiver sensors both comprise one transmitter coil and six receiver coils and operate at a frequency of 9 kHz. The usability of this sensor setup for archaeological mapping has been demonstrated by De Smedt et al. (2013 & 2014) and Saey et al. (2016 a & b). Different receiver coil orientations (figure 2.5) and separations (figure 2.6) allow measurements to be integrated across different depths. The 0.5 m, 1.0 m, 2.0 m and 4.0 m transmitter-receiver pairs form a horizontal coplanar dipole mode (HCPH, 1HCP, 2HCP and 4HCP), while the 0.6 m, 1.1 m, 2.1 m and 4.1 m pairs form a perpendicular dipole mode (PRPH, 1PRP, 2PRP and 4PRP).

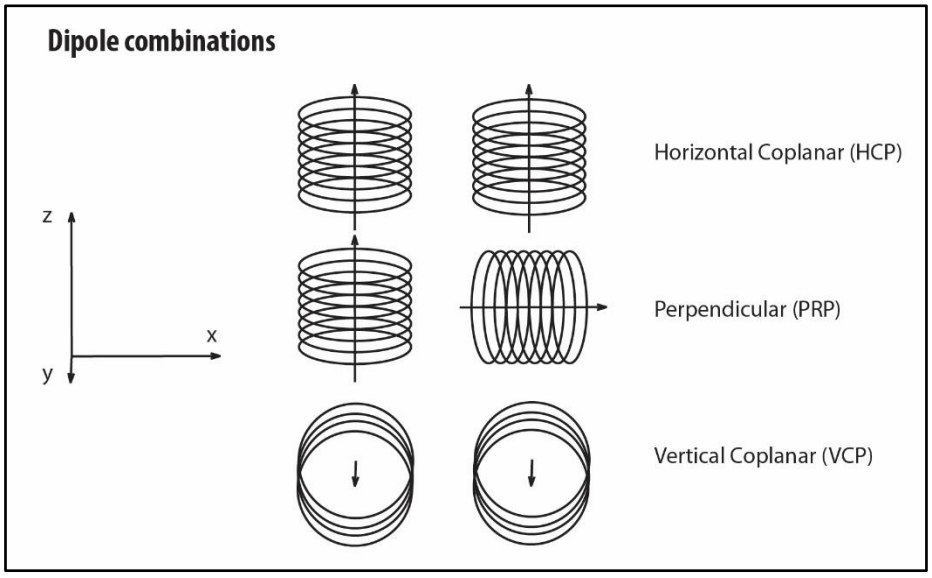



**Figure 2.5:** The coil orientations of the DUALEM sensors.

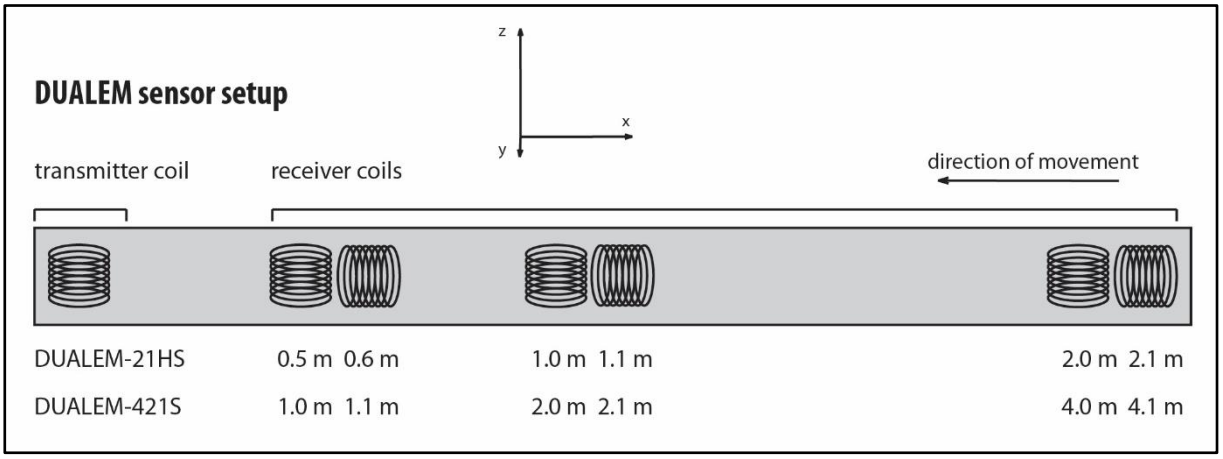



**Figure 2.6:** The coil combinations and separations of the 21HS and 421S DUALEM sensor.

### Survey setup

The DUALEM sensors are pulled within a high-density polyethylene (HDPE) sled behind a quad bike (figure 2.7), crossing the field in parallel lines of 1.2 - 1.4 m (medium resolution) or 0.7 m (fine resolution) apart. The instrument centre is situated at 0.16 m above the soil surface. Measurement intervals within the lines were at about 0.20 – 0.25 m at a median survey speed of 7-8 km/h. All measurements were georeferenced by an RTK-GNSS antenna and logged by a rugged field computer. Basic post-processing includes coordinate transforms, shift and sensor drift corrections (Delefortrie, 2016) and image gridding.

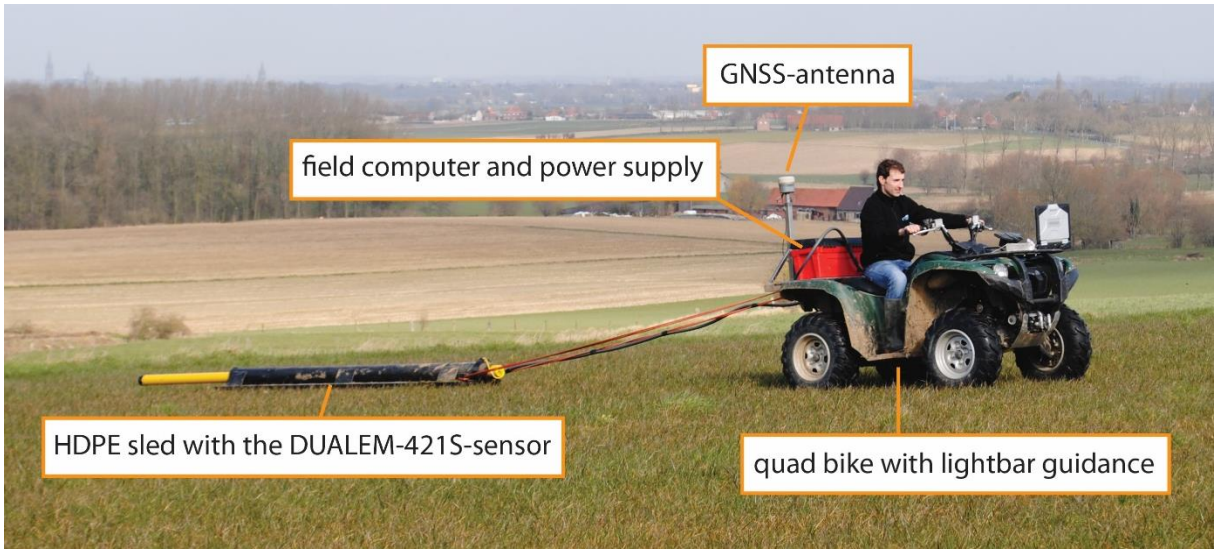



**Figure 2.7:** The DUALEM-421S survey set-up.

### Depth response

The cumulative electrical conductivity response (expressed as % of the measured signal, relative to 1) from the soil volume above a depth $z$ (in m) was given by McNeill (1980) for the horizontal coplanar ($R_{sHCP}(Z)$) dipole mode, and by Wait (1962) for the perpendicular ($R_{sPRP}(Z)$) dipole mode with *s* being the transmitter-receiver spacing in m.

$$R_{sHCP}(Z) = 1 - \left(4 \cdot \frac{Z^2}{S^2} + 1\right)^{-0.5} \qquad (2.10)$$

$$R_{sPRP}(Z) = 2 \cdot \frac{Z}{S} \cdot \left(4 \cdot \frac{Z^2}{S^2} + 1\right)^{-0.5} \qquad (2.11)$$

The DOE (depth of exploration), conventionally taken as the depth at the 70% cumulative response for the apparent electrical conductivity (figure 2.8), are 0.25 m, 0.5 m, 1.0 m, 2.0 m, 0.8 m, 1.6 m, 3.2 m and 6.4 m for the PRPH, 1PRP, 2PRP, 4PRP, HCPH, 1HCP, 2HCP and 4HCP coil configurations respectively. The cumulative magnetic susceptibility response (expressed as % of the measured signal, relative to 1) from the subsurface volume above a depth $z$ (in m) was given by McNeill and Bosna (1999) for the horizontal coplanar ($S_{sHCP}(Z)$) dipole mode:

$$S_{sHCP}(Z) = \frac{1 - 8 \cdot \frac{Z^2}{S^2}}{\left(4 \cdot \frac{Z^2}{S^2} + 1\right)^{2.5}} \qquad (2.12)$$

These depth-weighting responses are less straightforward to interpret: the DOE values cannot be determined in an unambiguous way (Saey et al., 2016a). The cumulative response curves, as deduced from equations (2.10), (2.11) and (2.12), are illustrated for all out-of-phase responses from the DUALEM-421S and DUALEM 21HS coil configurations (see figure 2.8 a) and for the in-phase responses of the HCP coil configurations (figure 2.8 b). Based on the depth responses from the multiple receiver coils, a rough depth estimation can be made of detected features.

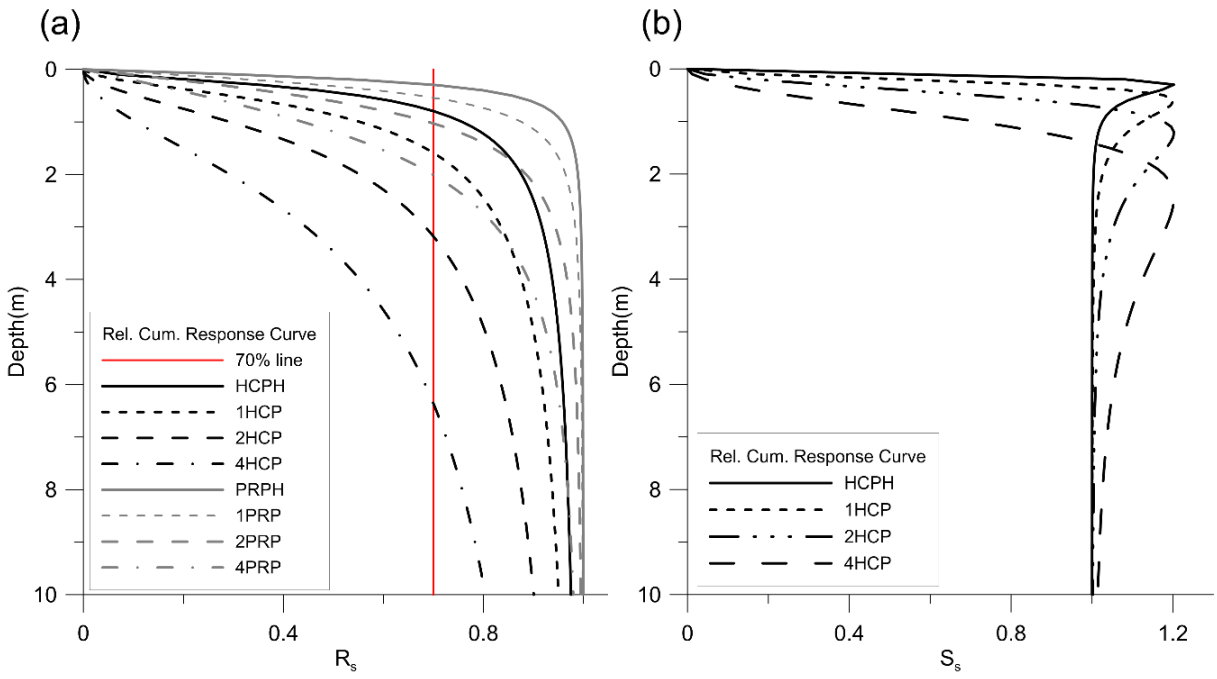



**Figure 2.8:** The cumulative relative response curve in function of depth (in m) for the apparent electrical conductivity (a) and for the HCP apparent magnetic susceptibility measurements (b) of the DUALEM 421S and DUALEM 21HS coil configurations.

## 2.2.4 Time domain electromagnetic induction

### Principle and characteristics

A time domain electromagnetic method uses an ungrounded loop as transmitter coil (Tx) in which a static electrical current is generated. Thereafter, the current in the transmitter coil is abruptly turned off and the rate of change of the secondary field ($H_s$) due to the induced eddy currents in the soil, is measured by the receiver coil (Rx). These eddy currents are caused by the turn-off of the electrical field (Maxwell equations: changes in electrical field causes a magnetic field). Figure 2.9 demonstrates this process. In graph A of figure 2.9, the on and off-time of the transmitting electrical current is shown in function of time. Graph B illustrates the transmitted primary magnetic field while graph C shows the measurement of the secondary magnetic field during the off-time moment of the electrical field. This secondary field will be weakened according to the soil's conductivity. Just after the Tx-loop is turned off, the current in the soil will be close to the surface, and the measured signal reflects the conductivity response of the top layers. At later decay times, the signal reflects deeper soil layers.

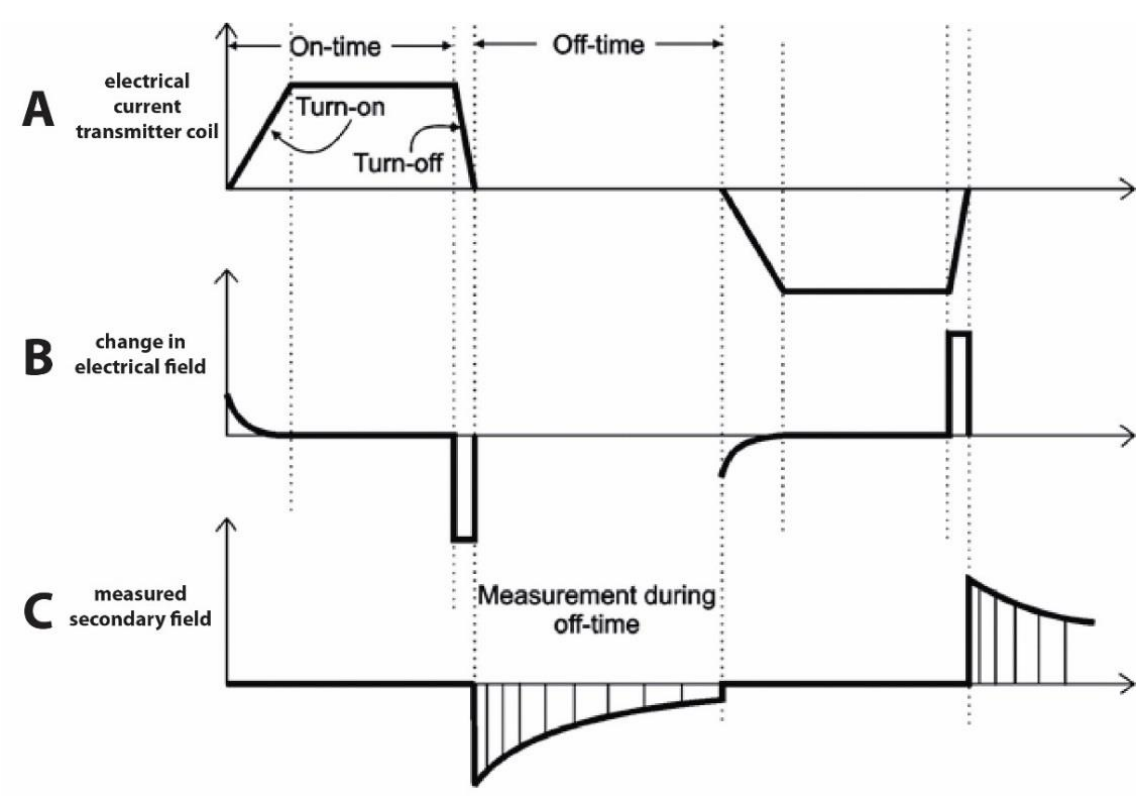



**Figure 2.9:** Visualisation in function of time of the on and off-time of the electrical field in the transmitter coil (A), the change in electrical field causing a primary induced magnetic field (B) and the measured response of the secondary field (C). (based on Sorensen et al., 2009)

**Sensor setup and skin depth**

Configurations with the receiver coil in the centre of the transmitting coil is called a central loop or an in-loop configuration. This is the configuration that is commonly used in metal detection for demining and artefact localisation in archaeology (= popular used metal detector). The second coil combination is the offset configuration with the receiver coil placed outside the Tx-loop. Both configurations are schematic represented in figure 2.10.

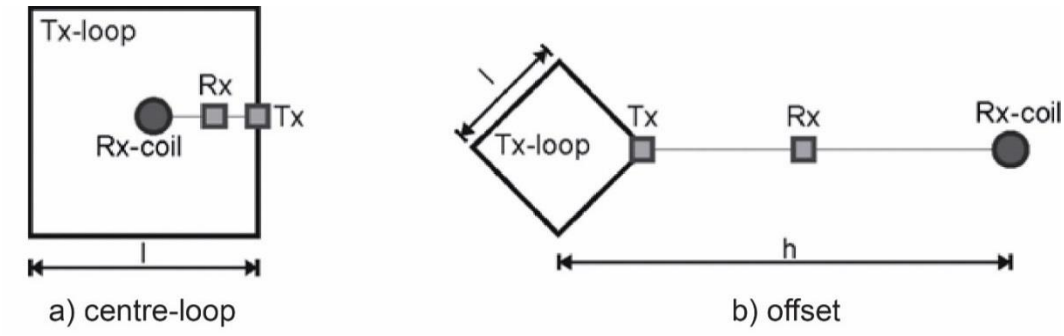



**Figure 2.10:** Coil configurations of a TD-EMI system: centre-loop (a) and offset configuration (b) (Sorensen et al., 2009).

The values of the secondary field are measured in $\mathrm{V}$ (volt). This response at period $\mathrm{t}$ can be written as:

$$\mathrm{V} = \frac{\mathrm{dH_s(t)}}{\mathrm{dt}} \qquad (2.13)$$

with $\mathrm{dH_s(t)}$ = response time secondary magnetised field

The penetration depth of the EM-signal can theoretically be expressed by equation 2.14. When the Tx is switched off at $\mathrm{t} = 0$, the penetration depth being measured is $\delta\,(\mathrm{m})$ (equation 2.14). In practice, the actual DOE is something complex to define and it will defer from this formula because parameters such as the transmitted frequency, Tx coil size, properties related to object magnetisation/material/size etc. are not included in this calculation.

$$\delta = \sqrt{\left[\frac{2\mathrm{t}}{\sigma\mu_0}\right]} \qquad (2.14)$$

with $\sigma$ (S/m) = conductivity of the earth / $\mu_0$ (H/m) = magnetic permeability in free space

### Survey configuration

As TD-EMI mapping system, the Sensys EMD2 survey setup (SENSYS Sensorik & Systemtechnologie GmbH, Bad Saarow, Germany) is suitable for archaeological prospection because it meets the properties of dense soil characterisation with a high planar precision at an acceptable fast coverage speed (Schmidt et al., 2015). This system uses a two level array of three receiver coils (six in total) in a pushcart setup, which not only produces a sharp image of the soil response, but also two responses in different levels. This property is ideal to perform a characterisation of magnetisable objects (depth, mass). The height distance between the two array tables (TD1 and TD2) is 0.64 m and the horizontal distance between the receiver coils in the array is 0.40 m. The transmitter coil is placed in the lower table and has the dimensions of 0.80 by 1.25 m. The coil configurations are shown in figure 2.12. The system operates at a pulse frequency of 610 Hz and samples at a rate of 20 Hz. The output response of both TD-levels is expressed in mV (millivolts). For georeferencing, a RTK-GNSS antenna was used in combination with an odometer, attached on one of the pushcart wheels. At walking rate, a coverage speed of 1 ha per day can be achieved. This TD-EMI setup (see figure 2.11) was originally designed for UXO detection and incorporates therefore a high planar precision to detect magnetisable objects.

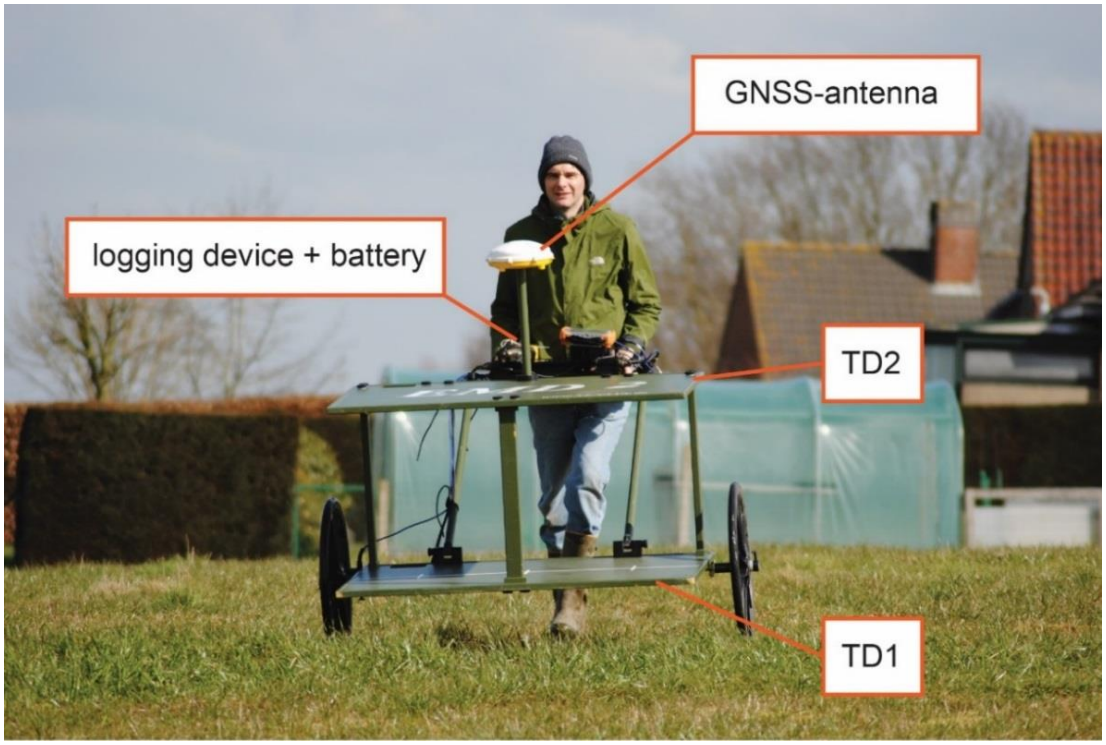



**Figure 2.11:** The Sensys EMD2 system in survey setup.

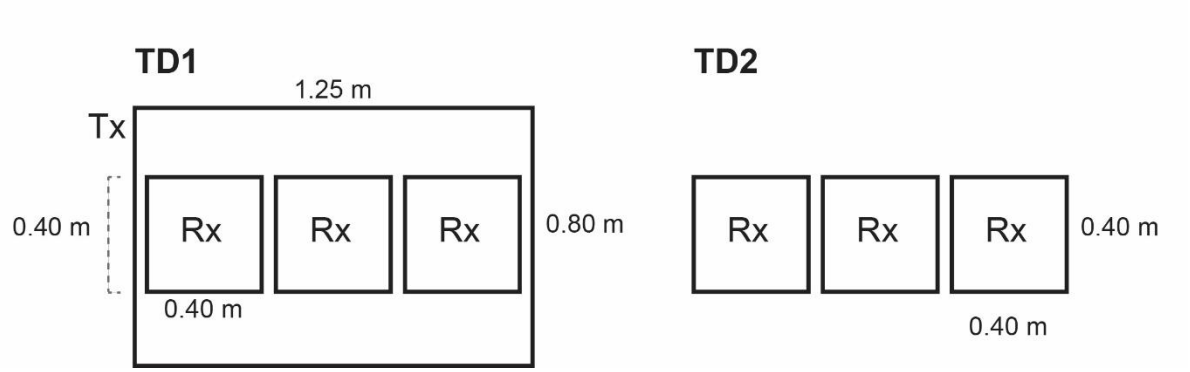



**Figure 2.12:** The EMD2 transmitter and receiver coil configurations of both TD-levels (tables).

## 2.2.5 Ground penetrating radar

### Principle and characteristics

A GPR antenna comprises out of at least one transmitter (Tx) and one receiver antenna (Rx). These systems use VHF (very high frequency) radio pulses in order of +/- 10 MHz up to 1.5 GHz to characterise the discontinuities in the soil by measuring the travelling time and intensity of the reflections caused by the transmitted radio pulses. Features of interest can found by detecting contrasts in dielectric permittivity. These contrasts are proportional to the amplitude (magnitude) of the received signal. The signal's amplitude decreases as it travels deeper into the soil until the point when it loses all its energy and no deeper detection is possible. The soil dielectric permittivity in combination with the transmitted signal frequency are decisive for the penetration depth of the system. The lower the relative dielectric permittivity, the deeper the skin depth of the antenna. The same goes for the signal frequency: the lower, the deeper the skin depth. The depth resolution on the other hand is depending on the wavelength of the EM-signal: the smaller, the more precise. The skin depth $\delta$ (m) of a GPR signal can be written as:

$$\delta = \frac{1}{\alpha} \qquad (2.15)$$

with $\alpha$ as the attenuation coefficient of the signal

The attenuation coefficient is proportional to the soil conductivity and inversely proportional the soil dielectric permittivity.

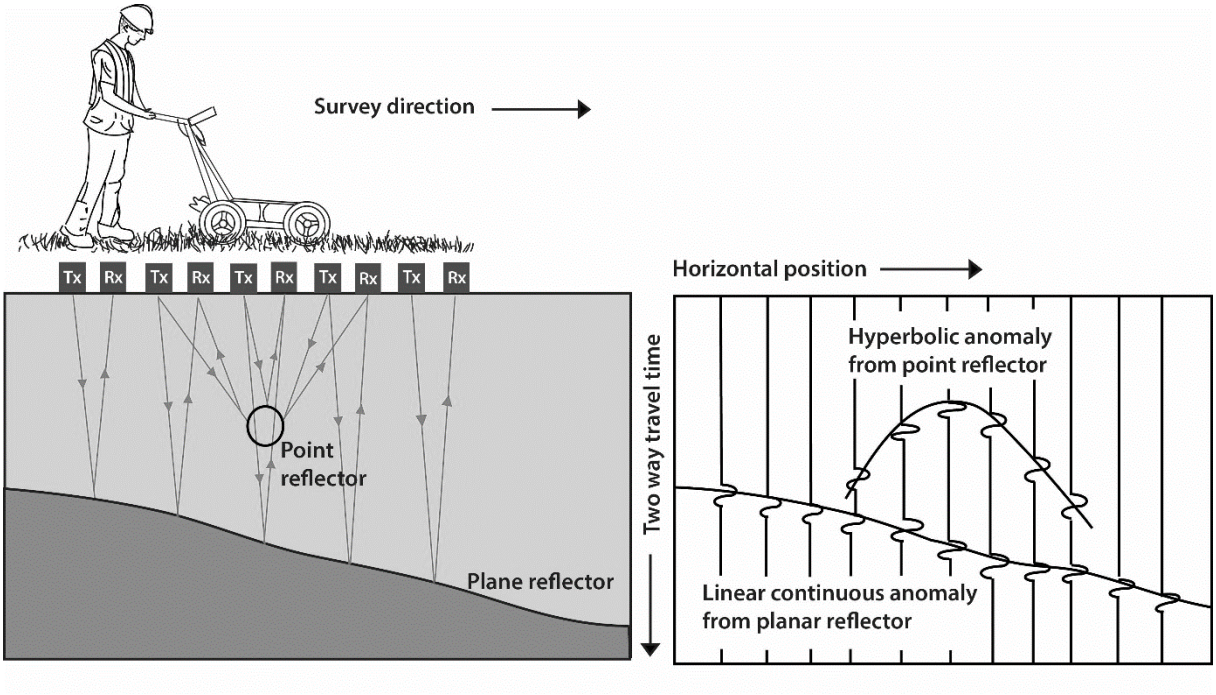



**Figure 2.13**: Display of the GPR-working principle on the field (left) and a schematic representation of the reflections (right), measured by the radar (Scantech Geoscience, 2018).

The scan data is often visualised in slices. A vertical slice visualises a 1D transect of the antenna in function of the depth response while a depth slice visualises the reflection response at a certain response time t in the XY-pane from several 1D transects. Contrasting anomalies (point or cylindrical objects) have a typical signature of a hyperbola while two contrasting soil layers will be detected as a linear anomaly (see figure 2.13). To convert the response time (expressed in ns) into a depth, the average dielectric permittivity is estimated according to reference values for different soil types. This was done according following formulas:

$$v = \frac{c}{\sqrt{\varepsilon_r}} \qquad (2.16)$$

$$z = \frac{v(t - t_0)}{2} \qquad (2.17)$$

$v$ (m/s) is the velocity of the EM-wave in a medium, expressed in function of $c$ (the speed of an EM wave in vacuum = $3 \cdot 10^8$ m/s) and the dielectric permittivity. $z$ (m) is the depth expressed in function of the velocity of the EM wave and the time interval between transmitting and receiving

the signal. The possibility for precise depth measuring compared to other GSS techniques, is the major advantage of GPR-systems.

### 3d-Radar survey configuration and principle

A stepped-frequency continuous wave GPR and a corresponding antenna array (3d-Radar AS, Trondheim, Norway) was applied in this research. To compare: a time-domain GPR system send a short pulse with a given pulse repetition frequency into the ground and receives the reflected signals as a function of time. This is the most common used system. The 3d-Radar (GeoScope-GS3F model) is a stepped-frequency continuous wave GPR, which transmits a frequency modulated wave with a stepped sweep over a determined frequency range (Daniels, 2004). This system generates a continuous-wave signal over a bandwidth between 100MHz and 3.0 GHz. The amplitude and phase of this signal is determined over a user-defined time (dwell time) at every frequency step. The resulting dataset is then inverted from the frequency to the time-domain using an inverse Fourier transform (3d-Radar, 2010). By mixing the transmitting and receiving signals in a quadrature mixer, it is possible to determine the deviation between both signals. The amplitude and phase shift from the reflecting signals are determined for the frequency between the minimum and maximum frequency. The width of the frequency step defines the resolution within the frequency-domain and determines, together with the specified frequency range and dwell time, the scan time of the antenna. For the research in this thesis, the stepped-frequency GPR system was configured to operate over a bandwidth of 100 MHz to 1.6 GHz. The 3D-radar antenna consists of seven transmitting and seven receiving antenna elements in array formation, creating 13 transmitter-receiver pairs with an offset of 10 cm between transmitter and receiver (figure 2.14). The antenna elements are arranged in a linear array where the transmitting and receiving antennas are displaced to each other. The radar-antenna is placed into a HDPE-sled and pulled behind an ATV. Parallel zigzagging lines are driven with an interline distance of 0.975 m to obtain a complete coverage of the study area with a horizontal resolution of 0.075 by 0.075 m. An additional odometer was used to enhance the spatial accuracy between the GNSS-logging points. The received antenna responses are send through a radar-processing unit to the laptop with logging software. This GPR-array is ideal for the execution of an exploring scan for archaeological purposes (dense sampling rate for complete coverage). The survey configuration is shown in figure 2.15.

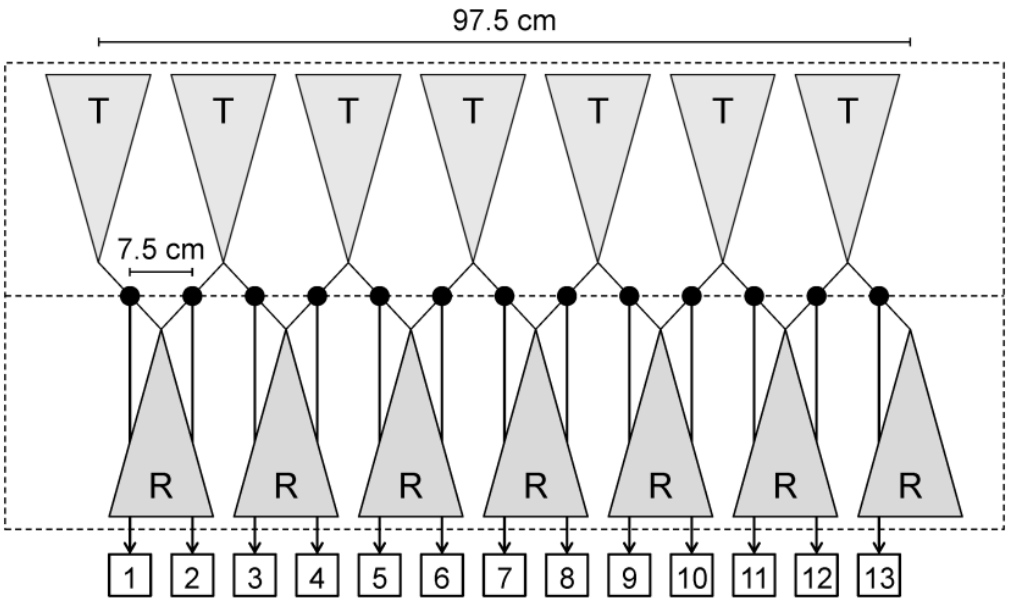



**Figure 2.14**: Schematic representation of the transmitter and receiver antennas of the Geoscope-GS3F radar, combining 13 transmitter-receiver combinations (black dots) (Van De Vijver, 2017).

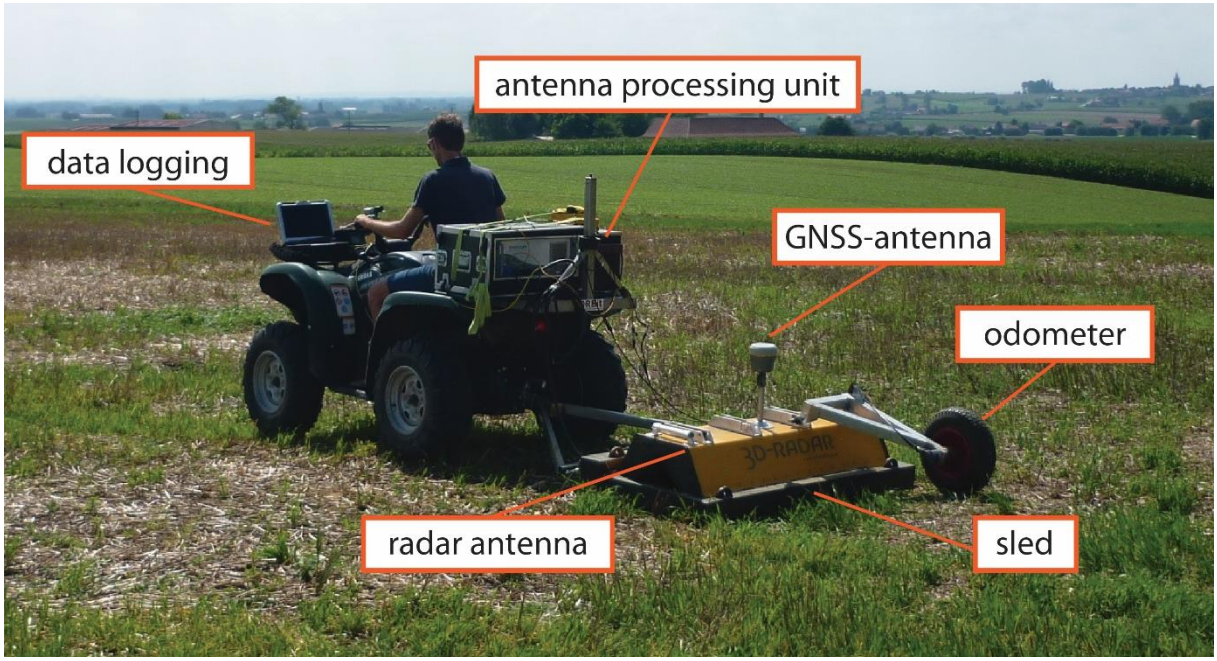



**Figure 2.15:** The 3d-Radar with multi-channel antenna design, power source, processing unit, logging device, odometer and GNSS-antenna.

## 2.2.6 Electrical resistivity

### Principle and characteristics

The principle of this technique is based on the measurement of the flow resistance of a transmitted electrical current into the ground. The soil electrical resistivity (ρ) is inversely proportional to the soil's electrical conductivity. Therefore, ER systems can be used to map the EC-properties of the soil. Clayey soils will have lower ρ values while sand has high ρ properties. Archaeological features of interest should have a contrasting value according to the background value of the soil resistivity and its variations. Building foundations, walls, rocks etc. will have a higher ρ contrast. Infillings of ditches with higher conductive material will sign as lower ρ anomalies. The difference between resistance and resistivity is that resistivity is a property of a material, while resistance is the potential difference measured over two potential electrodes when an electrical current is transmitted. The resistance $R$ is expressed in Ohm (Ω) and can be written as:

$$R = \frac{V}{I} \qquad (2.18)$$

with $V$ (volt) = electric potential = / $I$ (A) = current of resistor

In equation 2.18, $I$ is the current, measured in Amperes (A), flowing through a medium of soil. $V$ is the change in voltage, expressed in Volts. Resistivity meters will often use four contact electrodes: two current electrodes ($C_1$ and $C_2$) and two electrodes sampling the voltage ($P_1$ and $P_2$). Those four electrodes can be arranged in several combinations. The simplest configuration is the Wenner array whereby the distance between the electrodes is equally spaced with $C_1$ & $C_2$ as outer electrodes and $P_1$ & $P_2$ as the electrodes within. A schematic representation of the Wenner array is shown in figure 2.16.

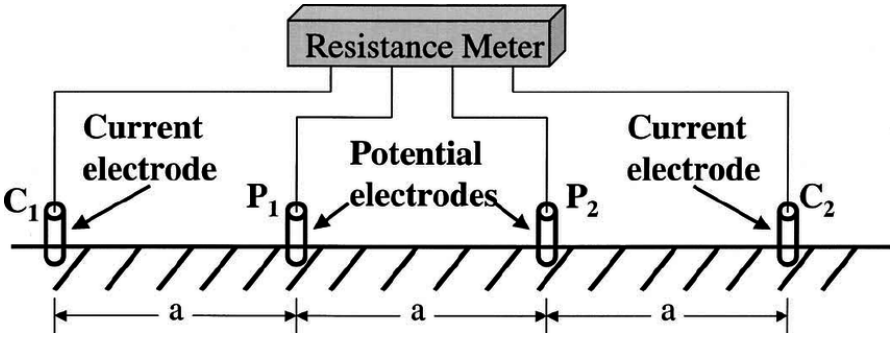



**Figure 2.16:** Schematic representation of the Wenner array (Rhoades and Halvorson, 1977).

The general equation for resistance measurement is:

$$R = \frac{V_{P1} - V_{P2}}{I} = \frac{\rho}{2\pi a}\left[1 - \frac{1}{X} - \frac{1}{X+Y-1} + \frac{1}{Y}\right] \qquad (2.19)$$

In equation 2.19, $a$ = distance (P1-P2), $X$ = distance (C1-P2) and $Y$ = distance (P2-C2). In a Wenner array, $X$ can be set to 2 and $Y$ to 1. Therefore, the resistance in a Wenner array can be expressed as in equation 2.20. The soil resistivity $\rho$ (Ω/m) can be derived from that equation.

$$R_{WENNER} = \frac{\rho}{2\pi a} \qquad (2.20)$$

Other electrode combinations exist as well. An example is the Twin-Probe (Aspinall and Lynam, 1970) whereby one P/C electrode pair has a fixed position and the second a changing one. Others are the double dipole and Schlumberger configurations (Gaffney and Gater, 2010; Milsom, 2002). Because there was obtained for a Wenner-based mobile survey system, the other array combinations will not further be discussed.

**Survey configuration**

The Veris Q2800 (Veris Technologies, Salina, Kansas, USA) is a by quad bike pulled resistivity system that uses coulter disc electrodes (diameter = 0.38 m) to measure EC derived from resistivity measurements. This device was originally developed for precision agriculture and most of its applications are located within this field. The user-friendly design makes this device easy to be pulled by a quad bike. The advantage of this system is its insensitivity to fine metal objects. If there is a need to detect soil disturbances and contrasts without the detection of individual pieces or a mass of interfering metal objects, ER offers a solution. The former WW1 battlefields in France and Belgium are areas covered in iron clutter, which can interfere with detecting the intended archaeology. The use of such systems in these regions would benefit archaeological soil sensing. On the other hand, a first disadvantage is the low measuring frequency (max 2 Hz) which influences the surveying speed. A second disadvantage is the fact that this technique is not really ‘non-invasive’. The discs have to penetrate the ground at least for a few cm. Its necessity for ground contact is important. Therefore, additional weights

are provided (4 x 39 kg) to push the coulter discs into the ground and improve ground contact. In figure 2.17, the Q2800 setup is shown where the 6 coulter electrodes can be seen. An AC-power source supplies a current flow between the 2nd and 5th electrode and the resultant voltage difference is measured between the 1st and 6th disc for $EC_{dp}$ (deep $EC_a$) and between the 3rd and 4th disc for the $EC_{sh}$ (shallow $EC_a$) response (see figure 2.18). A GNSS antenna with RTK corrections is implemented for the georeferencing of the $EC_a$ data.

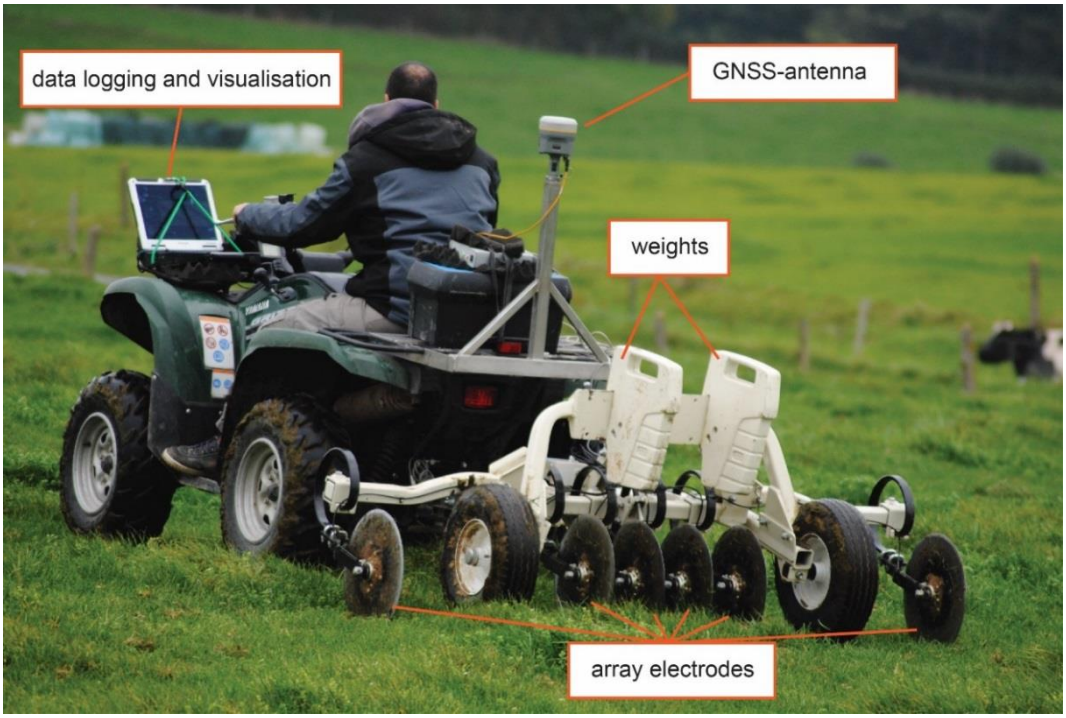



**Figure 2.17:** The Q2800 mobile survey setup with GNSS antenna and Toughbook for data logging.

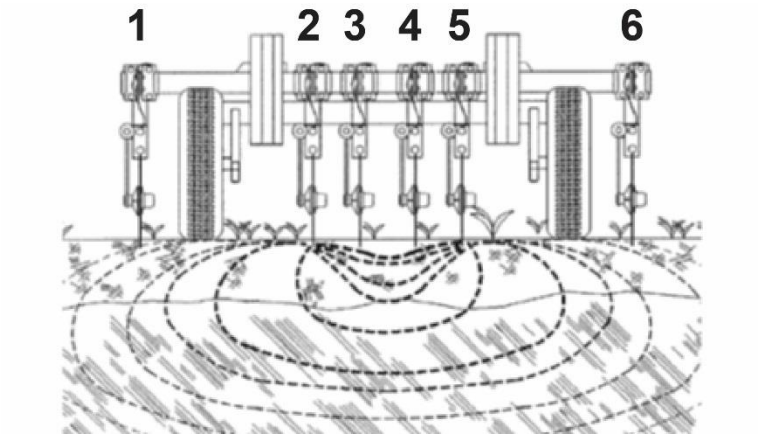



**Figure 2.18:** Schematic rear view of a Veris resistivity system, which hold the same principle as the Q2800. The coulter electrodes are numbered: current electrodes 2 & 5; shallow $EC_a$ measurement electrodes 3 & 4; deep $EC_a$ measurement electrodes 1 & 6.

### Depth response

The theoretical depth response of the Veris resistivity system is written as the Depth Investigation Characteristic (DIC) for Wenner arrays (Roy and Apparao, 1971) equation 2.21. The distance between the two extreme active electrodes is c. This is 0.535 m or $EC_a$ shallow and 1.94 m for $EC_a$ deep. z is the depth value in m. Based on these experimental measured distances for the used instrument, the DIC for the shallow and deep response are given in equation 2.22 and 2.23. A relative response ($R_c$) of 90% is applied as DOE. Based on equation 2.24, a DOE of 0.24 m is reached for $EC_{sh}$ and 0.87 m for $EC_{dp}$ (see figure 2.19). These numbers illustrate the next disadvantage of the Q2800 system: its limited depth response. Other similar systems with electrodes on larger distances will deliver a larger DOE such as the Geophilus Electricus (Lueck and Ruehlmann, 2013) by using an equatorial dipole-dipole array.

$$\mathrm{DIC(N)_{WENNER}} = \int \frac{1}{3}(8cz)\left\{\left(\frac{c^2}{9}+4z^2\right)^{-1.5} - \left(\frac{4c^2}{9}+4z^2\right)^{-1.5}\right\}dx \qquad (2.21)$$

$$\phi_{Vdp} = 5.173z\left\{\left(0.418+4z^2\right)^{-1.5} - \left(1.673+4z^2\right)^{-1.5}\right\} \qquad (2.22)$$

$$\phi_{Vsh} = 1.427z\left\{\left(0.0318+4z^2\right)^{-1.5} - \left(0.127+4z^2\right)^{-1.5}\right\} \qquad (2.23)$$

$$R_c(\%) = \left(9c\left(\frac{1}{9\sqrt{c^2+9z^2}} - \frac{2}{9\sqrt{c^2+36z^2}}\right) - 1\right)100 \qquad (2.24)$$

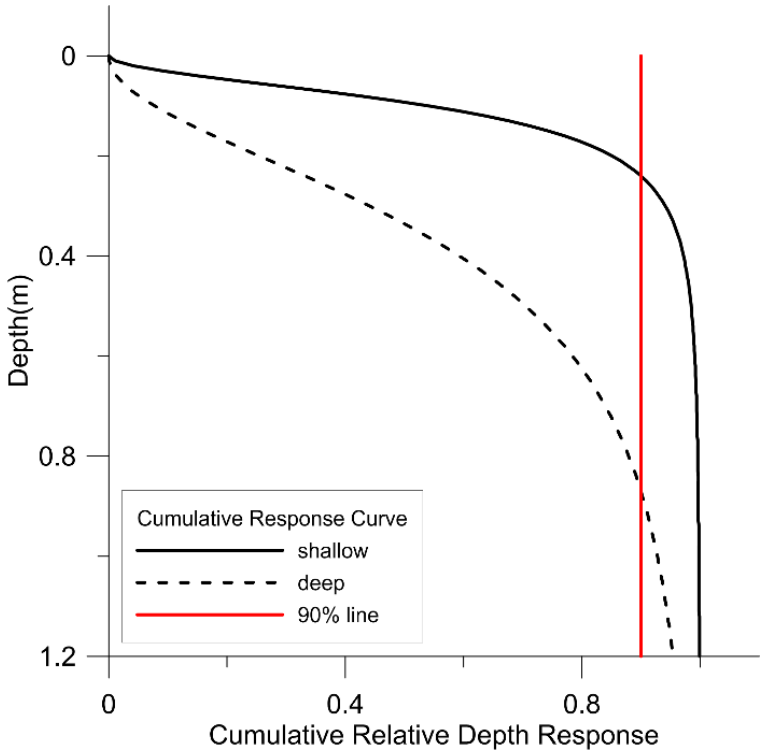



**Figure 2.19:** The cumulative relative response curve for de $EC_a$ data layers (shallow and deep) in function of depth (m) for the Veris Q2800 electrode pairs.

### 2.2.7 Fluxgate gradiometer magnetometry

#### Principle magnetic prospection

The principle of magnetic prospecting techniques such as magnetometry is based on the detection of weakly magnetised iron oxides in the soil which are caused by two phenomena: (1) thermoremanence and (2) magnetic susceptibility.

Thermoremanence is the phenomenon whereby a material has been magnetised when heated over the Curie temperature of haematite ($Fe_2O_3$) or magnetite ($Fe_3O_4$) (magnetisable particles). When this temperature threshold (+/- 725 °C) is reached, all magnetisation is lost. After crossing the Curie point, the material has to cool down. During this process, magnetisation of the surroundings has been given to the cooled down material. Bricks (heated clay) can easily be detected by making use of this property.

The spatial variations of magnetic susceptibility ($\kappa$) in the topsoil can be used as an indicator to localise archaeological features. Top soils are more magnetised because of burning and fermentation than sub soils (Le Borgne, 1960). If the above-described phenomena were transferred into a feature of interest, it can be detected by a magnetic prospecting technique. Both phenomena are depending on the concentration of iron oxides in the soil matrix. The intensity of magnetisation can be described in function of the magnetic susceptibility ($\kappa$) of a material and the field in which it is placed ($H$). $M$ is the volume-normalised magnetisation. $M$ and $H$ have the same units, so $\kappa$ is dimensionless.

$$M = \kappa \cdot H \qquad (2.25)$$

with $M$ (A/m) = volume-normalised magnetisation / $H$ (A/m) = magnetising field

**Characteristics**

Fluxgate magnetometry in gradiometer setup (FGM) is a commonly applied technique in the field of archaeology (Gaffney and Gater, 2010) and has become established as a mainstream technique for UXO detection (Billings et al., 2002; Billings, et al. 2009; Byrnes, 2009). The system uses the earth magnetic field as inductor and measures its vertical component. The strength of this field is situated around +/- 48000 nT in Belgium, but is locally varying. The vertical component is large near the poles and small near the equator. Near surface objects or structures with a locally magnetic deviation (because of the inducing earth magnetic field or thermoremanence), can be detected with magnetometers.

Fluxgate magnetometers have a low noise level and are therefore suitable for the detection of very small changes in magnetic susceptibility (0.1 – 1 nT). Ferromagnetic metals, heated materials (e.g. bricks) and fireplaces as well as magnetic contrasting fillings or ditches can all be detected. Where strong magnetic anomalies are absent, it is possible to detect subtle anomalies caused by soil disturbances or organic matter. The strong impact of artillery bombardments at the former Western Front caused a wide scattering of ferrous magnetic objects (metal fragments and war debris) that may cover subtle anomalies of interest. The mapping of anomalies as dipoles is one of the characteristics of FGM sensors. Fluxgate gradiometers can be directional sensitive which exposes them to tilt-introduced noise (Note et al., 2017; Schmidt et al., 2015). A significant advantage of these instruments is their

employment in array combinations. These multiple-sensor set-ups enable fast coverage of large areas, especially when they are towed by motorised vehicles (Trinks, et al., 2013).
Caesium magnetometers (total field instruments), which are the second most frequently used magnetic technique in archaeology (Schmidt et al., 2015), only have an advantage to fluxgate when their use is compatible with the detection of subtle anomalies. The relatively recent and strong impact of WW1 onto the soil does not meet the suitable conditions for using the caesium type. The instrument's higher sensitivity will result, in the case of WW1 battlefields, in more saturation of the high magnitude anomalies caused by the metal war debris (Schmidt et al., 2015). For some of the less-sensitive fluxgate surveys performed for this thesis (see chapter 4), metallic objects in the topsoil are significantly disturbing the location background values. The use of caesium will only increase the occurrence of this phenomenon. Based on this characteristic, it was decided to only carry out FGM surveys in the former front area.

**Sensor setup**

The fluxgate gradiometer system consists of two fluxgate sensors wound around a ferromagnetic core and placed one above the other in a vertically held cylindrical tube (Aspinall et al., 2008). This principle is shown is figure 2.20. The sensor output is the difference between both measurements, expressed in nanotesla (nT) units. Because of the vertical held position, near surface magnetic deviations will influence the lowest fluxgate sensor more than the one positioned in the top of the cylindrical sensor. In figure 2.20, $\overrightarrow{B_1}$ is measured by the upper fluxgate sensor to compensate $\overrightarrow{B_2}$, measured by the fluxgate sensor closer to the ground. A typical readout for $\overrightarrow{B_1}$ would be 48032.4 nT and 48074.6 for $\overrightarrow{B_2}$. The output value $\overrightarrow{B_2}$-$\overrightarrow{B_1}$ recorded by the sensor would then be 42.2 nT. The influence of the earth magnetic field onto both fluxgate sensors is considered as equal and therefore eliminated by the extraction of $\overrightarrow{B_2}$ from $\overrightarrow{B_1}$. The difference in readout is caused by nearby magnetised features (soil, bricks, metal…).

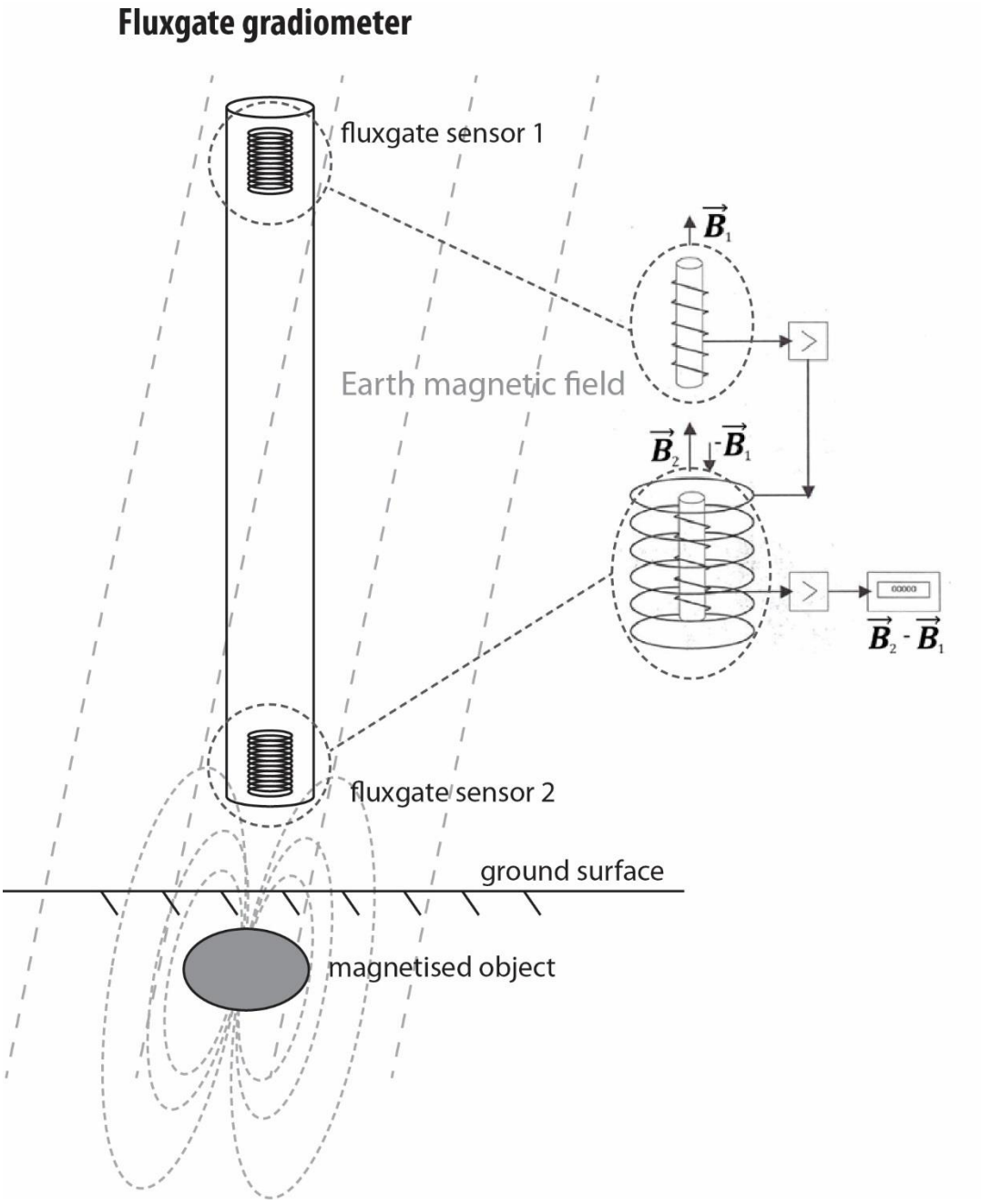



**Figure 2.20:** The fluxgate magnetometer sensor in gradiometer setup, measuring a magnetised object (after Aspinall et al., 2008).

### Survey configuration

For the surveys carried out in this thesis, a pushcart manufactured by SENSYS Sensorik & Systemtechnologie GmbH (Bad Saarow, Germany) with their five-channel fluxgate magnetometer system (MXPDA) was used. The carrier frame, which advances on two wheels, is made of fiberglass and plastic (figure 2.21) and allows sensor spacing of 0.50 m or 0.25 m.

For archaeological purposes, 0.50 m spacing is an acceptable option (English Heritage, 2008) and is the standard applied for the surveys in this thesis. The FGM650 series gradiometers measure at a frequency of 20 Hz within a range of +/-10 000 nT (www.sensys.de, 2016) and have a maximum depth response of roughly 3 m (Clark, 1990). A rugged waterproof PDA (handheld PC) was employed for data logging. A GNSS antenna with RTK corrections was acquired to obtain an absolute two-dimensional precision of a few cm. Around 85 measurements per metre were recorded at a walking rate. Scanning speeds of 3 hours per ha were achieved with a cart pushed manually and <1 hour per ha with a motorised pull cart (both with a scan line width of 2.5 m). Data processing includes coordinate transforms, overlap correction, median levelling, noise reduction and image gridding.

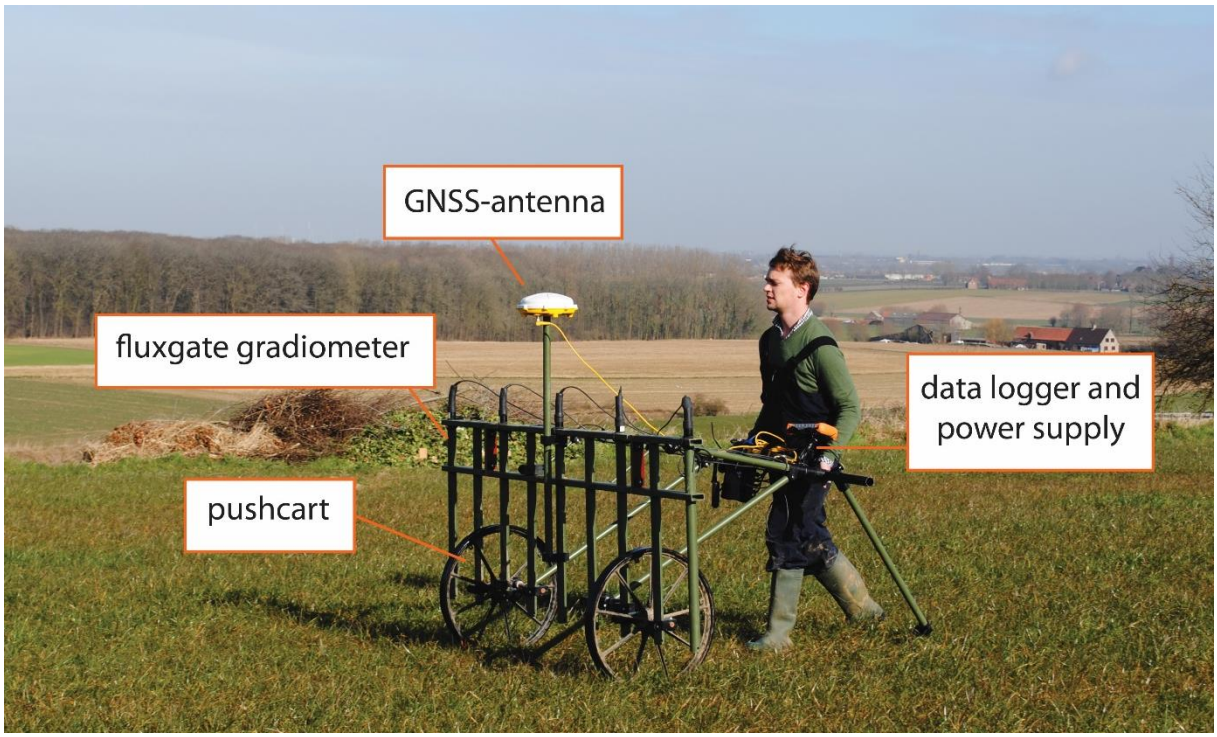



**Figure 2.21:** The Sensys pushcart with a five-channel sensor array, logging device and GNSS antenna.

## 2.3 Other non-invasive techniques

### 2.3.1 Aerial photography

#### WW1 period – military infrastructure

At the end of 1914, military aviation became the new eyes of the armies – millions of aerial photographs were taken of all theatres of war as a source of military intelligence and to map the extent of the vast networks of field defences and enemy artillery positions (Carlier, 1921). Over 500 000 historical photographs have been preserved in archives around the world, providing a visual record of the progress of war and destruction of the landscape (Cowley and Stichelbaut, 2012). In the past decade, over 18 500 of these aerial photographs of the frontlines in Belgium have been inventoried, digitised, georeferenced and studied (Stichelbaut, 2011; Stichelbaut, et al., 2017a), providing a unique primary dataset, including the vectorisation of all visible war features. The majority of these images were digitised from the archives of the Imperial War Museum (IWM), Australian War Memorial (AWM), Royal Army Museum Brussel (KLM-MRA), Bayerisches Hauptstaatsarchiv (BH), Service Général du Renseignement et de la Sécurité (SGRS) and the In Flanders Fields Museum (IFFM) (Stichelbaut and Chielens, 2013). The digitisation and database maintenance method is described by Stichelbaut (2009). The aerial photograph coverage and vectorised/interpreted war features coverage for the Western Front in Belgium can be seen in figure 2.22. This interpretation covers 1500 $km^2$ and contains 235 500 structures whereof 5000 km trenches. The database of interpreted features, which is important for heritage management, is being used to identify WW1 structures in archaeological excavations and in geophysical scans (Gheyle et al., 2016; Saey et al., 2016b). This reference is not absolute (as some features are unidentified or masked) but includes most of the aboveground structures (Van Hollebeeke et al., 2014). Georeferenced aerial photographs were obtained instead of trench maps because this source provide more (interpretable) information and the geospatial accuracy is better which is needed to validate geophysical scan results. In this thesis, the features detected by aerial photography are used as reference (considered as 100%) to compare the features detected by geophysics. Deriving information from aerial photography is often a standard approach in archaeological desktop studies. The air photo and GIS-mapping database which was created in the past 15 years is therefore a key-tool to investigate former WW1 conflict areas.

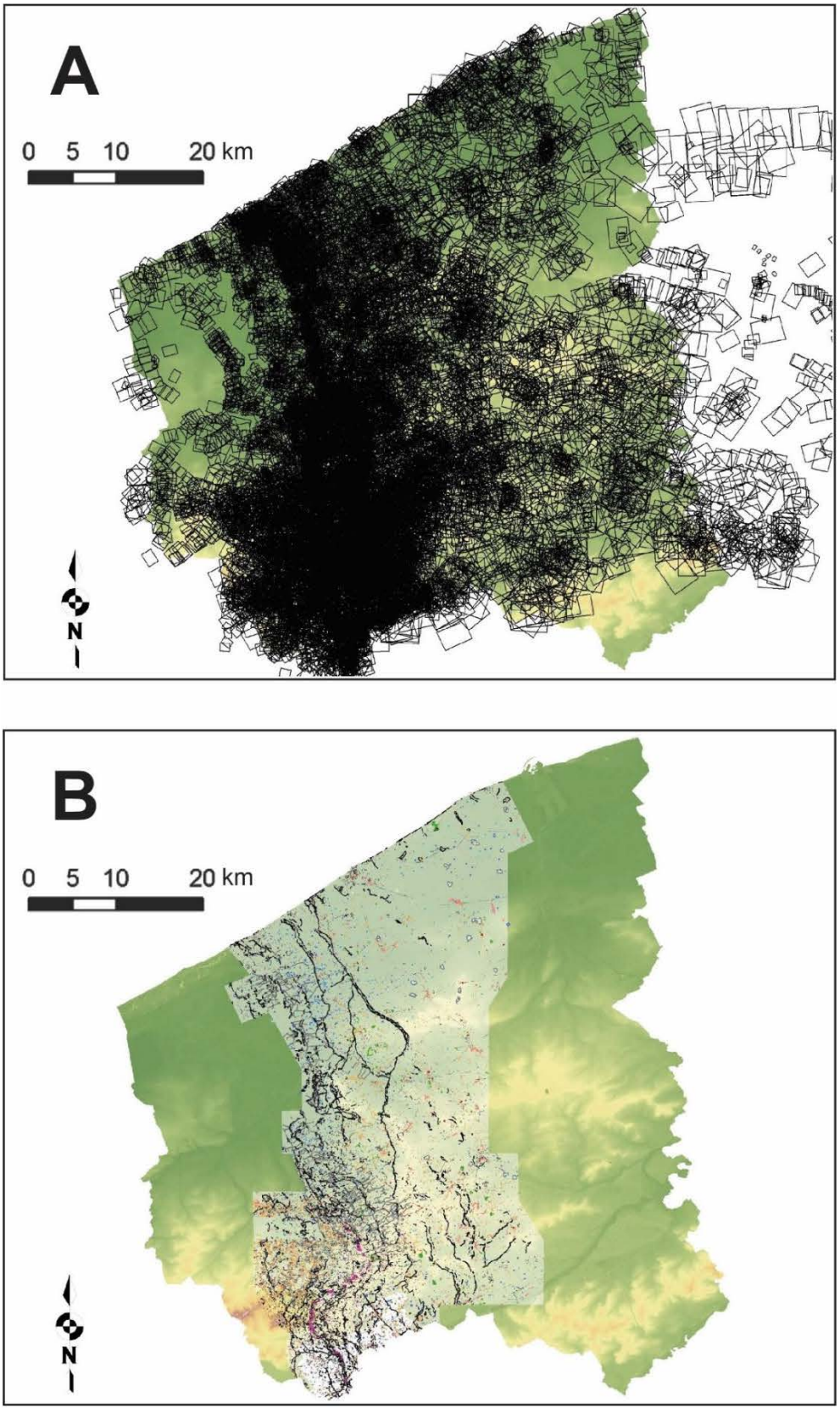



**Figure 2.22:** The situation in 2016 of the aerial photograph coverage (A) and vectorised feature database of interpreted military infrastructure (B) near the WW1 front in Belgium. Background: DHMV I visualisation of the province of West-Flanders.

### Post WW1 – land use changes

To analyse the post-war land use changes, aerial photography is consulted to monitor the impact on the still buried WW1 infrastructure. Woodland and continuous pasture ground do often contain WW1 traces (shell craters/trenches) on the surface whereby the land use conditions definitely contributed to this preservation quality (Gheyle et al., 2018). Agentschap Informatie Vlaanderen (AIV) provides several series of orthophotographs, covering the Flanders region to study those conditions and changes. The first complete covering dataset was established in 1971. Since then, 12 timeframes of orthophoto series were made for the Flanders territory. The series used for this research together with their specifications are given in table 2.2. In addition to these images covering the 1971 – present day period, 1939-45 WW2 images were used (National Collection of Aerial Photography, NCAP). By constructing a timeline of land use changes/conditions, a prediction on the preserving conditions of the buried near surface WW1 structures can be made.

**Table 2.2**: Series or aerial photographs used for the study of land use changes

| Period of survey | Data owner | Provider | Ground resolution (m) | Colour |
|---|---|---|---|---|
| 1915 - 18 | IWM/KLM/AWM/IFFM/BH/SGRS | CHAL | variable | BW |
| 1939-45 | NCAP | NCAP | variable | BW |
| 1971 | AIV | AIV | 1.00 | BW |
| 1989 - 90 | AIV | AIV | 1.00 | RGB |
| 2000 | Province of West-Flanders | AIV | 0.25 | RGB |
| 2014 - 17 | AIV | AIV | 0.25 | RGB |

## 2.3.2 LIDAR

### Definition and principle

LIDAR (Light Detection And Ranging) is a topographical measuring technique that uses pulsed laser light to determine the accurate position of a surface or object (Dong and Chen, 2017). A rotating mirror in the laser scanner distributes the transmitted pulses in a short amount of time to a certain predefined area (scanning footprint). Based on the time measurements between transmitted and received laser pulses, the transmitting/receiving angle and the by GNSS received coordinates and ground reference points, a 3D point cloud can be constructed as raw output result. LIDAR as an aerial application is called Airborne Laser Scanning (ALS). For this,

an airplane (or helicopter/aerial drone) is provided with a laser scanner, flying parallel scan strips over the area according to an optimised flight plan. Because a flying platform has to be carefully monitored to reach good quality results, an internal measurement unit is used next to GNSS receiver and ground control points to improve the precision of the point cloud.

### Applications ALS

LIDAR is applied for several purposes in different domains. A first derivative is a digital elevation model (DEM). Before LIDAR, land survey and photogrammetry were used to create a DEM, which was time consuming. LIDAR made this process easier and it has the property to penetrate through the vegetation. By only considering the last received signal of a transmitted pulse, vegetation can be filtered out and the ground surface can be extracted. A popular application of LIDAR is the deployment as exploring technique to cover large areas for archaeology to detect surface features (Hesse, 2013). By using a variety of specialist visualisation techniques (Opitz and Cowley, 2013), a large variety of archaeological sites can be detected, even below a tree canopy. Some other applications are: coastline and river monitoring, yield monitoring, erosion and water shed line calculation, solar energy simulation, glacier monitoring, architecture etc.

### Flanders dataset

In 2017, the Flemish government released an aerial LIDAR dataset covering the Flanders and Brussels area. This survey was recorded during the period of 2013-15 to update the former height model, which was based on LIDAR data with 1 point per 4 $m^2$. The new-recorded LIDAR data has an average point density of 16 per $m^2$; the planar precision is 0.10 m and the Z accuracy 0.05 m (AIV, 2013). Simultaneously, RGB-values were recorded for the rectification of high quality orthophotographs. These higher precision recorded datasets produced more opportunities to be used for other purposes such as remote sensing archaeology. The *.LAZ tiles (compressed format of *.LAS, containing point cloud data) can be downloaded from a geo-portal of the Flemish government. Between adjacent flight lines, there is a minimum overlap of 50%. The derived height model from this ALS survey is the Digital Height Model Vlaanderen II (DHMV II) in GeoTIFF format. The ground resolution of this model was set to 1 x 1 m and is also available in 5 x 5 m resolution.

### Usability for WW1 archaeology

In a first step, the 1 x 1 m DTM is used as indicator for the presence/absence of WW1 features in the micro topography. This data set in GeoTIFF format is comfortable to process in GIS-programs to visualise these per topographical map section (20 x 13.8 km). To study detected features in detail, the raw *.LAZ-files can be used to extract more detailed DEM's

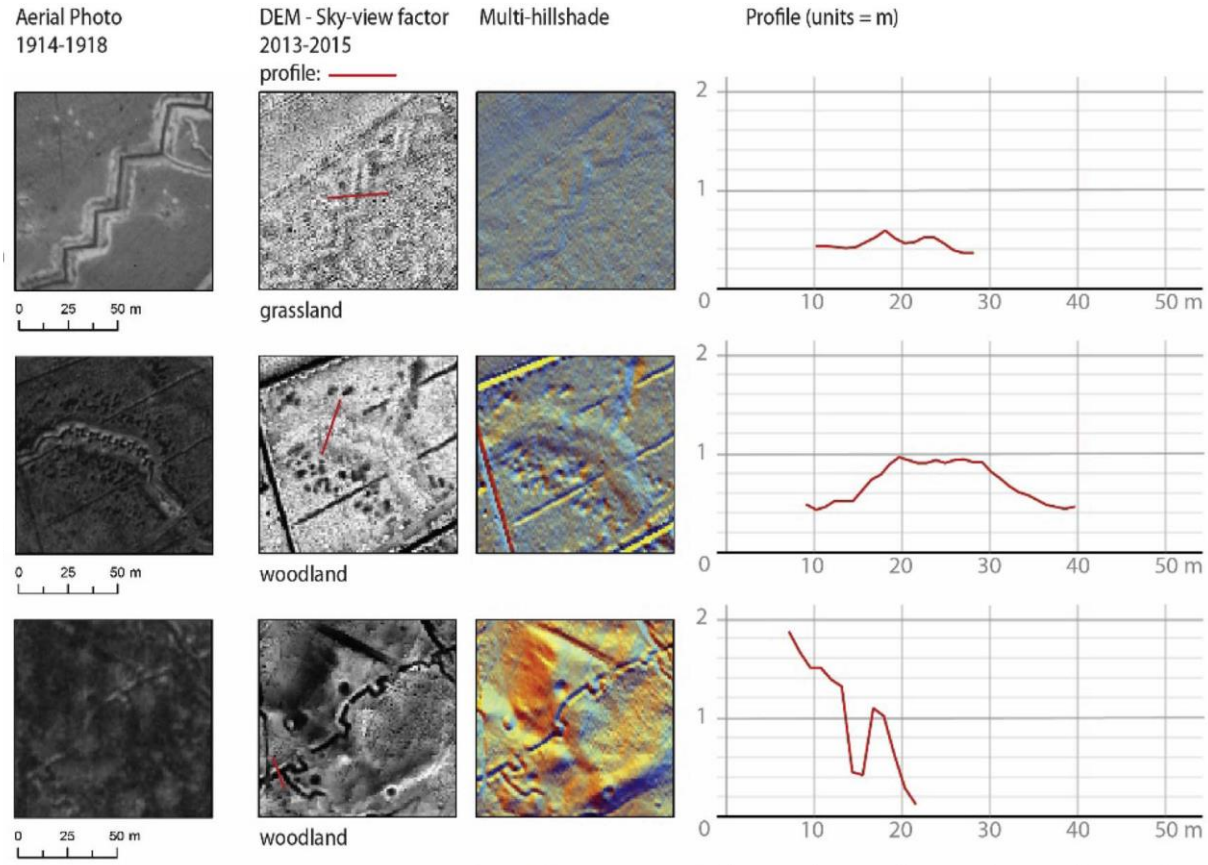



**Figure 2.23:** Three examples of war heritage (trenches) observed on both wartime historical aerial photographs (left) and the Flemish DHMVII (AIV) 1 m raster DTM: sky-view factor (10 m search radius in 16 directions) and multi-hill-shading (35° sun elevation from 16 directions) visualisation with a profile intersecting war features on the DTM (modified from Gheyle et al., 2018).

or profiles. These files can be obtained for small areas, which makes data processing much faster and more goal-oriented. Some LIDAR-visualisation techniques can be applied to improve the visibility of the micro relief, which is beneficial for the detection of archaeological features (Gheyle et al., 2018). The most satisfactory techniques for archaeological purposes are 'Sky-view factor' (SVF) and 'Multi-hill-shading' (MHS) which are calculated by using the RVT toolbox (Kokalj et al., 2011; Zaksek et al., 2011). A few examples of detected WW1 features with LIDAR are shown in figure 2.23, processed to SVF and MHS. The DMHV II raster

was beneficial to characterise the still preserved WW1 traces in the micro topography. In all research areas, the consultation of LIDAR-derived visualisations in combination with available time-series of aerial photographs is an important first step. This gives and excellent insight on what can be expected to be preserved at the surface.

## 2.4 WW1 battle phases and study area

### 2.4.1 Battle phases on the Western Front during the war in Belgium

This section gives an overview of some dates related to important offensives and front movements. This is needed because during this thesis, temporal references are frequently made to these events. It helps the reader to broadly understand the course of war.

The date of the start of the war in Belgium is the 2nd of August 1914 (declaration of war by Germany). After the quick movements of the armies from the eastern part of the country to the west, the war's front stabilised in October 1914 in western Belgium where it remained for four years. The combating parties on Belgian territory were the Allies (France, the British Empire and Belgium) and the Central Powers (Germany). During the war, a number of large-scale offensives shaped the front area and caused the front to shift over a maximum distance of 10 km. In between these offensives, there were longer periods of static warfare in which most of the defences were constructed.

Main offensives:

- Battle of the Yser (16-31 October 1914) and First Battle of Ypres (19 October – 22 November 1914: shaped the frontline along the Yser river and the higher ridges around Ypres (Edmonds, 1925).
- Second Battle of Ypres (22 April – 25 May 1915): subsequent series of German (gas) attack caused the frontline to shift towards Ypres (Edmonds, 1928).
- Battle of Messines (7-14 June 1917) and Third Battle of Ypres (31 July – 10 November 1917): Allied attempt to break though the stalemate and advance towards the Belgian harbours (Edmonds, 1948).
- German Spring Offensive / Battle of the Lys (9-29 April 1918); German advance beyond the 1917 battlefields towards Ypres (Edmonds, 1935).

In August 1918, the Allies started a counter offensive, which resulted in the withdrawing of German forces and finally the Armistice on the 11th November (and the peace truce of Versailles in 1919). The main frontlines for the Belgian territory are visualised in figure 2.24. The front from the cities of Nieuport to Dixmude remained constant during the war (except near the Yser mouth). The main theatre of operations was the Ypres Salient and the higher ridges to the south (Kemmel, Wytschaete and Messines).

### 2.4.2 Study area

A selection of fields was made near the frontlines in Belgium to investigate the former front region with geophysical prospecting techniques. These fields are mainly located in the study area of the '*Non-Invasive Landscape Archaeology of the Great War'* project (wo1.ugent.be, 2018). This project's study area is defined by three rectangular areas (transects) with the dimensions of 19 – 27 km in length and 3-4 km in height, crossing the frontlines from west to east (see figure 2.24). The first one is located just south of the city of Nieuport, covering an area from Ramskapelle to Gistel. The second covers the city of Ypres and intersects the Ypres Salient. The third reaches from Kemmel to Wervik and includes a part of the Messines ridge. These study areas will be set in a broader context (soil / topography) in chapter 7. Outside these areas, additional surveys – i.e. opportunities from landowners or additional case studies – complement this dataset. For some chapters, a limited number of additional surveys - measured outside the former conflict area - were added. To define all sites used in this thesis, detailed information was added to the appendices (appendix 2.4).

Within the transects, the parameters of site selection were: conditions of agricultural fields (easy to access), contained during WW1 interesting or unique war features (verified by aerial photography) and the landowner/user had to agree with the terrain access to execute the geophysical survey. 55 locations, totalling 243.5 ha, were surveyed near the former Western Front. All of those locations were scanned with FD-EMI. 12 of them (17.5 ha) were targeted with FGM, 9 (3.1 ha) with GPR, 4 (4.4 ha) with ER and 1 (1 ha) with TD-EMI. These surveys took a total of 86 field days of data collection. The total coverage and spread of these locations are visualised in figure 2.24. In some areas, clusters of fields can be found and some are empty. This was caused by coincidence (access given by landowner, availability of the field),

parameters of field selection (near frontlines: more interesting features to cover) or scan priority given to the field.

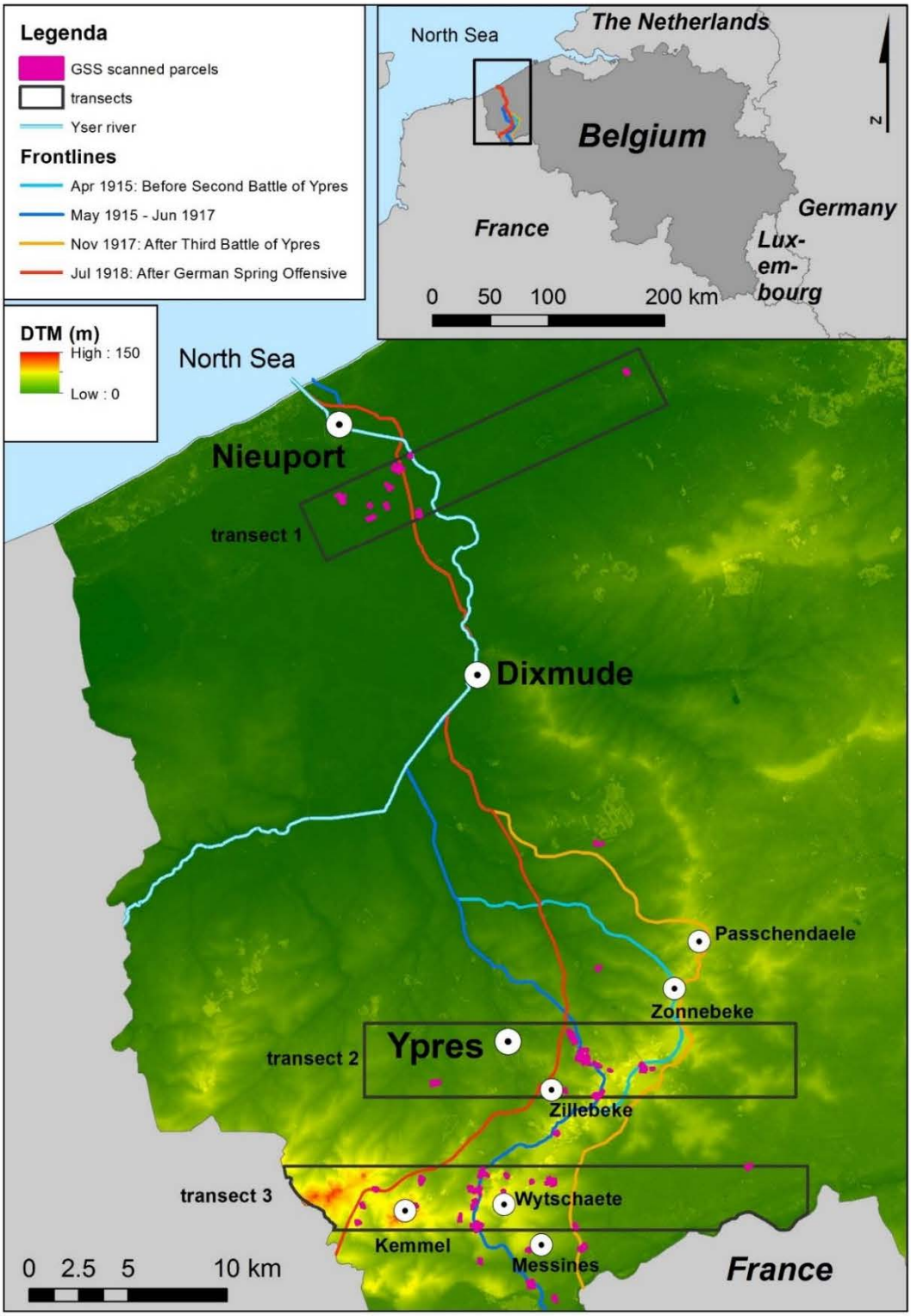



**Figure 2.24:** Overview of the former Western Front in Belgium, including the four main phases of the frontlines and cities/villages with importance during the war. In addition, the by geophysical techniques targeted fields and research areas (transects) are displayed. (DTM: copyright AIV)

# Chapter 3

## Optimising fluxgate magnetometer survey data

This chapter is partially modified from:

> **Note, N.**, De Smedt, P., Saey, T., Gheyle, W., Stichelbaut, B., Van den Berghe, H., Bourgeois, J., Van Eetvelde, V., Van Meirvenne, M. (2017). Removal of sensor tilt noise in fluxgate gradiometer survey data by applying one dimensional wavelet filtering. *Archaeological Prospection*, 24(4), 353-360.

## 3.1 Introduction

Optimising geophysical survey data is an important step to provide clear and unambiguous images for the end-user. This was the motivation to first analyse the noise-sensitive FGM recorded datasets for this thesis and improve the result before interpreting these for WW1 archaeology. Tackling the noise-problems could be done in two ways: preventing errors during data recording and eliminating unwanted phenomena in post-filtering procedures. In this chapter, errors experienced in the applied FGM surveys will be covered by describing them and providing a solution to reduce these errors. By using the Sensys FGM650 series gradiometers (Sensys, DE), a built-up of experience was gained to record good quality datasets onto the field and to filter out multiple errors afterwards. The software provided with the Sensys equipment (Sensys MAGNETO) covered only basic image gridding, zero-mean traversing and some standard output formats (sensysmagnetometer.com, 2019). Therefore, literature was consulted to integrate basic processing.

A first solution by using as few as possible post processing tools, is making small adjustments to the FGM configuration and survey strategy. This can produce significant improvements during data recording. One of those adjustments is the use of a small GPS-antenna when mounted on top of the sensor array. Antenna's in this position cause an influence onto the gradiometers which produces an offset to the zero-point of the data output (Aspinall et al., 2008). Other electronics and components from the sensor setup result in a similar effect. These elements should be firmly attached to avoid fluctuating errors (caused by movement reverberations). One solution to the constant influences is median levelling of data recordings per sensor or per survey line for each sensor. This is a successful operation, which is frequently performed for FGM processing (Aspinall et al., 2008). Another possibility is the attachment of the GPS-antenna and power supply on a backpack to reduce its influence. This option is preferred and used in terrain conditions with subtle magnetic traces.

A second practical issue is the performance of straight parallel survey lines. Experience taught that by looking on the PDA-screen where the survey lines are displayed in real-time, winding paths are performed. The operator's experience but mainly the terrain conditions play a major role in the quality of the survey path linearity. The use of two reference pickets to indicate the future positions at each end of the two following survey lines, showed to be more successful. By walking towards those reference pickets, generally straight lines are achieved. The optical angle error increases with increasing survey line size. Therefore, the length has to be limited with this technique (Gaffney and Gater, 2010). A maximum of 100 m is experimentally found as comfortable. Inevitable, overlap errors will be included. These overlaps are seen in the gridded data as interfering phenomena, which causes striping effects in the direction of movement. By removing the overlapping parts by a post-processing algorithm, those striping effects can be eliminated.

Regardless of the FGM configuration, gradiometer probes should be set in a stable vertical position to allow reliable data collection (Aspinall et al., 2008). This 'ideal' condition is sometimes difficult to uphold under field circumstances, and any sensor tilt induces noise into resultant survey data. Such motion-induced 'tilt' noise often displays specific wave patterns related to survey mode and speed, and coincides partly with operator step frequency (for manual surveys) or mechanic reverberations of mobile setups. The use of cart systems tend to adversely affect motion-induced noise as subtle motions of operator or operating vehicle are propagated, and sometimes enhanced, through the cart handle or towing rod. While adding suspension to cart-systems can help reduce the impact of micro-relief onto the operating tilt, the need for remediating resultant noise through post-processing persists.

Within this chapter, the effect of zero-median traversing, overlap and interfering data filtering will be demonstrated as important processing steps in section 3.2 'basic post processing'. To most magnetometer software packages, these procedures are not new but visualising the influences onto the data is something that is often missed in 'black box' software. The tilt-induced noise will be tackled in a separate section. Therefore, wavelet-based filtering on raw data is developed and demonstrated to provide a solution to this problem. In archaeological data processing, this procedure is new and tackles the problem before data gridding. Overall,

this chapter will provide solutions to a few common seen undesirable influences in FGM surveys. The MATLAB processing codes can be found in the appendices.

## 3.2 Basic post processing

### 3.2.1 Datasets

To demonstrate zero-median levelling and overlap processing, three datasets are included in this section. The first dataset is measured in the eastern part of Flanders, in the hamlet of Zelk (Halen). Potential remains of a late medieval moated site were detected. No hard validation (excavation or historical source analysis) was available but the signature of the detected elements produced a strong indication. The second site is located near Ninove, East Flanders. Here, Roman period anomalies were prospected (ovens, road). The third dataset is located to the east of Zillebeke, near Hill 62 and the Canadian WW1 memorial site. WW1 trenches and strong metallic anomalies are covered. In the first two datasets, the parallel survey lines are walked by using reference pickets. Both surveys cover a subtle archaeological structure which is ideal to demonstrate the effect of sensor-drift and sensor-offset onto the original recorded data. In the Zillebeke dataset, strong winding lines were performed because the survey paths were real-time displayed for the operator on the PDA screen. Therefore, this survey was chosen to enhance the negative effects of slovenly walked survey paths onto the data interpolation. All locations were surveyed by employing a 5-probe array pushcart.

### 3.2.2 Zero-median levelling

The constant influence of the FGM equipment produces an offset to one or multiple gradiometers in the sensor array. In addition, sensor drift is a known influence (Aspinall et al., 2008).These phenomena are causing difficulties to interpret the output of each sensor together in an interpolated grid. Therefore, the original data needs to be levelled for constant offset influence and drift before gridding. To tackle the constant zero-shift per sensor, median values for each sensor are removed. As a result, the new median for the sensor-output is equal to zero (zero-median correction). By doing this for each sensor in the array separately, all outputs can be interpret at the same zero-point. This effect can be seen in figure 3.2 B1 and 3.3 B1 for

the Ninove and Zelk dataset. This procedure creates an image that is more or less usable for interpretation but shift effects between lines caused by sensor drift are still noticed. When the data output is visualised in a graph for one sensor probe, significant drift over time can be seen (figure 3.1). Therefore, zero-median correction per survey-line per sensor is applied (figure 3.2 C1 and 3.3 C1). In literature, this procedure is known as zero-mean traversing (Aspinall et al., 2008). This process offers an option to choose between mean or median levelling. The median is less sensitive to outliers (strong anomalies) and therefore often more suitable than the mean. After completing this processing, acceptable good quality datasets are achieved which can be used for archaeological interpretation (figure 3.2 C1 and 3.3 C1). This zero-median/mean traversing is often standard in magnetometer software packages. When the length survey lines increase (>300 m), drift correction will be needed within the lines. This can be done by performing median levelling by applying a moving window. The choice of the size of this window is subjective and should be at least +/-10 times the largest anomaly. A too small window will filter out all significant variations or produce striping effect in extend of strong anomalies. In figure 3.4, the effect of a moving median levelling window with a size of 35 m is seen. The main amelioration can be detected in the north of the dataset: the heavy disturbed area, which covers up a magnetic ditch, is levelled whereby the magnetic output produces a stronger contrast and an extra part of a ditch can be seen.

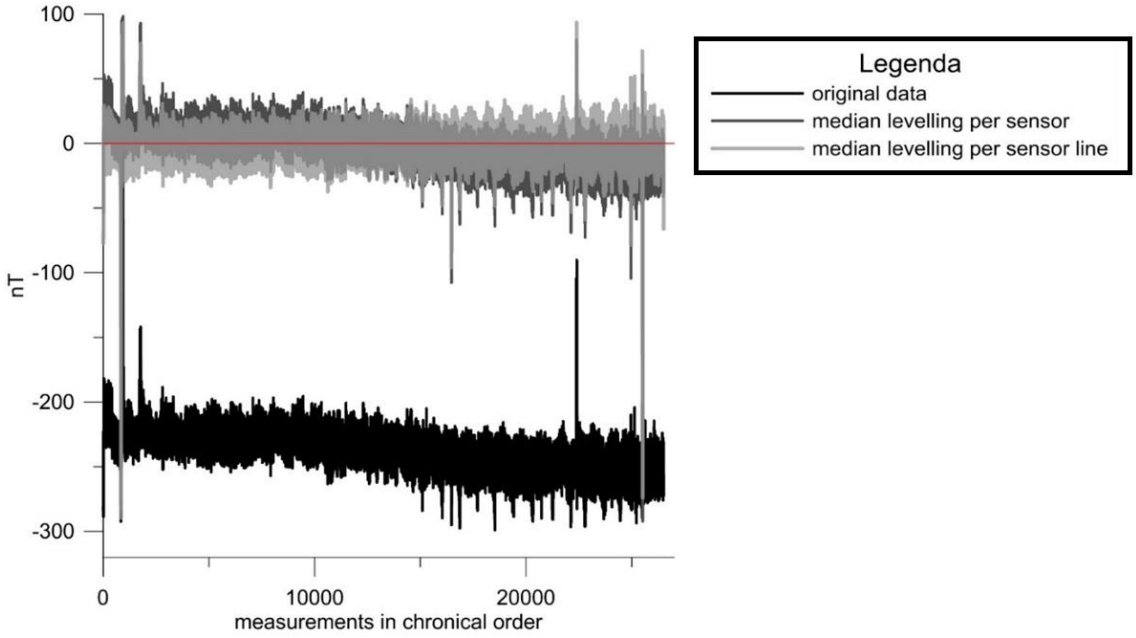



**Figure 3.1:** Data output for one sensor probe during a 2 h survey. The original data output (black), the median levelled output for the whole sensor (dark grey) and the median levelled output per survey line (light grey) are visualised in a graph.

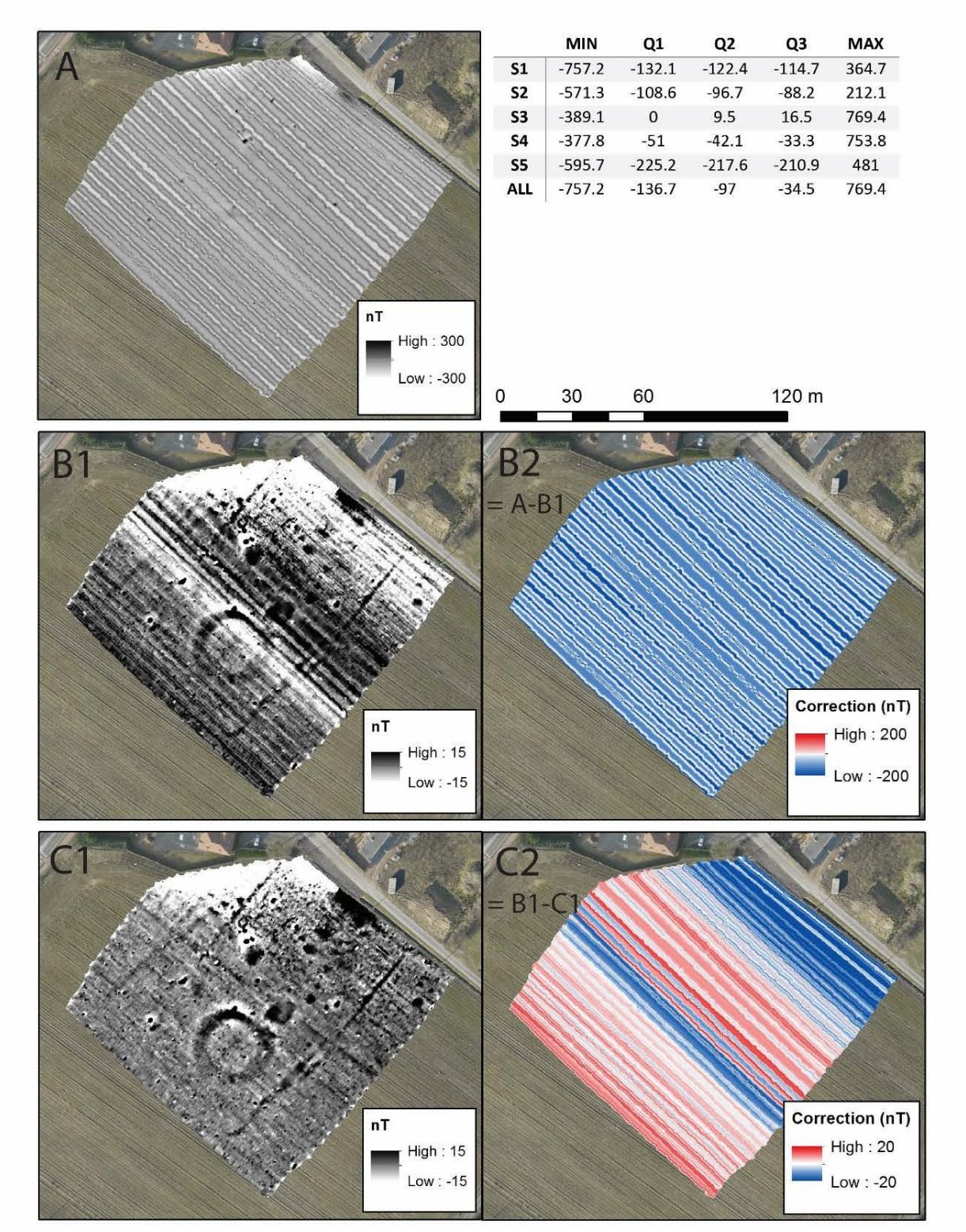
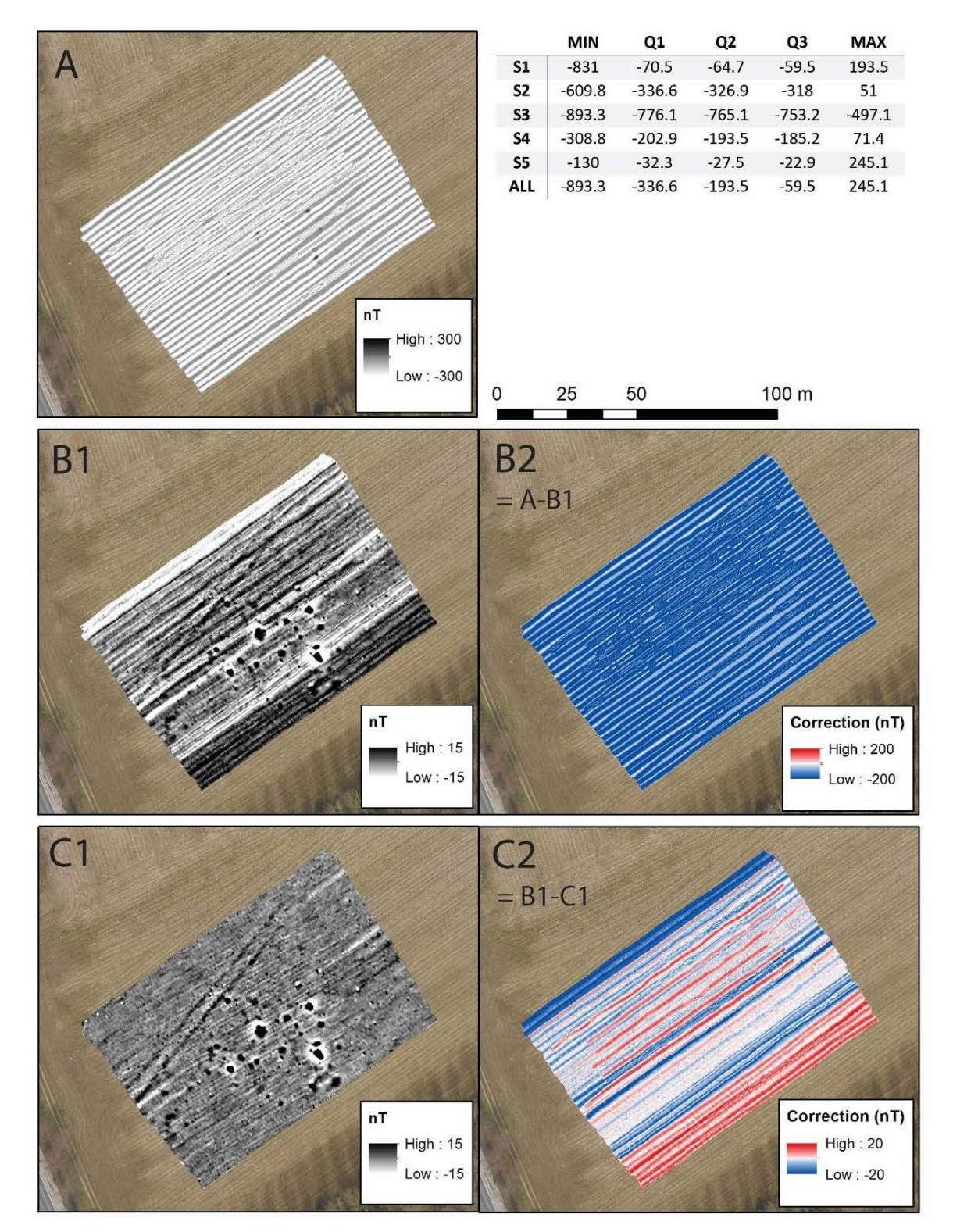



**Figure 3.2:** Display of the Zelk dataset: (A) original data; (B1) zero-median levelled data per sensor; (B2) residuals after zero-median levelling per sensor; (C1) zero-median levelled data per survey line per sensor; (C2) residuals after zero-median levelling per survey line per sensor. (orthophoto: copyright AIV)




| | MIN | Q1 | Q2 | Q3 | MAX |
|---|---|---|---|---|---|
| S1 | -831 | -70.5 | -64.7 | -59.5 | 193.5 |
| S2 | -609.8 | -336.6 | -326.9 | -318 | 51 |
| S3 | -893.3 | -776.1 | -765.1 | -753.2 | -497.1 |
| S4 | -308.8 | -202.9 | -193.5 | -185.2 | 71.4 |
| S5 | -130 | -32.3 | -27.5 | -22.9 | 245.1 |
| ALL | -893.3 | -336.6 | -193.5 | -59.5 | 245.1 |

**Figure 3.3:** Display of the Ninove dataset: (A) original data; (B1) zero-median levelled data per sensor; (B2) residuals after zero-median levelling per sensor; (C1) zero-median levelled data per survey line per sensor; (C2) residuals after zero-median levelling per survey line per sensor. (orthophoto: copyright AIV).

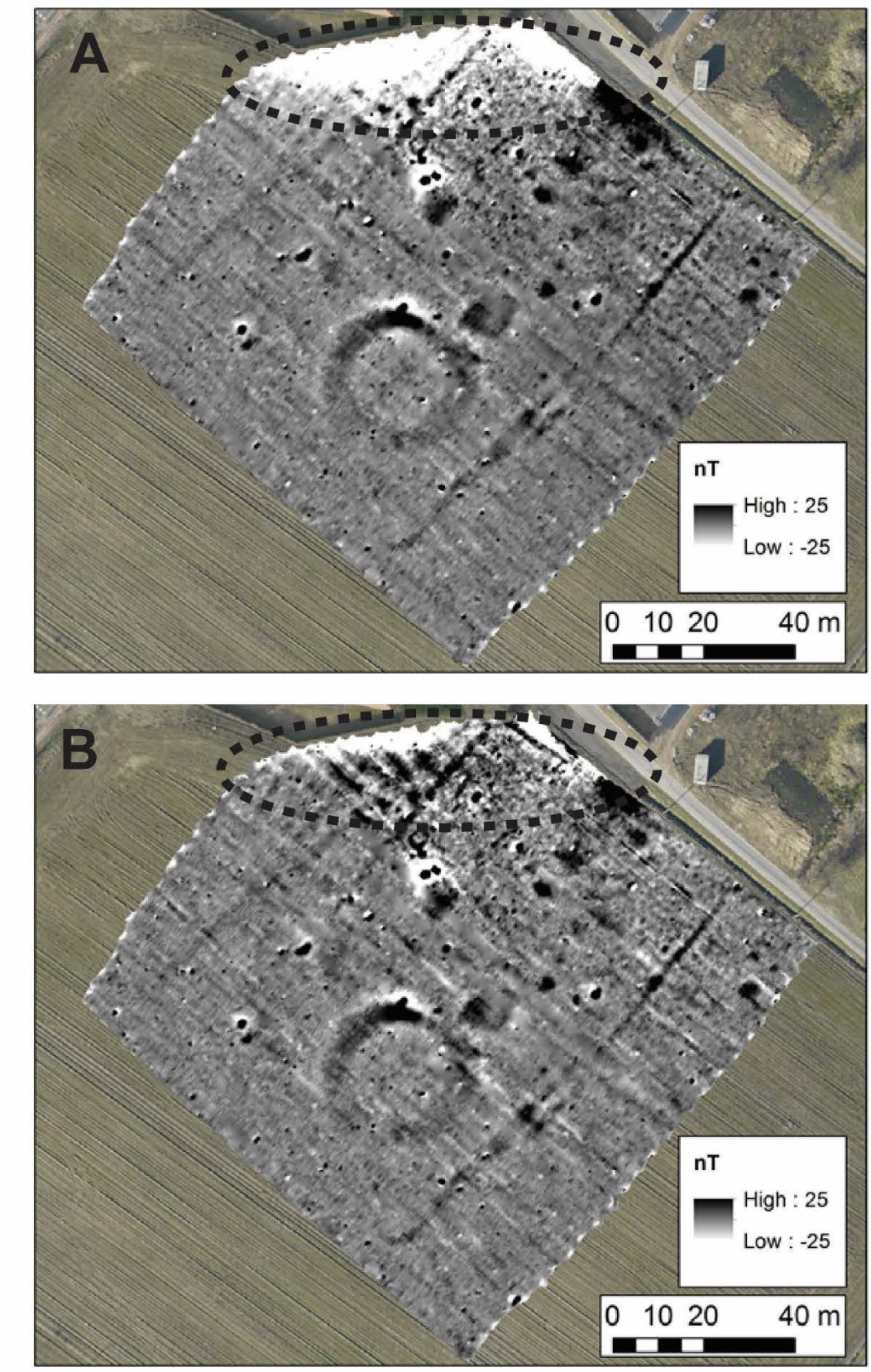
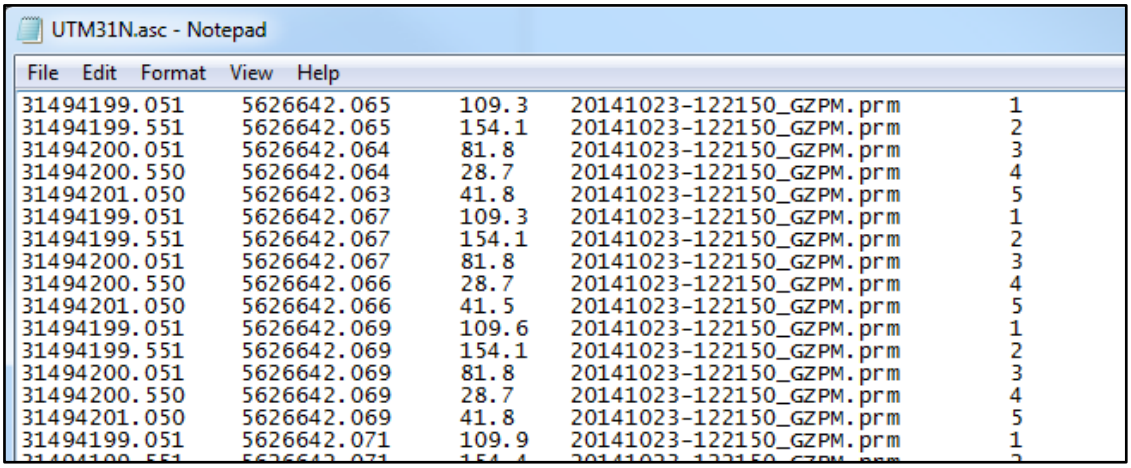



**Figure 3.4:** Display of the Zelk dataset after zero-median levelling per sensor line (A) and zero-median levelling by a moving window of 35 m. In the north of the survey, the magnetic ditch is visible after zero-median levelling by a moving window. (orthophoto: copyright AIV)

To understand the processing procedure, an example from the raw exported data file is shown in figure 3.5. A first step consists out of ranging the magnetic outputs per sensor and per sensor line in chronological order of measurement. This makes the suggested median filtering easy to perform. The MATLAB-code for importing the *.asc output file, ranging and selecting the output of each sensor and performing the median filtering, can be found in appendix 3.1.


UTM31N.asc - Notepad

File Edit Format View Help

| | | | | |
|---|---|---|---|---|
| 31494199.051 | 5626642.065 | 109.3 | 20141023-122150_GZPM.prm | 1 |
| 31494199.551 | 5626642.065 | 154.1 | 20141023-122150_GZPM.prm | 2 |
| 31494200.051 | 5626642.064 | 81.8 | 20141023-122150_GZPM.prm | 3 |
| 31494200.550 | 5626642.064 | 28.7 | 20141023-122150_GZPM.prm | 4 |
| 31494201.050 | 5626642.063 | 41.8 | 20141023-122150_GZPM.prm | 5 |
| 31494199.051 | 5626642.067 | 109.3 | 20141023-122150_GZPM.prm | 1 |
| 31494199.551 | 5626642.067 | 154.1 | 20141023-122150_GZPM.prm | 2 |
| 31494200.051 | 5626642.067 | 81.8 | 20141023-122150_GZPM.prm | 3 |
| 31494200.550 | 5626642.066 | 28.7 | 20141023-122150_GZPM.prm | 4 |
| 31494201.050 | 5626642.066 | 41.5 | 20141023-122150_GZPM.prm | 5 |
| 31494199.051 | 5626642.069 | 109.6 | 20141023-122150_GZPM.prm | 1 |
| 31494199.551 | 5626642.069 | 154.1 | 20141023-122150_GZPM.prm | 2 |
| 31494200.051 | 5626642.069 | 81.8 | 20141023-122150_GZPM.prm | 3 |
| 31494200.550 | 5626642.069 | 28.7 | 20141023-122150_GZPM.prm | 4 |
| 31494201.050 | 5626642.069 | 41.8 | 20141023-122150_GZPM.prm | 5 |
| 31494199.051 | 5626642.071 | 109.9 | 20141023-122150_GZPM.prm | 1 |

**Figure 3.5:** Display of the data output format, written in an asci-file. Data-order per column: x-coordinate, y-coordinate, magnetic output in nT units, filename survey line, sensor probe number in array.

### 3.2.3 Removal of overlapping and too close recorded data

After interpolating the median levelled point data, interfering effects appear at the overlapping and too close recorded points. These effects can be seen in figure 3.6 A. To tackle these artefacts before gridding, a processing code was written to remove the duplicate interfering data between survey lines. In this code, each line was reduced in data points to make the processing code more efficient and faster. One point per metre was often applied. Next, this simplified spatial approach is put in a geometric equation where the too close recorded data points are determined between sensor paths of different survey lines. In this procedure, the distance of points in neighbouring sensor lines are calculated according to the principle of Euclidian distance. If points are closer than a predefined threshold ($t$), the data points are removed from the dataset in one of the two interfering sensor lines in the range of a predefined radius ($r$). If the reduced point spacing within the line is equal to $a$, than this radius is preferable set to $r = 1.5a$. Applying this procedure offers significant improvements of the interpolated

datasets. An example can be seen in figure 3.6. The MATLAB-code can be found in appendix 3.2 and should be applied after execution of the code in appendix 3.1.

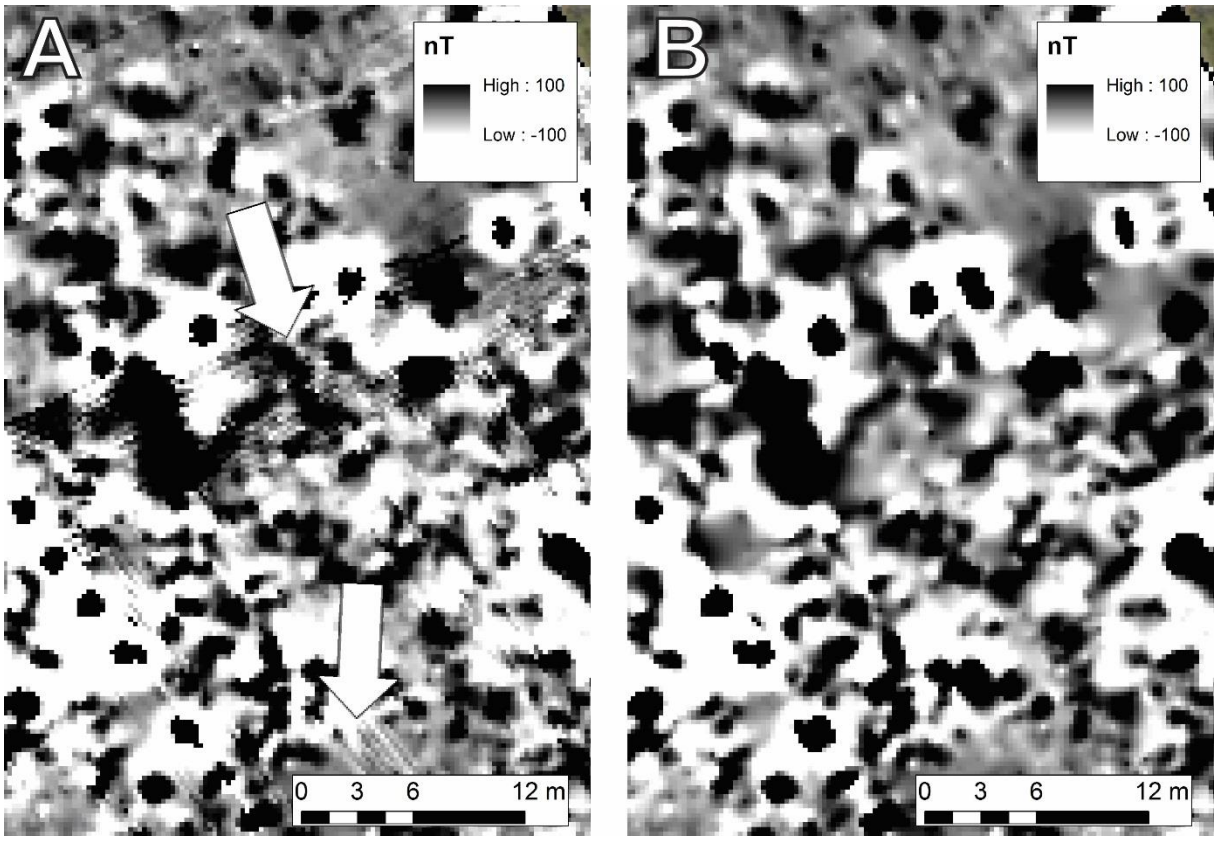



**Figure 3.6:** Visualisation of the overlapping and interfering data patterns in image A. An arrow indicates example spots of messy parts. In image B, the patterns are removed by the algorithm.

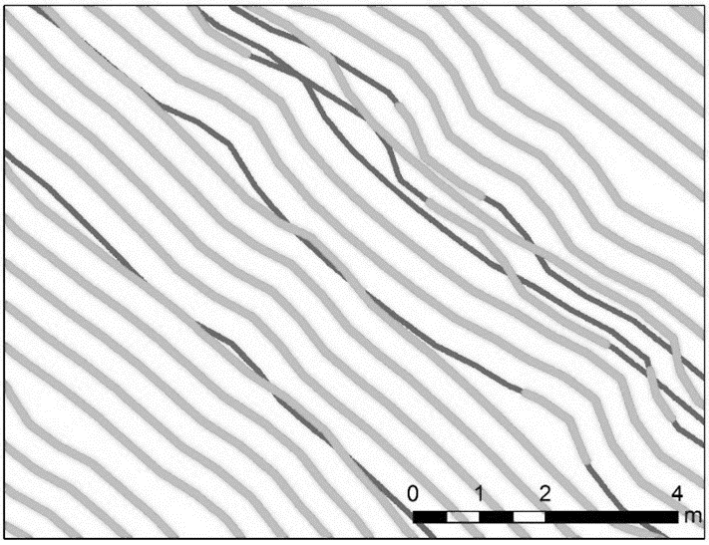



**Figure 3.7:** Example of corrected survey lines after proximity-processing: remaining lines (light-grey) and the by algorithm removed interfering parts (dark-grey).

## 3.3 Tilt noise filtering

Commonly, image filtering is applied to reduce the influence of tilt noise. Hereby, 2D low-pass filters (based on e.g. Gaussian, median or moving average filtering) are used to remove the tilt-noise. However efficient in producing a more levelled data visualisation, these techniques come with a smoothing penalty and produce blurred images (Bovik, A., 2000; McVeigh et al., 1985; Paoletti et al., 2007; Tsivouraki & Tsokas, 2007). For tilt noise particularly, the risk of artefact creation and removal of relevant information burdens adaptive filtering, as motion-induced noise often has the same high frequency content as anomalies in data registration (Tsivouraki and Tsokas, 2007). Nevertheless, in order to fully exploit data potential, tilt noise has to be addressed in post-processing as it can both mask relevant magnetic variations and create artefacts that make data plots difficult to interpret. Therefore an alternative filtering procedure is proposed that allows targeting tilt-noise variations more accurately through an adaptive processing scheme.

As motion induced noise is essentially independent of measurement positioning, but introduced as a function of sensor setup and the method of propagation, the resultant effect can be addressed in the time domain. Tilt noise generally causes repetitive patterns that occur perpendicularly to the direction of motion. However, as the frequency characteristics of such interference can vary slightly throughout the entire dataset, a flexible noise identification is pivotal in avoiding the introduction of artefacts. Therefore a filtering procedure is proposed, based on the 1D wavelet transform whereby the survey dataset is addressed as a time-series. The inherent flexibility of wavelet analysis allows targeting the appropriate variations by selection of a suited mother wavelet and considering different scales of variation simultaneously. For processing magnetometer data, wavelet analysis is often used to drive filtering methods aimed at removing undulation errors between survey lines in ground surveys (Tsivouraki and Tsokas, 2007) and directional trends in airborne survey data (Fedi and Florio, 2003), albeit primarily in 2D image processing procedures. For addressing unwanted measurement interference by 1D signal processing, De Smedt et al. (2016) used a 1D discrete wavelet filtering applied on electromagnetic induction data to remediate micro drift fluctuations. Here, an adaptive filtering procedure is proposed, equally based on the 1D wavelet transform that allows isolating unwanted motion-induced noise in FGM datasets. After defining the cause

and specific influence of sensor tilt, the way how adaptive wavelet filtering can help overcome the burden of tilt noise in magnetic survey data is investigated. In addition, the efficiency of the procedure is evaluated on three test cases.

### 3.3.1 Test sites

To evaluate the proposed procedure, FGM data from three test locations were considered. These surveyed sites are located in Belgium and display different magnetic contrasts (summary statistics are shown in table 3.1). The first site is located at the World War I frontline in Kemmel, situated 10 km from Ypres. The foundations of a barrack camp were prospected. The phenomenon of metal debris pollution originating from WW1 causes strong anomalies in the whole area (Note et al., 2018). The second site is located at Oostkerke in the Bruges area (Trachet et al., 2015). This survey was conducted at the location of a former medieval town. Settlement foundations (bricks) and a road were buried beneath the surface. The third location is a roman settlement in East-Flanders, named Alkeveld. Unlike the previous test sites, magnetic field variations have a more restricted range (table 3.1). All three datasets are visualised in figure 3.8 with addition of a window containing a detail of the noisy wave pattern and the direction of profiling.

**Table 3.1:** Summary statistics of the three test datasets.

| Values in nT | Kemmel | Oostkerke | Alkeveld |
|---|---|---|---|
| **mean** | 3.67 | 4.14 | -0.23 |
| **median** | -0.3 | -0.3 | -0.3 |
| **max** | 10000 | 2563.9 | 6013.9 |
| **min** | -9863.8 | -1265.3 | -6965.8 |
| **IQR** | 45.8 | 23.7 | 3.4 |
| **stdev** | 273.17 | 49.54 | 61.34 |

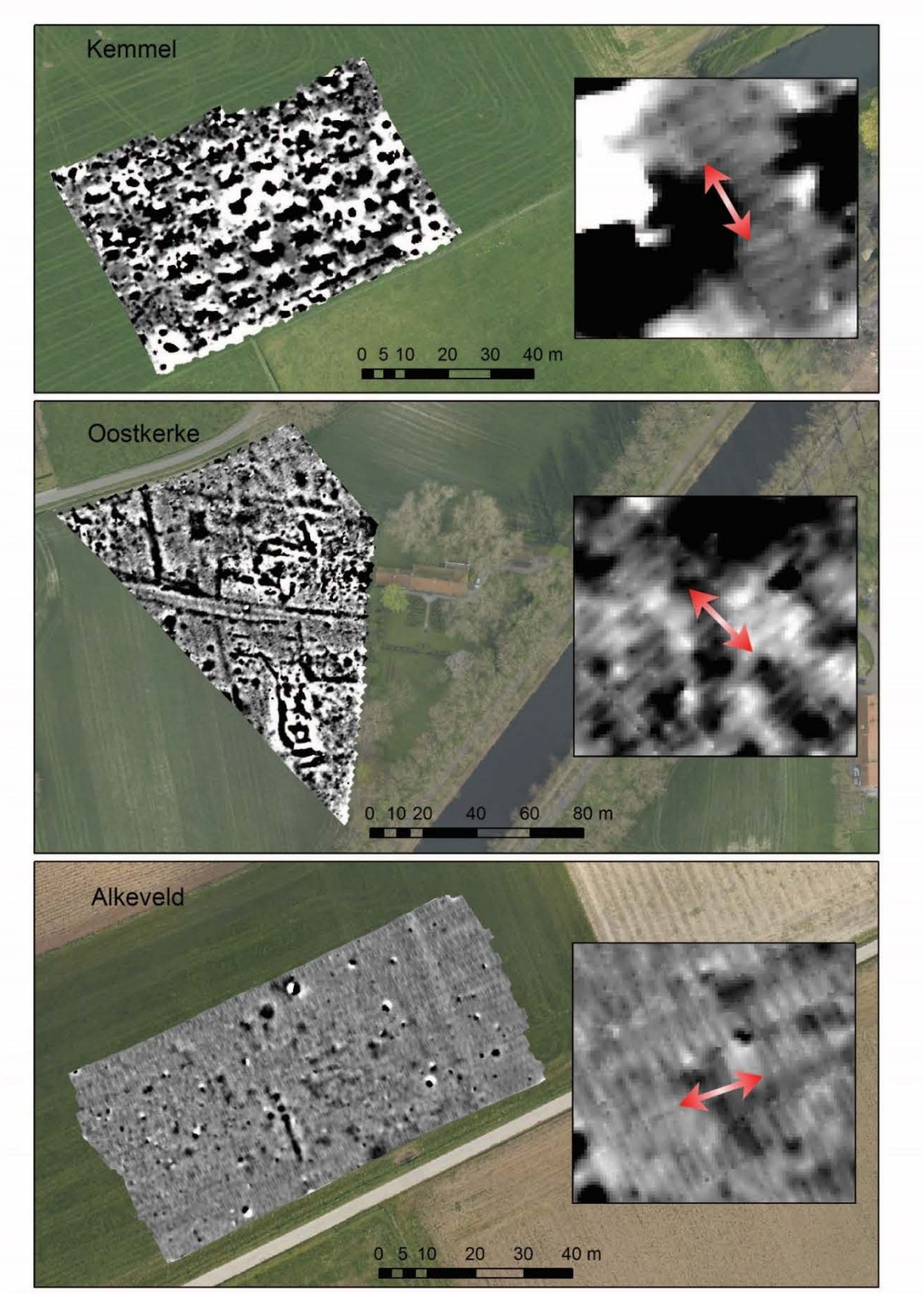



**Figure 3.8:** Display of the three magnetometer datasets with a greyscale set from -25 nT (white) to 25 nT (black). The direction of profiling is indicated by a double arrow on a zoomed in detail of the dataset where the noisy wave pattern is visible. (orthophoto: copyright AIV)

### 3.3.2 Noise identification

After interpolating FGM pushcart data, a repetitive wave pattern was detected with fluctuations around 5-10 nT perpendicular to the survey direction in every acquired dataset and in all separate probe measurements (figure 3.8). To isolate the cause of this noise pattern, two tests were conducted, aimed at assessing the influence of measurement drift and sensor tilt.

In a first test, stationary measurements were conducted with a fluxgate gradiometer probe at a fixed location (figure 3.9). The observed variations display a range smaller than 1 nT in field circumstances which corresponds with the sensor's stability in its technical sheet (Sensys, 2016). However, these small amplitude variations do not explain the repetitive noise pattern. If longer stationary recordings are considered (five minutes or more), drift over time becomes clearly visible. As such drift introduces low frequency trends in final data plots, this phenomenon can also be excluded as possible noise factor for the repetitive noise.

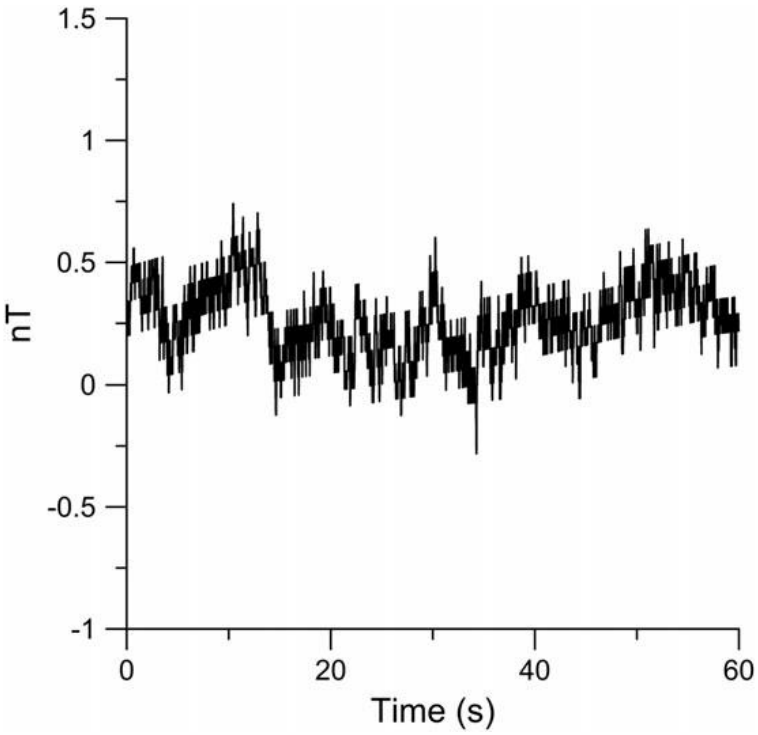



**Figure 3.9:** A 60 seconds FGM650 gradiometer stationary data example.

A second test was conducted with a sensor moving along one trajectory to test the effect of tilting on the signal acquisition. In the first measurement, a gradiometer was moved vertically in one direction. In the second measurement, a subtle tilting motion was introduced to the sensor (figure 3.10). These data show how sensor tilt results in noise with a similar range and sinusoidal pattern as observed in the field data (figure 3.8). A simplified representation of the cart carrier frame is shown in figure 3.11 with indication of the two relevant tilt axes (the vertical yaw axis does not influence the vertical sensor position and is therefore not taken into account). Axis 1 is orientated parallel to the direction of motion. Any roll around this axis is caused by the terrain's roughness and the absence of suspension on the cart wheels. Micro-relief causes the carrier frame to rotate and vibrate. The use of more than two wheels and/or suspension on the cart would give the system a better stability. The pitch around Axis 2 is caused by the operator movement (step frequency, walking speed, the ability to keep the sensor array stable, operator faults, etc.). This results in tilt noise as demonstrated in figure 3.10 and displayed in the datasets in figure 3.8.

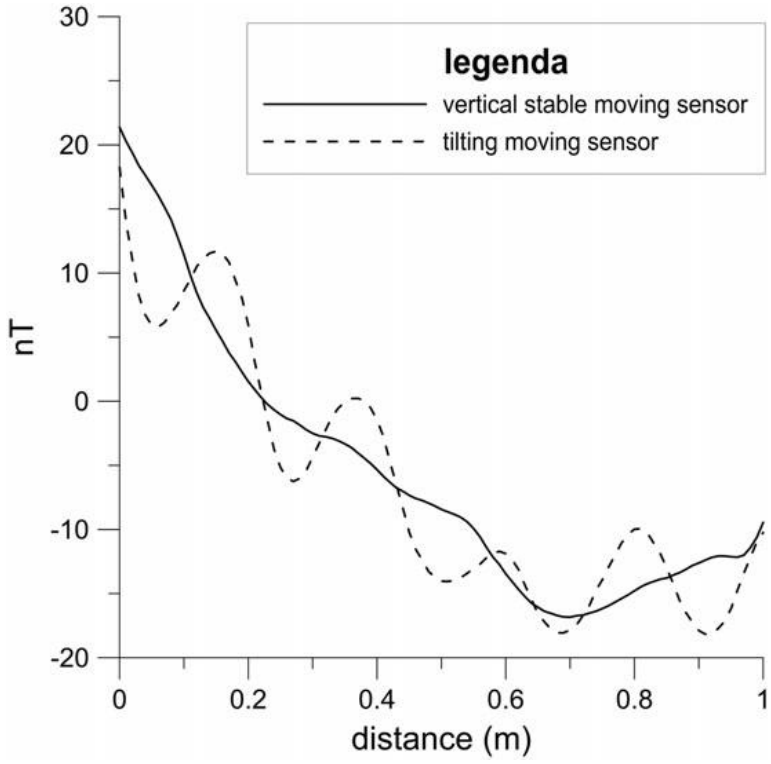



**Figure 3.10:** Gradiometer signals of a vertical stable moving sensor (full black line) and a subtle tilting moving sensor (dashed line) along the same trajectory.

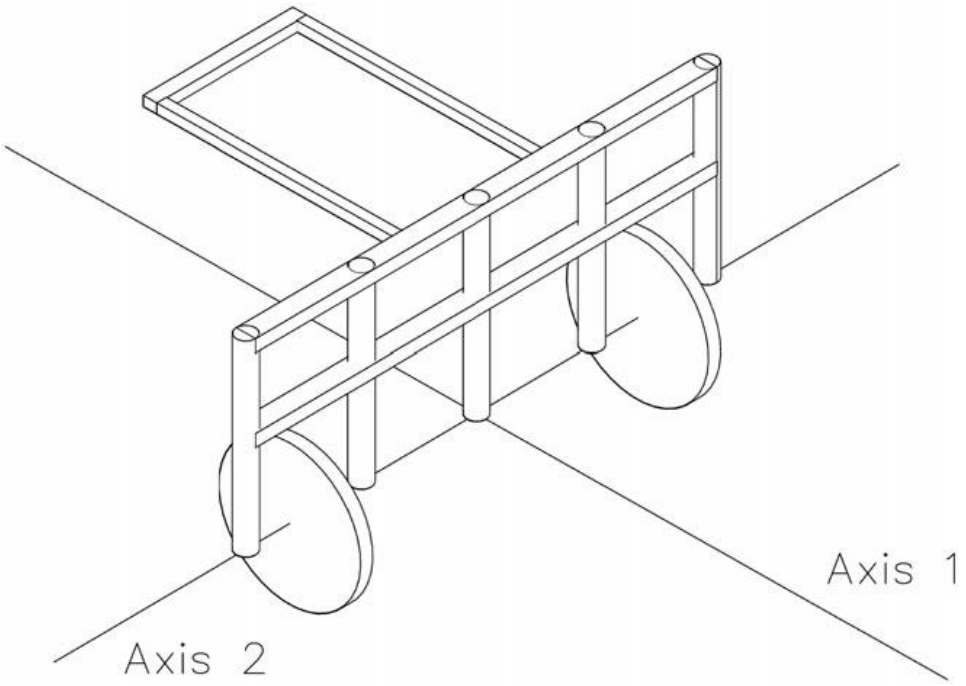



**Figure 3.11:** Schematic representation of the magnetometer pushcart with an indication of the tilt axes. Axis 1 aligns with the direction of movement while Axis 2 is perpendicular to Axis 1 at the height of the sensor array through the wheel basis.

### 3.3.3 Wavelet-based filtering procedure

#### *3.3.3.1 1D wavelet analysis*

Wavelet analysis is based on translations (~time/location) and dilations (~frequency/scale) of a predefined mother wavelet function $\psi(x)$ to divide a signal in components of different resolution respective to the applied scales of the mother wavelet (Daubechies, 1992). Original signals $(s_o)$ are divided into approximations $(a_j)$ and detail $(d_i)$ until a certain level $(j)$, whereby details contain the high-passed extraction and approximations the low-passed information for each decomposition level. It follows that the original signal can then be reconstructed by the summation of the obtained details and approximations as:

$$s_o = (\sum_{i=1}^{j} d_i) + a_j \qquad (3.1)$$

Selecting an appropriate mother wavelet is pivotal in any wavelet analysis, and highly dependent on the characteristics of the targeted signal. For analysing magnetometer data, Shen et al. (2008) and Tsivouraki and Tsokas (2007) proposed that Daubechies 2 (db2), Daubechies 4 (db4) and Coiflet 1 (coif1) wavelets (Härdle et al., 1998) are the most suited. After evaluating the efficiency of different wavelets to isolate tilt noise present in the test case datasets, the db2 and coif1 wavelets were deemed the most apt to drive the filtering procedure.

#### *3.3.3.2 Isolating tilt noise*

To compensate for the effect of tilt noise in data collected with mobile sensor arrays, a first step consists of considering measurements for each sensor probe separately. Next, the signal components of each data series are evaluated through the 1D discrete wavelet transform. The resultant details and approximations are interpolated to a resolution of 0.15 m. These grids are examined in a decomposition tree structure to determine at which scale the tilt pattern appears. After identifying decomposition details coinciding with the targeted noise pattern, these can be removed from the original signal. In figure 3.12, a decomposition tree, obtained by using a coif1 mother wavelet, is presented with part of the gridded Alkeveld dataset. Here, the tilt pattern is isolated in details $\mathrm{d}_4$ to $\mathrm{d}_6$. Consequently, removing these detail levels would reduce the influence of tilt noise of final data plots. Filtering out details of level 7 or higher, however, would introduce artefacts, i.e. data deformations in the direction of survey motion.

To evaluate the effect of removing the relevant detail levels, visual inspection along with the assessment of the relative signal energy loss ($\varepsilon_\mathrm{r}$) (Münch et al., 2009), i.e. the relative mean squared error between original and filtered signal can serve as a quick indicator for how strongly the wavelet filtering influences the overall data variation. Hereby, a combination of satisfactory removal of visible tilt noise and a low $\varepsilon_\mathrm{r}$ is pursued. Consequently, the mother wavelet that enables removing sensor tilt noise with the lowest energy loss $\varepsilon_\mathrm{r}$ is most apt for any wavelet based filter procedure targeting such interference. Transect-wise evaluation of filtering a low range (figure 3.13, left) and high range (figure 3.13, right) field dataset using coif1/db2/db4 mother wavelets, shows that:

- use of Daubechies mother wavelets (db2 & db4) introduces artefacts around strong anomalies (> 100 nT). The db2 wavelet is the least sensitive to this phenomenon, and can

therefore be considered the most suited to filter magnetometer data. When analysing the small data range example, too many dissimilarities with the original signal (amplitude underestimation and peak stretching) were introduced in the filtered data. This effect increases with large anomalies. In addition, the Daubechies wavelets also affect the spatial location of the detected objects (stretching and peak translation). Combined, these signal deformations are reflected in large relative energy losses ($\varepsilon_r$ db2 = 30.9% & 10.5%; $\varepsilon_r$ db4 = 16.8% & 34.9%).

- use of the Coiflet1-wavelet does not cause large artefacts around strong anomalies. In both data series, the Coiflet1 filtered data fits best to the original signal and produces the lowest relative energy losses ($\varepsilon_r$ = 3.4 & 4.4%). While some peaks are introduced due to the shape of the Coifet1-wavelet, this limited artefact creation is outweighed by the efficient tilt pattern filtering.

Based on these observations, the Coiflet1 mother wavelet was implemented in the processing procedure. However efficient in reconstruction the magnetometer signal, wavelet filtering adversely affects data quality where large peaks (e.g. >100 nT) are present (figure 3.13, right column). As the targeted tilt effect is dominant in the more narrow data range, isolating data within a predefined range ($\mathrm{rt}$) can help overcome the introduction of artefacts. Within these boundaries wavelet filtered data is used integrally. For data beyond these limits, the original signal is retained. Hereby, peak introduction and response over-/under estimation are successfully avoided (e.g. figure 3.13, right column, bottom graph). To prevent this method from introducing large data jumps at transition points, a threshold defining the allowed maximum difference ($\mathrm{d_{max}}$) is set between the original and filtered signal. When this difference is greater than $\mathrm{d_{max}}$, the original data is again retained. For the presented datasets, $\mathrm{rt}$ was set at ±50 nT, while a $\mathrm{d_{max}}$ of 20 nT was allowed between the original and filtered signal. These applied adjustments result in a much lower $\varepsilon_r$ which indicates that tilt noise removal has only a relatively small effect on the total signal energy content. The threshold effect is particularly apparent in the high range dataset (figure 3.13, bottom, right), where only 0.003% of energy loss occurs after wavelet filtering when only the $\mathrm{rt}$-range is targeted. The remaining data points fall beyond the set threshold range and are therefore not addressed by the filtering algorithm.

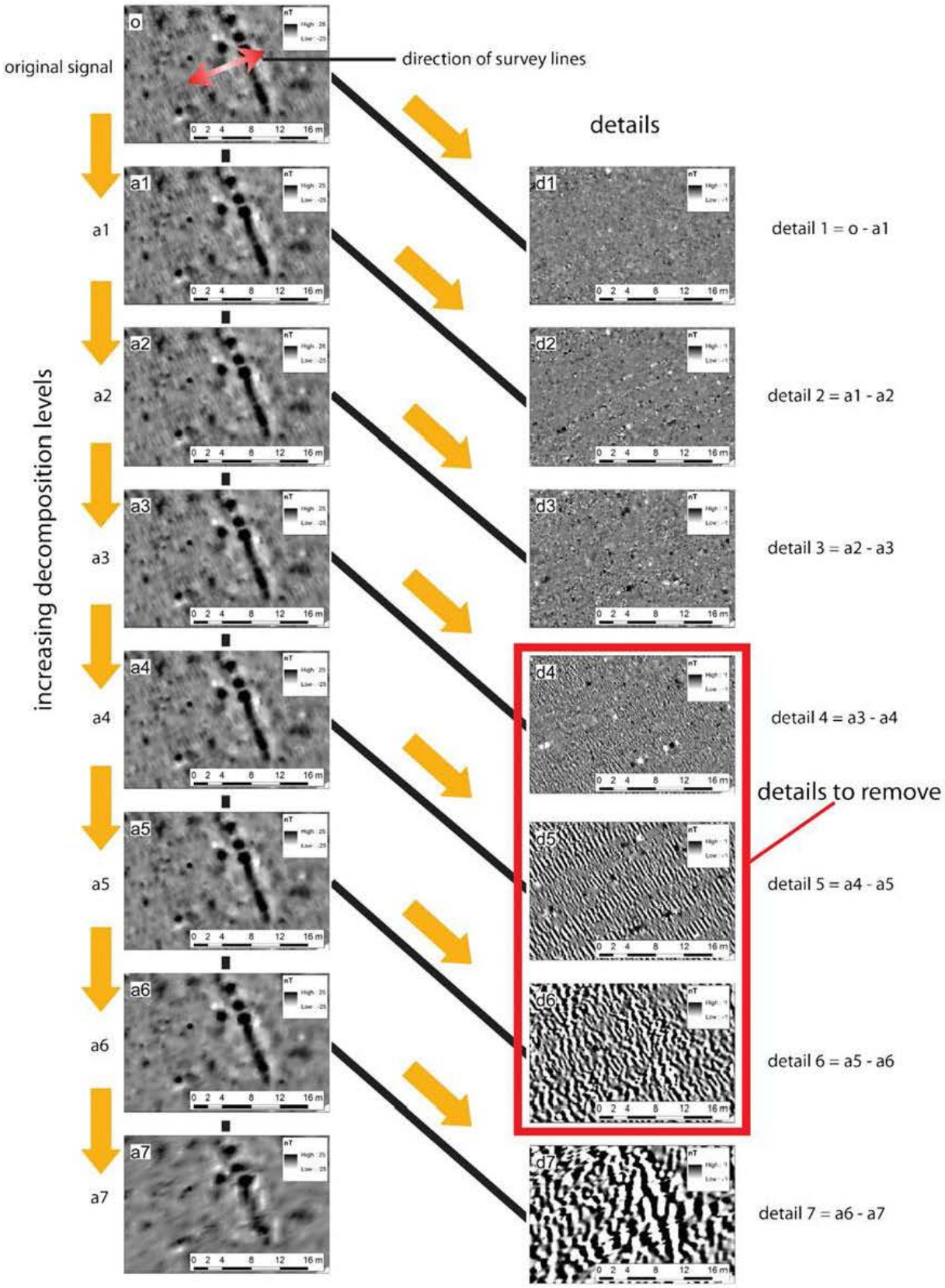



**Figure 3.12:** Interpolated details and approximations from a part of the Alkeveld dataset. For this wavelet decomposition, the Coiflet 1 wavelet is applied from level 1 to 7. The details with the perpendicular striping pattern are selected.

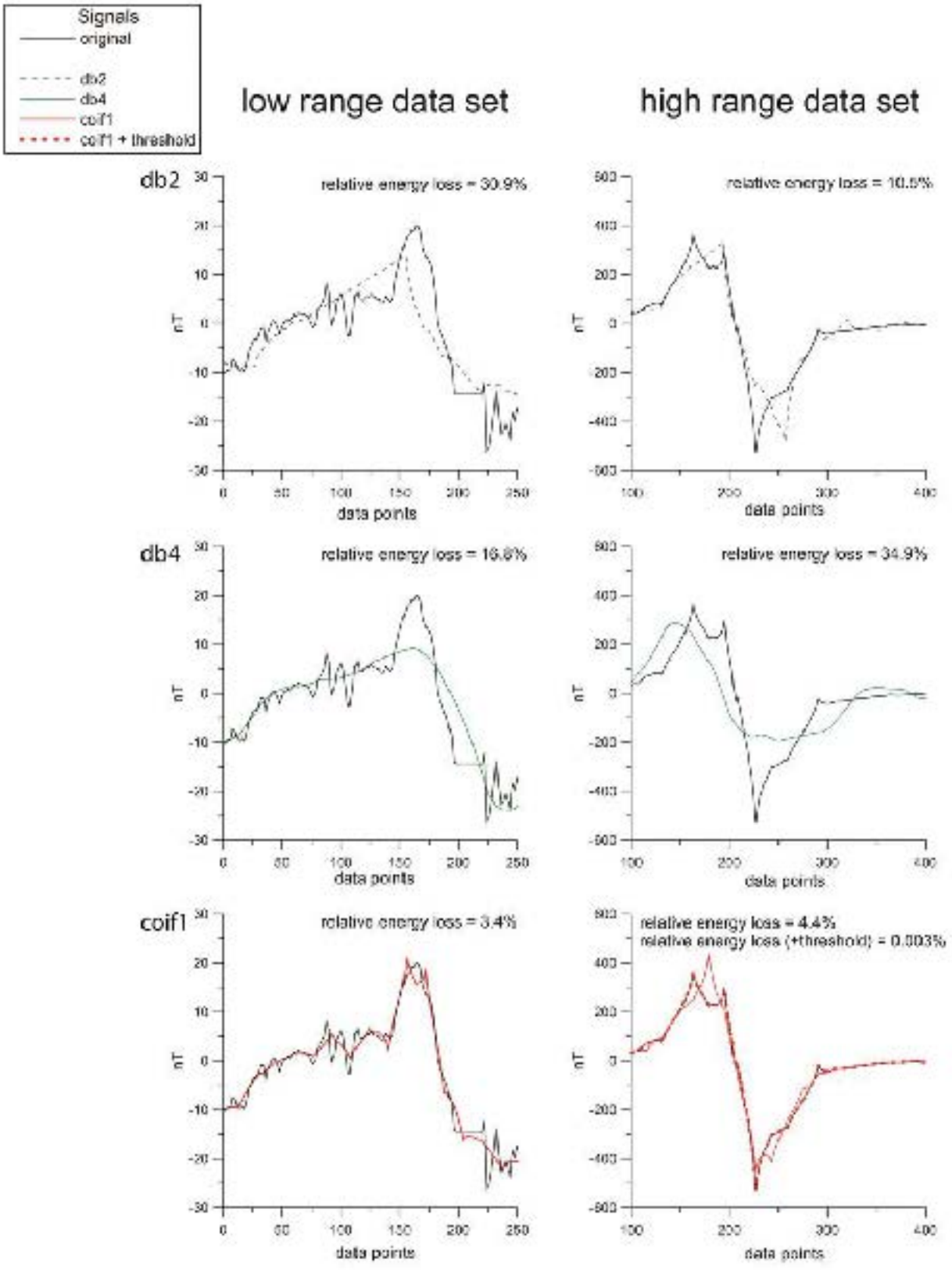



**Figure 3.13.** Display of two samples of denoised signals and their relative energy loss $\varepsilon_r$, visualised for three types of analysing mother wavelets: Daubechies 2 (db2), Daubechies 4 (db4) and Coiflet 1 (coif1). The two example evaluation datasets represent a low range and a high range data set to assess the results in two conditions.

#### *3.3.3.3 Result evaluation*

The original and filtered datasets of the three prospected areas are gridded at a resolution of 0.15 m and partially visualised in figure 3.14 & 3.15 based on the processing choices made in the previous sections. A grey scale with boundaries of + and - 25 nT is chosen to compare the results in a similar manner.

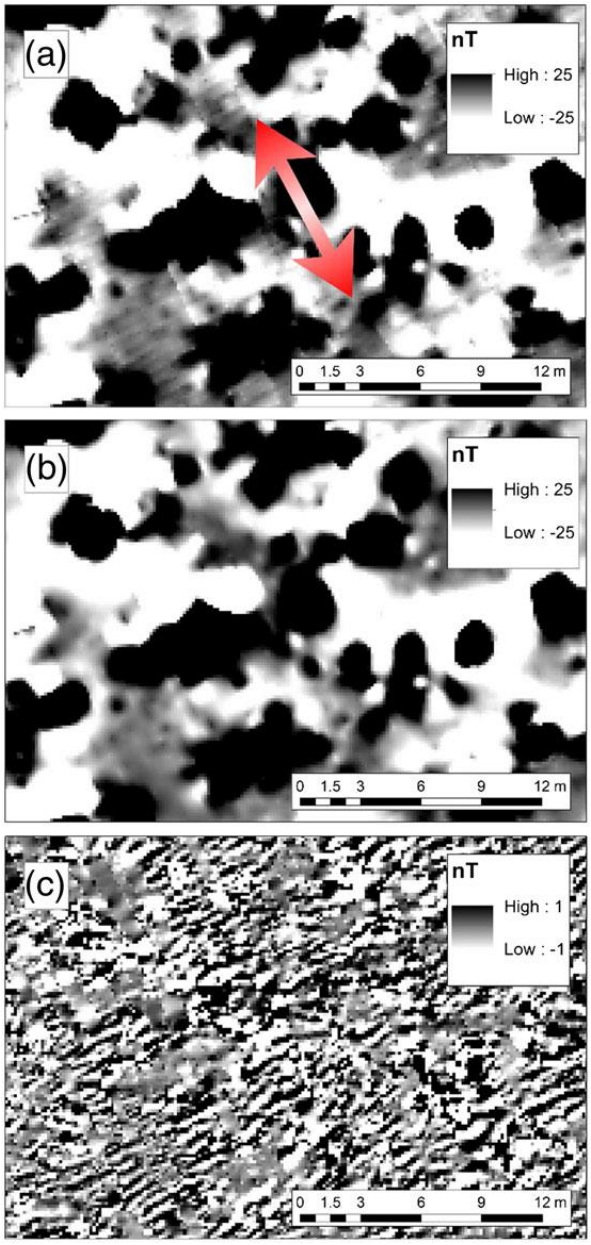



**Figure 3.14:** A comparison between the original (a) and filtered (b) interpolated signal and the residuals (c) between (a) and (b) of the Kemmel dataset. The double arrow indicates the survey line direction.

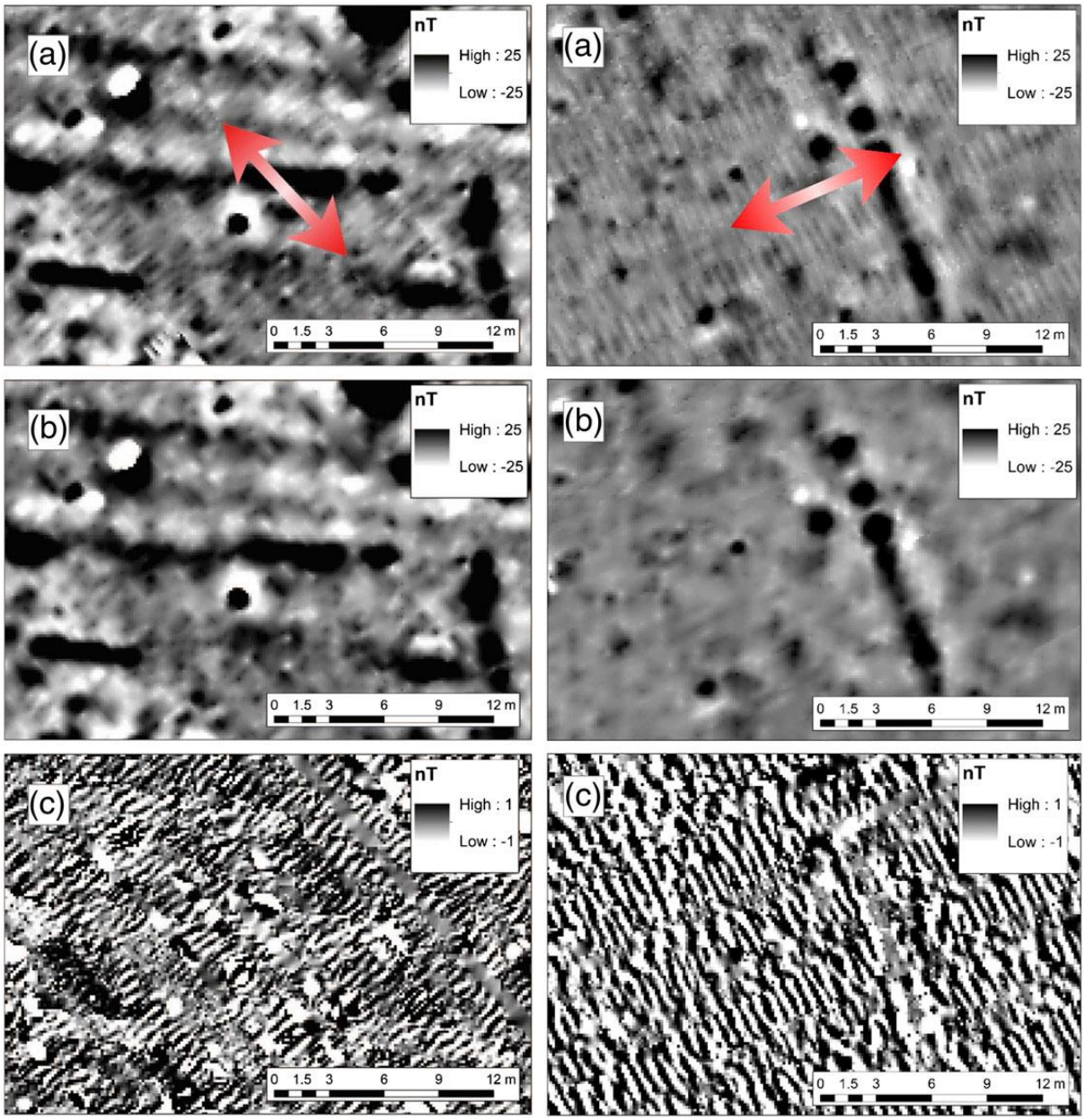



**Figure 3.15:** A comparison between the original (a) and filtered (b) interpolated signal and the residuals (c) between (a) and (b) of the Oostkerke (left) and Alkeveld (right) dataset. The double arrow indicates the survey line direction.

On all investigated datasets, the applied procedure allowed to reduce the effect of tilt noise to an extent where it could no longer be discerned clearly in the final data plots. When the filtering residuals are examined (figure 3.14c & 3.15c) the targeted repetitive tilt pattern is isolated with little added variation included. While high amplitude anomalies do influence the filtering result, and, particularly for the Oostkerke dataset (figure 3.15 left), affect the tilt pattern residuals (figure 3.15c), this effect remains limited and without observable consequences in the filtered

data plot (figure 3.14b and 3.15b). As can be expected, the effect of wavelet filtering is most apparent in the narrow range dataset (Alkeveld, figure 3.15 right), resulting in a practically tilt noise free result.

To evaluate the processing quality of wavelet filtering with traditional applied techniques, a visual comparison with a 2D Gaussian (3 X 3 kernel, 5 passes) and a moving average filtered dataset (3 X 3 kernel, 5 passes) was made. This is shown in figure 3.16, applied on the Alkeveld dataset. This figure demonstrates that the chosen filter parameters mask the tilt errors sufficient. If looked just at the tilt-induced noise, the suggested wavelet procedure produces the best result in terms of image sharpness. Despite that, other effects such as pixel outliers and traces from which the direction of motion can be distracted, remain present. To deal with this problems, 2D low-pass filters are more suitable. Also the phenomenon of peak stretching is visible, resulting in anomaly deformation in the direction of motion. This phenomenon is absent in the moving average or Gaussian low pass filtered data. In practice, a combination of the wavelet based filtering, outlier detection algorithms and 2D smoothing techniques will be applied on the same dataset to process different kinds of noise.

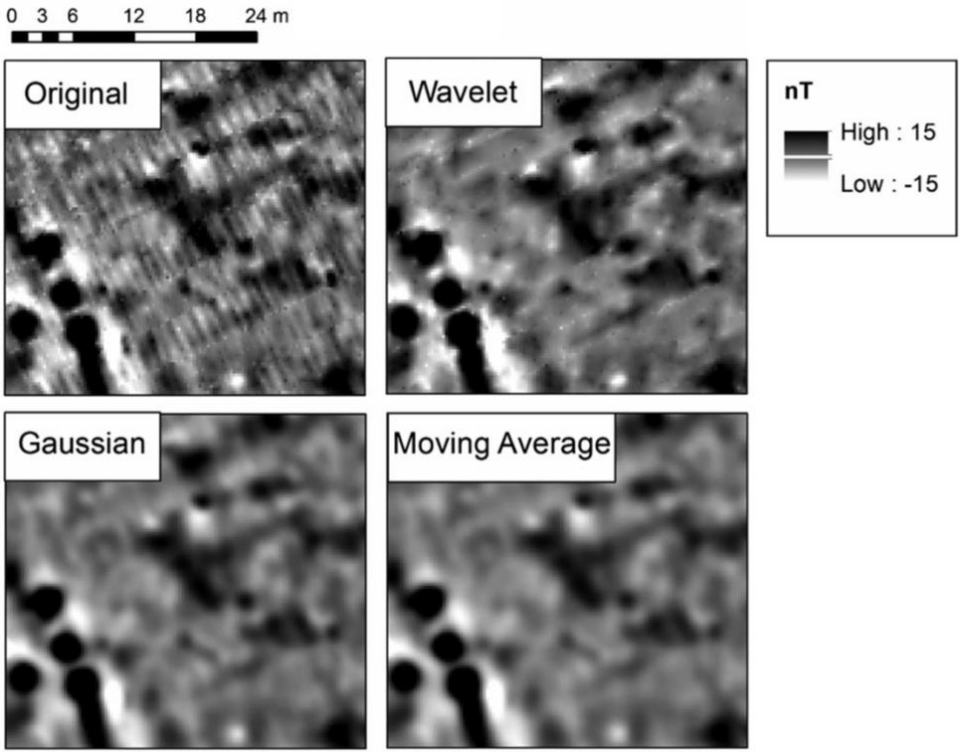



**Figure 3.16:** Focus window on a part of the Alkeveld dataset for the original dataset, a 1D wavelet based filtered result, a 2D Gaussian low pass filtered result (five passes of a 3 × 3 kernel) and a moving average filtered dataset (five passes of a 3 × 3 kernel).

### *3.3.3.4 Other applications*

While processing several datasets, two extra applications of this wavelet based filtering procedure were found. During one survey with a manual pushcart, one of the two operators had steel tips in his boots. This caused a similar wave pattern like the tilt noise induced in the data (figure 3.17 A). Based on the proposed procedure, it was possible to filter out this pattern (figure 3.17 B). Because of the filtering of this influence pattern, the two WW1 trenches in this survey were easier to identify. A second application of this method is the removal of the effect of a high voltage cable from the data signal. While modelling the details, one data plot contained fluctuations related to the trajectory of the cable (figure 3.18). Because the strong influence of the metal objects in the soil, the measurements are evaluated on a +/- 100 nT greyscale. In addition, many anomalies with values higher that the grey scale borders are located under the cable trajectory. That is why the cable influence in not noticeable in this survey. If this site would contain more subtle anomalies, the grey scale boundaries could be narrowed down and this pattern would appear.

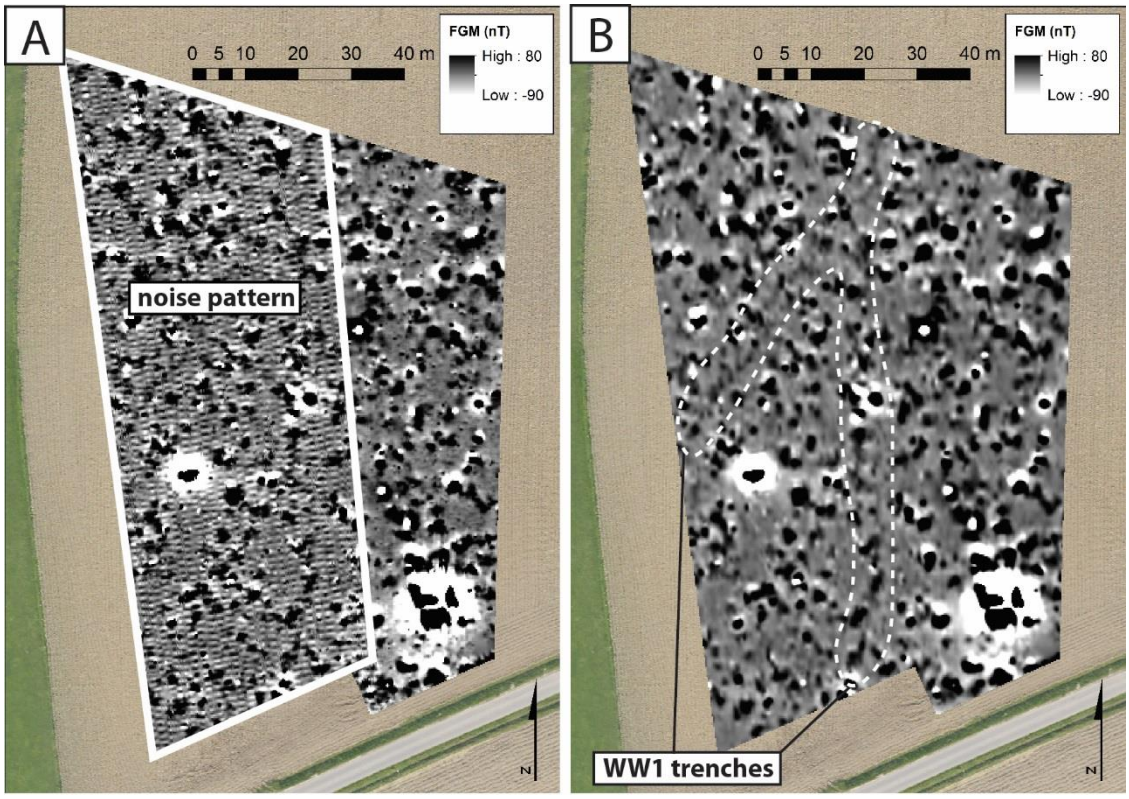



**Figure 3.17:** A WW1 battlefield FGM survey, containing an error pattern caused by steel tips in the operator's boots (A). In image (B), the noise pattern is filtered out by applying the wavelet-based procedure. Two WW1 trenches can now clearly be distinguished. (orthophoto: copyright AIV)

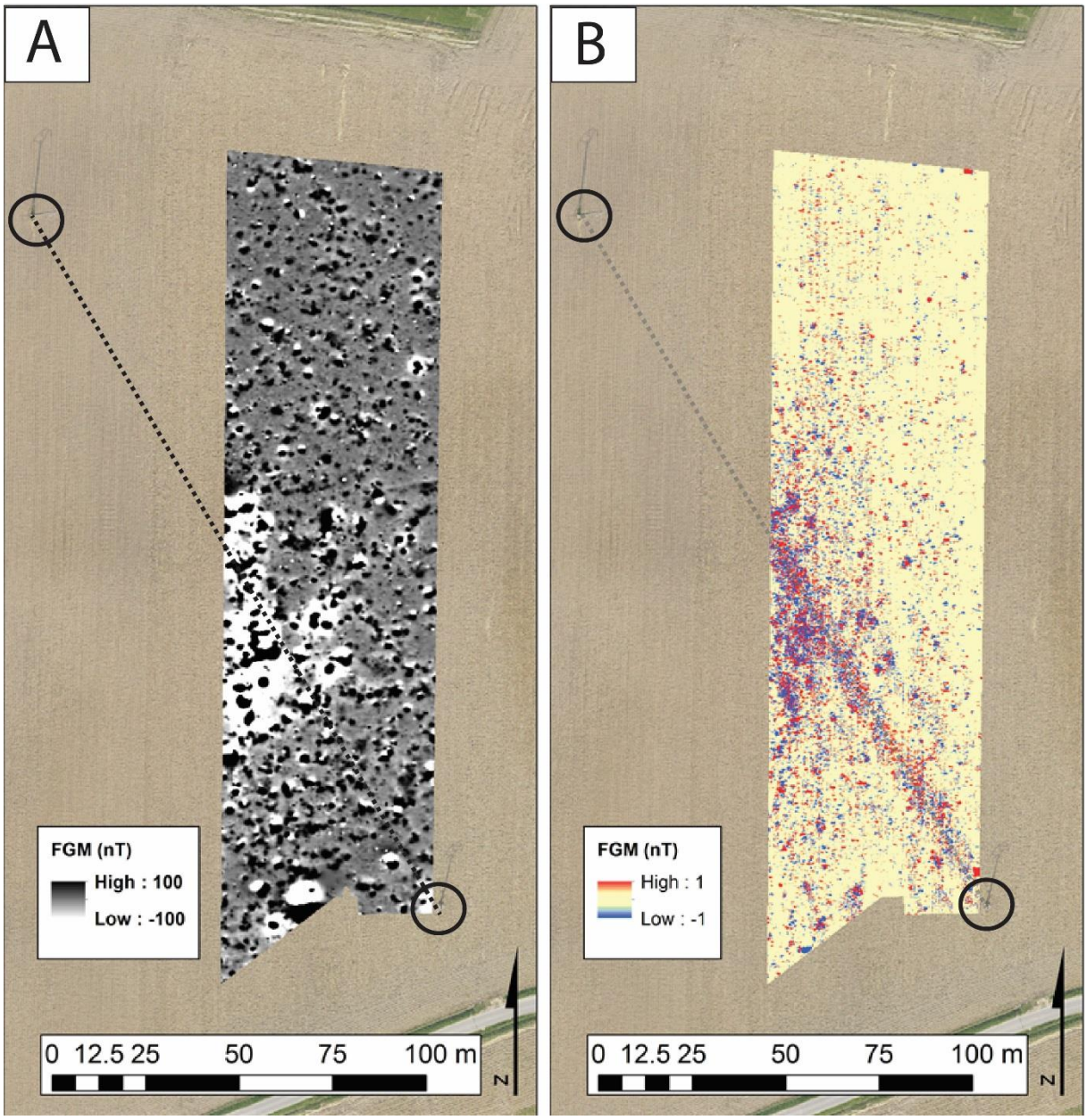



**Figure 3.18:** A FGM survey was recorded on a former WW1 battlefield under a crossing high voltage power cable (A). The trajectory of cable is indicated by a dashed line. In two detail data layers in the wavelet-filtering procedure, the influence of this cable is noticed. One of the two data layers is displayed in image (B). (orthophoto: copyright AIV)

## 3.4 Conclusions

For each proposed problem (need for data levelling, overlap and tilt issues) in the FGM data, an adapted solution was proposed. These solutions are successful in improving the interpolated result before data gridding. Tackling data issues before image creation is important because errors can be targeted more precise. Smoothing filters in traditional applied image processing tackle multiple source errors at once.

The procedure of median traversing is an inevitable step which produces a zero-point calibration between sensors. The median deviation is different per sensor and often a few times the data range. After this procedure, data is still difficult to interpret. This is caused by sensor drift over time. For the FGM650 series gradiometers, this drift covers an experimentally found range of 20 nT in three hours of survey time. Median levelling per survey line (= median traversing) is successful in levelling the data into a coherent and interpretable image. The above-described procedures are able to visualise the influences and errors onto the gradiometers readings in the FGM setup. Even when this filtering is included in processing software, visualising these errors can be useful to guide the survey strategy.

The processing code to remove overlapping and too close recorded interfering data patterns is successful in cleaning the dataset and producing an improved interpolated image. The art of filtering is to focus as close as possible onto the error without removing too much significant data. According to visual interpreted data, this is not the case except for some minor issues in very whimsical survey patterns. Badly recorded survey lines should be avoided in the first place.

The sensor tilt found in the data is related to different external factors including the terrain's micro-relief, motion characteristics and operating specifications. The signature of the repetitive tilt pattern in the direction of profiling enables applying a 1D discrete wavelet transformation directly on the gradiometer signal to subsequently reduce the influence of motion induced noise. By identifying tilt patterns in the wavelet decomposition levels, noise related details could be selected and removed from the original signal. As the proposed filtering procedure relies heavily on the selected mother wavelet, using a poorly suited wavelet function can adversely affect the shape and positioning of magnetic anomalies. The Coiflet 1 mother wavelet was demonstrated to be the most suited for isolating tilt noise in FGM datasets, reducing the risk of artefact introduction. In addition, there has been shown how tilt noise can

be targeted more precisely by defining threshold values that ascertain filtering only the narrow data range, resulting in a more adaptive and performant filtering procedure. If needed, other types of unwanted data variations can subsequently be filtered through more adaptive processing procedures. While the proposed filtering allows achieving a tilt-noise free result, the mechanical origin of such interference should be equally addressed. Improving survey conditions by using suspended cart systems or through the integration of real-time axis compensation will partly relieve the burden on subsequent filtering procedures. As the use of both manually and vehicle operated cart-systems in archaeological prospecting increases, the need for integrated and adaptive means of overcoming associated data issues grows.

The three above-mentioned processing steps were necessary to achieve good quality datasets. Other algorithms such as despiking and outlier filters, data subsampling, image smoothing, etc. are preferable but not determinant for the image quality. If necessary, these filters can be added to the processing flow. To summarise the proposed procedure in this chapter, a processing scheme is suggested in figure 3.19. This scheme starts with median levelling of the raw data strings (2). At this level, optional data filters can be applied to remove outliers. Important is that each interim result is evaluated as a data string and a 2D gridded result. Next, the spatial sensor paths are analysed to detect and remove sensor path interference. When sensor tilt is dominant, optional 1D wavelet based filtering can be applied before final image gridding (4). As interpolation technique for raw data points in MATLAB, the nearest neighbour principle is the best option to achieve a satisfactory result. If some undesirable errors still show up, extra image smoothing can be applied (e.g. Gaussian median filtering). This proposed processing flow (figure 3.19) should provide guidance in delivering good quality datasets for archaeological purposes. Processing steps such as median levelling and survey line overlap removal can easily adapted for other geophysical survey techniques, which was done for ER and TD-EMI processing in this thesis.

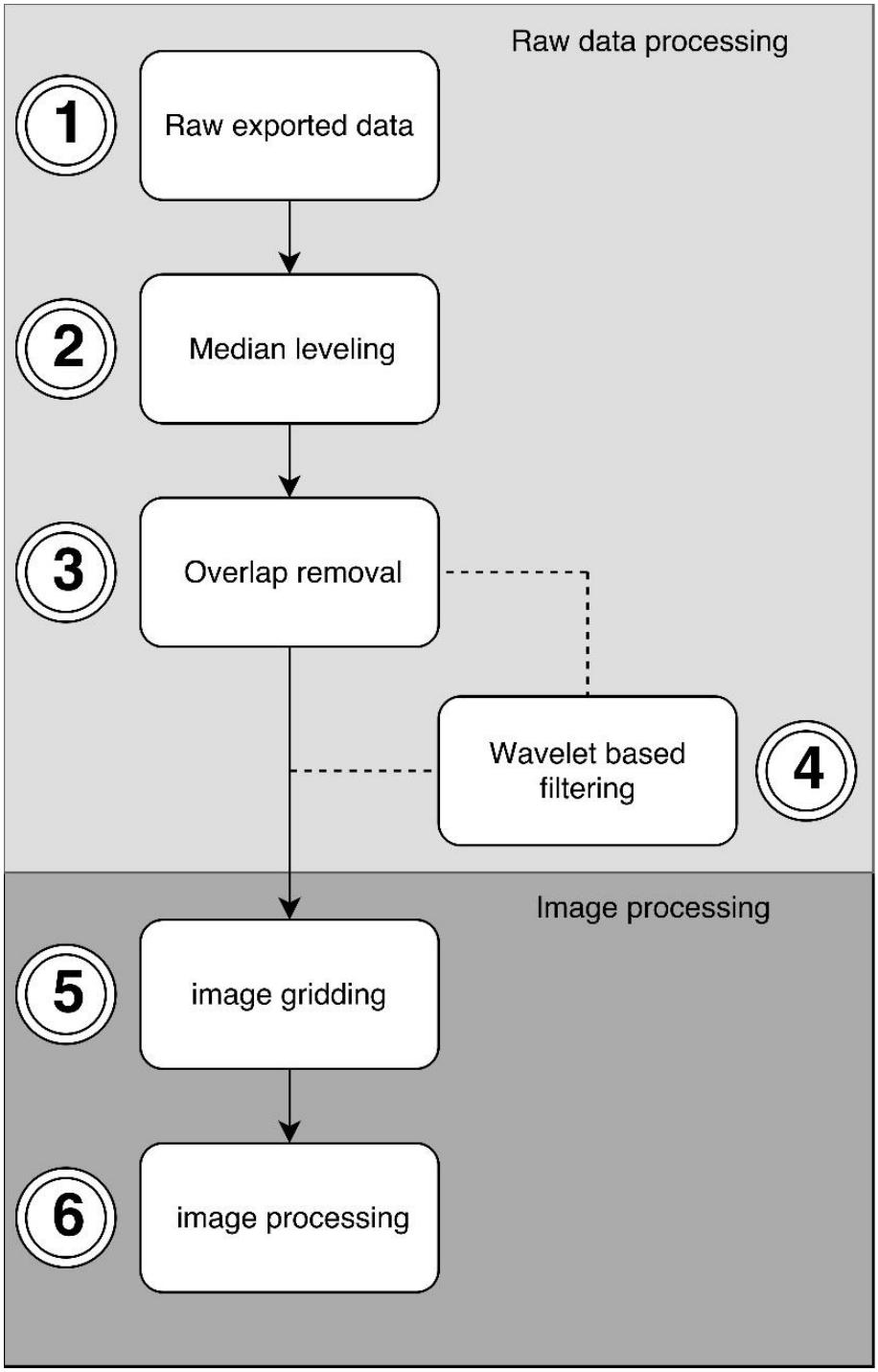



**Figure 3.19:** Suggested FGM processing diagram: Raw data processing includes median levelling (2), overlap removal (3) and optional wavelet based filtering (4); Image processing includes gridding options (interpolation parameters) and traditional applied smoothing filters (6).

# Chapter 4

## Evaluation of soil sensing techniques to characterise buried features in WW1 conflict areas

This chapter was partially modified from:

> **Note, N.**, Saey, T., Gheyle, W., Stichelbaut, B., Van den Berghe, H., Bourgeois, J., Van Eetvelde, V., Van Meirvenne, M. (2018). Evaluation of Fluxgate Magnetometry and Electromagnetic Induction Surveys for Subsurface Characterization of Archaeological Features in World War One Battlefields. *Geoarchaeology*, published online.

## 4.1 Introduction

ER, EMI (frequency and time domain), magnetometry (mainly FGM, but also alkali vapour instruments etc.) and GPR are popular geophysical prospecting techniques (English Heritage, 2008; Gaffney and Gater, 2010; Schmidt et al., 2015). This chapter evaluates the potential of these techniques to prospect non-invasively the WW1 conflict areas in Belgium. Only the ER devices are not completely 'non-invasive' as the sensors must penetrate the ground. In addition, this technique is almost completely insensitive to (fine) metal objects. Because of the importance of 'non-invasiveness' (avoiding contact with buried unexploded ordnances (UXOs), no damage to agricultural ground and the archaeological heritage) and the ability to detect metal objects, GPR, fluxgate magnetometry (FGM) and FD-EMI are deployed in a first selecting phase to draw up an inventory of WW1 relicts within the former Western Front in Belgium (battlefield, no man's land and hinterland on both sides).

During preliminary surveys for this research, the suitability of FGM and FD-EMI for prospecting was demonstrated (Masters and Stichelbaut, 2009; Saey et al., 2016a). GPR, on the other hand, revealed far fewer archaeological features because the clayey and wet soils attenuated the signal (Doolittle et al., 2007). Several surveys (N = 9, see appendix 2.4) confirmed the lack of success when using GPR in the western part of Belgium. Therefore, FGM and FD-EMI will be evaluated in a first section on their potential to: (1) detect a wide range of buried WW1 archaeological features; (2) characterise different feature types; and (3) localise buried metal objects (UXOs, metal debris, construction materials, etc.). Caesium magnetometers are kept out this evaluation because their higher sensitivity (Aspinall et al., 2008) is unnecessary in the highly magnetic disturbed soils near the frontlines. The experiences with the GPR technique and a mobile ER-device will be covered in separate sections to motivate their inferior applicability in the study area. In addition, small loop TD-EMI as mainstream technique for UXO-detection and characterisation will be compared to FD-EMI and FGM for its suitability for archaeological prospection.

## 4.2 FD-EMI / FGM evaluation

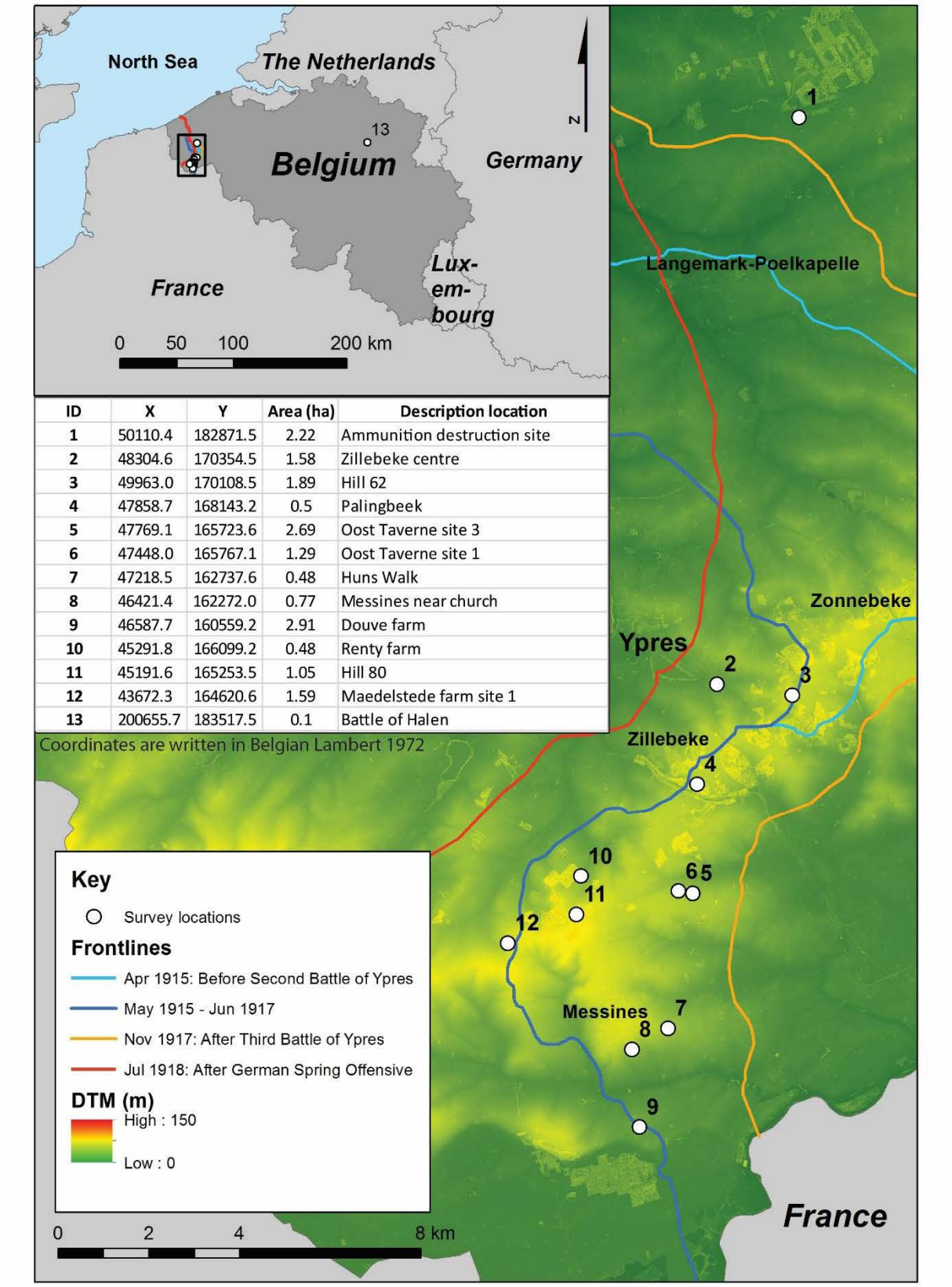
The FD-EMI / FGM study is based on the framework of the large-scale EMI investigation applied for this thesis near the former Western Front in Belgium (+/-240 ha, see chapter 2 section 2.4.3). In locations with interesting anomalies, additional targeted FGM surveys were carried out to compare both techniques.

### 4.2.1 Study area

For this evaluation, an area totalling 17.5 hectares was measured using both techniques at 12 different locations at the Western Front in Belgium. An extra dataset (see figure 4.1 ID 13) was added from the eastern part of Belgium, to include a WW1 case that is not related to the Western Front but to activities in the earlier stage of the war (the advance of German troops in the summer of 1914). All survey locations are shown in figure 4.1, including additional survey details and a location ID.

If the first 2.5 - 3 meters of the soil profile are considered, similar conditions are found for each site. All survey locations on the former Western Front are situated along the Westrozebeke Ridge. This elevated area rises just south of the city of Dixmude (around 20 m above sea level), and goes east around the town of Ypres then south to the West-Flemish hills (end ridge: 60-80 m above sea level, peak: Kemmel Hill, 156 m). These heights comprise Paniselian sands and clays, which dominate the relatively flat surrounding area (see figure 4.1, yellow on the colour scale of the height model). On top of this ridge, the soil profile consists of loam or sandy loam around 1 - 1.5 m deep covering layers of sand and clay underneath. Both Allied and German armies preferred these heights because the soil was better suited to trenching and tunnelling than the wet clay plain near Ypres (0.5 - 3 m loam-sand with clay underneath) and provided strategic advantages. This elevated terrain not only provided a topographical advantage but also better drainage and lower groundwater conditions. The profile of the site in the eastern part of Belgium is based on a loamy sand top layer (0 – 2 m) with homogeneous sand underneath (2 - 3 m). This profile information was obtained by using self-performed on-site augering descriptions, completed with information from the Flanders soil database (http://www.dov.vlaanderen.be, 2017). Because the first three meters of the soil matrix at the Western Front contain variations in clay, sand and loam layers (and moisture), contrasts in FD-EMI electrical conductivity will provide additional useful information alongside the magnetic

output of FGM and FD-EMI. These variations are limited to the sandy and more homogenous soil in the east-Belgian site.




| ID | X | Y | Area (ha) | Description location |
|---|---|---|---|---|
| 1 | 50110.4 | 182871.5 | 2.22 | Ammunition destruction site |
| 2 | 48304.6 | 170354.5 | 1.58 | Zillebeke centre |
| 3 | 49963.0 | 170108.5 | 1.89 | Hill 62 |
| 4 | 47858.7 | 168143.2 | 0.5 | Palingbeek |
| 5 | 47769.1 | 165723.6 | 2.69 | Oost Taverne site 3 |
| 6 | 47448.0 | 165767.1 | 1.29 | Oost Taverne site 1 |
| 7 | 47218.5 | 162737.6 | 0.48 | Huns Walk |
| 8 | 46421.4 | 162272.0 | 0.77 | Messines near church |
| 9 | 46587.7 | 160559.2 | 2.91 | Douve farm |
| 10 | 45291.8 | 166099.2 | 0.48 | Renty farm |
| 11 | 45191.6 | 165253.5 | 1.05 | Hill 80 |
| 12 | 43672.3 | 164620.6 | 1.59 | Maedelstede farm site 1 |
| 13 | 200655.7 | 183517.5 | 0.1 | Battle of Halen |

**Figure 4.1:** Localisation of the scanned zones, including the four main phases of the frontline and details on the surveyed fields. (DTM: copyright AIV)

### 4.2.2 Feature type identification

In this section, the most common basic features, such as trenches, shell holes and mine craters, are evaluated (as these features reflect the main types of battles undertaken in WWI). In addition, the ability to detect communication cables and former building traces is discussed. Besides these omnipresent Western Front features, two specific cases are highlighted to demonstrate and evaluate FGM and FD-EMI on WW1 structures. In the first example, foundations of a military camp consisting of semi-buried huts are surveyed and characterised prior to an archaeological excavation. In the second case, both techniques were tested to detect the precise location of horse mass grave from a one-day battle in early 1914 in the east of Belgium (ID 13). Here, the effect of intense and long-term shelling is absent.

#### *4.2.2.1 Trenches*

For the detection of trenches using FD-EMI or FGM instruments, the function and duration of use of the trench during warfare must be considered. Firing trenches, for example, are often more strongly built than communication trenches (Storey, 2014; Gheyle et al., 2016b), and many types of trenches are used by the different fighting parties. Also general trends in the use of trench construction materials between nationalities were documented (Bull, 2014). As an example, German trenches were known to be better equipped (electricity, toilet) and stronger built (using concrete and timber) because they were convinced that entrenching would go on for a longer period than the British soldiers (Bull, 2014). The British trenches were (in a first phase) more hastily dug and considered as something temporary. These trenches differed in general from others by consisting out of sand bags (breastworks) and corrugated iron sheets. Although this general classification between nationalities could be an indicator to consider, the reality is much more complex and is depending on multiple not well estimable factors. This was also experienced in testing the relation of this indicator to the detection differences in trench systems. According to the duration of use, structures with a long period of service might depict stronger signatures in the scans than hastily dug and quickly abandoned or destroyed trenches. This is similar for metal reinforced trenches and intact structures that were used in the post-war period to dump military waste (Debaeke, 2013). Trenches built at the end of the war have a better chance of being preserved, as indicated by information derived from time-series analysis of aerial photographs. The next significant

parameter is the density of metal debris in the soil. This background distortion has a major effect on magnetic deviations recorded with FGM. A high metal debris density caused by heavy shelling can mask the underlying weaker anomalies. Note et al. (2018) showed that these metal densities can be derived from shelling densities seen on aerial photographs. By identifying these preconditions, we can determine which survey technique is the most favourable. A trench and its environment can be considered in two extreme conditions: with or without metal objects. In this comparison (see table 4.1), the conditions are listed to evaluate both FD-EMI and FGM. In practice, the intermediate state of those conditions will appear. Four examples of trenches can be seen in figure 4.2, and each example was examined on the actual scan result (type of trench, iron-clutter density background, period of construction). Each survey example is graded per technique (good/acceptable/weak/bad) to judge the quality of the result. In example A (figure 4.2), a communication trench from the last year of the war was surveyed. Because of the low density of iron clutter, good results should be achieved with both FD-EMI and FGM. This prediction was confirmed by the scans. Example D (figure 4.2) shows a communication trench dating from a year before the Battle of Messines (June 1917). In this example, there are no metal objects within the structure itself, but a high density of iron clutter was detected in the soil composition. In this case, identification of the structure is difficult and FD-EMI is the preferred ideal technique because of the contrasts in $EC_a$ values. Examples B and C are two firing trenches with metal structural parts. In both examples, a better delineation could be performed by employing FD-EMI, because of the masking effect of the prominent anomalies caused by buried metal. The main difference between the two examples is that in B, there are strong anomalies in the close vicinity of the trench that prohibit a precise delineation of the structure with FGM, while in C, this effect is weaker and a good localisation of the firing trench can be performed.

**Table 4.1:** Guidance table based on metal parameters concerning the trench contents and surroundings (soil condition) to obtain the preferred technique to achieve the best result. A quotation is given per condition for each technique, ranging from well suited (++) to bad result (--) with intermediate assessments of good (+), average (0) and weak (-).

| Situation | FD-EMI | FGM |
|---|---|---|
| Metal-free trench with low metal-scatter content in subsoil | ++ | ++ |
| Metal-free trench with high metal-scatter content in subsoil | + | -- |
| Metal-filled trench with low metal-scatter content in subsoil | + | + or 0 |
| Metal-filled trench with high metal-scatter content in subsoil | + | - |

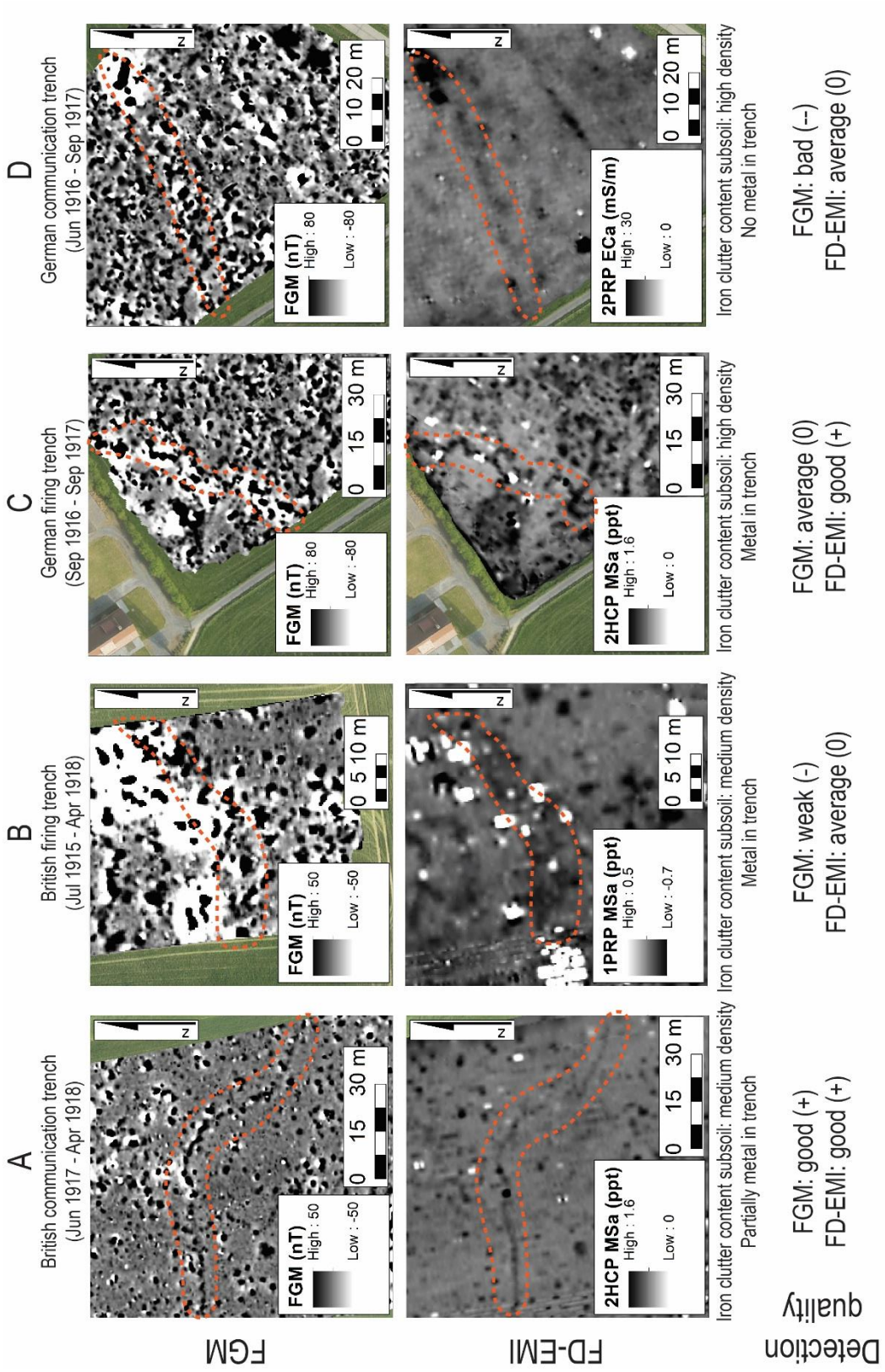



**Figure 4.2:** Four examples of trenches surveyed using both FD-EMI and FGM, containing different properties: (A) British communication trench (June 1917 – April 1918); (B) British firing trench (July 1915 – April 1918); (C) German firing trench (September 1916 – September 1917); (D) German communication trench (June 1916 – September 1917). (orthophoto: copyright AIV)

### *4.2.2.2 Communication cables*

In most surveys, one type of linear feature is only detected by FD-EMI: communication cables. These cables are often made of copper which, in its pure state, cannot be detected by magnetometry (figure 4.3 A). A typical FD-EMI response for a communication cable can be seen in figure 4.4. In the HCP $EC_a$ configuration, the cable is seen as a 'glow-worm' signature (figure 4.3 C, positive border values with negative centre values), while a 'fishbone' structure is found in the PRP $EC_a$ response (figure 4.3 B, due to the irregular shape of the PRP response and the zigzagging survey lines). These features are often found in trenches, but they can also follow a random path between trenches. If the cable ditch is not freshly dug or the cable is lying on the surface when the photograph is taken, this trajectory is often missed in remote-sensing archaeology. A camouflaged trench was found in the 'Messines near church site' (ID 8) by detecting a communication cable with FD-EMI (the FGM data showed no traces). This pointed to the advantages of FD-EMI surveys when these kinds of structures are missed by remote-sensing archaeology or FGM surveys.

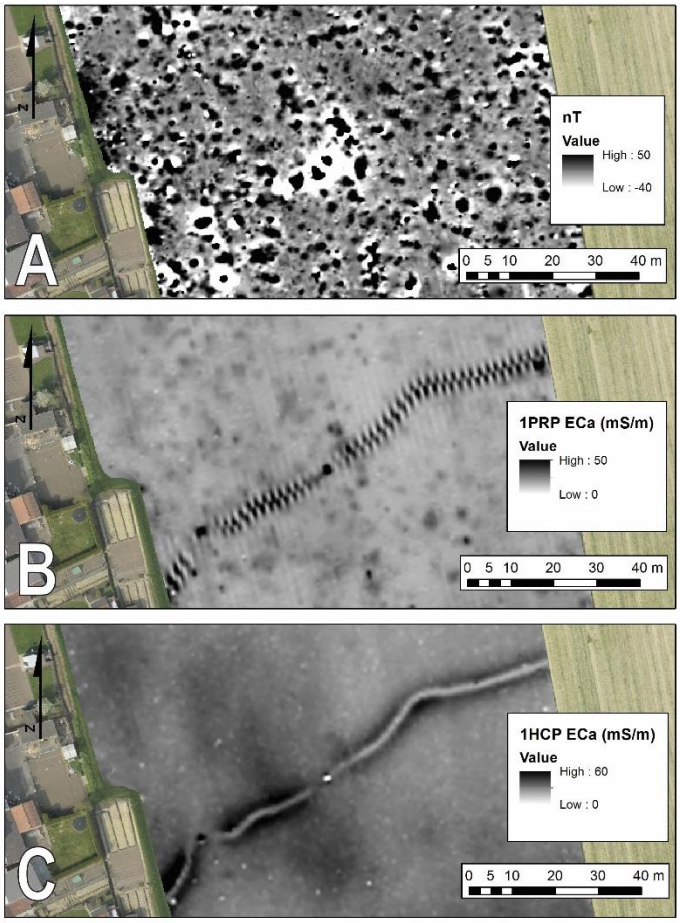



**Figure 4.3:** FGM (A) and FD-EMI measurements (B & C) of a communication cable, carried out at the Zillebeke centre site (ID 2). (orthophoto: copyright AIV)

### *4.2.2.3 Destroyed buildings*

For destroyed buildings (not rebuilt after the war), there are two ways of detecting building remains. In the first case, the foundations are mainly intact and include compacted and magnetic materials (bricks, concrete). In these conditions, both EMI and magnetometry allow the foundations to be localised. In the second case, either the building and foundations were destroyed or there were no substantial foundations. The EMI 1HCP $MS_a$ data layer shows an interesting property: a trace of destruction by artillery is included in this layer (figure 4.4), visualised as a spot of magnetic materials contrasting in an area of +/- 20 - 30 m around the building location. For FGM, this is often not possible due to the omnipresence of ferromagnetic clutter.

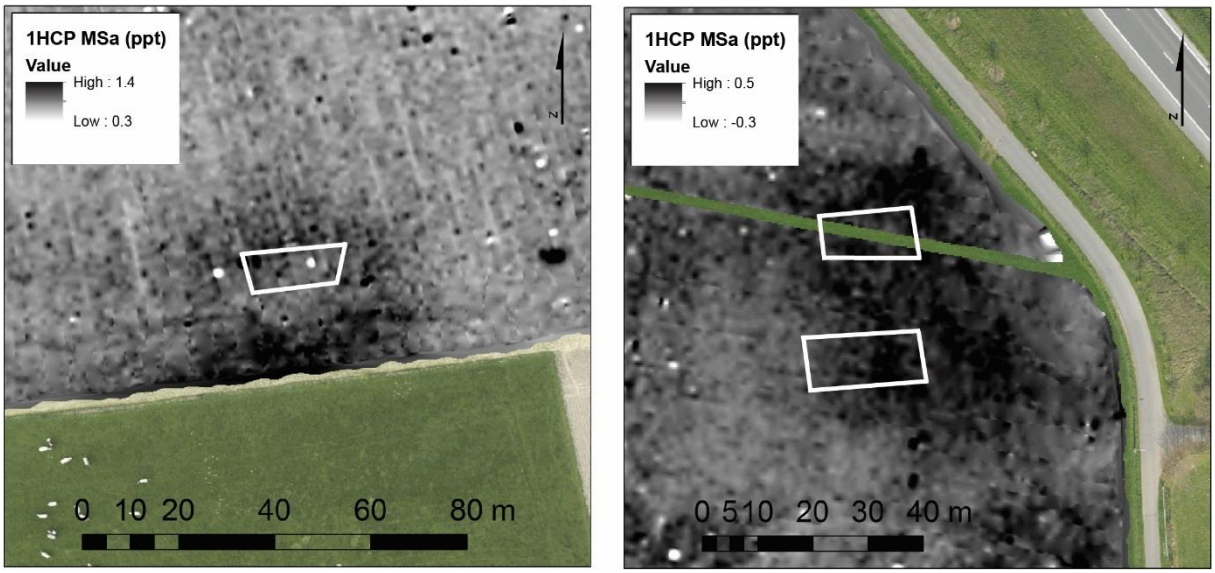



**Figure 4.4:** Two surveyed locations including a magnetic contrasting area around the former building locations (polygons), indicating destruction by artillery fire. (orthophoto: copyright AIV)

### *4.2.2.4 Shell holes and mine craters*

After 100 years, shell holes (caused by artillery) and mine craters (the result of underground war) are still visible as scars in the soil. By looking at the EMI $EC_a$ data layers, separate shell holes and mine craters can be distinguished, whereas FGM does not have the ability to discriminate between the individual craters and other magnetic deviations. Instead of detecting the actual crater, the magnetic impact on the soil (metal fragments, burned soil) is mapped by this passive technique. In the survey results, craters give the best signature in the EMI 1PRP

$EC_a$ and 2PRP $EC_a$ data layers. These anomalies can easily be classified as soil disturbances in the FD-EMI data (Saey et al., 2016b, see chapter 5). Both mine craters and shell holes are displayed in figure 4.6 in which image A and C show a British mine crater in the German 1917 frontlines near Hill 62 (ID 3). In the FD-EMI scan, a circular spot with greater $EC_a$ was detected, including some smaller strong anomalies in the crater (metal objects). In the FGM survey, metal objects at the crater location are dominant anomalies with large lateral dimensions, masking the subtle signature of mixed soil by bombturbation (Hupy and Schaetzl, 2006). Similar signatures can be seen for shell craters. Figures 4.6 B and 4.6 D show a cluster of craters.

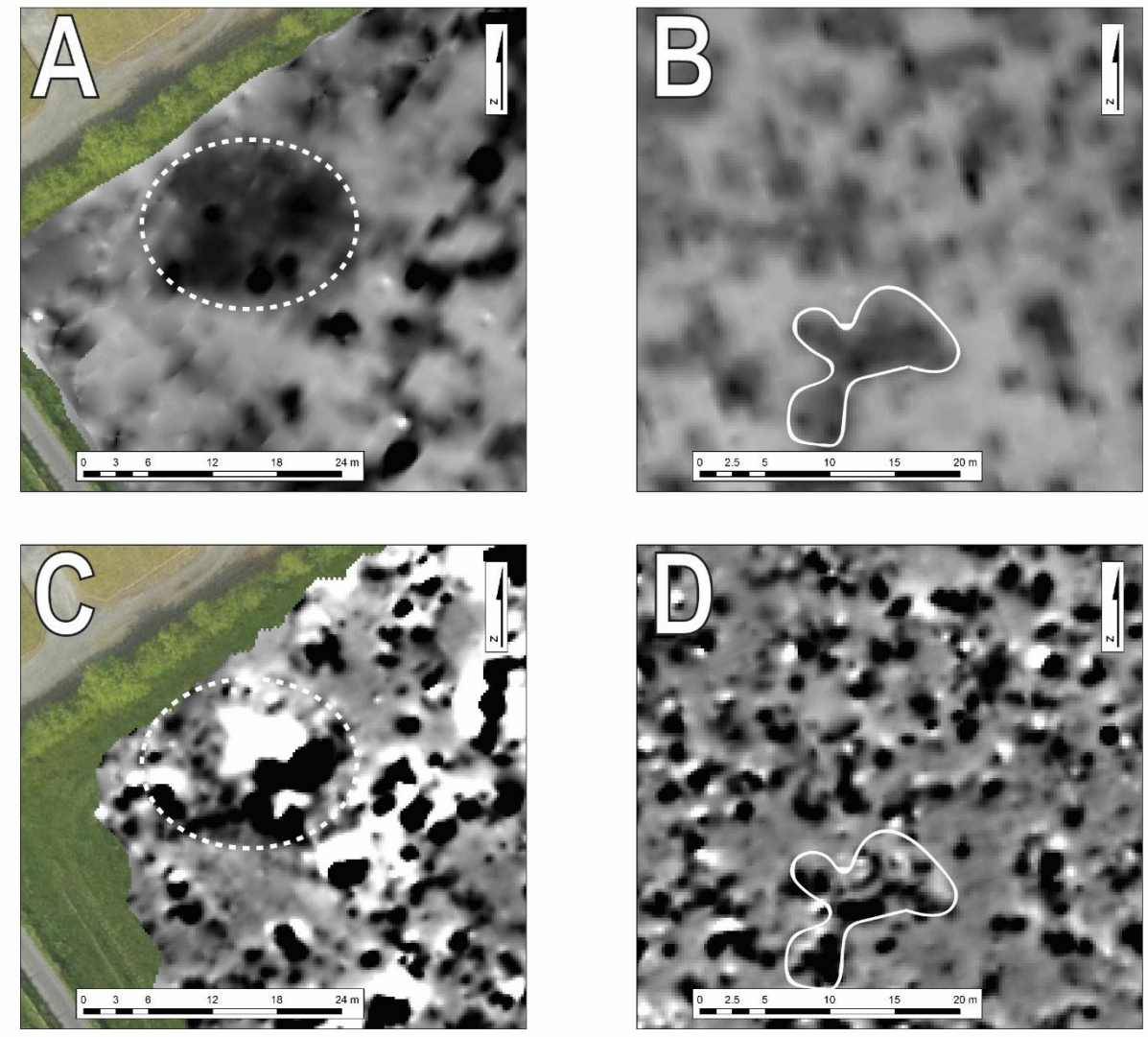



**Figure 4.5:** Two locations surveyed by using FD-EMI and FGM, including a mine explosion (A & C) and shell craters (B & D): (A) mine crater detected by EMI and seen in the 1PRP $EC_a$ data layer; (B) merging shell craters seen in the EMI 1PRP $EC_a$ data layer; (C) mine crater detected by FGM; (C) merging shell craters detected by FGM. (orthophoto: copyright AIV)

#### *4.2.2.5 Case 1: Characterisation of a British-Australian barrack camp*

In the spring of 2015, an exploratory FD-EMI survey discovered the foundations of what later appeared to be a WW1 barrack camp. This regular structure comprises 30 small rectangular shapes (6 by 5 rectangles, measuring 4 by 7 m each) and an enveloping structure (40 m by 60 m). An oblique, low-altitude aerial photograph from September 1918 (figure 4.6 A) shows the camp after destruction by the German Spring Offensive. At the end of 1917, this complex was erected in the former no-man's-land between the Allied and German frontlines. In preparation for characterising this camp with trial trenching, the barrack structure was scanned again with FD-EMI but at a substantially higher resolution (with a line spacing of 0.7 m). The site was also surveyed using FGM (sensor spacing 0.5 m). From the results seen in figure 4.6 B and C), the camp's shape and structure are clearly visible. In both surveys, the enveloping line (ditch) was detected. In the EMI interpolated data, this line was more continuous compared to the FGM scan. Both scans indicate magnetic barrack foundations, which after excavation, were seen to originate in general from brick floors. In addition, the effect of the fence or ditch in the south of the surveyed area is less distinct in the EMI scan. The same is true for the iron anomalies in the soil masking the underlying camp structure within the FGM data. Based on the completeness and clarity of the image, the FD-EMI scan results were chosen to define the location of two trial trenches. These trenches cut the site from north to south and from east to west, going over the first, eastern column of barrack foundations and over the second row of barracks from the north. At these locations, scan results showed the most interesting (metallic) anomalies that potentially could be used to identify the camp. The EMI survey is also used to guide the excavators towards possible buried UXOs. Metal object intensity (Saey et al., 2011) and depth discrimination (Saey et al., 2011 and 2016b) were performed to localise the possible position of the retrieved buried metal objects. The near-surface soil disturbances (Saey et al., 2016b) within the EMI $EC_a$ data allow for the identification of shell craters and waste pits. These waste pits prove archaeologically interesting because it may be possible to retrieve information about the way of life of the people who inhabited the barracks (food, waste, personal objects…). The scan results appeared ideal to guide the efficient archaeological excavation.

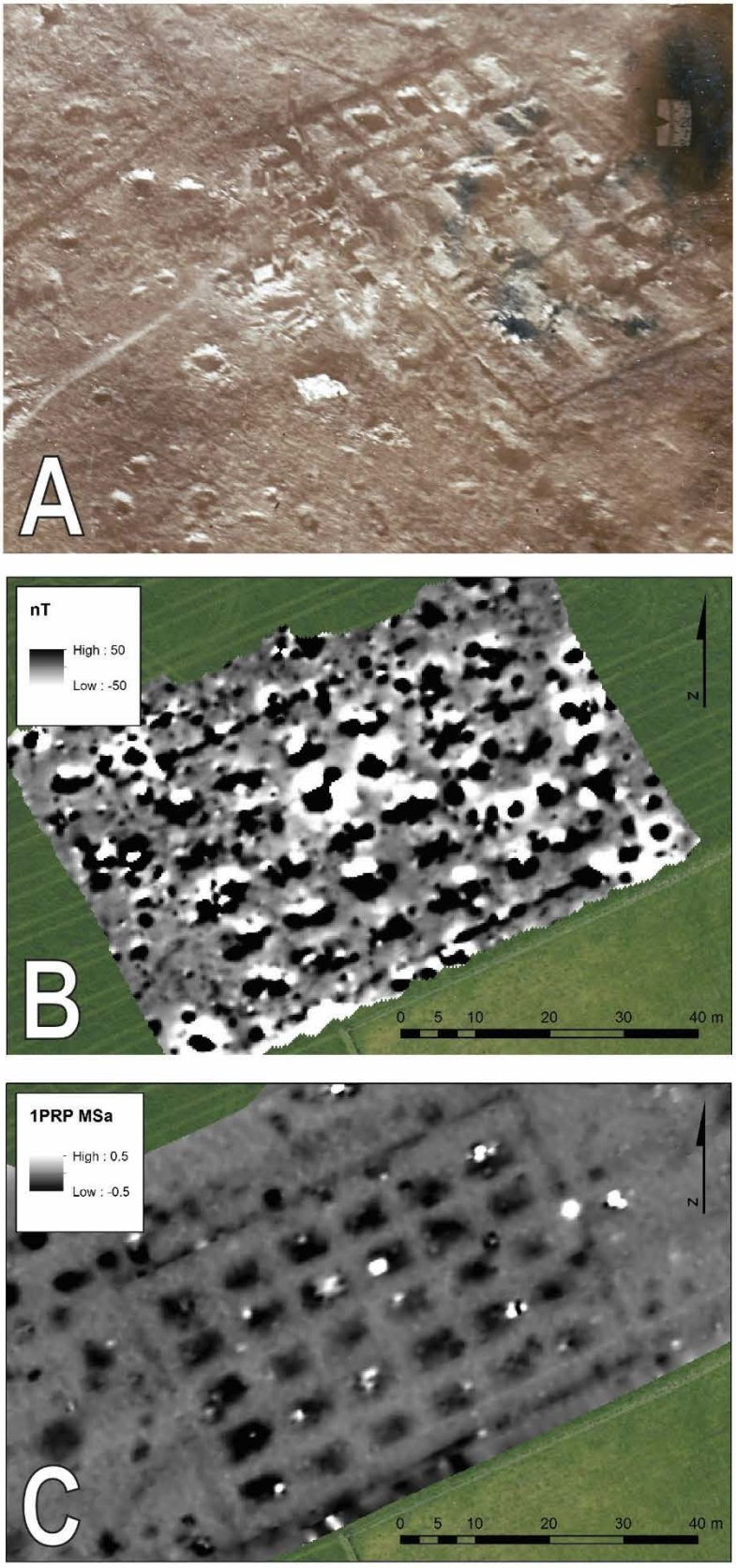



**Figure 4.6:** A WW1 barrack camp detected using three techniques: (A) an oblique aerial photograph taken in September 1918 (IFFM collection); (B) an FGM survey conducted in March 2015; (C) a magnetic data layer from a FD-EMI survey conducted in September 2014. (orthophoto: copyright AIV)

#### *4.2.2.6 Case 2: Localisation of a horse mass grave*

On 12 August 1914, during the German advance on Belgian territory, the Belgian soldiers faced a German cavalry attack with drawn sabres in the Battle of Halen (east Belgium), the so-called Battle of the Silver Helmets. The Belgian lieutenant general in charge had only two Hotchkiss machine guns at his disposal (compared to the German light infantry's 12 Maxim machine guns) and placed his regiments of lancers, cyclists, guides and artillery in tactical positions, with the knowledge of the terrain to his advantage. The German forces decided to attack with a traditional cavalry charge, but the horses and riders had no defence against the Belgian gunfire. This battle made it clear that traditional warfare had no answer to the newer technologies. Symbolically, this was considered as one of the last cavalry charges in Western Europe. After this battle, the 400 killed horses had to be buried in the area. From one picture (figure 4.7 A), it is possible to derive an approximate location of one horse grave. In this picture, which was taken near the hamlet of Zelk, people can be seen digging a horse mass grave perpendicular to the Staatsbaan road. Based on this information, it was possible to pinpoint the exact field (an area of 4 ha) where the grave in figure 4.7 A was dug. A FD-EMI scan was taken with an inline distance of 1.2 m. Based on this scan, a linear structure perpendicular to the road could be identified, measuring 2-3 m by 45 m. This anomaly was seen in both $EC_a$ and $MS_a$ responses. Based on the anomaly location, a few augerings were made and animal bone and mixed ground were found in the soil samples, giving a positive identification of the location of the mass grave seen in figure 4.7 A. For a further comparison, this anomaly was surveyed using FGM (figure 4.7 B). By comparing both images, it is possible to conclude that the magnetometer survey is sharper (due to sensor spacing) and has greater contrasts than the FD-EMI datasets. Within these loamy-sand soils and without the strong influences of metal objects similar to those on the Western Front, the magnetometer greyscale can be narrowed down to indicate weaker anomalies. The delineation of the anomaly and its subdivisions can be performed more precisely with this technique. A less favourable effect is the strong magnetic influence of the road and its surrounding elements, which blank out part of the structure (figure 4.7 B). Although this influence is weaker or even absent in the EMI data, FGM surveys can be considered equally as efficient or even more so for this purpose and within these soil conditions. To conclude, FD-EMI has proved its significant potential as a robust prospection technique, while a small-scale magnetometer survey provides a more detailed image and confirmation of this archaeologically interesting structure.

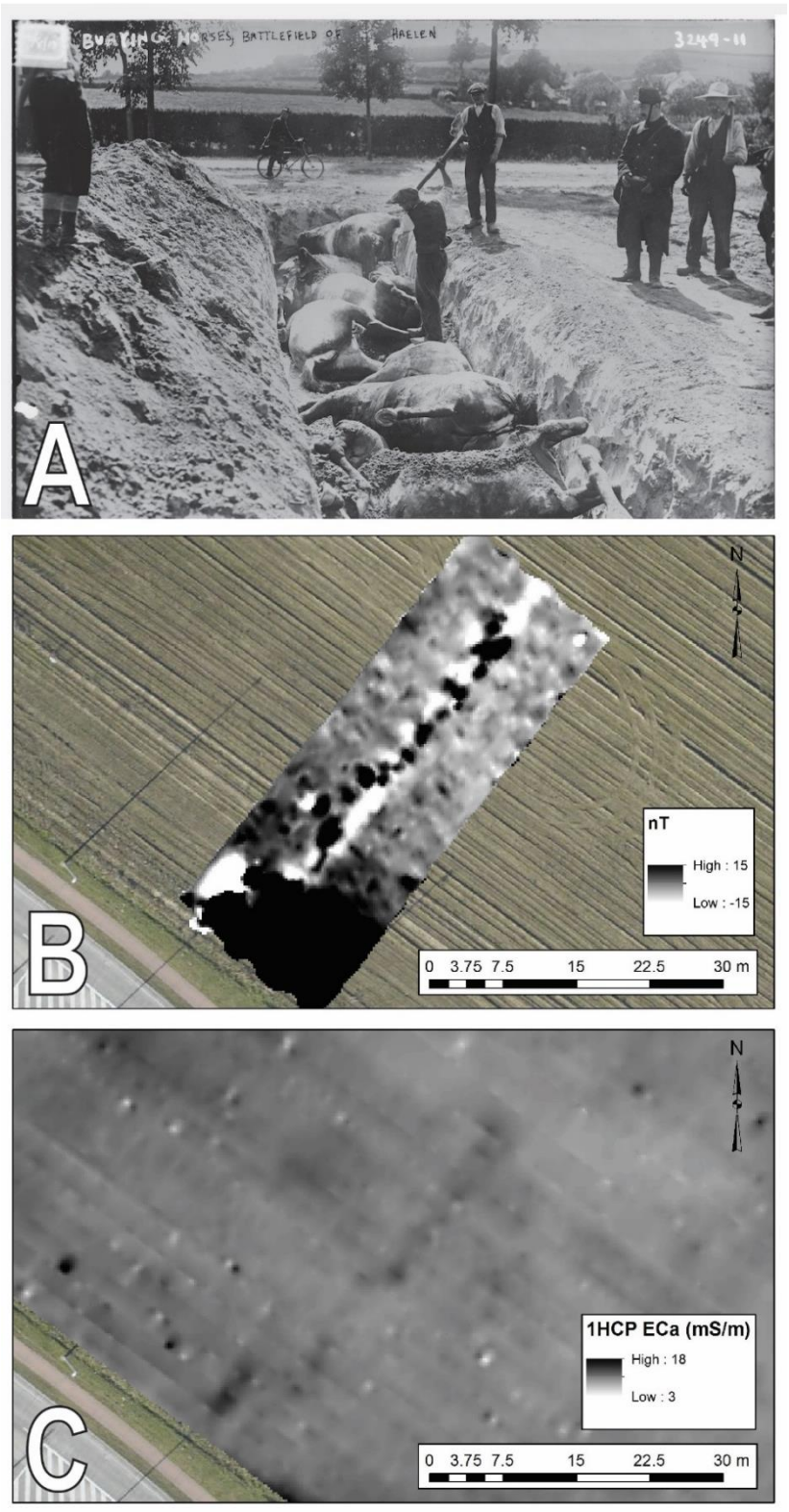



**Figure 4.7:** The location of a horse mass grave registered using three techniques: (A) an historical photograph taken in August 1914 (Library of Congress collection); (B) an FGM survey conducted in November 2016; (C) an electrical conductivity data layer from an EMI survey conducted in November 2016. (orthophoto: copyright AIV)

### 4.2.3 Feature detection: quantitative evaluation

In archaeological pre-studies, exploring geophysics are used to locate as many as possible archaeologically interesting hot spots. In this comparison, the technique that can potentially identify the greater part of the archaeological features is preferred. As a reference for this quantitative comparison, the features seen on aerial photographs are captured as a denominator in this test because this is often included in the pre-study standard approach. On 10 sites across the southern part of the Western Front in Belgium (12.7 ha in total), surveys were carried out using both techniques. The detected WW1 features were quantified as follows: in a first analysis, point (bunkers, shelters…) and linear features (trenches, roads, cables…) were counted (per section). In a second analysis, the length of the detected linear features was determined and compared to the length derived from a time series of aerial photographs. The results from this analysis are shown in tables 4.2 and 4.3. In 9 out of 10 surveys, more features were detected with FD-EMI than with FGM. By counting the length of the linear features, it can be seen that FD-EMI was able to detect 44% more linear features, a similar number of point features and 31 % more segments of linear features. The type of features, the detection characteristics of the sensors and the kind of environment can partially explain the differences between the two detection techniques.

**Table 4.2:** Number of detected point features (PF) and line segments (LF) for 10 sites, ordered by detection technique.

| | | | | FGM | | FD-EMI | | Overlap | |
|---|---|---|---|---|---|---|---|---|---|
| **Site ID** | **Area (ha)** | **TOTAL PF** | **TOTAL LF** | **PF** | **LF** | **PF** | **LF** | **PF** | **LF** |
| **2** | 1.57 | 0 | 1 | 0 | 0 | 0 | 1 | 0 | 0 |
| **3** | 1.89 | 1 | 18 | 0 | 11 | 1 | 16 | 0 | 9 |
| **5** | 1.25 | 6 | 6 | 4 | 3 | 5 | 5 | 3 | 2 |
| **6** | 0.85 | 1 | 2 | 0 | 1 | 1 | 2 | 0 | 1 |
| **7** | 0.48 | 0 | 7 | 0 | 6 | 0 | 7 | 0 | 6 |
| **8** | 0.77 | 2 | 5 | 1 | 4 | 2 | 5 | 1 | 4 |
| **9** | 2.91 | 0 | 13 | 0 | 9 | 0 | 13 | 0 | 9 |
| **10** | 0.48 | 0 | 5 | 0 | 3 | 0 | 5 | 0 | 3 |
| **11** | 1.05 | 5 | 11 | 5 | 10 | 2 | 7 | 2 | 6 |
| **12** | 1.43 | 30 | 18 | 30 | 13 | 30 | 18 | 30 | 13 |
| **TOTAL** | 12.68 | 45 | 86 | 40 | 60 | 41 | 79 | 36 | 53 |

**Table 4.3:** Detected length of linear features using both prospection techniques, compared to the total length of linear features detected with aerial photography.

| Site ID | FGM (m) | FD-EMI (m) | RSA (m) | r_FGM to RSA (%) | r_FD-EMI to RSA (%) |
|---|---|---|---|---|---|
| **2** | 0.0 | 110.0 | 99.4 | 0.0% | 110.7% |
| **3** | 495.0 | 692.8 | 1284.0 | 38.5% | 54.0% |
| **5** | 94.1 | 230.7 | 501.2 | 19.2% | 44.0% |
| **6** | 39.5 | 120.0 | 304.0 | 12.9% | 39.2% |
| **7** | 191.4 | 225.8 | 244.0 | 77.8% | 91.8% |
| **8** | 137.8 | 244.0 | 284.3 | 48.1% | 85.2% |
| **9** | 479.1 | 642.4 | 1574.6 | 30.4% | 40.8% |
| **10** | 54.9 | 142.1 | 285.4 | 18.9% | 49.8% |
| **11** | 394.9 | 377.5 | 504.1 | 77.8% | 74.6% |
| **12** | 424.2 | 549.2 | 944.5 | 44.8% | 58.0% |
| **TOTAL** | 2310.9 | 3334.5 | 6035.5 | 38.3% | 55.2% |

### 4.2.4 Metal objects

Because of the omnipresence of metal objects on the former Western Front (as mentioned earlier in this chapter), the ability to filter or distinguish these objects in scan results plays an important part in prospecting these conflict landscapes. Each metal indication could point to construction materials, ammunition or shell fragments, soldier-related utensils collected in waste pits, etc. which can provide extra information about the site being prospected. In addition, an acceptable precision in pinpointing the exact location of the detected metal hot spots is important during targeted excavations. On this topic, a problem for the FD-EMI sensor setup arises when a terrain has been exposed to agricultural practices, for instance. Gullies can influence the EMI sled position while in motion, disturbing the alignment of the quad bike (GNSS antenna) and sensor. In these conditions, a similar result such as the data obtained by the FGM set-up (fixed GNSS antenna-sensor position) is not possible. As a nearly flat terrain is needed, one logical solution to improve the planar precision on rough terrain is to mount the GNSS antenna on the sled. The influence of the GNSS antenna on the data registration is noticeable and preferably avoided. To investigate and compare both FD-EMI and FGM survey set-ups on their ability to pinpoint metallic objects, a modest 2D precision test is included in this study.

#### *4.2.4.1 Filtering*

In FGM data, the noise floor (clipping threshold) can be changed experimentally according to mass/size of the objects of interest and depth of exploration (Billings et al., 2002). Metal objects are mostly found in the outer ranges of the dataset. By lowering the noise floor closer to 0 nT, it is possible that non-metallic magnetised objects, such as ditches, fireplaces and bricks, are included in the anomalies. Experienced surveyors know how to interpret metallic objects (dipole shape, magnetic moment, etc.) taking into account the magnetic influences of a certain environment. For archaeological purposes, metallic objects often mask more subtle features within the data (Johnson, 2006). The large spatial influence of these objects in datasets covers many underlying features. On the former Western Front, high densities of iron clutter are found (Note et al., 2018) which result in the dominance of strong anomalies in the survey results. Under these conditions, the inversion of FGM data to obtain accurate object parameters is difficult to perform. EMI is less sensitive to those effects and therefore more suitable for significantly disturbed sites. Both ferrous and non-ferrous metallic objects can be detected with DUALEM-sensors by combining data layers from the 21S coil configuration (Saey et al., 2011). The linear formula used for this metal filter is the FEMP (fused electromagnetic metal prediction, see chapter 5) which indicates metal objects between the soil surface to roughly 1 m in depth.

#### *4.2.4.2 2D precision*

At 13 locations on the Maedelstede farm site 1 (ID 5), multiple metal objects (with WW1 origin) were dug in for a 2D precision test. Characteristics of the test objects are presented in table 4.4. The reference coordinates for the buried metal objects were determined by a photogrammetric recording before closing the object pit. The average X and Y coordinates (= centroid), derived from the resulting orthophotographs, are used as the reference location. These photographs are georeferenced by RTK-GNSS with 2-3 cm planar precision. The object anomaly locations within the geophysical surveys are obtained in a similar way. In magnetometer data, location and intensity of mono or dipole peaks are considered in the Sensys Magneto software to determine object location (Sensys, DE). For the FD-EMI survey, the centroids of the FEMP identified object peaks are used as a reference location. The results of this planimetric accuracy test are given in table 4.5. A distance of 0.25 m was found to be

the average deviation between photogrammetric centroid and geophysical anomaly location for both techniques, with a standard deviation of 0.12 m for FGM and 0.18 m for FD-EMI.

**Table 4.4:** Object characteristics

| ID | Weight (kg) | Depth (m) | Planimetric dimensions (m) |
|---|---|---|---|
| 1 | 35 | 0.50 | 0.25 X 0.50 |
| 2 | 30 | 0.45 | 0.40 X 0.40 |
| 3 | 25 | 0.43 | 0.40 X 0.40 |
| 4 | 52 | 0.43 | 0.95 X 0.25 |
| 5 | 5 | 0.47 | 0.35 X 0.35 |
| 6 | 10 | 0.52 | 0.30 X 0.40 |
| 7 | 16 | 0.50 | 0.20 X 0.50 |
| 8 | 40 | 0.49 | 0.50 X 0.50 |
| 9 | 16 | 0.68 | 0.30 X 1.00 |
| 10 | 16 | 0.37 | 0.40 X 0.30 |
| 11 | 32 | 0.32 | 0.50 X 0.25 |
| 12 | 20 | 0.39 | 0.35 X 0.40 |
| 13 | 25 | 0.43 | 0.50 X 0.30 |

**Table 4.5:** Object and geophysical anomaly parameters

| ID | Photogrammetry | | FGM | | FD-EMI | | Δ FGM (m) | Δ FD-EMI (m) |
|---|---|---|---|---|---|---|---|---|
| | x | y | x | y | x | y | | |
| 1 | 47794.11 | 165652.64 | 47792.92 | 165652.49 | 47792.83 | 165652.77 | 0.24 | 0.31 |
| 2 | 47802.50 | 165664.55 | 47802.84 | 165664.69 | 47802.37 | 165664.51 | 0.37 | 0.13 |
| 3 | 47804.94 | 165684.79 | 47805.05 | 165684.89 | 47804.98 | 165684.84 | 0.15 | 0.07 |
| 4 | 47805.31 | 165724.84 | 47804.93 | 165724.81 | 47805.37 | 165724.87 | 0.38 | 0.07 |
| 5 | 47801.90 | 165754.65 | 47801.75 | 165754.19 | 47801.97 | 165754.95 | 0.48 | 0.31 |
| 6 | 47807.44 | 165769.79 | 47807.63 | 165769.88 | 47807.02 | 165770.22 | 0.21 | 0.61 |
| 7 | 47791.38 | 165774.83 | 47791.27 | 165774.97 | 47791.38 | 165774.88 | 0.18 | 0.05 |
| 8 | 47792.70 | 165784.22 | 47792.96 | 165784.56 | 47792.73 | 165784.47 | 0.42 | 0.25 |
| 9 | 47780.58 | 165784.62 | 47780.55 | 165784.85 | 47780.65 | 165784.80 | 0.23 | 0.19 |
| 10 | 47777.50 | 165797.58 | 47777.41 | 165797.70 | 47777.38 | 165797.62 | 0.15 | 0.12 |
| 11 | 47775.96 | 165824.26 | 47775.94 | 165824.18 | 47774.23 | 165824.73 | 0.08 | 0.54 |
| 12 | 47784.09 | 165819.49 | 47785.89 | 165819.61 | 47785.87 | 165819.93 | 0.24 | 0.50 |
| 13 | 47788.38 | 165830.73 | 47788.31 | 165830.57 | 47788.29 | 165830.85 | 0.17 | 0.15 |

## 4.3 GPR

On ten selected sites near the front, small-scale GPR surveys were executed to test the ability of this technique to detect WW1 infrastructure. After the first tests with two GPR systems (GSSI utility scan & 3d-Radar), the surveys were delivering poor results. These higher frequency GPR-systems, suitable for near surface prospection, have some difficulties to overcome in the Flanders's WW1 area. The first difficulty is the presence of alluvial soils. Clay and loam makes it often difficult to penetrate much deeper than 0.5 -1 m. These grounds are ideal to hold moisture for a longer period. Because the ground was bombturbated (mixed by bombing), heavily disturbed topsoil in combination with omnipresent metal shrapnel and other clutter appears. This background makes contrasting reflections of WW1 features of interest hard to distinguish. Next, the top layer for which this technique delivers the best results (0 – 0.5 m), was often affected by agricultural activities. A third limitation is the groundwater table, which can be found between 0.7 and 1.5 m (DOV, 2015). To demonstrate the results of this technique, 4 surveys were carried out where at least a reference scan was deployed with another successful technique. For these surveys, the Geoscope 3d-Radar system. This GPR-setup is ideal for archaeological prospection to survey larger area's with high coverage resolution. Saey et al. (2013) demonstrated the potential of this radar to map a WW1 trench system at the Stonehenge World Heritage Site. This trench was constructed for fighting practices and was excavated in limestone. Because of the soil structure (0.1 – 0.4 m loess on top limestone), GPR was ideal to map this trench system (good contrast between limestone and loess). In Flanders where alluvial deposits are found, the 3D-radar scans delivered no useful results for the characterisation of buried WW1 features. At the Kemmel barracks site which was also surveyed with FD-EMI and FGM (see paragraph 4.2.2.4), GPR could only detect near-surface irregular patterns which probably correspond with the near surface preserved shelling marks. In addition, a part of the camp ditch and one brick barrack floor could vaguely be distinguished (figure 4.9). Without the aerial photographs or the other scan results as guidance, the localisation of these very subtle traces were almost impossible. At the site of the horse mass grave (also surveyed with FGM and FD-EMI, see paragraph 4.2.2.5), the linear graves were not detected. This site contained the best soil conditions of all test sites: homogeneous loamy sand soil, not disturbed by intense war fare or other activities. On the other hand, a late medieval moated site just next of the mass graves, was partially detected

by the 3d-Radar system. In terms of completeness of coverage, GPR was in this case also inferior to FGM and FD-EMI. The main advantage of GPR is the more precise depth estimation of the discovered features (high resolution in three dimensions). Two other surveys (Messines and Petit Bois) demonstrated that mainly superficial tracks were detected and that the signal has difficulties to penetrate the heavily disturbed ground. In figure 4.8 (Messines survey), the compacted grass caused by the quad bike in the scan setup, are clearly contrasting in the depth slice at 21 ns. At all GPR prospected sites, the advantage was given to FGM and FD-EMI because of the high WW1 feature coverage ability and success rate.




**Figure 4.8:** Visualisation of the 3d-Radar scan (21 ns) at the Messines site, revealing mainly superficial traces (quad bike tracks) which are also observable on the aerial photograph, used as background image (orthophoto: copyright AIV).

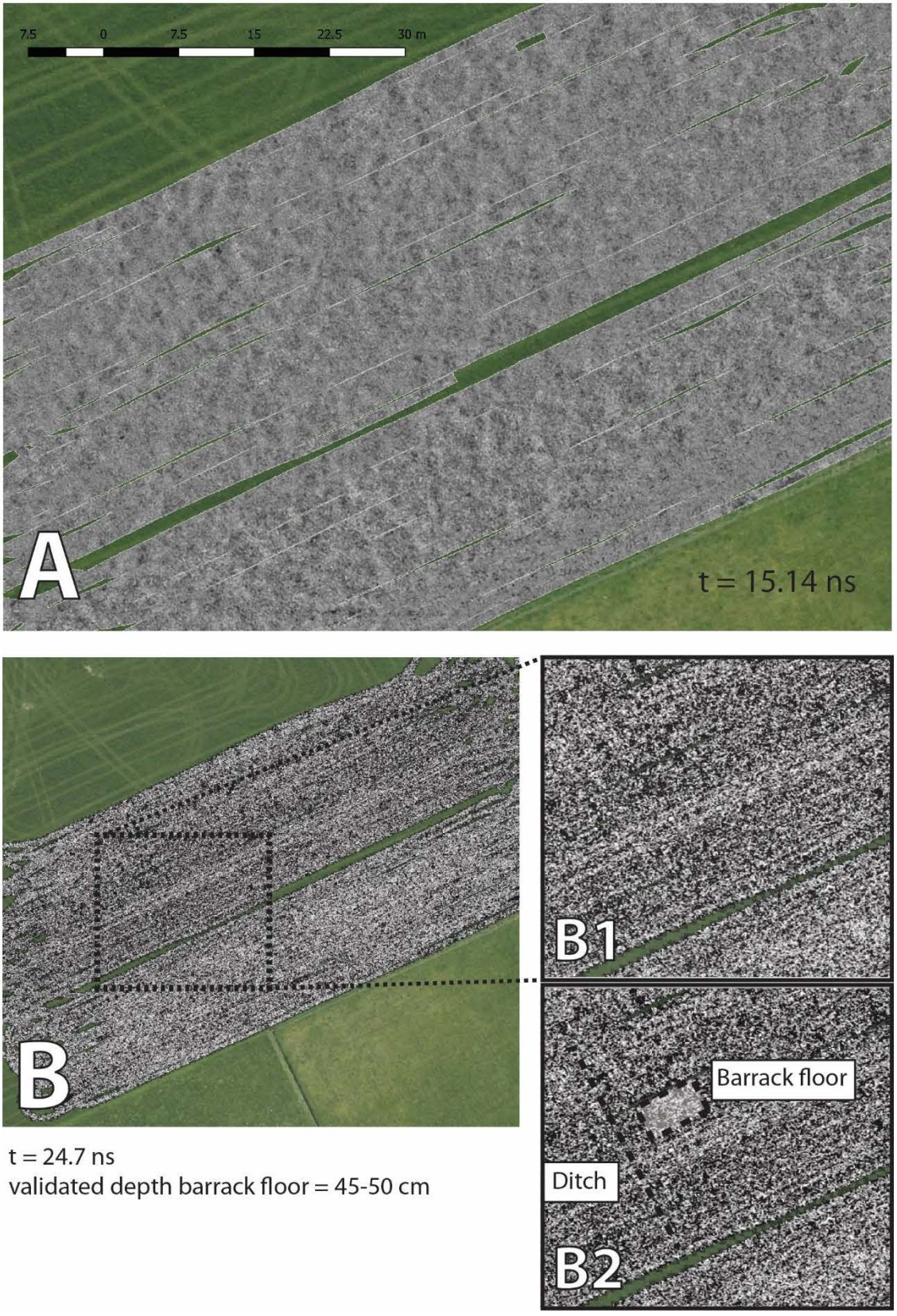



**Figure 4.9:** Display of the 3d-Radar results at the Kemmel barracks site, revealing some subtle contrasting traces. In image A, the 15.14 ns magnitude response is visualised, showing patterns which could correspond with the dense shelled topsoil. Image B demonstrates the magnitude response at 24.7 ns, which reveals subtle traces of the camp ditch and one barrack floor. (orthophoto: copyright AIV)

## 4.4 ER

Earth resistivity profiling for archaeological purposes was one of the first implemented geophysical techniques in Archaeology (Atkinson, 1946). Today, a manually operated pole-dipole configuration is the most popular technique. This method is relatively cheap but very time-consuming to cover larger areas. Therefore, it was passed in popularity by other techniques (magnetometry, GPR). A change came in the 2000's when mobile ER devices (pulled by an ATV) were constructed for Precision Agriculture (PA) to measure the soil variability on large sites. ER as indicator for soil EC in combination with pH-measurements are today commercially used to improve the productivity in agriculture. For PA, Veris technologies constructs mobile ER-systems whereby the contact electrodes of the array consists of spinning coulter disks which are pushed into the ground by the setup's weight. Other similar systems exists but these are not commercially available (e.g. Geocarta ARP system). Terron et al. (2015) tested the Veris 3150-system for archaeology whereby it was described as useful for largescale mapping. This system appeared to be ideal for pointing out hotspots of archaeological finds but the resolution is relatively rough compared to other techniques (GPR and magnetometry) and the soil conditions are important to take into account. This was the only publication so far that tested a Veris earth resistance system for archaeology. Starting from the few published information on this mobile system, the ability and the limitations of this sensor to detect WW1 archaeology in combination with a few test and survey examples will be shown in this section. Therefore, four sites were surveyed to analyse this instrument and setup. In addition, some important post-processing steps will be suggested to remove noise/data errors and to improve the visualised image.

### 4.4.1 Limitations

The ER device used in this this chapter is the Veris Q2800, a compact and 'light' resistivity system that can be pulled by a small ATV. This system produces a shallow (0 – 0.25 m) and deep EC value (0 – 0.90 m), ideal for near surface phenomena. Because of this sensor output in mS/m, it can be compared to similar depth responses measured by FD-EMI. For archaeological purposes, the interline distances of the ER survey is set to 1 m. A spatial resolution reference of 1 X 1 m to 0.5 X 0.5 m is suggested by English Heritage (2008). The inline resolution is depending on several aspects. The first one is the logging and measuring

speed of this active system. The system uses a measuring frequency of 1Hz or lower for PA purposes and the suggested maximum moving speed was set to 24 km/h (www.veristechnologies.com, 2018). For archaeological prospection, a minimum frequency of 4 Hz is preferable if the ATV speed lies between 5 – 10 km/h (0.35-0.70 m inline resolution). The maximum achievable measuring and logging speed of the Veris system is set to 2 Hz, which produces an inline resolution of 70 cm between data points at a speed of 5 km/h. Higher measuring frequencies are causing a delay in the data output which eventually fails after a few seconds. This was mentioned by the Veris support engineer and experimentally tested. A technical improvement to adapt the system will be necessary for high-resolution archaeological purposes. In these conditions, it cannot compete to achieve a similar high-resolution scan such as FGM, EMI or GPR in combination with a similar ATV speed. With the 2Hz measuring speed, the ATV its moving speed is limited at +/- 5-7 km/h for archaeology (1 x 1 m resolution). At this speed, it takes 1.5 – 2 h per ha.

A second limitation is related to soil moisture: the system needs at least 10% of the soil moisture wilting point to achieve a high rate of good-recorded values. Therefore measuring in a dry or wet period of the year will affect the measurement as well (Schmidt et al., 2015). Sediment soils (found in the study area) are ideal terrain for ER (= good moisture distribution in soil matrix).

A third and more decisive limitation is the system's need for ground contact. When the disks come off the ground, negative values are logged in the data file. This is often the case for the two outer disks. By this phenomenon, deep EC – measurements will fail. When the system is moved through an area containing puddles or surface water, the measurements will fail as well (short circuit).

### 4.4.2 Error codes

When a data logging problem shows up that obstructs the measurement of an EC-value, an error code is written into the logging file. Because negative EC-values does not exist, these values are used to indicate problems during the survey: ground contact loss (-1), short circuit (-2), lack of moisture (-4) and erratic contact of with the spring plungers or disks (-8 and -16). Other negative values represent the combination of multiple error sources. The error codes in the test surveys are listed in table 4.4. Each code can uniquely be identified. Based on these error codes, the survey quality can be analysed in several conditions.

**Table 4.6:** Error codes of the Veris Q2800 resistivity system.

| Error definition | Main error code | Combined error code |
|---|---|---|
| Ground contact | -1 | |
| Short circuit | -2 | |
| Ground contact \|\| short circuit | | -3 |
| Moisture | -4 | |
| Ground contact \|\| moisture | | -5 |
| Erratic contact | -8 | |
| Short circuit \|\| erratic contact | | -10 |
| Ground contact \|\| short circuit \|\| erratic contact | | -11 |
| Erratic contact | -16 | |
| Erratic contact | | -24 |

### 4.4.3 Survey examples and tests

A first test contains a survey of two fields near the Hollandse Schuur farm at Wytschaete. The first field is an arable plot where corn was harvested. The soil was slightly loosened up because of primary land treatment after harvesting. The second plot which is used as pasture, is located next of the first one. These two land conditions influence the quality of the Veris Q2800 survey because ground contact of the coulter disks works better on compacted grassland than loser surfaces. Secondly, because of the compaction of pasture, soil moisture can be kept better into the ground. In a first analysis, 0.2% of the data on the arable plot contained an error for $EC_{sh}$ and 2.2% for $EC_{d}$. The main errors for deep EC were moisture issues (49%) and ground contact loss (26%). Low moisture content is no problem for shallow EC. On the pasture plot, no errors were recorded for $EC_{sh}$ and only 0.08% of $EC_{d}$ values. Here the problem diagnostics are almost nihil. When the interpolated image is analysed, large EC value drops on the arable plot are noticed. This causes mainly small peaks in the interpolated image (= noise). These results confirmed the expectations: the employability on pasture is better than on arable land. Figure 4.10 demonstrates the ground contact loss issue for the outer coulter disks. These are acting frequent on irregular surfaces as a lever. Figure 4.11 shows the result of $EC_{sh}$ and $EC_{d}$ of both plots near the Hollandse Schuur farm. In the arable field interpolated data, no fine detail can be distinguished. Also the EC-drops (low peaks) are dominant. On the pasture area, fine detail and a low level of noise are found. In the western part of the survey, higher conductive

linear structures are detected, which were identified as communication trenches by RSA. The FD-EMI scan showed a similar result to interpret those structures.

The second Q2800 case is a pasture field near Bellewaarde that was scanned in a period of dry weather conditions (June 2016). At this site, a part of a medieval moat is covered and one trench appears in the data (figure 4.12). Because of the dried-out ground, 7.5% of the measurement were classified as an error related to the lack of soil moisture. Those errors are mainly located west in the scan results, visible as a zone containing many low-conductive values (near 0). This was one of the main reasons to quit this survey.




**Figure 4.10:** The Veris Q2800 applied on the arable plot near the Hollandse Schuur farm, demonstrating the effect of irregular and lose surfaces on the contact loss of the outer coulter disks.

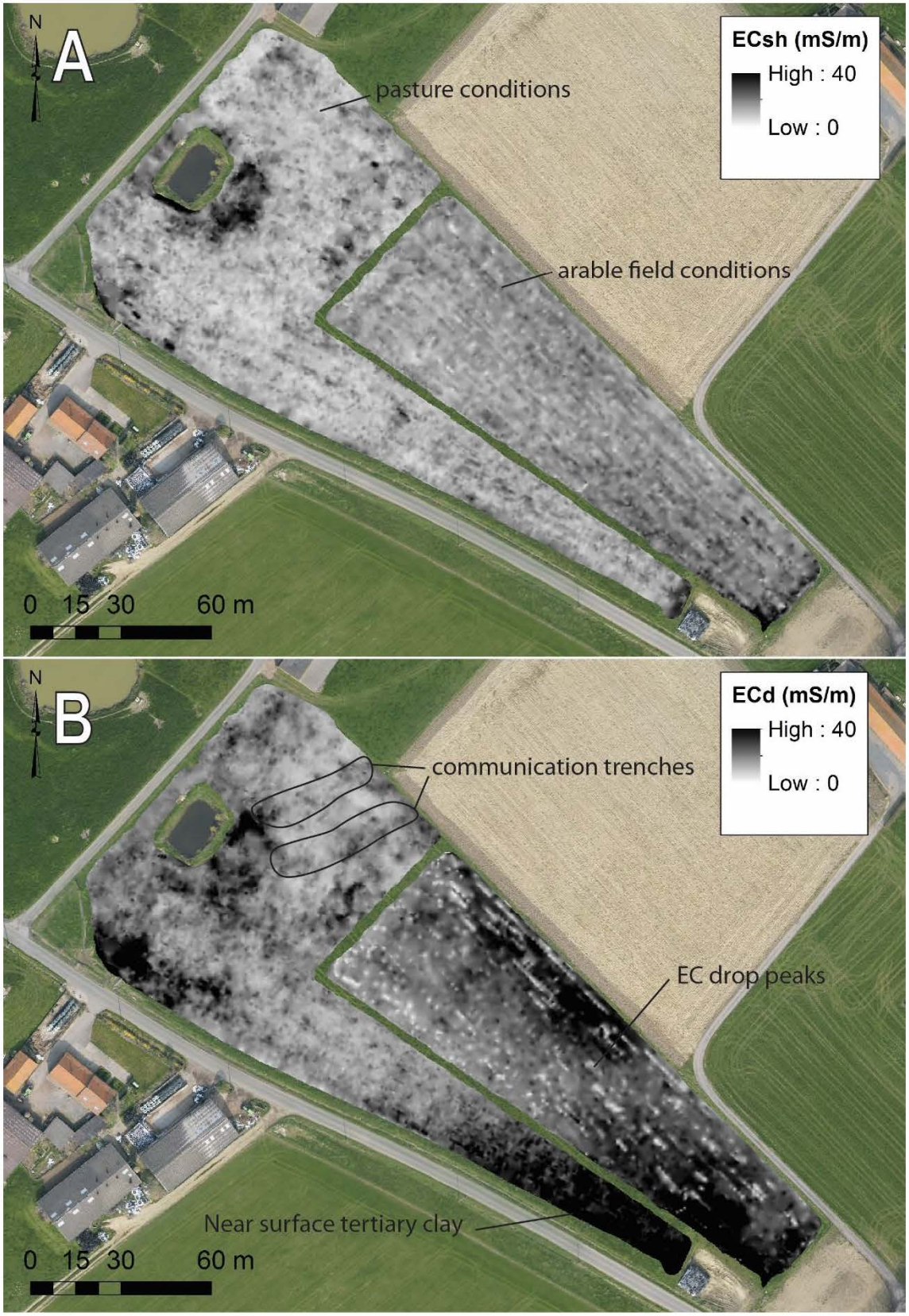



**Figure 4.11:** Visualisation of the Veris Q2800 shallow EC (A) and deep EC (B) for the Hollandse Schuur farm survey. (orthophoto: copyright AIV)

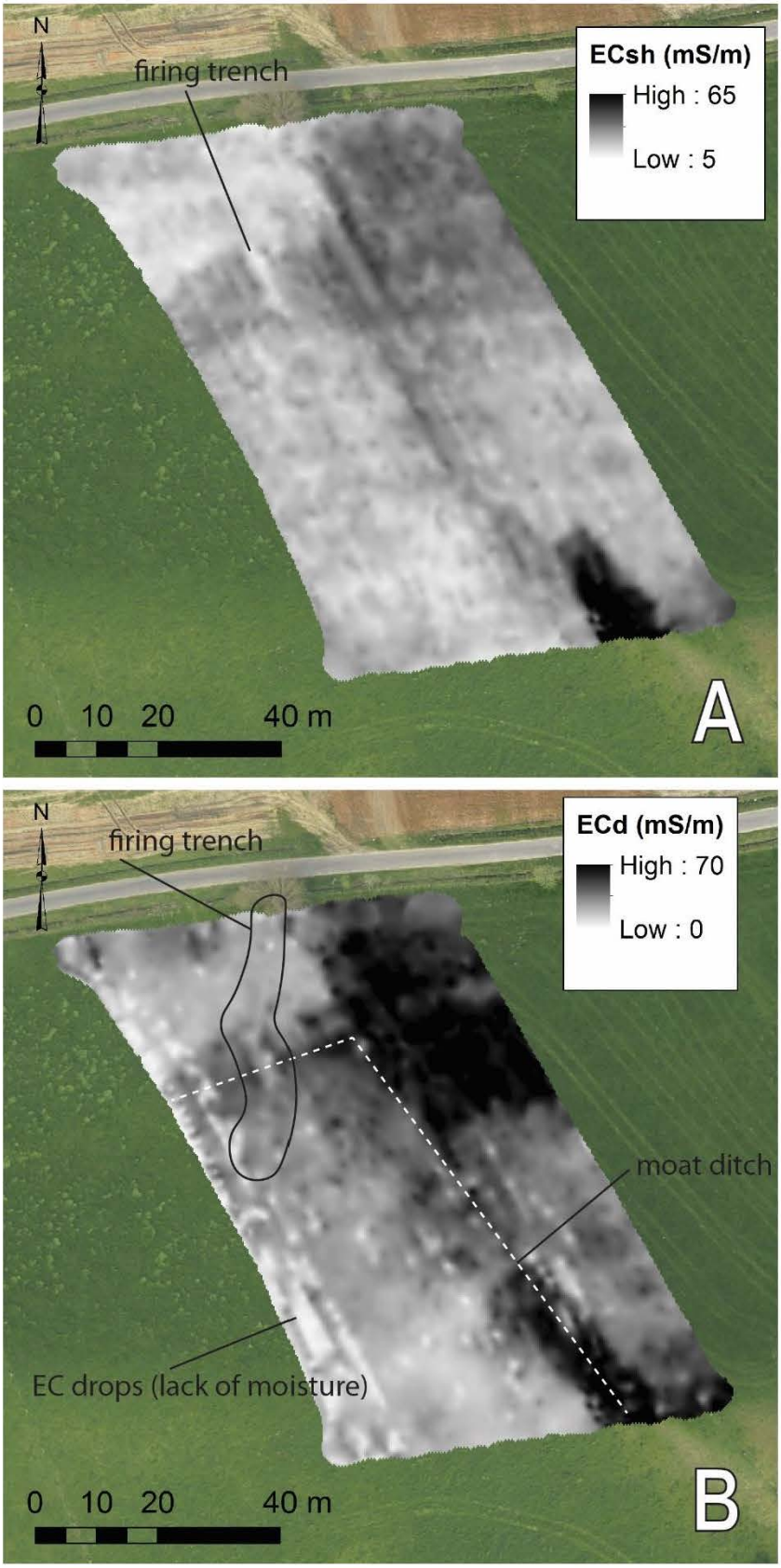



**Figure 4.12:** Visualisation of the Veris Q2800 shallow EC (A) and deep EC (B) for the Bellewaarde survey. (orthophoto: copyright AIV)

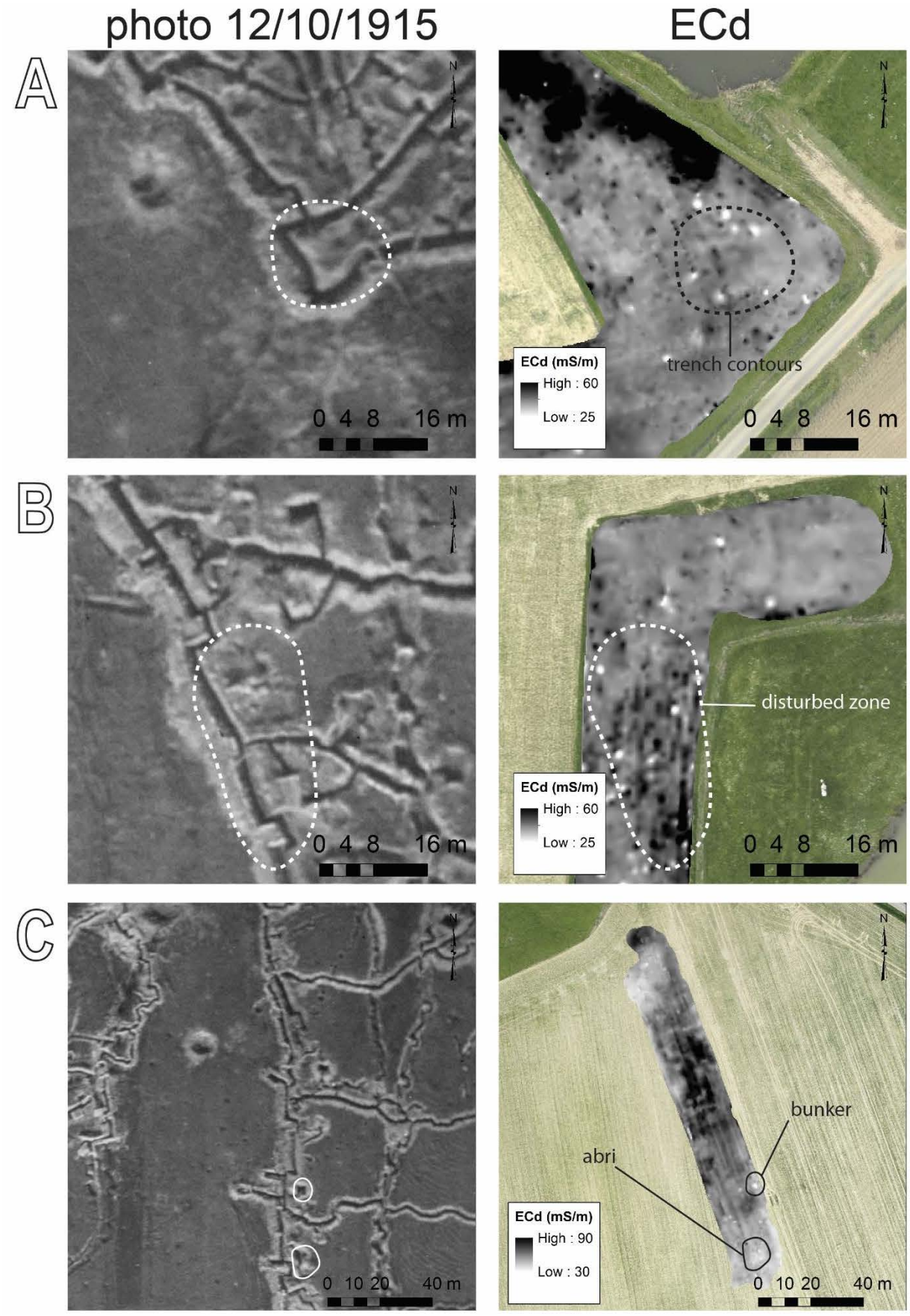



**Figure 4.13:** Details of an aerial photo (IWM collection) and ER survey near the Kruisstraat craters, indicating traces of trenches (A & B) and abri/bunker (C). (orthophoto: copyright AIV)

In figure 4.13, three detailed views of the $EC_d$ are shown, measured near the Kruisstraat craters between the villages of Kemmel and Wytschaete. At image A, vague contours of a 1915 trench system were found. At detail image B, a disturbed zone at the location of a firing trench was detected (confirmed by EMI). At image C, two low conductive (= higher resistive) areas were found on the location of an abri and bunker. This would indicate that some building foundation traces are still present but this is not as clear as the interpreted result from the FD-EMI scan where the building remains could easily be located (= strong anomalies). This information corresponds with Terron et al. (2015): this technique can be used for larger building foundations but smaller single building structures are difficult to identify. This identification was not possible based on the information of the ER scan alone.

### 4.4.4 Processing

To improve the data processing and interpolated image, some additional data-adjustments were made. The negative values (data errors) are filtered out and spatial overlapping and interfering data points were removed from the logging file (principle see chapter 3). Because there is an offset between the electrodes and the GNSS-antenna, a shift correction was applied. When spiking noise appears in the data recording, outlier removal based on the normal distribution is applied (e.g., 5% outliers are excluded). Another technique to remove those outliers is to calculate the local median within a window and setting an experimental derived tolerable offset. Those techniques worked well to eliminate the peaking noise (EC-drops). When this phenomenon is locally dominant (large area lacking moisture, see Bellewaarde survey figure 4.12), this filtering is not possible.

### 4.4.5 Suitability on WW1 sites

Limitations and advantages should be carefully weighted to subscribe for this technique. A first limitation which deserves major attention when executing fieldwork is a safety issue: disks cutting into the ground can hit unexploded shells. Every year, accidents happen with agricultural machines, cultivating the top layer of soil. Those actions have a much larger magnitude but despites that, the extra provided weights on the system (=156 kg) were abandoned on ploughed grounds to avoid hitting UXO with great force. The system was also set to penetrate only the first 5 cm of soil in combination with walking speed survey movement

to minimise the hitting impact. Safety is one of the reasons why only small areas were scanned with great caution. Based on this information alone, a negative recommendation can be given. On these terrains, the manual operated resistivity array systems are much safer and therefore advised. The second limitation are the weather conditions. A too dry period will cause a lack of soil moisture, influencing the measurement with noise and resulting in sudden EC-drops next to the negative values. Too wet conditions also influence the operability of the system: loose soil will stick between the system's wheels and when the weights are attached onto the sensor frame, these will slowly pull the sensor deeper into the ground while moving forward (muddy and wet Flanders clay plain effects). Land use conditions influence the survey quality as well: grass and pasturelands are preferred before arable fields and urban areas. One main advantage is that the omnipresent distributed metal objects, which influence other sensing techniques, can be avoided or minimised in the scan data. This works similar for pipelines etc. In areas disturbed by fine metal objects (where magnetometry and GPR are unsuccessful), this technique can contribute to the find buried military infrastructure (Banks, 2014). Despites this advantage, the sampling speed (and therefore spatial resolution) is lower than EMI / FGM / GPR devices.

## 4.5 TD-EMI

Short loop time domain electromagnetic induction is one of the mainstream techniques used by demining companies to determine the position of buried metallic objects. Sensor manufacturer Sensys (DE) constructed two array systems of TD-EMI receivers (AMOS and EMD2) to map the magnetic buried objects and structures in advance. Because of the array system, a dense spatial resolution is achieved which gives a sharper image than the DUALEM results and it is not highly sensitive like the FGM array system to ferromagnetic objects, which makes de localisation and identification of buried metal easier. Therefore, this sensor is mainly applied for UXO detection. The theoretical DOE of TD1 is situated around 1 m, which is comparable of the metal classification in the FD-EMI data surveys by the FEMP but smaller than the theoretical 3 m of FGM. The Kapellerie site, known during the war as Hill 80 (German: Höhe 80), was surveyed with the EMD2 system in March 2018. Compared to FGM, the influence of metal objects onto the surrounding elements is significant smaller. The anomaly

size of these objects are also better delineable which makes pinpointing more efficient. This characteristic is also interesting for the detection of archaeological features within heavily disturbed sites. In figure 4.14, the results of the TD1 data layer are presented with indication of the main archaeological features. In figure 4.15, the FGM result and a magnetic data layer from the FD-EMI scan are visualised as reference to compare TD-EMI. Next to the omnipresent metal objects, foundations of buildings and bunkers can sharply be delineated by TD-EMI. This is demonstrated in figure 4.12 where the foundations of a former windmill (1), bunker (4) and farm site containing building foundations (5) are detected. A trench without large infillings of metal (2) can sharply be distinguished. The contrasts of the filled trench with the surroundings are 20 mV, which makes the delineation of the trench system accurate according to the archaeological excavation results (see chapter 5). In the north of the study site, a part of a metal filled trench was found. The non-metal connecting trench structures were not detected by TD-EMI. These trenches were found by the FD-EMI survey (figure 4.13). Based on the completeness of trench detection (lengths + delineation), the advantage was given to FD-EMI (compared to TD). This finding was also expressed in the results for the linear feature detection rate: 75% for FD-EMI, 78% for FGM and 57% for TD-EMI.

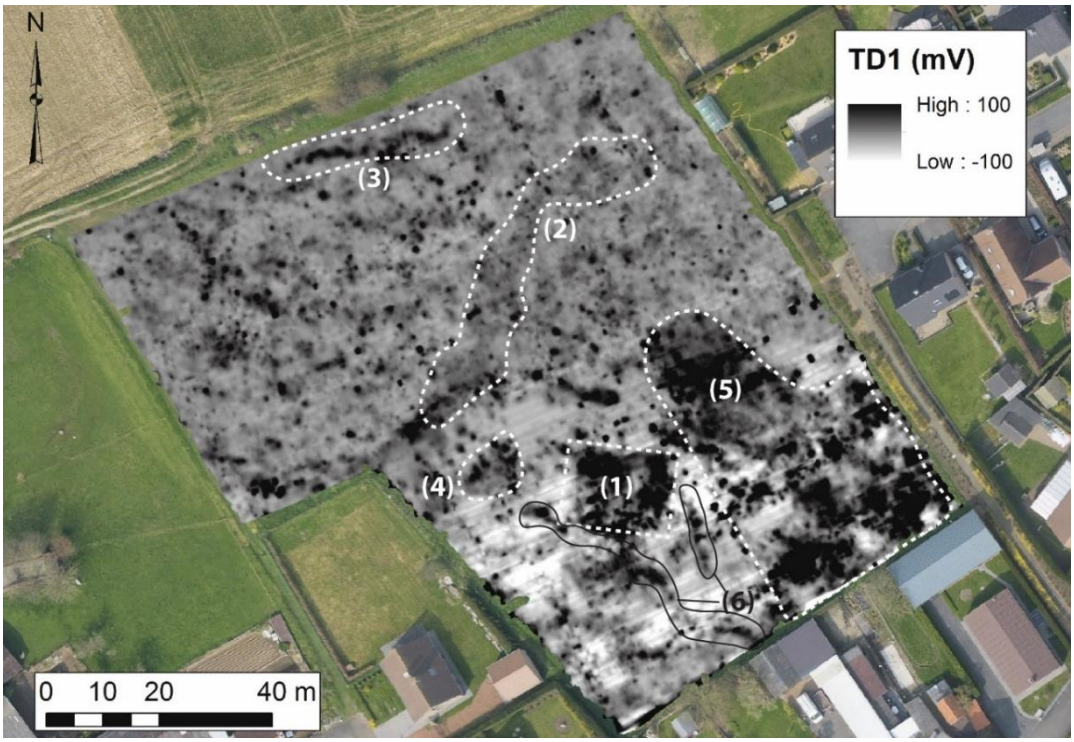



**Figure 4.14:** Visualisation of the EMD2 DT1 data layer with indication of the most dominant WW1 features. (1) is the foundation of the former Wytschaete windmill, (2) is a German 1917 firing trench, (3) are metal objects within a 1915 German firing trench, (4) are the remains of a possible bunker, (5) are the traces of the pre-WW1 farm activities and building foundations and (6) are two communication trenches. (orthophoto: copyright AIV)

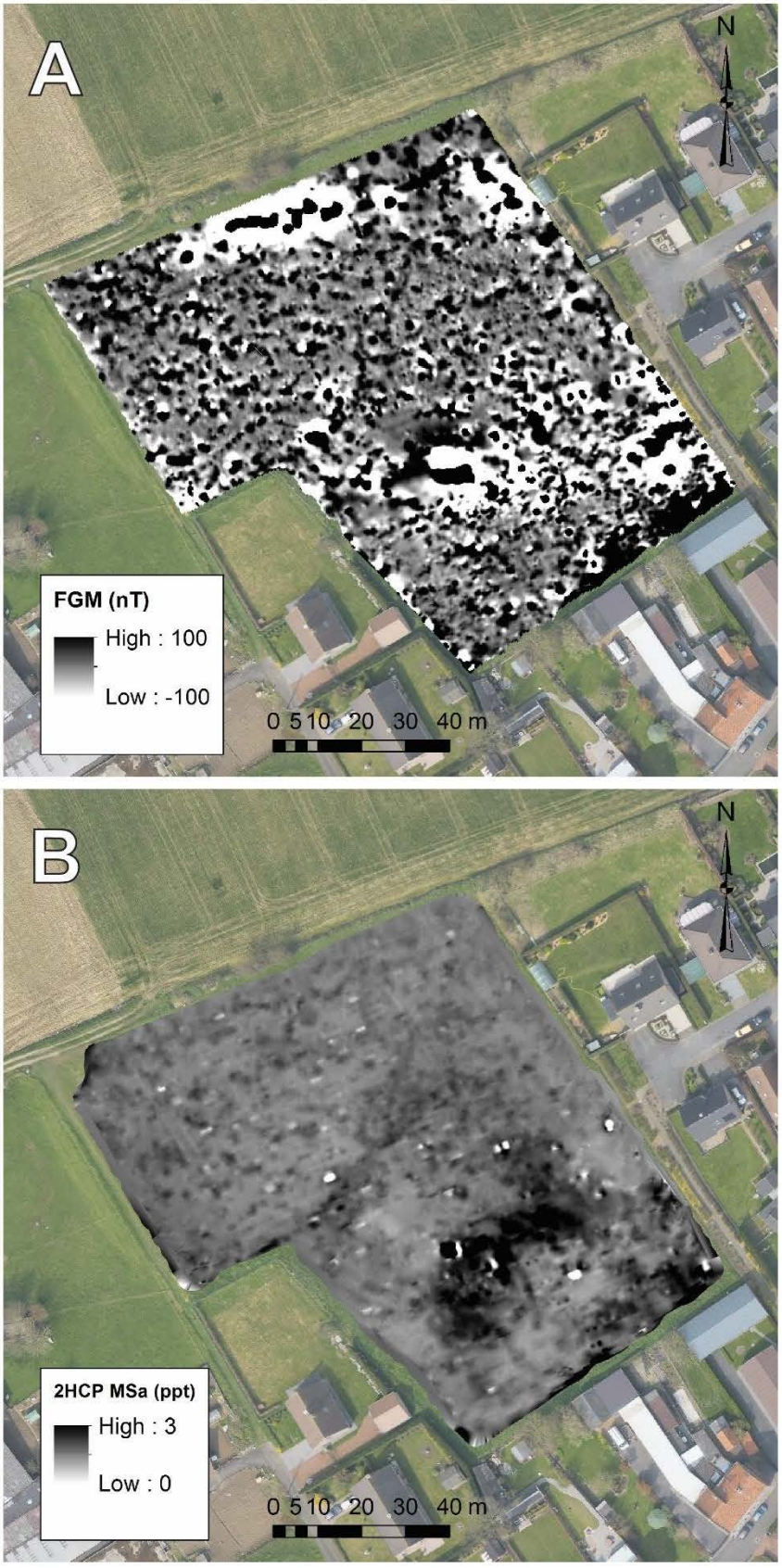



**Figure 4.15:** Visualisation of the Hill 80 survey, performed with FGM (A) and FD-EMI (B, 2HCP $MS_a$ data layer). (orthophoto: copyright AIV)

## 4.6 Conclusions

Without any question, FGM and EMI are more suitable for WW1 archaeology at the former Western Front in Belgium than GPR and ER. Next to the lower spatial resolution of ER, safety is a major concern by penetrating the surface (hitting UXO's). Based on this fact, a logical exclusion of this technique can be made. On the other hand, a manual operated ER system is safer and can be an answer to the strongly magnetic disturbed conditions (metal debris) which are strongly influencing the FGM surveys. For GPR, the wet Flanders's alluvial soils and heavy clays are attenuating higher frequency GPR-systems, which are the most suited radar systems for archaeological prospection. The penetration depth and the contrasts are often poor in the WW1 study area. In addition, the bombturbated grounds create complex mixed soil conditions that are not beneficial for the GPR technique. Therefore an acceptable rate of success is not achievable. This was confirmed by executing multiple surveys. By analysing the FGM / FD-EMI database compiled for this chapter, both of the evaluated techniques have pros and cons for prospecting WW1 battlefields. The main determining parameter in this comparison is the presence of ferrous metallic objects in the soil. If this impact is limited or absent, both techniques are favourable for feature detection (depending on the survey specs to match). By using shelling densities derived from aerial photographs (Note et al., 2018) or a test scan as proxy for metal object impact, a primary terrain characterisation can be made. This analysis is the first and important indicator when deciding on the scanning technique. If a fast scan coverage is considered with a high planimetric and steady resolution, an FGM array pulled by a motorised vehicle is suitable for the job. In addition, pinpointing anomalies is much more reliable compared to FD-EMI. When an FD-EMI scan is taken, flat and obstacle-free terrain conditions are needed to achieve similar precision results as those from FGM. If focused on the detection of front archaeological features, it is advisable to use FD-EMI, based on maximum coverage results and structure-type identification. This is partly explained by the multiple signals received at multiple depths (active system), its sensitivity for soil-related properties (texture, moisture) as well as its weaker sensitivity for metal objects. Shell craters and communication cables can easily be classified by FD-EMI, which is more challenging or even impossible using FGM. The scans in this study showed that in 9 out of 10 cases, FD-EMI produced the best 'complete coverage' result, which demonstrates that FGM is not always inferior but that overall FD-EMI is the more reliable option.

The results of the TD-EMI survey with the EMD2 equipment were satisfactory for WW1 archaeology. This mainstream technique developed for UXO detection was able to deliver the best quality result in the delineation of trenches and building foundations in these soil conditions. In has a comparable sampling resolution as FGM but it is less sensitive to strong magnetic anomalies, which in FGM data are blanking out the other more subtle anomalies. Also pinpointing of metal objects delivered an improved result (sharper delineable) in highly magnetic disturbed areas, compared to the FGM scans. The main limitation is the limited DOE (inferior to FGM and FD-EMI) which also resulted in a lower detection rate of linear WW1 features. Therefore, FD-EMI and FGM are getting priority over TD-EMI for archaeological purposes.

# Chapter 5

## Identification and validation of geophysical anomalies in WW1 battlefields

This chapter contains sections, derived from following publications:

Stichelbaut, B., **Note, N.**, Bourgeois, J., Van Meirvenne M., Van Eetvelde, V., Van den Berghe, H., Gheyle, W. (2018). The archaeology of world war I tanks in the Ypres Salient (Belgium): A non-invasive approach. *Archaeological Prospection*, published online.

Saey, T., **Note, N.**, Gheyle, W., Stichelbaut, B., Bourgeois, J., Van Eetvelde, V., Van Meirvenne, M. (2016). EMI as a non-invasive survey technique to account for the interaction between WW I relicts and the soil environment at the Western front. *Geoderma, 265*, 39 – 52.

Stichelbaut, B., **Note, N.**, Saey, T., Hanssens, D., Van den Berghe H., Bourgeois, J., Van Meirvenne, M., Van Eetvelde, V., Gheyle, W. (2017). Non-invasive research of tunneling heritage in the Ypres Salient (1914–1918) – research of the Tor Top tunnel system. *Journal of Cultural Heritage*, *26*, 109-117.

## 5.1 Introduction

In this chapter, three topics will be covered related to the identification and validation of geophysical anomalies, mapped by FD-EMI sensors. This technique is successful in characterising buried WW1 features (see chapter 4) and therefore its potential will be demonstrated in this chapter. Because the information was derived from several papers[1], reports and cases, a hybrid structure was chosen for this chapter. The separate parts in this compilation are covering identification and validation procedures, which were applied on multiple surveyed sites within this thesis or contained unique information about validated geophysical anomalies.

In the first part, a technique will be demonstrated to distinguish both metal objects and shell holes in scan results, since these features are both strongly present in the same data layer. By integrating other FD-EMI data layers, this distinction can be made (Saey, 2011; Saey et al., 2016). This data discrimination is relevant because shell holes and metal objects are remnants of war, present at each field near the former front. Therefore covering these procedures is essential. These techniques were performed as standard analysis for site and anomaly characterisation in this thesis.

The second goal in this chapter is to check the detection rate of a geophysical scan compared to a site-covering archaeological excavation. This is an uncovered issue for WW1 sites. For a complete investigation, at least multiple sites should be included. Site-covering excavations which are available at the same time of a research project, are rare and therefore lacking to perform large-scale research. In 2018, an exceptional opportunity occurred: a 1 ha site near the village centre of Wytschaete (Hill 80) was selected for an extended archaeological excavation. The results of a comparing test on these data will be a first indication of the comparison of geophysics, aerial photography and excavation results, performed on buried WW1 archaeology.

[1] Sections from papers containing original research from the author of this thesis are included. These were extracted and modified to fit in this chapter. The author's name is second on these papers as a result of compromise between the project collaborators.

The final topic investigates what is actually measured when an anomaly related to the WW1 activities is found. When an anomaly corresponds to the location and the shape of an identified war feature, a clear link between both data sources can be made. Still, the buried detected anomaly can be related to a partial remain, a derivative or an indirect measurement of the actual structure. The validation of what is measured can only be performed by archaeological excavation or augering. In this chapter, these techniques will be applied in combination with the interpretation of the geophysical scan results to validate traces related to four remarkable sites: derelict tanks, military barracks, a horse mass grave and a deep dugout system. The number of structures is limited but these types are unique among the range of WW1 features. Each case will be linked to the historical background, a specific research question set for the case (related to the original purpose of excavation, see papers and reports) and the conditions of the structure to determine what made it possible to be detected. Overall, this chapter will provide information of what is possible to characterise by applying FD-EMI scans with detail for specific cases.

## 5.2 Metal debris and shell craters: direct indicators of warfare

### 5.2.1 Metal identification

Saey et al. (2011) concluded that massive metal objects within the topsoil (0–0.4 m) sign as very negative anomalies within the DUALEM 1HCP $EC_a$ response. Therefore, this data layer is considered as very sensitive for metal objects within the topsoil. Moreover, it is able to distinguish metallic objects with very large masses below a depth of 0.4 m as positive anomalies. Whereas the 1PRP $EC_a$ response proves to be very sensitive to small buried metallic objects up to a depth of 1.0 m, the 2PRP and 2HCP configurations only depict very large metal masses as negative anomalies within their data. This allows for an integrated analysis of both 1PRP and 1HCP measurements. When an anomaly is positive within the 1PRP $EC_a$ data and negative within the 1HCP $EC_a$ data, it can be considered as situated within the top (0–0.4 m) soil layer. When an anomaly causes highly positive values in the 1PRP $EC_a$, but only a negligible or a positive response in the 1HCP $EC_a$, it can be considered to be present within the soil layer from 0.4 to 1.0 m depth.

Extra depth information about identified metallic objects can be extracted from the magnetic data layers. The cumulative response of the $MS_a$ coil responses have a signal change below a certain depth which means that high magnetic features appear as anomalies with a reduced $MS_a$ compared to the surrounding area and vice versa. For the 1HCP coil configuration, a high sensitivity can be obtained for the top 0.4 m, and a very low sensitivity between 0.4 m and 0.6 m because the tipping point is situated at a depth of about 0.5 m. Below 0.6 m, the cumulative response decreases, but the slope of the curve remains relatively small. This means that only objects with a very high magnetic susceptibility compared to the surroundings can be observed if they are situated below a depth of 0.6 m. However, this coil configuration is very sensitive to magnetic objects in the 0 to 0.4 m depth range, so this signal is considered to be representative for (subtle) magnetic anomalies within the topsoil. In analogy with the 1HCP configuration, the 2HCP coil configuration is very sensitive to features within the top 0.8 m, insensitive for objects between 0.8 and 1.4 m, and again (slightly) sensitive for objects within the layer from 1.4 up to 2.0 m depth. By integrating this information within the depth estimation of metal objects, depth intervals of 0 – 0.4 m / 0.4 – 0.8 m / 0.8 – 1.0 m can be suggested for the detected metal objects based on the several data layer results.

To standardise the classification of metal by applying DUALEM surveys, Saey et al. (2011) defined a linear combination of the DUALEM 21S $EC_a$ data layers which is called the FEMP (fused electromagnetic metal predictor). Values above an experimental determined threshold are used to identify metal objects within the soil by the FEMP calculation. The FEMP equation can be considered as standardised because the local median (in a radius of 10 m) has been removed from the $EC_a$-data layers (Δ-symbol). The median eliminated $EC_a$ data layers are combined within the result calculation. The FEMP is written as:

$$\text{FEMP (mS/m)} = 2.05 \cdot \Delta 1\text{PRP } EC_a - 1 \cdot \Delta 2\text{PRP } EC_a - 0.82 \cdot \Delta 1\text{HCP } EC_a - 1.89 \cdot \Delta 2\text{HCP } EC_a \quad (5.1)$$

To perform a targeted metal classification and properties estimation (depth / distinguish metal debris – massive objects), the following strategy can be used: First, a binary map can be generated to classify the pixels as metal containing (1) or metal absent (0). This is performed by the reclassification of the FEMP layer with a 15 mS/m threshold. This threshold is

experimentally determined for the WW1 front areas but in less disturbed environments this threshold can be adjusted (closer to 0 mS/m). Next, the properties of the different coils and responses (see beginning section 5.2.1) are used to estimate the depth of the detected objects. After classifying the metal objects per depth interval, the intensity of the FEMP and the peak shape can be considered. The FEMP intensity is related to the mass of the object but decreases rapidly with increasing depth. That is why only objects with a large size / high mass can be classified deeper than 1 m. Nevertheless, a FEMP peak-intensity data layer in combination with an estimated depth can deliver additional information. Small WW1 shells (18 pounder, +/- 6 kg) have experimentally derived FEMP values of > 50 mS/m (Saey, 2011) within the first metre of soil, which can be a calibration point of what to expect. A similar data evaluation flow can be seen in figure 5.1. Three detected and validated buried metallic items successfully demonstrated this strategy in appendix 5.1 and 5.2.

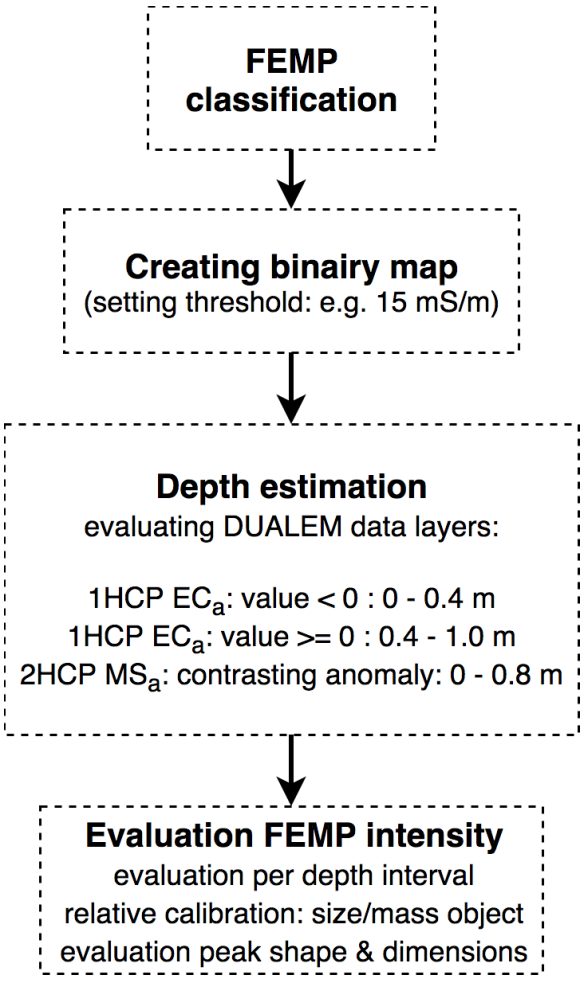



**Figure 5.1:** Data analysis flow to classify, interpret and estimate metal objects, detected by DUALEM scans.

### 5.2.2 Shell craters

When the topsoil only is partially affected by agricultural activities (no excavations or earthworks), shelling traces remain present in the top layer of the soil. When observing DUALEM $EC_a$ data, the 1PRP $EC_a$ stands out in mapping such shallow traces. Because of its limited depth response (0-0.5 m), the soil just below the ploughing activities (containing undisturbed war traces) is included in the measurements. Therefore, on such sites, evaluating this data layer is essential to get an insight in the remaining traces in the top layer. When the shelling marks match the traces on the aerial military photography, this information can be used as primary parameter to evaluate preservation of the war impact. Figure 5.2 displays a comparison between aerial photography and the 1PRP $EC_a$ data.

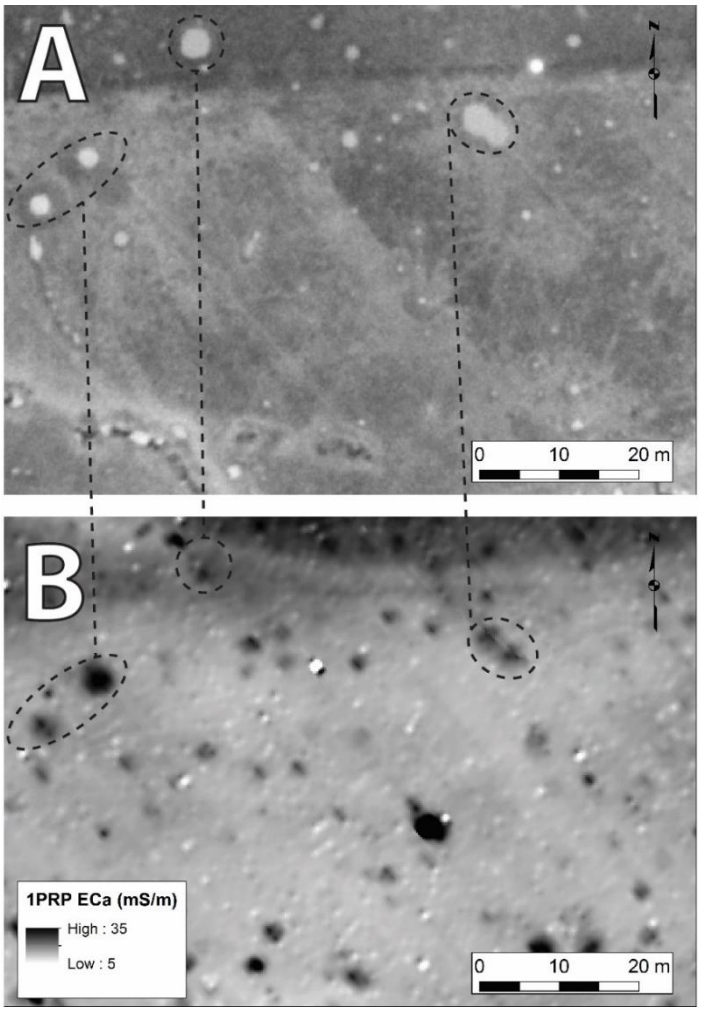



**Figure 5.2:** (A) represents an aerial photograph taken in May 1918 near the village of Loker (AMW collection), (B) is the 1PRP $EC_a$ data layer, measured in 2011 at the same location of image A. Three examples of detected and by aerial photograph validated shell holes are marked and matched between the two images.

To classify or extract those shallow soil disturbances, $EC_a$ depth slicing can be used, as proposed by Saey et al. (2016b). Because the shelling marks are vaguely present or absent in the other $EC_a$ data, those layers can be used to model the $EC_a$ response for the same depth as the 1PRP. Next, the modelled data layer (1PRP $EC_a$*) has to be subtracted from the measured 1PRP $EC_a$ layer, which will help to accentuate the shallow soil disturbances (= shell craters). By setting a threshold in this new layer, the shallow soil disturbances can be classified in a binary map. The schematic procedure to extract the soil disturbances is shown in figure 5.3 through data plots.

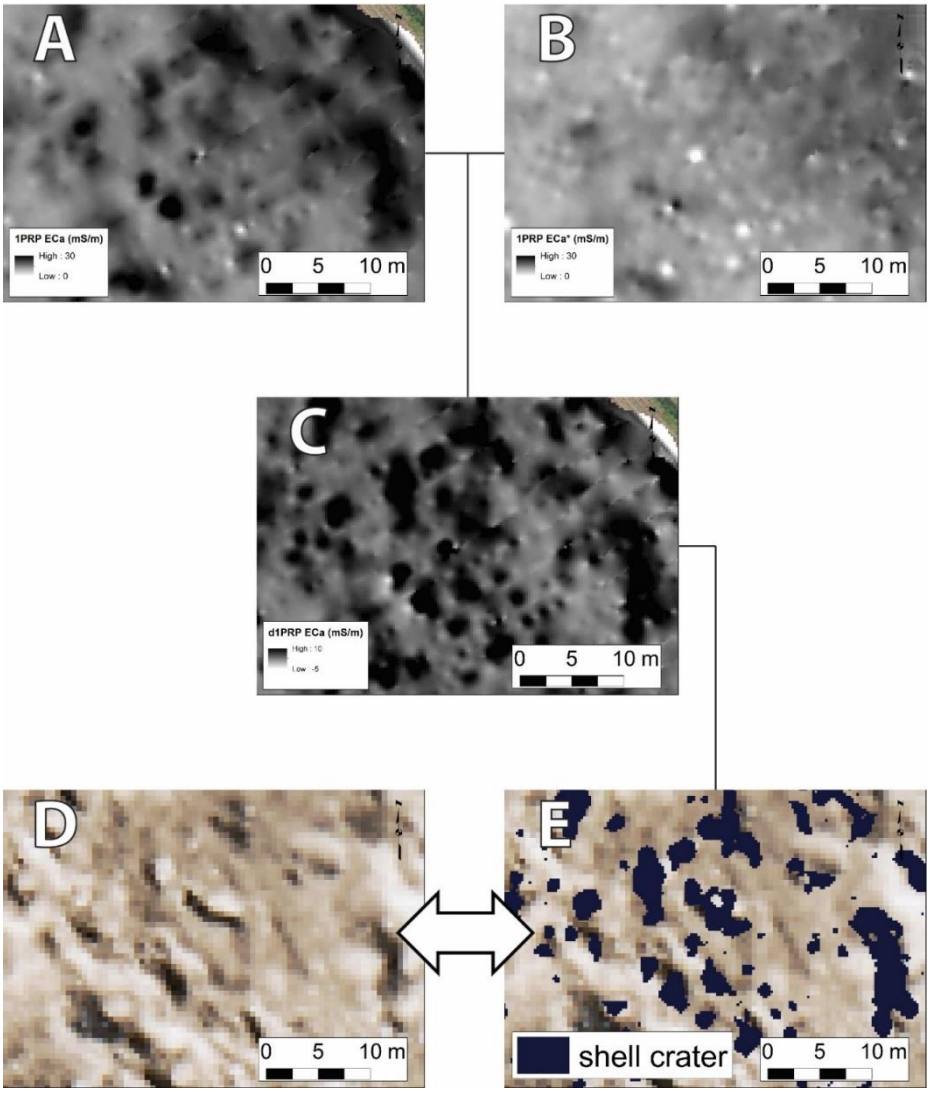



**Figure 5.3:** Visualisation of the 1PRP $EC_a$ data layer of a site near Wytschaete (A); the modelled 1PRP $EC_a$* response based on the other $EC_a$ data layers of the DUALEM 21S (B); the extraction of 1PRP $EC_a$* from 1PRP $EC_a$ (C); an aerial photograph of 1917 (IFFM collection) (D); the classification of shallow soil disturbances in a binary map by setting a threshold (= 8 mS/m) in layer C (E), whereby the zero-response was replaced by the historical aerial photography in image D.

The crucial processing step in the shell crater classification procedure is the process of $EC_a$ depth slicing to create the modelled 1PRP $EC_a$* layer. This step is briefly discussed in this section. The depth slicing procedure starts from the simultaneous $EC_a$ measurements (by the DUALEM configuration) and a three-layered model with a fixed conductivity of the topsoil (0–0.4 m), which was modelled to be 39.9 mS/m. This was done because the 1PRP $EC_a$ measurement proves very disturbed while the other measurements proved less sensitive to these shallow disturbances. Subsequently, this 1PRP $EC_a$* layer was modelled from the other $EC_a$ measurements by solving the set of equations below, together with the conductivity between soil layer $Z_1$ and $Z_2$ ($EC_2$*) and the conductivity of the soil material below $Z_2$ ($EC_3$*), with a given $EC_1$ of 39.9 mS/m.

$$\text{sHCP } EC_a = \left[R_{sHCP}(Z_1^*) - R_{sHCP}(Z_s)\right] \cdot EC_1 + \left[R_{sHCP}(Z_2^*) - R_{sHCP}(Z_1^*)\right] \cdot EC_2^* + \left[1 - R_{sHCP}(Z_2^*)\right] \cdot EC_3^* \quad (5.2)$$

$$\text{sPRP } EC_a = \left[R_{sPRP}(Z_1^*) - R_{sPRP}(Z_s)\right] \cdot EC_1 + \left[R_{sPRP}(Z_2^*) - R_{sPRP}(Z_1^*)\right] \cdot EC_2^* + \left[1 - R_{sPRP}(Z_2^*)\right] \cdot EC_3^* \quad (5.3)$$

With s = coil spacing in configuration

Whereby:

$$\text{1PRP } EC_a^* = \left[R_{1PRP}(Z_1^*) - R_{1PRP}(Z_s)\right] \cdot EC_1 + \left[R_{1PRP}(Z_2^*) - R_{1PRP}(Z_1^*)\right] \cdot EC_2^* + \left[1 - R_{1PRP}(Z_2^*)\right] \cdot EC_3^* \quad (5.4)$$

In equation 5.4, $\left[R_{1PRP}(Z_1^*) - R_{1PRP}(Z_s)\right]$, $\left[R_{1PRP}(Z_2^*) - R_{1PRP}(Z_1^*)\right]$ and $\left[1 - R_{1PRP}(Z_2^*)\right]$ are the cumulative responses for the three layers. Within this equation, 1PRP $EC_a$*, $EC_2$* and $EC_3$* were modelled at every measurement location by using the Levenberg–Marquardt non-linear least-squares algorithm (Marquardt, 1963), which converged to a stable solution to identify the unknown parameters. The FSOLVE function in MATLAB was used to automate this calculation. The complete modelling procedure for a three-layered model by using DUALEM results is described in Saey et al. (2012). When comparing the measured 1PRP $EC_a$ with the modelled 1PRP $EC_a$*, the global pattern appears quite analogue, with the difference that the patches caused by either extreme anomalies from the massive metallic objects, the scattered small metal pieces and soil disturbances in general are absent on the modelled data plot. The

residual map allows to identify the slight anomalies identified as soil disturbances, which are likely to be interpreted as shell craters.

## 5.3 GSS-scan vs. surface covering excavation results

### 5.3.1 Introduction

The only way to validate the detection ability of a geophysical sensor is to compare the scan results with the outcome of an extended archaeological excavation. In Flanders, most research areas are assessed by trial trenching to investigate the archaeological potential of an area (mostly threatened by development). In some cases, when valuable heritage is found, a surface covering excavation follows. Such an excavation containing valuable WW1 remains, took place from April until July 2018 at a 1 ha site near the village centre of Wytschaete. Before the investigations started, an FD-EMI scan with an interline resolution of 0.85 m was executed. This opportunity made it possible to evaluate the detection ability of the DUALEM sensors according to excavation results.

### 5.3.2 Site description

The Wytschaete study site (Hill 80) is located 900 m behind the 1915-1917 frontline on top of the Messines ridge. This area was mainly occupied by the German army. The Kapellerie windmill (built in the 17$^{th}$ century) can be found in the centre of the field with farm buildings in the southeast corner. Aerial photographic research showed that during the war, all civilian structures were incorporated in the military defence network. Around May 1917, the entire Messines ridge was heavily targeted by Allied artillery (Edmonds, 1948) as preparation for the Battle of Messines which was a prelude to the Third Battle of Ypres. The increased artillery fire was meant to weaken the enemy lines before the 19 depth mines were detonated (to ease an Allied attack and force a frontline shift). This shelling had a strong impact onto the site. From then on, the area was converted into the lunar-like landscape. After the Messines battle, the village of Wytschaete was in Allied hands and the front has been pushed back 2.5 km to the east of the study site towards the hamlet of Oosttaverne. During the Allied occupation, not

much changed in terms of military infrastructure on the study site (Stichelbaut, 2015). After the German Spring Offensive (German army occupation on the site), British trench maps mentioned the presence of some earthworks/bunkers at the site which could be linked to the reuse of the infrastructure (Stichelbaut, 2015). This can further not be proven. From the period after the liberation offensive, not much information was available to further analyse the site.

### 5.3.3 Results

The digitised contours of the excavated features were provided by Ruben Willaert Archeologie (Brugge, Belgium) who excavated the site. The site contours and classified features of the excavation are shown in figure 5.4.

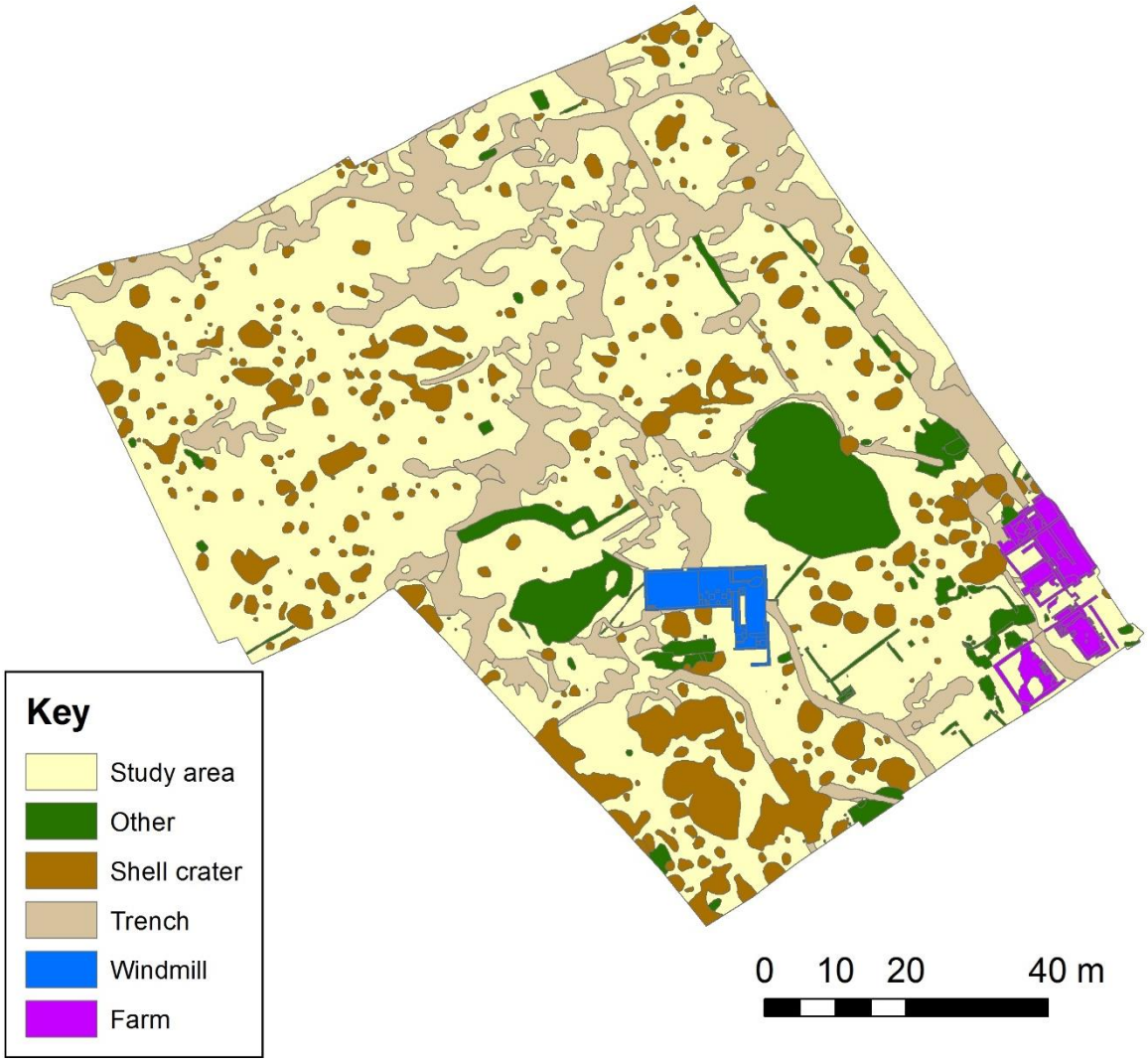



**Figure 5.4:** Display of the map representing the contours of the excavated archaeological features of the Hill 80 excavation.

The two main categories of WW1 structures on the map in figure 5.4 are trenches (covering 28.7% of the study area) and shell craters (covering 12.7% of the study area). The FD-EMI scan was able to detect 62% of the (approximate) trench trajectories[2] while aerial photography detected 81% (both compared to the excavation results). Trenches (2), (6) and (10) were missing in the RSA analysis (see figure 5.6). A possible cause for this absence is the lack of a denser temporal photo coverage, the lack of contrast of features in the images and the often slightly blurred quality of the high altitude aerial photographs.

In the scan results, trench (2) was detected (not seen by RSA) while trenches (6), (7), (10) and half of trench (3) were not revealed (figure 5.6). This short analysis proves the complementarity of both RSA and GSS techniques to reach a maximum coverage in non-invasive archaeological pre-studies. The main reason for the coverage difference between GSS and the excavation results are the scale of the features, the complexity of the area and the misinterpretation of features. In the southern part of the field, smaller and less extended trenches were found. The FD-EMI scan shows that this area is more (magnetically) disturbed and because of that, the majority of the finer structures were not always distinguished. The trenches in this area were often found near other dug structures or building remains (see classification 'other', 'Farm' and 'Windmill' in figure 5.4) which makes the discrimination between both difficult, as not impossible. At the northern part of the site, the well-developed trenches can clearly be distinguished. The derived scan signature of those trenches match the excavation results well. The precision of delineation is partially depending on the spatial scan resolution but also on the scan technique. The TD-EMI scan with the Sensys EMD2 delivered a sharper image of trench (5) (see figure 5.7) due to the finer spatial resolution. The shape from the by TD-EMI scanned trench matches the excavation results better than the FD-EMI results (see figure 5.7). On the other hand, the TD-EMI technique had the disadvantage that the total coverage of trenches is lower (see chapter 4) because not all structures had a magnetic distinguishable footprint. Therefore, FD-EMI was the better option.

If the detected building remains are considered, the windmill building and the former farm foundations were found during the excavation. Both structures could be located in the RSA data and GSS results whereby mainly the Kapellerie windmill could be distinguished in the FD-

[2] Approximate trajectory lengths: this is measured in GIS and includes the main trajectory of the trench. Small bulges and variations were not included in this measurement.

EMI scan. Its signature in the 1PRP $EC_a$ layer is displayed in figure 5.5. From this signature and without any additional information, this sharply delineable and strong contrasting L-shape structure could be identified as possible building remains. The bricks in the image are producing a contrast by causing increased magnetic and electrical conductive values compared to the surroundings. The anomalies at the farm location are not contrasting with the surroundings in a way that these foundations could identified based on the scan results alone. Because these traces are at the edges of the surveyed field, survey turning-effects of the sensor are noticed in the data interpolation, which are not favourable for feature detection.
Overall, the GSS scans delivered a satisfying result according to the excavated features with the localisation of unseen structures compared to RSA. The localisation of the general trench trajectories and building remains can be accurately performed when the scan information is used as guidance.

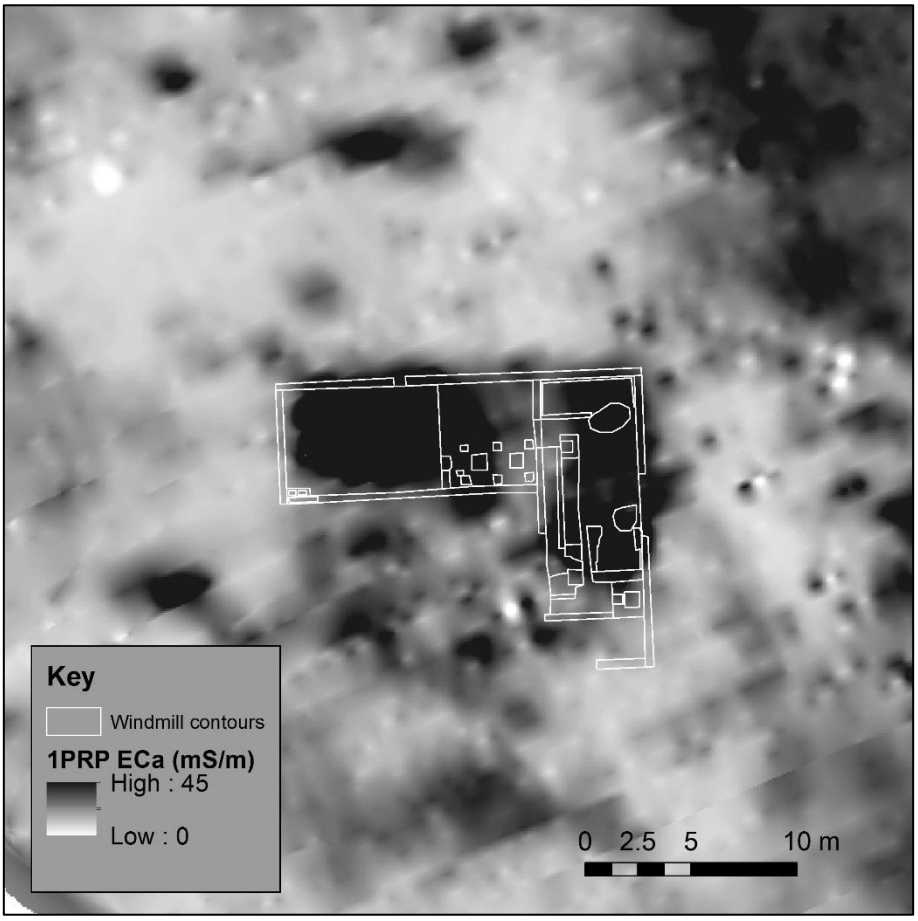



**Figure 5.5:** Display of the 1PRP $MS_a$ data layer on the location of the former Kapellerie windmill with indication of the excavated building contours.

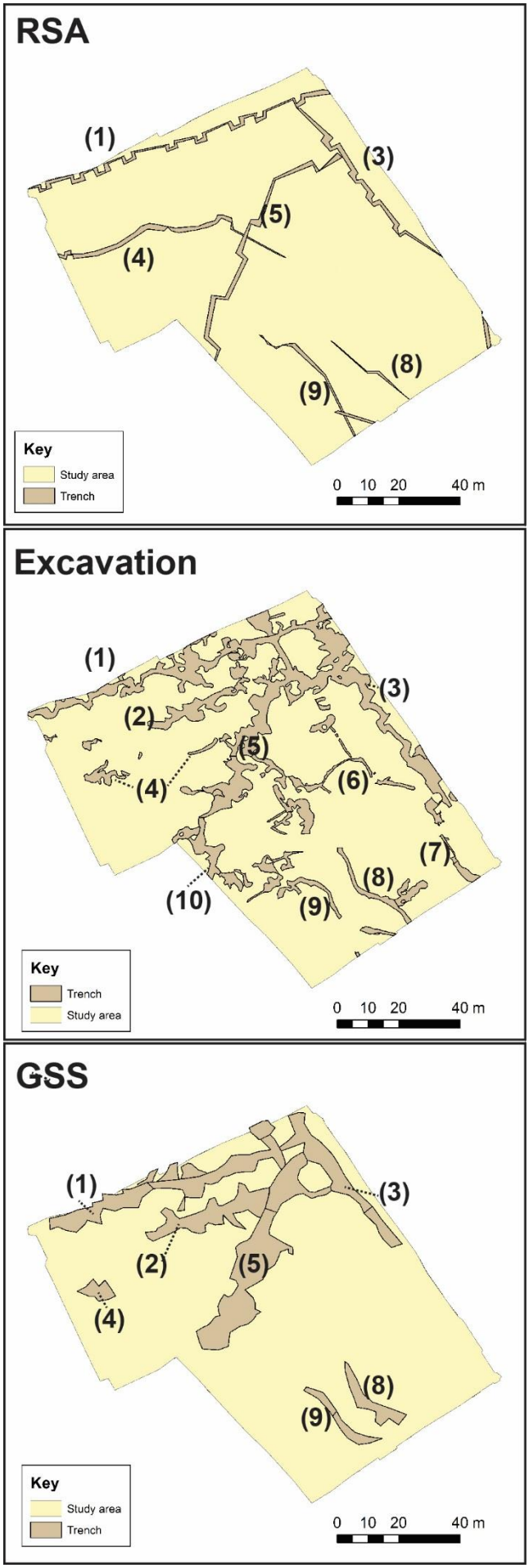



**Figure 5.6:** Display of the digitised trenches derived from aerial photography (top); archaeological excavation (middle); FD-EMI scan (bottom). The corresponding trenches are identified in all three maps by a number ID.

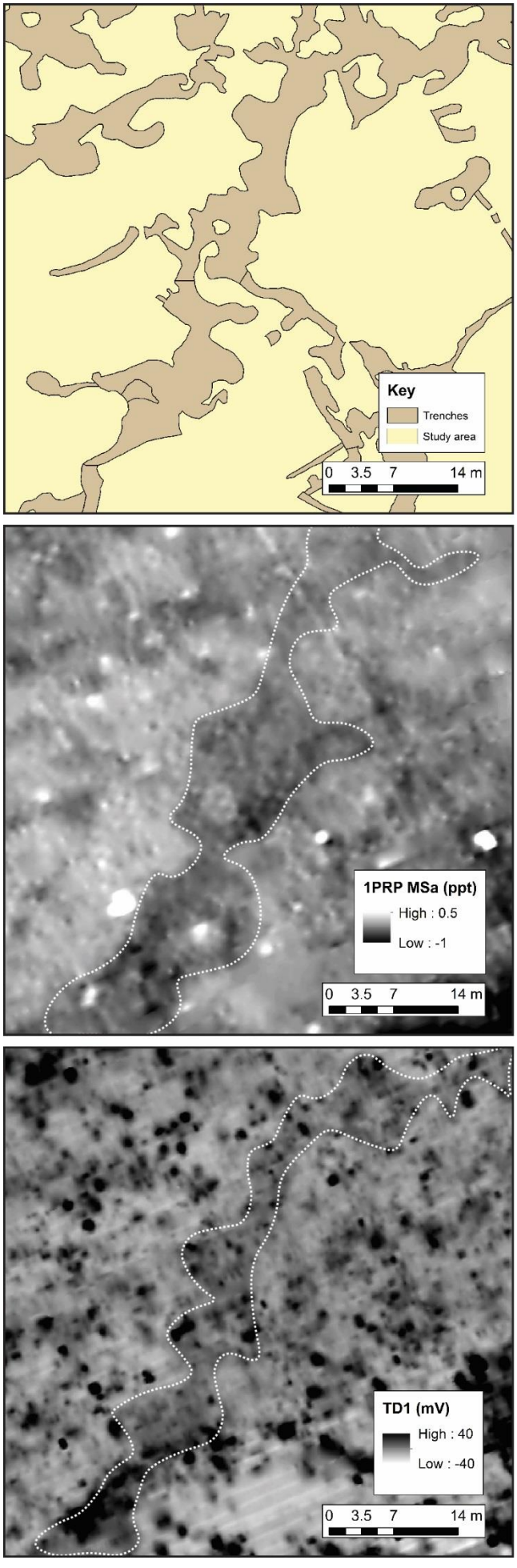



**Figure 5.7:** Display of trench 5 (see figure 5.6) at the Hill 80 site by the digitised excavation contours (image top), by the 1PRP $MS_a$ data layer of the FD-EMI scan, by the TD1 data layer of the TD-EMI scan. The dashed line delineates the detected trench anomalies.

## 5.4 Validation of military structures

### 5.4.1 Dugout

#### *5.4.1.1 Introduction*

As the war progressed and the impact of the artillery became more powerful, protection was sought below the surface. Therefore, the armies started with the construction of underground sheltering structures. The first type of underground works are dugouts which can either be covered shelters with reinforced roofs or deeply excavated or even tunnelled with sufficient ground cover to resist artillery fire, the so-called deep dugouts (Doyle et al., 2001). The purpose of these was to accommodate troops close to the frontline while protecting them from artillery fire. Deep dugouts were constructed as deep as 15 m below the surface. The largest systems could shelter a complete battalion (Barton et al., 2004). A third type of underground works consists of covered approach trenches or underground communication passage tunnels – the so-called Russian saps and infantry subways – to conceal troop movements from enemy ground observation and give advancing troops the necessary protection (Grieve and Newman, 1936). Despite the significant potential along the Western Front and other theatre of war sites, only very limited field research has been carried out. This is partly because of the difficulties in pinpointing the sites but also because tunnel explorations are both hazardous and expensive due to the subsurface nature of the sites. In this section, the potential of the FD-EMI scanning technique will be investigated to characterise underground activities.

**Geophysical scan**

The detection of underground tunnels or deep-dugouts is presumed to be difficult and mostly out of the depth range of geophysical prospection techniques that are adapted to map archaeological sites. Therefore, a test case was established, with the knowledge of the construction of dugouts at this case's area during WW1. The aim of this case is to try to map remains or indications of presence of the former tunnelling activities and dugout systems in the Ypres Salient with geophysical techniques, supported by other non-invasive sources.

#### *5.4.1.2 Study area – Tor Top*

The study area for this dugout-test is located in the central part of the Ypres Salient on a dominant ridge with strategic views towards Ypres. The area was selected because historical records indicate that it was a military mining and tunnelling hot spot (Barton et al., 2004; Stichelbaut et al., 2016). This sector of the front was known by Allied cartographers as Hill 62 or Tor Top. During the Second Battle of Ypres (22 April–25 May 1915), the frontline shifted towards the study area and both warring parties entrenched themselves in a positional trench warfare lasting more than two years. As was the case with many of the strategically important ridges, the area became a dangerous hotspot in the mining war (Stichelbaut et al., 2016). During the first week of June 1916, just prior to the German offensive, work had begun on a mineshaft (War Diary 2nd Canadian Tunnelling Company, weekly mine report 5th June 1916). After the recapture of the ground, work recommenced. By August 1916, deep dugout chambers and stairs were constructed almost 6 m deep in sandy soils, forming the complex tunnel system known as 'Tor Top' (Barton et al., 2005). Two partial plans of the dugouts – dated November 1916 and March 1918 (figure 5.8) – show the internal organisation of a section of the tunnel system (Barton et al., 2004) (3rd Canadian Tunnelling Company War Diary). It shows a complex network of dugout chambers, with connecting and defensive galleries housing listening posts to signal German offensive mining schemes. During spring 1917, three mines were detonated from within tunnel galleries causing craters almost 15 m wide just in front of their own frontline, most probably as counter-mines. As a result of the Allied 1917 offensive (Third Battle of Ypres, 31July–10 November 1917), the frontline shifted and the study area moved 1700 m behind the new Allied frontline. The dugouts continued to be used as the brigade headquarters and in 1918 provided safe shelter for up to 30 officers and 500 infantrymen in chambers fitted out with bunks (Barton et al., 2005). The structure remained in use until the area was lost following the 1918 German Spring Offensive.

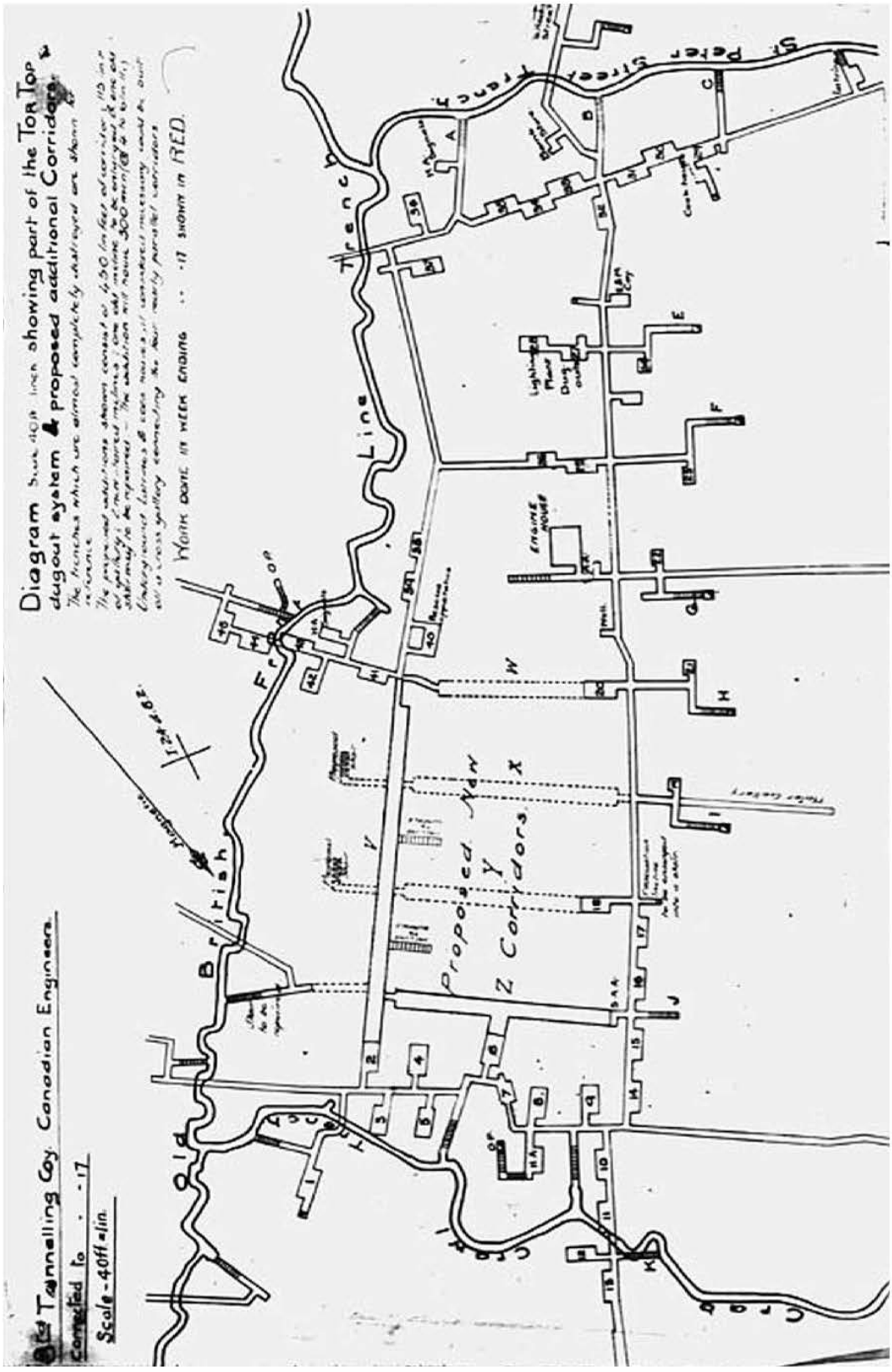



**Figure 5.8:** Plan drawing of the Tor Top dugout system in March 1918 (source: War Diary 3rd Canadian Tunnelling Company, Canadian Engineers, Library and Archives Canada).

#### *5.4.1.3 Results DUALEM 421S scan*

Comparison with the historical evidence reveals the preservation of large parts of both the Allied and German trench system, despite heavy artillery fire during the war. Features such as trenches (figure 5.9 C) and two stretches of a trench railway (figure 5.9 B) clearly left an archaeological footprint in the soil. The EMI survey also reveals that large parts of the landscape are peppered with shell holes and mine explosions (figure 5.9 A). The most prominent and intriguing features at the site are revealed in the $MS_a$ measurements (figure 5.9). The $MS_a$ measurement of the soil volume up to an approximate depth of 1.5 m shows five connecting linear features (figure 5.9 E). Those features are also vague visible in the 1PRP $EC_a$, 2PRP $EC_a$ (figure 5.9 centre) and 1HCP $EC_a$ but those elements were only identified in combination with the dugout plan drawing (figure 5.8) and the 2PRP $MS_a$ dataset (figure 5.9). These linear anomalies correspond to parts of the Tor Top dugout. A 75-metre-long section of the eastern main gallery and a 110-metre-long section of the western gallery – which both run parallel to the frontline – are visible in the 2 PRP $MS_a$ dataset, together with three transverse galleries each 30 m long. The latter are indicated on the tunnel plans as 'proposed additional corridors'. The geophysical measurements clearly indicate that the construction also took place. In the 4PRP $MS_a$ measurements, similar parts of the dugout are revealed, although these are much more subtle and partially interrupted. Two linear features correspond to the two main galleries and measure approximately 175 and 125 m (figure 5.9 F–F' and G–G'). They even go beyond the area covered by the two tunnel plans, thereby providing new information on the extent of the tunnel network. By georeferencing the historical plans, more parts of the dugout can be identified. At least four dugout chambers (figure 5.9 H) and parts of the defensive tunnel network in front of the Allied frontline are revealed. Of equal importance to notice is the absence of other features, which are invisible in the dataset. None of the entrances or tunnel ad its show up as a signal which can be differentiated from the signals of trenches or battlefield debris. In general, it is much more difficult to identify point features than linear ones. Without further integration of historical data, the identification of such sites will remain extremely difficult.

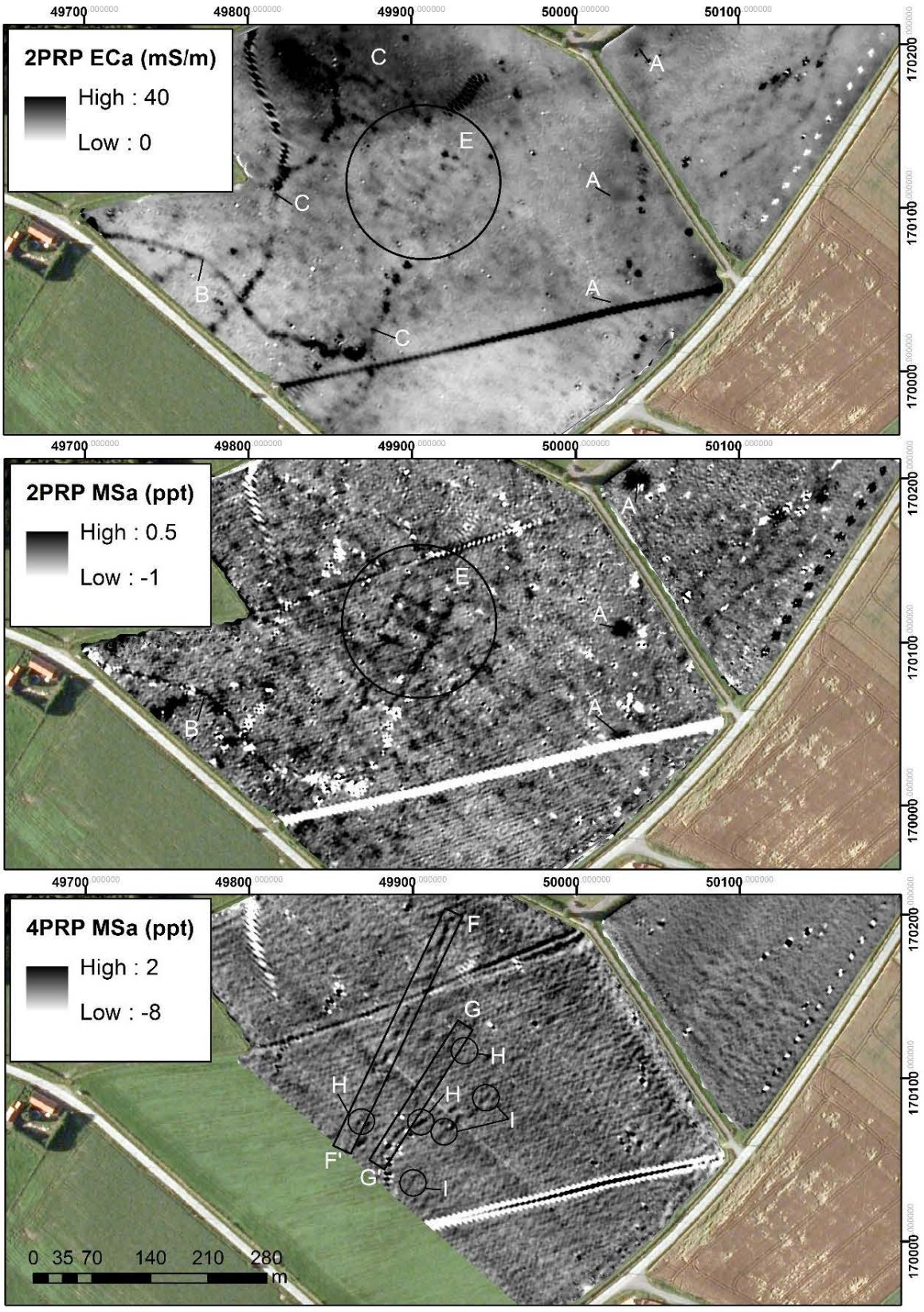



**Figure 5.9:** Top to bottom: 2PRP $EC_a$ measurement with a DOE of 0.8 m; 2PRP $MS_a$ of the measurement of the soil volume up to an approximate depth of 1.5 m; the 4PRP $MS_a$ measurement of the soil volume up to an approximate depth of 2 m. (orthophoto: copyright AIV)

#### *5.4.1.4 Augering validation*

Although there is no doubt that the geophysical anomalies in the EMI data are related to the dugout system, questions remain as to what exactly caused the anomalies that were picked up by the EMI measurements. In order to use these geophysical methods to detect similar sites in other sections of the front, this important question must be answered. The historical records of the 2nd Canadian Tunnelling Company mention that the tunnel system has been constructed at a depth of 5.5–7.6 m. Consequently, theoretically this is too deep to be picked up by the $MS_a$ measurements, which have a maximum exploration depth of approximately 2 m. Based on the theoretical possibilities of the sensors, we can suggest several hypotheses: either the historical records are inaccurate, or another shallow tunnel system shows up, or the anomalies are caused by the physical characteristics of the soil above the tunnels. Based on depth responses of the multi-receiver EMI, the anomaly can be estimated between roughly 0.5 and 1.5 m deep. To better understand what was causing this anomaly, further research was needed to test these hypotheses and provide an answer to the following questions: why is only a part of the network visible; what causes the geophysical anomaly; and how can a feature, which according to historical sources is situated at a depth of approximately 6 m, show up on the EMI survey.

**Hand augering**

Initially, hand augering (3 cm gouge auger) on the geophysical anomalies of the transverse galleries of the tunnel system (figure 5.9 E) validated the interpretation of the features as a dugout system. At 3.5 m deep, the auger penetrated through the degraded but still in situ wooden tunnel frame. The augering and soil profile (figure 5.10) revealed a hollow or loosely filled space above a solid wooden construction, probably the tunnel floor, at a depth of 5.1 m. Two additional augerings revealed similar results, although in these latter soil profiles no hollow space was observed and the tunnel appeared either to have been filled in with loose sand or may even have entirely collapsed. This ground truthing corroborates the interpretation of the geophysical anomalies as being part of the Tor Top dugout system and corresponds more or less with the historical records, which mention a construction at a depth of 5.5 – 7.6 m below the surface.

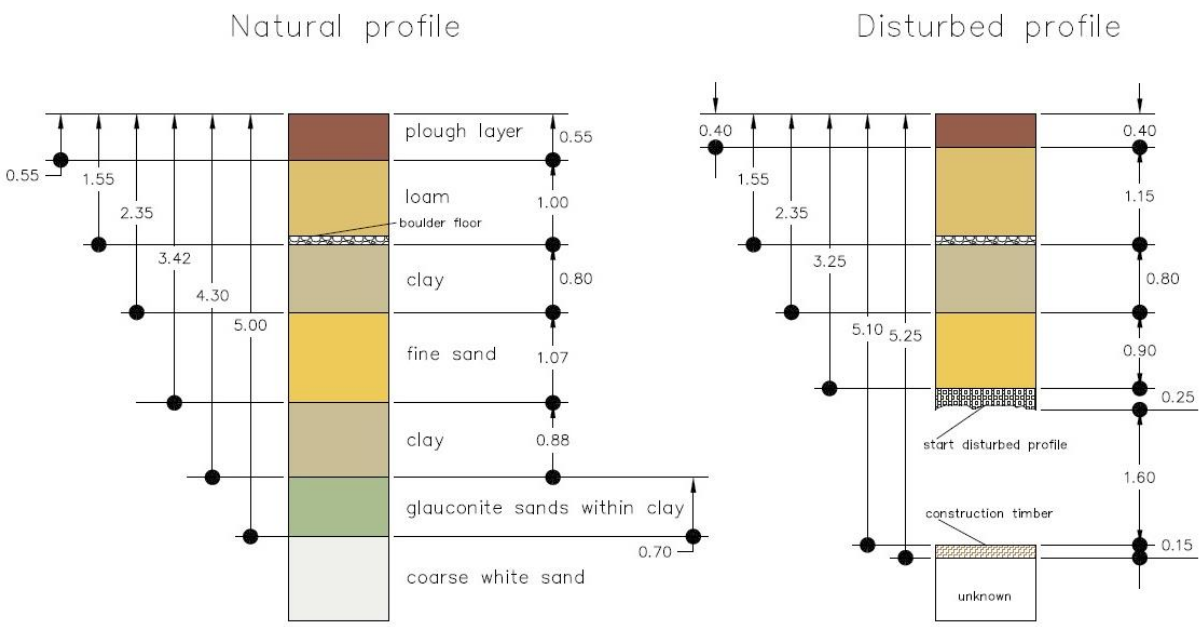



**Figure 5.10:** Results of the augering: a natural soil profile compared to a soil profile showing the presence of the 1916–1918 tunnel system.

### Magnetic susceptibility profiles

To further explain why the tunnel shows up on the geophysical dataset and to evaluate the $MS_a$ data, magnetic susceptibility profiles were established with a Bartington MS2 magnetic susceptibility system. This system allows to measure MS-values in a borehole to make a depth-related MS-profile. First, in situ soundings were performed with a Bartington MS2H downhole probe. Measurements were taken at 10 cm intervals, to a depth of 1.9 m beneath the surface, there by targeting the relevant depth interval indicated by the variations in the $MS_a$ data. Soundings B1 and B2 (figure 5.11) are situated in the magnetic anomaly of the transverse galleries, whereas B3 was placed outside of it. While the latter only displays a slightly higher susceptibility in the top layer (0 – 0.5 m), B1 and B2 display values over $100 \times 10^{-5}$ SI, recorded beneath this top layer as well, and most prominently deeper than 0.50 m below the surface (see figure 5.12). At B2, the higher susceptibility even persists throughout the entire profile depth, as is explained by the numerous small metal fragments (battlefield debris) along the whole length of the auger profile. Additional lab-based susceptibility measurements of soil samples were made using a Bartington MS2B sensor. Samples were taken using a 5-cm

diameter Dutch auger, before bulk samples were taken at each coring interval. These were then subsampled to avoid any direct interference from chunks of metal debris. The results, shown in figure 5.13, confirm the pattern observed in the field soundings (figure 5.12). Both B2 and B4, located in the magnetic structure detected in the EMI data, indicate higher magnetic susceptibility concentrated between 1 and 1.5 m deep. However, there is a significant difference between susceptibility values observed in the in situ soundings and the lab-based measurements (figure 5.13). This can be attributed to the in situ presence of metal object fragments, which were not taken into account in the laboratory analysis. At locations B3 and B5, higher susceptibilities are once again only present in the top layer.

In the light of these MS measurements, it can be said that outside the dugout's magnetic footprint, the top layer relates to battlefield debris and higher magnetic susceptibility (0–0.5 m; MS2B median: 20 X $10^{-6}$ SI; MS2H median: 35.5 X $10^{-6}$ SI) than the soil below the plough layer, which is more homogeneous and of low magnetic susceptibility (MS2B median: 12.5 X $10^{-6}$ SI; MS2H median: 21 X $10^{-6}$ SI). There is a difference at locations bearing the magnetic anomaly corresponding to the transverse galleries. Here, a heterogeneous soil with a higher magnetic response (median MS2H at B2: 52.5 X $10^{-6}$ SI) is found just under the plough layer. This could be explained by filling in from the subsidence caused by the collapse of those tunnels with higher magnetic top layer soil. Location B1 (figure 5.12) corresponds with the hollow space detected (see hand augerings). This location has lower deviations in $MS_a$ than in B2 (EMI scan), which can be explained by the higher magnetic disruptions at a depth of 1–1.90 m in the magnetic augering (figure 5.12). Extrapolating this principle, it can be concluded that the darker the image (higher values in the 2PRP $MS_a$ measurement, figure 5.11), the more heterogeneous magnetic soil is used to fill in the subsidence and the less likely the tunnel will be intact.

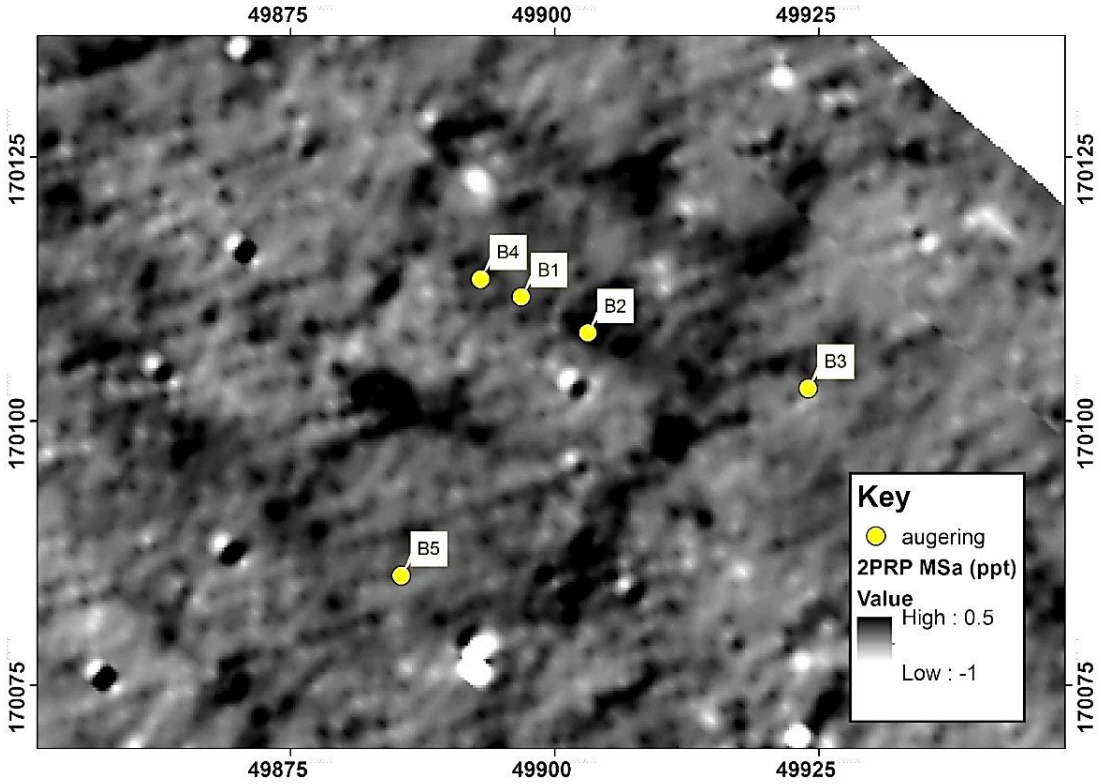



**Figure 5.11:** A detail of the 2PRP $MS_a$ measurement, with a focus on the magnetic structure and augering locations.

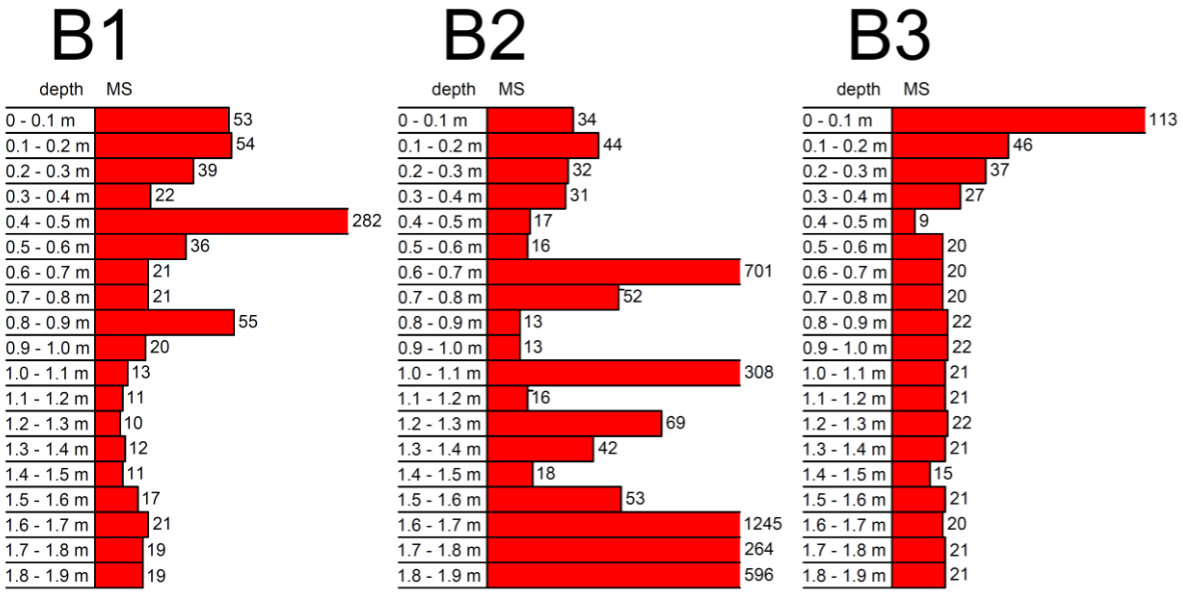



**Figure 5.12:** Magnetic depth profiles (MS) at the augering locations measured by the MS2H downhole probe. MS values are expressed in X $10^{-6}$ SI units.

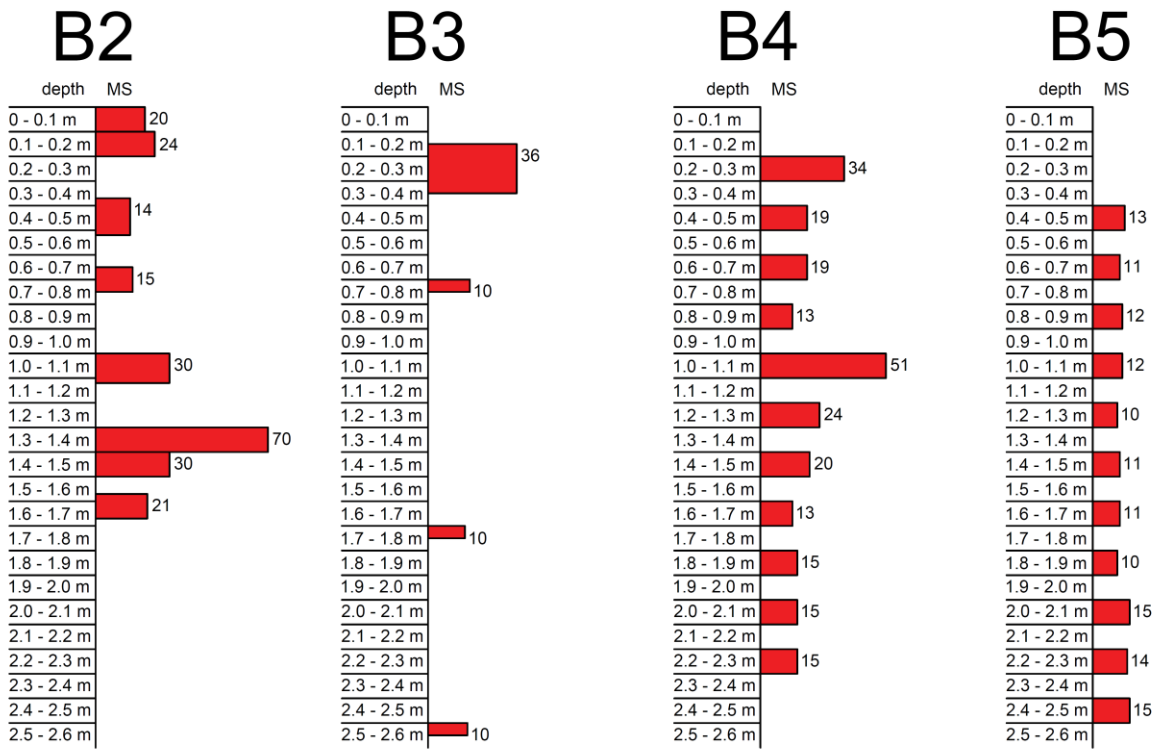



**Figure 5.13:** Results of the MS2B analysis. MS values are expressed in X $10^{-6}$ SI units.

### Borehole camera and LIDAR data

To support the theory of collapsed dugout galleries, small subsidences were noticed in the ALS data (figure 5.14). Even after agricultural activities that levelled out older subsidences, still ongoing degradation of the dugout can be observed in the recent micro-topography (2016 land use state: grassland). The second extra element to support this theory is the exploration of the borehole with an imaging device. Therefore, a sewer camera was used to enter the borehole at an augering location. At the position where the gouge auger made an abrupt shoot through, a penetrated wooden roof board of a dugout gallery was seen, containing a cavity underneath. The reason why the auger made a depth shoot trough of more than 1.5 m is because of the loose sand in the filled up corridor. At the bottom of this infrastructure, a wooden floor was found (wood flakes gathered in auger by scratching, obstruction of deeper penetration). The roof plate in the borehole can be seen in figure 5.15.

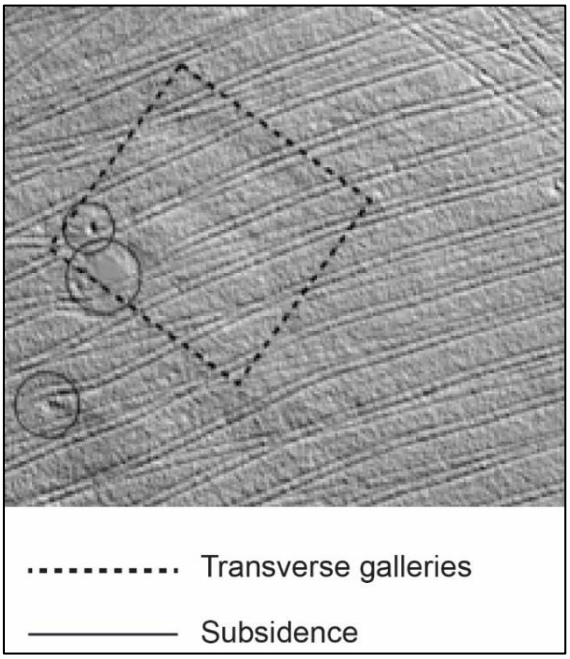



**Figure 5.14:** Hill shading (40° azimuth, 15° angle) of the high-resolution ALS dataset with indications of subsidence and transverse tunnel galleries.

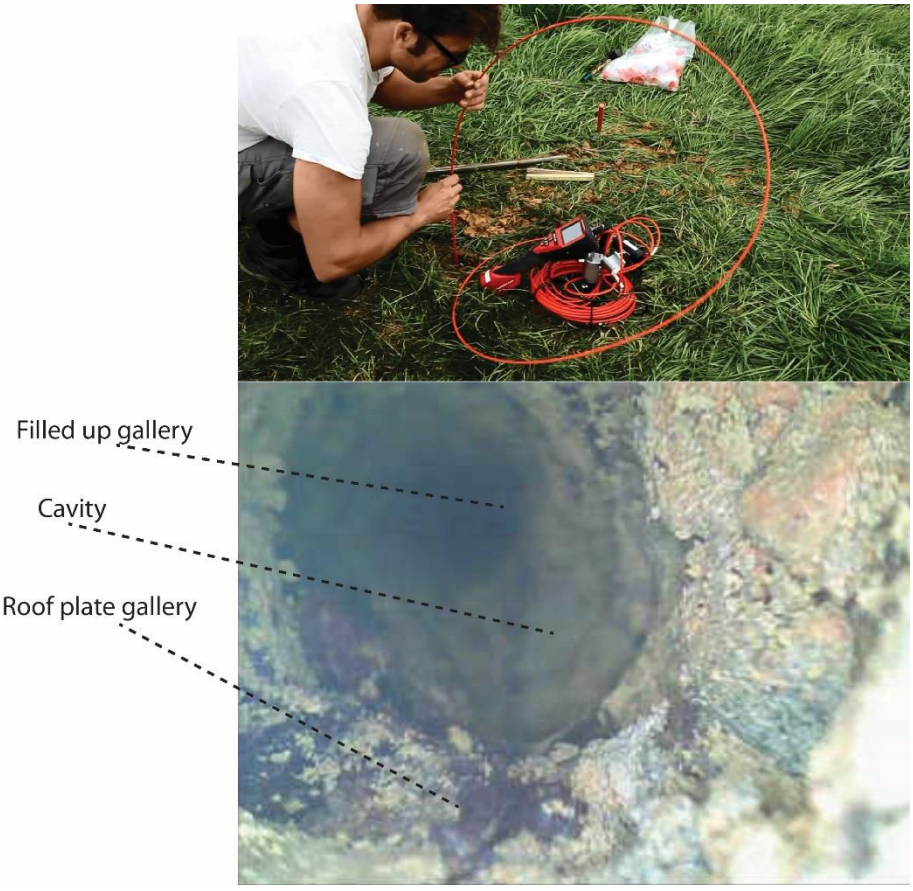



**Figure 5.15:** Borehole camera (top) and image of the penetrated roof plate of the dugout system (bottom).

## 5.4.2 Tanks

### *5.4.2.1 Historical background*

To unlock the almost static trench warfare, new weapons were introduced, one of which was a self-propelled armoured fighting vehicle capable of travelling cross-country as a weapon carrier (Liddell Hart, 1959). These 'landships' – as they were originally known – saw action for the first time on 15 September 1916 during the Battle of the Somme. Their goal was to act as 'land battleships' and break through the impregnable networks of trenches which were protected with barbed wire, pillboxes and machine-guns.

In Belgium, tanks were used for the first time in 1917. Field Marshal Douglas Haig, the supreme commander of the British Expeditionary Force, planned a large-scale offensive to break through the defences of the German Fourth Army in the Ypres Salient – the belt of fortifications around the town of Ypres – and capture the logistical networks in Roeselare and Torhout (Edmonds, 1948). The ultimate goal was initially to straighten the Wytschaete-Messines Ridge, then subsequently to break the stalemate in the Ypres Salient and advance further to capture the German submarines bases along the North Sea coast which threatened the British fleet. To support this offensive, 216 Mark IV tanks were employed, measuring 8.05 m long and weighing 28 tonnes and operating with a crew of seven, either equipped with six machine-guns (female tanks) or four machine-guns and two six-pounder canons (male tanks) (Edmonds 1948). The German army lagged behind in developing tanks and did not use them on the battlefields in Flanders.

### *5.4.2.2 Localisation at the front*

Aerial photo interpretation was quite successful to accurate localise logged or destroyed tanks at the battlefields (Stichelbaut et al., 2018). The wealth of available aerial photographs made it possible to identify 97 tank wrecks at the Ypres Salient. All were identified on photographs dating from after the tanks had been in action, thereby excluding any being photographed while they are still in action. This number is most definitely an underestimation of the historical reality. Although the research area is extensively covered with aerial photographs, in some areas there is no coverage with either large-scale or high-quality photography.

Interpretation of the air photos and GIS mapping resulted in the first detailed and accurate overview map of tank cemeteries in the Ypres Salient. Besides being a valuable addition to the historical narrative, a departure point for further targeted heritage research was created. Looking at the present day, land use indicates that over 47% of these sites have already been lost and overbuilt by roads and buildings (n=46). This leaves 51 sites of unknown potential where geophysics can be applied to verify if remains of these tanks can still be found.

#### *5.4.2.3 GSS validation sites*

To investigate the potential of encountering any material remains related to tank warfare in Belgium, two high-potential areas were selected (based on the aerial photograph analysis) to carry out non-destructive geophysical surveys in order to assess the heritage potential. As geophysical prospection technique to perform a non-invasive characterisation, FD-EMI was applied on these sites.

**Site 1: Clapham Junction**

One of the most famous tank cemeteries in the Ypres Salient is in the historical literature and in captions of photographs often described as near 'Hooge' and 'Clapham Junction'. It was photographed numerous times by official war photographers and as attraction for battlefield tourists in the post-war years. Historical aerial photographs of the area located the tanks accurately and revealed seven hulks of disabled tanks close to each other.

The site is situated near a strategic position in the Ypres Salient, on the edge of the Geluveld plateau, the heights east of Ypres in an area which played a key role in the German defences. On the opening day of the Third Battle of Ypres, tanks of the Tanks Corps 2nd Brigade supported the ground offensive of the British II Corps. Of the 52 tanks in this brigade, 19 were hit and 22 broke down or were ditched (Edmonds, 1948). It proved to be the most difficult sector in the area under attack because of the bad state of the ground and the narrow gaps in which the tanks had to manoeuvre. The area became infamous as '*the tank graveyard'* with many being knocked out by a well-positioned anti-tank gun in a nearby concrete bunker with excellent observation of the limited approaches to the ridge (Liddell Hart, 1959). More tanks were knocked out in this area during successive attacks in August and September 1917. The

tanks remained in situ during the remainder of 1917 and 1918. They came under intensive German artillery fire during the Third Battle of Ypres. The area was retaken by the German Army during the 1918 Spring Offensive and shelled again by British artillery. Ground photographs taken during and after the war show many traces of the intensive damage suffered by the tanks. This research indicates that these sites probably still contain a number of construction parts and instruments related to tank warfare.

In 2017, an area of 0.88 hectares near Clapham Junction was surveyed with a DUALEM sensor. Historical aerial photographs identified four hulks of tanks in the study area (three more are just outside of the survey limits) (figure 5.16). As a surprise, on all four spots there was a geophysical anomaly which corresponds to magnetic contrasting traces. Each spot was identified as containing metal. On tank location A, FEMP values of 150 to 300 mS/m are found which indicate the possible presence of massive pieces of metal (larger tank parts). The other three locations indicate much lower values (20 – 100 mS/m) which could relate to smaller objects or rust traces in the topsoil. Based on the coil responses, these anomalies should be located just beneath the surface.

At tank location C, agricultural groundwork activities revealed preserved traces in the soil: shallow metal objects were found and identified as metal-plate construction bolts. Most of them were only found with the 'head' intact, which could point to activities to dismantle the tank for scrap metal (see photo in appendix 5.2). In addition, numerous rust traces and weathered metal were noted at a shallow depth. The continued use of the land as pasture since the end of the war, contributed to preserving these targeted finds.

Based on the non-invasive research published in Stichelbaut et al. (2018), a detailed archaeological excavation was executed on the 1st of December 2018 at this site. More specific, a window of 10 by 10 m was opened up at tank location B and D to validate the cause of these anomalies. At both locations, concentrations of bolts and rust traces were found which were sharply delineable in the soil matrix. For sure, compaction had an influence on the measurements (28 ton tank, detectable in EC) but the level of influence of metal and shell craters exceed this. There can be concluded from the archaeological investigation that both anomalies can be linked to the careful stripping of the tanks after the war, whereby almost all parts (with the exception of the bolts and nuts) were collected (Bracke et al., 2019).

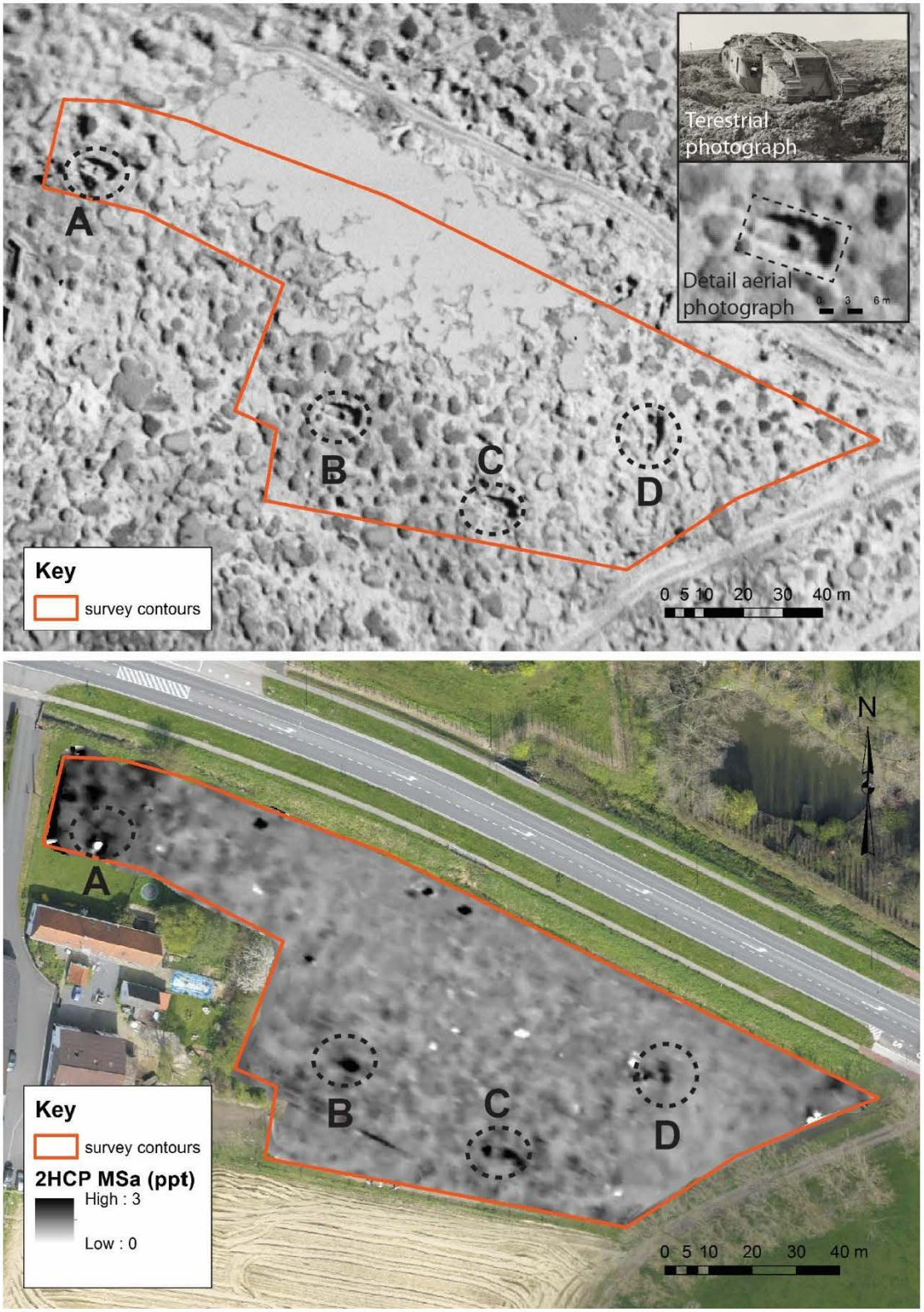



**Figure 5.16:** Top: visualisation of an aerial photograph (27th May 1918, IWM collection) with indication of four spotted tanks (A-B-C-D) within the scanned study site borders. A detail of a terrestrial and aerial view of a Mark IV tank is shown (IWM collection). Bottom: the 2HCP $MS_a$ data layer with indication of four anomalies corresponding with the locations of the four tanks in the photograph above. (orthophoto: copyright AIV)

### Site 2: Sint-Juliaan

Based on the positive detection results of the Clapham Junction case study, a second area was selected to validate the historical remote-sensing data: a site near the hamlet of Sint-Juliaan was chosen where aerial photography indicated an abandoned tank hull.

On the first day of the third Battle of Ypres, the front shifted almost two kilometres and reached Sint-Juliaan. Throughout August 1917, the hamlet was the scene of numerous costly actions as regards human life, although further progress was very limited. On 20 September 1917, the offensive was renewed all over the frontline (Battle of the Menin Road, 20-25 September 1917) (Edmonds, 1948). In the research area, the British 58th division advanced with the aid of tanks from the E Battalion. The aim of the tanks engaged was to support the attacking infantry and create strong points in the new frontline. The Allies were able to advance almost one kilometre; during the action, eight of the nine supporting tanks were ditched, broke down or were hit by German artillery (Martin, 2017). Just south-east of the hamlet, an area of 1.9 hectares has been investigated using geophysical survey techniques (figure 5.17). One tank is identified on the aerial photographs – most probably these are the remains of tank E7 ‘Explosive’ which proceeded along the Sint-Juliaan road. It got stuck in the mud, was ’un-ditched’ then ditched again and disabled by a shell exploding underneath the vehicle (Martin, 2017).

The FD-EMI survey successfully located a magnetic anomaly corresponding with the tank visible on the historical aerial photograph. This measures 4 by 5 m with a metal-filter intensity of 20-80 mS/m. These dimensions correspond with the tank’s ground contact area (maximum dimensions: 4.12 m by 8.05 m) and indicate the possible location of small metal pieces and rust traces (no large tank parts). Based on the coil responses, this anomaly should be found deeper than 0.4 m. These results are comparable as the ones of the Clapham Junction site.

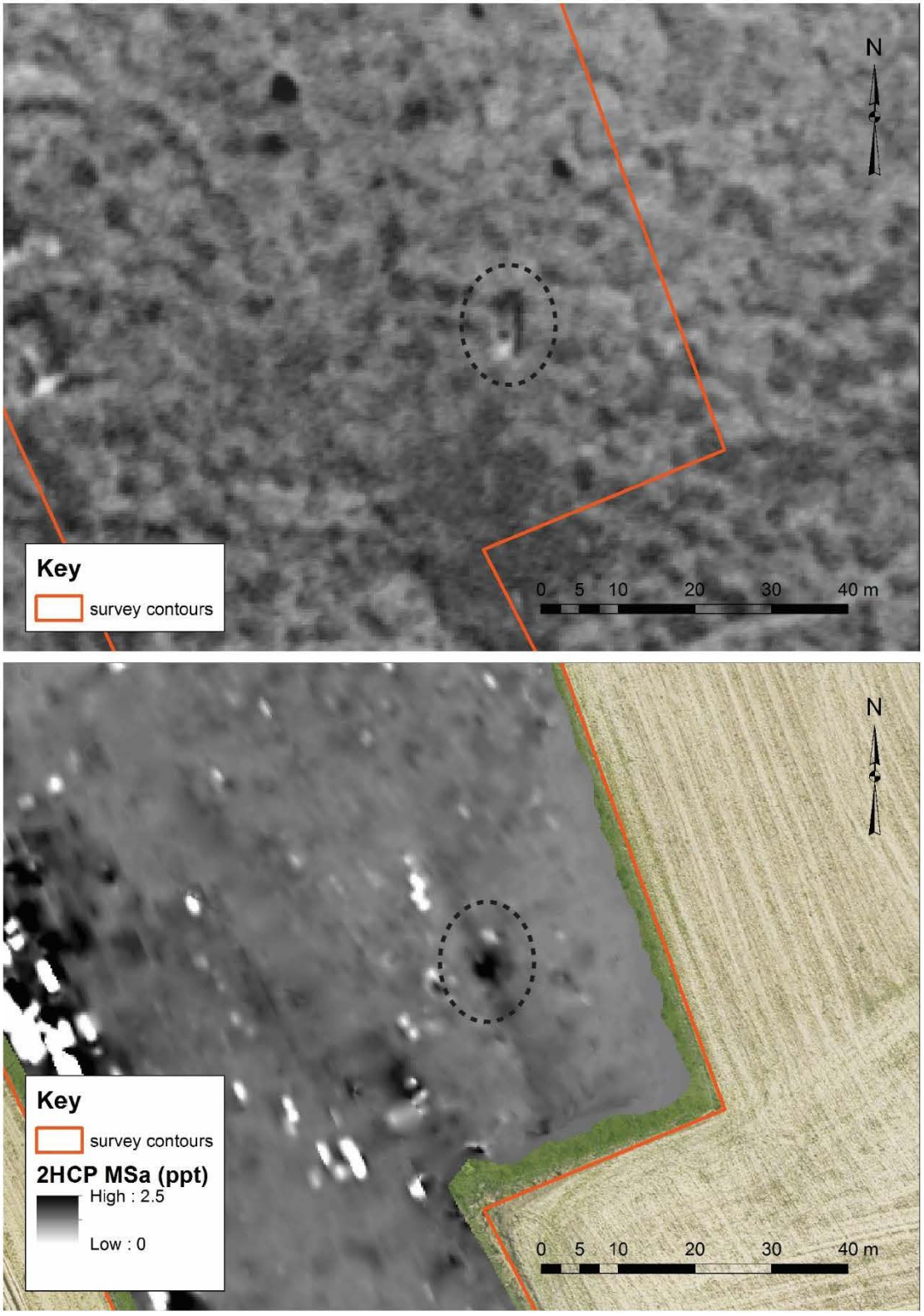



**Figure 5.17:** Top: visualisation of an aerial photograph (17th February 1918, IWM collection) with indication of one spotted tank within the scanned study site borders. Bottom: the 2HCP $MS_a$ data layer with indication of the anomaly corresponding with the tank location in the photograph above. (orthophoto: copyright AIV)

## 5.4.3 Military barracks

### *5.4.3.1 Introduction and non-invasive research*

In 2015, an exploring FD-EMI scan was executed on a pasture field near Peckham crater (between Kemmel and Wytschaete, close to Maedelstede farm), which was selected as part of the large-scale geophysical research. On this field, Allied frontline trenches dating from November 1914 until the battle of Messines (June 1917) were situated. In the FD-EMI scan (see figure 5.18), the Allied frontline could clearly be seen as a heavily disturbed area containing a dense network of trenches. A more remarkable feature appears in the former 1915-1917 no-man's-land: a rectangular structure of 40 by 60 m containing 30 smaller rectangular structures (5 by 6). On aerial photographs the feature looks similar and appears from the end of 1917 until medio 1918 (see figures 5.19). This structure has the properties to be a camp that was built when the frontline shifted +/- 4-5 km to the east in 1917. This camp was constructed in the less disturbed no-man's land (less targeted by artillery than the frontline trenches). This offered often better conditions to erect new infrastructure. This camp was mainly in use as base for soldiers which were occupied with the construction of other soldier camps. On an oblique aerial photograph from September 1918, the camp is seen as partially destroyed: several barracks have been collapsed. Based on the scan data and the aerial photography, a surrounding ditch was spotted. Also some trenches are connected to the camp, which could indicate that it was provided with a sheltering function.

If the camp's position is compared according to the front position after the 3rd battle of Ypres, it was one of the barrack camps which was located the closed to the front. Compared to all other FD-EMI scans performed on WW1 battlegrounds, none of other detected structures had a similar sharp delineation in $EC_a$ and $MS_a$. To determine the function of the camp and the reason what made it so suited to be sharply detected by geophysical techniques, a test-trenching campaign was executed.

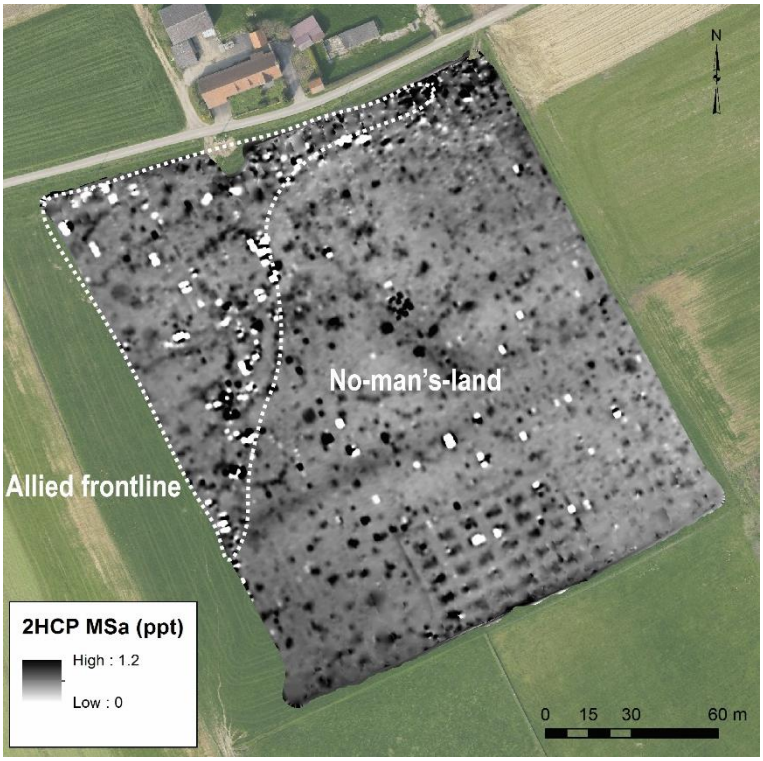



**Figure 5.18:** Visualisation of the 2HCP $MS_a$ data layer of the exploring FD-EMI scan. In the south of the scanned area, the barrack camp's footprint appears. In addition, the 1915-17 Allied frontline and no-man's-land are marked. (orthophoto: copyright AIV)

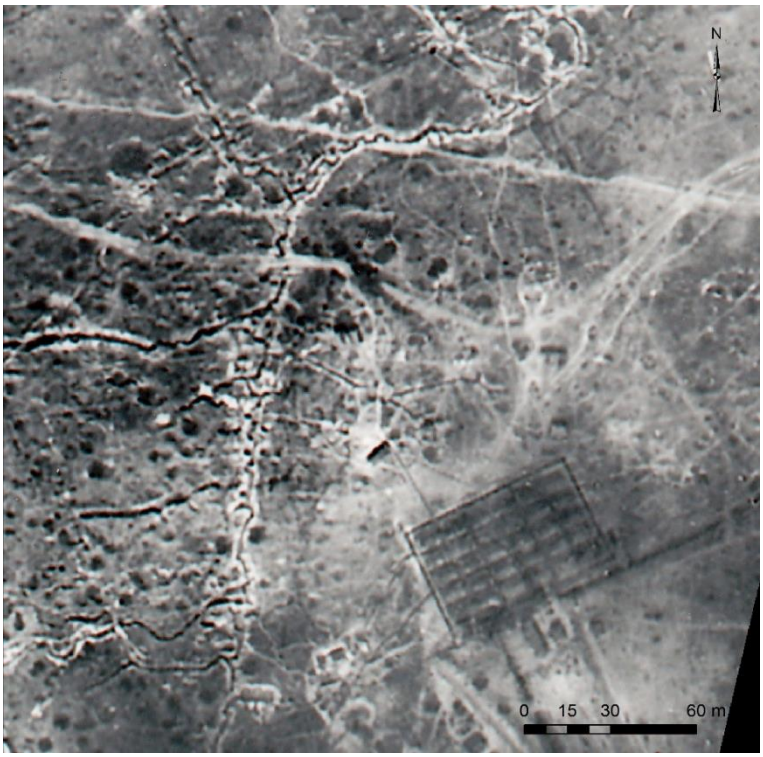



**Figure 5.19:** Visualisation of the aerial photograph taken on the 26th March 1918 (Bayerisches Hauptstaatsarchiv collection).

### *5.4.3.2 Validation by test-trenching*

#### Positioning of the validation trenches

To prepare the archaeological dig, a new and denser FD-EMI scan was executed to improve the detection quality of the first rougher executed exploring scan. The rough scan had a 1.4 m interline spacing with a north-south orientation. The turning circle of the sensor crosses partially over the camp anomaly. The denser scan had an interline distance of 0.7 m with turning circles outside the study area. The second purpose of this extra scan was to improve the coverage for metal detection to guide the executers safely during the dig to encounter the possible finds of UXO. The classification of metal objects and shell craters (shallow soil disturbances) was performed as described in paragraph 5.2. Next, all this (filtered) scan information was analysed to define the location of two test-trenches. The first column and second row of the barrack matrix were intersected (according to north-orientation) by the two proposed trenches. These cover also the camp's ditch and an area outside the camp. The parameters to define these validation trenches are: the presence of shallow soil disturbances, metallic objects and the barrack footprints. By the proposed position of the trenches, 10 barracks, 4 parts of camp ditch and 9 hotspots of metallic objects (whereof 4 with a high intensity over 100 mS/m) were investigated by excavation.

#### Excavation results

In September 2016, the archaeological excavation was executed. Underneath the organic top layer of 0.35-0.40 m (A-horizon), a sharp transition to the brighter coloured B-horizon can be found. The top of the C-horizon (0.55-0.60 m) is heavily disturbed by the war-activities. At these depths, the traces related to the barrack camp and other war activities can be found. An overview image of the archaeological excavation can be seen in figure 5.20. A visualisation of the validation trenches in combination with the scan results can be found in figure 5.21. In this figure, the barrack contours are numbered from 1 to 10 and other traces were marked by a small letter, ranging from 'a' to 'e'.



**Figure 5.20:** Overview of the excavation process of the validation trenches, shown from the west side of the study area.

In the work pits, the barrack contours were noted as enveloping rust traces, presumably originating from metal roof plates. The barracks were slightly excavated into the soil and eight out of ten had a brick floor. The other two floors were made of wood. The bricks in combination with a contrasting filling above the barrack foundation and the rust traces aligning the barrack contours, make these features easy to detect for geophysical survey techniques such as EMI or FGM. A completely excavated brick floor (barrack no. 6) and a docked cross-section of a barrack with wooden floor (barrack no. 1) can be seen in figure 5.23. In barrack no. 3, the metal anomaly (see figure 5.21) was identified as a bucket, penetrated with holes to be used as a stove (object: see photo in appendix 5.1). The large metal anomaly in barrack no. 4 was identified as three bars of narrow gauge railway (object: see photo in appendix 5.1). The difference between both anomalies are the intensity and shape of the FEMP peak. The bucket anomaly is more concentrated and has a higher peak which is more concentrated in one place while the metal bars anomaly is more flattened out over the barrack foundation (see figure 5.22). These FEMP-properties could directly be linked to the type and conditions of the metal objects: the bucket shape is very concentrated at one place while the three metal bars are more spread over the barrack's footprint. The weak FEMP anomaly in barrack 8 was related to the find of military waste containing small pieces of metal (bullets, utensils). On the other hand, shell craters 'a' and 'b' (figure 5.21) were marked as shallow soil disturbance in the EMI data and validated as filled up shell holes. The shallow soil disturbances near 'c' are indicated by a low FEMP-intensity and were validated as waste pits. These waste pits (c and in barrack

8) were useful to find objects from the daily life at the camp which helped to identify the function of this infrastructure, information about the daily life of the soldiers who stayed there and identifying their nationality. Near the camp ditch, a screw picker was found as part of a barbed wire fence around the camp. At the northeast part of the camp (facing towards the enemy lines), the surrounding ditch (figure 5.21 d) was deepened to be used as trench. After analysing the excavation results and the archaeological finds, the camp was identified as a British-Australian soldier camp, which was partially destroyed and left behind during the German Spring Offensive.

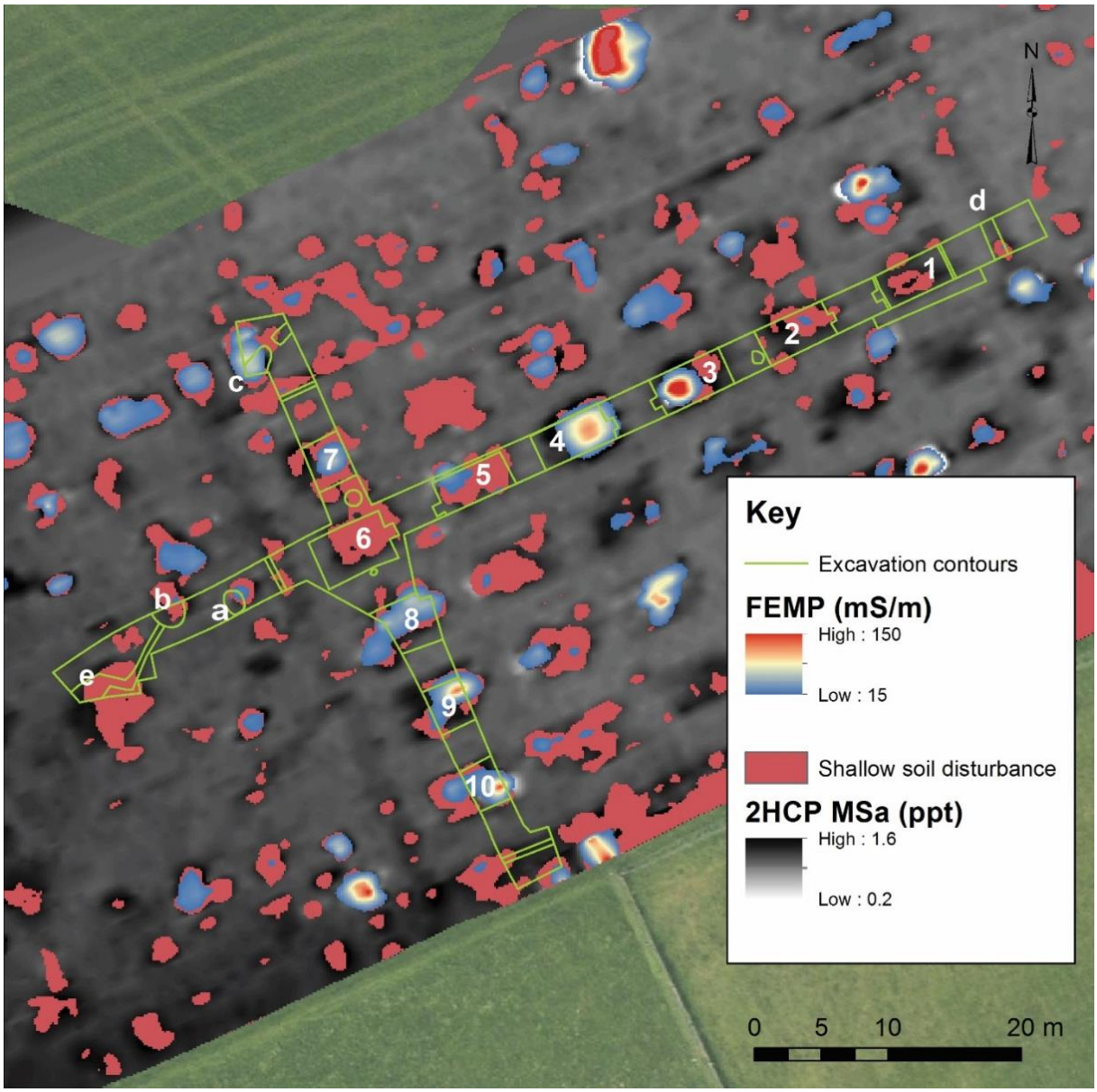



**Figure 5.21:** Visualisation of the 2HCP $MS_a$ data layer with indication of shallow soil disturbances, metal objects with their intensity and the numbering of the excavated features (barracks 1 – 10, a – e). The contours of the validation trenches and the excavated traces are visualised by a green line. (orthophoto: copyright AIV)

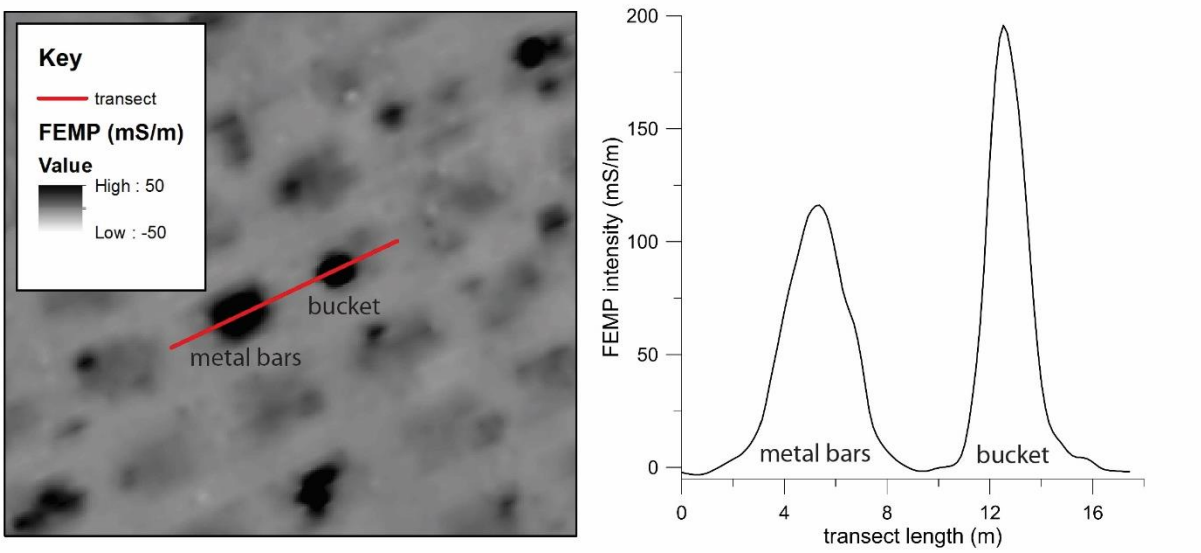



**Figure 5.22:** Visualisation of the peak dimensions (as a profile) of the magnetic anomalies caused by the metal bars in barrack 4 and the bucket in barrack 3.

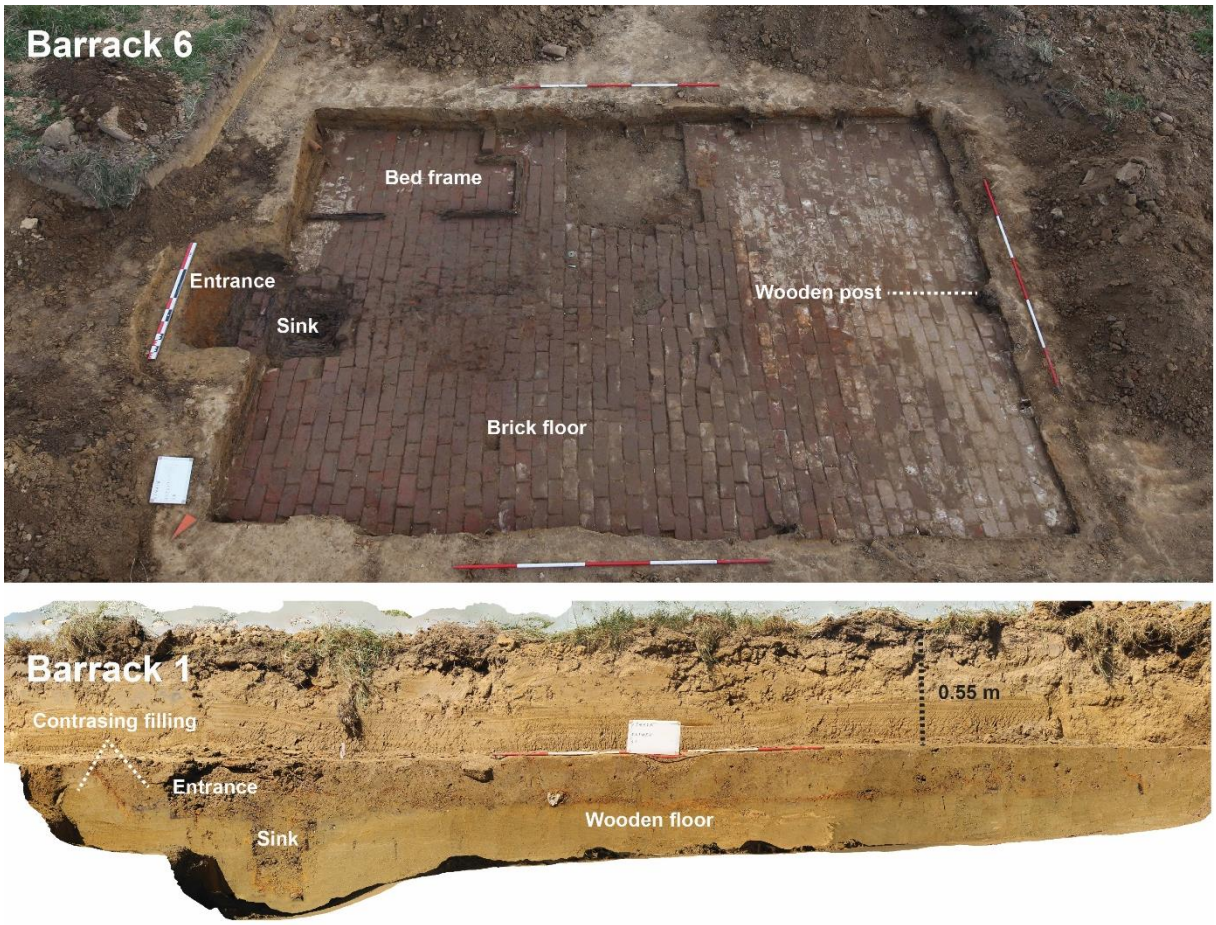



**Figure 5.23:** Visualisation of two barrack foundations: barrack 6 has a brick floor while barrack 1 has a wooden floor. Each barrack entrance contained a sinkhole. In barrack 6, parts of a wooden bed frame were found. At the section of barrack 1, clear contrasting infillings above the barrack foundation can be seen.

### 5.4.4 Horse mass grave

In section 4.2.2.6, survey results were displayed of FD-EMI and FGM scans which were able to detected the potential location of one or two horse mass graves, shortly dug after the Battle of Halen (12 august 1914, east Belgium). In this section, the validation of these graves will be covered. The graves were dug to bury the horses of the fallen cavalry. The approximate burial location of one mass grave could be determined by terrestrial photographs, taken just right after the battle. In this grave, only horses were buried. The fallen soldiers were also given a resting place near the Staatsbaan road, but at the west corner of the same field. More historical information about the Battle of Halen can be found in section 4.2.2.6.

#### *5.4.4.1 Geophysical scans*

An exploring EMI-scan discovered in November 2016 two linear structures, perpendicular to the Staatsbaan road (figure 5.24 A1 and A2). These structures correspond with the size and orientation towards the road of the mass grave (derived from historical photographs). A1 has the dimensions of 2-3 m by 45-50 m and A2 2-3 m by 30-35 m. Both structures could be seen in the $MS_a$ measurements whereby mainly the A1 signature was found in the $EC_a$ data. This anomaly was found, starting at a depth of 0.25-0.50 m, which corresponds to the position just below the agricultural ground works. In the FGM scan, only A1 was found and a 3d-Radar scan delivered no clear contrasts at the location of the potential graves. North of these anomalies, signatures of a possible late medieval moated site were found (B1 and B2 indication). In addition, two strong contrasting anomalies C1 and C2 were marked. Because the focus of this case was set on the horse graves, no extra investigation was performed on the B and C anomalies.

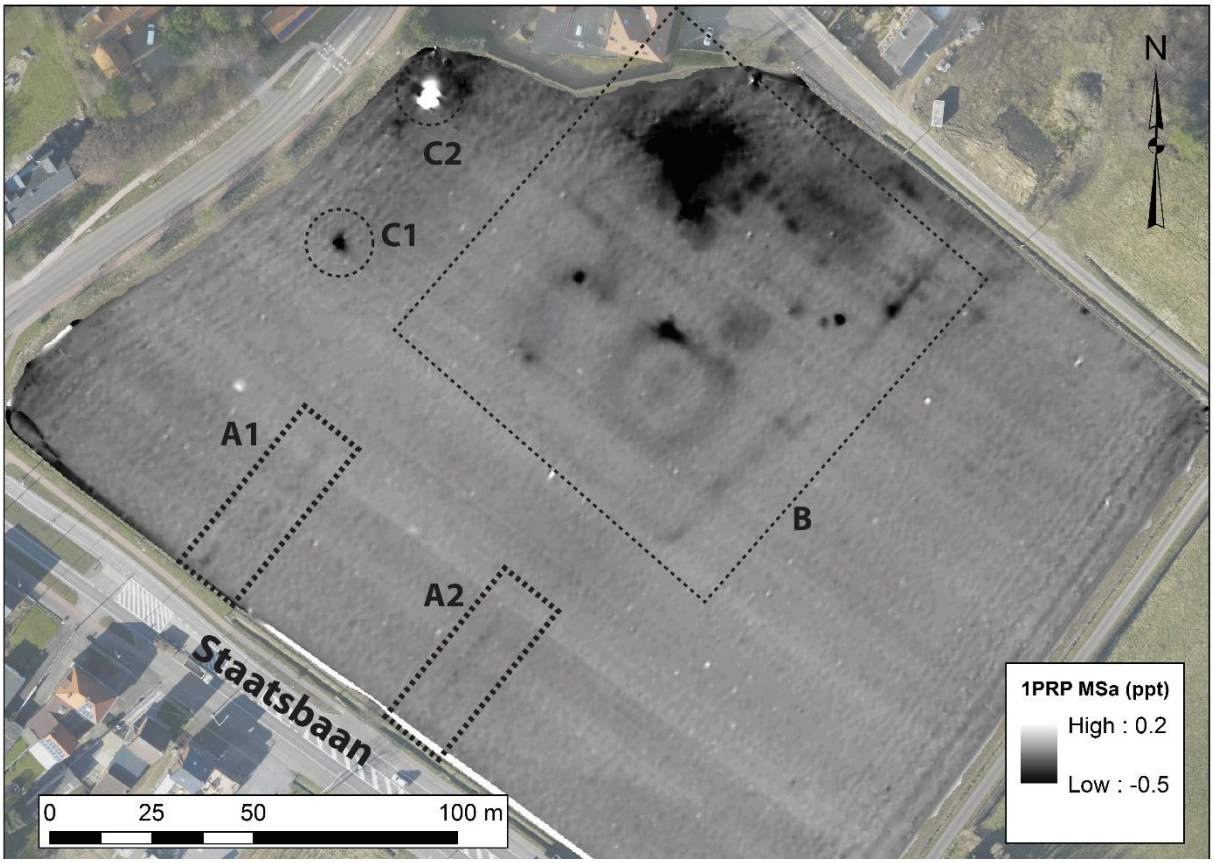



**Figure 5.24:** $MS_a$ data of the 1PRP coil configuration. The most prominent anomaly areas were identified and marked with a unique ID consisting of 1 letter and an optional number. A1 and A2 represent the anomalies related to the possible location of one or two horse mass graves. (orthophoto: copyright AIV)

### *5.4.4.2 Augering validation*

To validate the A-anomalies, augerings were executed on both structures with a Dutch auger. The four augering locations (3 on the anomalies and 1 natural profile) are visualised in figure 5.25 (location) and 5.26 (profile). The natural profile consists of 40 cm of plough layer containing organic material followed by 1.6 m of sand-loam with sand underneath. There is a sharp delineation between the sand-loam and the sand layer. The augerings which are situated on top of the linear anomalies, exist of 0.50-0.55 m of plough layer, with disturbed sand-loam underneath (mixed with darker material from the plough layer = organic material). At the depth of 2 m, undisturbed sand is situated. At a depth of 0.85 - 1.0 m at augering location 3 (anomaly A1), animal bone fragments were found. This bone material was already degraded in a distant stage (figure 5.27). There can be concluded that with great certainty, anomaly A1 is the horse mass grave seen in the photographs just taken after the battle of Halen. At the moment of the

survey, the grave is 102 years old which can be used as reference of what is still possible to detect after that amount of time in these soil conditions. Anomaly A2 shows similar dimensions and a parallel alignment according to A1, perpendicular to the road. The information of the two augerings on this anomaly demonstrated that the soil is similar disturbed as on anomaly A1 but shows no traces of animal bone. If historical maps and aerial photographs are consulted, a parcel border (with possible draining ditch) can be seen on the location of A2. Presumably, this trace has something to do with the A2 anomaly. No definitive conclusion can be drawn for A2.

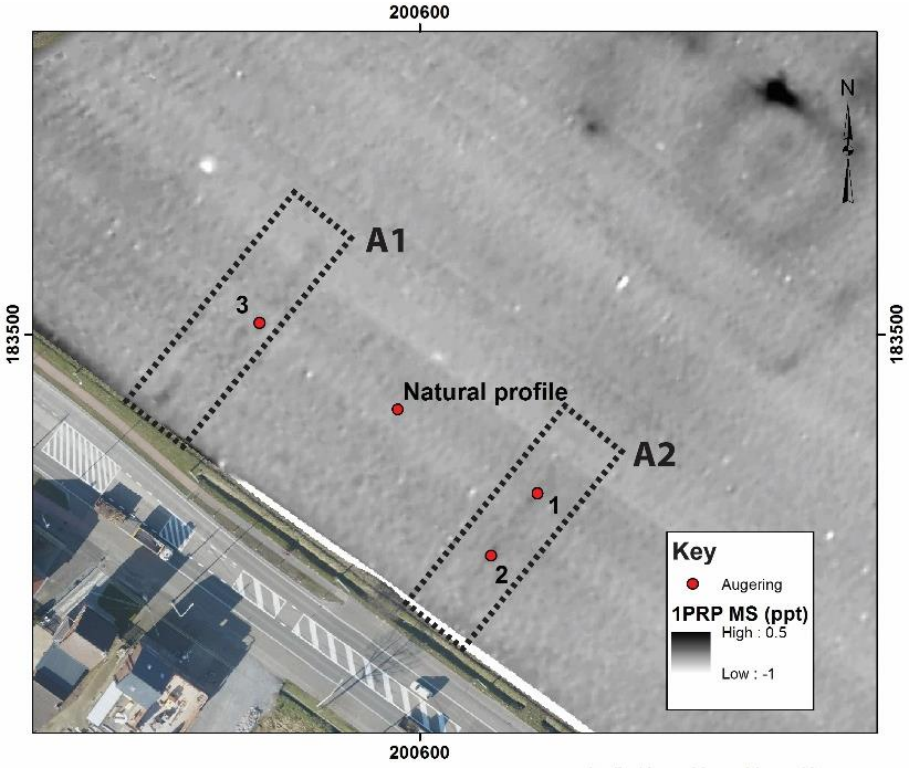



**Figure 5.25:** The 1PRP $MS_a$ data layer with visualisation of the augering locations.

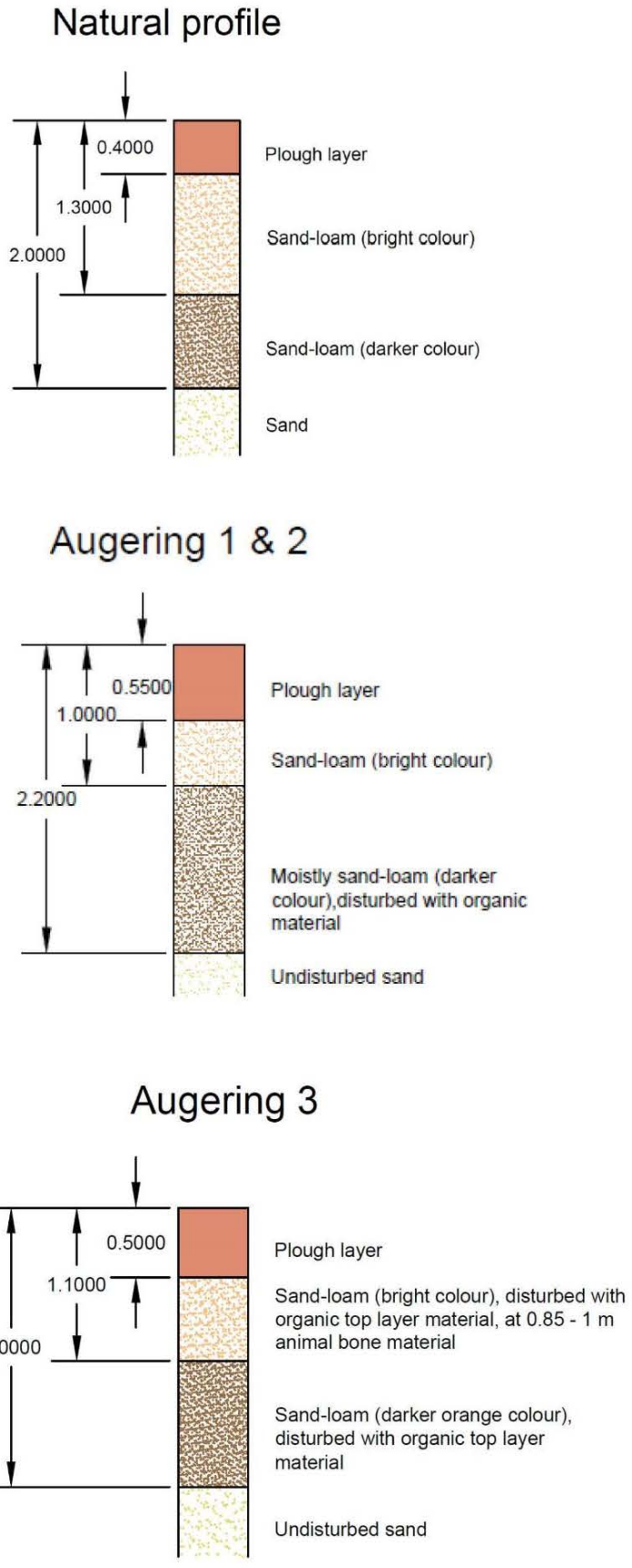



**Figure 5.26:** Description of the augering locations at the mass grave site near Halen.




**Figure 5.27:** Disturbed soil as at augering location 1/2/3 (left) and animal bone fragments, found at 0.85 - 1 m depth (right) at augering location 3.

## 5.5 Conclusions

The results have shown that:

- A classification and parameter estimation (object state and depth assessment) can be made by using FD-EMI for shallow metal objects (depth: 0 – 1 m). The former WW1 conflict areas are saturated with war related metal objects. Therefore, metal classification is a necessary ability, which can be met with FD-EMI for archaeological and demining purposes.
- Shelling traces and other soil disturbances – preserved in the first half metre of soil – can be classified by using EC depth modelling that is based on a three-layered model. Shell craters were often filled during or after the war with military waste. Identifying those traces can lead to the finds of war related features.
- A case including a surface covering excavation of a WW1 archaeological site demonstrates that aerial photography and GSS are able to accurately characterise a large share of the buried WW1 traces. When GSS and RSA – as non-invasive techniques – are used in a complementary way, this combination provides more information about the buried military infrastructure then each technique on its own.

- Dugout infrastructure could be indirectly detected by FD-EMI scan by measuring the magnetic infillings of the aboveground ditches, caused by the dugout gallery collapse. The geophysical detection in combination with other validation techniques (augering, ALS) were able to determine the conditions of this dugout. The successful combination of these techniques opened up an improvement to the localisation of dugout systems in the Ypres Salient.
- Two cases which included positions of beached WW1 tanks, signed positive in the performed FD-EMI surveys. This was mainly caused by dismantling traces in the top layer of the soil (0.2 – 0.5 m): bolts and nuts as left-behind construction parts from the tanks.
- It is possible to detect a WW1 horse mass grave with GSS. Grave structures are often difficult to find with GSS. A mass grave (large size) in ideal undisturbed soil conditions led to the possibility to detect this grave with both FD-EMI and FGM. A similar case in the intense affected areas near the former Western Front are more challenging for grave localisation as these traces have often a lower impact than trenches and shell craters.
- The soldier camp excavation could be guided by the FD-EMI scan to define the test-trenches. The metal and shallow soil disturbance classification was useful to localise waste pits, utensils, construction materials etc. The delineation of the barrack floors could sharply be performed because of contrasting infillings of these slightly buried barracks and the presence of brick floors. The use of non-invasive techniques for this archaeological excavation resulted in a focussed and efficient approach.

# Chapter 6

## Shell holes: A proxy for destruction intensity and buried iron clutter

This chapter was modified from:

> **Note, N.**, Gheyle, W., Van den Berghe, H., Saey, T., Bourgeois, J., Van Eetvelde, V., Van Meirvenne, M., Stichelbaut, B., 2018. A new evaluation approach of World War One's devastated front zone: A shell hole density map based on historical aerial photographs and validated by electromagnetic induction field measurements to link the metal shrapnel phenomenon. *Geoderma*, *310(C),* 257-269.

## 6.1 Introduction

During WW1, the intense and concentrated artillery shelling at the front area completely obliterated villages, towns and countryside. The landscape was in many places converted into a lunar-like environment peppered with innumerable shell holes (Debaeke, 2013; Stichelbaut, 2006). The artillery's environmental impact was amongst the most impressive in history (Pearson et al., 2010). The effect of heavy shelling had an enormous destructive impact on the landscape. By looking at the number of shells fired during the preliminary bombardments prior to the two most heavily fought over battles in Belgium (battles of Messines and Passchendaele, 1917), an accumulated 7.8 million projectiles were used (His Majesty's Stationery Office, 1922). The battles in this region reached a climax during the summer of 1917. Hundred years after the start of WW1, the actual extent of the destroyed landscape and its traces within the soil are still unclear. Iron clutter such as metal debris, shrapnel, shells and construction materials are still omnipresent, even after clearance of the fields directly after the war (Desreumaux, 2011).

Unlike the French government, the Belgian authorities allowed a repopulation of the Western Front without any restrictions. As a result, even today the inhabitants and ground workers on the former WW1 battlegrounds are confronted with war related dangers. A detailed and objective historical destruction map on parcel level does not exist, although such map and its derivatives would be useful instruments in government related administrative procedures, such as decision-making steps for land development. Therefore a high quality map is needed to classify and delimit the heavily and less impacted zones. This classification is essential to define zone-linked guidelines (procedures or safety restrictions) for invasive practices. This map could be used as an indicator to suggest actions to handle the remnants of war, including the valuable war heritage and the still eminent danger of unexploded ordnances (UXO). The map would also create an insight in the war's impact on the cultural heritage (above and belowground) or could be used for soil monitoring, agriculture practices, archaeological prospection, construction permits, risk communication, etc. Even the increase of heavy metal

concentrations in the soil caused by the war (Bausinger and Preuß, 2005; Bausinger et al., 2007; Van Meirvenne et al., 2008; Meerschman et al., 2011) could possibly be simulated.

In this chapter, a method based on historical aerial photography to map and assess the destruction of the landscape and soil archive at the former Western Front is proposed. This new approach will allow a classification of well-defined destruction levels to indicate a gradation of the once destroyed landscape. To simulate the iron clutter phenomenon, the destruction parameter will be converted into a metal debris indicator after a calibration based on geophysical measurements. The final aim is a high quality historical destruction map.

## 6.2 Prior attempts in France and Belgium

Shortly after the war, attempts were made to delimit and map the scale of the destruction within the former war zones. Descriptive observations of the destroyed areas at the former Western Front in France were drawn on a topographical map and based on the registration of destroyed buildings, roads and land use. These maps entitled ‘Carte Spéciale des Régions Dévastées’ (1920) were published by l'Institut Géographique National. A detail extract of one of the map sheets is shown in figure 6.1. Derived from those maps, Guicherd and Maîtrot (1921) described a three-zonal classification, categorising the actions organised by the government to re-establish residential and agricultural land use (figure 6.2). The ‘Blue Zone’ is mainly characterised by ‘average damage’ and abandoned equipment. Here, the inhabitants are responsible for regaining land use without any governmental actions. The ‘Yellow Zone’ is related to battles fought behind the frontlines and is clearly affected by destruction. Land levelling and demining were advised and it would take several years to regain its agricultural productivity. The so-called ‘Red Zone’ (French: ‘Zone Rouge’) covers areas close to the frontlines. This third zone represents ‘total destruction’ with almost no remaining infrastructure at the end of the war. This zone required the removal of human remains, neutralising the decomposing animal cadavers and performing extensive demining campaigns. Through time, the Red Zone was reduced but never disappeared. Today, around 17,000 of the original 120,000 ha are still restricted for housing and farming. In some parts, the original flora even refuses to grow (Bausinger et al., 2007).

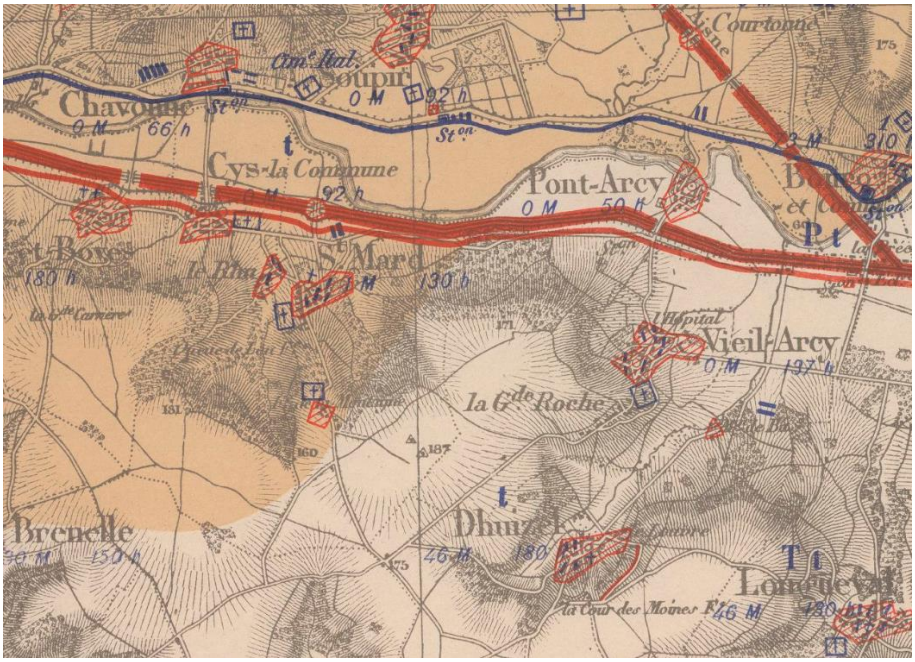



**Figure 6.1:** A detailed extraction of sheet 33 NE from 'Les Cartes Spéciales Des Régions Dévastées' (IGN, 1920), with indication of the destroyed grounds (orange colour, contains shell holes and trenches), destroyed buildings (red hatched polygons) and destroyed roads and water networks (red) marked on the French topographical base map.

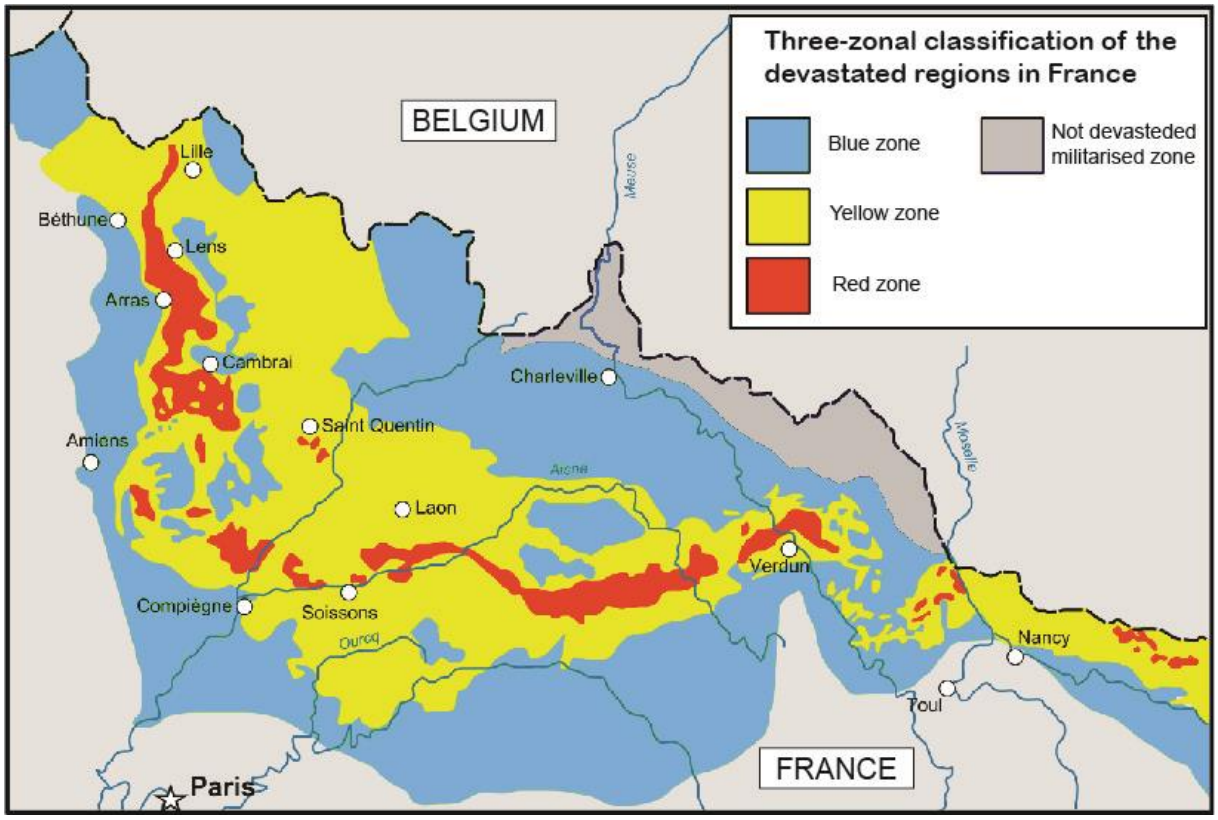



**Figure 6.2:** Map of the devastated regions in France, categorised by a three-zonal classification (after Guicherd & Maîtrot, 1921; https://commons.wikimedia.org, 2018).

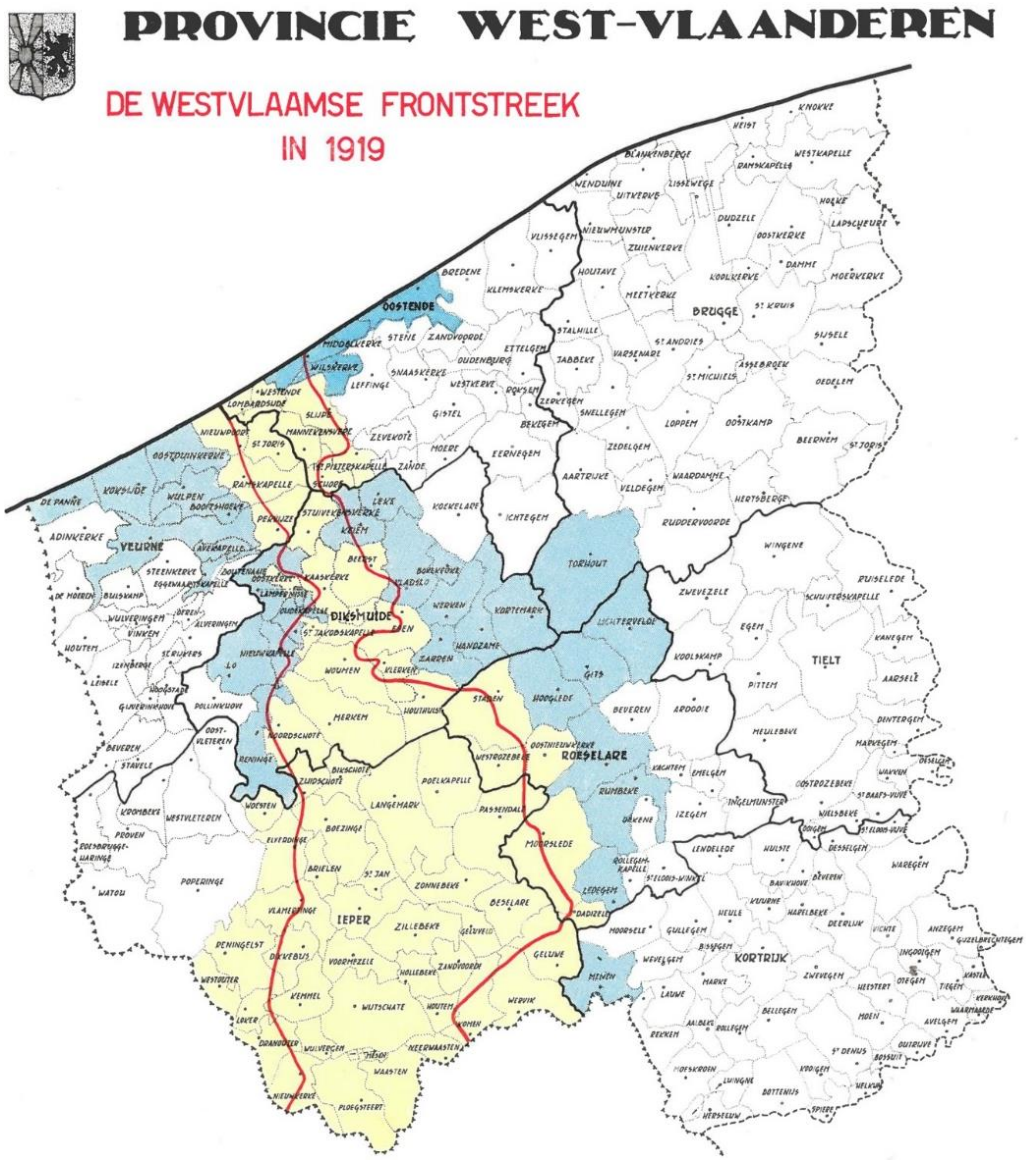



**Figure 6.3:** The map of the devastated regions in Belgium, published by Van Outryve d'Ydewalle and Viaene (1958), indicating the destroyed villages (yellow), the partial destroyed villages (blue) and the complete destroyed agricultural grounds (between the red lines).

A similar classification map for the former Western Front in Belgium does not exist. In 1920 the ORD (Office des Régions Dévastées) published a map indicating the towns and villages that suffered from war destruction to identify which one would qualify for governmental reconstruction support. This destruction classification was reproduced by Van Outryve d'Ydewalle and Viaene (1958) and led to an inventory of the province of West-Flanders indicating ‘destroyed villages’, ‘partially destroyed villages’ and ‘completely destroyed agricultural grounds’ (figure 6.3). Since the map was based on war damage inventories, it only gives a general classification on the level of the municipalities. There is no detailed and

accurate understanding of the extent of the devastated regions in Belgium and its impact on the soil. This lack of information needs to be completed if a spatial analysis tool for multiple soil applications has to be developed.

## 6.3 New approach: Shelling as proxy

### 6.3.1 Method and study area

To establish a method for a high-resolution map, a new approach was chosen to indicate the actual destruction: instead of mapping the destroyed infrastructure, the density of the shelling itself was directly derived from aerial photographs. This method is more objective than interpreting destroyed buildings or land use and it allows classifying almost every parcel in this mainly agricultural area. The test area to evaluate this novel mapping method is located on the infamous Messines Ridge, just south of Ypres and includes the villages of Kemmel, Wytschaete, Wervik, Comines-Warneton and Messines. It is similar to the 3rd transect area of the '*Non-invasive landscape archaeology of the Great War*'-project. This area has the dimensions of 28.5 by 5 km and covers all frontlines from 1914 to 1918 and the areas behind the frontline battlefields (figure 6.4).

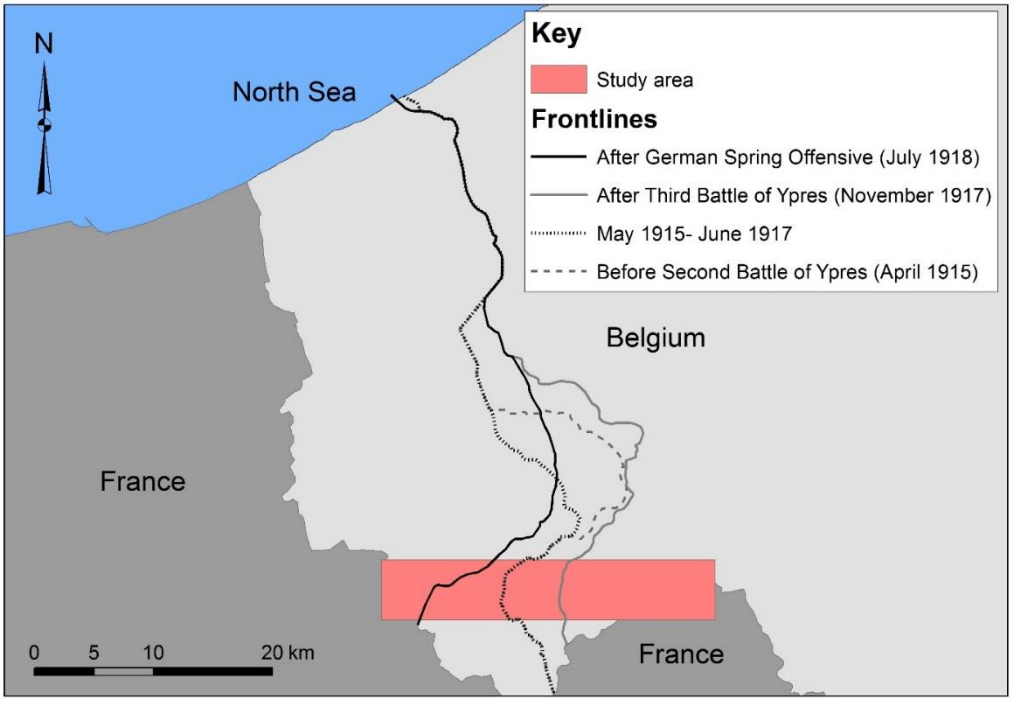



**Figure 6.4:** Study area in relation to the four main WW1 frontline phases in Belgium.

In the methodology, the photographs taken after the heaviest battles (period second half 1917 and 1918) are selected to digitise shell holes manually. This procedure demands knowledge from a war expert. The selected photographs must also have a substantially high resolution to identify individual shell holes. A sample strategy for operator-based interpretation is preferred with 50 by 50 m samples in a staggered grid (figure 6.5). This grid is derived from a regular grid with an inclination angle of 45° and the sample size is chosen to be large enough to indicate a representative value per sampling location, but small enough to be applied to an entire study area without making the process too labour intensive. The horizontal distance between samples is 1000 m and the minimum distance between samples from two adjoining rows is 707.1 m. This strategy covers 0.54% (0.7675/142.5 $km^2$) of the study area and satisfies the conditions of digitising intensity, usage and prediction quality (validation with independent test).




**Figure 6.5:** Demonstration of the sampling strategy: the squares represent the sample locations. (orthophoto: copyright AIV)

For the proposed study area, shell holes in the sample areas are digitised. It is important that shell hole interpretations are unambiguously defined for multiple operators. Mixed interpretations would lead to operator depended variations in the destruction map. At a certain point, individual impact holes in heavy shelled areas cannot be distinguished any longer. The maximum number of discernible shell holes was obtained experimentally and is set to 180 in

a 50 by 50 m sample (720 per ha). In total, 319 sample areas were defined in the study area (figure 6.6). The following step in the map creation procedure is the interpolation of the samples. As one of the most common used spatial data interpolation techniques, Ordinary Kriging was found suitable because the shelling density parameter has the characteristic of spatial autocorrelation, the covariance showed local stationarity (mean unknown) and no spatial trend was detected (Hengl, 2007). The variogram applied for this interpolation is shown in figure 6.7. Therefore, 307 grid points and 40 random points (see figure 6.6) are used to determine the experimental variogram. An exponential function was chosen with a nugget effect of 120 and a sill of 6400. Up to 3000 m, the exponential function fits the lag points well. At larger distances, fluctuations appear in the variogram, which are related to border effects and the stretched shape of the study area. As a result, the experimental variogram does not reach a state of equilibrium. Based on the size of the study area, the short distance variations of the parameter and the experimental variogram, the maximum range of the search ellipse for this dataset is limited to 3000 m. The interpolated result of the 307 regular grid samples is shown in figure 6.8.

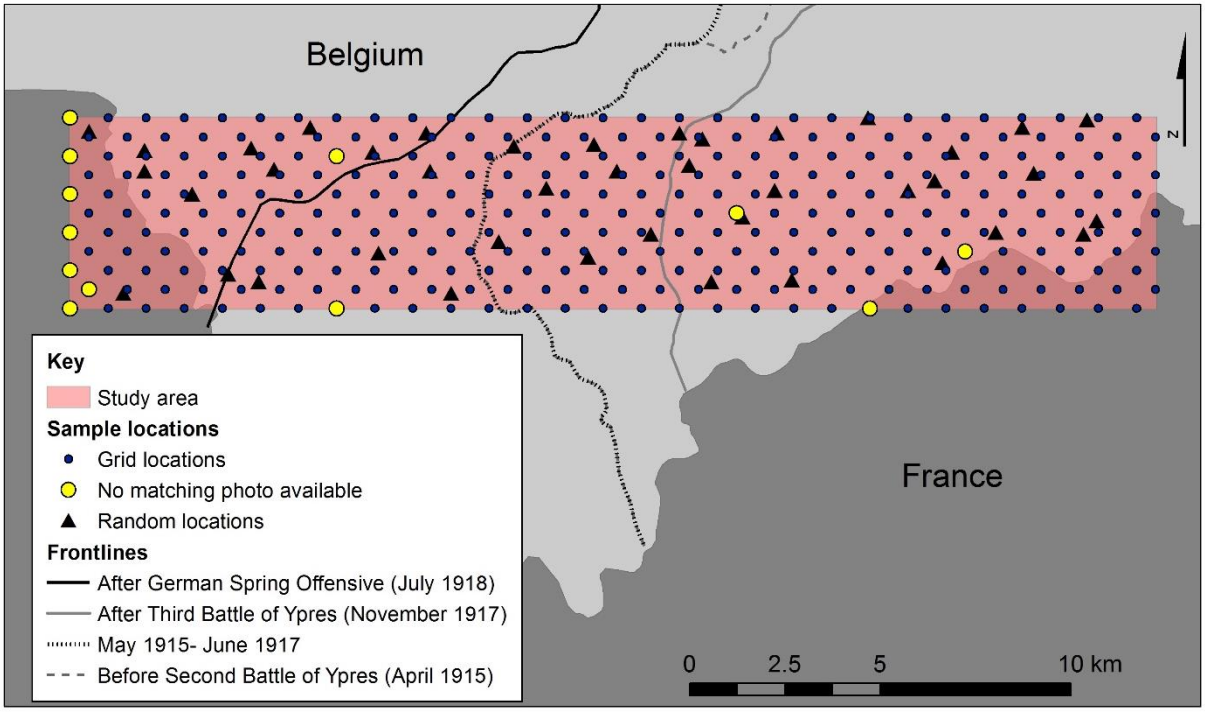



**Figure 6.6:** Demonstration of the sampling strategy: random samples and samples in a staggered grid with indication of the missing data.

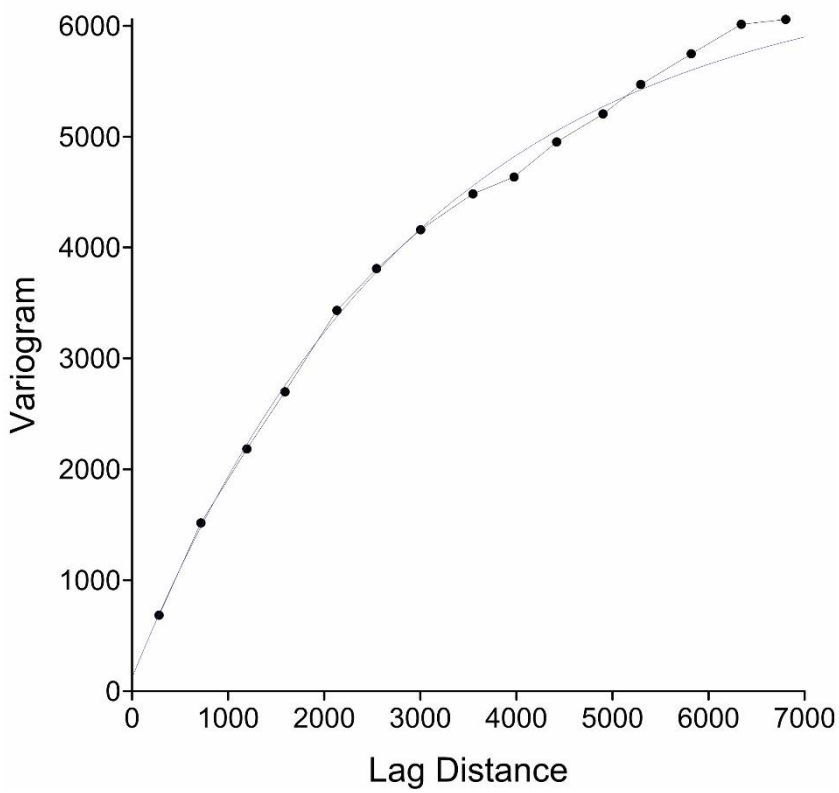



**Figure 6.7:** Variogram applied for the shelling density map (Surfer parameters: type = exponential, lag distance = 466.66 m, nugget = 120 m, sill = 6400 m, length (A) = 3000 m).

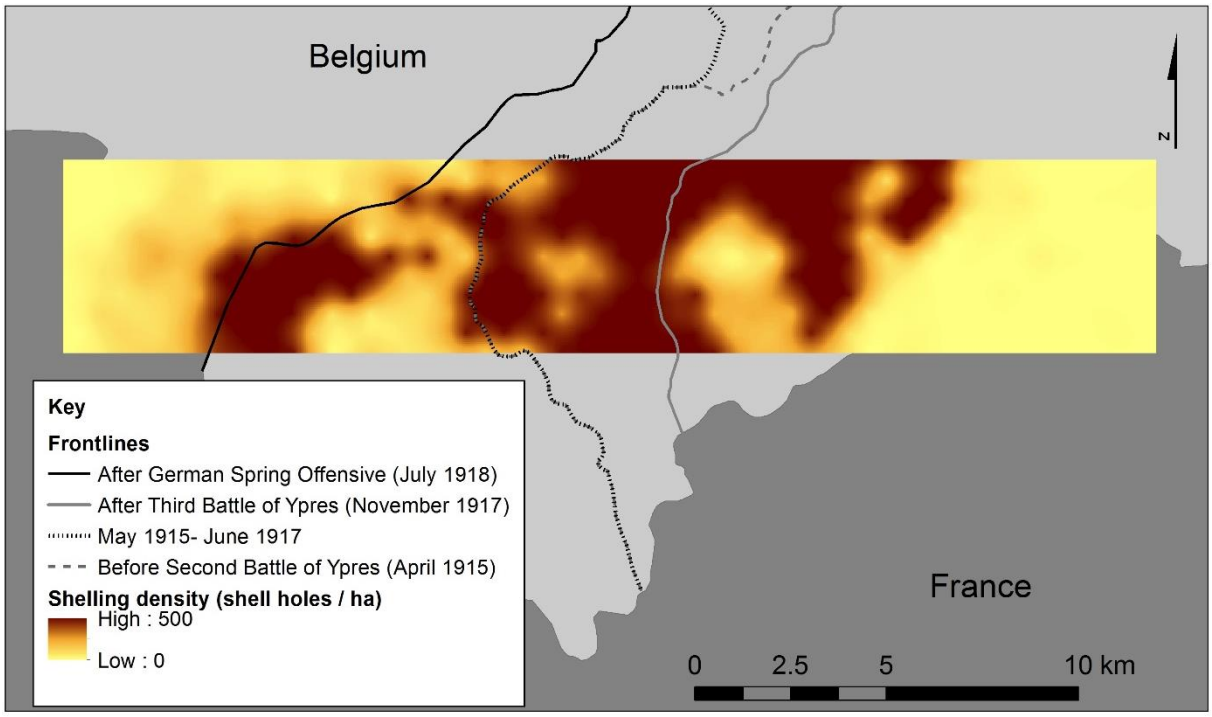



**Figure 6.8:** Interpolated shelling density map with a heat map color scale ranging from 0 to 500 shell holes/ha.

### 6.3.2 Class division and validation

To translate shelling densities into destruction intensity, the data values are split up in five subdivisions ranging from ‘no destruction’ to ‘total destruction’. These divisions were chosen by visually examining the aerial photographs (expert input). The limits of these classes are applied in the classification of the density map and described in figure 6.9 with addition of a visual example. The first zone is the one with the lowest impact and is called ‘intact’. Here, no real damage is done to landscape and infrastructure. Only a few lost impact holes from a single attack or shooting practice can be seen (density: 0 – 20 shell holes/ha). The second class represents a zone of light destruction (density: 20 – 80 shell holes/ha). In this area, some artillery firing took place, marking the landscape with a visible shelling scar. The presence of military structures and destroyed infrastructure can be noticed. The third zone is described as medium destruction (density: 80 – 200 shell holes/ha). Here, every field and the majority of the buildings were affected by incoming artillery. Parcel borders and roads are damaged by impacts but still distinguishable in the landscape. In the fourth zone, almost every single $m^2$ is affected. Here, between 200 and 480 shell holes per ha are detected. The military infrastructure is dominant and almost all roads and buildings are destroyed. The fifth and final zone is associated with total destruction where shelling densities of 480 holes per ha or higher are observed. The entire landscape from before WW1 is wiped out and even the military infrastructure is hard to distinguish. This zone is the so-called lunar-like landscape. This classification applied on the study area's shelling density map is shown in figure 6.10.

To test the success of the classification, 41 random generated locations (sample size 50 × 50 m) were digitised (table appendix 6.1: ID range 0 – 43) and shell holes were counted. Based on the location of the samples, the predicted destruction class was derived from the destruction map itself. An independent test was performed by comparing both (true and predicted) classifications per sample. This test pointed out that 7 locations were wrongly classified. Only at one location, the predicted class differed 2 classes from the modelled class. The other 6 samples were located in an adjacent class. So, the classification has a success rate of 83%. A second similar test was performed by completely digitising 19 parcels (table appendix 6.1: ID range 100–122). Based on this selection, 5 parcels were misclassified in an adjacent class.

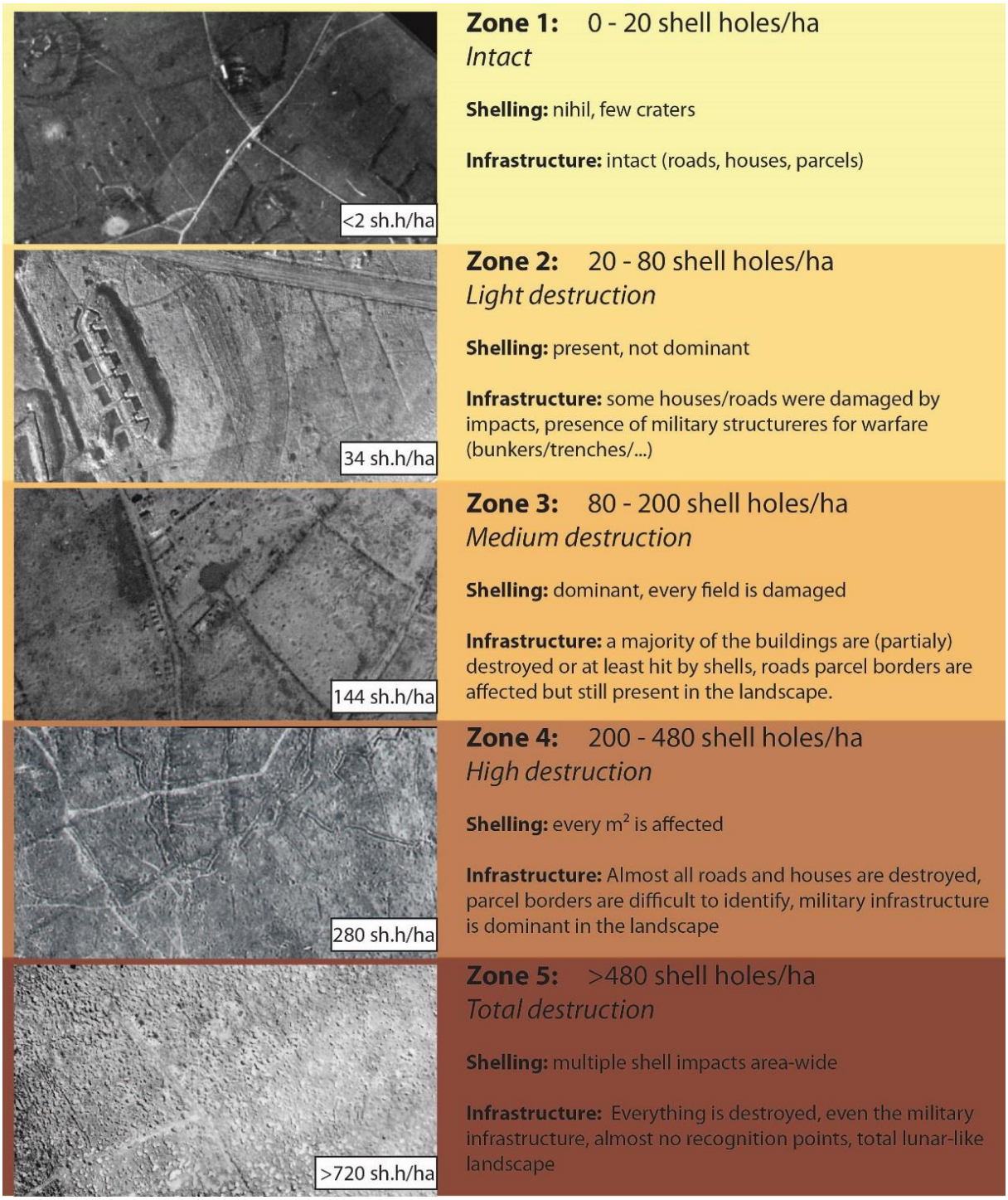



**Figure 6.9:** Classification of the shelling density zones, translated to the level of destruction. (photos: IFFM, IWM, Service Général du Renseignement et de la Sécurité, Section Archives)

A destruction map based on shelling densities does not only delineate zones with different destruction levels but it can probably be translated to the intensity of metal debris and shrapnel pollution (MSP). This phenomenon is the direct result of the intense shelling. During WW1,

around 25–30% of the shells did not explode (Debaeke, 2013), which means that shelling densities could also be related to the possibility of encountering UXO. If these parameters correlate with the shelling densities, the applications of this destruction map would increase.

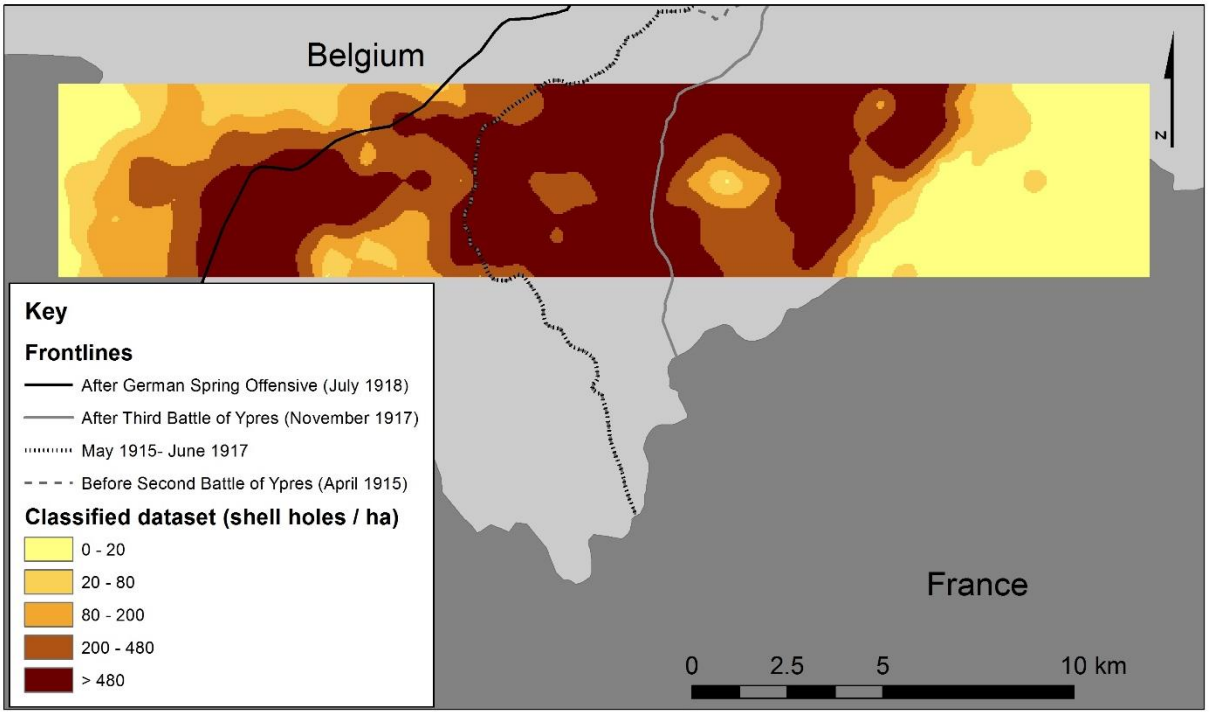



**Figure 6.10:** The shelling density map divided in five defined classes.

## 6.4 Geophysical integration

To validate the correlation hypotheses of the previous section, excavations of sample areas would be ideal to test these relations but this validation method would be too intense to perform at a large scale. Therefore the performance of geophysical measurements is preferred, which can indicate the presence of buried metal objects. From those scans, derived metal related parameters are used to determine the relationship between shelling and metal object densities. Electromagnetic induction surveys with a DUALEM 421S sensor were chosen to map the subsoil at 16 different locations in the study area. This sensor has the potential to map metallic objects between the soil surface and roughly 1 m deep (Saey et al., 2011). This allows estimating the buried metal objects, which predominantly represent WW1 shells.

### 6.4.1 Metal filtering and parameters

This classification is a first step in localising metal objects originating from heavy shelling and warfare during WW1. It is difficult to quantify the amount of metal objects detected by the FEMP filter (see chapter 5) in each survey. Therefore, two parameters are derived from each dataset: the percentage of pixels that are classified as metal (% area FEMP) and the amount of isolated metal object hotspots (MOH) per hectare. These hotspots are FEMP indicating pixels that are isolated from other similar classified pixels. To make an interpretation about a certain area, both parameters should be considered. As a typical signature for the former Western Front, both parameters are expected to score high. The expected behaviour for both parameters in function of an increasing metal object density is shown in figure 6.11.

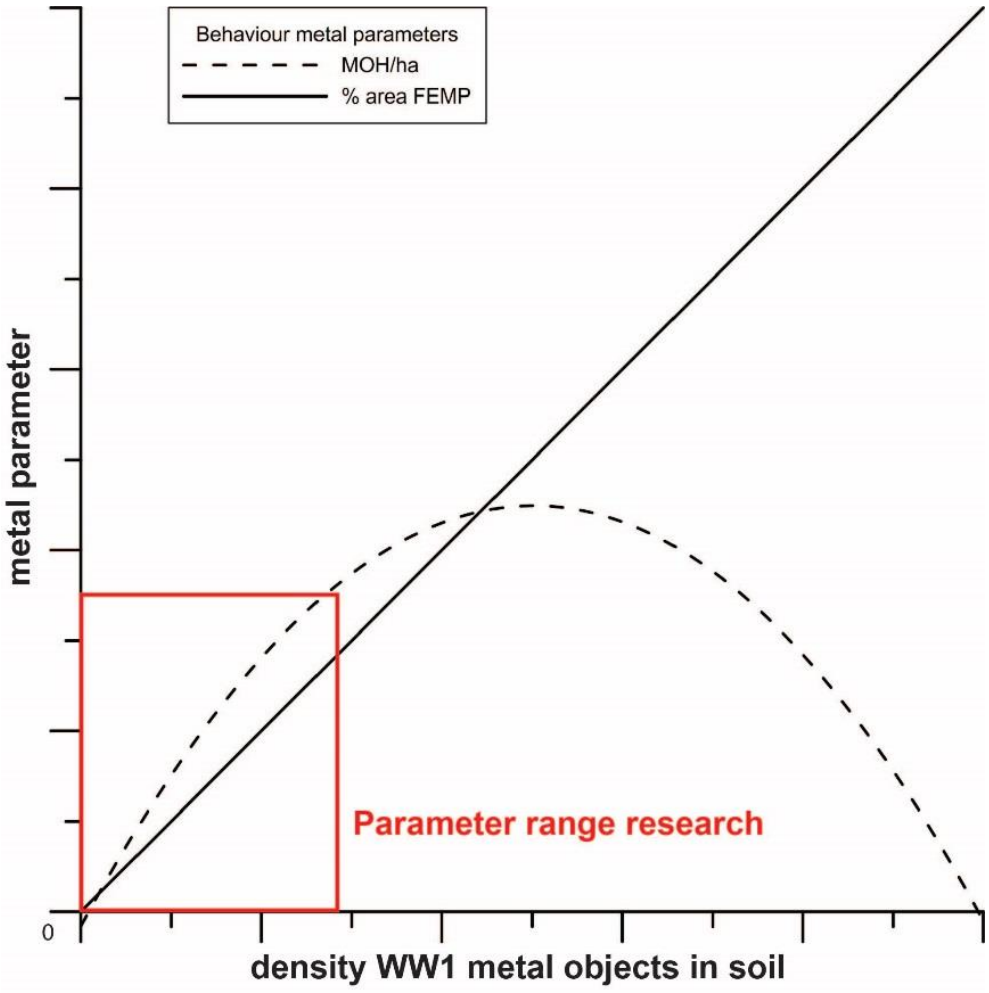



**Figure 6.11:** The expected behaviour for the MOH/ha and % area FEMP metal parameters with indication of the data range for this research.

### 6.4.2 Metal parameter description

To test the relationships between shell hole densities and geophysical survey parameters, a training dataset of 16 records was compiled from the former Western Front in Belgium (table 6.1). Because of the absence of some parameters (blurred photographs), only 12 complete records could be provided. For both parameter correlations, a linear function could be fitted with an increase of metal objects. In theory, the MOH/ha will reach a critical point after which the MOH densities will decrease (see figure 6.11). Therefore, a 2$^{nd}$ order polynomial function was used for this parameter. Both functions are shown in figure 6.12. The best correlation is reached with the FEMP metal indicating hotspots (even when both are linear). Therefore this parameter and its correlation equation will be used to translate the shelling density sampling dataset into FEMP hotspot values, describing the MSP-phenomenon.

**Table 6.1:** Training dataset for parameter correlation.

| ID | % area FEMP | MOH/ha | area (ha) | region | shell holes/ha (photo) |
|---|---|---|---|---|---|
| 1 | 10.4% | 420.7 | 0.82 | S | 289.02 |
| 2 | 0.3% | 9.9 | 6.12 | S | 1.17 |
| 3 | 3.0% | 177.0 | 3.65 | S | - |
| 4 | 3.1% | 161.3 | 6.96 | S | 69.80 |
| 5 | 3.6% | 217.5 | 1.7 | S | 142.94 |
| 6 | 4.3% | 154.3 | 3.15 | S | 111.11 |
| 7 | 4.8% | 261.0 | 6.7 | S | 110.82 |
| 8 | 6.4% | 304.7 | 2.16 | S | 149.07 |
| 9 | 7.3% | 366.4 | 1.08 | S | 181.48 |
| 10 | 8.9% | 493.9 | 1.03 | S | - |
| 11 | 9.4% | 282.9 | 2.42 | S | 117.36 |
| 12 | 0.6% | 27.1 | 6.84 | N | - |
| 13 | 1.6% | 111.9 | 3.21 | N | 34.54 |
| 14 | 1.0% | 56.9 | 11.75 | N | - |
| 15 | 1.4% | 56.5 | 4.95 | N | 46.32 |
| 16 | 10.6% | 394.1 | 1.88 | S | 193.59 |

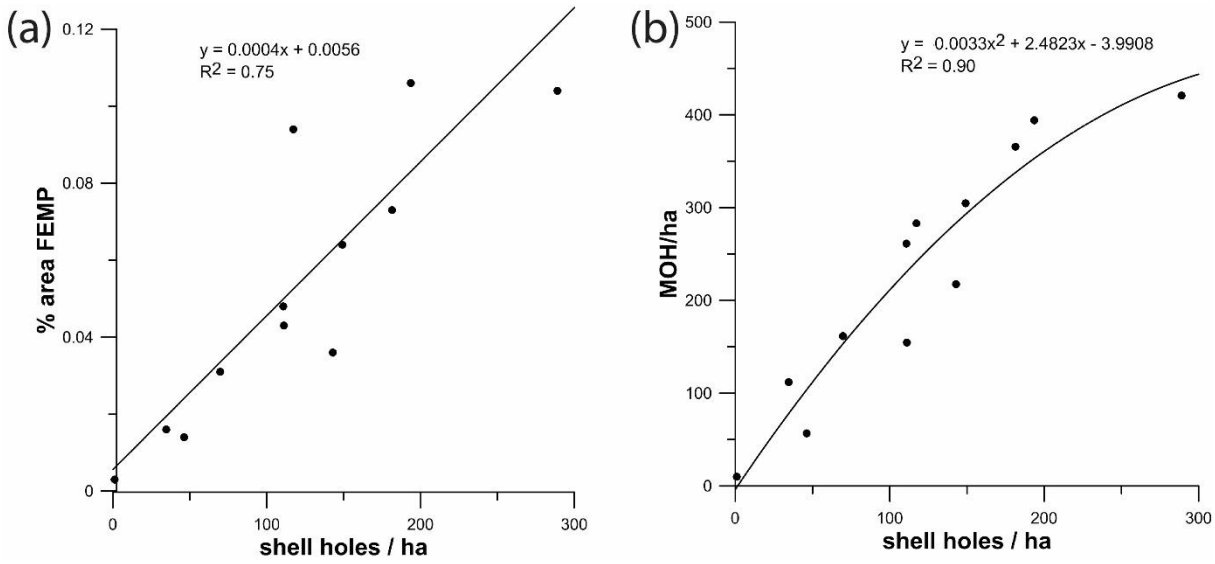



**Figure 6.12:** Correlation functions between shelling densities and both EMI metal parameters: (a) % area FEMP, (b) MOH per hectare.

To determine at which rate the level of buried metal objects exceed the 'normal' (no Western Front area) values, a reference dataset of 12 surveyed fields (appendix 6.2) was integrated in this study. These fields are situated outside the former Western Front area and located in Flanders and Holland. For this dataset, the FEMP hotspots have a range between 0 and 30 MOH/ha and cover up an area between 0 and 1% of the surveyed field. The parameters for the northern part of the Western Front in Belgium indicate a slight incline (between 0 and 1.65% area FEMP and 8–111 MOH/ha). This area was less shelled compared to the Ypres region and therefore included as a separate zone. By looking at data for the southern area of the former Western Front in Belgium, a coverage of 3 to 10% area FEMP and a MOH/ha range between 150 and 500 are found. This third area is clearly exceeding what can be described as 'normal'. The parameters for each field are shown in appendix 6.2. Based on these findings, three MSP zones are defined as: normal (0–30 MOH/ha), low MSP (30–150 MOH/ha) and high MSP (> 150 MOH/ha). Based on the correlation formula between shelling densities and FEMP hotspots, the shelling density map is transformed into a FEMP hotspot map where the above described class division is applied (figure 6.13). In this map, the darker zones can be seen as increased metal shrapnel and debris indicating areas, caused by the war.

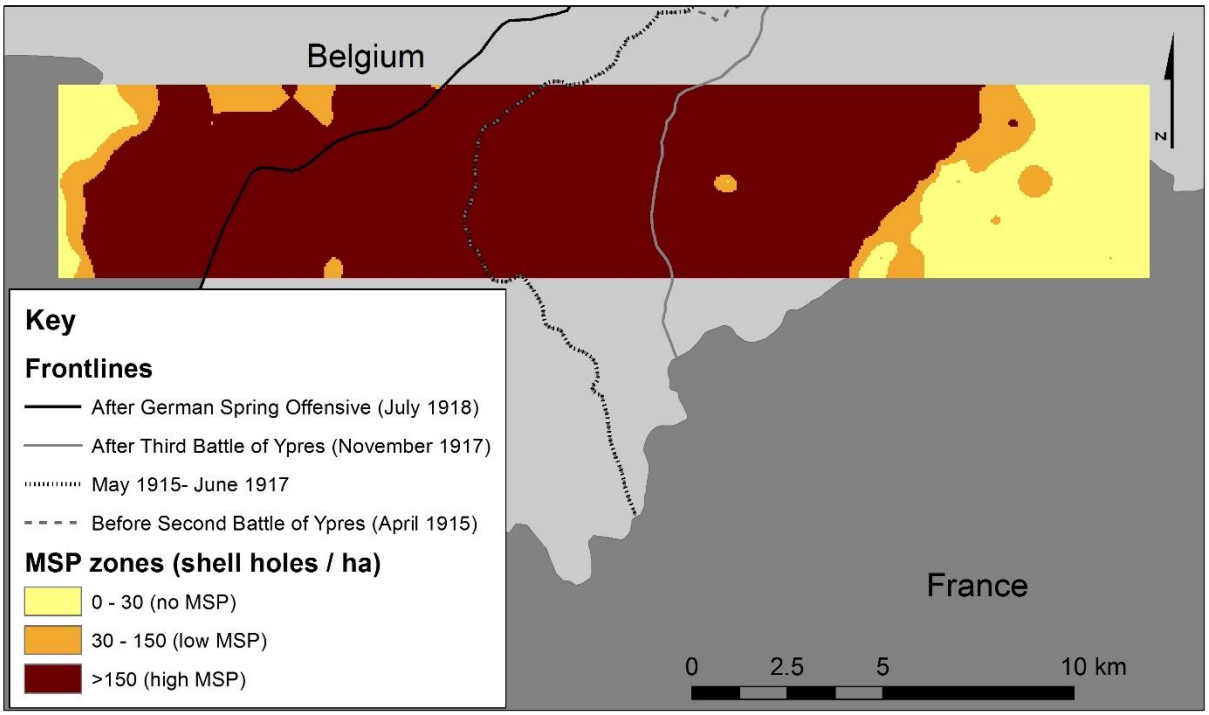



**Figure 6.13:** Based on the relationship between shelling densities and the metal parameter characterisation, a map with MSP zones is constructed.

## 6.5 Conclusions and discussion

Based on a sampling strategy to manually digitise shelling densities on historical aerial photographs, the simulation of the level of destruction for the former Western Front in Belgium is satisfactory.

This applied method is not perfect and has some limitations. The first obstacle to overcome is obtaining a full coverage of the mapping area with good quality historical aerial photographs. In less surveyed areas, the availability of photographs is rather limited which can result in an incomplete coverage with influence on the map's prediction quality. A second determining parameter is the sampling strategy resolution. For the test in this chapter, a relative rough resolution has been applied according to the higher frequency variations in shelling densities. Even with this low-resolution approach, 80% of the test areas (60 in total) were correctly classified in one of the five well-defined destruction classes and almost all mishits were found in an adjacent class. If a higher success rate of classification is desired, a strategy with an increased sampling density will be required. Therefore automatic shell hole detection algorithms (Jensen, 2008) are suitable to decrease de labour intensity of digitising. Unlike the

current orthophotographs, these WW1 photos have a strong varying quality, which is not ideal for automated algorithms. Therefore, human interpretation remains preferable. The second objective in this study, which includes correlating the density of metal debris and shrapnel correlation with the shelling intensities seen on aerial photographs, was proven valid. The geophysical measurement parameters showed an increasing metal object hotspot density and coverage with increasing shell hole densities. The only drawback are the limited number of complete sample records used for the correlation function (only 12). For future research, an increased number of records is needed but despites that, this strong relationship cannot be denied. The creation of a MSP prediction map is useful to localise the MSP-phenomenon in space for risk assessment in soil applications. This map could be implemented in desktop studies and government related procedures with applications in agriculture, demining, construction works, archaeology, etc… Increasing the correlation dataset and optimising the sampling resolution are two important elements that need to be dealt with in future studies. EMI surveys were applied as an indirect method for metal clutter measurements. If the estimation of real metal quantities is needed, test excavations will be necessary to define the relationship. This gap in the MSP definition is an interesting topic for additional research. Despite the unknown quantities, the suggested relative reference zones are effective enough to localise the MSP for spatial analysis.

As result of this study, the workflow for destruction mapping is proposed in appendix 6.3. This procedure has the potential to be applied on every conflict area with artillery shelling. Its strength lies in the availability of a centralised photograph database and war expertise. In addition, the electromagnetic induction measurements are easy to perform and low-cost compared to test-excavations. This unique combination could be the answer to the present need for a high quality destruction map with multiple applications, describing the former Western Front in Belgium.

# Chapter 7

Preservation of WW1 features in the soil on a regional scale

## 7.1 Introduction

The outbreak of the war on the 3rd August 1914 in Western Europe started as a German invasion through neutral Belgium. The flat alluvial territory of Flanders was ideal terrain to move the invading armies as quick as possible to the French harbours in the north, to eventually reach Paris as part of the Schlieffen-plan[3]. This route was a well-chosen detour to reach the French capital because it avoided the strongly developed French fortifications along the French-German border and it contained a lower topographical barrier. Topography in warfare is something that never can be underestimated (Doyle, 2017). In November 1914, the German invasion on Belgian territory was called to an end in Western Flanders near the cities of Nieuport and Dixmude in the north and near Ypres and the Messines in the south. The armies had to take shelter for the constant artillery fire and therefore, soldiers started to dig trenches and underground shelters. This resulted in the Western Front, which was a stalemate in the trenches. The front standstill had an enormous impact onto the land, not only for the vast network of trenches but also during the long period of warfare in this relatively narrow zone. Initially, both parties believed that 'entrenching' was a temporary phase, which would eventually result in front movement. This 'temporary' phase became the norm until the end of the war. In Belgium, the battlefields were partially cleaned and quickly reused after the war (Debaecke, 2013). Until today, remaining military infrastructure is still found. These discoveries are on a daily basis made by ground workers (archaeologists, construction workers, farmers…). For inhabitants, local governments, war enthusiasts, archaeologists and historians, the question rises how many war features are still buried within the soil today and what factors can explain this preservation, both related to human activities (land use) and to soil characteristics (soil type, profile, groundwater …). This information can be useful because land cleaning actions were not well tracked.

[3] An invasion plan, developed at the beginning of the 20th century by the German general Alfred von Schlieffen. The plan's purpose was to overwhelm the French as quickly as possible, in case of an attack.

To gain information about this this problem, a regional study was conducted which investigates the preservation of WW1 traces in the soil. First, the soil properties and their variations were evaluated along the front. This was done to understand its influence on the construction method of trench infrastructure and warfare but also the effect of preservation on buried construction materials.

The second part of the research objective focusses on geophysical prospection to detect buried military infrastructure in a selected number of agricultural fields, mostly distributed along the frontline in the three transect study areas of the '*Non-Invasive Landscap Archaeology of the Great War'*-project (see chapter 2). In this part, the detection results will be compared according to WW1 period aerial photographic research as a reference dataset. In addition, time-series of post-war aerial photographs and ALS data will be used to extract non-invasive information related to the selected fields. As large-scale geophysical mapping technique, FD-EMI was obtained. The choice of this technique can be supported by the findings in chapter 4 and the experience gathered in the period of 2008-14 (see chapter 1). By analysing the large-scale FD-EMI scans, detected linear feature trajectory lengths related to WW1 infrastructure (trenches, roads, railway and communication cable ditches) were extracted and used as a proxy for preservation characterisation. Linear features are chosen because identification of their signatures is more straightforward than it is the case with point anomalies (the shape of a linear feature is more unique and therefore easier to discriminate and to identify in a network of dense military infrastructure). Other parameters related to shelling and metal object finds (in geophysical scans) are used as indicator for the (un)destroyed state of a field.

In general, this chapter will provide archaeologists and WW1 battlefield investigators insights in what can be detected, which soil conditions have an influence on the ability to detect those structures, what are the numbers of linear features lengths – shell craters traces – metal objects that were detected (indicator for preservation) and what is their relationship to land use activities. The integration of aerial photography, ALS, geophysical exploration, soil conditions and land use influences is the core of this chapter to investigate the preservation of WW1 features on a regional scale by using non-invasive proxies.

## 7.2 Soil conditions at the former Western Front in Belgium

Because WW1 was mainly a stalemate in the trenches, soil and topography played a key role in variations of trench construction along the front. Since the end of war, large parts of the subsoil remained untouched because of the mainly rural character of this area. The buried construction materials and war features are degrading over time and soil related parameters are influencing this degradation. Understanding soil related influences in the spatial context of the former Western Front in Belgium would partially explain why certain areas show a better preservation of buried war features than others. In this section, there will be shown how soil composition and soil related factors influence the above and underground trench construction in the former front region in Belgium. Preservation parameters of construction materials (wood/metal) will also be briefly covered.

### 7.2.1 Soil, warfare and trench construction

According to the Belgian soil map, the former Western Front can be divided in 4 main pedo-landscape units: dunes, polder, sand-loam and loam area (overview map see figure 7.5). Starting north at the coast, a short 2 – 3 km wide dune belt is situated between the North Sea and the city of Nieuport. This belt starts in Dunkirk (France) and is reaching just to the North-East of Nieuport where it becomes narrower (0.5 km). The first kilometres of defence lines of the Western Front were built in these dunes (figure 7.1). In a first phase, these lines were situated to the east of the 'Yser' estuary. After the *Strandfest*[4] operation in June 1917, these lines reoriented on both riverbanks (Sheldon, 2007). The defence lines consisted of trenches, shelters, barbed wire and shallow tunnels (subways). Because of the loose sand, the strength of trench and dugout constructions was low. Nevertheless, these dunes had a strong short-distance varying relief (0 – 20 m) which provided cover for soldiers. The vast network of military defences in these dunes were necessary because no inundation was possible except for the tidal flood area of the Yser estuary. Exploding shells had a limited effect in the loose sand, so shelling was limited here, certainly compared to the massive artillery barrages around Ypres and elsewhere along the front. In addition, these grounds have a good drainage ability. By following the front from Nieuport to Dixmude, wet clay alternated with sandy layers can be

[4] German attack on 10 June 1917 whereby the British positions were taken at the eastern side of the Yser estuary at Nieuport.

found (source: DOV). These polder grounds consist out of littoral and estuarine sediments which were formed by fluctuations of dry and flooded periods in the Yser basin (coastal swamp, polders since the late middle ages) (Boterberge, 1962).



**Figure 7.1:** German sailors pose by their shelters in the dunes near Nieuport beach during the winter of 1917 (KLM-MRA collection).

Beneath the polder clay and sandy soil, peat layers appear. Because this land was regained as agricultural land from the coastal swamp, a network of canals is managed to control the drainage of the polder land but also the possible flooding upstream the Yser river caused by the tidal movements of the North Sea. The lock and sluice complex to control this water household is located near the city centre of Nieuport, popularly called 'Ganzenpoot' (goose claw) (figure 7.2). During WW1, the water lock system played a crucial role in stopping the German army (Rash & Declercq, 2018). By flooding some parts of the polders on the western Yser bank between Nieuport and Dixmude, a natural barrier was created. On the Allied side, the water was blocked by the railway Nieuport-Dixmude, which was slightly elevated according to the polder fields. Because of the clayey lowlands, the modified railway dike and an organised water control management, the flood could be sustained until the end of the war. This railway inundation was crucial to consolidate the position of the front. Groundwater is often near surface in these lowlands and during the year (except dry summers), the land is difficult to advance through. With addition of the tactical inundation, large army advances were no longer possible. Because of the high groundwater levels, trench construction was limited to half a metre down with breastworks made out of sand bags, compacted soil or concrete. The parapet (breastwork towards enemy) had to at least 3 m thick on the top to be bulletproof, with a slight

slope toward the enemy lines (His Majesty's Stationary Office, 1916). The parados is the breastwork at the back of the trench, which is often higher than the parapet to avoid the outlined contours of the men in the trenches against a contrasting background (sky) (His Majesty's Stationary Office, 1916; Army War College, 1917). Its main function was preventing death and injuries from shrapnel shells that burst behind the lines. On later trench constructions, this was often optional. A borrow pit in front of the parapet provides drainage. A transverse section of a trench in wet soil conditions can be seen in figure 7.3. In addition, ruins of left-behind houses and farms were often turned into strongpoints. These locations were the highest points in the surrounding area, which were just rising above the water level. Because of the poor soil drainage conditions, shell craters contained mud, flood and rainwater. This omnipresent micro topography contributed to the front standstill.



**Figure 7.2:** French oblique aerial photograph (January 1916) of the city of Nieuport (in foreground), with the sluices complex central in the photograph and parts of the inundations in the background (KLM-MRA collection).

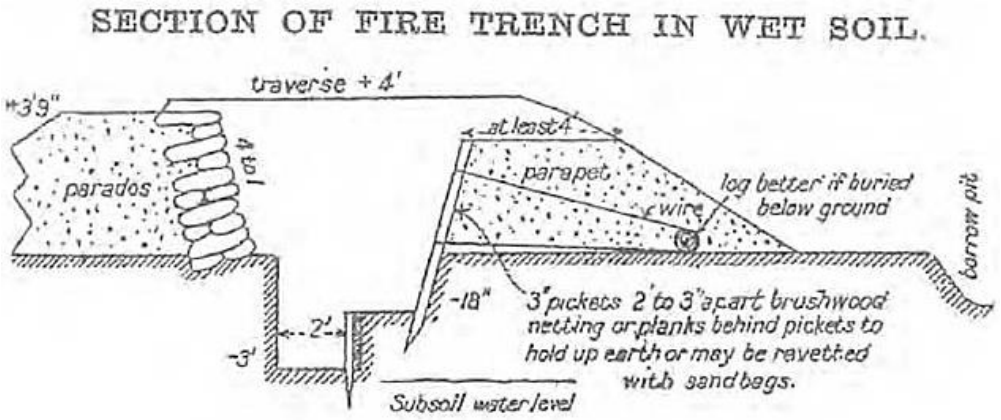



**Figure 7.3:** Section of a typical fire trench for wet soils (shallow ground water level) such as the polder plains in Flanders. This drawing appeared in 'Notes for Infantry Officers on Trench Warfare' (His Majesty's Stationary Office, 1916).

To the east of Dixmude (see map figure 7.5), the soil in the German back areas consists of dry/wet sands while on the west, polder grounds remain. When the Germans occupied Dixmude on the 10th November 1914, the decision was made by the Allies to inundate the 'Blankaart', a swamp area to the south of Dixmude (Demerre & Termote, 2013; Simoens 2016). To create this inundation, a dike was built on the Yser nearby the village of Sint-Jacobskapelle. This move caused also an unwanted inundation to the east of Dixmude in the Handzame valley (a bulge of polder grounds into sand-loam and sand country where the Handzame canal is located). In January 1915, the French demanded the inundation of Knokke (to the west of the Blankaart, upstream the Yser). This inundation was possible up to the hamlet of Fintele where the Yser river and the Lo-canal meet. To inundate the Knokke area, water was pumped out of the Lo-canal. The possibility to inundate the Yser banks is supported by the Belgian soil map and height model (figure 7.4 and 7.5). The inundations derived from the British trench maps are similar as the footprint of the polder bulges entering the higher grounds of the sand-loam area. These inundated polder areas are lowlands that also reflect in the elevation model (figure 7.4). At the time of the war, a detailed soil map was lacking. Instead, geological maps were used to inform soldiers about the expected soil profile. Belgian scientists performed pioneering work from the beginning of the 19th century to explore the geology within national borders (De Béthune, 1961). This information was useful during the war for military geological engineers. The height model to guide armies through the relative flat relief could be derived from the first Belgian topographical base map (scale 1:20000, revision 1903-1912), which was used as background reference for trench maps.

North of Ypres (see map figure 7.5), the front no longer followed the Yser river and was positioned in a wide arc around the city, the so called Ypres Salient. Here, the elevation starts to rise and the soil changes into sand-loam (0.5 – 3 m thick) with Ypresian clay (Kortrijk formation) underneath. These typical blue-grey clays are very suitable for tunnelling and (deep) dugout structures and are largely water impervious. When exposed to air, the clay colour changes into grey-brown after oxidation. The blue colour (when freshly dug) had to be hidden because this would give information to the enemy lookouts that tunnelling is taking place (Doyle, 2017). Above the clay, the loam-sand layer allows water through and when infiltration reaches the Ypresian clay, this impermeable layer stops the water drainage. This soil property gave problems for trenching in areas where the sand-loam layer is thinner than 1 m. In addition,

when the landscape was completely shelled, mud and rainwater would fill the shell holes. For the British, the uncountable numbers of undrained shell holes is the reference image for the battles fought at the Ypres Salient.

To the east of Ypres, an elevated area arises which starts from the south of Dixmude (+/- 20 m TAW) and reaches to Mt. Kemmel (156 m TAW). These higher grounds (see figure 7.4) called the 'Mid-West-Flemish Hillside' (or Westrozebeke ridge), played a strategic role during the war. Around the village of Passchendaele (before 2nd battle and after 3rd battle of Ypres) and Mount Sorrel (between 2nd and 3rd battle of Ypres), frontlines coming from Langemark are reaching these heights that consists out of Eocene sands and clays. This elevated landscape is also found to the south of Ypres around Wytschaete and Messines (loam and clay soils) where the ridge is flowing over in the West-Flemish hills (60-80 m TAW). From there, the topography is again lower and the front moves to the Lys-plain south into France. The British army named the hills to the east of Ypres the 'Passchendaele ridge' and the ones to the south the 'Messines ridge'. The soil profile of these hills (alternating clay and sand layers) are more favourable to build structures in better-drained soil conditions than the wet Ypres clay plain. The elevation above the surrounding area gave armies also a tactical advantage for enemy surveillance. The German forces occupied these heights most of the time enabling artillery fire from several directions around the city of Ypres. In addition, trenches could be dug at sufficient depth without building large breastworks (see figure 7.6). In very wet and muddy plains, trenches are more difficult to maintain than the dryer Eocene sand and clay hills. When water saturation reaches its maximum, the topsoil (sand-loam) loses its plasticity. Degradation of trenches in these conditions are unavoidable. Therefore, the dryer ridges surrounding Ypres were preferred for (deep) trenching. Because the soil types vary by depth and the groundworks increased in depth in the southern part of the front in Belgium, a depth profile following the frontlines, was made out of information from the DOV database (www.dov.vlaanderen.be, 2018). This profile's path is marked in figure 7.4 and 7.5 (A to F) and displayed as a cross-section in figure 7.7.

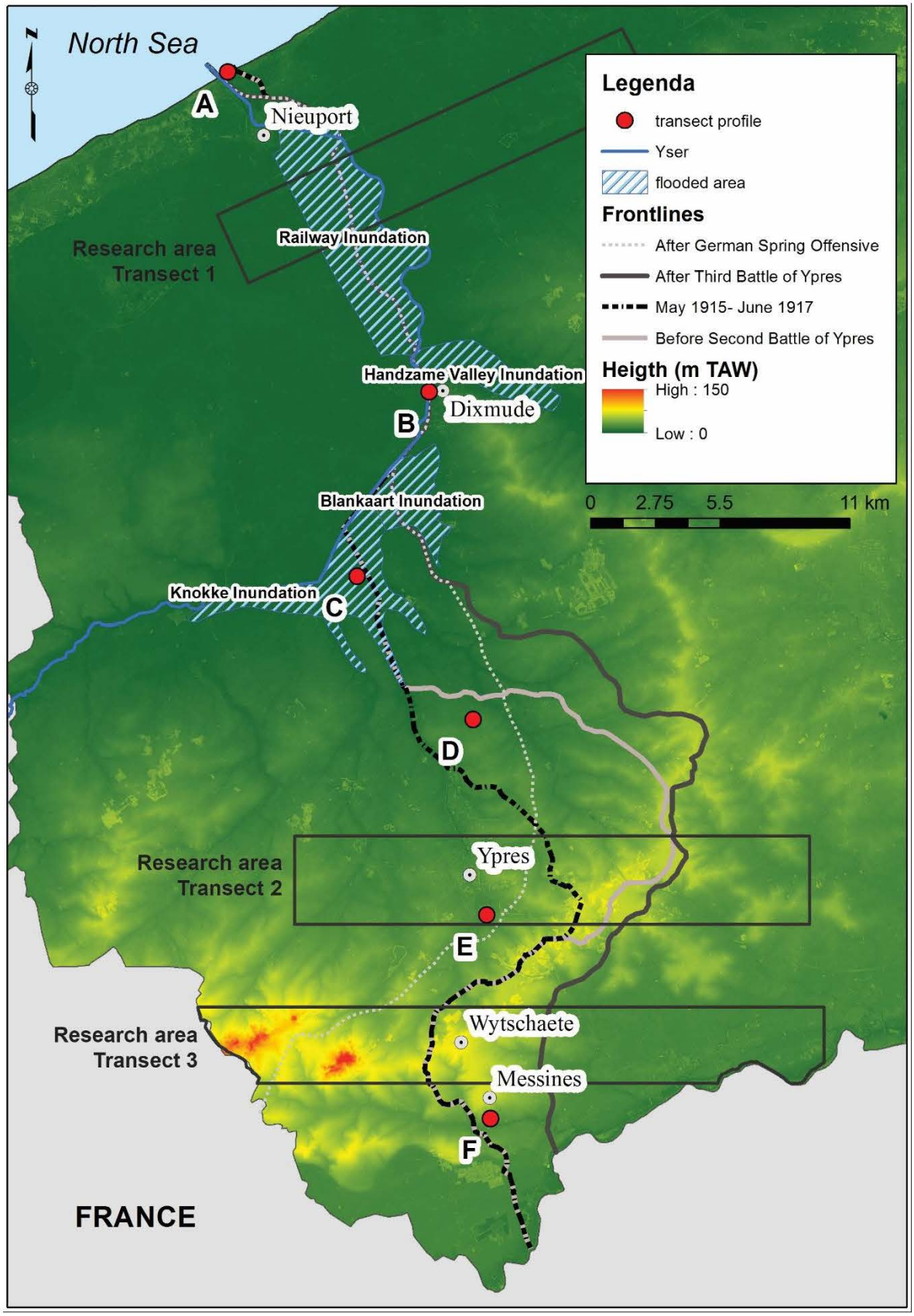



**Figure 7.4:** Overview of the Flanders digital elevation model (DHVII, copyright AIV) along the former Western front in Belgium. A soil profile was taken by following the transect from A to F (see figure 7.7).

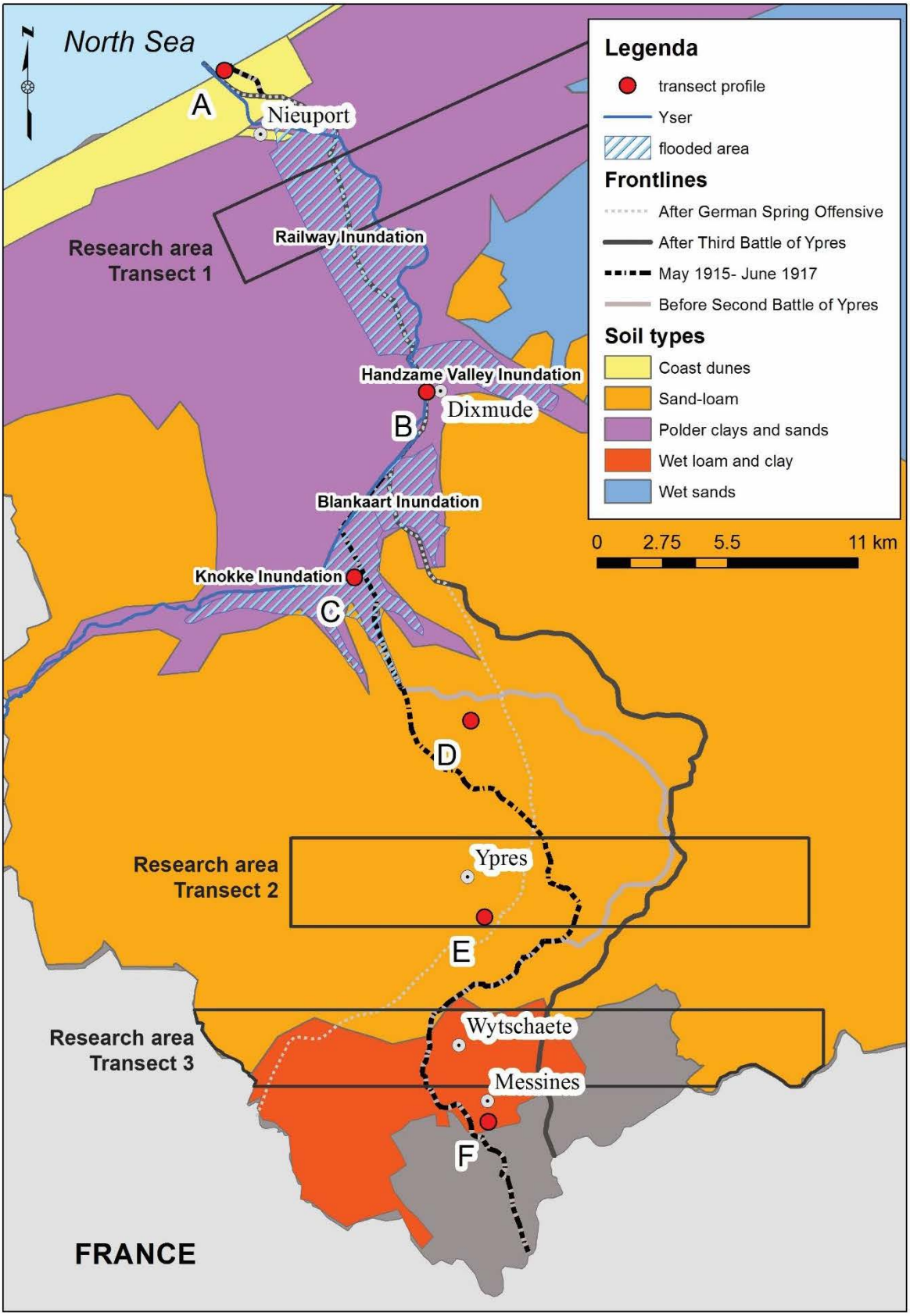



**Figure 7.5:** Overview of the soil classification by the Belgian soil map in generalised groups along the former Western Front in Belgium. A soil profile was taken by following the transect from A to F (see figure 7.7).

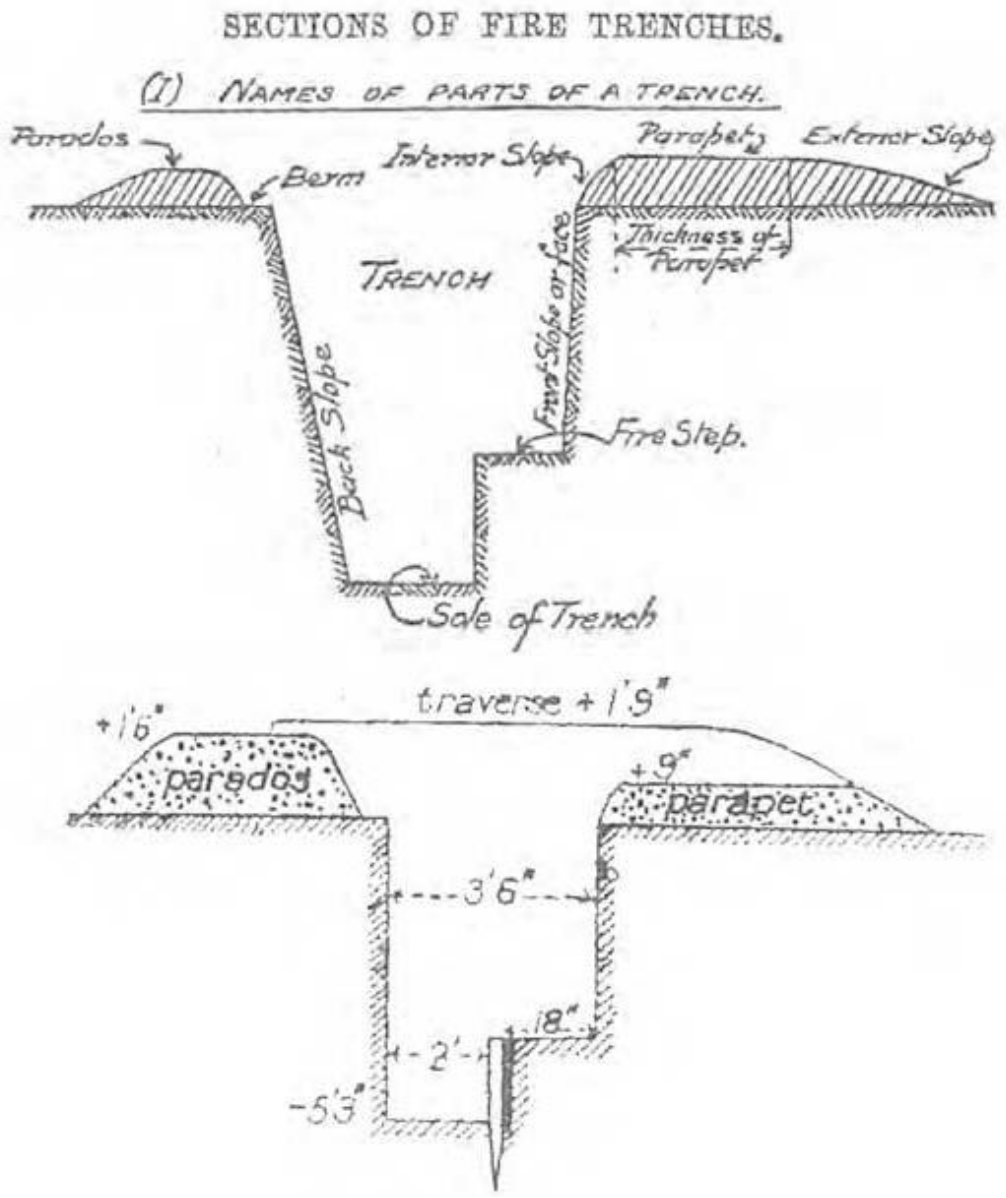



**Figure 7.6:** Section of a typical fire trench in soils with good drainage (not limited by groundwater table). This trench construction was ideal on the sand and clay ridges surrounding Ypres. This drawing appeared in 'Notes for Infantry Officers on Trench Warfare' (His Majesty's Stationary Office, 1916).

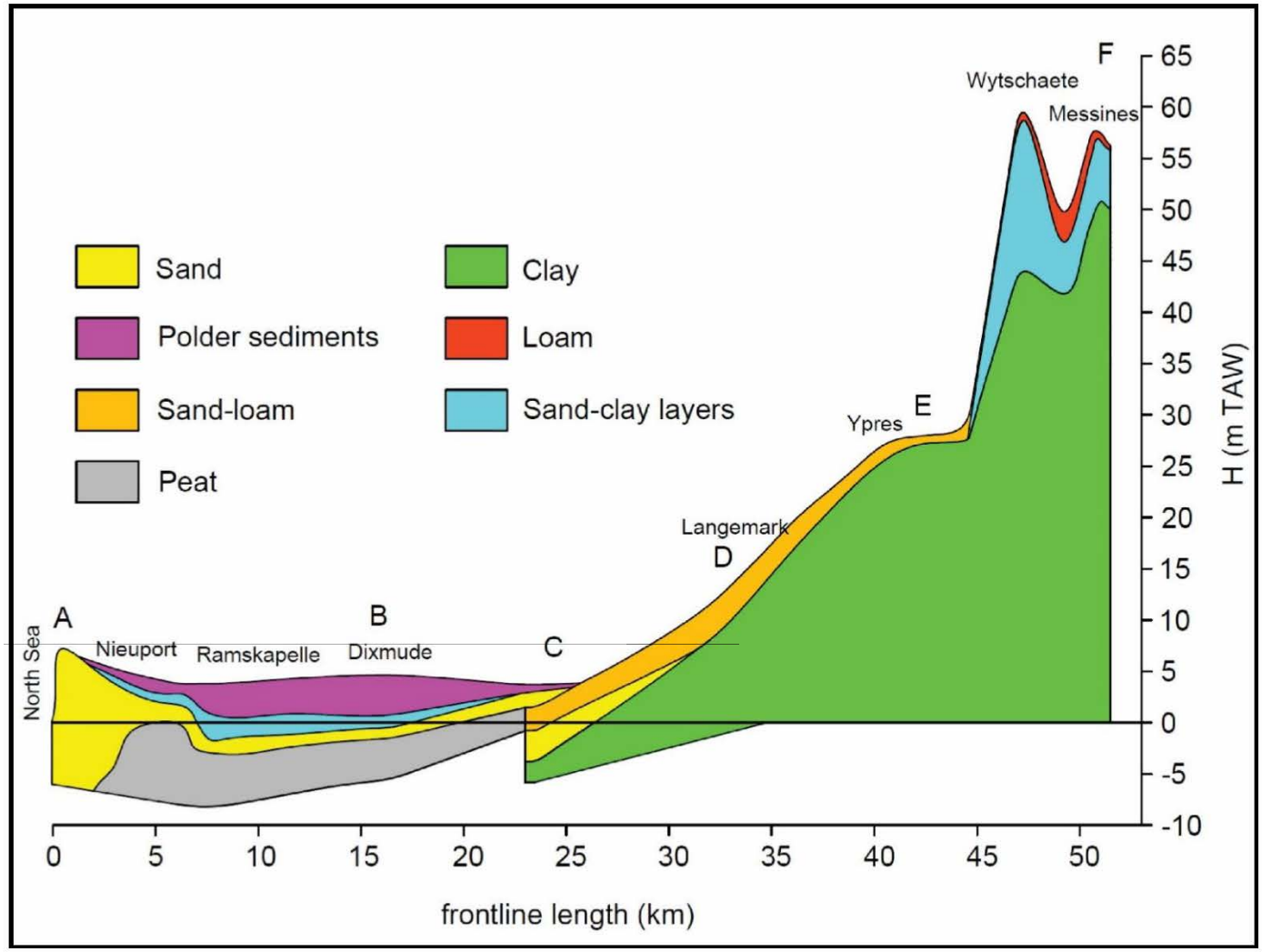



**Figure 7.7:** Cross-section along the Western Front in Belgium based on descriptions of soil profiles derived from DOV. The section trajectory is marked in figure 7.4 and 7.5.

### 7.2.2 Degradation of WW1 construction materials vs. soil conditions

The two major materials used during WW1 next to sandbags and concrete are timber and metal alloys (His Majesty's Stationary Office, 1916). Timber became a precious material during the war, and was imported by all fighting parties as wood became scarce. It was generally used as reinforcement for trenches (wall reinforcements, duckboards, dugout support…), to build infrastructure (shelters, bridges, railway, soldier camps…), to support constructions for artillery or as heating raw material. Metal alloys on the other hand are the main component of guns, ammunition, barbed wire, nails, railway tracks, roof plates, corrugated sheets as trench support etc. Both materials degrade in similar conditions: in the presence of oxygen, fluctuating dry/wet conditions and by increasing temperature (Revie, 2011; Shupe et al., 2008). The first two parameters are the most determent because temperature in the subsoil can be considered as quite stable. In addition, the smaller the soil particle size, the better materials are isolated from the air.

To predict the preservation conditions for one particular WW1 site, following parameters should be considered: soil profile (texture), dissolved oxygen in groundwater, groundwater level and its variations. Other less important influences are ion content, pH, chlorides, sulphates, bacteria and microorganisms, which have a limited influence since the end of WW1 and therefore not taken into account. Measurements of the groundwater are based on the DOV database containing measurements of the 2004-2014 period (https://www.dov.vlaanderen.be/portaal, 2015).

**Groundwater**

Water plays an important role in the process of metal corrosion and wood degradation. The groundwater table determines the soil depth to where circulating air can travel through the soil pores and degrades timber and metal. This level can fluctuate seasonally. In heavily saturated soils, air is transported by diffusion, which is a slow process. The zone just below the ground surface is provided with pores. This ensures that air can penetrate the soil smoothly, but the lack of moisture can ensure a relatively low degradation rate. The zone just above the ground water table is favourable for degradation. Both air transport via pores and capillary moisture derived from groundwater, ensures a high degree of degradation (Mattsson et al., 1996). In natural soils, the degree of water saturation varies. The frequency from saturated to

unsaturated determines the increase in corrosion (Romanoff, 1985). Fluctuating dry/wet soil conditions can be caused by two phenomena: rainfall and groundwater fluctuations (seasonal variations). Objects and structures below the groundwater table are sealed from air contact. In this case, degradation is depending on the amount of dissolved oxygen (DO) in the groundwater. The oxygen content that is absorbed by the groundwater depends on a number of parameters: temperature, air pressure, depth (hydrostatic pressure) and salt. The average $O_2$ content in transect zone 1 (due to higher salt concentrations) is 0.95 mg/l, for transect zone 2 this is 1.5 mg/l and for zone 3 this is 1.25 mg/l (DOV database). To analyse the corrosive effect of DO onto steel pipes, the redox potential (Eh°) of groundwater is used as alternative indicator (Starkey & Wight, 1945). Values between 0-100 mV and 100-200 mV represent respectively high and moderate corrosive effects, which are found in the dunes and polder areas. These high values are caused by the presence of ions (mainly chlorides) and not because of significant differences in DO. The sand-loam area represents values between 200-400 mV, indicating a low corrosivity of metals. On the other hand, salts are good preservatives for construction timber against rot.

In addition, groundwater regulates the heat distribution in the soil. At the former Western Front in Belgium, values are measured between 10-12°C with a standard deviation of 3-4°C. Generally, the edge of 10°C is determining for timber degradation (Shupe et al., 2008). Higher temperatures create conditions (together with moisture) for bacteria to affect the wood. For metal alloys, soil temperature changes doesn't have a large effect (Quaranta, 2009). Climatic differences for wood or metal degradation are decisive when the temperature factor is used. For Belgium, this is not the case.

**Soil texture**

The soil is the medium in which buried metals and timber degrade. Soil is a mixture of minerals, organic material, water and air. The combination and composition of these components determines the aggressiveness of the degradation. The larger the pores, the easier air and water can travel trough. Minerals are a conglomerate of sand, silt and clay. Their relative composition (see texture triangle figure 7.8) determines the soil texture.

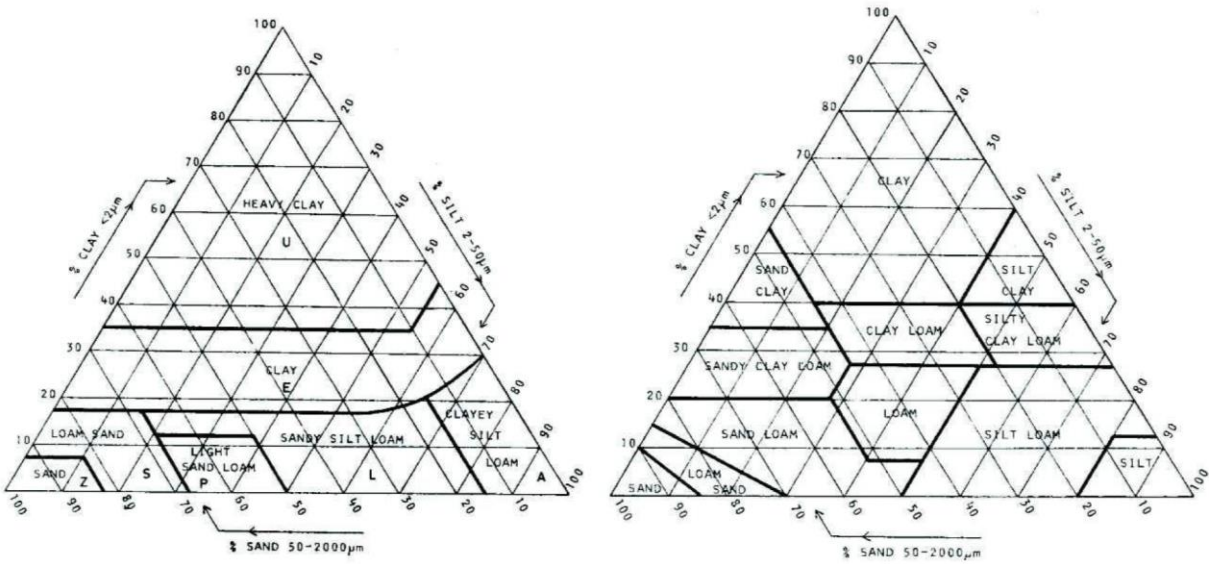



**Figure 7.8:** The Belgian texture triangle (left) and the international texture triangle (right).

**Sand** (63 µm - 2 mm) consists of relatively large particles with a small specific surface (area, volume ratio) that create a structure with pores that allow air and water to circulate easily.
**Loam (silt)** (2 µm - 63 µm) consists almost exclusively of uninterrupted minerals, smaller than sand particles and has a small specific surface area. The particles are variable in size, which promotes soil compaction. The mobility of water in this medium is very small. Loam has a large moisture-holding capacity.
**Clay** (<2 µm) is the product that remains after the decomposition of various igneous rocks and consists of hydrated aluminium silicates, often contaminated with Fe and Mg. The particles have a large specific surface area and small dimensions so that this medium has a very large water-bearing capacity. Water causes clay to swell. As a result, clay has a very compact mass, making it inaccessible to air.

Based on the Belgian soil map, the first and second transect study areas mainly consist out of sand-clay or sand-loam combinations. In the third transect, loam in combination with outcropping tertiary clay appear which are more favourable conditions for WW1 feature preservation than the two other transects.

### 7.2.3 Anthropogenic effects of the post war period

After the war, inhabitants came back to the former front areas to rebuild the infrastructure and cultivate the land. Cleaning parties such as the Chinese labour force, German war prisoners and Belgian army units helped to turn the battlefields into habitable land again (Debaecke, 2013). After rebuilding the railway infrastructure in the spring of 1919, workers from all over the country's came to clean and level the battlefields. In a first phase, the trenches and shell craters were filled and the near-surface UXO was removed (Dendooven, 2007). In a second phase, the soil was turned over to remove war materials and UXO below the ploughing depth (approximate 0.5 m) (Dewilde, 2010). Depending on the position along the front, the cleaning was done with different levels of precision.

In the polder area where inundation was the general defence tactic, no front movement took place in this relative calm area. This made the localisation and removal of the military infrastructure easier than in other parts of the front. In addition, the depth of trenching and tunnelling was limited: mainly above ground structures had to be removed and dense shelling was absent, except for the area of Dixmude, Nieuport and the sluices system which were completely whipped out at the end of war.

The water saturated sand-loam soils on the impermeable clay-plain near Ypres caused soaked mud-areas, densely perforated with shell holes. This complex mud area caused a part of trench infrastructure to disintegrate. The frontlines shifted a few times over a distance of 5 km with the largest changes in 1918 caused by the German and Allied offensives. This caused a wider area of left-behind structures and materiel. Trenches that did not survive the heavy artillery fire were often missed by cleaning actions. On the other hand, open trenches were often reused to dump the military waste. Therefore, waste filled battle-surviving structures should be easier to find with geophysical prospecting techniques.

On top of the ridges surrounding Ypres, dryer grounds favoured the usability conditions of men-dug structures. This was mainly because of the better drained soil conditions which caused a better situation for trench infrastructure to stay intact in wet conditions. This situation had possible an effect on the retraceability of WW1 structures with non-invasive techniques.

**The importance of land use changes & ALS**

After the reconstruction which mainly took place in the 1920's, the impact and intensity of land use influenced the preservation conditions of buried structures. The former front area is mainly a rural landscape, dominated by pasture and arable fields. Plots that intensively have been ploughed would hypothetically contain less traces in the shallow soil layers than pasture fields that have been in the same land use conditions since the end of WW1. Also compaction improves preservation which can be found in pastureland or pavements.

One source to study land use changes are periodic recordings based on topographical maps and aerial photographs. The analysis of these time series is a first indicator of post-war changes. By giving weights to land use conditions for several time series of photographs, different plots can be compared with each other based on the effects of land use. Also similar conditions over the years can have a different impact: fields were more intense and deeper ploughed since the 1970's than before. Therefore a different quotation can be given to similar land use for different time frames.

A second indicator is based on the processing of ALS data to extract indications of micro-topographical variations, related to WW1 traces (Gheyle et al., 2018). Long-time grass and woodland score best on micro topographic traces. Classifying an area based on an ALS study is a recent developing technique that is promising for battlefield studies (Taborelli et al., 2017).

### 7.2.4 Summary soil influencing parameters

A table containing a selection of preservation defining parameters is given as a synthesis of section 7.2. This overview can be used as guidance (hypothesis) when studying a specific site on the Western Front in Belgium. Four main determine parameters (linked to the soil) are given a score (between -1 = bad and 1 = good), indicating its influence on the possibility to find/detect WW1 traces. The purpose of these scores is to make a general overview of the described parameters, linked to the four pedo-landscape zones (table 7.1). Based on the averages per zone, a relative indication can be given. In this quotation, the loam-clay area on the southern part of the Westrozebeke ridge indicates better properties to retrieve structures from the soil (see table 7.1). The Polder areas score lower because of the presence of mainly above ground military infrastructure, which was easier to remove during the post-war period. The scores per

zone will be linked to the large-scale geophysical surveys (section 7.3), performed as proxy for preservation characterisation.

**Table 7.1:** A quotation table containing four main indication parameters to predict the expectation of WW1 feature finds in the soil matrix per pedo-landscape zone.

| | **ZONE 1**<br>**Dunes** | **ZONE 2**<br>**Polder** | **ZONE3**<br>**Clay plain** | **ZONE 4**<br>**Higher ridges** |
|---|---|---|---|---|
| **Groundwater** | Weak (-1) | Moderate (0) | Moderate (0) | Moderate (0) |
| **Drainage** | Moderate (0) | Weak (-1) | Weak (-1) | Moderate (0) |
| **Soil texture** | Weak (-1) | Moderate (0) | Moderate (0) | Moderate-Good (0.5) |
| **Trench construction** | Deep (1) | Shallow (-1) | Shallow-deep (0.5) | Deep (1) |
| **GENERAL quotation** | Weak (-0.25) | Weak (-0.5) | Moderate (-0.125) | Good (0.375) |

## 7.3 Field research: large-scale geophysical investigation

Highlights of the large-scale FD-EMI investigation are described in this section per transect zone of the '*Non-Invasive Landscape Archaeology of the Great War'* – project (see chapter 2). Each investigated field is analysed to understand the conditions that determined the presence or absence of WW1 traces in the subsoil. Proxies such as the detection rate[5] (DR) of linear features[6], the density of linear features seen on aerial photography[7], extra detected linear feature lengths[8], EMI metal parameters[9] and shelling densities[10] (described in chapter 6) are calculated to compare fields and areas. The definition of the above described parameters can be found in the footnotes. For the field research, a clear distinction is made between the polder areas from transect 1 and the sand-loam and loam-clay area from transect 2 and 3. In addition, ALS and land use changes are merged to the GSS investigation to connect information about land use to the finds of military infrastructure while trench maps and aerial photograph information are used as reference for the by GSS detected features.

### 7.3.1 Transect 1: The polders

This transect, which crosses the frontlines south of Nieuport, can be divided in three main areas: the Belgian sector on the western side of the railway inundation (see figure 7.9), the by inundations dominated area between the railway and the Yser river with both Belgian and German outposts and the German sector to the east of the Yser. In this polder area, 10 locations were surveyed (see figure 7.9). According to the function of the sites during the war, the sites can be classified in four different groups: (1) fortified farms near the Belgian frontline,

[5] Detection rate (DR) are the total lengths of linear features seen in the EMI data compared to the validated lengths by aerial photography (RSA). Linear traces with no validation reference in RSA data are not included. This variable is expressed in m/ha.
[6] Linear WW1 features are: trenches, narrow gauge railway, military roads and communication cables. These traces can be detected by EMI-investigation.
[7] This is the RSA density of linear features, expressed in m/ha.
[8] Extra detected lengths of linear features with a signature of WW1 infrastructure in the EMI scan data and not validated (=seen) on aerial photography.
[9] EMI metal parameters are: (1) percentage scan area classified as metal by the FEMP filter (= % area FEMP); (2) density separate hotspots classified as metal by the FEMP filter within the scan area (= metal hotspots per hectare or MOH/ha). These parameters are described in chapter 6.
[10] Shelling densities are described as shell holes per hectare (Sh.h/ha). Dese values are derived from aerial photography. Therefore, a photograph at the end of the war, close to the final offensives are used. This parameter is described in chapter 6.

(2) advanced posts near the frontline in the inundated area, (3) frontline locations and (4) hinterland sites. In total, an area of 50.0 ha was surveyed.

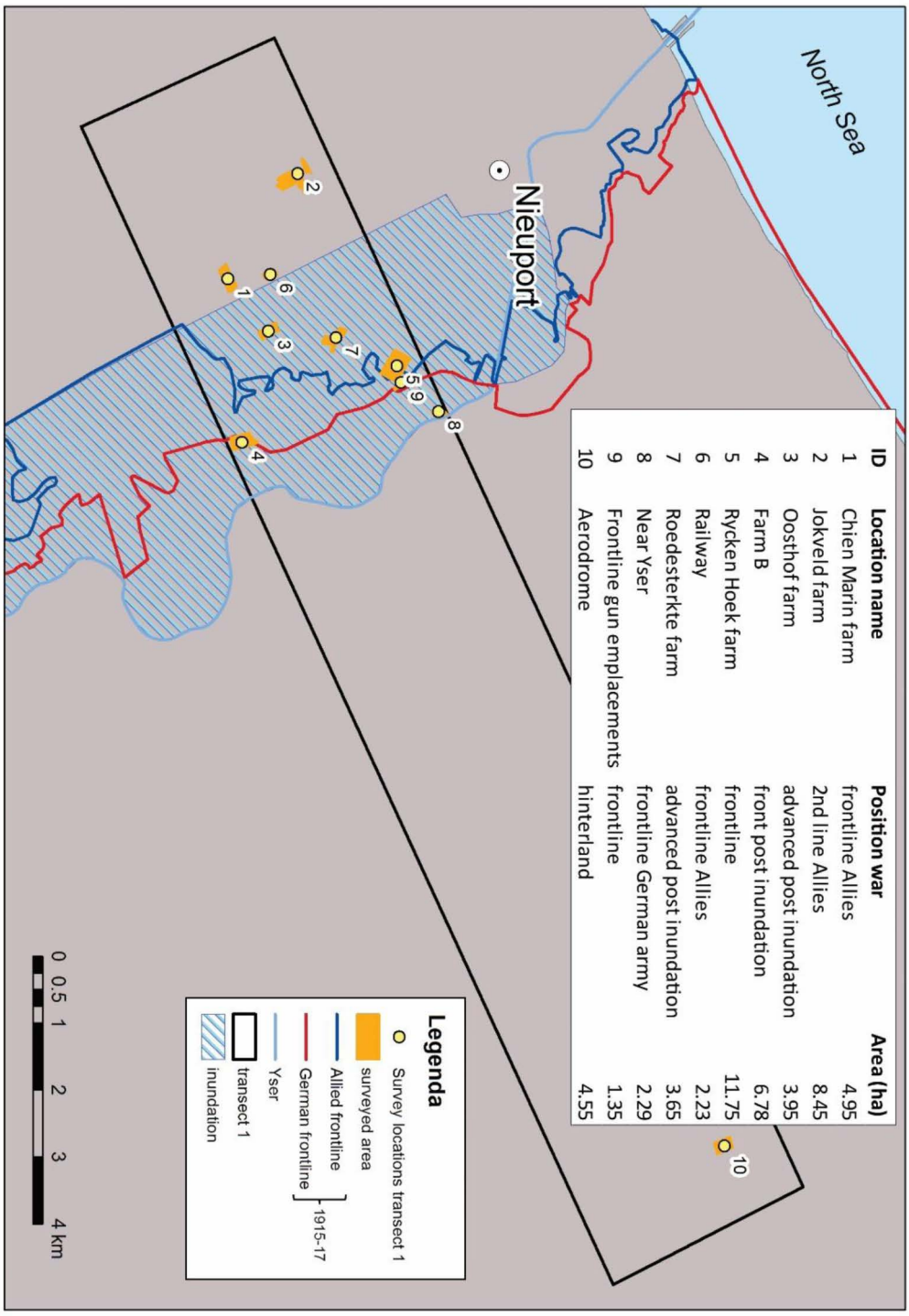



**Figure 7.9:** Overview of the surveyed sites according to the 1st transect zone. Each site has its own ID.

#### *7.3.1.1 Chien Marin and Jokveld, fortified farms near the Belgian frontline (ID 1 & 2)*

Both farms played a major role as fortified posts for the Belgian army. The German army targeted these farms many times with their artillery but because of the lack of offensive actions, these sites remained behind the Belgian frontline. During the summer of 2015, the fields around both farms were scanned. The results of the linear feature detection analysis showed two different outcomes. Near Chien Marin farm, 42.7% of the linear feature transects (DR) were found. In general, the outer contours of trench breastworks were detected with both $EC_a$ and $MS_a$ responses. This can be explained by the detection of the (dug) borrow ditch on the outer side of the breastwork. Contrasting magnetic infillings of this ditch reveal the trench contours in the result of the EMI survey. On the other hand, the locations of the breastworks are relatively 'clean' (the above ground breastworks apparently protected the soil and prevented war debris from penetrating in the surface) while the surrounding areas are showing more magnetic anomalies). By locating the 'undisturbed' breastwork footprint (see figure 7.11 C) trench locations can be identified. In addition, a communication trench between the farm fortifications and the first line (along the railway bank) was detected by the magnetic response (see figure 7.11 B). Overall, the 2HCP $MS_a$ data layer was the most useful for this site.

In contrast, at Jokveld farm no WW1 features were detected. The absence of these has many possible causes. A first difference between both farms is their position in relation to the first defence line. Chien Marin was connected with the front posts as direct support. It is located only 300 m behind this line while Jokveld is 1000 m further away. Next, the inundated area between Chien Marin and the front was much narrower on the Allied side. These factors can form a possible explanation why the fortifications around Chien Marin were more intensively used with the result of a stronger footprint in the soil. A second factor are the changes of land use since the end of war and the intensity of agricultural practices. The surrounding fields of the Chien Marin farm were classified as pasture since the end of war until the 1970-80's, when it was converted into arable ground. Compaction of polder grounds is ideal for magnetic trace preservation. South of the Chien Marin site, a zigzagging communication trench was detected by modelling the micro topographic changes from the elevation model (DHMV II). This is one of the very rare fields in the first transect where trenches appear in the LIDAR model. This was one of the trenches to provide a connection between the farm and the frontline trenches. The presence of this topographical signature is explained by the constant state of pasture conditions. At the Chien Marin site, only some old field boundaries of the pré-landconsolidation

phase (<1980's) are visible in the ALS data. The small micro-topographical changes related to the war were ploughed out. The land use conditions seem to have an important role to detect the few remaining traces. This is because trench construction was mainly performed above ground in combinations with breastworks. When a trench was dug, its depth was often limited to 0.5-0.8m, just above ground water level. For firing trenches, the draining/borrow ditch in front was often the only features which was actually dug into the soil. Sometimes parcel canals were integrated in the trench system for drainage. Therefore, it is often difficult to make the distinction between trenches and parcel canals in the geophysical results. When a field was constantly ploughed after the war, the remaining traces were destroyed by agricultural practices. This is probably what happened around Jokveld farm.

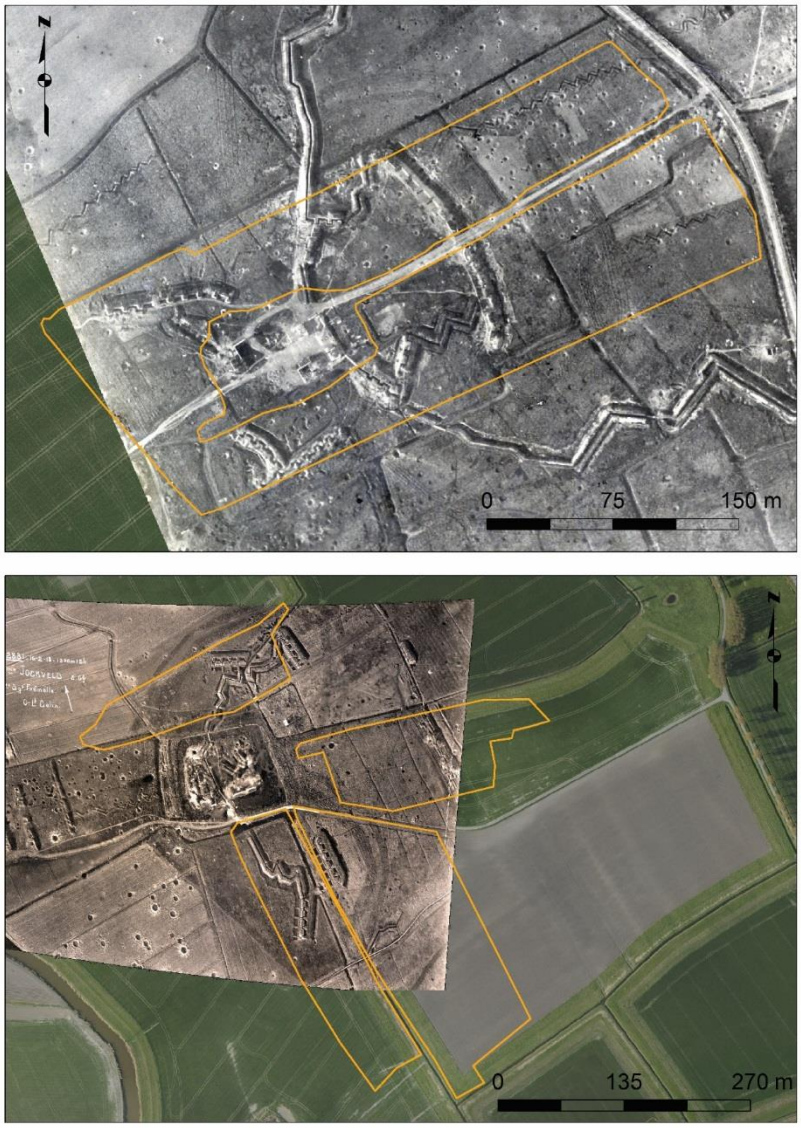



**Figure 7.10:** Visualisation of war period aerial photographs taken at Chien Marin farm (top, KLM-MRA collection) and Jokveld farm (bottom, collection Service Général du Renseignement et de la Sécurité, Section Archives), indicating fortified farms, surrounded by trenches. The surveyed areas are marked by a full enveloping line. (orthophoto: copyright AIV)

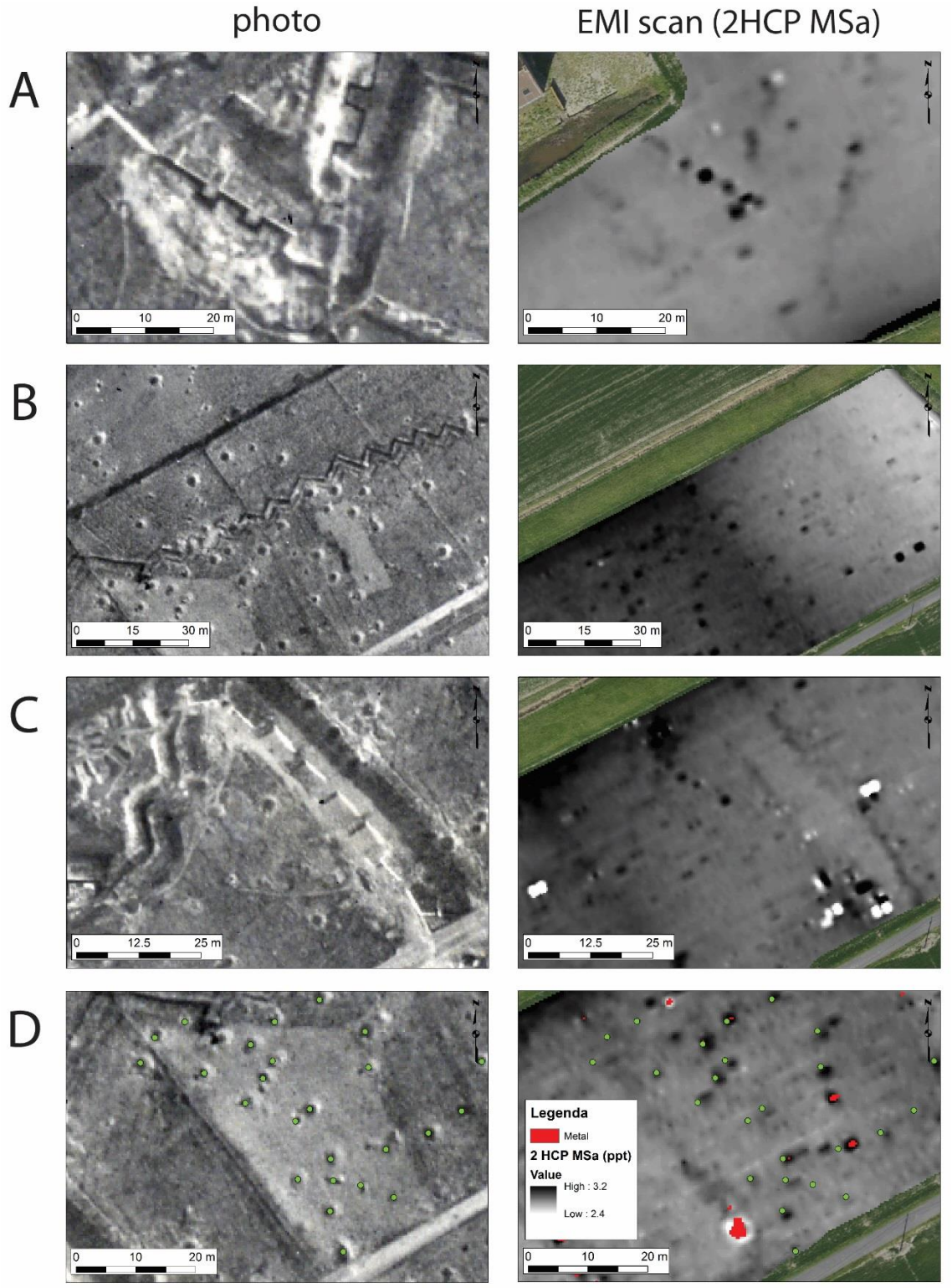



**Figure 7.11:** Visualisation of four remaining WW1 traces in the soil around Chien Marin farm: (A) firing trench with breastworks, retraced by the surrounding magnetic ditches / (B) communication trench with very subtle magnetic signature / (C) communication and firing trench found by their magnetic surrounding ditches, magnetic 'clear' footprint on the breastwork locations firing trench / (D) shelling traces: 21/27 shell holes (indicated with green dots) in the presented sample area were detected by EMI, some contained metal. (aerial photograph KLM-MRA collection; orthophoto: copyright AIV)



**Figure 7.12:** Aerial photographs taken in 1971 of the Chien Marin farm (copyright AIV). This image indicates pasture surrounding the farm buildings.

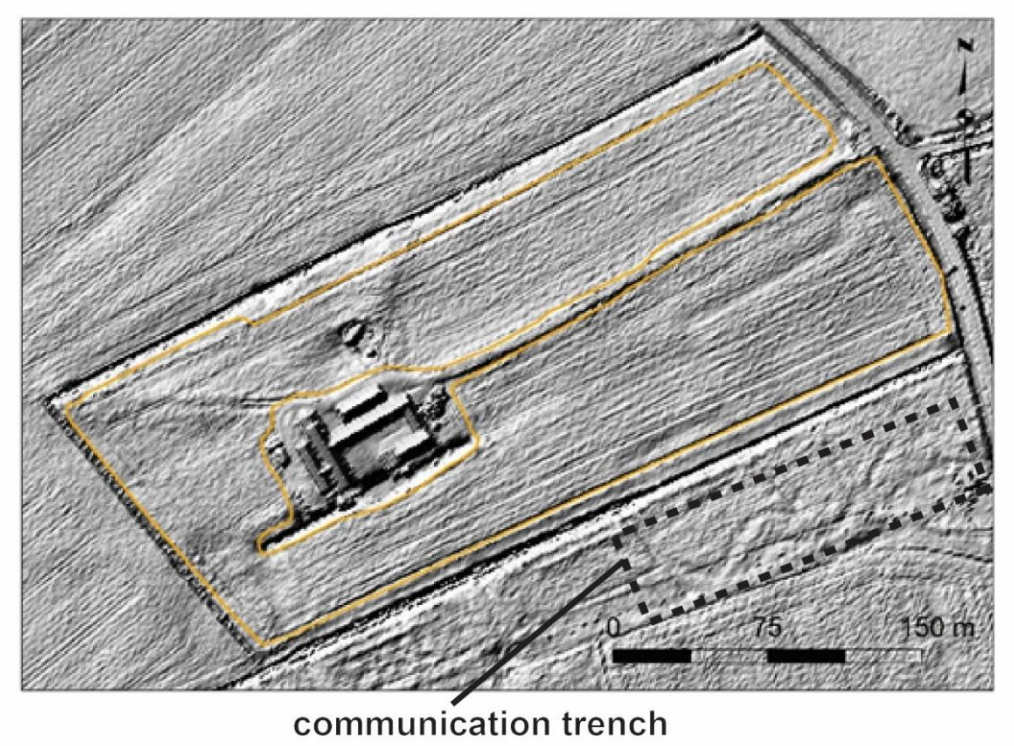



**Figure 7.13:** Visualisation of the micro relief changes near the Chien Marin farm. On the by EMI prospected site, no war related traces were seen. In a parcel that is for the current moment pasture just south of this site, a zigzagging communication trench appears in the micro relief (DHMV II: copyright AIV).

#### *7.3.1.2 Advanced posts in the inundated area near the front: sites near Oosthof (ID 3) and Roedesterkte farm (ID 5)*

Oosthof and Roedesterkte farm were two strategic locations in the inundation zone that were used as outposts by the Belgian army. These advanced posts were guarded by sections of 25 to 50 men and from those sites, several raids were held to keep the German army occupied with counter attacks without the thought to regain ground (Simoens, 2016). This was done to avoid German troop shifts and deployments to other sections of the front. Both farms were occupied by Belgian soldiers which were facing the 'Groote Hemme' farm (occupied by German soldiers). A few hundred metres to the east of both farms, firing trenches were constructed facing the enemy with 500 - 1000 m of no-man's-land in between.

On the prospected field near Oosthof, two firing trenches including breastworks were constructed. The parcel canal in front of the trench system was integrated as drainage ditch and a bunker was built in the middle of both trenches. The dry part of elevated polder grounds between the Oosthof site and Chien Marin farm, made it possible for the enemy to reach the Belgian first line. Therefore, this advanced post was constructed.

Considering the EMI scan, breastwork and bunker traces were found on the Oosthof site in the 2HCP magnetic data layer (see figure 7.14). After ground levelling and removing the breastworks in the post-war period, a footprint was left in the soil. This footprint remains in agricultural grounds where ploughing did not affect the trench traces over its complete depth. Magnetic contrasting infillings of the parcel and trench ditch are typical remnants of WW1 trenching in the polder areas. A schematic visualisation in figure 7.15 demonstrates what remains after post-war clearance and levelling. In total, 69% of the trench trajectories on the Oosthof site were detected by the EMI scan. The grounds around Roedesterkte farm delivered similar results. Only here, the magnetic traces were more subtle. If land use is considered, the prospected Roedesterkte fields are classified as pasture in all-time series, except for one field, which was seen in arable conditions on the 1971 image. Therefore, the LIDAR data shows a lot of micro-relief changes such as a slight ditch related to the firing trench breastworks detected by EMI (see figure 7.16). At the Roedesterkte site, around 48% of the by RSA detected trench trajectories were found by EMI.

Because of the results obtained at Chien Marin and Oosthof, the experience was build up to look at the specific breastwork pattern in the 1 and 2 HCP $MS_a$ data layers from other scans.

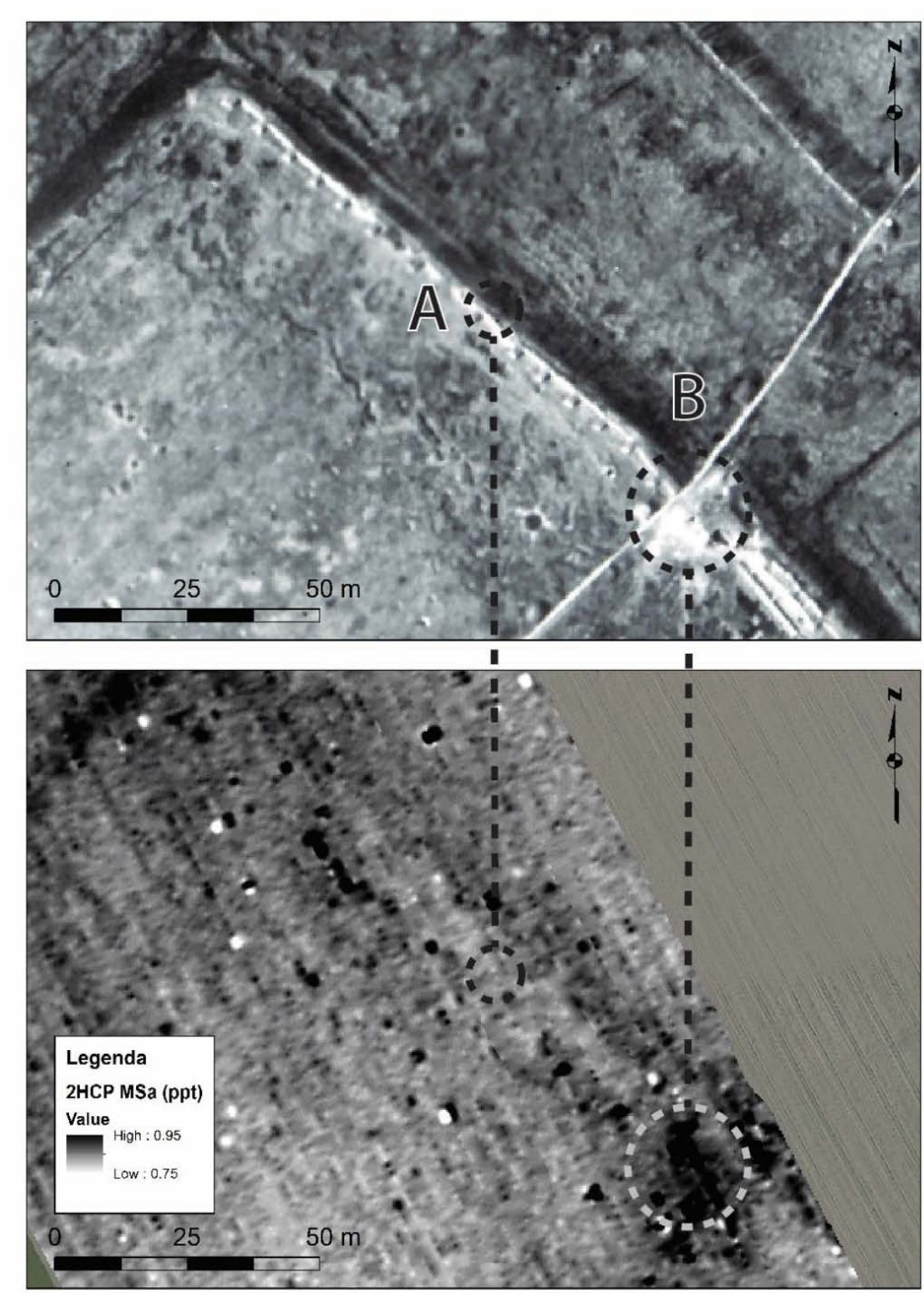



**Figure 7.14:** Comparison for the Oosthof site between an aerial photograph (23/03/1918, KLM-MRA collection) and the 2HCP magnetic data layer from the EMI scan (11/08/2015). On both images, (A) points the location of breastworks of a firing trench while (B) gives indication of a bunker. (orthophoto: copyright AIV)

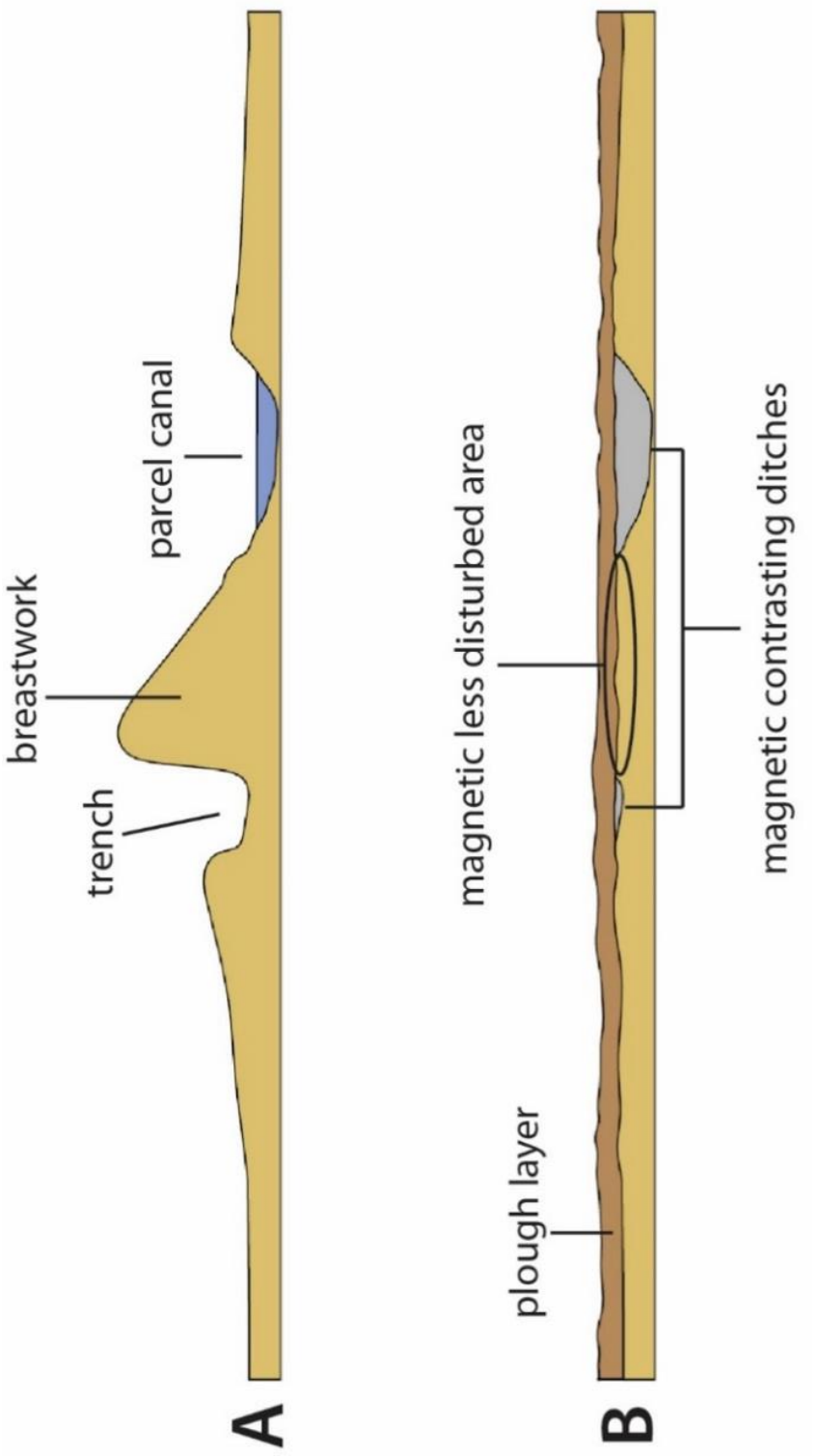



**Figure 7.15:** Schematic representation of preserved trench traces in the soil at the Oosthof site. Sketch (A) is the trench during the war while (B) refers to the current situation.

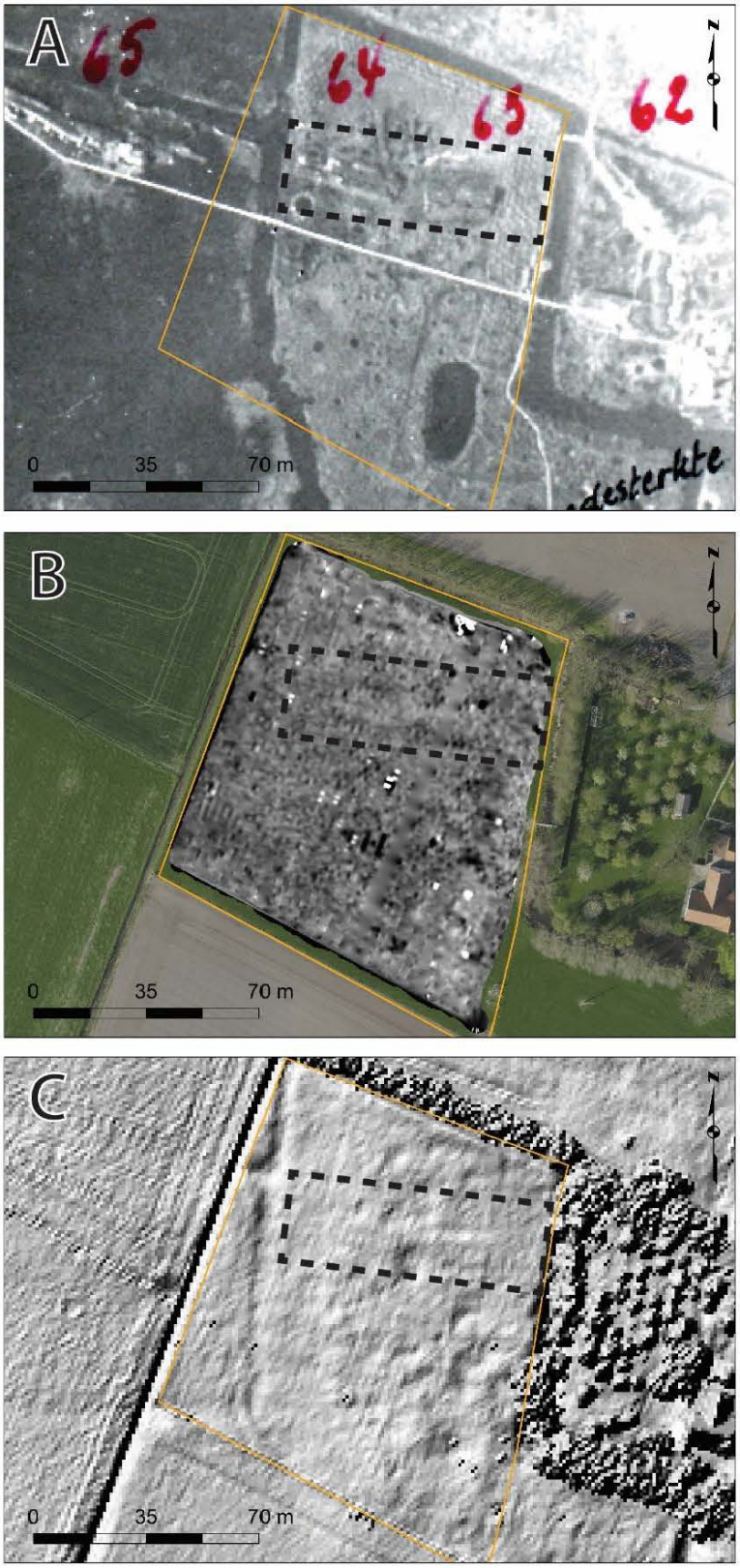



**Figure 7.16:** Comparison of results near Roedesterkte farm between a WW1 aerial photograph (A), a magnetic data layer (2HCP) from an EMI scan (B) and the current micro relief derived from a LIDAR scan (C). A slight signature of the firing trench on (A), can be found in the scan results from (B) and (C). (LIDAR and orthophoto: copyright AIV)

### *7.3.1.3 Scanned area between Rycken Hoek, Violette and Ter Stille farm (ID 5 & 9)*

In a first phase of war, several attacks were launched from Rycken Hoek by the Belgian first division to conquer the farms nearby (Ter Stille and Violette farm), occupied by the German army (Simoens, 2016). Approximately 12.5 ha near those farms were scanned during the summer of 2015 (ID 5 & 9), covering the military infrastructure in-between. These grounds contain frontline fortifications and no-man's-land (see figure 7.17). From the scan results, subtle magnetic traces were seen, related to gun emplacement (figure 7.18 B, field ID 9) and firing trench contours (figure 7.18 A field ID 5). The signatures of the detected WW1 features on photo and EMI-scan are displayed in figure 7.18. On field ID 5, 8.5% of the firing trench trajectories were detected by EMI. This low trace preservation could be linked to agricultural activities that are mainly arable field cultivation and some minor parts of pasture (images 1940 – 1958). On the photographs of 1971 until now, this field is classified as arable. No significant traces were seen on the LIDAR images. A second possible influence on the low traceability is the effect of inundation onto the military structures at this site.

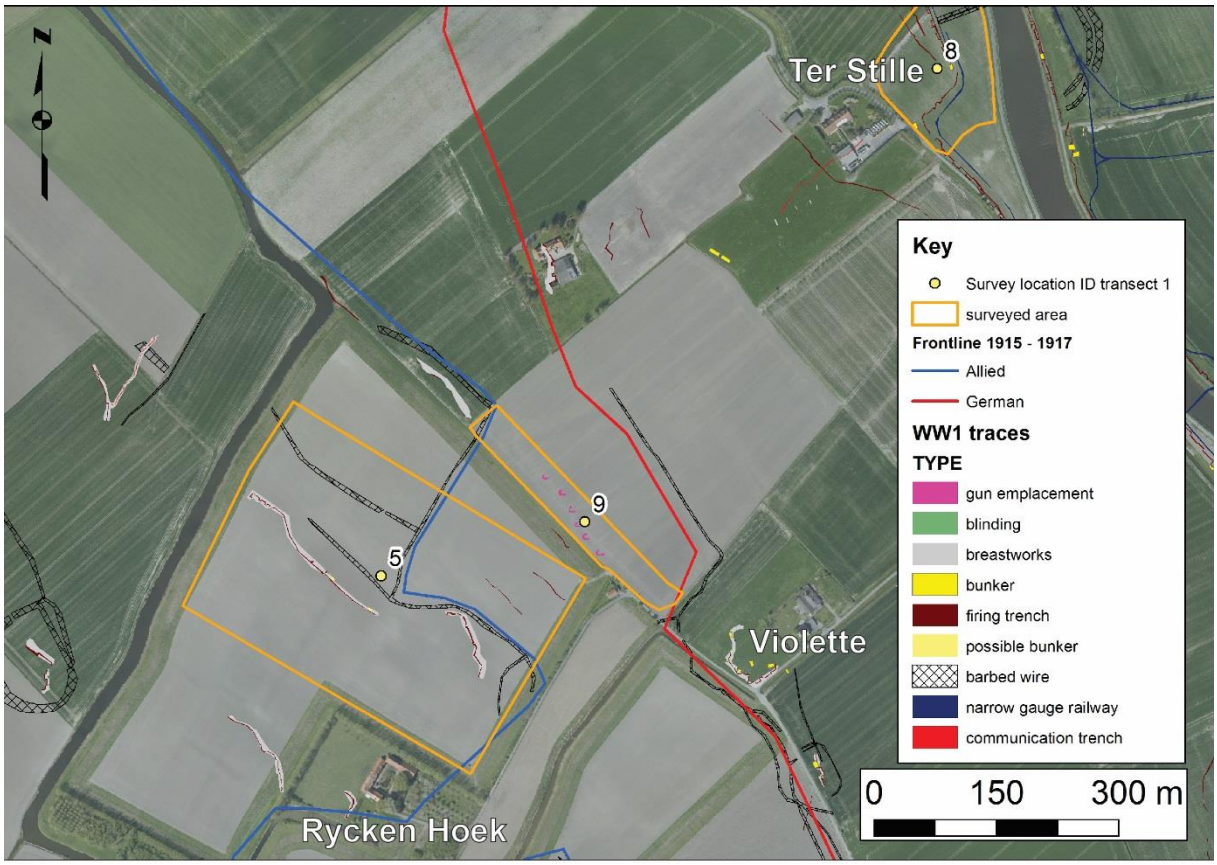



**Figure 7.17:** Localisation of Rycken Hoek, Violette and Ter Stille farm with respect to the surveyed fields. (orthophoto: copyright AIV)

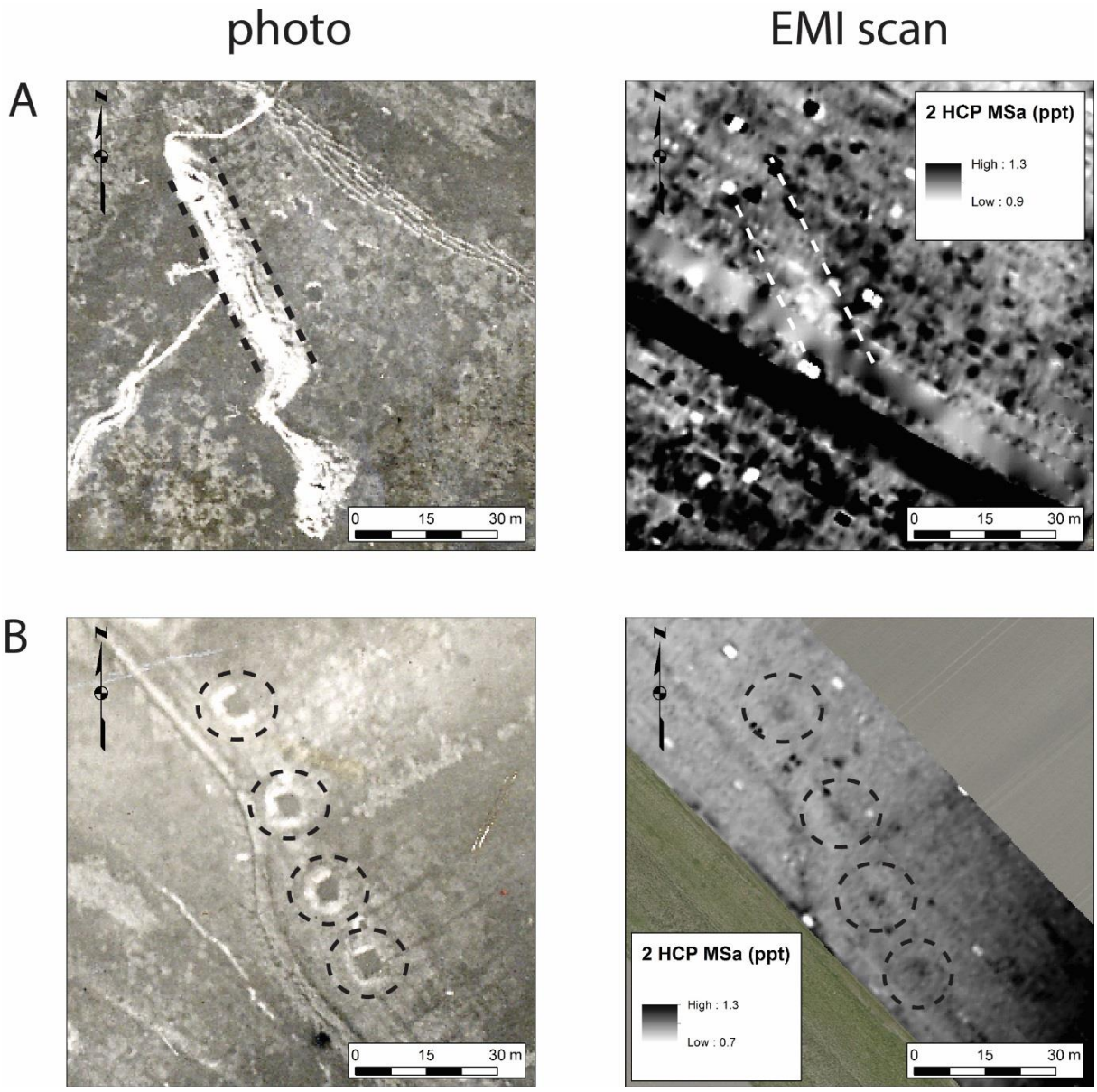



**Figure 7.18:** Visualisation of two types of remaining WW1 traces in the soil matrix near Rycken Hoek farm: (A) firing trench with breastworks, retraced by the subtle magnetic footprint of the breastwork coverage / (B) magnetic signatures of gun emplacements. (WW1 aerial photograph: KLM-RMA collection; orthophoto copyright AIV).

#### *7.3.1.4 Absence of identifiable traces in the soil: Farm B (ID 4) / Railway (ID 6) and Near Yser site (ID 8)*

At Farm B, the German forces converted the buildings into a stronghold with additional bunkers. This front post in the inundation was connected to the German first line by

passerelles[11]. In both shallow EC and MS responses of the scan results, contours of the former farm are still visible. On the field, brick fragments are present and in the scans, pre-war parcel canals are detected. Based on the combination of WW1 photography and EMI scan results, no clear distinction can be made between war and pre/post-war relicts. Only south-west in the scan-image, a linear trace appear in the magnetic data layer (figure 7.19). This trace could be related to an inundated trench but photograph interpretation was not able to identify this with great certainty. Because bunker remains are not present in the soil, the suspicion exists that the farm was reused after the war. The topographic maps from 1934 and 1949 confirmed this. Compared to destroyed farms around Wytschaete and Kemmel where the infrastructure is often rebuilt on a different spot close to the original farm, here it was reconstructed on the same location. This was done because of the higher position in the landscape to escape possible flooding. A low rate of destruction combined with long-term inundation during the war are additional supporting factors. On the aerial photographs of 1971, the farm buildings can be seen as broken down. Scan results and war-period photographs are shown in figure 7.19.

The railway site (ID 6) is located 600 m north of Chien Marin. During the war, a communication trench connected the firing trenches at the railway fortification with the firing trenches located 500 m behind this first line. After scanning the site with EMI, no recognisable traces were seen related to the communication trench. A scan result can be found in appendix 7.1.

A similar result was obtained for the 'Near Yser' site (ID 8), which is located between Ter Stille farm and the Yser river. Firing trenches and a narrow gauge railway were seen on the aerial photographs, located on the trajectory of a former road. The road traces were detected without clear indications of WW1 features. Contrary to the Farm B and Railway site, shelling traces were seen in both MS and EC data layers with massive metal objects on the shelling locations. This result could indicate that the clearance of the trench system was well done (reuse of road) except for the metal object removal in the area next to the road. A scan result of this site can be found in appendix 7.2.

[11] Passerelle: footbridge; during WW1 constructed in wood and used as connection infrastructure in flooded or muddy areas.




**Figure 7.19:** Visualisation of an aerial photograph taken on the 16th of July 1918 (KLM-RMA collection), indicating an outpost on the prospected field, containing three bunkers which are connected by passerelles to the German first line and nearby frontline posts. The second image visualises the magnetic scan results. In both images, a linear traces is marked by a dashed line. This is a possible WW1 trace. (orthophoto: copyright AIV)

#### *7.3.1.5 Hinterland site: German Aerodrome near Gistel (ID 10)*

The German army started in November 1914 with the construction of an airfield north of the city of Gistel (11 km from the frontline), near the Belgian coast (Deneckere, 1998; http://www.luchtvaarterfgoed.be, 2018). This airfield was given a misleading name: *Brieftaubenabteilung Ostende* (carrier pigeon unit Ostend) which was meant to fool the Allied forces and to camouflage the real intention of the airfield: bombing the United Kingdom from the sky (ginter.kindereninbezetgebied.be, 2018). At this site, importance was given to the

drainage of the airfield and wooden sheds were built to protect the airplanes (bombers) from gusts. This airfield, which was located west of the 'Zomerloos' farm, was partially scanned. The results show shallow magnetic traces of the aerodrome buildings, airstrip, drainage and military road. The only sharp identifiable structure in the scans are a power cable from the nearby windmills and one or more paleo gulls in the $EC_a$ data. An aerial photograph and a shallow $MS_a$ scan result are shown in figure 7.20 with indication of the detected WW1 traces.

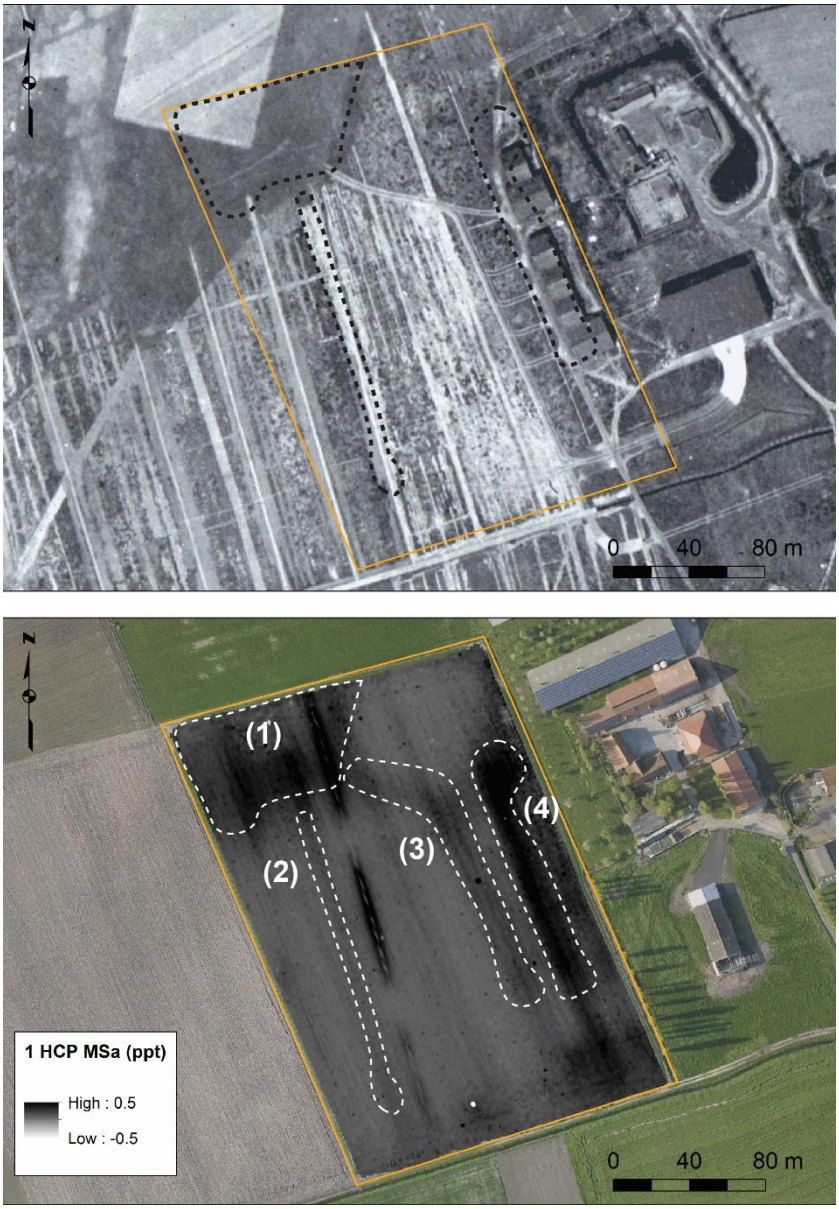



**Figure 7.20:** Visualisation of an aerial photograph taken on the 17th of May 1917 (KLM-RMA collection), indicating an aerodrome with hangars next to the 'Zomerloos' farm. On the 1HCP $MS_a$ scan result, magnetic traces of the airfield are found: (1) is a part of the (partially wooden) landing strip, (2) is a (drainage) track on the levelled extension of the airfield, (3) is a military road connecting the airplane sheds to the airstrip (not visible on photograph) and (4) relates to the plane hangars.

### *7.3.1.6 An overview of the Polder results*

The measurable proxy parameters of the scanned fields in transect 1 are shown in table 7.2 and 7.3. These indicate that limited linear traces were detected by EMI and LIDAR. This can be explained by the combination of a lower intensity of warfare and a less dense trench network compared to other sections of the front. In addition, this area contains more arable land (in which the first half metre of depth is cultivated) than other parts of the study area (transect 2 and 3). This influences the amount of detectable traces because the military infrastructure in those fields was situated mainly above ground and the traces at shallow depth are influenced by agricultural activities. The third factor is the effect of the inundation onto the front: this caused a situation where the need for a dense and strong fortified trench system was low. The inundation as natural defence barrier fluctuated in time which could also affect the maintenance of the military infrastructure, adjacent to the inundated areas.

Of all ten prospected sites in this transect, Chien Marin (ID 1) showed the best results: a high linear RSA feature density with more than 40% of those detected in the soil. The large breastworks ensured firing trenches to make a better chance to be detected than communication trenches (60% compared to 26% on this site, see table 7.2). This is because communication trenches could not be identified with large breastwork traces in the aerial photography. Elements that contributed to good detection results are the long state of pastureland (end of war until +/- 1970-80), an intense use of this fortified farm during the war, absence of inundation and probably a limited post-war clearance indicated by the presence of numerous shell craters with metal objects within. The nearby communication trench that is visible in the LIDAR data proves the importance of land use conditions on the grade of preservation. The field in which this structure is located, is since the end of war used as pastureland. Because there were many land use changes between pasture and arable land, not many features were detected by LIDAR in the transect 1 area. Most of the pastureland is nowadays converted into arable fields which are ploughed until the depth of 0.3 - 0.4 m (with an increased intensity and depth in the last few decades, < 1970's : 0.15 – 0.25 m). Most of the trenches built in these polder grounds are dug not much deeper than the current ploughing depth. That is why only subtle traces were detected by EMI and rarely LIDAR.

The best coil configuration to identify features in the EMI data is the 2HCP $MS_a$ data layer. This coil distance has a theoretical depth response for the magnetic signal between 0 – 0.8 m, which reaches sufficient beneath the plough layer, but not too deep to be averaged out by the

volume measurements. If land use is considered as an indicator, the field with the highest and only strong positive quotation (see table 7.5, Roedesterkte farm ID 7) is the only site containing subtle WW1 traces in the LIDAR data. The sites which were found in more than 50% of the post-war period aerial photograph time series as pasture (ID 1 & 7, see table 7.4), contained by EMI detectable traces. Three other sites with a long state of arable land, contained detectable features as well such as the Oosthof site that includes the most dominant traces, recorded by EMI. This is remarkable because this field was constantly in arable conditions since the end of war. This site has also the highest DR of all the sites (68.6%). These trenches were dug on locally higher grounds where the possibility exists to dig deeper than other lower locations (lower ground water levels and absence of inundation). Deeper dug trenches have a better chance to escape (partially) the ploughing activities. If the shelling densities are considered, Jokveld (ID 2), Chien Marin (ID 1) and the 'Near Yser' site (ID 8) were targeted the most. Those sites score in the middle / top range of the metal proxy indicators (see table 7.2) which points out the still existing connection between WW1 and the impact of metal object presence in the soil. Despites the lower intensity of warfare and the shallow effect of military infrastructure onto the soil in transect 1, important traces can still be found in the subsoil. Half of the scanned sites showed increased scores on the metal proxy parameters (see chapter 6), which could be linked to the effect of warfare.

**Table 7.2:** Detected feature lengths, expressed in percentage detected by EMI compared to RSA-data for each site. The grey-scale saturation is linked to the score of the parameter.

| ID & Name | Com. trench | Firing trench | Lin. density RSA (m/ha) | Detection rate | Extra |
|---|---|---|---|---|---|
| **1 Chien Marin farm** | 26.0% | 60.4% | 182 | 42.7% | 0.0% |
| **2 Jokveld farm** | 0.0% | 0.0% | 49 | 0.0% | 0.0% |
| **3 Oosthof farm** | - | 68.6% | 47 | 68.6% | 0.0% |
| **4 Farm B** | - | - | 0 | - | - |
| **5 Rycken Hoek farm** | - | 8.7% | 38 | 8.7% | 0.0% |
| **6 Railway** | 0.0% | 0.0% | 84 | 0.0% | 0.0% |
| **7 Roedesterkte farm** | - | 48.1% | 22 | 48.1% | 0.0% |
| **8 Near Yser** | 0.0% | 0.0% | 249 | 0.0% | 0.0% |
| **9 Frontline gun emplacements** | - | - | 0.0 | - | - |
| **10 Aerodrome** | - | - | - | - | - |

**Table 7.3:** Metal parameters and shelling densities expressed per hectare for each site.

| ID & Name | MOH/ha | % area metal | Sh.h/ha |
|---|---|---|---|
| 1 Chien Marin farm | 66.5 | 1.35% | 29.3 |
| 2 Jokveld farm | 84.9 | 1.34% | 27.8 |
| 3 Oosthof farm | 8.9 | 0.08% | 15.2 |
| 4 Farm B | 27.1 | 0.56% | - |
| 5 Rycken Hoek farm | 58.0 | 0.97% | 16.8 |
| 6 Railway | 102.6 | 1.11% | 5.8 |
| 7 Roedesterkte farm | 111.9 | 1.65% | 21.6 |
| 8 Near Yser | 80.5 | 1.84% | 38.0 |
| 9 Frontline gun emplacements | 62.2 | 0.57% | 12.6 |
| 10 Aerodrome | 8.1 | 1.11% | 0.0 |

**Table 7.4:** Time series of land use for each site (P = pasture / A = arable land).

| ID | Name | 1940-45 | 1971 | 1989-90 | 2000 | 2014-18 |
|---|---|---|---|---|---|---|
| 1 | Chien Marin farm | P | P | A | A | A |
| 2 | Jokveld farm | A & P | A | A | A | A |
| 3 | Oosthof farm | A | A | A | A | A |
| 4 | Farm B | A & P | A | A | A | A |
| 5 | Rycken Hoek | A & P | A | A | A | A |
| 6 | Railway | A | A | A | A | A |
| 7 | Roedesterkte farm | P | A & P | P | P | P |
| 8 | Near Yser | A | A | A | A | A |
| 9 | Frontline gun emplacements | A | A | A | A | A |
| 10 | Aerodrome | / | A | A | A | A |

**Table 7.5:** Definition of weights given to each type of land use, divided over two periods which represents a different grade of intensity (representing effect on preservation traces).

| Land use | 1940-1971 | 1989 - 2018 |
|---|---|---|
| A | 0 | -1 |
| P | 1 | 1 |
| A & P | 0.5 | 0 |

**Table 7.6:** In this table, weights are given to each period of land use verification. The sum of those weights gives a general quotation of land use. If WW1 features are detected by EMI of LIDAR, a grade of signature detection is given: clearly visible (++), subtle present (+) or absent (-).

| ID | Name | 1940-45 | 1971 | 1989-90 | 2000 | 2014-18 | Land use quotation | Features EMI | Features LIDAR |
|---|---|---|---|---|---|---|---|---|---|
| **1** | **Chien Marin farm** | 1 | 1 | -1 | -1 | -1 | -1 | ++ | - |
| **2** | **Jokveld farm** | 0 | 0 | -1 | -1 | -1 | -3 | - | - |
| **3** | **Oosthof farm** | 0 | 0 | -1 | -1 | -1 | -3 | ++ | - |
| **4** | **Farm B** | 0 | 0 | -1 | -1 | -1 | -3 | - | - |
| **5** | **Rycken Hoek** | 0 | 0 | -1 | -1 | -1 | -3 | + | - |
| **6** | **Railway** | 0 | 0 | -1 | -1 | -1 | -3 | - | - |
| **7** | **Roedesterkte farm** | 1 | 0.5 | 1 | 1 | 1 | 4.5 | + | + |
| **8** | **Near Yser** | 0 | 0 | -1 | -1 | -1 | -3 | - | - |
| **9** | **Frontline gun emplacements** | 0 | 0 | -1 | -1 | -1 | -3 | + | - |
| **10** | **Aerodrome** | - | 0 | -1 | -1 | -1 | - | - | - |

### 7.3.2 Transect 2: A section through the Ypres Salient

In the second transect, 13 sites were surveyed, mostly situated east of the city of Ypres near the frontlines (figure 7.21). Here, two soil conditions appear: (1) fine sand-loam top soil with underneath the thick layer of clay to the west of the Passendale ridge and (2) sands on top of the Westrozebeke ridge. Generally, the Bellewaarde ridge defines the boundary between the Ypres clay plain on one side and the dry sands on the other. In this transect, the Hill 62 site (ID 10), Clapham Junction (ID 11), Palingbeek (ID 2) and Black Watch Corner site (ID 13) are situated on the sandy ridge. All sites are visualised in figure 7.21. In total, 77.8 ha were surveyed. If the location of the scans are considered in relation to the front, one hinterland site (Vlamertinge, ID 1) was scanned, four large areas at the 1915-1917 front (Bellewaarde, Cambridge road, Hill 62 and Palingbeek) and one site near the front before the 2nd Battle of Ypres (Black Watch Corner, ID 13). A short evaluation containing highlights of these sites will be covered in this section.

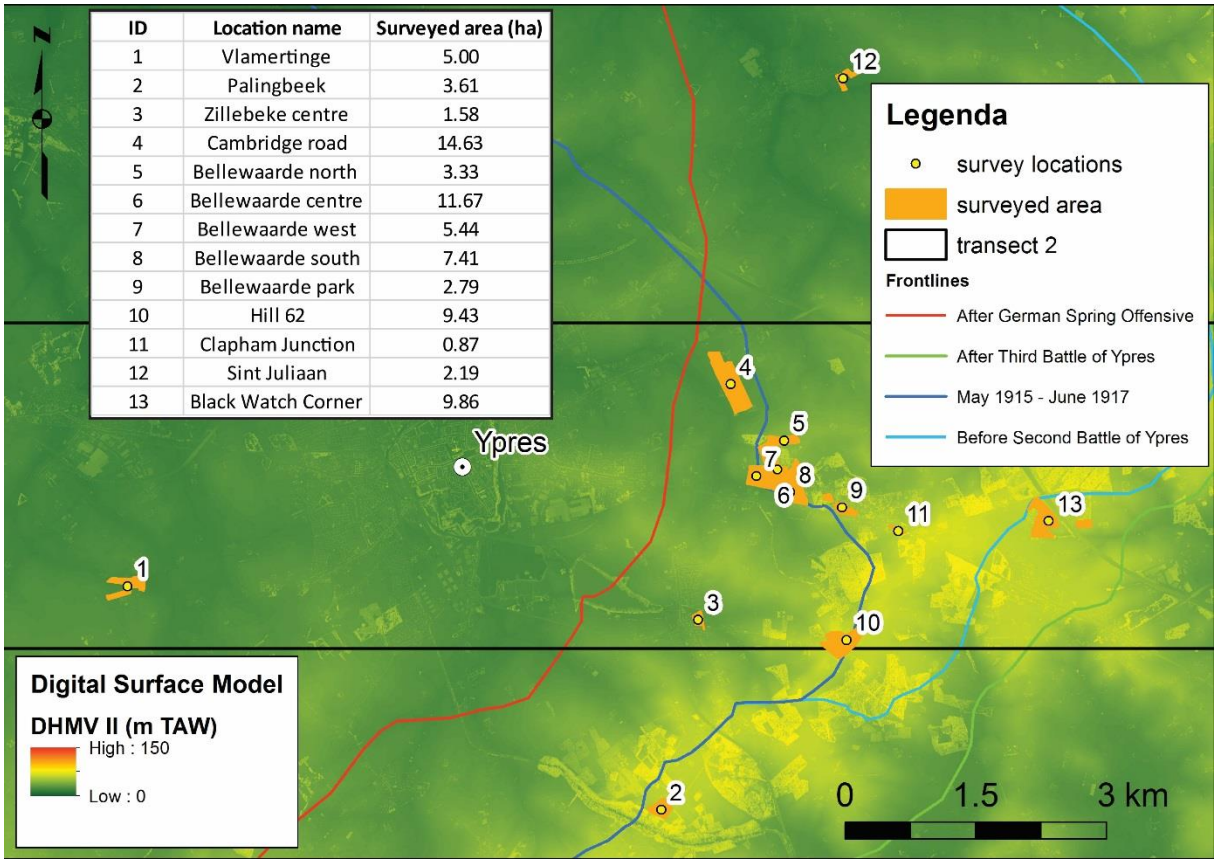



**Figure 7.21:** Overview of the surveyed sites according to the second transect zone. Each site has its own ID. As background image, the DHMV II is used (copyright AIV) to locate the Westrozebeke ridge.

### *7.3.2.1 Hinterland site: Vlamertinge (ID 1)*

The area around the 'De Roo Balie' farm in Vlamertinge was prospected in February-April 2018. A hundred years earlier, this site was occupied by Allied troops. At that moment, the farm consisted out of three buildings. After destruction during WW1, only the northern building was reconstructed. During the entire war, the site remained Allied territory and was located 3 to 12 km behind the front. This continuous hinterland position makes it easier to identify the coverage of WW1 structures (only one occupant, absence of dense shelling). On these unconquered sites, aerial photography is often sufficient to characterise the above ground visible military infrastructure. Besides the numerous barrack camp buildings, narrow-gauge railway tracks and trenches appear on the aerial photographs. The majority of this site is pastureland which is favourable for LIDAR to reveal some of the traces. In the northern part of the survey, a railway bed slightly appears while in the eastern area, hut contours show up in

the grassland. Both types of structures were found in the EMI data as well. Details of those structures on aerial photo and in the EMI data are shown in figure 7.22. Additional linear features - identified as cables - were found in the scan. Despite these results, no clear traces were found of trenches. Only a vague magnetic signature, supported by the integrated parcel borders as draining ditches, was identified as a firing trench (figure 7.22 C). Metal parameters and the density of linear features are the lowest compared to the values of the 2nd transect sites. These results were expected from this hinterland position.

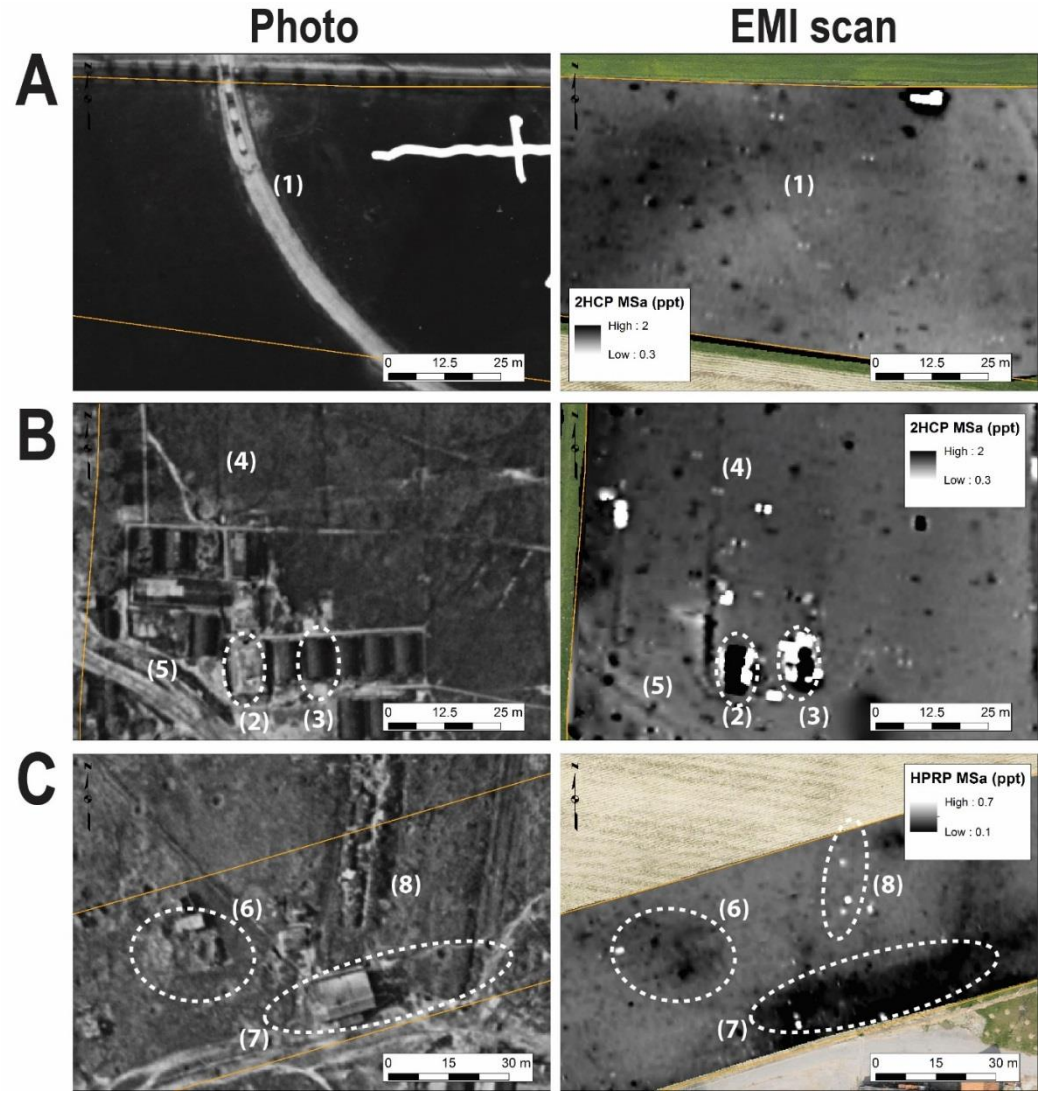



**Figure 7.22:** Detailed views of specific features within the Vlamertinge study area: (A) a narrow gauge-railway (with train on the aerial photograph); (B) huts (2 & 3) where drainage ditches (4) are visible on both datasets next to a narrow gauge-railway bed (5); (C) ploughed magnetic traces of barracks and buildings show up in the shallow magnetic data layers (6 & 7). In addition, borrow ditches around the firing trench (8) were detected (in $EC_a$ and $MS_a$) as linear anomalies and metal objects on the firing trench position. (WW1 aerial photograph: IWM collection; orthophoto: copyright AIV)

### *7.3.2.2 Bellewaarde Ridge (ID 4-9)*

The Bellewaarde Ridge area is known as one of the most contested sites in Belgium. At the beginning of the war, Bellewaarde was situated 3 km from the front. After the 2nd Battle of Ypres, the Ypres Salient shrank and the shifted front was now only 4 km away from the city centre near the heights of Bellewaarde. The ridge was the frontline for more than two years (May 1915 – July 1917). With an average rate of 300 casualties a day in this area for the commonwealth forces (www.ww1battlefields.co.uk, 2018), this was one of the most dangerous areas at the Western Front. On 31 July 1917, the opening day of the Third Battle of Ypres, the area was conquered and as the battle slowly proceeded towards Passchendaele, it became British back area until the German forces reconquered the ridge in April 1918 (German Spring Offensive). South of the prospected Bellewaarde site (figure 7.23), the Menin road intersects the frontline from west to east. At this intersection, the small hamlet of 'Hooghe' was situated. Characteristic for this area are the underground tunnelling activities and the mine explosions. Georeferenced tunnelling maps indicate a dense network of tunnels below the Bellewaarde site (Dewilde et al., 2014; Stichelbaut et al., 2016). These tunnels were used to set up explosive charges under the enemy lines or to use them as shelter (deep dugout) or listening posts. Its strategic lookout position towards Ypres was the main reason for these fights. For example, in the spring of 1917, dozens of mine explosions took place around the Bellewaarde farm. This complete destroyed landscape makes it difficult to characterise and interpret the detected WW1 features. The crater wood just south of the Bellewaarde north site is one of the best-preserved relicts related to the shelling and mine explosions (Dewilde et al., 2014). After the 3rd Battle of Ypres, warfare by using dense networks of trenches and tunnels was abandoned in this area whereby parts of those systems were reused to convert them into strongpoints (Dewilde et al., 2014). Based on the aerial imagery, this site is probably one of the most dense trench networks at the Western Front in Belgium (>500 m/ha).

The EMI surveys performed at this site are divided in 5 sub-areas near the Bellewaarde lake (figure 7.23) and one site north of these five adjacent fields (Cambridge road site, ID 4). The first one to discuss is Bellewaarde north site (ID 5), located north of the crater wood (figure 7.23). The state of this terrain is pastureland during the post-war period. This site scores the highest on DR for the Bellewaarde sites (26%) together with the Bellewaarde park site (ID 9, DR 25%). At Bellewaarde north, trenches and mine craters appear next to the late-medieval

moat ditch of the farm in the scan results. If looked at the 1HCP $EC_a$ data layer, two well delineated area's contain shallow metal objects (0 – 0.40 m range, strong negative peaks) while the rest of this site does contain almost none of these shallow objects (figure 7.24 E). Selective soil clearance in combination with dumps in mine craters is a plausible explanation. Dewilde et al. (2014) mentioned that there was no ground clearance directly after the war. In that area, some of the detected trenches were archaeological investigated in 2010-11 and were despite the great devastation, found in excellent preserved conditions (Dewilde et al., 2014).

The soil at Bellewaarde park site (ID 9) was covered since the 1970-80's with a layer of gravel and used as parking space for the amusement park 'Bellewaerde'. This situation protected the subsoil from agricultural activities, weathering and erosion. At the other three Bellewaarde zones: Bellewaarde centre (ID 6), Bellewaarde west (ID 7) and Bellewaarde south (ID 8), trenches are more difficult to identify. Intensive land cultivation (arable conditions) in combination with the high rate of destruction by shelling made it difficult to clearly identify linear features such as trenches. The shallow $EC_a$ data layers (1PRP $EC_a$) do not contain sharply delineable crater disturbances. Unlike other heavily destroyed areas, the metal parameters score average for the front area (MOH/ha: 170-240; 4.8-6.4% area FEMP) except for the Bellewaarde park site (ID 9) where the operation of the amusement park had an influence on near surface metal objects. On one hand, the low scoring average values for the metal parameters for the Bellewaarde sites with agricultural function is remarkable but on the other, harvest and ploughing activities took place on the majority of the scanned area. The suspicion of post-war ground clearance actions is a track for further investigation. This is a second plausible reason for the lower scores.

On the Bellewaarde park site where Hooghe castle was built (and destroyed during the war), high conductive and magnetic traces were found on the former building location. Some additional regular linear traces similar to the contours corresponding to the formal castle park layout (derived from the Ferraris Maps, 1777) appear as well (in $EC_a$ and $MS_a$). This is a clear indication that the WW1 battles on heavy contested locations did not always destroy all of the subsoil archaeological elements. These former park-contours were detected on grounds with a post-war castle park function. This kind of land use possibly contributed to the find of this structure (=better preserving conditions).

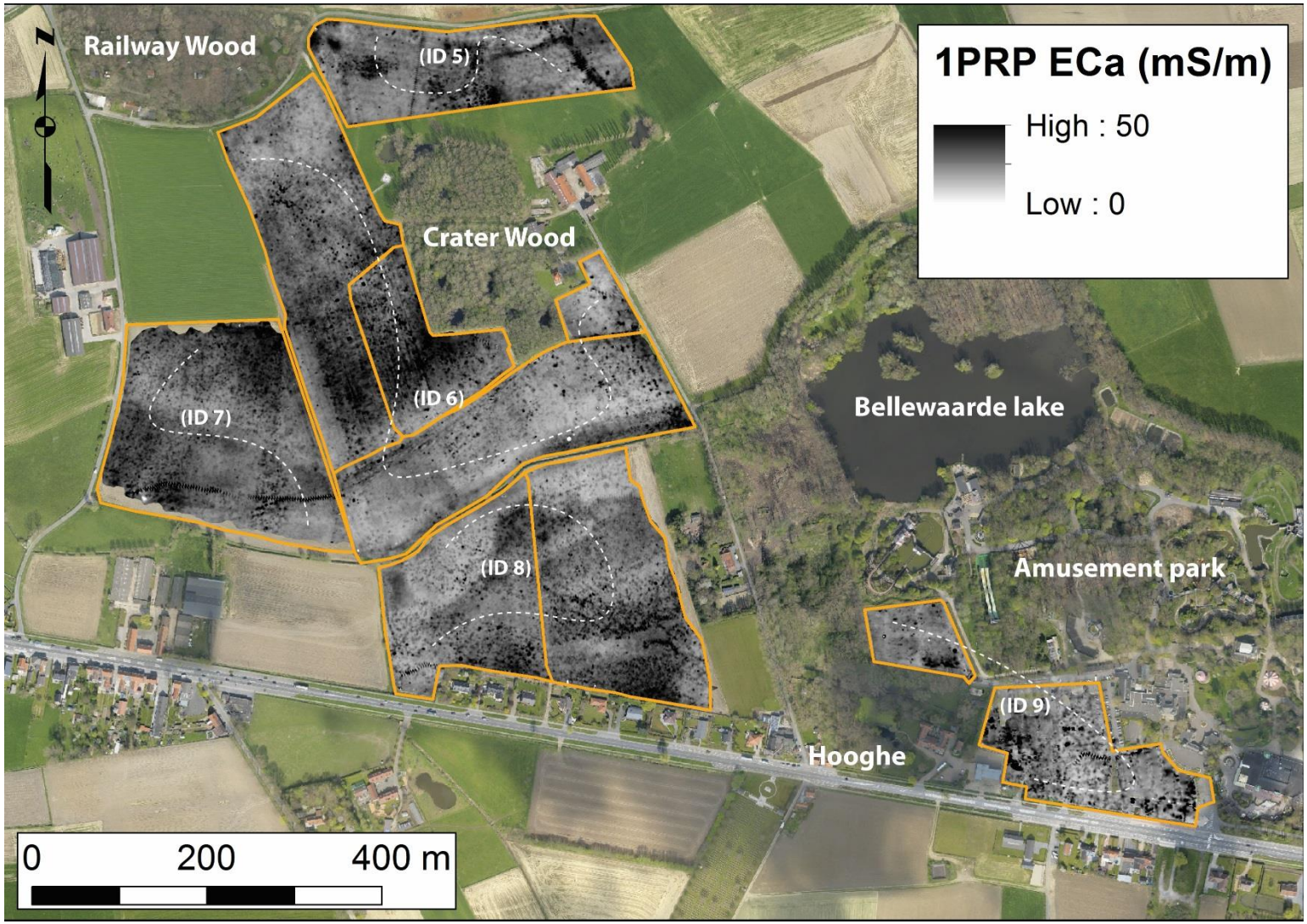



**Figure 7.23:** Overview of the Bellewaarde survey with the subdivision of the different areas: Bellewaarde north (ID 5), Bellewaarde centre (ID 6), Bellewaarde west (ID 7), Bellewaarde south (ID 8) and Bellewaarde park (ID 9). The white dashed lines cover the scanned fields related to the nearby corresponding ID number.

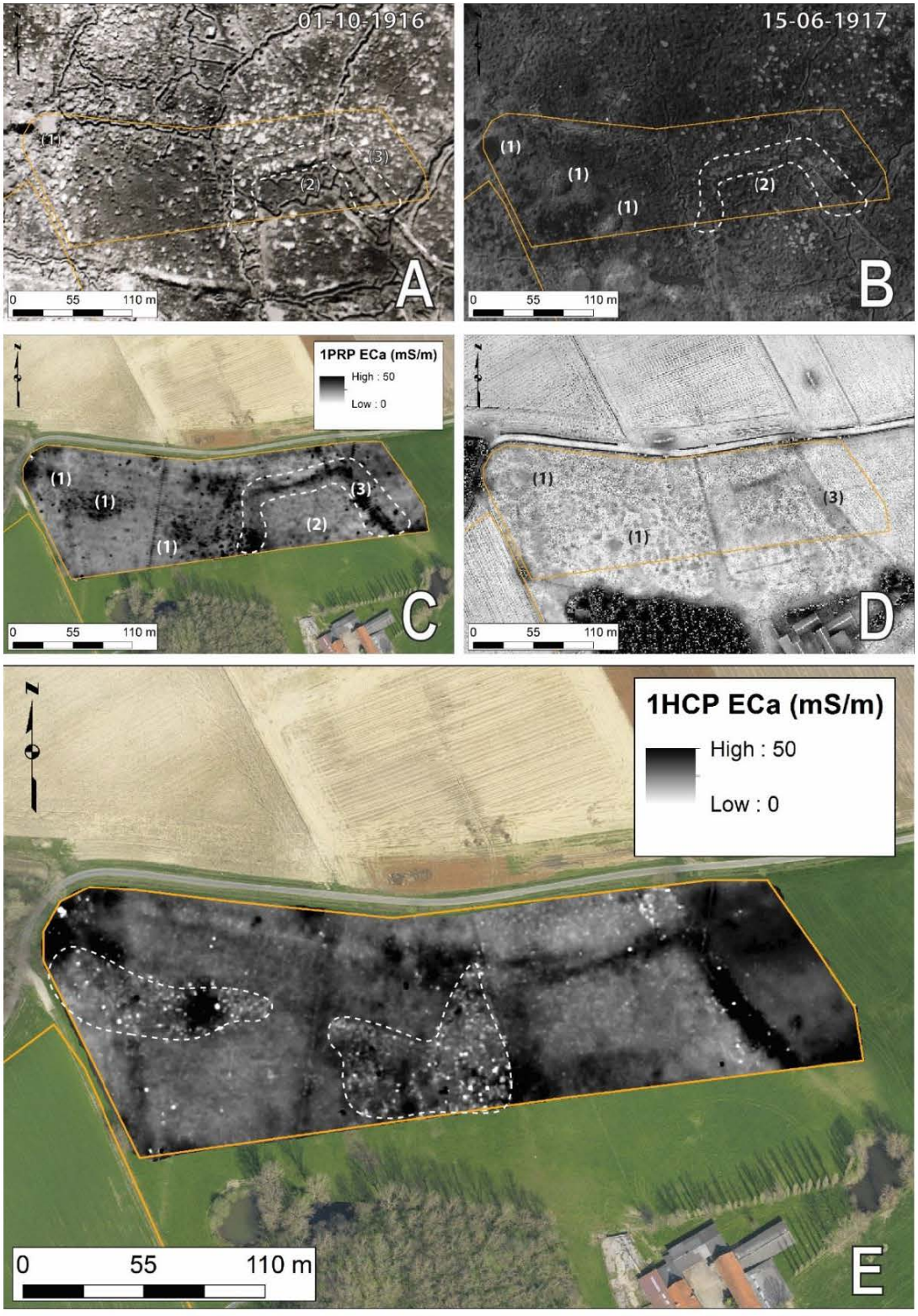



**Figure 7.24:** Detailed multi data source view of the Bellewaarde north area. (A) and (B) are aerial photographs dating from October 1916 and June 1917 (A: AWM collection; B: IWM collection); (C) is the 1PRP $EC_a$ data layer; (D) is the micro topography derived from the DHMVII (copyright AIV) and (E) the 1HCP $EC_a$ data layer. Some WW1 elements are pointed out on these images: (1) are exploded mine craters; (2) are communication trenches and (3) is the ditch around the farm moat. On image E, two zones with high concentrations of shallow metal objects (0-0.4m; 1HCP $EC_a$ strong negative peaks) are defined.

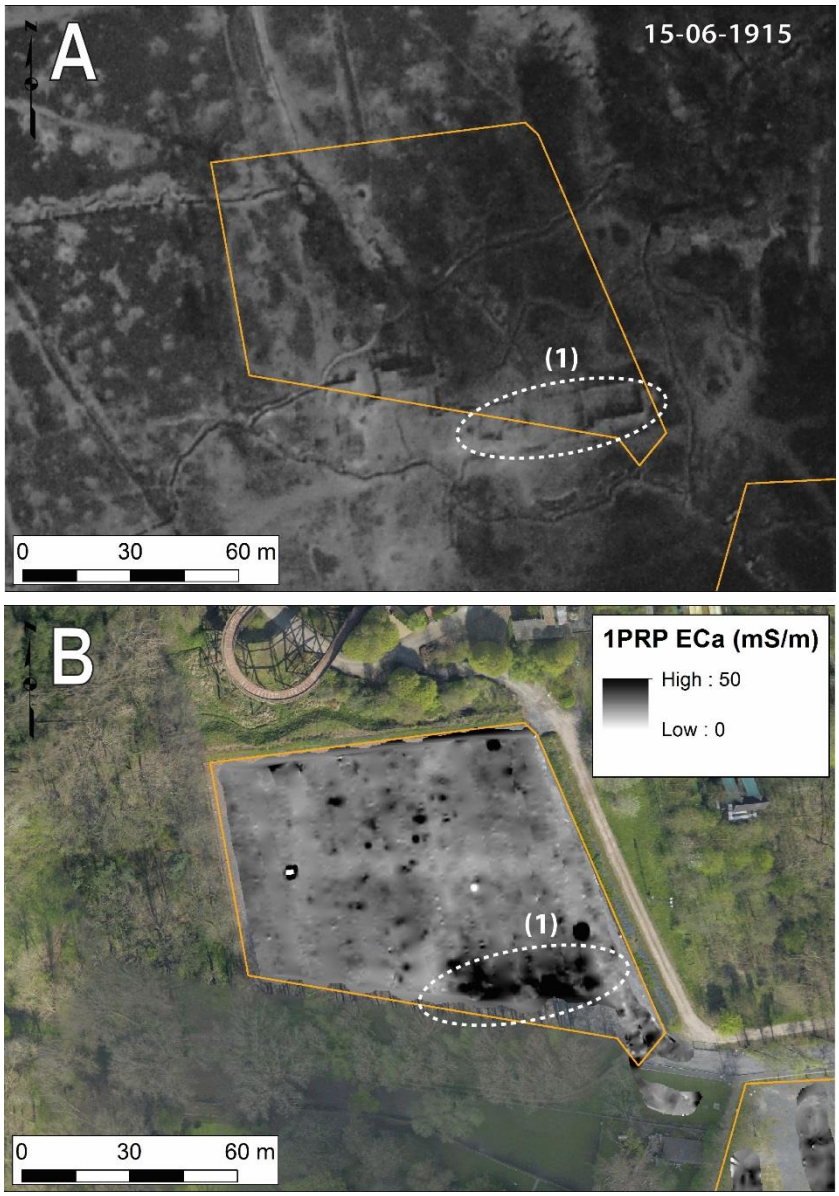



**Figure 7.25:** Detailed image of the western area of the surveyed parking space of the Bellewaerde amusement park. On the 1915 aerial photograph (A) (IWM collection), the ruins of the Hooghe castle are still visible (1). Anomalies corresponding with this building were found in the EMI scan (B). Next to the castle remains, contours of the ornamental garden (low-conductive cross-shape) were detected.

Cambridge road site (ID 4) is located 0.5 km north-west of the Bellewaarde site. It is one of the most densely trenched areas, together with Bellewaarde and Hill 62. It mostly covers the Allied lines of 1915-17. It has a similar DR like the Bellewaarde north and south site (27%) but remarkable are the even lower scoring metal parameters: 2.3% area FEMP and 134 MOH/ha. The constant post-war arable conditions had an effect on the lower metal finds on this site but probably ground levelling and clearing actions took place. The landowner explained that wet areas were raised. This is a possible third cause of the low scoring metal parameters. These raised areas correspond with the two highly magnetic and electrical conductive areas in figure 7.26. These high $EC_a$ zones make it hard to distinguish WW1 features because of the

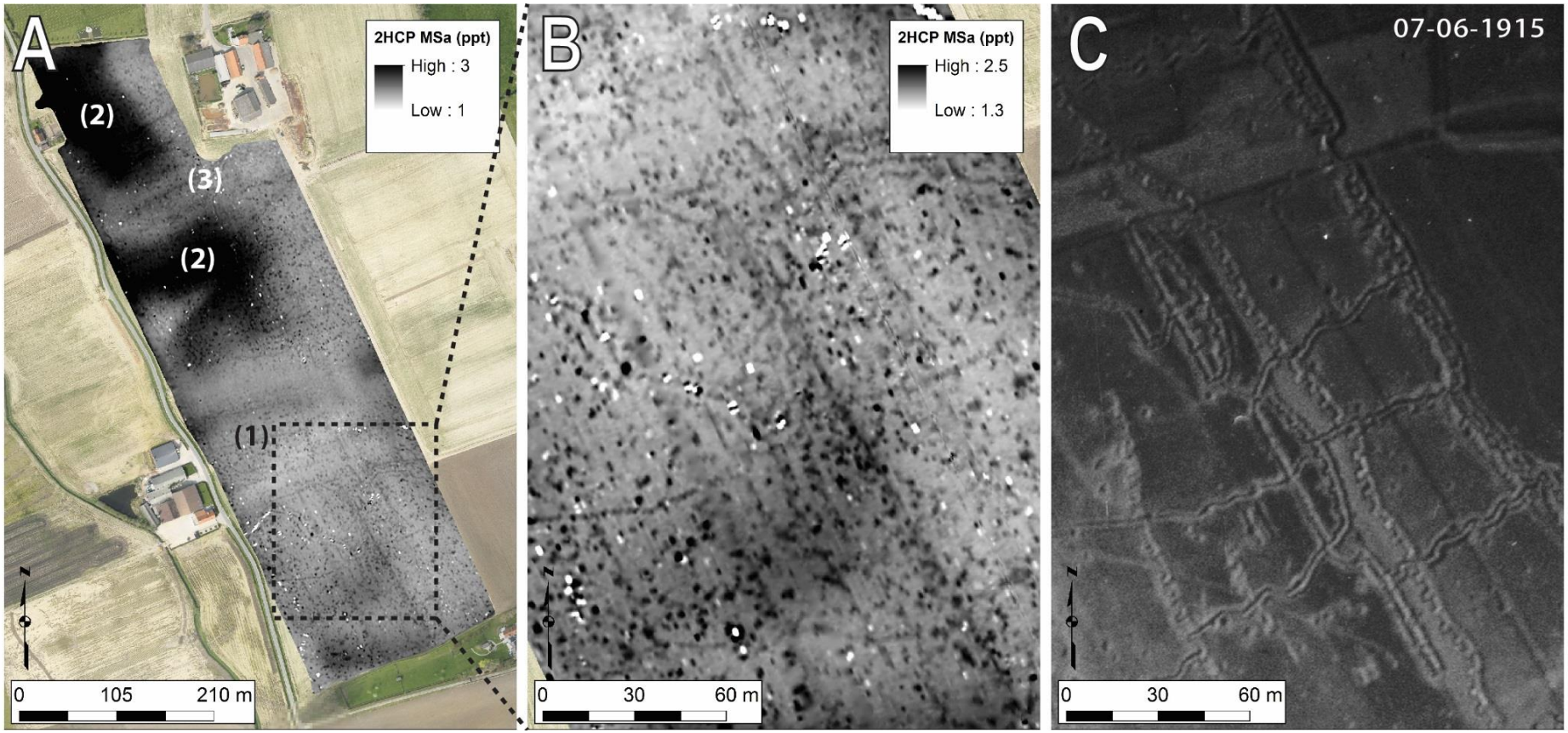



**Figure 7.26:** Overview and detail from the Cambridge road site. (A) Shows the overview image of the 2HCP $MS_a$ data layer. (1) Represents the detail box that refers to the detailed view in image B of the 2HCP $MS_a$ data layer and the 1915 aerial photograph (C) (IWM collection). (2) are two area's with a high magnetic and electrical conductive background in which WW1 feature identification is difficult. (3) are digging traces originating from soil drainage tubes. (orthophoto: copyright AIV)

absence of contrasts between feature and background. The higher background values are caused by the tertiary clay which is near surface (derived from the Belgian soil map, DOV). Based on the scan, clay depth can be estimated at 0.3-0.6 m. These grounds have the property to be water logging (reason to raise surface). Recently placed drainage tubes are visible in the scan, which are located near the high scoring $EC_a$ and $MS_a$ zones. The near surface clay (slightly magnetic and high $EC_a$) in combination with the increased moisture content (influence on $EC_a$) make the background values of $EC_a$ an $MS_a$ to be high. Therefore, most of the WW1 features were identified in the southern half of the survey. By locally adjusting the greyscale limits, traces can be identified.

#### *7.3.2.3 Hill 62: a heavily contested site (ID 10)*

This site was the scene of heavy fighting because of its strategic view towards Ypres. It is also known as a mining and tunnelling hotspot (see chapter 5). In October-November 2016, the grasslands and pasture grounds southeast of the Hill 62 Sanctuary Wood Canadian memorial were scanned. Based on the high quality of the WW1 features in the scan images, Hill 62 can be considered as one of the best examples to demonstrate the potential of EMI research on WW1 battlegrounds. Figure 7.27 displays the shallow soil disturbances (1PRP $EC_a$): trenches and shell crates can be found in the best detectable conditions. Also three mine craters (diameter: 5 - 10 m) appear from north to south, central in the image. The soil conditions (sand-loam-clay along the depth profile causing contrasts in $EC_a$) in combination with land use conditions (mainly pasture-grassland) are the main determining factors of the preservation conditions of the site and the possibility to detect these soil disturbances. Because of the 'heavy soil' (clay rich), farmers kept these areas more than others in grassland conditions. Another characteristic is that groundwater is not found in the top few metres (confirmed by 5 m deep augerings). The above ground military infrastructure and shell holes were probably quickly filled up after the war and no clear indications were found of ground cleaning actions. Despite the high grade of destruction and the dense network of linear features (480m/ha), a DR of 43% was achieved. This is the highest number obtained at a frontline site with a dense network of trenches. The immense high values for the metal parameters (318 MOH/ha, 11.5% area FEMP) indicate dense shelling and probably untouched subsoil. These shell crater and metal properties are one indicator of many to predict the quality of preserved archaeological

finds. If these proxies are at the level of expectation (according to the intensity of warfare, see chapter 6), this can indicate that post-war activities had a limited effect onto the situation of the subsoil.

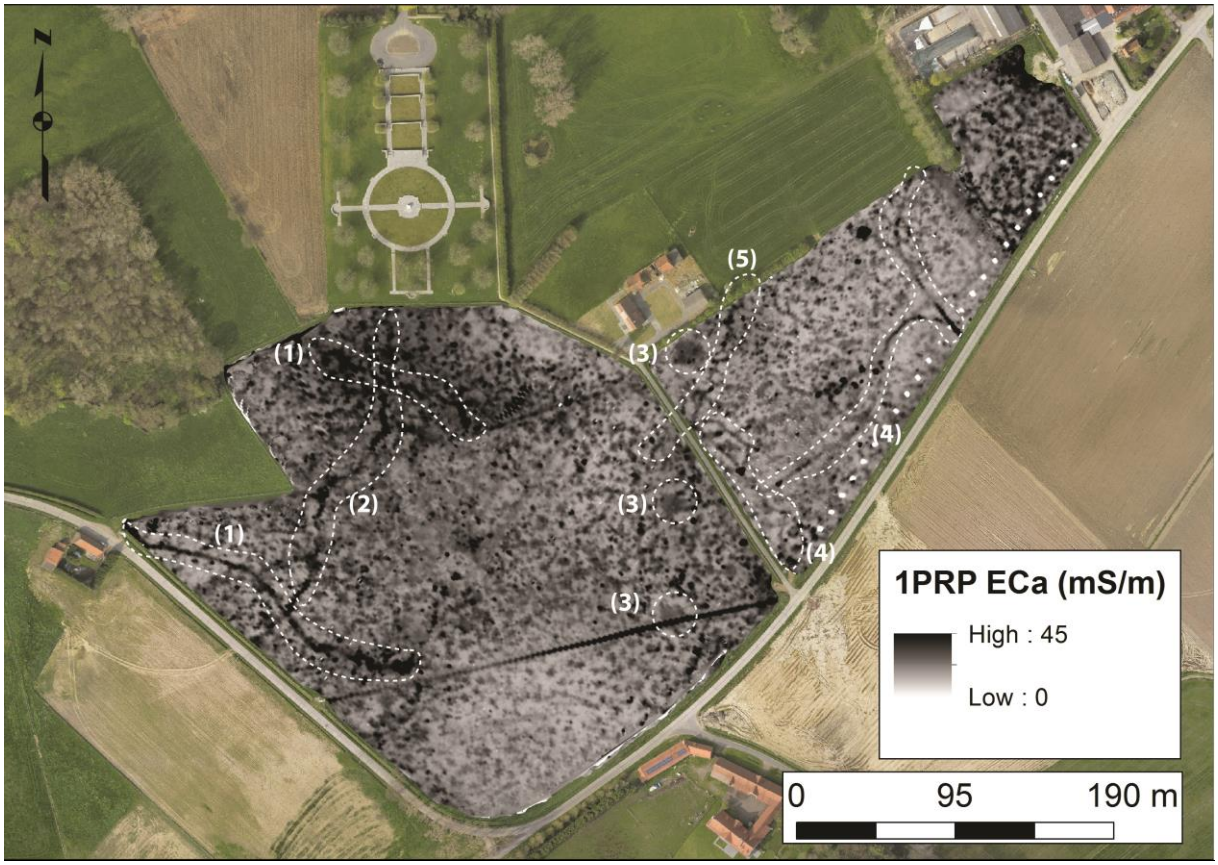



**Figure 7.27:** Overview of the Hill 62 survey, by displaying the 1PRP $EC_a$ data layer. North of the site, the Canadian memorial 'Sanctuary Wood' is located. Dominant traces of detected military infrastructure within the study area are indicated with dashed lines and an identification number. (1) are British communication trenches; (2) British firing trenches; (3) exploded mines, dug by the British from their side of the frontline under the frontline trenches of the German army; (4) German communication trenches; (5) German firing trench. (orthophoto: copyright AIV)

### *7.3.2.4 Black Watch Corner, on top of the Westrozebeke ridge (ID 13)*

The 10 ha 'Black Watch Corner**'** site is situated on top of the Westrozebeke ridge where the dry Eocene sands and clays appear. The surveyed area is found south of Polygon Wood near the A19 highway. The site's name was derived from the Black Watch Battalion, a part of the British army which was active in the area. Before the 2nd battle of Ypres, the frontline reached this site which was at that time in German hands. In November 1915, the site became German

2nd line and after the 3rd Battle of Ypres, it was near the front again (500 m after frontline). Some of the trenches, communication cables, a bunker and shell craters were found by the scans (figure 7.28). This site was originally selected to validate if early 1914 trenches can be found. This was the case and displayed in figure 7.28 (2).

At this site, the difference between areas which were levelled and cleared from metal objects (by land cleaning actions or agricultural practices) on one hand, and areas with well-preserved shell craters on the other hand, are clearly visible as rectangular patterns in the 1 PRP $EC_a$ layer. An example is given in figure 7.28 by (4) and (5). The identified WW1 feature signatures were mainly found in the areas with preservation of shallow shell crater traces. The absence of metal objects in the first 1 m of depth is noticed in those 'cleaner' areas. Despites these current field conditions, metal parameters of 210 MOH/ha and 6.4% area FEMP were derived. A DR of 19% was found, which is close to the average value of the transect.

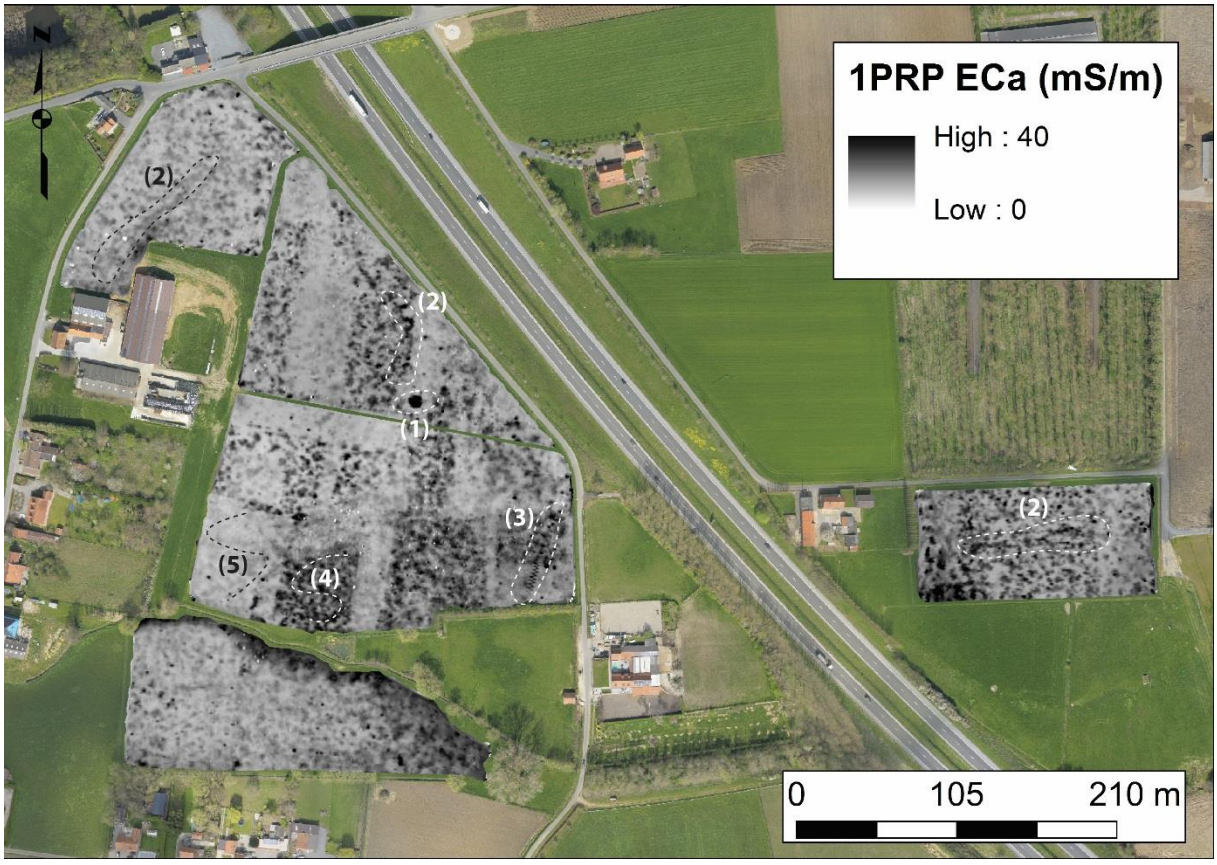



**Figure 7.28:** Overview of the Black Watch Corner survey by the 1PRP $EC_a$ data layer. (1) indicates concrete remains of a destroyed bunker; (2) are three clearly detectable trenches; (3) is a communication cable leading to the former farm location which is situated just above number '3'; (4) is an area with strong detectable shell craters and near surface metal objects; (5) is an area without identifiable metal objects in the first 1m of soil and weaker detectable shell craters. (orthophoto: copyright AIV)

#### *7.3.2.5 Other sites: Palingbeek, Sint-Juliaan and Clapham Junction*

The Palingbeek (ID 2) site is located on top of the Westrozebeke ridge, 3 km south-west of Hill 62. It is located near the frontline related to the period between the 2nd and 3rd Battle of Ypres. Based on the 2nd transect values, this site scores average on DR (23%). The metal parameters are relatively high: 10.7% area FEMP and 274 MOH/ha. Based on the land use scoring scheme, it scores a positive value which can explain the high scoring metal parameters, typical for this part of the front. The 1PRP $EC_a$ data layer indicates good preserved shallow shell crater traces. This scan result can be found in appendix 7.3.

The Sint-Juliaan (ID 12) and Clapham Junction (ID 11) sites were surveyed in order to validate if traces of tanks can be found with EMI scans. This is displayed and discussed in chapter 5. Therefore, no results are shown in this chapter. The derived scan parameters can be found in table 7.7-7.11.

#### *7.3.2.6 Summary of the 2nd transect results*

- Most of the sites were surveyed at the 1915-17 frontline (8 out of 13). At those locations, an average linear feature density based on aerial photography of 504 m/ha was found. This high number indicates the importance of these sites which cannot be disconnected from a high rate of destruction and contesting: the dense military trench network is related to intense warfare over a longer period. The immense devastation makes it difficult to identify WW1 features because the signature of those elements is often hard to distinguish. In these areas, aerial photography is necessary for feature identification in the soil scans. This was mainly the case for the Bellewaarde battlegrounds. These battlefields were the most photographed to map the almost monthly changing situation (several small frontline shifts).
- Metal parameters and the quality of preserved shell craters in first half to one metre deep give an indication how ground clearing actions and agricultural activities influenced the conditions of the topsoil where WW1 features are partially located. Absence of metal objects or lower quantities as expected could indicate the anthropogenic post-war influence. This was the case for the Bellewaarde, Cambridge road and Black Watch Corner

sites. On the opposite, the well-preserved and detectable craters at Hill 62 in the first half metre of soil were found together with a high rate of complete trench signatures.

- The near surface heavy clay deposits are often an obstacle for farmers to turn these sites into arable land and to cultivate them with ease (ploughing). These 'heavy grounds' protect the buried infrastructure from mechanical damage. Pasture or grassland are often the chosen options in this mainly agricultural region. The 'heavy grounds' is probably one of the reasons why the DR at Hill 62 is higher than on other similar sites. The DOV-database confirms that the dryer sand-loam-clay conditions of the soil are more ideal for pasture or grassland.
- Despites the destructive effect of war at Bellewaarde, former ornamental garden contours could be detected from the Bellewaarde castle (Hooghe).

**Table 7.7:** Detected feature lengths, expressed in percentage detected by EMI compared to RSA-data for each site

| ID | Name | Com. trench | Firing trench | Lin. density RSA (m/ha) | Detection Rate | extra |
|---|---|---|---|---|---|---|
| 1 | Vlamertinge | 0.0% | 21.7% | 54 | 43.7% | 67.7% |
| 2 | Palingbeek | 20.6% | 22.9% | 509 | 23.6% | 2.2% |
| 3 | Zillebeke centre | - | 0.0% | 49 | 0.0% | 246.7% |
| 4 | Cambridge road | 38.5% | 13.1% | 575 | 27.4% | 3.0% |
| 5 | Bellewaarde north | 32.5% | 15.7% | 430 | 26.0% | 6.8% |
| 6 | Bellewaarde centre | 5.3% | 8.7% | 551 | 6.7% | 8.0% |
| 7 | Bellewaarde west | 15.4% | 30.9% | 568 | 19.3% | 12.0% |
| 8 | Bellewaarde south | 20.5% | 27.9% | 329 | 25.3% | 12.4% |
| 9 | Bellewaarde park | 9.8% | 30.5% | 446 | 21.2% | 27.4% |
| 10 | Hill 62 | 43.3% | 42.4% | 480 | 42.8% | 11.7% |
| 11 | Clapham Junction | 0.0% | 0.0% | 95 | 0.0% | 0.0% |
| 12 | Sint-Juliaan | 0.0% | 0.0% | 212 | 0.0% | 13.9% |
| 13 | Black Watch Corner | 20.0% | 15.2% | 242 | 19.1% | 2.9% |

**Table 7.8:** Metal parameters (MOH/ha and % area FEMP) expressed per hectare for each site

| ID | Name | MOH/ha | % area metal | Sh.h/ha |
|---|---|---|---|---|
| 1 | Vlamertinge | 86 | 1.8% | 59 |
| 2 | Palingbeek | 274 | 10.7% | 425 |
| 3 | Zillebeke centre | 162 | 4.0% | 227 |
| 4 | Cambridge road | 134 | 2.3% | 168 |
| 5 | Bellewaarde north | 172 | 6.0% | 404 |
| 6 | Bellewaarde centre | 224 | 4.8% | 262 |
| 7 | Bellewaarde west | 192 | 5.5% | 317 |
| 8 | Bellewaarde south | 234 | 6.4% | 362 |
| 9 | Bellewaarde park | 374 | 16.5% | 448 |
| 10 | Hill 62 | 318 | 11.5% | 267 |
| 11 | Clapham Junction | 274 | 7.2% | 431 |
| 12 | Sint Juliaan | 156 | 3.9% | 329 |
| 13 | Black Watch Corner | 210 | 6.4% | 340 |

**Table 7.9:** Time series of land use for each site (P = pasture or grassland / A = arable land/ G = gravel, Park = castle/amusement park)

| ID | Name | 1940 | 1971 | 1989-90 | 2000 | 2014-18 |
|---|---|---|---|---|---|---|
| 1 | Vlamertinge | NA | A & P | A & P | A & P | A & P |
| 2 | Palingbeek | NA | A & P | A & P | A & P | P |
| 3 | Zillebeke centre | A | A | A | A | A |
| 4 | Cambridge road | A & P | A | A | A | A |
| 5 | Bellewaarde north | P | A & P | P | P | P |
| 6 | Bellewaarde centre | A | A | A | A | A |
| 7 | Bellewaarde west | A | A | A | A | A |
| 8 | Bellewaarde south | A | A | A | A | A |
| 9 | Bellewaarde park | Park | Park & A | Park & G | G | G |
| 10 | Hill 62 | A & P | A | A & P | A | P |
| 11 | Clapham Junction | P | P | A | P | P |
| 12 | Sint Juliaan | NA | A | A & P | A & P | P |
| 13 | Black Watch Corner | A & P | A & P | A & P | A & P | P |

**Table 7.10:** Definition of weights given to each type of land use, divided over two periods which represents a different grade of intensity representing the effect on preservation of traces (P = pasture / A = arable land/ G = gravel, Park = castle/amusement park).

| Land use | 1940-1971 | 1989 - 2018 |
|---|---|---|
| **A** | 0 | -1 |
| **P** | 1 | 1 |
| **Park** | 1 | 1 |
| **A & P** | 0.5 | 0 |
| **Park & A** | 0.5 | 0.5 |
| **G** | 1 | 1 |
| **Park & G** | 1 | 1 |

**Table 7.11:** In this table, weights are given to each period of land use verification. The sum of those weights gives a general quotation of land use. If WW1 features are detected by EMI of LIDAR, a grade of signature detection is given: present (+/++) or absent (-).

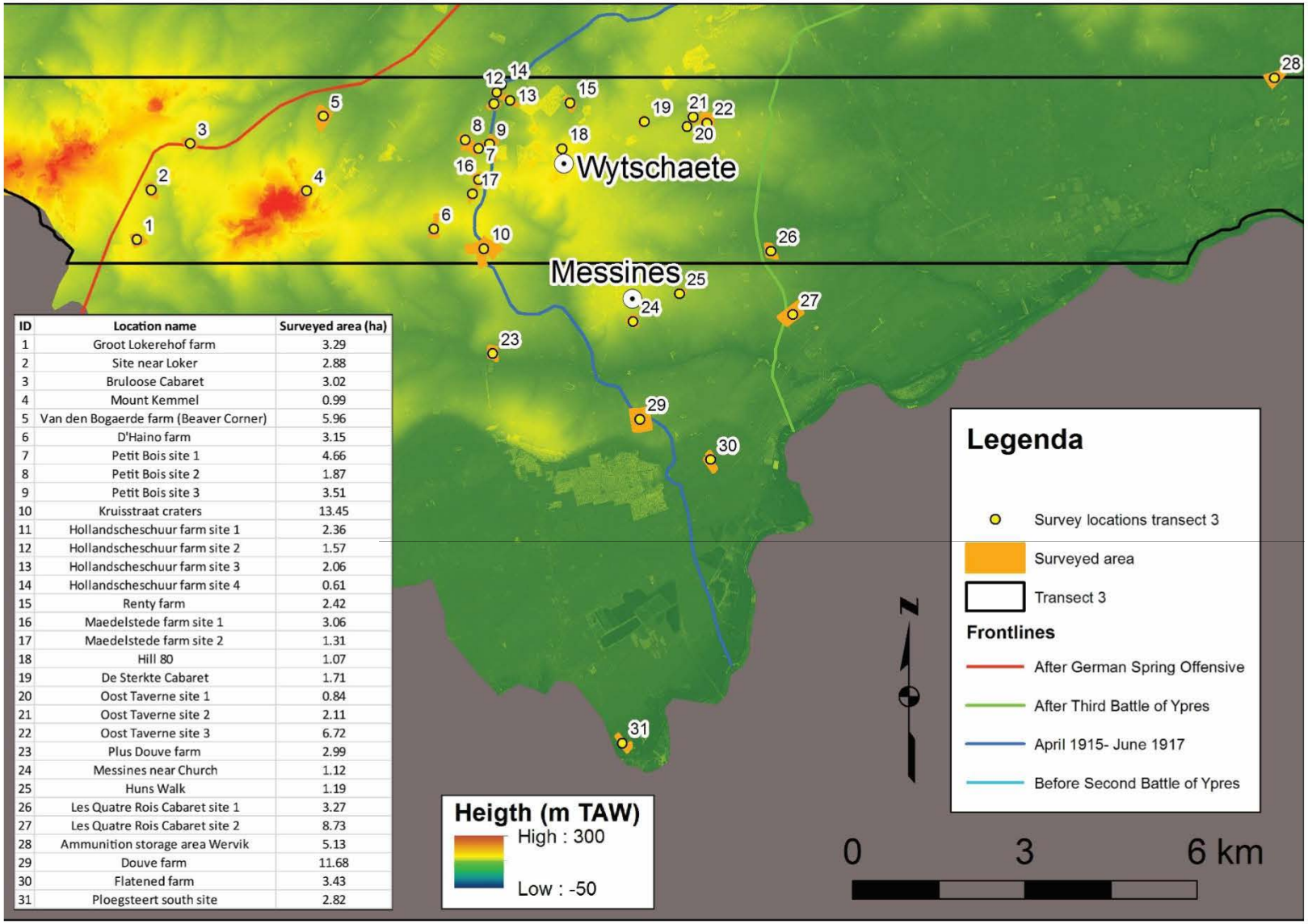
| *ID* | *Name* | *1940-45* | *1971* | *1989-90* | *2000* | *2014-18* | *Land use quotation* | *Features EMI* | *Features LIDAR* |
|---|---|---|---|---|---|---|---|---|---|
| ***1*** | **Vlamertinge** | NA | 0.5 | 0 | 0 | 0 | 0.5 | ++ | ++ |
| ***2*** | **Palingbeek** | NA | 0.5 | 0 | 0 | 1 | 1.5 | + | - |
| ***3*** | **Zillebeke centre** | 0 | 0 | -1 | -1 | -1 | -3 | + | - |
| ***4*** | **Cambridge road** | 0.5 | 0 | -1 | -1 | -1 | -2.5 | ++ | - |
| ***5*** | **Bellewaarde north** | 1 | 0.5 | 1 | 1 | 1 | 4.5 | ++ | ++ |
| ***6*** | **Bellewaarde centre** | 0 | 0 | -1 | -1 | -1 | -3 | + | - |
| ***7*** | **Bellewaarde west** | 0 | 0 | -1 | -1 | -1 | -3 | + | - |
| ***8*** | **Bellewaarde south** | 0 | 0 | -1 | -1 | -1 | -3 | + | - |
| ***9*** | **Bellewaarde park** | 1 | 0.5 | 1 | 1 | 1 | 4.5 | ++ | - |
| ***10*** | **Hill 62** | 0.5 | 0 | 0 | -1 | 1 | 0.5 | ++ | + |
| ***11*** | **Clapham Junction** | 1 | 1 | -1 | 1 | 1 | 3 | + | + |
| ***12*** | **Sint Juliaan** | NA | 0 | 0 | 0 | 1 | 1 | + | - |
| ***13*** | **Black Watch Corner** | 0.5 | 0.5 | 0 | 0 | 1 | 2 | + | + |

### 7.3.3 Transect 3: A section through the Messines Ridge

The locations surveyed in this transect can be divided in three main areas representing the main frontlines: (1) the 1915-17 front, (2) the British advances after the Third Battle of Ypres (1917) and (3) the front shift after the German Spring Offensive (April 1918). The elevated area south of the Ypres clay plain contains thirty-one locations, visualised in figure 7.29. Seven are located outside the 3rd transect but included in this section. In total, an area of 108.9 ha was surveyed. All sites are located on the dry sand-clay ridges, except for one hinterland site near Wervik (ID 28), Flatened farm site (ID 30) and Ploegsteert south site (ID 31).

#### *7.3.3.1 Sites near Loker: from Allied hinterland to 1918 frontline (ID 1-2-3)*

The Groot Lokerhof farm (ID 1) was situated between 6 km (after 2nd Battle of Ypres) and 11 km (after 3rd Battle of Ypres) behind the front. When the German Spring Offensive took place in 1918, the frontline shifted towards Loker. Despites the area's safe position during the majority of the war, the landscape and civilian infrastructure were destroyed in the last phase. The aerial photograph dating from the 3rd of May 1918 recorded a targeted but still intact Lokerhof farm (see figure 7.30 A). The aerial recording from the 29th July 1918 (3 months later) shows a completely destroyed site. At that moment, the site was located near the frontline and was therefore heavily targeted by artillery fire (see figure 7.30 B). The EMI scan executed in March 2012 showed that the building remains are still present underneath the surface (see figure 7.30 C). These are situated at the location of the medieval outer court of this historical farm. The associated moated site surrounded by a ditch and palisade is located just south of the farm buildings. When WW1 started, the moated site was already broken down and levelled. Despites the destructive effect of WW1 (170 shell craters per ha, = transect 3 average), ditch and palisade remains are still present in the soil and micro topography. After the war, a new farm was built north of the Lokerhof farm (former outer court). In 2013, an extra shed was placed on top of the outer court.




| ID | Location name | Surveyed area (ha) |
|---|---|---|
| 1 | Groot Lokerehof farm | 3.29 |
| 2 | Site near Loker | 2.88 |
| 3 | Bruloose Cabaret | 3.02 |
| 4 | Mount Kemmel | 0.99 |
| 5 | Van den Bogaerde farm (Beaver Corner) | 5.96 |
| 6 | D'Haino farm | 3.15 |
| 7 | Petit Bois site 1 | 4.66 |
| 8 | Petit Bois site 2 | 1.87 |
| 9 | Petit Bois site 3 | 3.51 |
| 10 | Kruisstraat craters | 13.45 |
| 11 | Hollandscheschuur farm site 1 | 2.36 |
| 12 | Hollandscheschuur farm site 2 | 1.57 |
| 13 | Hollandscheschuur farm site 3 | 2.06 |
| 14 | Hollandscheschuur farm site 4 | 0.61 |
| 15 | Renty farm | 2.42 |
| 16 | Maedelstede farm site 1 | 3.06 |
| 17 | Maedelstede farm site 2 | 1.31 |
| 18 | Hill 80 | 1.07 |
| 19 | De Sterkte Cabaret | 1.71 |
| 20 | Oost Taverne site 1 | 0.84 |
| 21 | Oost Taverne site 2 | 2.11 |
| 22 | Oost Taverne site 3 | 6.72 |
| 23 | Plus Douve farm | 2.99 |
| 24 | Messines near Church | 1.12 |
| 25 | Huns Walk | 1.19 |
| 26 | Les Quatre Rois Cabaret site 1 | 3.27 |
| 27 | Les Quatre Rois Cabaret site 2 | 8.73 |
| 28 | Ammunition storage area Wervik | 5.13 |
| 29 | Douve farm | 11.68 |
| 30 | Flatened farm | 3.43 |
| 31 | Ploegsteert south site | 2.82 |

**Figure 7.29:** Overview of the surveyed sites according to the 3rd transect zone. Each site has its own ID.

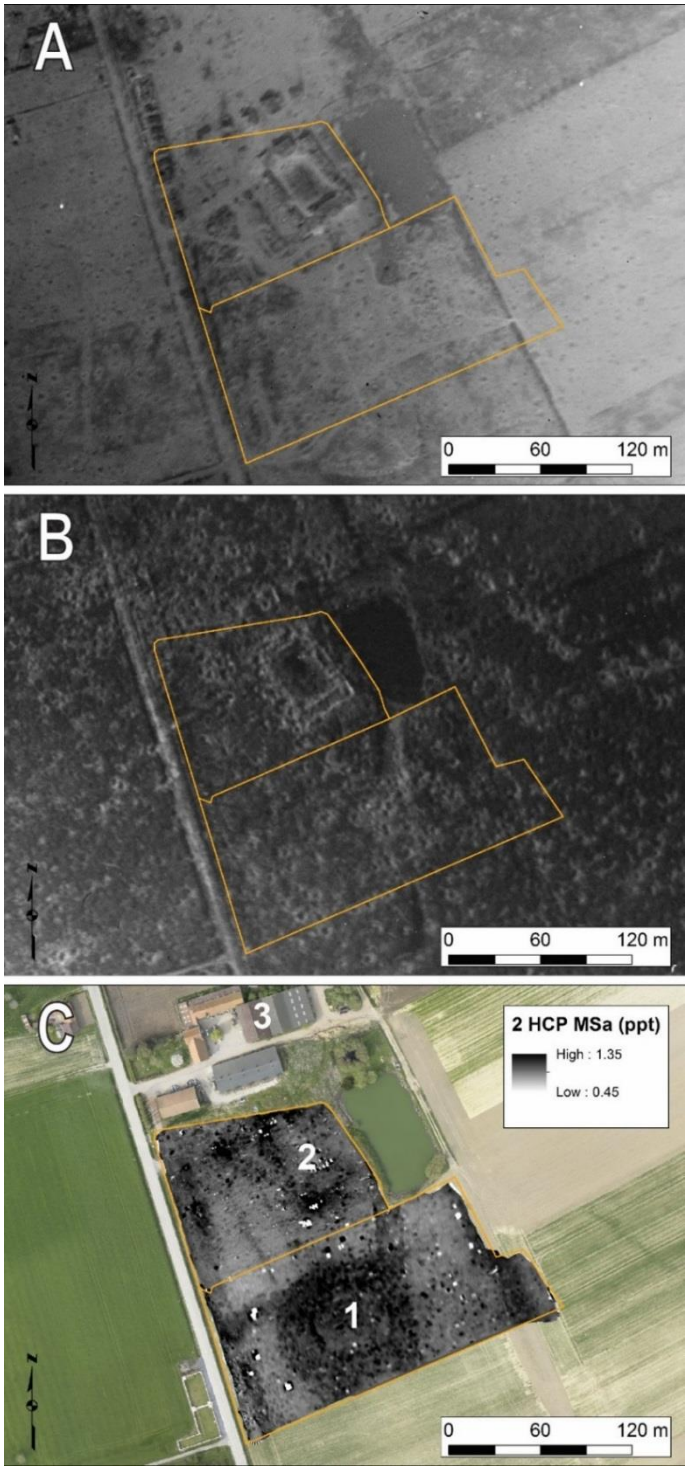



**Figure 7.30:** Visualisation of the 'Groot Lokerhof' by aerial photography before total destruction (A, 03/05/1918, IWM collection), after total destruction (B, 29/07/1918, IWM collection) and the EMI scan performed on the 15th March 2012 (C). On the 2HCP magnetic data layer, the moated site is indicated by number '1', the outer court and farm buildings during WW1 by number '2' and the current farm by number '3'.

On the 2nd site near Loker (ID 2), newly dug communication cable ditches are seen on the aerial photograph of 1916 (figure 7.31 A) while trenches can be found at the same area after the German Spring Offensive (figure 7.31 C). Both structures were (partially) found in the scan results (figure 7.31 B). This site shows a case where cables were recently dug and therefore traceable by RSA. This is partially due to the intact landscape before the Spring Offensive

where shelling did not camouflaged the cable ditch. The post-war land use as orchard and some parts as pasture enhanced the traceability of these war features today.

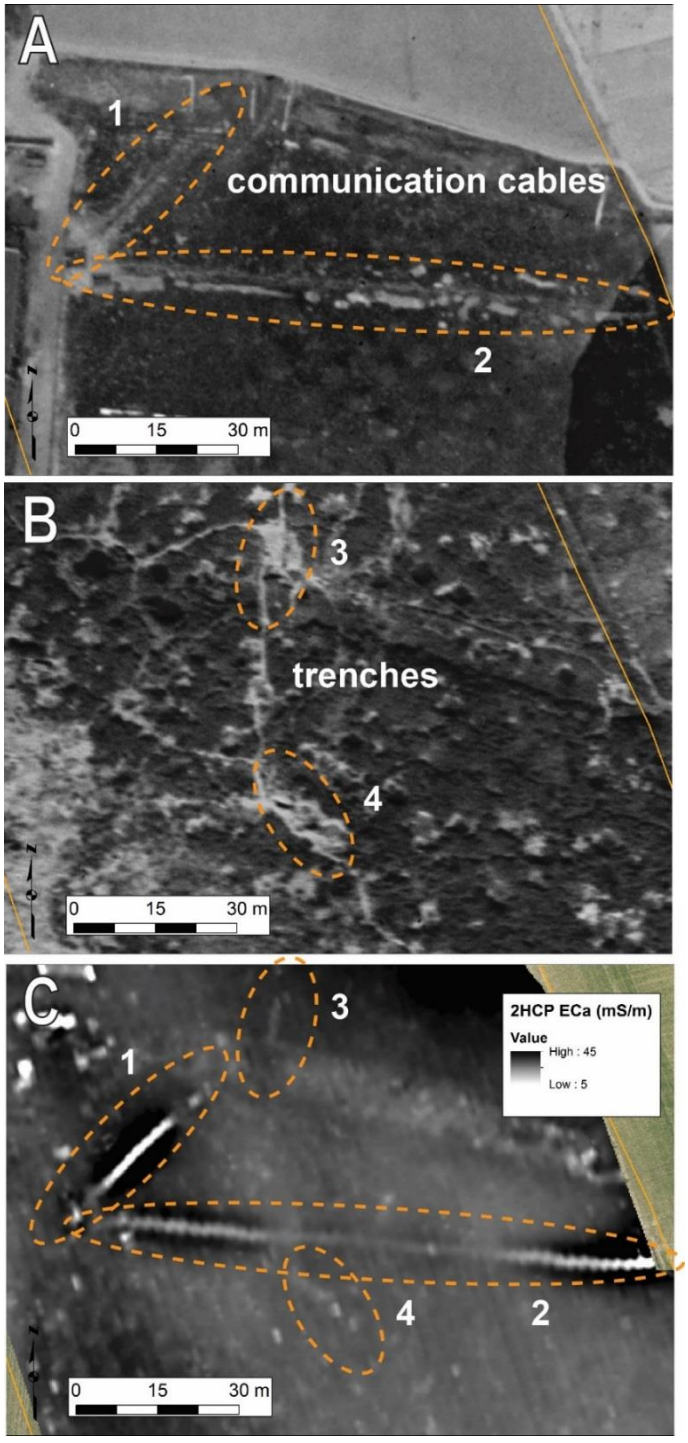



**Figure 7.31:** Visualisation of the Loker site (ID 2) by aerial photography before destruction (A, 04/05/1917, IWM collection) with indication of digging traces for communication cables, after destruction (B, 21/08/1918, IWM collection) with indication of trenches and the EMI scan (C). On the 2HCP $EC_a$ data layer, the detected communication cables (1 & 2) and trenches (3 &4) are marked.

The third site near Loker is Bruloose Cabaret (ID 3), named after the nearby hamlet. Here, a British firing trench and military road are crossing this site from west to east. Both structures date from the German Spring Offensive period and were firstly seen on aerial photographs at

the beginning of May 1918. These were heavily shelled between spring and summer of 1918. Despites the constant state of arable land, a strong signature of the trench in the scan data was found. No clear traces were detected of the military road. Saey et al. (2013) already published these results as short report in advance of the *Non-Invasive Landscape Archaeology of the Great War* project. Therefore, the scan results are only shown in the appendices (see appendix 7.4).

#### *7.3.3.2 Kemmel sites: a well-targeted lookout hill and Allied 1915-17 hinterland (ID 4-5)*

Kemmel Hill (French: Mont Kemmel) is a tactical lookout dominating the surrounding flat area, with evidence of that tactical use as early as the Bronze Age. During the war, it acted as an Allied observation post until it was heavily shelled and conquered in April 1918 by the German forces. The battles in this area continued until the end of July. On September 5$^{th}$, the Allies reconquered the hill. At the end of the battles, the tree-covered hill was completely turned into a bare landscape with innumerable craters. A site of one hectare was surveyed on its north-eastern flank. Due to the trees and constant post-war pasture conditions, shell craters and trenches not only could be detected in the EMI data but also above-ground by LIDAR (see figure 7.32). Metal parameters in the EMI data are one of the highest in this area (7.3% area FEMP, 475 MOH/ha). These high numbers are related to the intense shelling of the hill (Note et al., 2018). Despite the heavy shelling, one early communication trench from September 1915 is well preserved in the EMI data and in the micro relief (figure 7.32). All the linear WW1 elements seen on aerial photographs in this small area were detected by the EMI scan. The second Kemmel site (ID 5) is situated near Van den Bogaerde farm, just 1 km north of the previous site. On this 1915-17 hinterland site, former farm remains were found and some trenches at the western part of this field. The magnetic footprint of these building remains (brick fragments) can be sharply delineated in the 1HCP $MS_a$ data layer (see figure 7.33 C). Due to ploughing activities, the magnetic content has been vaguely distributed around these former building locations. This can be concluded because the ploughing direction can be extracted from the scan data. The other two examples are moderately preserved firing trenches which can be detected in the top 50 cm (just below the ploughing activities). If the EMI metal parameters are considered, the numbers are indicating typical values for a shortly heavily targeted hinterland site (177 MOH/ha & 3% area FEMP).

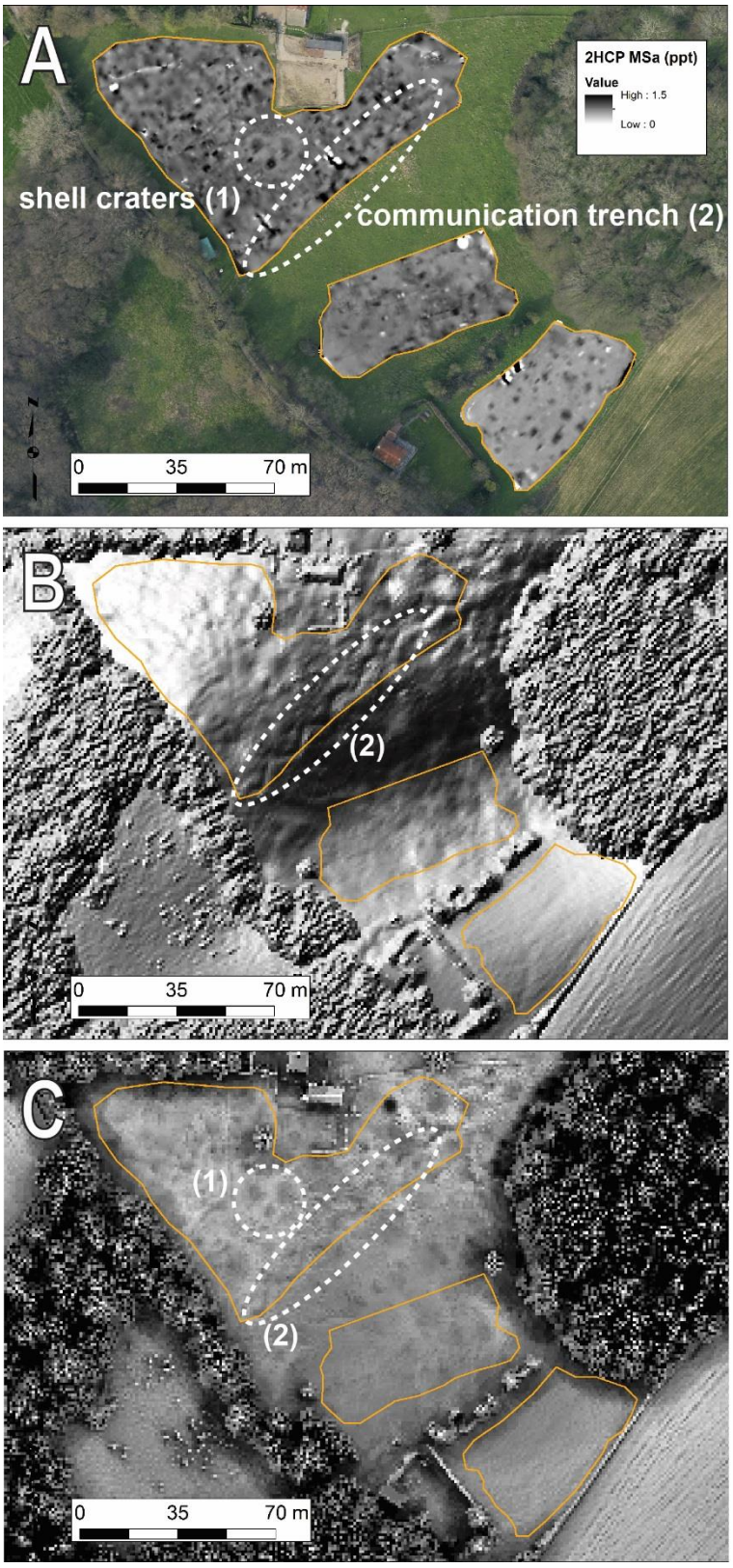



**Figure 7.34:** Visualisation of the Kemmel Hill site. Image A displays the survey results of the EMI scan with indications of three well-preserved shell craters and a well-preserved 1915 communication trench. Both structures can be seen in the LIDAR data (B, multi-hill shade visualisation) and the derived micro relief (C) (copyright AIV).

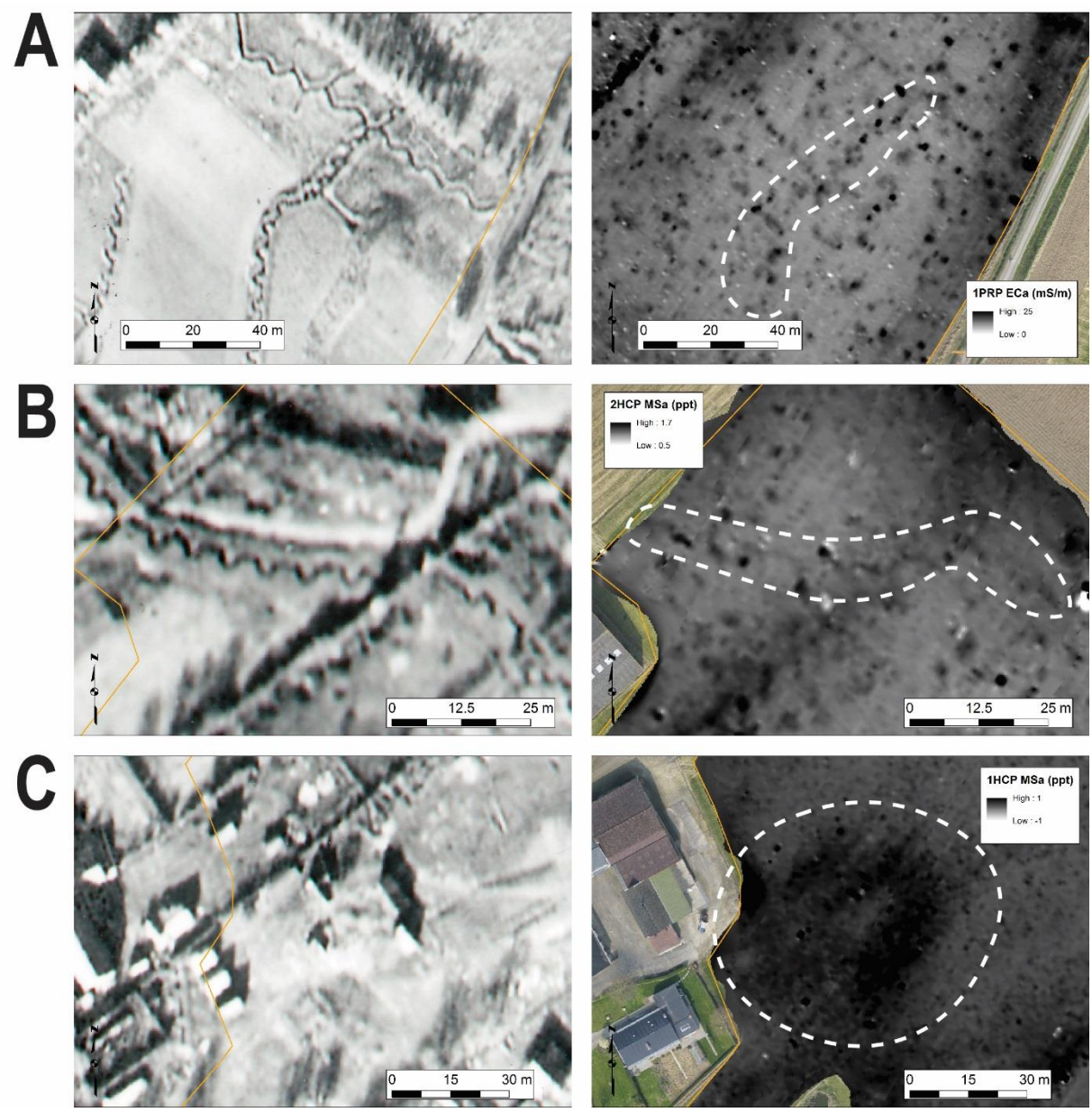



**Figure 7.35:** Visualisation three details in aerial photography (left, Bayerisches Hauptstaatsarchiv collection) and EMI data (right) from the Van den Bogaerde farm site (ID 5). A & B are the results from two firing trenches while C demonstrates the suitability of the 1HCP $MS_a$ coil configuration to sharply delineate the magnetic remains of the former farm buildings (destroyed during WW1). (orthophoto: copyright AIV)

### *7.3.3.3 The 1915-1917 frontline sites: complex area's (ID 7 – 18, 23 & 29)*

The closer to the frontline, the denser and more complex the WW1 structures and networks become. If the density of above ground linear networks of the 1915-17 hinterland sites (ID 1 – 5) are compared to the frontline sites, a density range of 100-200 m/ha detectable linear features are found for hinterland (average 119 m/ha) and 250 – 600 m/ha for frontline sites (average 411 m/ha). These near frontline sites are often more difficult to interpret by aerial photography despite the dense recording of time series of photographs. Not only the complexity of the linear network makes it harder to recognise or distinguish some linear structures but also the intense shelling. On these sites, the armies went underground to find shelter or to force a breakthrough towards the enemy lines. These underground activities accompanied with camouflaged infrastructure are often missed by RSA. On these sites, EMI-surveys demonstrated its potential to detect the unseen features by RSA. On the 1915-17 frontline sites, EMI was able to detect 14.7% extra potential linear WW1 features compared to the 4.2% of the other frontline sites in this transect (other frontline phases). Four areas were surveyed along and three within a proximity of 1 km of this 1915-17 frontline (see figure 7.34).




**Figure 7.34:** Visualisation of the surveyed sites ID 7-18 between Kemmel and Wytschaete. The near frontline zones are marked in a bold font style. (orthophoto: copyright AIV)

D'Haino farm site (ID 6), the first area to discuss, is situated on the Allied side at approximate 500 m of the first line. At this site, a complex situation of war features can be found (figure 7.35). There is a high indication of extra-detected linear features by the soil scan (31%) (see table 7.12) which are generally identified as communication cables. Because of the depth of some cables (>2m), there can be assumed that these features were placed in a covered trench/ditch and not just on top or just below the surface. The complexity of linear features at this site led to a possibly difficult situation to identify all features. Some of these detected cables are connecting to by RSA identified communication trenches. This fact contributes to the assumption that these cables were put in a camouflaged ditch/trench. Because the cables are mostly leading to abri's/barracks from the last period of the war (first seen around April 1918, see figure 7.35), there can also be assumed that these cables are dating from the same period. None of the cable ditches were detected by aerial photography.

Another complex site including extra linear features caused by communication cables is the Petit Bois site (ID 7-8-9). In this area, two craters (+/- 70-80 m in diameter) are dominating the landscape as relicts from the great explosions that started the 1917 Battle of Messines (located to the east of this survey, see figure 7.36). At the western part of the prospected area near Vandamme farm, tunnel galleries were dug towards the German lines (current Petit Bois craters). The first mining operations in this area took place in the summer of 1915. As soon as the Messines ridge mining scheme was developed (+/- 20 mines under the enemy frontline, south of Ypres), the 250$^{th}$ Tunnelling Company took over the mining sector in November 1915, starting the activities for the deep tunnelling system. Because of the slow progress of the works at the Petit Bois site, an experimental mechanical excavator (Bridgland, 2003) was tested. The machine was not a great success. After being started at 4 march 1916, it was capable of drilling a 2 meter diameter tunnel. However, because of the heavy weight of the drilling apparatus and the difficult operational circumstance in the clay, it was not able to maintain a straight trajectory and by the end of the month, the machine was abandoned in a tunnel 'covered in shame and 80 odd feet of Flanders soil' (Grieve and Newman, 1936). Normal clay kicking (digging technique) was recommenced to complete the tunnel. The gallery extended over 1.600 feet (488 m) before splitting in a Y shape leading towards two galleries of 210 and 260 feet (64 and 79 m). The deep mine galleries are located out of the detection limits of the DUALEM sensor but shallow structures or anomalies related to those tunnelling activities could still be detected.

To begin, a trajectory of communication cables was detected, which was missed during the RSA analysis. Several cables start from an underground location near Vandamme farm. One cable trajectory is leading to the British first line. From tunnel and dugout discovery reports (Barton et al., 2005), it was possible to link the communication cable cross point to an underground commando post. Based on the EMI-responses, the sections of cable can be estimated for the majority of the trajectory between 0 - 0.7 m and 0.7 - 1.4 m. Other cables revealed camouflaged trenches. In addition, one entrance of a subway tunnel (+/- 3-5 m deep) was found. Images of those structures are displayed in figure 7.36.

A third frontline site is located around the Pool of Peace (Spanbroekmolen crater) and the Kruisstraat craters (ID 10). In this 13.5 ha survey, a good representation is found of Allied and German frontline structures with the no man's land in-between. A well-preserved German firing trench dating from 1915-17, is dominating the other traces in the scan. This is partially explained by the large amounts of buried metal in this trench. Probably, this was a strongly fortified trench (quality, strength and thoroughness were characteristic for German trenches)(Bull, 2014) or this structure was used to dump the military waste. Because of the high density of metal objects around this linear feature, the signature can be seen in both $EC_a$ and $MS_a$. The 1915-17 trenches on the eastern flank of this site (figure 3.35 B 3) were most likely not filled with military waste and therefore only detected by $EC_a$ response. Their magnetic signature is often too subtle to be detected in a strong magnetic disturbed area like the former Western Front. A metal classification and depth analysis for the whole site reveals that that the majority of the objects are buried deeper than the top 40 cm. This is explained by the constant arable conditions: agricultural machines sift out the metal objects and clutter. Next to the agricultural effects, there is a height difference of 16 m between the highest and lowest point of this terrain, which makes it exposable to slope erosion. In the eastern part of this site, a damped crater from the 1917 mine battles appears. Bulldozers illegally filled this crater in July 1972 (www.wo1.be, 2018). This crater only appears in the $EC_a$-data layers because of the different characteristics of the filled and the surrounding soil content. Today, this crater remains invisible, even the micro relief (LIDAR) does not reveal any traces.

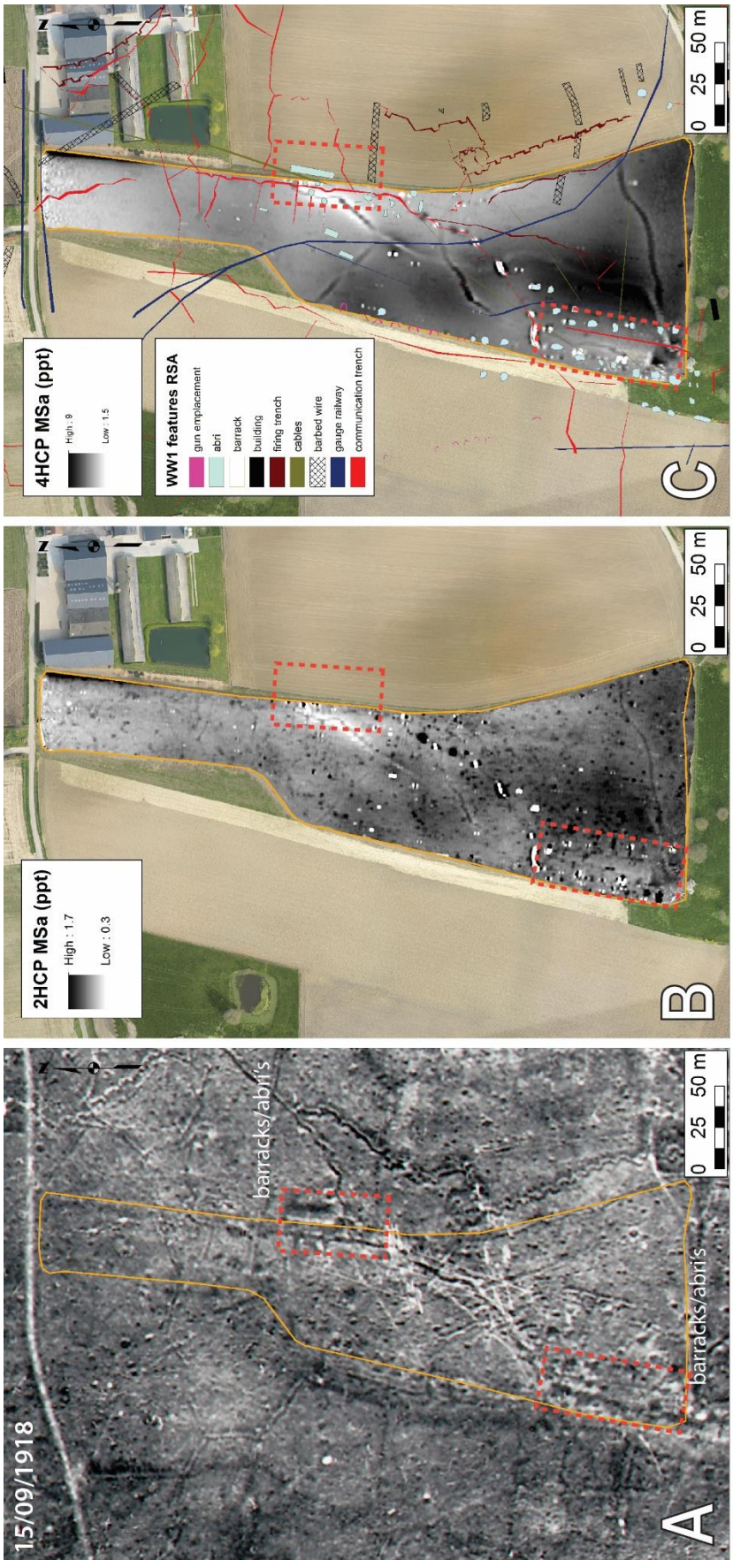



**Figure 7.35:** Visualisation of the D'Haino farm site. Image (A) represents an aerial photograph taken on 15 September 1918 (Bayerisches Hauptstaatsarchiv collection), image (B) shows the magnetic response for the 2HCP coil configuration and (C) the magnetic response for the 4HCP coil configuration with indication of the detected WW1 features by RSA. On all three images, a box is drawn over abri's/barrack structures. (orthophoto: copyright AIV)

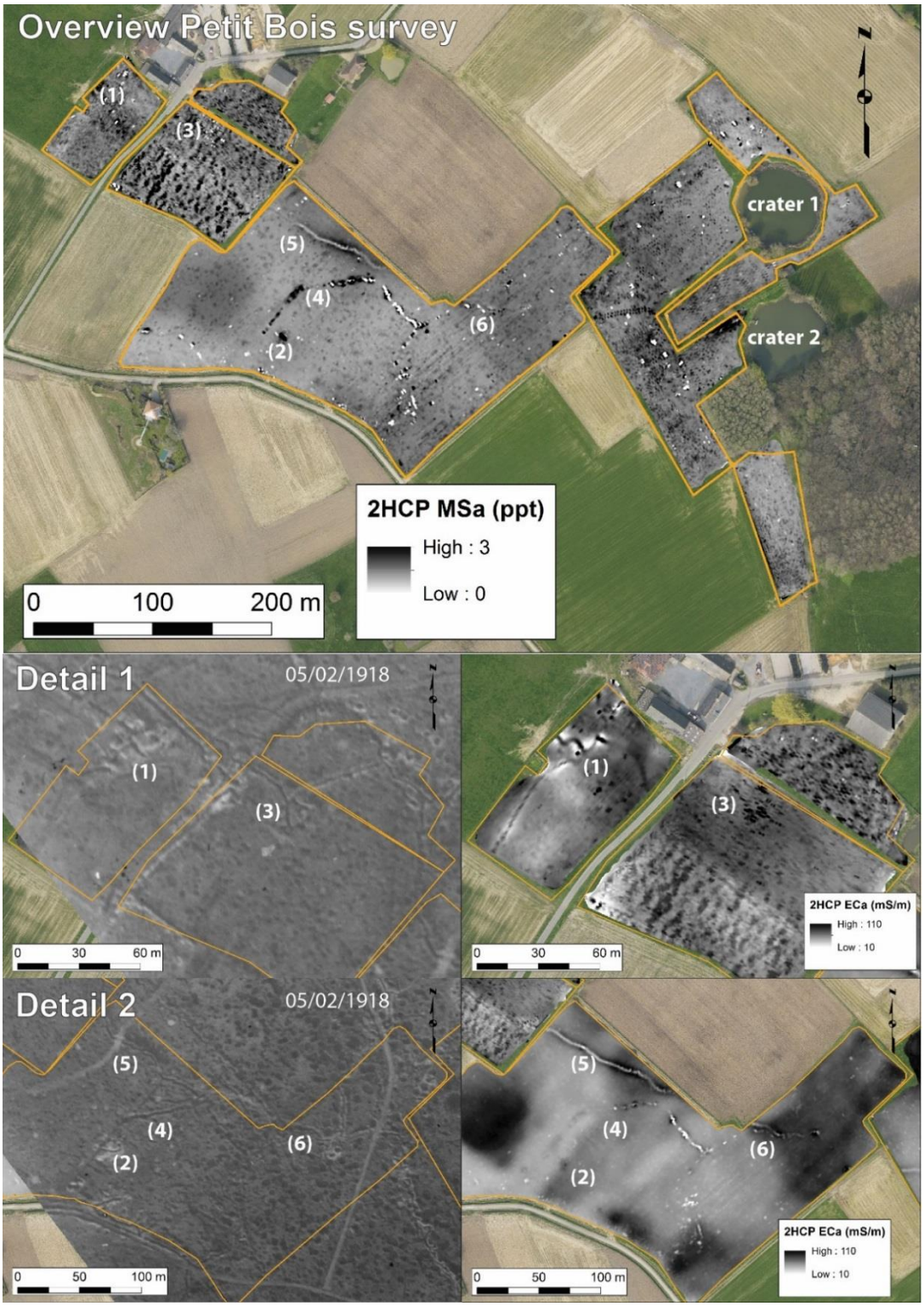



**Figure 7.36:** Overview of the Petit Bois survey with the 2HCP magnetic data layer. Two zoomed in details with the 2HCP $EC_a$ data layer are giving a clear image about the interesting detected features. Those features are: (1) cross point of communication cables, situated on the ruins of the former Vandamme farm, the entrance of the deep dugout is situated in this plot (2) the location of a subway entrance (3) anomaly on the location of a former abri, (4) metal filled communication trench, (5) a communication cable situated 0 - 0.7 m of depth and situated in the vicinity of a former communication trench, (6) a communication cable situated within a communication trench. (WW1 aerial photograph: IWM collection; orthophoto: copyright AIV)

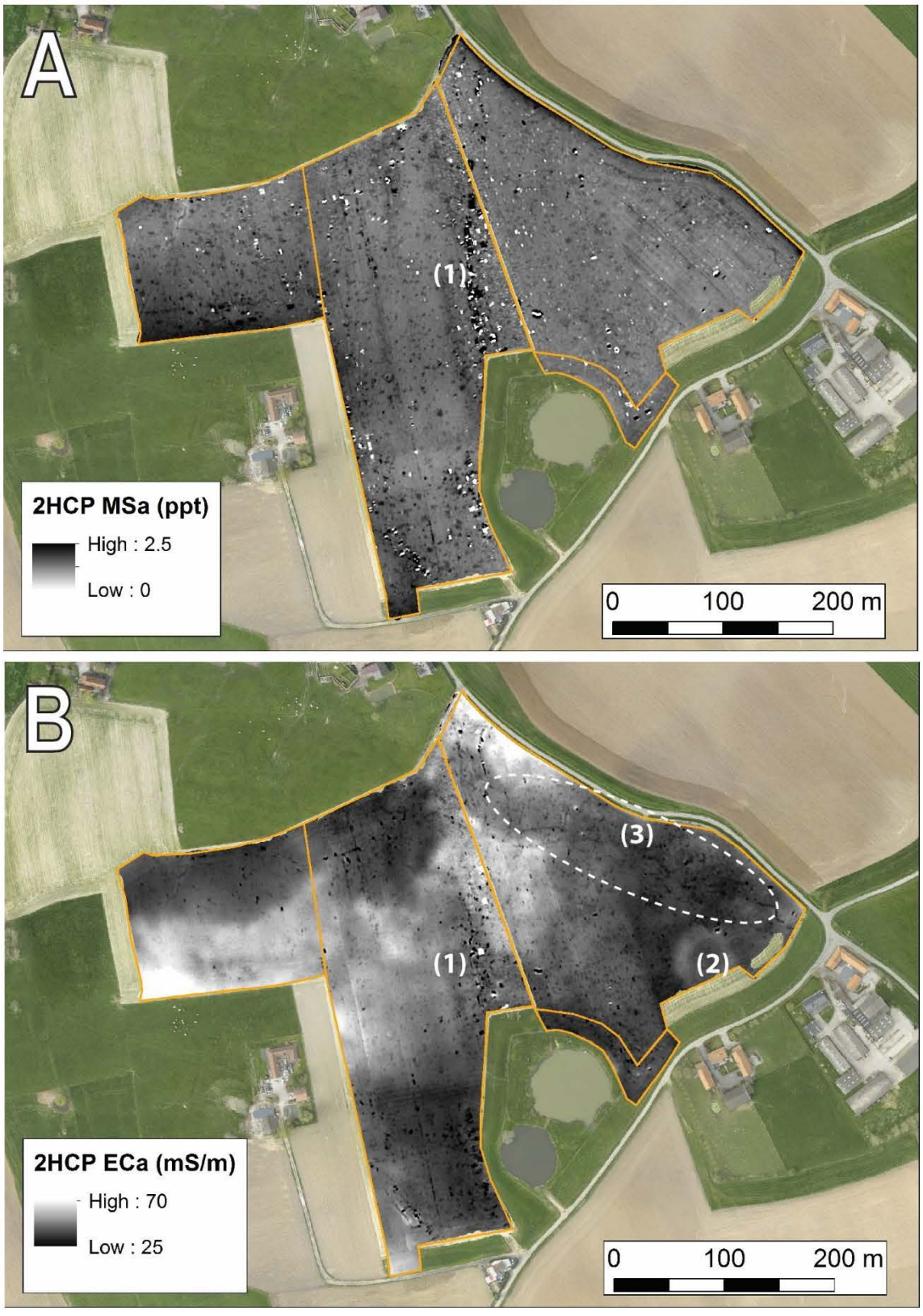



**Figure 7.37:** Overview of the Kruisstraat craters survey. Image (A) shows the 2HCP magnetic data layer while image (B) represents the 2HCP electrical conductivity layer. In the middle of the survey, a metal filled firing trench crosses the area from north to south (1). Label '2' refers to the damped mine crater. In the east of the field, a dens network of firing and communication trenches appear in the $EC_a$ data (3). (orthophoto: copyright AIV)

Near the Hollandse Schuur farm, 6.6 ha were scanned. This area was targeted as well by the mine explosions. Three similar craters as the Petit Bois and Kruisstraat craters mark the area near the farm buildings. After the war, this farm was rebuilt at the same location. On other sites in the 3rd transects, farms are often rebuilt next to the former building locations just like the buildings south of the Hollandse Schuur farm, which were moved to the south-west of the former farm location. Traces of these southern buildings were detected by EMI survey (figure 7.39 - 7). Next to the numerous shell craters, there is a special WW1 feature present in the micro topography and in the soil scans: a long trajectory of one of the railway beds from the 1917 British goods station is clearly retraceable. Even the extend of the bed up north is visible by colour differences of the crop plants. This station was built after the Allied advances to the east after the mine explosions. Some of the tracks are positioned in no-man's-land because this area was less destroyed compared to the first lines. These tracks can partly be seen on LIDAR (figure 7.38). The best signature for the railway beds in the EMI data can be found in the 1PRP/2HCP $EC_a$ and the 1 & 2 HCP $MS_a$ data layers. Because of the shallow responses of the beds in EMI and the presence in the LIDAR image, those traces can be considered as 'near surface' (0-0.5m) for the beds marked by '(2)' and under the ploughed layer (0.4-1.0m) for the bed marked by '(1)' in figure 7.39.

A rarer feature to detect than railway beds are military roads because these structures are located 'on the surface' and have no metal parts (as opposed to parts of rails). On the Renty farm survey (ID 15), a 1918 military road location was detected (seen from January – April 1918). This is the only example of a preserved military road found by soil sensing in all surveys. Its signature can be found in both $EC_a$ (vage in 1PRP) and $MS_a$ (2HCP) responses. Correlation between those two layers is often found (Saey et al., 2016b). The magnetic outer road contours are detected which give a similar signature like the breastwork trenches from the polders. These two parallel lines are road ditches that were filled by a magnetic contrasting content. The vicinity of the road near woodland (pre and post-war) is a possible favourable effect for the detection of this road (preserving effect tree roots). Between the woodland and the road, traces of a 1916-17 British firing trench are detected. An aerial image and scan result are shown in figure 7.40.

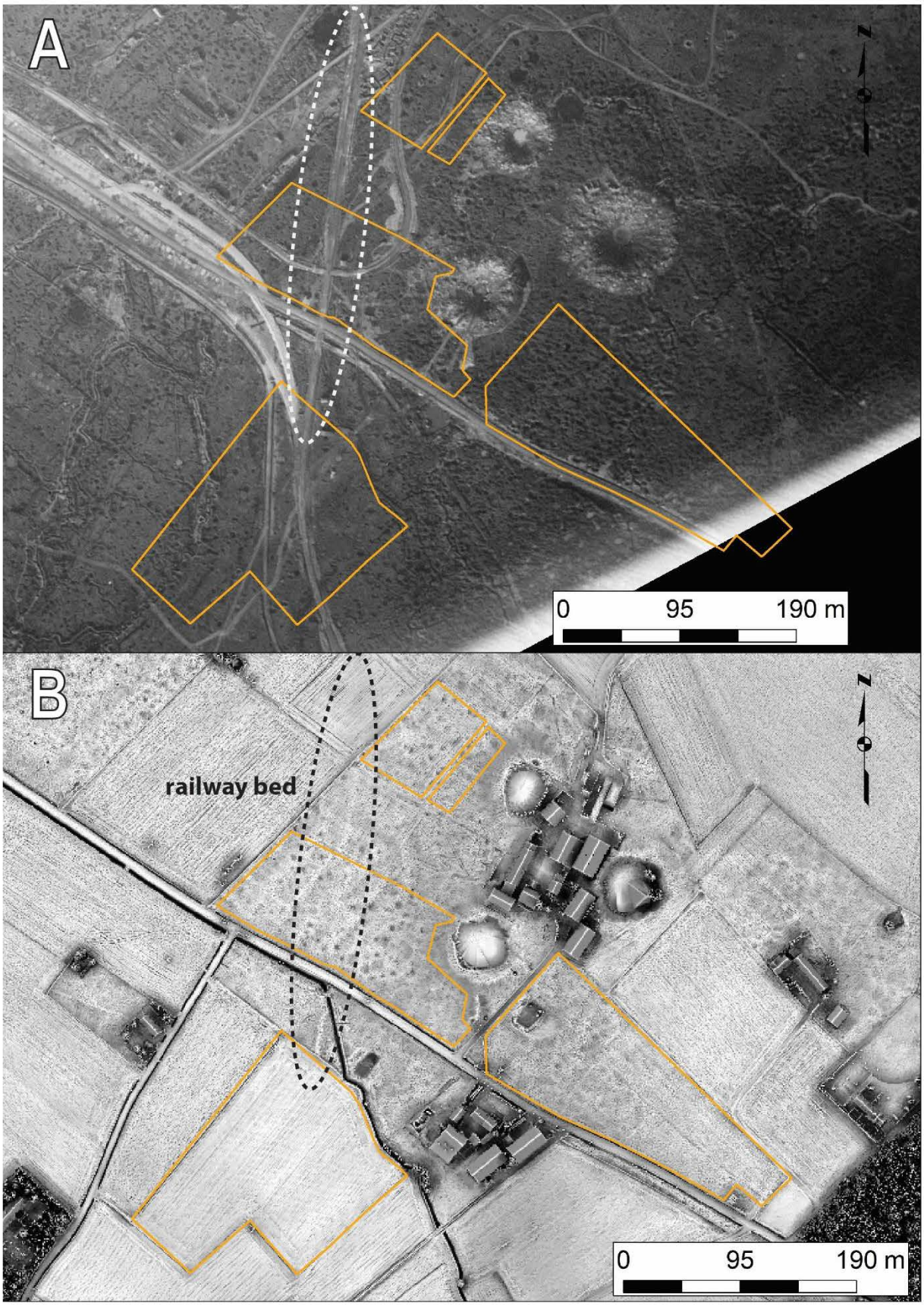



**Figure 7.38:** Visualisation of narrow-gauge railway bed on an aerial photograph taken on 05/02/1918 (A, IWM collection) and the micro relief accentuated LIDAR data (B, copyright AIV).

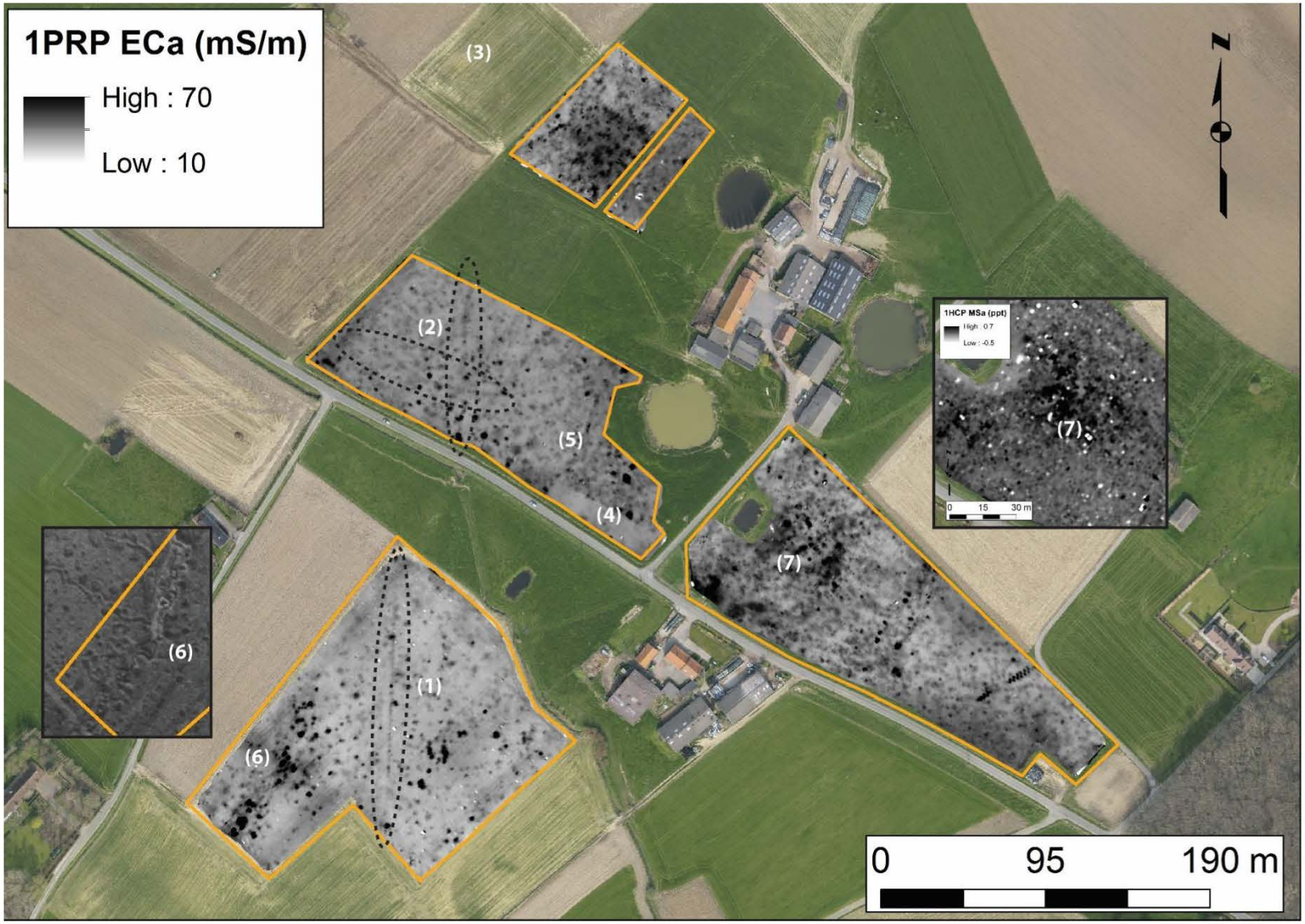



**Figure 7.39:** 1PRP $EC_a$ measurement of the Hollandseschuur site. On this site following structures are identified: (1 & 2) narrow-gauge railway beds, (3) narrow-gauge railway bed visible in the crops, (4) area without shallow WW1 traces, (5 & 6) firing trenches, (7) farm building traces. (WW1 aerial photograph: IWM collection; orthophoto: copyright AIV)

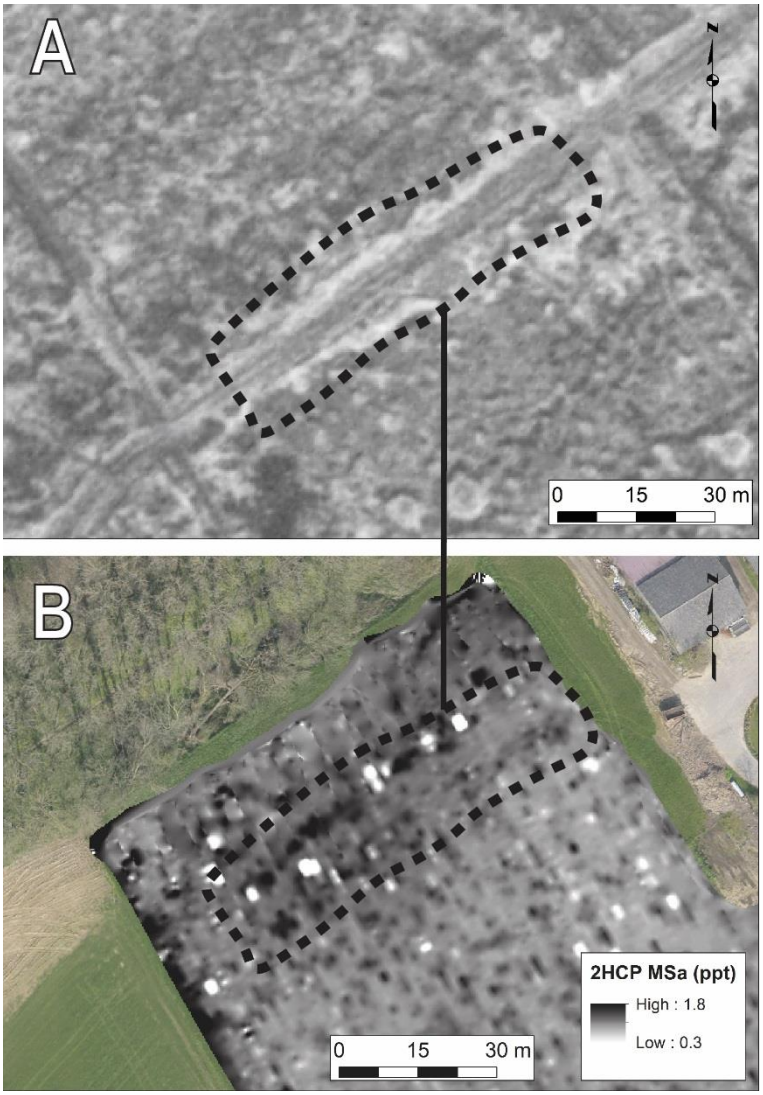



**Figure 7.40:** A detailed view of the detected road at the Renty farm survey: (A) aerial photograph from 1918 (IWM collection), (B) 2HCP $MS_a$ scan result with indication of a detected military road. (orthophoto: copyright AIV)

Maedelstede (ID 16-17) is situated along the frontline between Petit Bois and Kruisstraat craters. This site contains in the north a well-fortified firing trench infrastructure. Several smaller communication trenches were seen on the aerial photographs but some extra linear structures (possible trenches) were confirmed by the EMI scan. This is one of the sites where scan information was helpful to map and identify the dense network of trenches in relation to this frontline. This resulted in 33% extra detected linear features (mostly communication/approach trenches). Next to the trenches, a remarkable and unique structure appears in the no-man's-land zone: A British-Australian barrack camp, built after the advances of the Allies to the east in 1917 (see chapter 4 & 5). The almost perfect fine (magnetic) delineation of the camp footprint

predicted that the foundations of the camp should be intact. This was confirmed by test trenching in September 2016 (Bracke et al., 2018; Gheyle et al., 2016a). The conditions of this site are similar to the ones from the Petit Bois survey containing the railway beds: less shelled no-man's land was used to install a new 'behind the front' structure. These conditions probably contributed to the possibility to detect these structures with more ease. German forces targeted the detected camp during the Spring Offensive in 1918. Destroyed barracks were noted in the aerial photography but the camp as one complete entity remained.

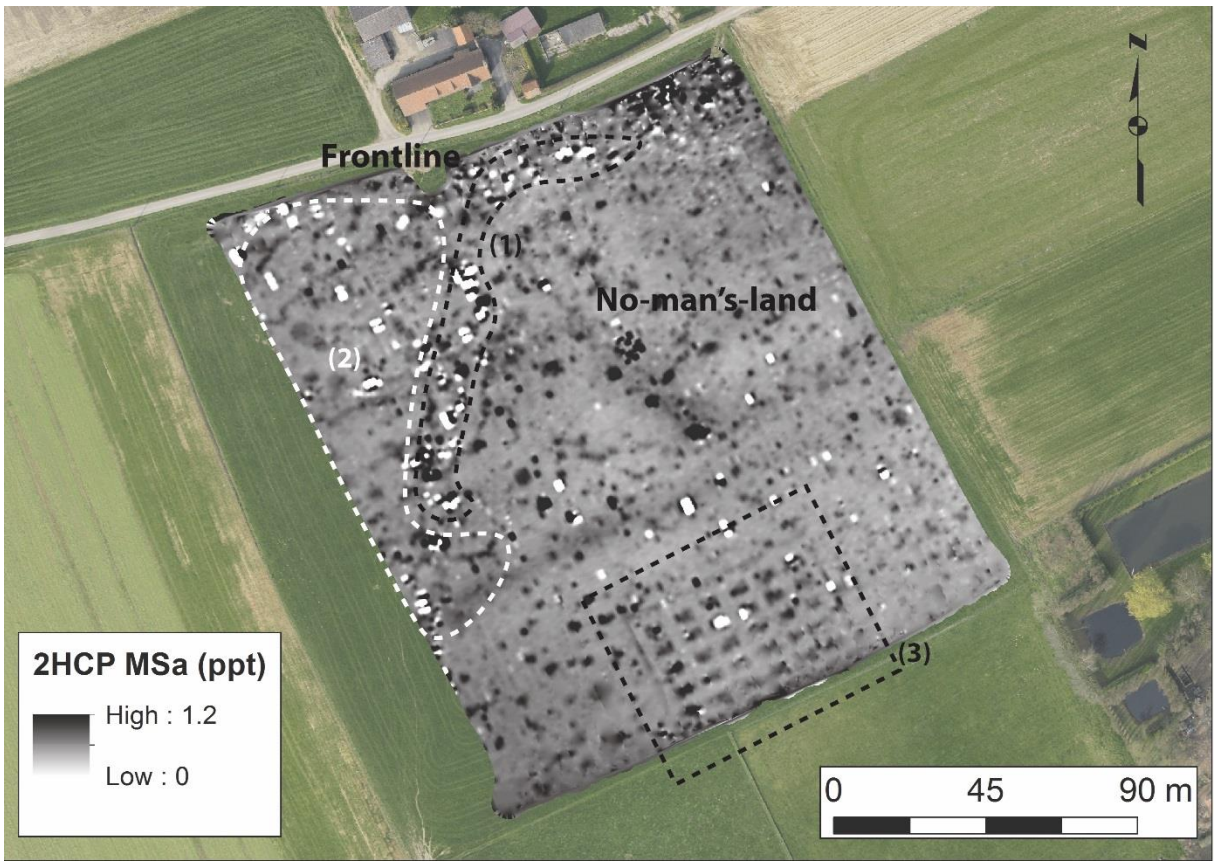



**Figure 7.41:** Visualisation of the 2HCP MSa data layer of the Maedelstede site suvey (ID 16). Here, the Allied frontline is indicated: metal containing firing trenches (1) and a dense network of communication trenches (2). In the 1915-17 no-man's-land, a magnetic footprint of a barrack camp (end of 1917) is found (3). (orthophoto: copyright AIV)

The scan results for the Plus Douve farm site (ID 23) are remarkable for two reasons. The first one is that different types of structures are represented in this survey. The detection quality of the main structures is high despites the long period of arable conditions and slope erosion. This survey is a perfect example for EMI feature interpretation. Second, the scan results produce also the 2nd best score on the linear feature detection rate (70%). This could be

explained by the low score on shelling/metal parameters (97 MOH/ha; 21 sh.c/ha) in combination with a low destruction impact seen on aerial photography. The scan result is displayed in figure 7.42.

The scans of Douve farm site (ID 29) show a high DR of linear structures as well: 66%. The number of MOH/ha (502) is the highest of all prospected sites. This is partially due to the dense shelling but moreover to the high number of metal containing trenches. More details about this site can be found in Saey et al. (2016a). One data layer of the Douve farm scan can be found in figure 7.43 with identification of the detected trenches. This field is situated north of the remembrance monument for the 1914 Christmas truces[12], which were held during the war in this area.

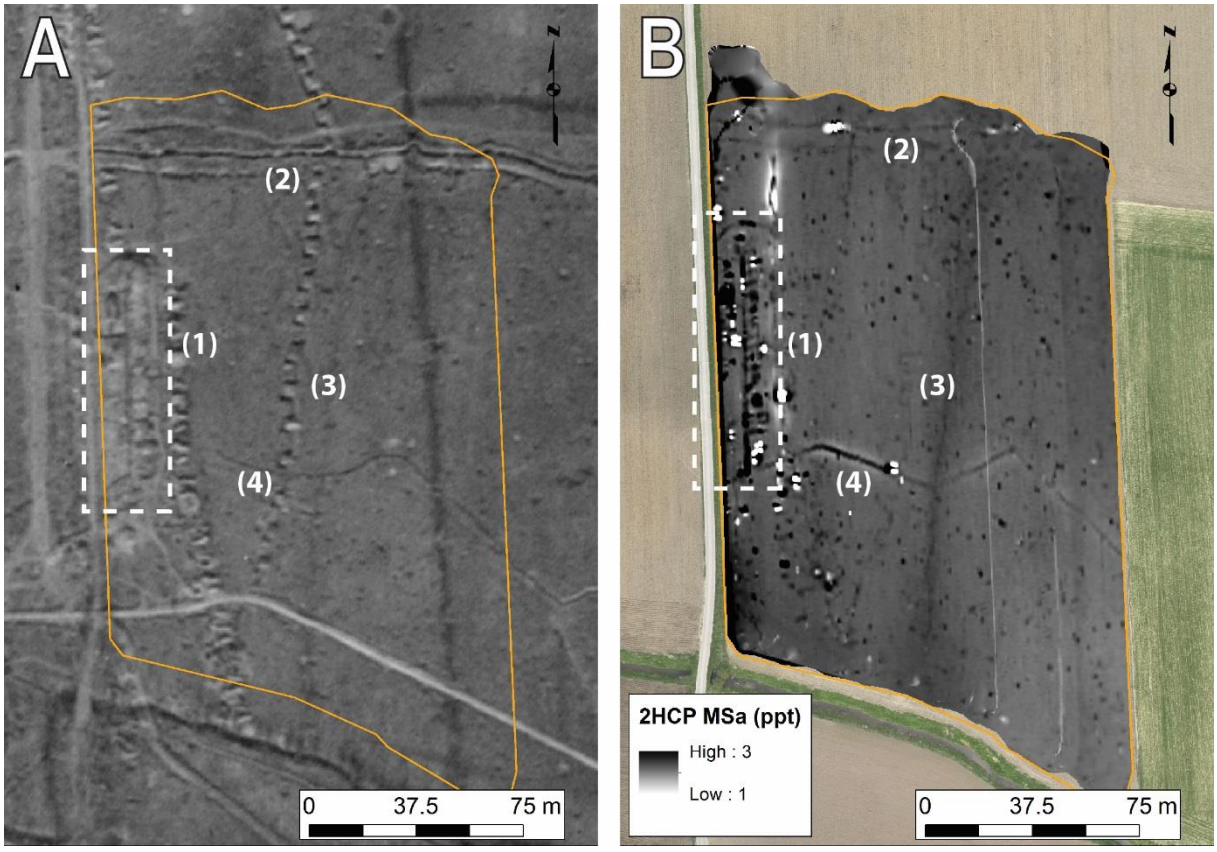



**Figure 7.42:** La Plus Douve site on 08/03/1918 (A, photo IWM collection) and scanned with EMI in 2014 (B). Both images contain deserted dugouts (1), an Allied 1915 firing trench with annexes (2), a firing trench (3) and a communication trench accentuated by a cable (4). (orthophoto: copyright AIV)

[12] Peace moment between Allied and Central forces to celebrate Christmas together. Football was played among soldiers.

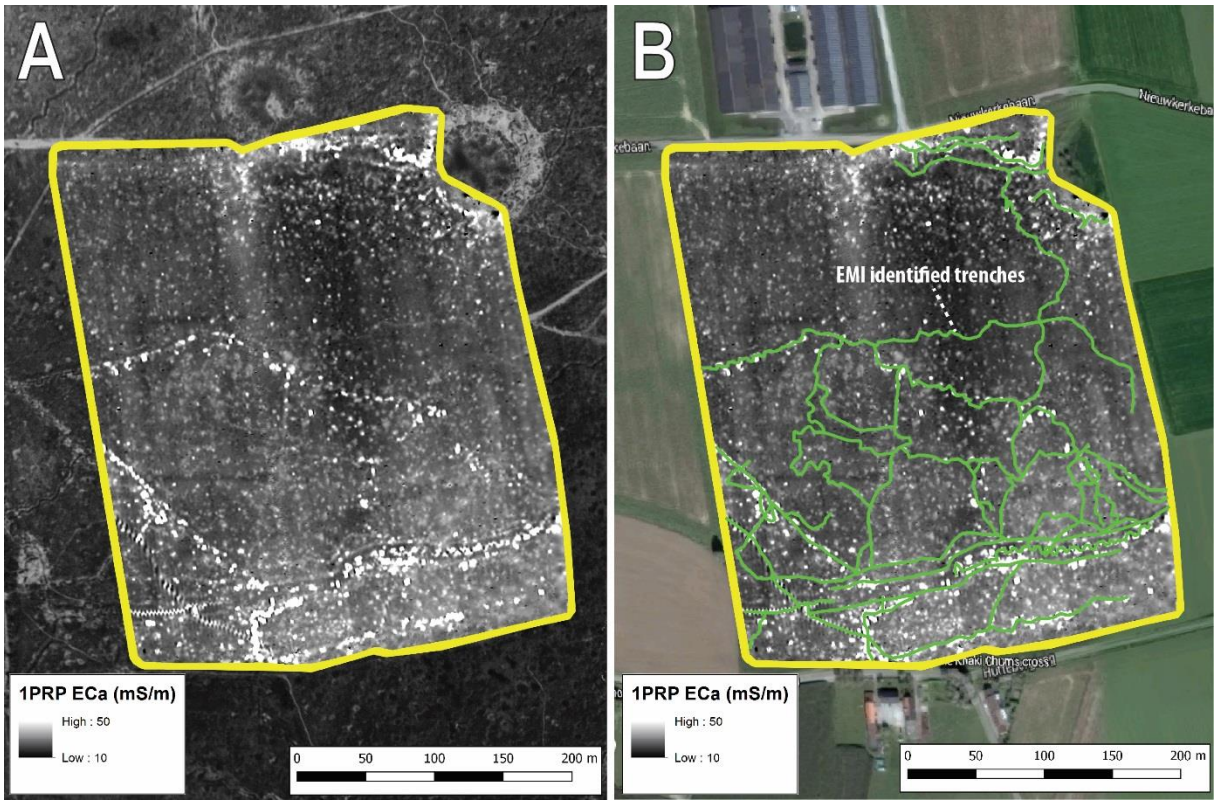



**Figure 7.43:** Visualisation of the 1PRP $EC_a$ data layer at the Douve farm site. In image (A), an aerial photograph of July 1918 (IWM collection). (background image B: copyright Google Maps)

### *7.3.3.4 Near frontline sites after the 3rd battle of Ypres (ID 20-21-22, 26-27)*

The Oost Taverne site 3 (ID 22) is located between the 1915-17 frontline and the front after the 3rd battle of Ypres. The first military activities at this site took place in 1915 when the structures were incorporated in the German military defences of the Messines ridge. The front shifted over this area to the east after the 3rd battle of Ypres. Based on the metal parameters and the detected linear structures, this site scores average values for this transect (DR: 39%, 276 MOH/ha, 4.8% area FEMP). This site was published in Saey et al. (2016b). The Oost Taverne sites 1 and 2 (ID 20 and 21) didn't include any detected linear features. The metal parameters of these sites score double compared to the Oost Taverne 3 site (= continuous post-war arable fields conditions). This can be explained by mainly pasture conditions of these fields after the war, especially for Oost Taverne site 2 which includes old farm remains (still pasture today). An overview of the Oost Taverne sites (ID 20-21-22) can be seen in figure 7.44.

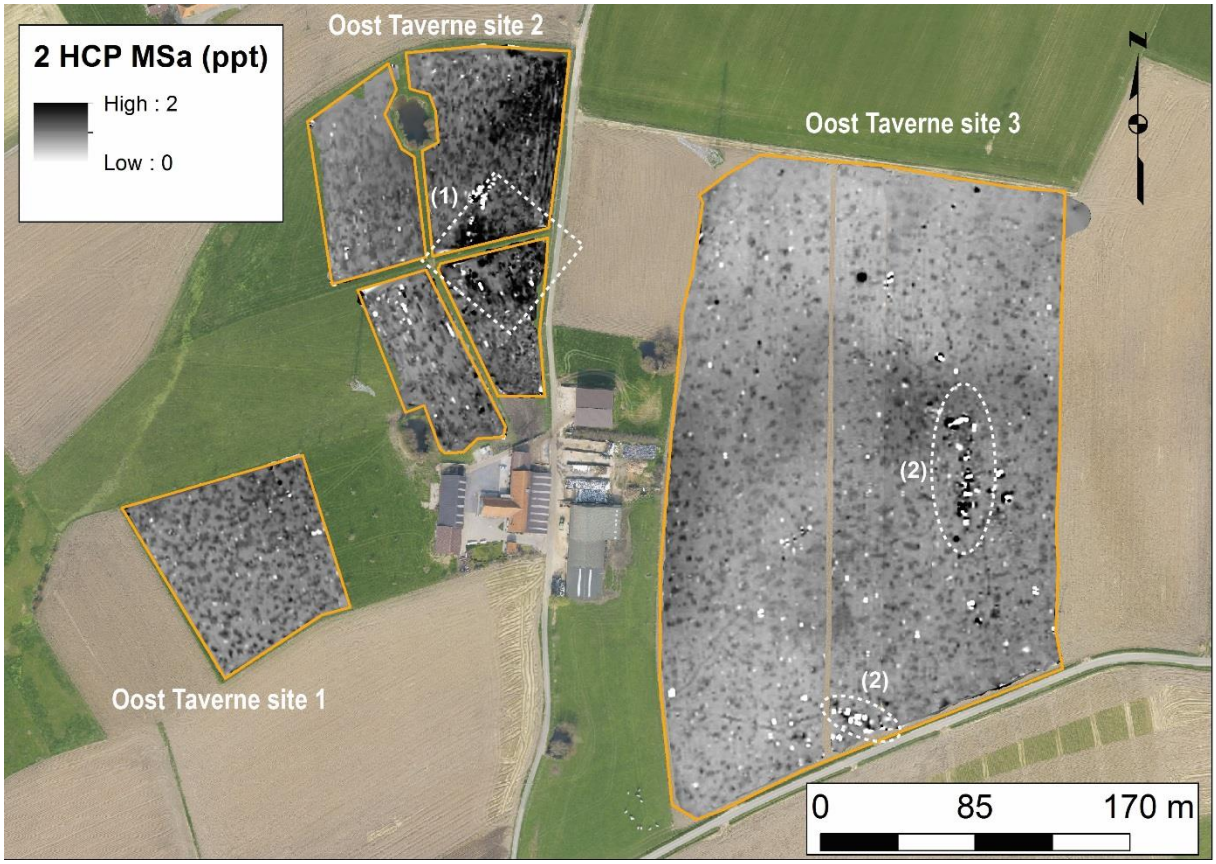



**Figure 7.44:** Visualisation of the 2 HCP $MS_a$ measurement of the Oost Taverne sites. Site 1 demonstrates nicely preserved shelling marks; site 2 contains the remains of the pre WW1 farm (1); site 3 includes gun emplacements (2) whereof poison gas was used. (orthophoto: copyright AIV)

The Quatre Rois Cabaret site 1 (ID 26) is located at the front after the 3rd battle of Ypres. Almost no linear features were seen on aerial photography. Several shell craters were reused as fortified craters (RSA interpretation) but no difference could be made between those shelters and other craters. Some of them have a stronger signature but this is no criterion to discriminate. Because of the absence of trench defences and arable conditions, low scores on metal parameters are found: 1.1% area FEMP and 69 MOH/ha. This site is in contrast to the Quatre Rois Cabaret site 2 (ID 27), 1km south along the frontline. More linear features, higher scoring metal parameters and good result on the detection rate of linear features (DR: 38%). Both Quatre Rois Cabaret sites are visualised in figure 7.45. In this figure, a detail of the detected shelters at site 1 is shown.

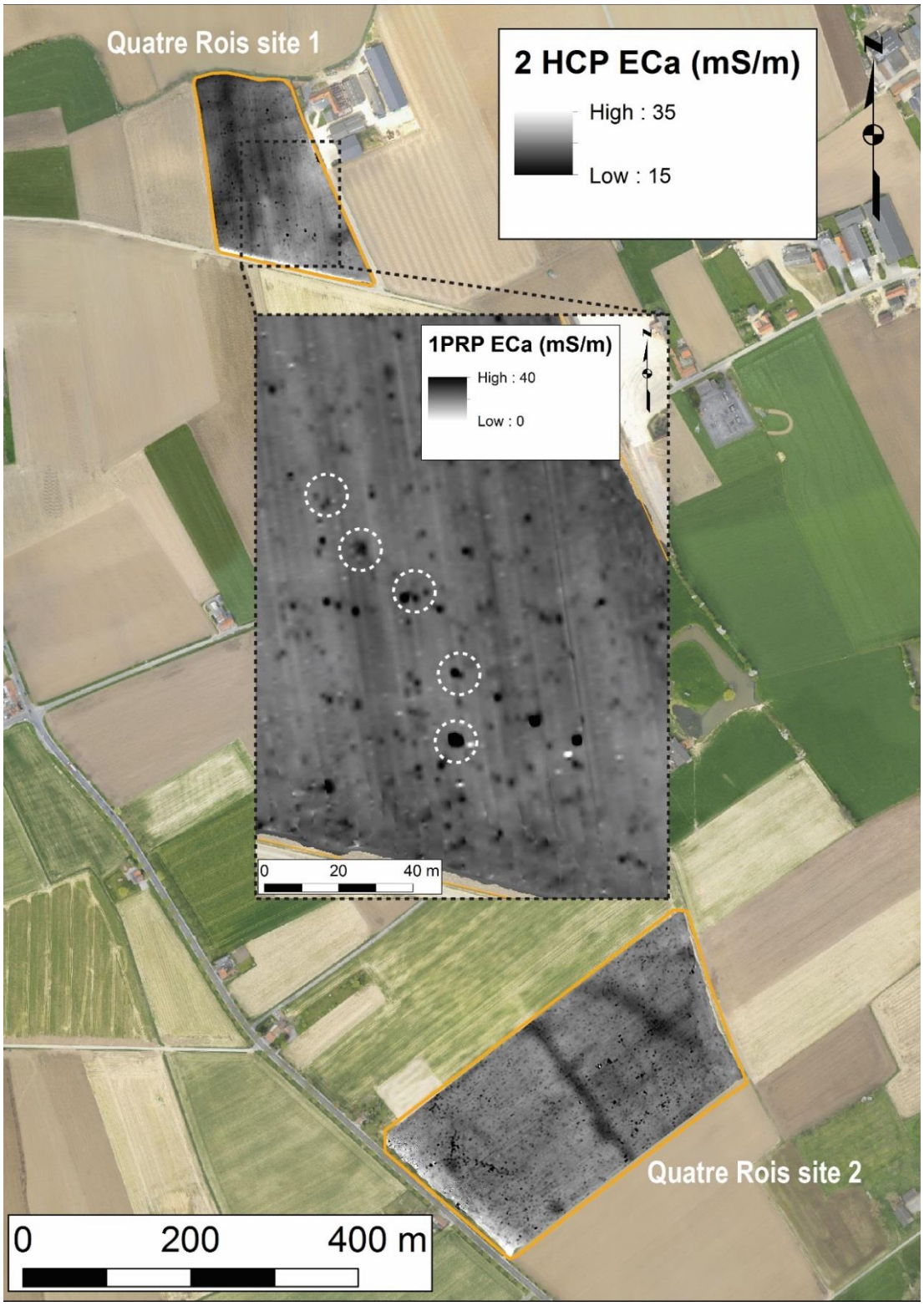



**Figure 7.45:** Display of both Quatre Rois sites with visualisation of the 2HCP $EC_a$ data layer. A detail of site 1 is shown containing detected shelters (dashed white circles). (orthophoto: copyright AIV)

#### *7.3.3.5 German hinterland site (ID 28)*

This former German ammunition storage terrain is situated near the Lanmosnier farm in Wervik and was surveyed during the spring of 2015. This area remained German hinterland during the war. The limited shelling results in low scoring metal indication parameters: 0.3% area FEMP and 10 MOH/ha. These numbers are under the threshold of the metal enrichment of the front area. On this site, only a few dug features were identified by RSA. The bunker in the middle of the parcel is the only trace that is dominant in this survey. Based on the indication of metal on the bunker location, it can be expected that reinforced concrete is still present. None of the other superficial traces were detected (ammunition storage infrastructure). Only some larger detected metal pieces can be associated with ammunition. The landowner confirmed that in the first decades after the war, ammunition was ploughed up. Nowadays, this phenomenon is rare. With 10 MOH/ha, this was be confirmed by the EMI scan. The low rate of shelling in combination with the above-ground WW1 structures (paths and ammunition storage buildings) and the constant arable conditions after the war, makes it explainable why almost no linear traces were detected (DR: 5%). One data layer of the EMI-scan can be found in figure 7.46.

#### *7.3.3.6 Other sites (ID 18 - 19 - 24 - 25 - 30 - 31)*

Not all sites related to transect 3, are discussed in this chapter but their parameters are included in this research to draw conclusions. This is because some of them did not include detected military infrastructure to discuss (ID 19 Sterkte Cabaret; ID 31 Ploegsteert South site), were discussed in another chapter (ID 18,Hill 80; see chapter 5) or would deliver no significant information or repetition (ID 24 Messines near church; ID 25 Huns Walk; ID 30 Flattened farm). Images of the scan results of these fields can be found in the appendices of this chapter.

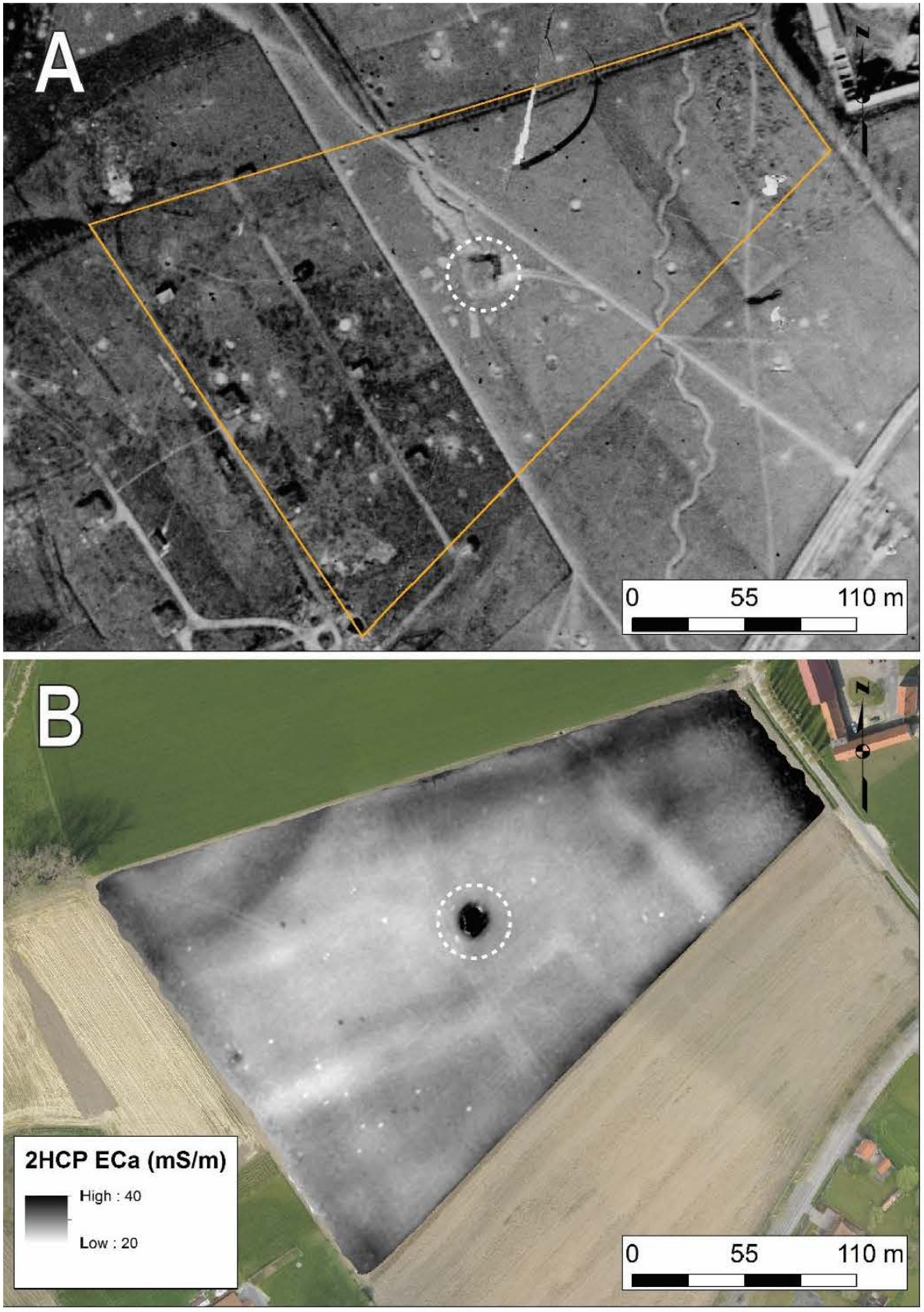



**Figure 7.46:** Visualisation of the ammunition storage site in Wervik (ID 28). Image (A) shows an aerial photograph from March 1918 (AMW collection). Image (B) shows the 2HCP $EC_a$ data scan result. At both images, the central bunker is visible and marked with a dashed line.

#### *7.3.3.7 An overview of the 3rd transect results*

A few trends are remarkable for this elevated area south of Ypres:

- On all scanned sites, traces from WW1 were found (shell crater/trench/bunker/cable/…). For the majority of the sites which are not located near the 1915-17 front, RSA provided sufficient information for the localisation and identification of linear features. For those areas, the rate of extra detected linear features is close to 0%. This means that by applying EMI scans, not many extra potential linear WW1 features were found (average 4.2%) compared to the aerial photography.
- The 'extra' detection score for the near 1915-17 frontline sites is higher (14.7%). At some of these sites such as D'Haino farm (ID 6), Petit Bois (ID 7-8-9) and Maedelstede site 1 (ID 16), the contribution of EMI in locating and identifying extra linear features was clearly demonstrated (up to 30% extra features). This was mainly caused by the complex situation of dense and long-term shelling in combination with a high density of linear structures.
- Because of the long-term shelling, it can be expected that the metal parameters for the near 1915-17 frontline sites are the highest. This was confirmed: 411 MOH/ha and 6.5% area FEMP for the 1915-17 front sites (N =12, 55.7 ha) compared to 146 MOH/ha and 3.6% area FEMP for the other southern front sites (N=10, 37.8 ha). Values for each site can be found in table 7.13.
- A large share of pasture or grass land in this area remained under the same land use conditions after the war. This results in beautifully preserved micro topographies that still hold the remnants of war. LIDAR is useful in this area because untouched post-war pastureland is not rare at this section of the front. In the land use quotation of the surveyed sites (table 7.16), terrains holding a positive quotation (such as pasture, grassland or orchard), are often linked to WW1 traces in the micro relief.

**Table 7.12:** Detected feature lengths, expressed in percentage detected by EMI compared to RSA-data for each site.

| ID & Name | Com. trench | Firing trench | Lin. density RSA (m/ha) | Detection rate | Extra |
|---|---|---|---|---|---|
| **01 Groot Lokerehof farm** | - | - | - | - | - |
| **02 Site near Loker** | - | 33.8% | 128 | 58.7% | 0.0% |
| **03 Bruloose Cabaret** | - | 93.8% | 131 | 62.6% | 0.0% |
| **04 Mount Kemmel** | 100.0% | 100.0% | 130 | 100.0% | 0.0% |
| **05 Van den Bogaerde farm** | 14.8% | 43.6% | 173 | 35.0% | 0.0% |
| **06 D'Haino farm** | 68.9% | 0.0% | 602 | 31.4% | 31.1% |
| **07-08-09 Petitbois** | 28.3% | 1.6% | 283 | 12.8% | 23.4% |
| **10 Kruisstraat craters** | 23.5% | 28.3% | 457 | 26.0% | 5.3% |
| **11 Hollandseschuur farm** | 14.3% | 78.3% | 136 | 45.6% | 39.0% |
| **12 Hollandseschuur farm** | 19.3% | 40.9% | 540 | 23.4% | 8.6% |
| **13 Hollandseschuur farm** | 28.9% | - | 261 | 28.9% | 4.5% |
| **14 Hollandseschuur farm** | - | 81.1% | 61 | 81.1% | 0.0% |
| **15 Renty farm** | 18.8% | 37.2% | 485 | 30.5% | 6.9% |
| **16-17 Maedelstede farm** | 17.0% | 30.9% | 347 | 26.2% | 33.3% |
| **18 Hill 80** | 0.0% | 62.7% | 432 | 49.2% | 31.1% |
| **19 De sterkte Cabaret** | - | 0.0% | 57 | 0.0% | 0.0% |
| **20 Oost Taverne site 1** | 0.0% | 0.0% | 330 | 0.0% | 0.0% |
| **21 Oost Taverne site 2** | 0.0% | 0.0% | 101 | 0.0% | 0.0% |
| **22 Oost Taverne site 3** | 41.6% | 36.7% | 300 | 38.9% | 6.0% |
| **23 Plus Douve farm** | 79.5% | 103.1% | 299 | 70.3% | 30.9% |
| **24 Messines near church** | 33.6% | 0.0% | 400 | 25.6% | 107.9% |
| **25 Huns Walk** | - | 64.8% | 331 | 72.6% | 0.0% |
| **26 Les Quatre Rois Cabaret site 1** | - | 0.0% | 8 | 0.0% | 0.0% |
| **27 Les Quatre Rois Cabaret site 2** | 73.2% | 42.9% | 121 | 38.3% | 17.8% |
| **28 Ammunition storage area Wervik** | 69.0% | 0.0% | 116 | 5.1% | 5.1% |
| **29 Douve farm** | 73.9% | 68.4% | 536 | 66.3% | 9.6% |
| **30 Flatened farm** | 68.0% | 46.7% | 311 | 54.9% | 14.8% |
| **31 Ploegsteert south site** | - | - | - | - | - |

**Table 7.13:** Metal parameters (MOH/ha and % area metal) and shelling densities expressed per hectare for each site

| ID & Name | MOH/ha | % area metal | Sh.h/ha |
|---|---|---|---|
| **01 Groot Lokerehof farm** | 243.9 | 1.7% | 170 |
| **02 Site near Loker** | 191.0 | 4.7% | 125 |
| **03 Bruloose Cabaret** | 115.2 | 2.6% | 72 |
| **04 Mount Kemmel** | 475.4 | 7.3% | 89 |
| **05 Van den Bogaerde farm** | 177.0 | 3.0% | 55 |
| **06 D'Haino farm** | 154.3 | 4.3% | 111 |
| **07-08-09 Petitbois** | 227 | 5.8% | 373 |
| **10 Kruisstraat craters** | 207.7 | 8.3% | 157 |
| **11 Hollandseschuur farm** | 156.4 | 5.0% | 219 |
| **12 Hollandseschuur farm** | 357.3 | 5.1% | 149 |
| **13 Hollandseschuur farm** | 359.7 | 10.6% | 273 |
| **14 Hollandseschuur farm** | 434.7 | 7.7% | 144 |
| **15 Renty farm** | 282.9 | 9.4% | 117 |
| **16-17 Maedelstede farm** | 163.7 | 6.7% | 135 |
| **18 Hill 80** | 365.4 | 7.3% | 181 |
| **19 De sterkte Cabaret** | 225.1 | 3.3% | 272 |
| **20 Oost Taverne site 1** | 385.7 | 10.6% | 319 |
| **21 Oost Taverne site 2** | 419.5 | 9.2% | 178 |
| **22 Oost Taverne site 3** | 261.0 | 4.8% | 111 |
| **23 Plus Douve farm** | 97.3 | 3.0% | 21 |
| **24 Messines near church** | 111.6 | 1.7% | 65 |
| **25 Huns Walk** | 200.0 | 3.3% | 238 |
| **26 Les Quatre Rois Cabaret site 1** | 69.1 | 1.1% | 256 |
| **27 Les Quatre Rois Cabaret site 2** | 147.4 | 3.0% | 185 |
| **28 Ammunition storage area Wervik** | 9.9 | 0.3% | 1 |
| **29 Douve farm** | 169.7 | 6.8% | 502 |
| **30 Flatened farm** | 118.7 | 2.3% | - |
| **31 Ploegsteert south site** | 100.5 | 2.0% | 83 |

**Table 7.14:** Time series of land use for each site (P = pasture / A = arable land/ O = orchard)

| ID | Name | 1940-45 | 1971 | 1989-90 | 2000 | 2014-18 |
|---|---|---|---|---|---|---|
| 1 | Groot Lokerehof farm | P | P | A | A | A |
| 2 | Site near Loker | O | O | A & P | A & P | A |
| 3 | Bruloose Cabaret | A | A | A | A | A |
| 4 | Mount Kemmel | P | P | P | P | P |
| 5 | Van den Bogaerde farm | A & P | A & P | A | A & P | A |
| 6 | D'Haino farm | A | A | A | A | A |
| 7 | Petit Bois site 1 | A | A | A | A | A |
| 8 | Petit Bois site 2 | P | P | P | P | P |
| 9 | Petit Bois site 3 | P | P | P | P | P |
| 10 | Spanbroeck Cabaret | A | A | A | A | A |
| 11 | Hollandscheschuur farm site 1 | A | A | A | A | A |
| 12 | Hollandscheschuur farm site 2 | P | P | P | P | P |
| 13 | Hollandscheschuur farm site 3 | A & P | A & P | P | P | P |
| 14 | Hollandscheschuur farm site 4 | P | P | P | P | P |
| 15 | Renty farm | A | A | A | A | A |
| 16 | Maedelstede farm site 1 | A | A | P | P | P |
| 17 | Maedelstede farm site 2 | P | P | P | P | P |
| 18 | Hill 80 | A | A & P | A & P | A & P | A & P |
| 19 | De Sterkte Cabaret | A | A & P | P | P | A |
| 20 | Oost Taverne site 1 | P | P | A & P | A | A |
| 21 | Oost Taverne site 2 | P | P | P | P | P |
| 22 | Oost Taverne site 3 | A | A | A | A | A |
| 23 | Plus Douve farm | A | A | A | A | A |
| 24 | Messines near Church | P | P | A | A | A |
| 25 | Huns Walk | A | A | A | A | A |
| 26 | Les Quatre Rois Cabaret site 1 | A | A | A | A | A |
| 27 | Les Quatre Rois Cabaret site 2 | A | A | A | A | A |
| 28 | Ammunition storage area Wervik | A | A | A | A | A |
| 29 | Douve farm | A | A & P | A & P | A | A |
| 30 | Flattened farm | A | A | A | A | A |
| 31 | Ploegsteert south site | A & P | A & P | A & P | A & P | A & P |

**Table 7.15:** Definition of weights given to each type of land use, divided over two periods which represents a different grade of intensity representing the effect on preservation of traces (P = pasture / A = arable land/ O = orchard).

| Land use | 1940-1971 | 1989 - 2018 |
|---|---|---|
| A | 0 | -1 |
| P | 1 | 1 |
| O | 1 | 1 |
| A & P | 0.5 | 0 |

**Table 7.16:** In this table, weights are given to each period of land use verification. The sum of those weights gives a general quotation of land use. If WW1 features are detected by EMI of LIDAR, a grade of signature detection is given: present (+/++) or absent (-).

| ID | Name | 1940-45 | 1971 | 1989-90 | 2000 | 2014-18 | Land use quotation | Features EMI | Features LIDAR |
|---|---|---|---|---|---|---|---|---|---|
| 1 | **Groot Lokerehof farm** | 1 | 1 | -1 | -1 | -1 | -1 | + | - |
| 2 | **Site near Loker** | 1 | 1 | 0 | 0 | -1 | 1 | + | - |
| 3 | **Bruloose Cabaret** | 0 | 0 | -1 | -1 | -1 | -3 | ++ | - |
| 4 | **Mount Kemmel** | 1 | 1 | 1 | 1 | 1 | 5 | ++ | ++ |
| 5 | **Van den Bogaerde farm** | 0.5 | 0.5 | -1 | 0 | -1 | -1 | + | - |
| 6 | **D'Haino farm** | 0 | 0 | -1 | -1 | -1 | -3 | ++ | - |
| 7 | **Petit Bois site 1** | 0 | 0 | -1 | -1 | -1 | -3 | + | - |
| 8 | **Petit Bois site 2** | 1 | 1 | 1 | 1 | 1 | 5 | + | + |
| 9 | **Petit Bois site 3** | 1 | 1 | 1 | 1 | 1 | 5 | + | + |
| 10 | **Spanbroeck Cabaret** | 0 | 0 | -1 | -1 | -1 | -3 | ++ | - |
| 11 | **Hollandscheschuur farm site 1** | 0 | 0 | -1 | -1 | -1 | -3 | + | - |
| 12 | **Hollandscheschuur farm site 2** | 1 | 1 | 1 | 1 | 1 | 5 | + | ++ |
| 13 | **Hollandscheschuur farm site 3** | 0.5 | 0.5 | 1 | 1 | 1 | 4 | + | + |
| 14 | **Hollandscheschuur farm site 4** | 1 | 1 | 1 | 1 | 1 | 5 | + | + |
| 15 | **Renty farm** | 0 | 0 | -1 | -1 | -1 | -3 | + | - |
| 16 | **Maedelstede farm site 1** | 0 | 0 | 1 | 1 | 1 | 3 | ++ | + |
| 17 | **Maedelstede farm site 2** | 1 | 1 | 1 | 1 | 1 | 5 | + | ++ |
| 18 | **Hill 80** | 0 | 0.5 | 0 | 0 | 0 | 0.5 | ++ | + |
| 19 | **De Sterkte Cabaret** | 0 | 0.5 | 1 | 1 | -1 | 1.5 | + | - |
| 20 | **Oost Taverne site 1** | 1 | 1 | 0 | -1 | -1 | 0 | + | + |
| 21 | **Oost Taverne site 2** | 1 | 1 | 1 | 1 | 1 | 5 | + | ++ |
| 22 | **Oost Taverne site 3** | 0 | 0 | -1 | -1 | -1 | -3 | + | - |
| 23 | **Plus Douve farm** | 0 | 0 | -1 | -1 | -1 | -3 | + | - |
| 24 | **Messines near Church** | 1 | 1 | -1 | -1 | -1 | -1 | + | - |
| 25 | **Huns Walk** | 0 | 0 | -1 | -1 | -1 | -3 | + | - |
| 26 | **Les Quatre Rois Cabaret site 1** | 0 | 0 | -1 | -1 | -1 | -3 | + | - |
| 27 | **Les Quatre Rois Cabaret site 2** | 0 | 0 | -1 | -1 | -1 | -3 | ++ | - |
| 28 | **Ammunition storage area Wervik** | 0 | 0 | -1 | -1 | -1 | -3 | + | - |
| 29 | **Douve farm** | 0 | 0.5 | 0 | -1 | -1 | -1.5 | ++ | + |
| 30 | **Flattened farm** | 0 | 0 | -1 | -1 | -1 | -3 | + | + |
| 31 | **Ploegsteert south site** | 0.5 | 0.5 | 0 | 0 | 0 | 1 | + | NA |

## 7.4 Conclusions

After more than 100 years, a considerable part of the original WW1 infrastructure is still present in the subsoil. The non-invasive research in this chapter supports this statement, which was due to a successful integration of GSS with aerial photography and ALS to evaluate the occurrence of buried WW1 remains on a local scale and extracting general trends from this to describe the front region (regional scale). The analysis on the information gathered with these techniques, provided the tools to evaluated trends in preservation of WW1 infrastructure without digging into the ground. The advantage of this research is its minimum impact onto the sites, soil and annoyance for land user/owner in combination with the low-cost gathered datasets compared to archaeological excavations. The general trends and findings discovered in this research, are discussed below.

- The average DR per transect area are shown in table 7.17. On DR, transect 1 & 2 score a similar result (TR1.DR = 21%; TR2.DR = 23%) while the DR of transect 3 is almost double in size (T3.DR = 39%). This higher scoring 3rd transect can partially be explained by the soil properties in relation to other aspects. This trend is similar as in the quotation given in section 7.2.3 to the pedo-landscape units along the former Western Front in Belgium. The 1st transect corresponds with the polder grounds, the 2nd transect mainly with the Ypres clay plain and a part to the higher ridges while transect 3 corresponds almost completely to the 'higher ridges' conditions. It is difficult to prove the direct link between soil conditions and the DR but the literature about soil properties (Doyle, 2017) and entrenching (Bull, 2014) suggested a similar trend whereby the result for the higher ridges (= dominant in 3rd transect) clearly are emerging in both evaluations (evaluation 1: section 7.2 / evaluation 2: section 7.3).

**Table 7.17:** Results of DR and the rate of extra detected linear features per transect zone.

| Transect | **DR** | **extra** |
|---|---|---|
| T1 | 21.2% | 0.0% |
| T2 | 23.0% | 9.0% |
| T3 | 38.6% | 14.1% |

- The impact of human activities on the detection of linear traces is difficult to evaluate. In addition, the EMI scan results proved that land use did not influence the DR. This does not mean that ploughing did not affect the conditions of a buried trench. In some cases, the distribution of the anomaly content in the proximity of the structure can be detected, which is often found in the shallow magnetic data layers of the EMI survey. This phenomenon can give indication of the preserving conditions. Pasture and woodland are known for their better preserving characteristics but the ability to detect those structures was not clearly influenced by different land use types. It is rarely the case that one land use type is maintained during the post-war period. Based on a land use quotation for several periods (derived from tables 7.6, 7.11 and 7.16) whereby positive values represent mainly better preserving grounds (pasture, grassland, grind cover…) and negative values ploughed grounds. The positive quoted grounds reached a median DR of 26% (quartile 0.25 = 9.5%, quartile 0.75 = 45.9%) while the negative quoted site have a median DR of 27.4% (quartile 0.25 = 7.7%, quartile 0.75 = 44.1%). By testing this statistically (Student t-test), no significant differences between both groups were found (t-value = 0.51 < 2.70 for $\alpha = 0.01$).

- A clear relationship was found between the iron clutter densities at the frontline sites and land use. In a first observation, this was determined at a local level. A clear example of this phenomenon in this thesis was found at the Oost Taverne sites (T3 ID 20-21-22) where at the same location of the front, two sites (ID 20-21) were found in continuous post-war pasture conditions and the 3$^{rd}$ site (ID 22) in continuous post-war arable state. Both pasture plots score double on EMI metal parameters compared to the plot in post-war arable conditions. Other observations at multiple sites in this thesis confirmed this influence as well. If this trend is compared for all surveyed sites in a similar way as the one for the detected linear traces and land use quotation, the positive quoted fields score almost double on metal indicators. This trend was confirmed in all three transects. Overall, average values of 272 MOH/ha and 6.8% area FEMP are found for positive quoted fields and 141 MOH/ha and 3.2% area FEMP for negative quoted fields. An important influence on this result is the intensity of warfare related to the metal debris in the soil. This is varying along the front and therefore influencing this comparison. If the sites from the 1$^{st}$ transect and the hinterland sites are excluded from the dataset because of their lower intensity of warfare, this trend is still confirmed on a statistical level (t-value: MOH/ha = 4.18; % area

FEMP = 3.64, both > 2.70 for α = 0.01). In ideal circumstances to avoid the influence of warfare intensity, each sampling location should contain two fields, each belonging to one of the land use groups. By selecting only the heavily concurred sites, the effect of variations in warfare intensity should mainly be avoided. From these results can be concluded that land use has certainly an effect onto encountering WW1 remains: the mechanical sifting by agricultural activities are clearly reducing the smaller pieces of metal debris and other military metal finds. The detection of war related micro topographies in ALS data is a second indicator which can point out the intensity of metal clutter finds, as it is strongly correlated with land use (Gheyle et al., 2018).

- There is only a little knowledge about the extent of soil cleaning and levelling actions on WW1 battlefields. EMI provides the possibility of studying this by detecting metal and shell craters as shallow WW1 features whereby the quality and the presence these two types of WW1 remains give an indication if metal debris was removed or shell craters were damaged (by ground levelling) in the first half metre of soil. Variations of both indicators within one field and one land use unit were several times found in the EMI scan results.

- Places where the Eocene clay is near surface or grounds with dry sands were often kept as pasture or grassland because of the 'heavy grounds' or dry conditions for crops. In these cases, WW1 features stand a better chance to be preserved in good conditions. To locate these grounds, the DOV-database (dov.vlaanderen.be) can be consulted.

- Because of complex situations such as fast evolving and often shortly used military networks in combination with continuous changing positions, heavy fighting and shelling at frontlines, the infrastructure is difficult to interpret with geophysical exploration alone. The additional use of aerial photography is necessary in those areas to reach a maximum of non-invasive information. More specifically, this is the fact for the 1915-17 frontlines the 2$^{nd}$ and 3$^{rd}$ transect. The intensive battles made feature identification not easy because of the high rate of destruction and the unmet need for a denser temporal aerial observation. Therefore, in these transects, extra WW1 related linear features were regularly found with GSS. This is displayed in table 7.17 where the percentages of extra detected linear WW1 features are given. These numbers peak around the 1915-17 front for both 2$^{nd}$ and 3$^{rd}$

transect. These extra features are trenches, camouflaged trenches or communication cables. In most cases, the detection of cables for archaeological purposes is not beneficial but in some cases, these cables can reveal unseen structures such as camouflaged trenches.

- No large differences were found between the detection of firing (DR = 41%) and communication trenches (DR = 43%). This was statistically tested (t-value = 0.33 < 2.66 for $\alpha = 0.01$) and proven valid. At the start of this analysis, the nationality of the trenches was considered to take in account because each fighting party had its own typical way of trench construction and use of materials (Bull, 2014). Because this is something complex (use of mixed materials by all parties, reuse of trenches by other parties, land cleaning etc.) and no indications were found in the scan results, this research track was abandoned.

- Traces of two moated medieval sites and a 17-18$^{th}$ century ornamental garden were detected in heavily shelled areas. These examples showed that WW1 battles at the front did not always destroy important older archaeological traces and that these traces remain detectable by geophysics.

# Chapter 8

Conclusions and future perspectives

The general aim of this research was to explore the potential of geophysical soil sensors to characterise the buried WW1 remains on the former Western Front in Belgium whereby following areas were examined:

- The weighting of geophysical soil sensors in relation to each other for the exploration of WW1 features.
- The validation of a limited number of buried WW1 features to get insights in the geophysical chartability of structures.
- A comparison between a geophysical scan, detected features by RSA and the results of a surface covering archaeological excavation.
- An effective method to identify and extract metal objects and shell craters in FD-EMI scans, as these features are omnipresent in this historical conflict region.
- A technique to map the destruction of WW1 based on aerial photography, with integration of GSS to simulate the metal debris and shrapnel pollution, caused by the intense artillery shelling during the war.
- The exploration on a regional scale of buried WW1 features by carrying out large-scale geophysical research, with feedback to other non-invasive archaeological techniques.

Next to the WW1-related research topics, an improvement in the domain of data processing for magnetometry was achieved. To give an overview of the covered topics, feedback is made on the original objectives, set in chapter 1.

**Objective 1**: *The evaluation of different geophysical soil sensing techniques for the prospection of WW1 conflict landscapes*.

The reason to investigate this objective was that fluxgate magnetometry and GPR are the main applied techniques in exploration geophysics, commercially available in Belgium. For the heavily (magnetic) disturbed sites at the former Western Front, these techniques seemed to have limitations to prospect non-invasively this former conflict region (Masters & Stichelbaut,

2009). By comparing a set of popular techniques, these findings were confirmed. The objective's conclusion pointed out that EMI-techniques were more adapted to characterise the WW1 archaeology in the soil conditions of the study area. This should be taken into account for all those who want to apply geophysics in that region to execute successful interpretable soil scans. By investigating this objective, suggestive guidelines were created for the professional field. The importance of the application of geophysical prospection is growing as new developments are increasing in this former conflict region. Therefore, sensor evaluation and the creation of guidelines was an important issue to cover. A summary of the technique evaluation can be found below.

**Summary**

Five popular geophysical techniques were evaluated on the base of their application near the former WW1 front whereof 3 of them delivered satisfying results: FD-EMI, TD-EMI and FGM. Based on maximum coverage of military infrastructure and the identification of different types of structures, FD-EMI produced the best results. A first advantage of FD-EMI is that it measures both magnetic and electric properties of the soil (FGM and TD-EMI only magnetic), whereby multiple data layers are provided with their own characteristics. Second, EMI-techniques are much less sensitive to strong magnetised objects than the highly sensitive FGM sensors, which makes them more suited for feature identification in heavily shelled areas. On the other hand, both FGM and TD-EMI sensors have a more concentrated spatial resolution (vertical vector measurements) and sampling density, which produce finer datasets. Therefore, these techniques are more suited for magnetised object localisation (bricks, metal bars/plates/debris, UXO) then FD-EMI.

Based on the examination of the GPR results, the wet and alluvial soils of the former Western Front in Belgium are attenuating the electromagnetic signals, which result in measuring mainly shallow near surface phenomena. As exploring scanning technique, GPR is not well suited. The bombturbated soils in combination with the metal debris produces extra noise to identify sharply delineable structures. The only case where GPR can deliver extra information is when another exploring survey is executed and extra depth information is needed of a localised detected feature but even that is no guarantee for success.

An exploring ER scan is more suited for archaeological prospection in these WW1 conflict landscapes than GPR. The moisture bearing alluvial soils in the study area are well suited for

this technique. Unlike the other sensors, this one is insensitive to (small) pieces of metal, which can be useful in heavily disturbed areas. The main disadvantages are the slow measuring/coverage speed, the lower spatial resolution and the issue whereby the contact electrodes (for this thesis: coulter discs) have to penetrate the ground and maintain good contact: this is risk-full to hit UXO. Manually operated arrays are a safer alternative.

**Objective 2**: *The improvement of fluxgate magnetometer data by developing a focussed approach to reduce interfering noise sources.*

Two disturbing noise sources were identified and tackled in this thesis to improve the FGM dataset: (i) A spatial filter to identify and remove overlapping data sampling areas, which were causing interfering striping effects; (ii) A one-dimensional filter based on wavelets, directly applied onto the data strings to reduce the wave effects caused by sensor tilt noise. This second filtering procedure is in the field of archaeology new and different to the 2D smoothing filters - often applied on the interpolated data grids - to reduce similar noise effects. This technique proved to be successful without producing blurred images (unwanted loss of information) and could be used to tackle other noise sources or implemented in the processing for other sensors. Its main advantage is that the tilt noise is better targeted than with the 2D image processing. Therefore, the development of this technique was completed and finetuned. The implementation of this filter into a geophysical data processing toolbox is something that should be considered in the future.

**Objective 3**: *The identification and validation of geophysical anomalies.*

Three topics were examined to research this objective. The first topic deals with a characterisation of metal objects and shell craters. FD-EMI offers the possibilities to identify metal features unambiguously in the topsoil (compared to other techniques). This identification is possible due to the multiple coil combinations of the sensor and the $EC_a$ response. For shell craters, additional WW1 period aerial photography is recommended as verification source to exclude other soil disturbances. The identification of both features is important because their presence can give information about the state of the surveyed field (ground-clearing actions,

indicator for preserved traces, high metal indications and UXO…) and it can be used to guide soil interventions in archaeological investigations (next to the aerial photograph identification). The second topic is a one-site study case whereby surface covering archaeological excavation results are compared to RSA and GSS. This comparison was the result of a rare opportunity whereby a scanned site (with multiple techniques) was completely invasively investigated. Comparing excavation reports with detection results from multiple scanning techniques, is something which was never done before on a WW1 site and it gave a unique insight in the mapping abilities of the three applied techniques. It was concluded for this site that no non-invasive technique delivered a full coverage of buried linear traces (compared to excavation results) and the combination of RSA and GSS provided a more complete result then both separately. In addition, the delineation of trenches and building remains could be sharply and accurately performed based on both EMI techniques.

For the third topic, four specific structures were measured with FD-EMI and identified based on RSA and historical information. By applying invasive validation techniques (augering/excavation), the reason why these structures are measured, was identified. These limited number of validation cases gave the answer to if remains of tanks, (deep) dugouts and a mass grave can still be detected after a century. The detectability of these features is less evident than the detection of e.g. trench remains. By investigating these cases, the possibility of detecting these features was demonstrated. The cases are unique in the field of applied geophysics in former WW1 conflict regions and were therefore covered in this thesis. The most remarkable case was the indirect detection of a dugout structure. This was possible due to the detection of shallow filled up cavities with magnetic contrasting topsoil. These cavities were caused by the collapse of the dugout galleries and filled up by agricultural activities. This phenomenon is regularly observed near tunnelling hotspots and can be used as indicator for degrading tunnelling infrastructure. This specific case showed the usability of the FD-EMI technique for the investigation of underground (degrading) WW1 infrastructure.

**Objective 4**: *The development of a non-invasive method to characterise the destruction of the war on a regional scale.*

To meet the need for a detailed destruction map, the answer was found in the extensive library of georeferenced aerial photographs (Stichelbaut, 2011a; Stichelbaut et al., 2017) which

covers most parts of the Western Front in Belgium and can be considered as a unique database, even at an international level. This database creates opportunities to investigate unexplored potential. One of these is the use of the dense aerial photograph coverage of the front region for mapping the destruction caused by the war. To execute this spatial analysis, a new parameter of shelling densities was introduced as objective approach. This approach is applicable at almost every location at the former Western Front and is different from the technique of destroyed landscape interpretation that was used by the French. To make this process of destruction mapping feasible on a regional scale, a sampling strategy was applied. This was tested in a 142.5 $km^2$ area where it was found successful in mapping the historical destruction by only sampling 0.54% of the area. This strategy is an instrument to study the impact of war onto the soil for several purposes. It allows visualising the former front as an area of varying intensities and not only as linear representations of the frontline phases or the trench infrastructure. It is the first time that this method was applied and it opened up opportunities to be used as a spatial analysis tool for several purposes. One example is the localisation and intensity characterisation of the metal war debris in the soil: from FD-EMI scans derived metal parameters correlate with the shelling densities on WW1 aerial photographs. Based on this information, areas with a higher chance of encountering UXO can be localised.

**Objective 5**: *Mapping buried war traces on a regional scale to characterise the current state of the subsoil of the former Western Front in Belgium.*

For this objective, 236 hectares divided over 54 different locations along the former Western Front in Belgium were prospected with FD-EMI. These scans successfully characterised the presence of buried military remains, which then was compared to the digitised and interpreted aerial photograph dataset. This objective covered a unique insight of what still can be found in the soil in this former conflict region. The way in which this research differs from others is the scale and the window it creates into the unknown state of the soil matrix by applying a non-invasive technique. In a first phase, the results were examined at an individual scale to 'understand' how WW1 can be seen in the data. In a second phase, parameters were derived from those scans to quantify the detection of linear features such as trenches. Also land use conditions and LIDAR were examined. In addition, metal parameters and shelling densities

were determined for each site to characterise the impact of artillery. These parameters were used to discover trends over all surveyed sites.

From this large-scale analysis, following general trends were discovered:

- The heights south of Ypres (transect 3) contained a higher rate (almost double) of detectable linear features than the Ypres clay plain and the polder area near Ramskapelle.
- In dense shelled areas near the 1915-17 front, extra detected linear features were often found with GSS compared to the aerial photograph database. These areas in the Ypres Salient contained the densest entrenched networks along the front with daily changing situations. This is the main cause for this trend. This means that GSS is useful in those areas to characterise unseen features by the aerial photograph coverage because of the intensity and long period of static warfare. For other less fought areas, aerial photography is often sufficient to map the trench networks.
- Despites the immense historical destruction near the former front, older archaeological remains can still be found by geophysics.
- Land use had an effect on the iron clutter in the subsoil in the post-war period: parcels under mainly pasture conditions contain increased scores on metal object indications if compared to mainly arable conditions. This information is useful for the domain of UXO clearance because it can give an indication of the intensity (=costs) of ground clearance.
- Selective land cleaning patterns were discovered. The possibility to map this is useful because land cleaning was not well tracked. This gains importance for areas where suitable terrains have to be chosen for new development works. The lower the presence of dangerous war remains (= better cleaned), the more suited to reduce the costs of archaeological investigation and UXO clearance. Therefore, this application of exploration geophysics can be a useful tool for the development businesses in that region.

**Future perspectives – Implementation results**

- The findings describing the application of GSS on WW1 sites, could be integrated as guidelines (basis) for carrying out geophysical surveys as part of the archaeological investigation process in Flanders or conflict landscapes with similar soil conditions.

- The non-invasive characterisation of sites is able to support the protection of archaeological landscapes: On August 21, 2018, a ministerial policy was carried out to protect the Crater Wood and Railway Wood near Bellewaarde as an archaeological landscape (besluiten.onroerenderfgoed.be, 2018). The scans carried out for this thesis near Crater Wood (T2.ID5 Bellewaarde North), were requested to be added to the protection dossier to establish the protective ministerial policy.
- The development of a destruction map for the whole former Western Front in Belgium (expansion of objective 4) is something that attracts much interest from several government departments. Therefore, this idea was integrated in a FWO-SBO project proposal to characterise and delineate the problem area with an increased intensity of UXO finds. From the historical-archaeological point of view, mapping the destruction after important war phases (time dimension) is a still unexplored opportunity. In this thesis, only the phase close to the end of the war was mapped in a limited test area.
- The fact that (collapsed) dugout structures can be retraced by an EMI scan, is a track to continue on because hundreds of deep dugouts were built in the Ypres Salient whereof their exact position is often unknown. These days, notifications of subsidences - caused by the underground tunnelling activities and related to these dugouts – are regularly made. Based on the combination of plan drawings, EMI scans, ALS, augerings and landowner information, the exact location and the condition of multiple dugouts could be examined by the combination of these techniques.
- The characterisation of the buried WW1 heritage with non-invasive soil sensing techniques on a regional scale should make policy makers aware that these former battlefields are still not cleaned from (hazardous) war remains. Nowadays, more projects are coming to this mainly agricultural dominating area. As Flanders has a high urbanisation rate, the open areas at the 'Westhoek' region are being reduced nowadays by residential expansion, recreation and industry. Therefore, a coordinated investigation of newly developing sites in the former WW1 front area is needed. When the open spaces at these former conflict areas are being selected for developments, establishing a cadastre of the subsoil as proposed by Dewilde (2010) is something that should be considered. The use of non-invasive techniques have been demonstrated to be successful to offer the tools to study conditions of new developing terrains.

# Appendices

# Chapter 2

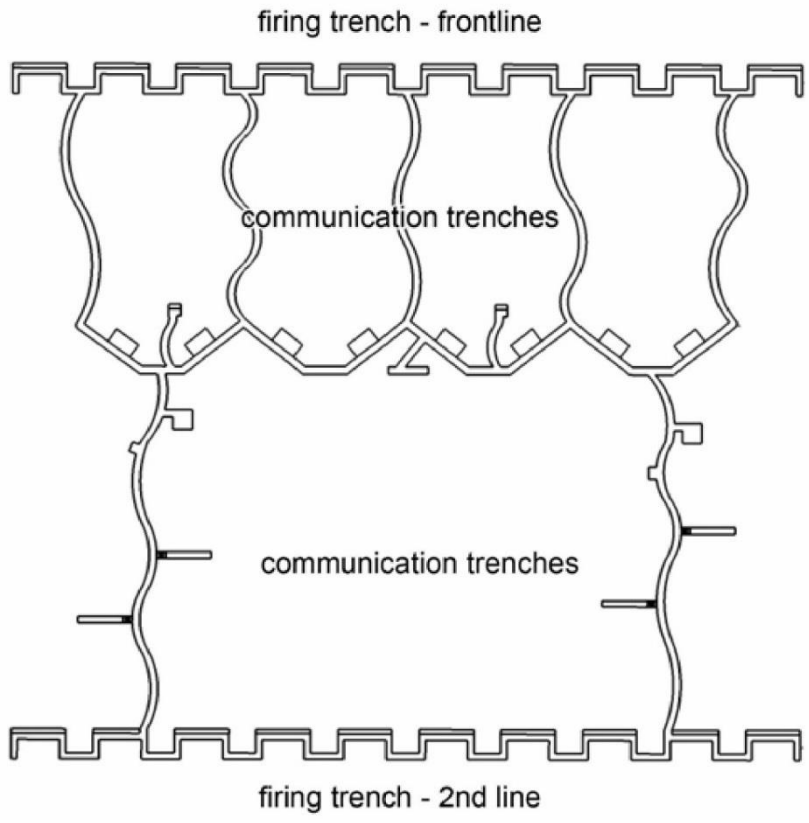
**Appendix 2.1**: Terminology of military infrastructure.

Main concepts of WW1 military infrastructure which are used in this thesis, are listed below (Axelrod et al., 2016).

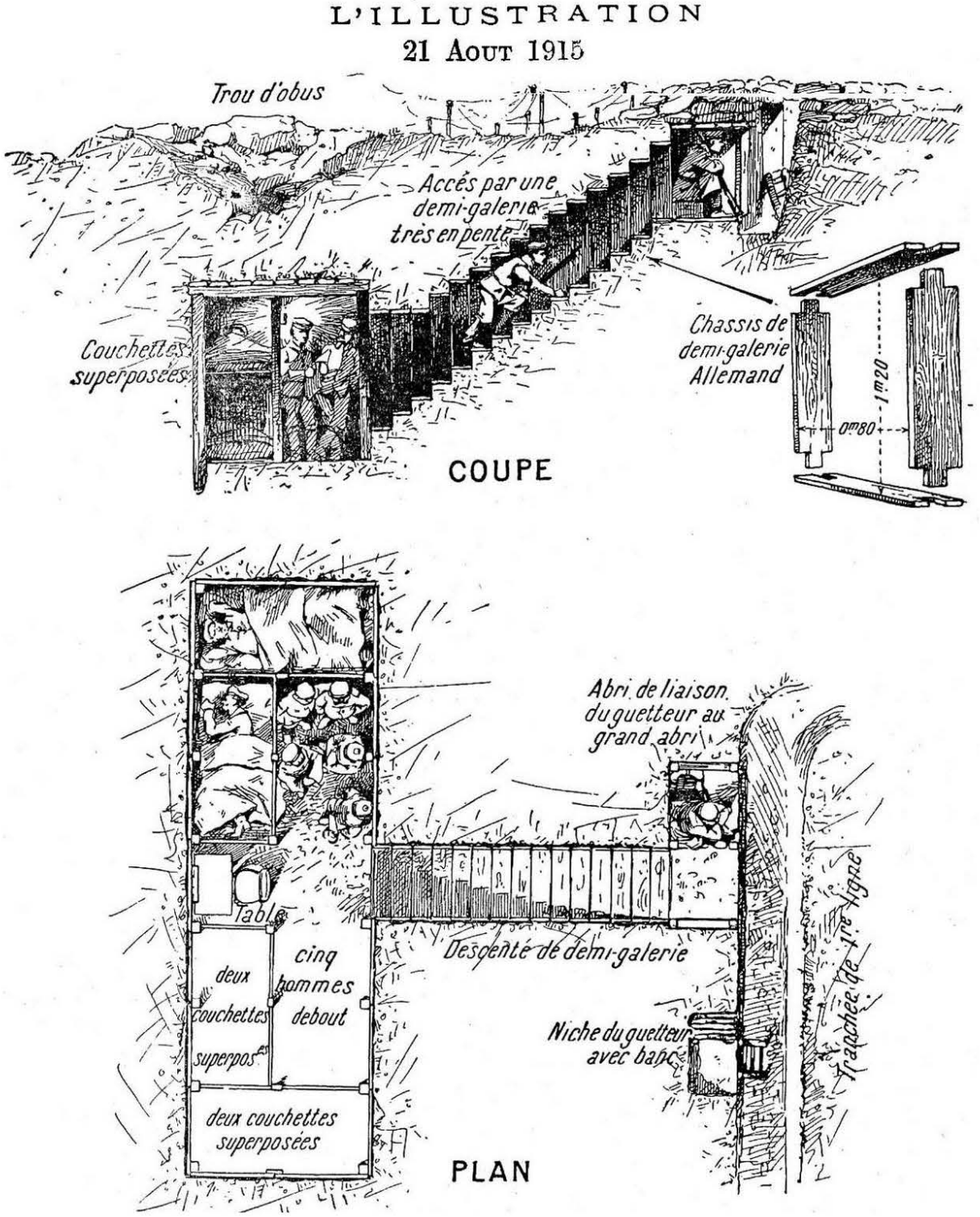
- Trench: a linear man-dug ditch to provide shelter, movement and firing options in war situations. A typical WW1 trench system (diagram) is shown in appendix 2.2.
- Fire trench (firing or fighting trench): Trench near the enemy line to position soldiers with small firearms. This is mostly a frontline construction. The winding shape caused by the fire bays, should prevent explosions/gunfire traveling through the whole trench. Also 2nd line or reserve trenches have a similar signature as the frontline trench, to provide the function when the front trench is taken by the enemy.
- Communication trench: Mostly zigzagging trench as connection between the lines (front-second-reserve line). These trenches are dug at an angle facing towards the enemy and were used to transport soldiers (arriving or wounded men), equipment and food supplies. The non-straight trajectory was used to avoid a direct line of fire from the enemy towards the fleeing soldiers.
- Support trench: This is the trench from which troops could offer support to the front line trench, to rotate troops out of the front line trench or the withdrawal of troops from the front towards this trench.
- Breastworks: Earth fortifications (earth works) around trenches to form a bulletproof protection. Parapet is the earthwork towards the enemy and the parados is the earthwork at the back of the trench system. This ground was used from the dug trench or a borrow pit.
- Sap: Trench excavated towards the enemy to approach them for attacking purposes.
- Bunker: Military defence structure to offer protection against artillery fire and bombing. During WW1, these were often made out of armoured concrete and have a roof.
- Dugout: Men-dug underground structure to protect soldiers and the military staff from the above ground battles and to provide accommodation (sleeping/eating/etc.). Dugouts are often connected to the trench systems. The shallow dugouts are constructed at the same level of the trenches. The deep-dugouts use staircases from the trenches towards the corridors which are located +/- 3 – 6 m beneath the surface. A drawing of such a dugout is shown in appendix 2.3.

- Abri: Small shelter. It is derived from the French word ‘Abrier’ which means shelter. These shelter structures have a roof.
- Shelter: Protective structure for soldiers against artillery fire with a military origin. It is often incorporated in a trench system. It’s a structure without a roof.
- Barrack: Building or group of buildings to house soldiers.
- Shrapnel: Lead or steel bullets within a shrapnel shell, also synonym for small ragged metal fragments.
- Barbed wire: Metal wiring, curling with sharp edges, to obstruct the passage for people.
- Communication cable: copper cable, placed within a ditch or trench, to pass messages by telephone or telegraph.
- Narrow gauge railway: Narrow placed railway tracks for small trains or carts, to move soldiers, food and equipment between hinterland and front. The French, British, German and Belgian armies used a narrow gauge spacing of 600 mm.

**Appendix 2.2**: A schematic representation of a generalised trench system, showing the positions and connections between the different trench types (based on www.homefrontlegacy.org.uk, 2018; His Majesty’s Stationary Office, 1916).



**Appendix 2.3**: Illustrations from a 1915 French soldier manual, visualising a coupe and plan of a German deep dugout system (www.oldmagazinearticles.com, 2018).



**Appendix 2.4:** survey details sites used in thesis.

**Part 1:** Sites in the near the front related to the three main research zones (T1/T2/T3)

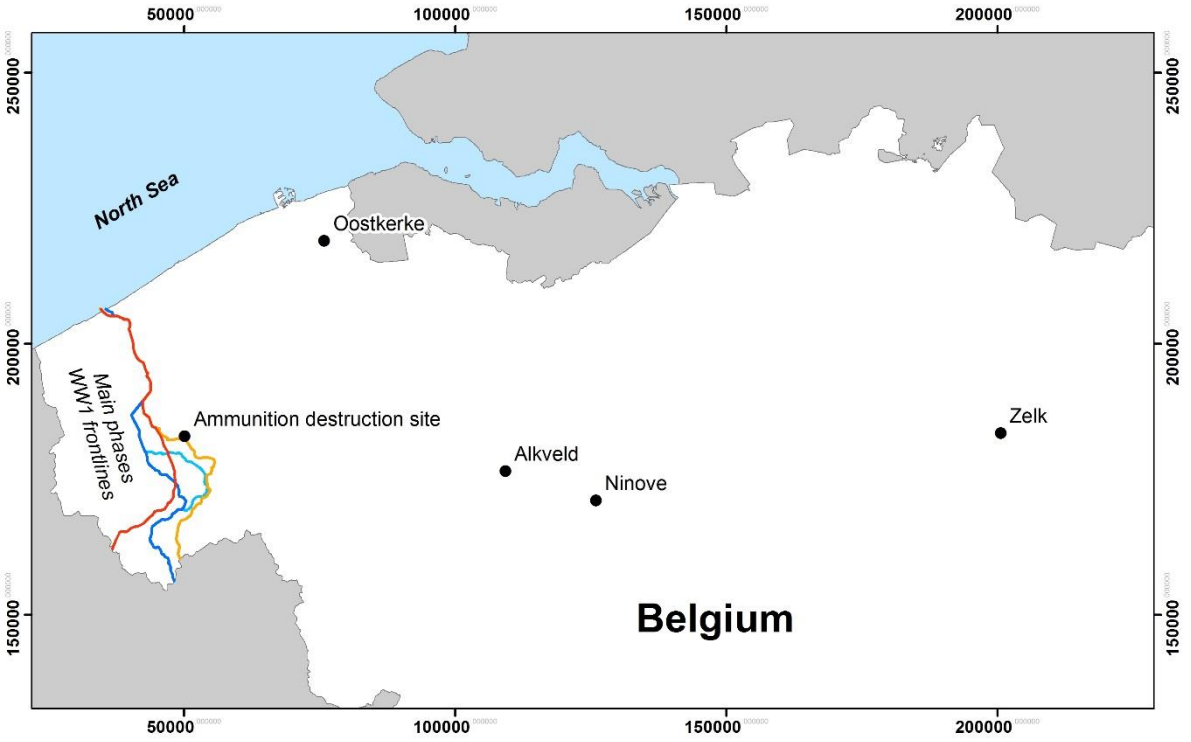
| ID | Name | area (ha) | FD-EMI | TD-EMI | FGM | GPR | ER |
|---|---|---|---|---|---|---|---|
| T1.1 | Chien Marin farm | 4.95 | x | | | | |
| T1.2 | Jokveld farm | 8.45 | x | | | | |
| T1.3 | Oosthof farm | 3.95 | x | | | | |
| T1.4 | Farm B | 6.78 | x | | | | |
| T1.5 | Rycken Hoek | 11.75 | x | | | | |
| T1.6 | Railway | 2.23 | x | | | | |
| T1.7 | Roedesterkte farm | 3.65 | x | | | | |
| T1.8 | Near Yser | 2.29 | x | | | | |
| T1.9 | Frontline gun emplacements | 1.35 | x | | | | |
| T1.10 | Aerodrome | 4.55 | x | | | | |
| T2.1 | Vlamertinge | 5.00 | x | | | | |
| T2.2 | Palingbeek | 3.61 | x | | x | | |
| T2.3 | Zillebeke centre | 1.58 | x | | x | | |
| T2.4 | Cambridge road | 14.63 | x | | | | |
| T2.5 | Bellewaarde north | 3.33 | x | | | | x |
| T2.6 | Bellewaarde centre | 11.67 | x | | | | |
| T2.7 | Bellewaarde west | 5.44 | x | | | x | |
| T2.8 | Bellewaarde south | 7.41 | x | | | | |
| T2.9 | Bellewaarde park | 2.79 | x | | | | |
| T2.10 | Hill 62 | 9.43 | x | | x | x | |
| T2.11 | Clapham Junction | 0.87 | x | | | x | |
| T2.12 | Sint Juliaan | 2.19 | x | | | | |
| T2.13 | Black Watch Corner | 9.86 | x | | | | |
| T3.1 | Groot Lokerehof farm | 3.29 | x | | | | |
| T3.2 | Site near Loker | 2.88 | x | | | | |
| T3.3 | Bruloose Cabaret | 3.02 | x | | | x | |
| T3.4 | Mount Kemmel | 0.99 | x | | | | |
| T3.5 | Van den Bogaerde farm | 5.96 | x | | | | |
| T3.6 | D'Haino farm | 3.15 | x | | | | |
| T3.7 | Petit Bois site 1 | 4.66 | x | | x | x | |
| T3.8 | Petit Bois site 2 | 1.87 | x | | | | |
| T3.9 | Petit Bois site 3 | 3.51 | x | | | | |
| T3.10 | Spanbroeck Cabaret | 13.45 | x | | x | x | x |
| T3.11 | Hollandscheschuur farm site 1 | 2.36 | x | | | | |
| T3.12 | Hollandscheschuur farm site 2 | 1.57 | x | | | | |
| T3.13 | Hollandscheschuur farm site 3 | 2.06 | x | | | | x |
| T3.14 | Hollandscheschuur farm site 4 | 0.61 | x | | | | |
| T3.15 | Renty farm | 2.42 | x | | x | | |
| T3.16 | Maedelstede farm site 1 | 3.06 | x | | x | x | |
| T3.17 | Maedelstede farm site 2 | 1.31 | x | | x | | |
| T3.18 | Hill 80 | 1.07 | x | x | x | | |

| | | | | | | | |
|---|---|---|---|---|---|---|---|
| T3.19 | De Sterkte Cabaret | 1.71 | x | | | | |
| T3.20 | Oost Taverne site 1 | 0.84 | x | | x | | x |
| T3.21 | Oost Taverne site 2 | 2.11 | x | | x | | |
| T3.22 | Oost Taverne site 3 | 6.72 | x | | x | | |
| T3.23 | Plus Douve farm | 2.99 | x | | | | |
| T3.24 | Messines near Church | 1.12 | x | | x | x | |
| T3.25 | Huns Walk | 1.19 | x | | x | | |
| T3.26 | Les Quatre Rois Cabaret site 1 | 3.27 | x | | | | |
| T3.27 | Les Quatre Rois Cabaret site 2 | 8.73 | x | | | | |
| T3.28 | Ammunition storage area Wervik | 5.13 | x | | | | |
| T3.29 | Douve farm | 11.68 | x | | x | | |
| T3.30 | Flattened farm | 3.43 | x | | | | |
| T3.31 | Ploegsteert south site | 2.82 | x | | | | |

**Part 2**: Other sites, measured to perform additional research in and outside the front area in Belgium.

| Name | area (ha) | FD-EMI | TD-EMI | FGM | GPR | ER |
|---|---|---|---|---|---|---|
| Ammunition destruction site | 2.22 | x | | x | | |
| Oostkerke | 0.91 | | | x | | |
| Alkeveld | 0.39 | | | x | | |
| Battle of Halen / Zelk | 3.90 | x | | x | x | |
| Ninove | 0.75 | | | x | | |

**Part 3**: Map indicating the location of the surveyed fields in part 2. The location of the sites in part 1 are well-defined in chapter 7 section 3 and illustrated in figure 2.24.



# Chapter 3

## **Appendix 3.1**: Script for median levelling of FGM data.

```
%%%%%%%%%%%%%%%%%%%%%%%%%%%%%
file = 'Filename.asc'; %file name, *.asc/*.txt/*.csv
%%%%%%%%%%%%%%%%%%%%%%%%%%%%%
gradiometer = 5; % number of gradiometers
sensor(1) = 1; %use sensor(1) = 1, don't use = 0
sensor(2) = 1; %use sensor(2) = 1, don't use = 0
sensor(3) = 1; %use sensor(3) = 1, don't use = 0
sensor(4) = 1; %use sensor(4) = 1, don't use = 0
sensor(5) = 1; %use sensor(5) = 1, don't use = 0
%%%%%%%%%%%%%%%%%%%%%%%%%%%%%
median_removal_per_sensor = 1; %median levelling per sensor
median_removal_per_line = 1; %median levelling per sensor line
median_removal_window = 0; %median levelling moving window
median_window_size = 200; %window size
%%%%%%%%%%%%%%%%%%%%%%%%%%%%%
s_input.dX = 0.25; %gridding resolution (m)
%%%%%%%%%%%%%%%%%%%%%%%%%%%%%
warning('off','all')
addpath('../functions/CSVwrite');
addpath('../data'); %datalocation

dispstat(' START A_sensorsplit_and_range','timestamp','keepthis');
%%
fileID = fopen(strcat(file)); %opgeven in te lezen text, ascii of csv-bestand
zzz = textscan(fileID, '%f %f %f %s %f'); %inlezen file
zzz2 = zzz{4};
no_rows = numel(zzz2);

% Extract data
[za,zb,zc] = unique(zzz2);
zb2 = [zb(2:end)-1;no_rows];
data_row_ID = zeros(no_rows,1);

for loopInd = 1:numel(zb)
    data_row_ID(zb(loopInd):zb2(loopInd),1) = str2num(zzz2{zb(loopInd)}(10:15));
end

% Put in double array
data_in = [zzz{1},zzz{2},zzz{3},data_row_ID,zzz{5}];
% Sort data
data_in_sort = sortrows(data_in,5);

%% select gradiometers

l = length(data_in_sort(:,1));
teller = 1;

for g = 1:gradiometer
    gradiometer_n(g) = l/gradiometer*g;
    sensor_select{g} = data_in_sort(teller:gradiometer_n(g),:);
    teller = gradiometer_n(g)+1;
end

data_in_sort(:,:) = [];

for g = 1 : gradiometer
   if sensor(g) == 1
      data_in_sort = vertcat(data_in_sort,sensor_select{g});
   end
end

%% median removal per sensor

if median_removal_per_sensor == 1
dispstat(' Median removal per sensor','timestamp','keepthis');
nTdata(:,1) = data_in_sort(:,3);
length_nTdata = length(nTdata);

        for dd = 1 : sum(sensor(:))

            aa = round((dd - 1) * (length_nTdata/sum(sensor(:)))) + 1;
            bb = dd * (length_nTdata/sum(sensor(:)));

            nTdata(aa:bb,1) = nTdata(aa:bb,1) - median(nTdata(aa:bb,1));
        end
data_in_sort(:,3) = nTdata(:,1);
end
```

**%% median removal per sensor line**

```
if median_removal_per_line == 1
    dispstat(' Median removal per sensor line','timestamp','keepthis');
    LijnID = data_in_sort(1,4);
    j = 1;
    teller = 1;
    lijnen_data = [];
    k = 1;

for kk = 1 : length(data_in_sort(:,1))

        if data_in_sort(kk,4) ~= LijnID

        LijnID = data_in_sort(kk,4);
        matrix_A(:,3) = matrix_A(:,3)- median(matrix_A(:,3));
        lijnen_data = vertcat(lijnen_data,matrix_A);

        matrix_A = [];

        k = k + 1;
        j = 1;
        end

    if data_in_sort(kk,4) == LijnID
         matrix_A(j,1) = data_in_sort(kk,1);
         matrix_A(j,2) = data_in_sort(kk,2);
         matrix_A(j,3) = data_in_sort(kk,3);
         matrix_A(j,4) = data_in_sort(kk,4);
         matrix_A(j,5) = data_in_sort(kk,5);
         j = j + 1;
         teller = teller + 1;
    end
end
matrix_A(:,3) = matrix_A(:,3)- median(matrix_A(:,3));
lijnen_data = vertcat(lijnen_data,matrix_A);
data_in_sort = lijnen_data;
end
```

**%% median removal window**

```
if median_removal_window == 1
    dispstat(' Median removal window','timestamp','keepthis');
nTdata(:,1) = data_in_sort(:,3);

length_nTdata = length(nTdata);

    for dd = 1 : sum(sensor(:));

    aa = round((dd - 1) * (length_nTdata\sum(sensor(:)))) + 1;
    bb = dd * (length_nTdata/sum(sensor(:)));

        for ff = (aa+(median_window_size)/2) : (bb-(median_window_size)/2)
            nTdata(ff,1) = nTdata(ff,1) - median(nTdata((ff-
median_window_size/2):(ff+median_window_size/2),1));
        end

      nTdata((bb-median_window_size/2):bb,1) = nTdata((bb-median_window_size/2):bb,1) -
median(nTdata(ff:(ff+median_window_size/2),1));
      nTdata(aa:(aa + round(median_window_size/2)),1) = nTdata(aa:(aa + round(median_window_size/2)),1) -
median(nTdata(aa:(aa + round(median_window_size/2)),1));
    end
    data_in_sort(:,3) = nTdata(:,1);
end

%%
header = '';
namefile = ['sensor_data.csv'];
writeCsvFile_format(namefile,data_in_sort(:,1:5),header,'%.2f\t%.2f\t%.2f\t%.2f\t%.0f\n');
```

**%% gridding**

```
dispstat(' Start gridding ','timestamp','keepthis');

    s_mesh = create_blank_2D(data_in_sort(:,1:2),s_input.dX,100,1);
    vqinterp = scatteredInterpolant(data_in_sort(:,1),data_in_sort(:,2),data_in_sort(:,3),'natural');
    vq_bl_h = vqinterp(s_mesh.rasX_bl,s_mesh.rasY_bl);
    vq = s_mesh.blank(:); vq(~isnan(vq)) = vq_bl_h;
    grd = reshape(vq,s_mesh.nrows,s_mesh.ncols);

save_ascii_raster_grid(strcat('sensor_data.asc'),flipud(grd),s_mesh.ncols,s_mesh.nrows,s_mesh.minX,s_mesh.m
inY,s_input.dX,'%.2f ',s_mesh.nodatavalue);
    fh = GUI_visualize_grd(grd,s_mesh,'originele data');
%%
dispstat(' A_sensorsplit_and_range DONE','timestamp','keepthis')
```

## **Appendix 3.2:** Script for removing overlapping errors in FGM data.

```
%%%%%%%%%%%%%%%%%%%%%%%%%%%%%%
%LINE APPROACH
sprong = 100; %% frequency subsampling step (data reduction): 1/sprong
%%%%%%%%%%%%%%%%%%%%%%%%%%%%%%
%NEARBY
execute_nearby = 1; %% Yes = 1 / No = 0
sensorafstand = 0.45; %% threshold (t)
remove_dist_nearby = 1.50; %% radius (r)
%%%%%%%%%%%%%%%%%%%%%%%%%%%%%%
%gridding resolution XY
s_input.dX = 0.25;
%%%%%%%%%%%%%%%%%%%%%%%%%%%%%%

%%
warning('off','all')
addpath ('../functions/CSVwrite')
addpath ('../functions/dispstat')
dispstat(' START Processing B_intersect_overlap_nearby','timestamp','keepthis');
fprintf('\n');
file = 'sensor_data.csv';
fileID = fopen(strcat(file)); %opgeven in te lezen text, ascii of csv-bestand
zzz = textscan(fileID, '%f %f %f %f %f'); %inlezen file

%% read double array
data_in = [zzz{1},zzz{2},zzz{3},zzz{4},zzz{5}];
LijnID = data_in(1,4);
j = 1;
k = 1;
teller = 1;

%% Deviding in separate sensor lines

for i = 1 : length(zzz{1})
        if data_in(i,4) ~= LijnID
        LijnID = data_in(i,4);
        lijnen_data{k} = matrix_A;
        matrix_A = [];
        k = k + 1;
        j = 1;
        end

    if data_in(i,4) == LijnID
         matrix_A(j,1) = data_in(i,1);
         matrix_A(j,2) = data_in(i,2);
         matrix_A(j,3) = teller;
         matrix_A(j,4) = data_in(i,3);
         j = j + 1;
         teller = teller + 1;
    end
end

lijnen_data{k} = matrix_A;
teller = 1;
teller2 = 0;
snijpunten = [];
matrix_F = [];

%% too close sampled model

for j = 1 : k
    for i = j : k
        a = lijnen_data{j};
        b = lijnen_data{i};
        lijn1x = a(1:sprong:end,1);
        lijn1y = a(1:sprong:end,2);
        lijn2x = b(1:sprong:end,1);
        lijn2y = b(1:sprong:end,2);

    if execute_nearby == 1;
        for m = 1 : length(lijn1x)
          teller4 = 1;
           for n = 1 : length(lijn2x)
           eucl_d_1 = sqrt((lijn1x(m) - lijn2x(n))^2 + (lijn1y(m) - lijn2y(n))^2);

            if eucl_d_1 < sensorafstand
                matrix_E(teller4,1) = lijn1x(m);
                matrix_E(teller4,2) = lijn1y(m);
                matrix_E(teller4,3) = j;
                matrix_E(teller4,4) = i;
                teller4 = teller4 + 1;
            end
           end
           matrix_F = vertcat(matrix_F,matrix_E);
           matrix_E = [];
        end
```

```
    end
    nearby_intersect_progress  = j/k*100;
    dispstat(strcat(' Processing nearby_intersect(BUILDING MODEL):     {',
num2str(round(nearby_intersect_progress)),'%}'),'timestamp');
    msg = strcat(' Processing nearby_intersect:     {', num2str(round(nearby_intersect_progress)),'%}');
end

dispstat(strcat(' Processing nearby_intersect:     {',
num2str(round(nearby_intersect_progress)),'%}'),'keepthis','timestamp');
```

**%% Removal of too close sampled and overlapping data**

```
if execute_nearby == 1
    for j = 1 : (length(matrix_F(:,1)))
    x_in = (matrix_F(j,1));
    y_in = (matrix_F(j,2));
    lijn = (matrix_F(j,3));
    lijn_ref = (matrix_F(j,4));
    lijn_matrix = lijnen_data{1,lijn};

    if lijn ~= lijn_ref
        for d = 1 : length(lijn_matrix)
        x_test = (lijn_matrix(d,1));
        y_test = (lijn_matrix(d,2));
        eucl_d = sqrt((x_in - x_test)^2 + (y_in - y_test)^2);

            if eucl_d < remove_dist_nearby
                lijn_matrix(d,:) = NaN;
            end
        end
    end
       lijnen_data{1,lijn} = lijn_matrix(:,:);
       remove_nearby_progress  = j/length(matrix_F)*100;
       dispstat(strcat(' Processing remove_nearby:     {',
num2str(round(remove_nearby_progress)),'%}'),'timestamp');

    end
       dispstat(strcat(' Processing remove_nearby:     {',
num2str(round(remove_nearby_progress)),'%}'),'timestamp','keepthis');

end
```

**%% writting final data matrix**

```
 eindmatrix = [];
 teller3 = 1;

 for i = 1:length(lijnen_data)
   matrix_D = lijnen_data{1,i};
   eindmatrix = vertcat(eindmatrix, matrix_D);
   teller3 = teller3 + length(matrix_D);
   eindmatrix_progress = i/length(lijnen_data)*100;
   dispstat(strcat(' Writing eindmatrix:     {', num2str(round(eindmatrix_progress)),'%}'),'timestamp');
 end
 dispstat(strcat(' Writting eindmatrix:     {',
num2str(round(eindmatrix_progress)),'%}'),'timestamp','keepthis');

%%
header = '';
namefile = ['data_intersect_remove.csv'];
writeCsvFile_format(namefile,eindmatrix(:,1:4),header,'%.2f\t%.2f\t%.2f\t%.0f\n');
```

**%% gridding data**

```
%remove NaN in eindmatrix
TF1 = isnan(eindmatrix(:,1)) == 1;
eindmatrix(TF1,:) = [];

%create UTMzone array
l = length(eindmatrix(:,1));
utm(1:l,1) = cellstr(UTMzone);

dispstat(' Start gridding ','timestamp','keepthis');
    s_mesh = create_blank_2D(eindmatrix(:,1:2),s_input.dX,100,1);
    vqinterp = scatteredInterpolant(eindmatrix(:,1),eindmatrix(:,2),eindmatrix(:,4),'natural');
    vq_bl_h = vqinterp(s_mesh.rasX_bl,s_mesh.rasY_bl);
    vq = s_mesh.blank(:); vq(~isnan(vq)) = vq_bl_h;
    grd = reshape(vq,s_mesh.nrows,s_mesh.ncols);

save_ascii_raster_grid(strcat('data_intersect_remove.asc'),flipud(grd),s_mesh.ncols,s_mesh.nrows,s_mesh.min
X,s_mesh.minY,s_input.dX,'%.2f ',s_mesh.nodatavalue);
    fh = GUI_visualize_grd(grd,s_mesh,'overlap remove');

%%
fprintf('\n');
dispstat(' END Processing intersect_overlap_nearby','timestamp','keepthis');
```

# Chapter 5

**Appendix 5.1:** Two detected anomalies are evaluated to make an estimation of the characteristics of these objects. During excavation works, these items were validated. Item 1 are narrow gauge railway bars and item 2 is a bucket. Measurable parameters are given per item.



**Item 1:** narrow gauge railway
Size: 2 x 2 m & 1 x 1 m
Weight: +/- 100 kg
Depth: 0.60 - 0.80 m



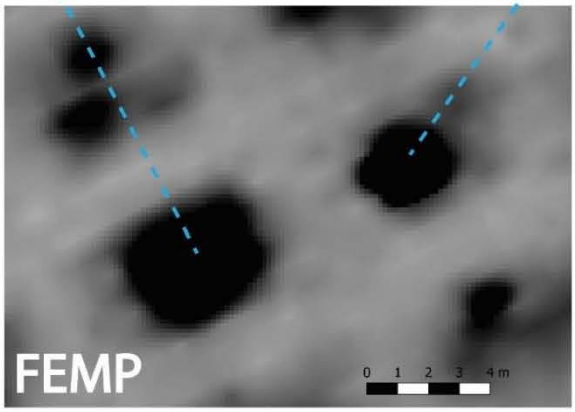
**Item 2:** bucket
Size: 0.4 x 0.25 x 0.25 m
Weight: 9.45 kg
Depth (center): 0.55m

**Item 1**

FEMP:
metal = positive
peak = 115 mS/m

1HCP ECa :
strong positive

2HCP MSa:
strong contrast with surroundings

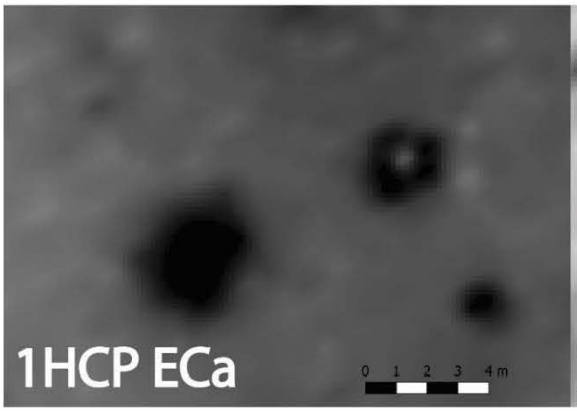


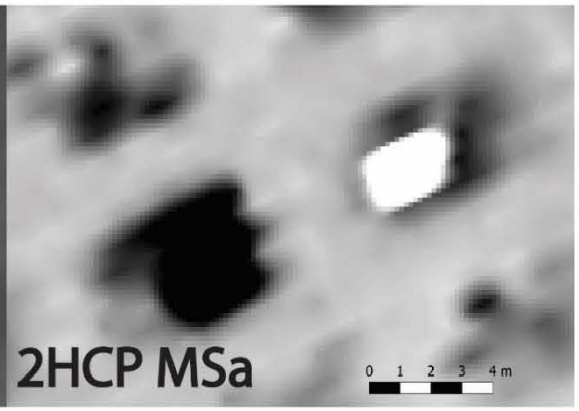

**Item 2**

FEMP:
metal = positive
peak = 211 mS/m

1HCP ECa :
strong positive

2HCP MSa:
strong contrast with surroundings




**Item 1 - estimation**

depth: 0.4 - 0.8 m

massive object

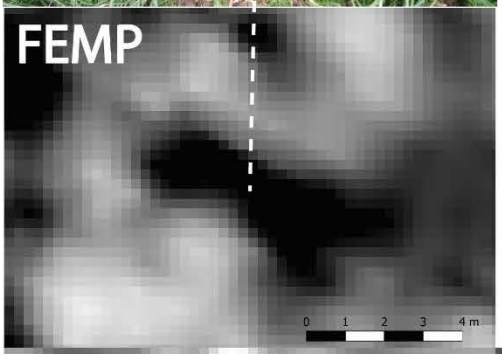
**Item 2 - estimation**

depth: 0.4 - 0.8 m

massive object

**Appendix 5.2:** The detected anomaly is evaluated to make an estimation of the object characteristics. During excavation works, this item was validated. Item 3 is a collection of construction bolts and other fine metal pieces. Measurable parameters are given for this item.






**Item 3:** construction bolts tanks

Multiple small objects (max 0.1 x 0.1 m)

Depth: 0.20 - 0.40 m

FEMP:
metal = positive
peak = 40 mS/m

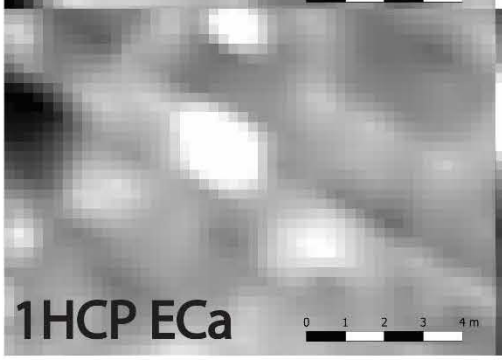
1HCP ECa :
negative

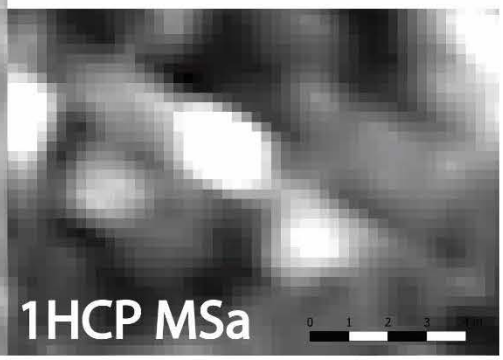
1HCP MSa:
strong contrast with
surroundings

**Item 3 - estimation**

depth: 0.0 - 0.4 m

smaller objects



# Chapter 6

**Appendix 6.1:** True and estimated shelling density classification of the random test locations and selected sites

| ID | Area (ha) | Estimated density | Predicted class | Real value | Real class | Difference | Class difference |
|---|---|---|---|---|---|---|---|
| **0** | 0.25 | 703.07 | 5 | 720 | 5 | 16.93 | 0 |
| **1** | 0.25 | 0.02 | 1 | 0 | 1 | 0.02 | 0 |
| **2** | 0.25 | 51.71 | 2 | 96 | 3 | 44.29 | -1 |
| **3** | 0.25 | 19.92 | 1 | 0 | 1 | 19.92 | 0 |
| **4** | 0.25 | 0.79 | 1 | 0 | 1 | 0.79 | 0 |
| **5** | 0.25 | 209.9 | 4 | 128 | 3 | 81.9 | 1 |
| **6** | 0.25 | 723.03 | 5 | 720 | 5 | 3.03 | 0 |
| **7** | 0.25 | 722.29 | 5 | 720 | 5 | 2.29 | 0 |
| **8** | 0.25 | 726.16 | 5 | 720 | 5 | 6.16 | 0 |
| **9** | 0.25 | 726.32 | 5 | 720 | 5 | 6.32 | 0 |
| **10** | 0.25 | 384.87 | 4 | 720 | 5 | 336.13 | -1 |
| **11** | 0.25 | 81.32 | 3 | 172 | 3 | 90.68 | 0 |
| **12** | 0.25 | 8.9 | 1 | 0 | 1 | 8.9 | 0 |
| **13** | 0.25 | 149.29 | 3 | 412 | 4 | 262.71 | -1 |
| **14** | 0.25 | 530.62 | 5 | 720 | 5 | 189.38 | 0 |
| **15** | 0.25 | 734.24 | 5 | 720 | 5 | 14.24 | 0 |
| **16** | 0.25 | 227.93 | 4 | 376 | 4 | 148.07 | 0 |
| **17** | 0.25 | 71.91 | 2 | 72 | 2 | 0.09 | 0 |
| **18** | 0.25 | 421.88 | 4 | 424 | 4 | 2.12 | 0 |
| **19** | 0.25 | 724.36 | 5 | 720 | 5 | 4.36 | 0 |
| **20** | 0.25 | 16.09 | 1 | 0 | 1 | 16.09 | 0 |
| **21** | 0.25 | 484.37 | 5 | 124 | 3 | 360.37 | 2 |
| **22** | 0.25 | 646.31 | 5 | 720 | 5 | 73.69 | 0 |
| **23** | 0.25 | 509.06 | 5 | 720 | 5 | 210.94 | 0 |
| **24** | 0.25 | 696.65 | 5 | 720 | 5 | 23.35 | 0 |
| **25** | 0.25 | 180.25 | 3 | 144 | 3 | 36.25 | 0 |
| **28** | 0.25 | 41.84 | 2 | 52 | 2 | 10.16 | 0 |
| **29** | 0.25 | 1.62 | 1 | 0 | 1 | 1.62 | 0 |
| **30** | 0.25 | 3.47 | 1 | 36 | 2 | 32.53 | -1 |
| **31** | 0.25 | 700 | 5 | 720 | 5 | 20 | 0 |
| **32** | 0.25 | 1.49 | 1 | 0 | 1 | 1.49 | 0 |
| **33** | 0.25 | 741.29 | 5 | 720 | 5 | 21.29 | 0 |
| **34** | 0.25 | 377.26 | 4 | 204 | 4 | 173.26 | 0 |
| **35** | 0.25 | 628.78 | 5 | 232 | 4 | 396.78 | 1 |
| **36** | 0.25 | 2.35 | 1 | 16 | 1 | 13.65 | 0 |
| **37** | 0.25 | 716.38 | 5 | 720 | 5 | 4.62 | 0 |
| **39** | 0.25 | 344.37 | 4 | 288 | 4 | 56.37 | 0 |
| **40** | 0.25 | 734.38 | 5 | 720 | 5 | 14.38 | 0 |
| **41** | 0.25 | 526.23 | 5 | 548 | 5 | 22.77 | 0 |
| **42** | 0.25 | 141.3 | 3 | 80 | 3 | 61.3 | 0 |
| **43** | 0.25 | 321.12 | 4 | 360 | 4 | 38.88 | 0 |
| **100** | 6.13 | 48.9 | 2 | 44 | 2 | 4.9 | 0 |
| **105** | 2.42 | 629.08 | 5 | 720 | 5 | 90.92 | 0 |
| **106** | 6.96 | 193.81 | 3 | 408 | 4 | 214.19 | -1 |
| **107** | 1.71 | 690.53 | 5 | 720 | 5 | 29.47 | 0 |
| **108** | 6.72 | 726.49 | 5 | 720 | 5 | 6.49 | 0 |
| **109** | 0.52 | 349.86 | 4 | 108 | 3 | 241.86 | 1 |

| | | | | | | | |
|---|---|---|---|---|---|---|---|
| **110** | 1.03 | 394.96 | 4 | 148 | 3 | 246.96 | 1 |
| **111** | 2.16 | 591.61 | 5 | 720 | 5 | 128.39 | 0 |
| **112** | 2.8 | 637.74 | 5 | 720 | 5 | 82.26 | 0 |
| **113** | 1.08 | 583.42 | 5 | 720 | 5 | 136.58 | 0 |
| **114** | 0.53 | 567.07 | 5 | 720 | 5 | 152.93 | 0 |
| **115** | 3.65 | 416.36 | 4 | 720 | 5 | 303.64 | -1 |
| **116** | 2.88 | 722.17 | 5 | 720 | 5 | 2.17 | 0 |
| **117** | 1.31 | 490.49 | 5 | 720 | 5 | 229.51 | 0 |
| **118** | 1.19 | 733.45 | 5 | 720 | 5 | 13.45 | 0 |
| **119** | 2.1 | 733.34 | 5 | 720 | 5 | 13.34 | 0 |
| **120** | 6.55 | 690.6 | 5 | 720 | 5 | 29.4 | 0 |
| **121** | 2.88 | 687.31 | 5 | 488 | 5 | 199.31 | 0 |
| **122** | 1.19 | 726.91 | 5 | 216 | 4 | 509.91 | 1 |

**Appendix 6.2:** Reference datasets with metal parameters (Flanders-Holland not front related sites, Northern part front and Southern part front in Belgium).

**Reference data**

| ID | Village | area size (ha) | % area FEMP | MOH/ha |
|---|---|---|---|---|
| **1** | Hoeke (B) | 1.26 | 0.28% | 9.5 |
| **2** | Doel (B) | 6.14 | 0.01% | 1.1 |
| **3** | Koksijde (B) | 2.73 | 1.14% | 23.1 |
| **4** | Everberg (B) | 1.17 | 0.23% | 11.1 |
| **5** | Aalter (B) | 1.29 | 0.84% | 14.7 |
| **6** | Spiere (B) | 0.97 | 0.81% | 20.6 |
| **7** | Ooike (B) | 4 | 0.04% | 3 |
| **8** | Koolkerke (B) | 1.45 | 0.09% | 20.7 |
| **9** | Nukerke (B) | 0.93 | 0.47% | 14 |
| **10** | Middelburg (NL) | 1.12 | 0.97% | 21.4 |
| **11** | Walcheren (NL) | 0.99 | 0.39% | 28.3 |
| **12** | Rijckholt (NL) | 1.35 | 0.21% | 14.8 |

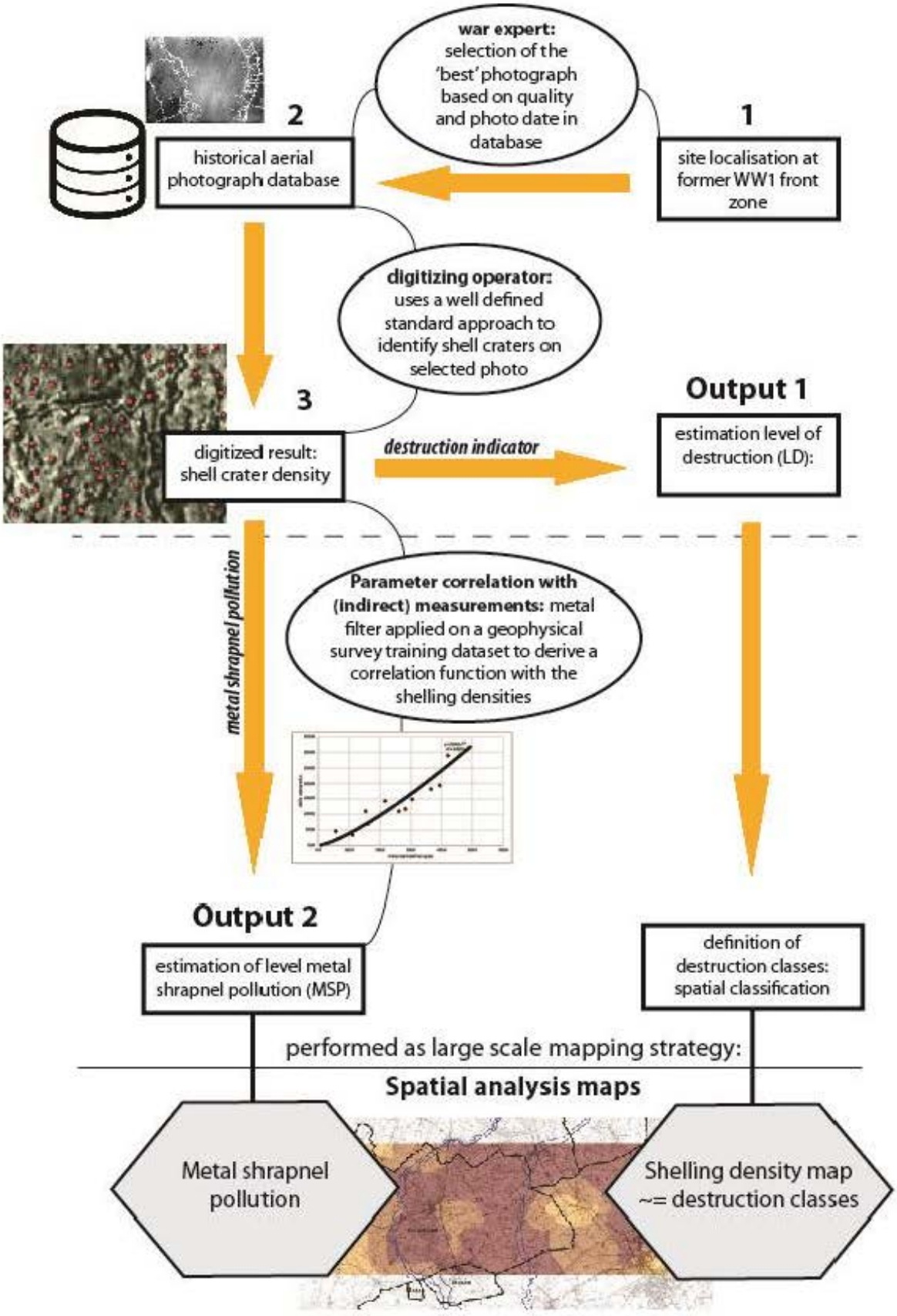
**Northern part front**

| ID | area size (ha) | % area FEMP | MOH/ha |
|---|---|---|---|
| **1** | 6.78 | 0.56% | 27.1 |
| **2** | 3.54 | 1.65% | 111.9 |
| **3** | 12.19 | 0.97% | 56.9 |
| **4** | 2.53 | 1.44% | 56.5 |
| **5** | 4.08 | 0.08% | 8.6 |
| **6** | 2.29 | 1.32% | 102.6 |
| **7** | 4.30 | 1.11% | 8.6 |

**Southern part front**

| ID | area size (ha) | % area FEMP | MOH/ha |
|---|---|---|---|
| **1** | 4.97 | 0.34% | 9.9 |
| **2** | 3.05 | 3.04% | 177 |
| **3** | 6.94 | 3.05% | 161.3 |
| **4** | 1.77 | 3.62% | 217.5 |
| **5** | 3.15 | 4.27% | 154.3 |
| **6** | 1.46 | 4.82% | 261 |
| **7** | 2.16 | 6.14% | 170.8 |
| **8** | 1.71 | 6.37% | 304.7 |
| **9** | 0.98 | 8.88% | 493.9 |
| **10** | 2.28 | 9.39% | 282.9 |

**Appendix 6.3:** Workflow suggested method for shelling density mapping.

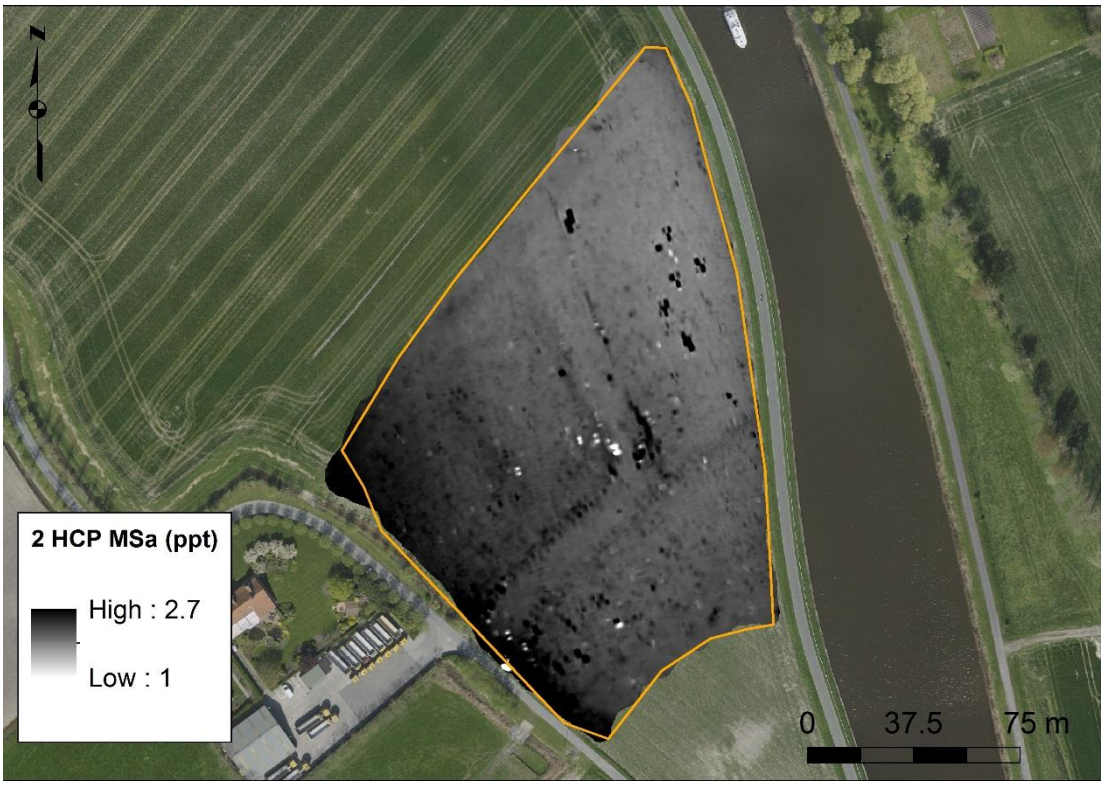


# Chapter 7

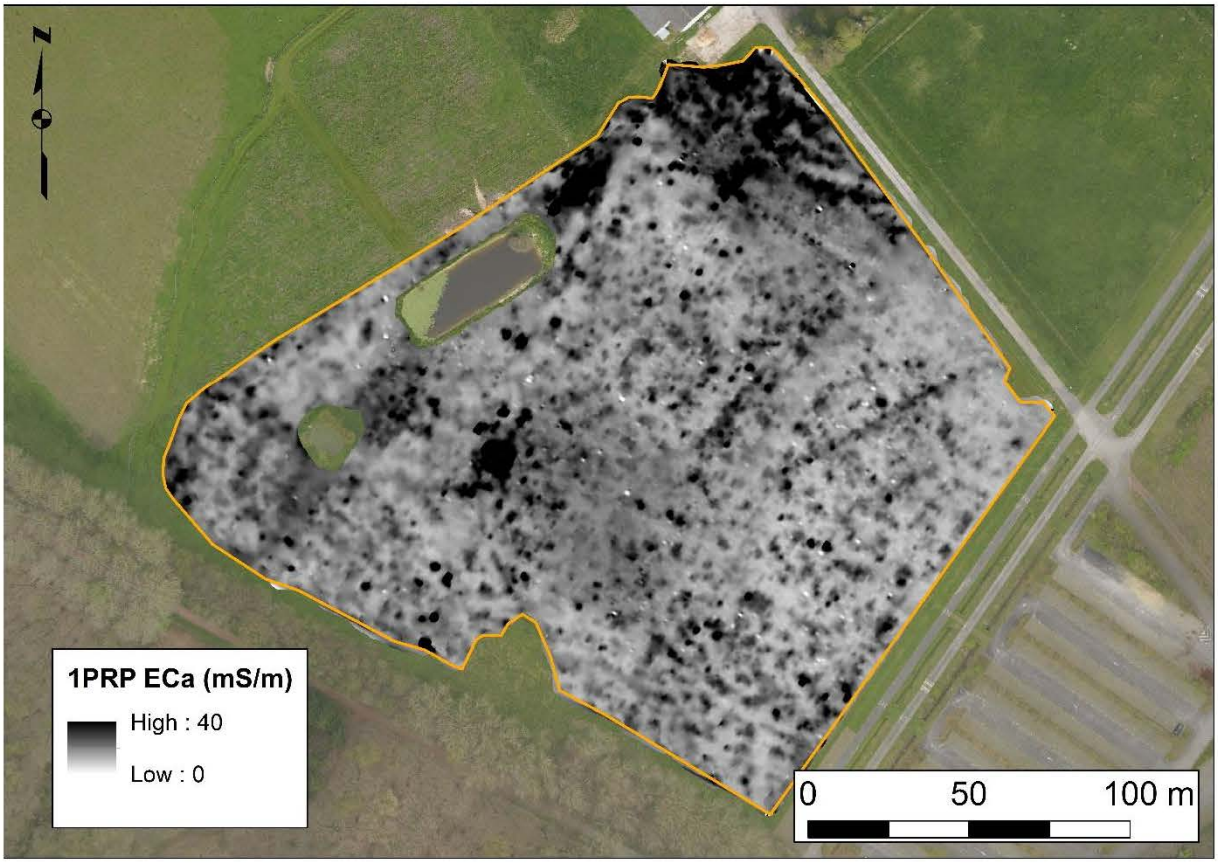
**Appendix 7.1**: The 1PRP $EC_a$ scan result of the railway site (T1 - ID 6).



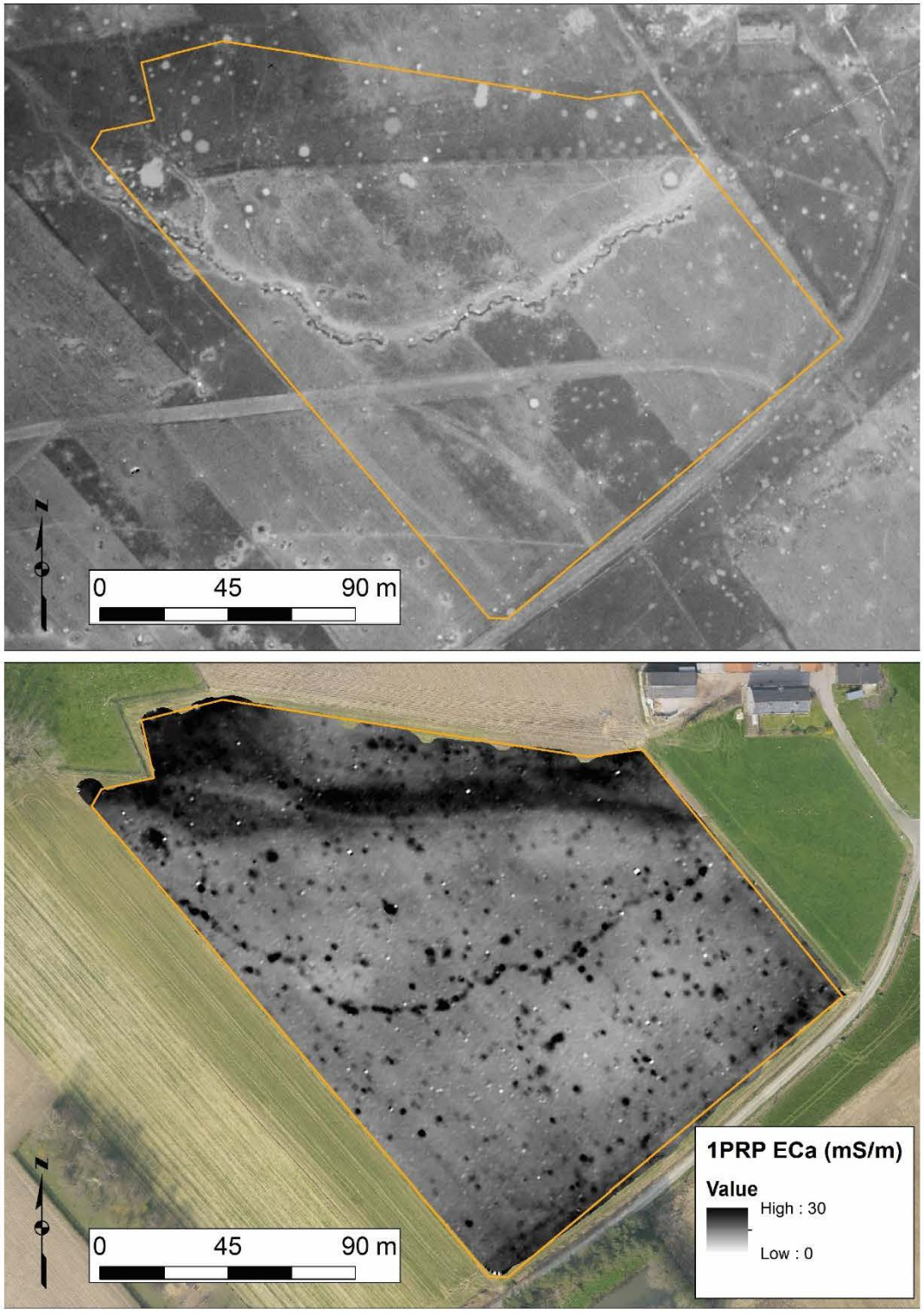

**Appendix 7.2**: The 1PRP $EC_a$ scan result of the Near Yser site (T1 - ID 8).



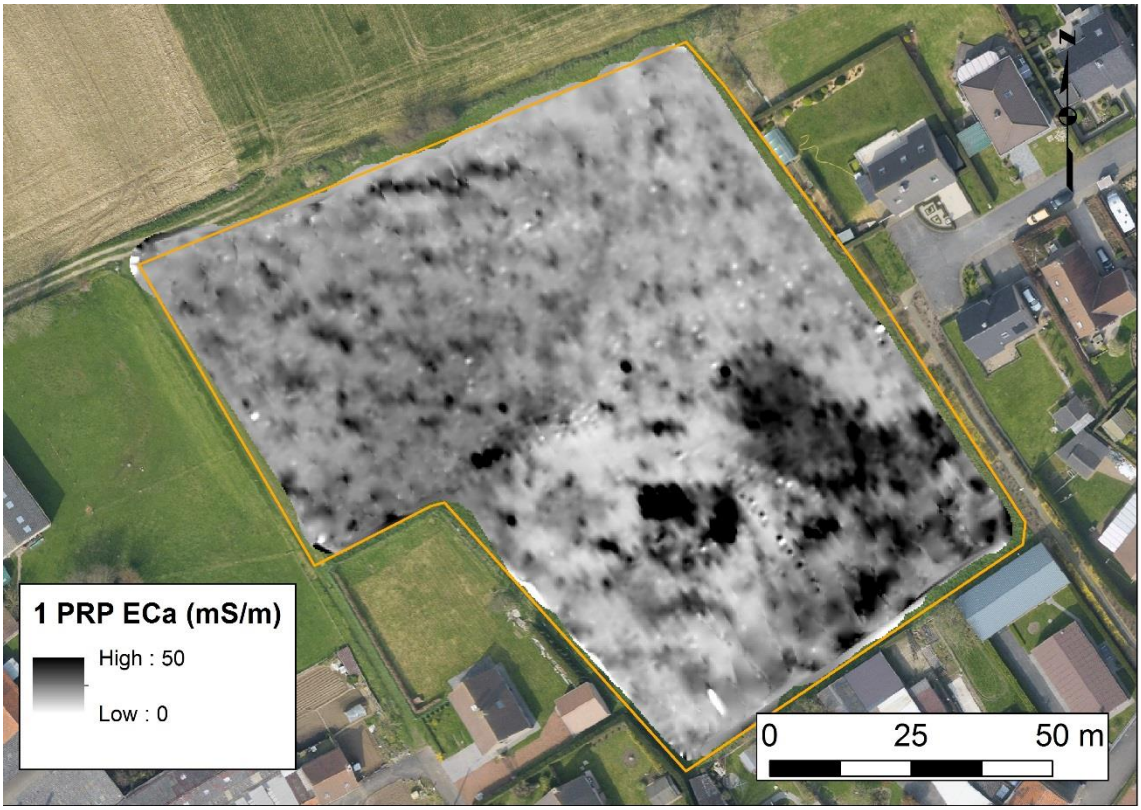
**Appendix 7.3**: The 1PRP $EC_a$ scan result of the Palingbeek site (T2 - ID 2).



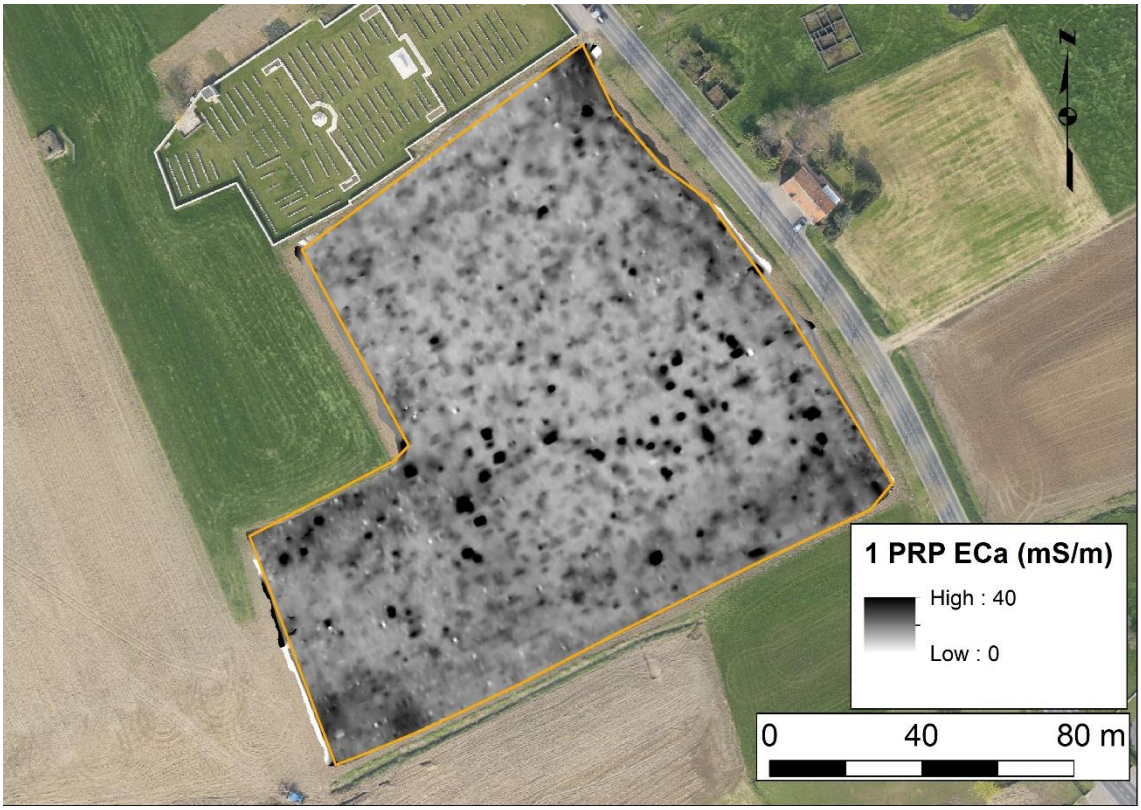
**Appendix 7.4**: The 1PRP $EC_a$ scan result of the Bruloose Cabaret site (T3 - ID 3). Aerial photograph was taken on 17/07/1918 (IWM collection).



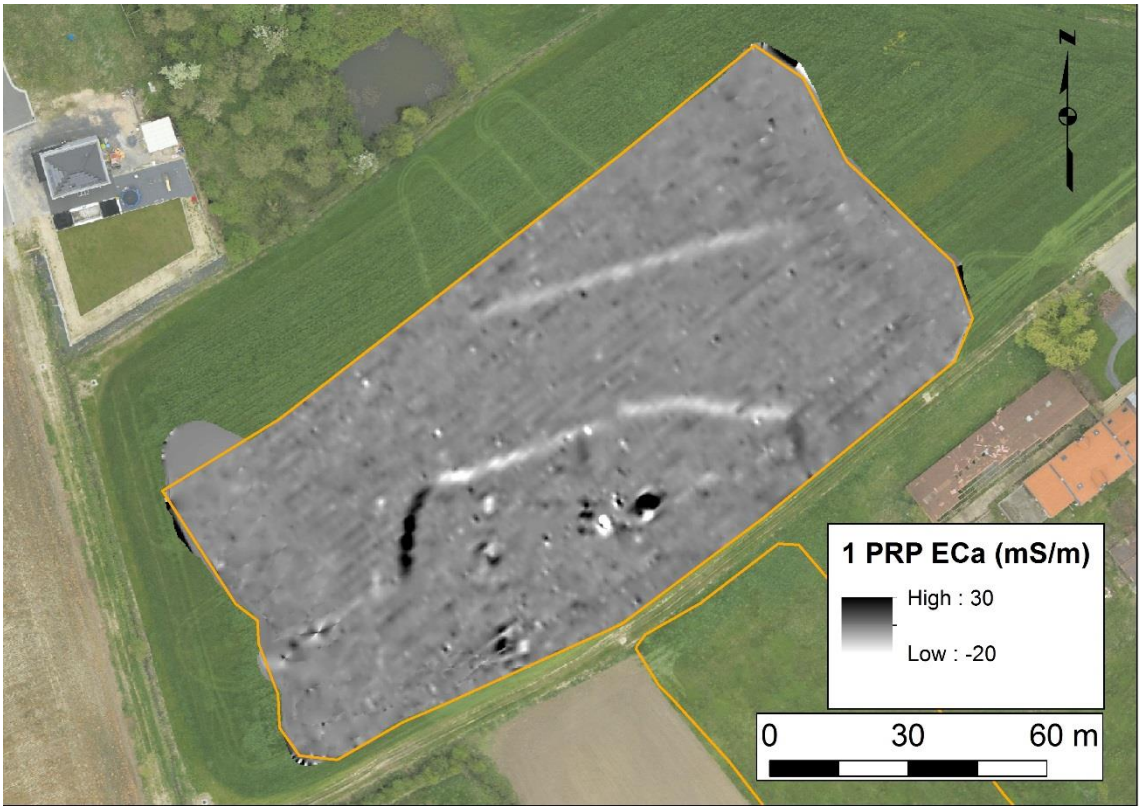
**Appendix 7.5**: The 1PRP $EC_a$ scan result of the Hill 80 site (T3 - ID 18).



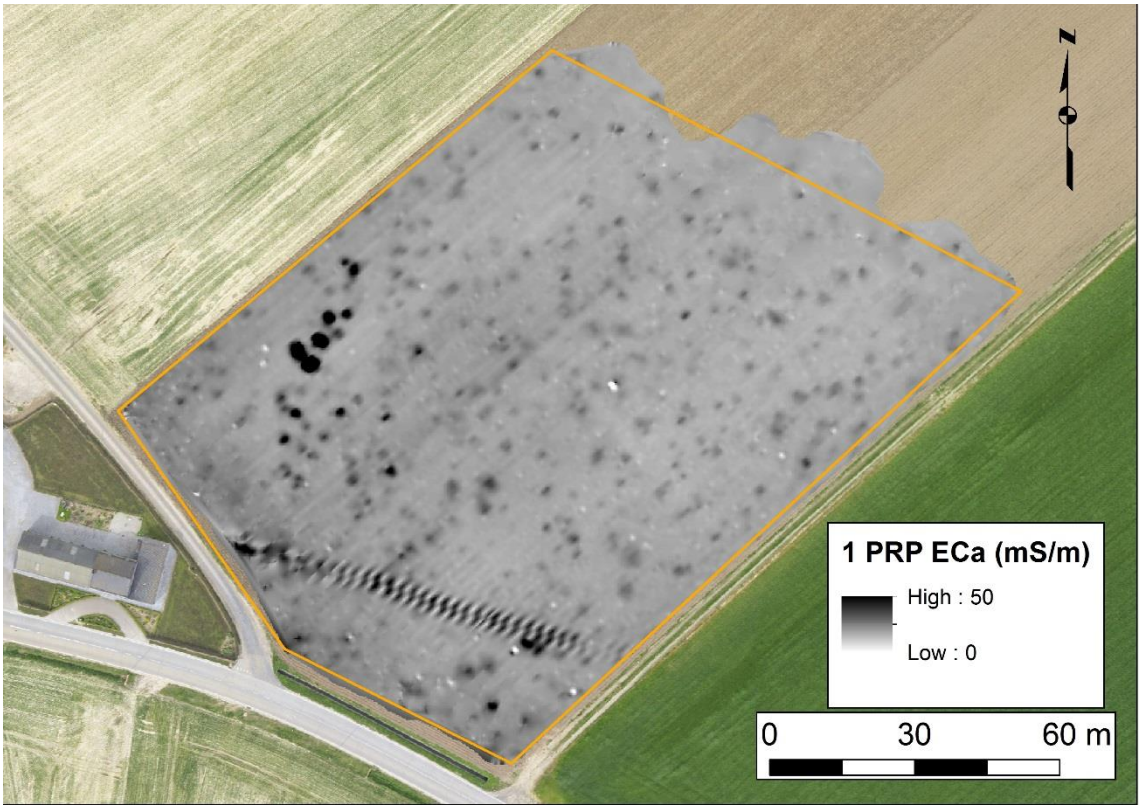

**Appendix 7.6**: The 1PRP $EC_a$ scan result of the De Sterkte Cabaret site (T3 - ID 19).



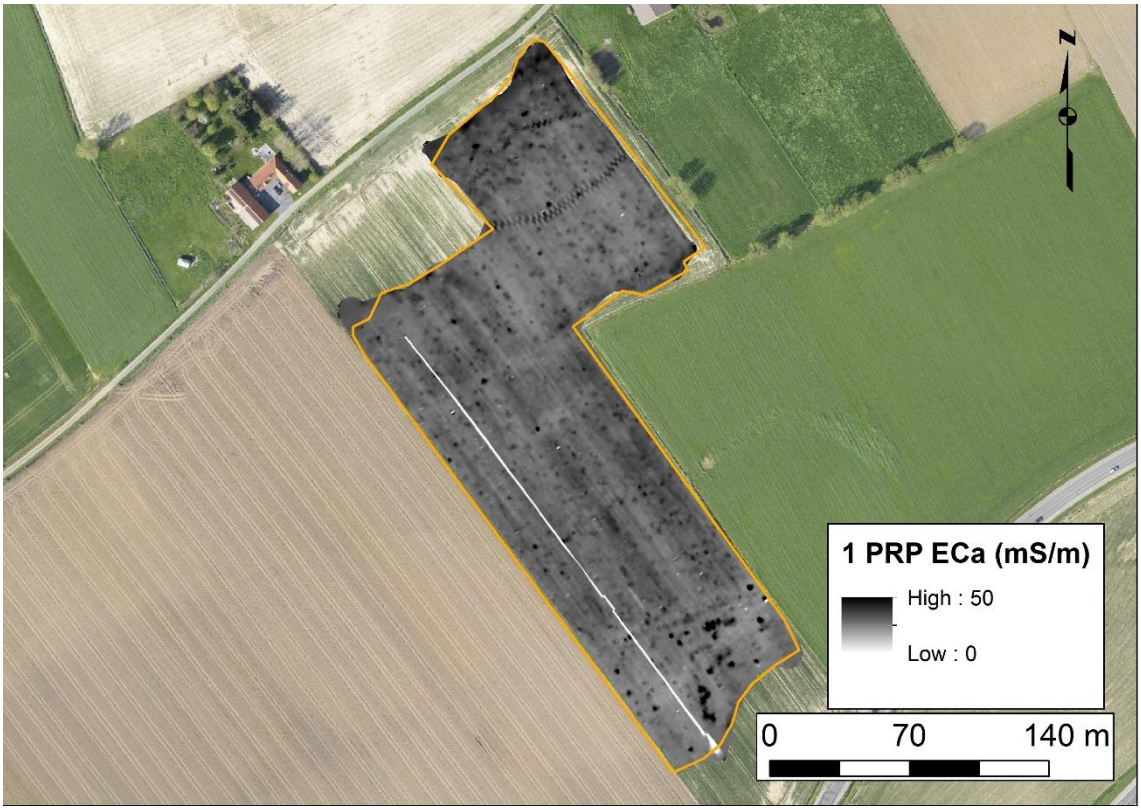
**Appendix 7.7**: The 1PRP $EC_a$ scan result of the Messines near church site (T3 - ID 24).



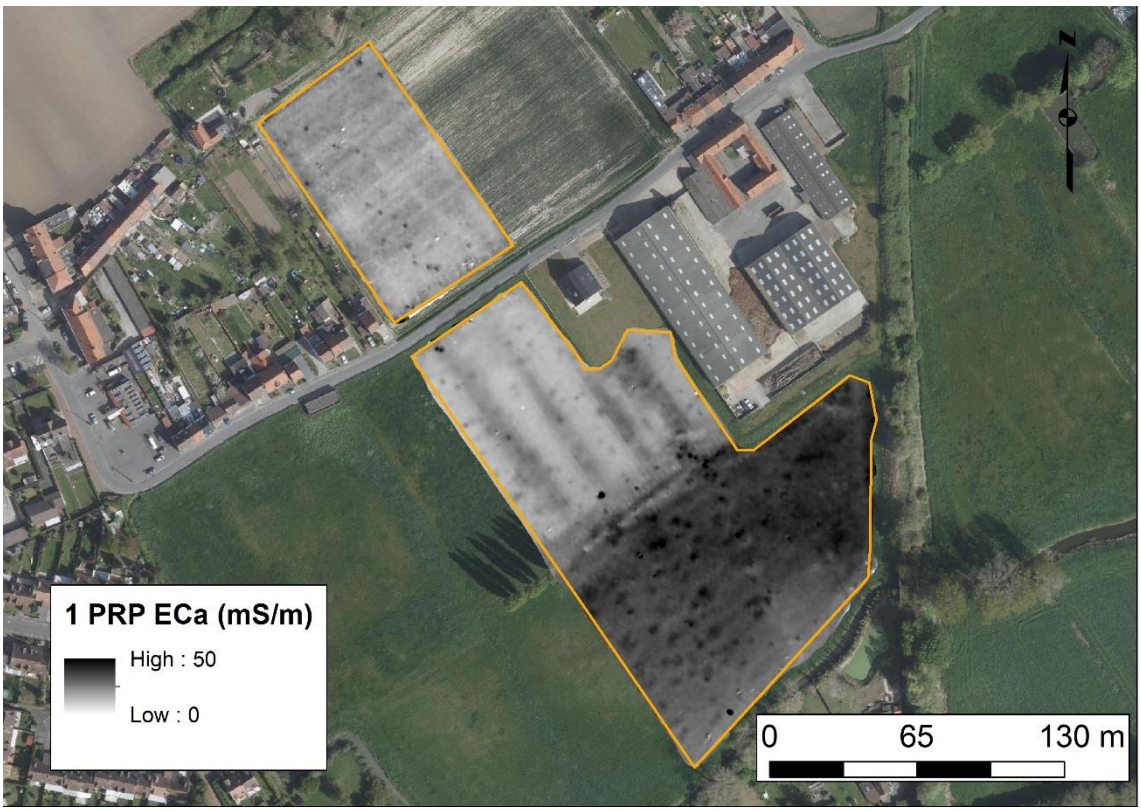

**Appendix 7.8**: The 1PRP $EC_a$ scan result of the Huns Walk site (T3 - ID 25).



**Appendix 7.9**: The 1PRP $EC_a$ scan result of the Flatened farm site (T3 - ID 30).




**Appendix 7.10**: The 1PRP $EC_a$ scan result of the Ploegsteert south site (T3 - ID 31).



# References

3d-Radar (2010). *GeoScope 3GHz*. Retrieved June 6, 2018, from http://3d-radar.com/wp-content/uploads/2010/04/2010-datasheet-geoscope-3ghz.pdf

Actiegroep voor Wereldoorlogarcheologie (2007). *Wat is de A.W.A.?* Retrieved October 8, 2018, from http://www.a-w-a.be/nl/index2.html

Agentschap Informatie Vlaanderen (2013). *Infosessie: brondata DHMV*. Retrieved June 27, 2018, from https://overheid.vlaanderen.be/sites/default/files/media/documenten/informatie-vlaanderen/producten/BVK/documenten/Infosessie_BVKOpenData_LiDAR_21022017%20%281%29.pdf?timestamp=1517955906

Agentschap Onroerend Erfgoed, (2017*). Code van Goede Praktijk*. Retrieved October 3, 2018, from https://www.onroerenderfgoed.be/nl/beheer/de-code-van-goede-praktijk/

Army War College (1917). *Notes on the construction and equipment of trenches*. Washington Government Printing Office, 109 pp.

Aspinall, A., Gaffney, C., Schmidt, A. (2008). *Magnetometry for Archaeologists*. Lanham, Maryland: AltaMira Press, 208 pp.

Aspinall, A., Lynam, J. (1970). An induced polarisation instrument for the detection of near surface features. *Prospezioni Archeologiche*, *5*, 67-75.

Atkinson, R. (1946). *Field Archaeology* (1st edition). London: Methuen.

Atkinson, R. (1953). *Field Archaeology* (2nd edition). London: Methuen.

Axelrod, A. (2016). *The Battle of the Somme*. Maryland: Rowman and Littlefield, 282 pp.

Banks, I. (2014). Digging in the Dark: The Underground War on the Western Front in WWI. *Journal of Conflict Archaeology*, *9(3)*, 156-176.

Barton, P., Doyle, P., Vandewalle, J. (2004). *Beneath Flanders Fields: the tunnellers' war 1914–1918*. Spellmount: Staplehurst.

Barton, P., Doyle, P., Vandewalle, J. (2005). *Beneath Flanders Fields. Tunnels en Mijnen 1914–1918*. Zonnebeke: Johan Vandewalle.

Bausinger, T., Bonnaire, E., Preuß, J. (2007). Exposure assessment of a burning ground for chemical ammunition on the Great War battlefields of Verdun. *Science of the Total Environment*, *382*, 259-271.

Bausinger, T., Preuß, J. (2005). "Environmental Remnants of the First World War: Soil Contamination of a Burning Ground for Arsenic Ammunition. *Environmental Contamination and Toxicology*, *74*, 1045-1052.

Bevan, B. (1983). Electromagnetics for mapping buried earth features. *Journal of field archaeology*, *10*, 48-54.

Billings, S.D., Stanley, J., Youmans, C. (2002). *Magnetic discrimination that will satisfy regulators?* UXO forum.

Billings, S.D., Li, Y., Goodrich, W. (2009). *Advanced UXO discrimination using magnetometry: understanding remanent magnetization.* SERDP Project MM – 1380.

Bossuet, G., Camerlynck, C., Brehonnet, C., Petit, C. (2001). Magnetic Prospecting of Diachronic Structures (Antiquity to First World War) on the Site of the Sanctuary of Ribemont-sur-Ancre (Somme, France). *Archaeological Prospection*, *8*, 67-77.

Boterberge, R. (1962). Historische Geografie van het Overstromingsgebied van de Ijzer in de Middeleeuwen. *Handelingen der Maatschappij voor Geschiedenis en Oudheidkunde, Gent*, *Nieuwe reeks*, *16*, 77-142.

Bovik, A. (2000). *Handbook of Image and Video Processing*. San Diego: Academic Press.

Bull, S. (2014). Trench: A history of trench warfare on the Western Front. Oxford: Osprey Publishing.

Bracke, M., Claesen, J., Benoot, N., Saey, T., Stichelbaut, B., De Decker, C. (2019). Berging Britse tanks Tank Cemetery Hoge Meenseweg (Ieper). Archeologierapport.

Bracke, M., Gheyle, W., Stichelbaut, B. (2018). Just behind the front line. In B. Stichelbaut (ed.), *Traces of War. World War 1 Archaeology*, 84-99. Veurne: Hannibal.

Bridgland, T. (2003). *Tunnel-master and arsonist of the Great War: The Norton-Griffiths story*. Barnsley: Leo Cooper.

Byrnes, J. (2009). *Unexploded Ordnance Detection and Mitigation.* NATO Science for Peace and Security Series B: Physics and Biophysics.

Carlier, A. (1921). *La Photographie Aérienne pendant la Guerre.* Paris: Librairie Delagrave.

Cassidy, N. (2009). Electrical and magnetic properties of rocks, soils, and fluids, In H. M. Jol (Ed.), *Ground Penetrating Radar: Theory and Applications*, 41-72. Amsterdam: Elsevier.

Cihlar, J., Ulaby, F. (1975). *Microwave remote sensing of soil water content*. Technical Report. NASA, Houston, Texas. 196 pp.

Clark, A. (1990). *Seeing Beneath the Soil: Prospecting Methods in Archaeology.* London: B.T. Batsford.

Cowley, D., Stichelbaut, B. (2012). Historic Aerial Photographic Archives for European Archaeology. *European Journal of Archaeology*, *15(2)*, 217-236.

Daniels, D. (2004). *Ground Penetrating Radar (1st edition Vol. 1)*. Herts, United Kingdom: Institution of Electrical Engineers.

Daubechies, I. (1992). Ten Lectures on Wavelets. *CBMS-NSF Regional Conference Series in Applied Mathematics,* Society for Industrial and Applied Mathematics, 369 pp.

Debaeke, S. (2013). *Oud ijzer. De frontstreek bedolven onder levensgevaarlijke oorlogsmunitie*. Bruges: Uitgeverij de Klaproos.

Desfossés, Y. (1998). *Préserver les Traces. L'Archéologie et la Grande Guerre 14-18 Aujourd'hui*, 36-51. Paris: La Sigogne.

Desfossés, Y., Jacques, A., & Prilaux, G. (2008). *L'Archéologie de la Grande Guerre*. S.l.: INRAP.

Delefortrie, S. (2016). Optimizing the reliability of small-loop, frequency domain electromagnetic survey data*. Doctoral dissertation*, Ghent University.

Demerre, G., Termote, J. (2013). De onderwaterzetting van de Ijzervlakte. *De Grote Rede – Vlaams instituut voor zee*, *36*, 47 – 52.

Dendooven, D. (2007). *De wederopbouw – Wonen in de Zuidelijke Westhoek*. Brochure Open Monumentendag. Retrieved August 13, 2018, from http://www.wo1.be/nl/geschiedenis/gastbijdragen/militaire-en-burgerlijke-geschiedenis/de-wederopbouw

Deneckere, B. (1998). *Luchtoorlog boven West-Vlaanderen in 1914-1918*. Kortrijk: Groeninghe Uitgeverij, 279 pp.

Desreumaux, J. (2011). *Land van schroot en knoken*. Leuven: Davidfonds uitgeverij.

Devos, A., Taborelli P., Dodici, M., Chalumeau, L., Buridant, J., Bollot, N., Combaud, A., Defossés, Y. (2015). Le rôle des conditions géographiques sur l'organisation spatiale des Réseaux de durant la Grande Guerre- Application à la Champagne (région de Reims). *PhysioGéo*, *9*, 157-174.

Dewilde, M. (2010). *Onderzoeksbalans Onroerend erfgoed Vlaanderen – Archeologisch erfgoed Eerste Wereldoorlog*. Retrieved September 2, 2018, from https://onderzoeksbalans.onroerenderfgoed.be/onderzoeksbalans/thematisch/eerste-wereldoorlogerfgoed/archeologie

Dewilde M., Pype P., de Meyer M., Demeyere F., Lammens W., Degryse J., Wyffels F., Saunders, N. (2004). Belgium's new department of First World War archaeology. *Antiquity, Project Gallery 78(301)*.

Dewilde, M., Stichelbaut, B., Van Hollebeeke, Y., Verboven, H., Wyffels, F. (2014). Bellewaarde en zijn turbulente oorlogsverleden. *Monumenten en landschappen*, *33(3)*, 30-47.

De Béthune, P. (1961). Atlas van België, Blad 8 – Geologie. *Nationale Atlas*, Brussel, 47 pp.

De Meyer, M. (2006). *Inventarisatie van archeologische resten uit de Eerste Wereldoorlog en de mogelijkheden voor onderzoek naar sporen van andere conflicten: Battlefield Archaeology in West-Vlaanderen*. In K. Cousserier, E. Meylemans, E. In't Ven (Eds.), CAI-II, VIOE, 43-74.

De Smedt, P., Delefortrie, S., Wyffels, F. (2016). Identifying and removing micro-drift in ground-based electromagnetic induction data. *Journal of Applied Geophysics*, *131*, 14-22.

De Smedt, P., Saey, T., Lehouck, A., Stichelbaut, B., Meerschman, E., Islam, M., Van De Vijver, E., Van Meirvenne, M. (2013). Exploring the potential of multi-receiver EMI survey for geoarchaeological prospection: A 90 ha dataset. *Geoderma*, *40(2)*, 1260-1267.

De Smedt, P., Van Meirvenne, M., Saey, T., Baldwin, E., Gaffney, C., Gaffney, V. (2014). Unveiling the prehistoric landscape at Stonehenge through multi-receiver EMI. *Journal of Archaeological Science*, *50*, 16-23.

Dong, P., Chen, Q. (2017). *LiDAR Remote Sensing and Applications*. In Q. Weng (Ed.), Taylor and Francis Series in Remote Sensing Applications. Beijing: CRC Press, 200 pp.

Doolittle, J., Minzenmayer, F., Waltman, S., Benham, E., Tuttle, J., Pleaslee, S. (2007). Ground-penetrating radar soil suitability map of the conterminous United States. *Geoderma*, *141*, 416-421.

Doyle, P. (2017). *Disputed earth: Geology and trench warfare on the Western Front: 1914-18*. London: Unicorn Publishing Group, 208 pp.

Doyle, P., Bostyn, F., Barton, P., Vandewalle, J. (2001). The underground war 1914–1918: the geology of the Beecham dugout, Passchendaele, Belgium. *Proceedings of the Geologist's Association*, 263–274.

DOV (2015). Grondwatermeetnetten. Retrieved July 2015, from https://www.dov.vlaanderen.be/portaal/?module=verkenner#ModulePage

Edmonds, E. (1925). *History of the Great War. Military Operations: France and Belgium, 1914. Volume II: Antwerp, La Bassé, Armentières, Messines and Ypres, October – November 1914*. London: Macmillan.

Edmonds, J. (1928). *History of the Great War based on official documents by direction of the Historical Section of the Committee of Imperial Defence. Military Operations. France and Belgium, 1915. Volume 1: Winter 1914-15, Battle of Neuve Chapelle, Battle of Ypres*. London: Macmillan.

Edmonds, J. (1935). *History of the Great War. Military Operations: France and Belgium, 1918. Volume I: The German march offensive and its preliminaries*. London, Macmillan.

Edmonds, E. (1948). *History of the Great War. Military Operations: France and Belgium, 1917. Volume II. 7th June - 10th November, Messines and Third Ypres.* London: His Majesty's Stationery Office.

English Heritage (2008). *Geophysical Survey in Archaeological Field Evaluation.* Swindon: English Heritage Publishing.

Fedi, M., Florio, G. (2003). Decorrugation and removal of directional trends of magnetic fields by the wavelet transform: application to archaeological areas. *Geophysical Prospecting, 51(4)*, 261-272.

Ferguson, N., Novotny, J., Trigg, J. (2010). Postgraduate Conflict Archaeology. *Journal of Conflict Archaeology, 7(3),* 161-163.

Foard, G., Morris, R. (2012). The Archaeology of English Battlefields (CBA Research Report). *Council for British Archaeology*.

Gaffney, C., Gater, J. (2010). Revealing the buried past: Geophysics for Archaeologists. Gloucestershire: The History Press.

Gemeente Zonnebeke (2014). *Inhuldiging van het monument aan Black Watch Corner.* Retrieved August 27, 2018, from http://www.wo1.be/nl/nieuws/48485/inhuldiging-van-het-monument-aan-black-watch-corner

Georges-Leroye, M., Bock, J., Dambrine, E., Dupouey, J-L. (2011). Apport du lidar a la connaissance de l'histoire de l'occupation du sol en forêt de Haye. *ArcheoSciences*, *35*, 117-129.

Gheyle, W., Bourgeois, J., Bracke, M., Dalle, S., Deconynck, J., Decorte, J., De Langhe, K., De Mulder, G., Hanssens, D., Heyvaert, B., Note, N., Saey, T., Stichelbaut, B., Van Den Berghe, H., Van Eetvelde, V., Van Hollebeeke, Y., Van Meirvenne, M., Verdegem, S. (2016a). *Interdisciplinair onderzoek naar een Brits-Australisch barakkenkamp in het niemandsland te Kemmel (W-VL)*. Gent: Conflict in Contact IV.

Gheyle, W., Dossche, R., Bourgeois, J., Stichelbaut, B., Van Eetvelde, V. (2014). Integrating archaeology and landscape analysis for the cultural heritage management of a World War One militarised landscape: the German field defences in Antwerp. *Landscape Research*, *39(5)*, 502-522.

Gheyle, W., Saey, T., Van Hollebeeke, Y., Verplaetse, S., Note, N., Bourgeois, J., Van Meirvenne, M., Van Eetvelde, V., Stichelbaut, B. (2016b). Historical aerial photography and multi-receiver EMI soil sensing, complementing techniques for the study of a Great War conflict landscape. *Archaeological Prospection*, *23(3)*, 149-164.

Gheyle, W., Stichelbaut, B., Saey, T., Note, N., Van den Berghe, H., Van Eetvelde, V., Van Meirvenne, M., Bourgeois, J. (2018). Scratching the surface of war. Airborne laser scans of the Great War conflict landscape in Flanders (Belgium). *Journal of Applied Geography*, *90*, 55-68.

*Great Arab Revolt Project – Second Fieldwork Season* (2007). Retrieved, 30 October, 2018, from http://www.jordan1914-18archaeology.org/prospectus/Second%20Season%20Prospectus-1.pdf

Grieve, W., Newman, B. (1936). *Tunnellers. The story of the Tunneling Companies, Royal Engineers, during the World War*. London: Herbert Jenkins Limited.

Guicherd, J., Maîtrot, C. (1921). Les terres des régions dévastées. *Journal d'Agriculture Practique*, *34*, 154-156.

Härdle, W., Kerkyacharian, G., Picard, D., Tsybakov, A. (1998). *Wavelets, Approximation, and Statistical Applications*. New York: Springer, 265 pp.

Hengl, T. (2007). *A Practical Guide to Geostatistical Mapping of Environmental Variables*. Luxemburg: Office for Official Publications of the European Communities.

Hesse, R. (2013). *The changing picture of archaeological landscapes: Lidar prospection over very large areas as part of a cultural heritage strategy*. In R. Opitz, D. Cowley (Eds.), Interpreting archaeological topography: Airborne laser scanning, 3D data and ground observation,171–183. Oxford: Oxbow.

*Het vliegveld van Gistel* (n.d.). Retrieved August 13, 2018, from http://ginter.kindereninbezetgebied.be/objecten/het-vliegveld-van-gistel

His Majesty's Stationery Office (1916). *Notes for infantry officers on trench warfare*. London: His Majesty's Stationery Office.

His Majesty's Stationery Office (1922). *Statistics of the Military Effort of the British Empire during the Great War 1914-1920*. London: His Majesty's Stationery Office.

Hupy, J., Schaetzl, R. (2006). Introducing "bombturbation", a singular type of soil disturbance and mixing. *Journal of Soil Science*, *171(11)*, 823-836.

IGN (1920). *Carte spéciale des régions dévastées, 33NE, Soissons*. Retrieved October 18, 2017, from https://gallica.bnf.fr/ark:/12148/btv1b8593492b?rk=128756;0

*Identifying First World War trenches* (n.d.). Retrieved August 23, 2018, from https://www.homefrontlegacy.org.uk/wp/case-studies/identifying-first-world-war-trenches/

Jacobs, K., & Pollard, T. (2008). *Vampir Dugout. Opgravingsverslag Archeologische prospectie*. Retrieved October 16, 2018, from https://onderzoeksbalans.onroerenderfgoed.be/node/31046

Jensen, L. (2008). *Automatische Detektion von Bombentrichtern*. Bonn: Rheinische Friedrich-Wilhelms-Universität.

Johnson, J. (2006). *Remote sensing in archaeology: an explicitly North American Perspective*. Alabama: University of Alabama Press, 255 pp.

Jones, S. (2010). *Underground warfare 1914–1918*. Barnsley: Pen & Sword.

Keegan, J. (2013). *The first World War*. New York: Vintage Books.

Kokalj, Z., Zaksek, K., Ostir, K. (2011). Application of sky-view factor for the visualization of historic landscape features in lidar-derived relief models. *Antiquity*, *85(327)*, 263–273.

*Krater 15 – Kruisstraat nr. 3* (n.d.). Retrieved August 27, 2018, from http://www.wo1.be/nl/db-items/krater-15-kruisstraat-nr-3

Le Borgne, E. (1960). Influence du feu sur les proprieties magnetiques du sol et du granite. *Annales de Geophysique*, *16*, 159-195.

Liddell Hart, B. (1959). *The tanks: the history of the Royal Tank Regiment and its predecessors Heavy Branch Machine-Gun Corps, Tank Corps and Royal Tank Corps*. Londen: Cassell.

*Loods van vliegveld* (n.d.). Retrieved August 13, 2018, from http://www.luchtvaarterfgoed.be/content/loods-van-vliegveld

Lueck, E., Ruehlmann, J. (2013). Resistivity mapping with GEOPHILUS ELECTRICUS – Information about lateral and vertical soil heterogeneity. *Geoderma, 199*, 2-11.

Marquardt, D. (1963). An algorithm for least-squares estimation of nonlinear parameters. *Journal of the Society for Industrial and Applied Mathematics*, *11(2)*, 431-441.

Martin, R. (2017). *Landships google Homepage - British Tank actions of the First World War*. Retrieved August 18, 2018, from https://sites.google.com/site/landships/home

Masters, P., Stichelbaut, B. (2009). From the air to beneath the soil – revealing and mapping great war trenches at Ploegsteers (Comines-Warneton), Belgium. *Archaeological Prospection*, *16(4)*, 279-285.

Mattsson, E., Nord, A., Tronner, K., Fjaestad, M., Lagerlöf, A., Ullén, I., Borg, G. (1996). *Deterioration of archaeological material in soil; Results on bronze artefacts*. *Konserveringstekniska Studier RIK, Riksantikvarieämbetet och Statens Historiska Museer 10*. Stockholm: Riksantikvarieämbetet Förlag.

McNeill, J. (1980). *Electromagnetic terrain conductivity measurement at low induction numbers*. *Technical NoteTN-6*. Ontario: Geonics Limited.

McNeill, J., Bosna, M. (1999). *Application of "dipole-dipole" electromagnetic systems for geological depth sounding. Technical Note TN-31*. Ontario: Geonics Limited.

McVeigh, E., Henkelman, R., Bronskill, M. (1985). Noise and filtration in magnetic resonance imaging. *Medical Physics, 12(5)*, 586-591.

Meerschman, E., Cockx, L., Islam, M., Meeuws, F., Van Meirvenne, M. (2011). Geostatistical Assessment of the Impact of World War I on the Spatial Occurrence of Soil Heavy Metals. *AMBIO, 40*, 417-424.

Meylemans, E., De Smedt, P. (2018). *Geophysical prospection in Flanders: a summary*. Conference: De rol van geofysisch onderzoek in het archeologieproces. Brussels: Agentschap Onroerend Erfgoed.

Milsom, J. (2002). *Field Geophysics* (3rd edition). London: University College, 235 pp.

*Ministerieel besluit tot voorlopige bescherming als archeologische site van het Eerste Wereldoorlog-slagveld van Bellewaarde Ridge in Ieper (Ieper, Zillebeke)* (2018). Retrieved October 16, 2018, from https://besluiten.onroerenderfgoed.be/besluiten/14681/bestanden/18330

Münch, B., Trtik, P., Marone, F., Stampanoni, M. (2009). Stripe and ring artifact removal with combined wavelet - Fourier filtering. *Optics Express. 10(17)*, 8567-8591.

Nabighian, M. (Ed.) (1987). *Investigations in Geophysics. Electromagnetic Methods in Applied Geophysics: Volume 1, Theory*. Oklahoma: Society of Exploration Geophysicists, 531 pp.

Nicholson, G. (1962). Official History of the Canadian Army in the First World War: Canadian Expeditionary Force, 1914–1919. Ottowa: Queen's Printer and Controller of Stationery.

Note, N., De Smedt, P., Saey, T., Gheyle, W., Stichelbaut, B., Van den Berghe, H., Bourgeois, J., Van Eetvelde, V., Van Meirvenne, M. (2017). Removal of sensor tilt noise in fluxgate gradiometer survey data by applying one dimensional wavelet filtering. *Archaeological Prospection*, *24(4)*, 353-360.

Note, N., Gheyle, W., Van den Berghe, H., Saey, T., Bourgeois, J., Van Eetvelde, V., Van Meirvenne, M., Stichelbaut, B. (2018). A new evaluation approach of World War One's devastated front zone: a shell hole density map based on historical aerial photographs and validated by electromagnetic induction field measurements to link the metal shrapnel phenomenon. *Geoderma*, *310(C)*, 257-269.

Opitz, R., Cowley, D. (2013). *Interpreting Archaeological Topography: Lasers, 3D Data, Observation, Visualisation and Applications*. Oxford: Oxbow.

Osgood, R., Brown, M. (2009). *Digging up Plugstreet. The Archaeology of a Great War Battlefield*. Yeovil: Haynes Publishing.

Paesen, J., Creemers, G., Meylemans, E., De Bie, M. (2010). Hernieuwd Celtic Fields onderzoek in de Limburgse Kempen (België). *Lunula Archaeologia Protohistorica*, *18*, 151-153.

Paoletti, V., Fedi, M., Florio, G., Rapolla, A. (2007). Localized cultural denoising of high-resolution aeromagnetic data. *Geophysical Prospecting*, *55(3)*, 421-432.

Pearson, C., Coates, P., Cole, T. (2010). *Militarized Landscapes, From Gettysburg to Salisbury Plain* (1st edition). Switserland: Bloomsbury Academic.

Pollard, T., Banks, I. (2014). Beyond recall: searching for the remains of a British secret weapon of World War I. *Journal of Conflict Archaeology*, *9(3)*, 119-155.

Pollard, T., Banks, I. (2007). Not so Quiet on the Western Front: Progress and Prospect in the Archaeology of the First World War. *Journal of Conflict Archaeology*, *3(1)*, iii-xvi.

Price, J. (2005). Orphan heritage: Issues in managing the heritage of the Great War in northern France and Belgium. *Journal of Conflict Archaeology*, *1(1)*, 181-196.

*Quad2800 specifications* (n.d.). Retrieved July 6, 2018, from https://www.veristech.com/the-sensors/q2800

Quaranta, M. (2009). On the degradation mechanisms under the influence of pedological factors through the study of archaeological bronze patina. *Doctoral dissertation*, University of Bologna.

Rash, F., Declercq, C. (2018). *The Great War in Belgium and the Netherlands: Beyond Flanders Fields*. Switserland: Palgrave Macmillan, 226 pp.

*Red Zone Map-fr.svg* (n.d.). Retrieved October 18, 2017, from https://commons.wikimedia.org/wiki/File:Red_Zone_Map-fr.svg

Rhoades, J., Halvorson, A. (1977). *Electrical conductivity methods for detecting and delineating saline seeps and measuring salinity in Northern Great Plains soils*. ARS W-42. Berkeley CA: USDA-ARS.

Romanoff, M. (1957). *Underground Corrosion*. U.S. Department of Commerce: National Bureau of Standards. Circular 579.

Roy, A., Apparao, A. (1971). Depth of investigation in direct current methods. *Geophysics*, *36(5)*, 943-959.

Saey, T. (2011). Fusing multiple signals of an electromagnetic induction sensor to characterize contrasting soil layers and buried features. *Doctoral dissertation*, Ghent University.

Saey, T., De Smedt, P., Meerschman, E., Islam, M.M., Meeuws, F., Van De Vijver, E., Lehouck, A., Van Meirvenne, M. (2012). Electrical conductivity depth modelling with a multireceiver EMI sensor for prospecting archaeological features. *Archaeological Prospection*, *19*, 21–30.

Saey, T., Gheyle, W., Stichelbaut, B., Bourgeois, J., Verplaetse, S., Van Eetvelde, V., Note, N., Van Meirvenne M. (2016a). The characterization of a former World War I battlefield by integrating multiple signals from multi-receiver EMI soil sensor. *Geoarchaeology*, *31(4)*, 267-281.

Saey, T., Note, N., Gheyle, W., Stichelbaut, B., Bourgeois, J., Van Eetvelde, V., Van Meirvenne, M. (2016b). EMI as a non-invasive survey technique to account for the interaction between WW I relicts and the soil environment at the Western front. *Geoderma*, *265*, 39-52.

Saey, T., Stichelbaut, B., Bourgeois, J., Van Eetvelde, V., Van Meirvenne, M. (2013). Short Report: An interdisciplinary non-invasive approach to landscape archaeology of the Great War. *Archaeological Prospection*, *20*, 39-44.

Saey, T., Van Meirvenne, M., Dewilde M., Wyffels, F., De Smedt, P., Meerschman, E., Islam, M.M., Meeuws, F., Cockx, L. (2011). Combining multiple signals of an electromagnetic induction sensor to prospect land for metal objects. *Near Surface Geophysics, 9*, 309-317.

Saunders, N. (2012). *Introduction: engaging the Materialities of twentieth and Twenty-first Century Conlict*. In Saunders (Ed.), Beyond the Dead Horizon: Studies in Modern Conflict Archaeology, 10-14. Oxford and Oakville: Oxbow Books.

Scantech Geoscience (n.d.). *About GPR*. Retrieved June 20, 2018, from http://scantech.ie/scantech-about-gpr.html

Schmidt, A., Linford, P., Linford, N., David, A., Gaffney, C., Sarris, A., Fassbinder, J. (2015). *EAC Guidelines for the Use of Geophysics in Archaeology: Questions to Ask and Points to Consider. EAC Guidelines 2*. Namur: Europae Archaeologia Consilium (EAC).

Schwertmann, V., Taylor, R. (1977). *Iron oxides*. In J. Dixon, S. Weed (Eds.), Minerals in soil environments, 145-180. Wisconsin: Soil Science Society of America.

Scott, D., McFeaters, A. (2010). The Archaeology of Historic Battlefields: A History and Theoretical Development in Conflict Archaeology. *Journal of Archaeological Research, 19,* 103-132.

Sensys Gmbh. *Vertical difference magnetometer FGM650 Series*. Retrieved January 17, 2016, from http://www.sensys.de/index.php/en/fgm650.html?file=files/pi/PI_FGM650_EN.pdf

Sheldon, S. (2007). *The German Army at Passchendaele*. South Yorkshire: Pen & Sword Books Ltd, 352 pp.

Shen, G., Sarris, A., Papadopoulos, N. (2007). Enhancing Geophysical Signals from Archaeological Sites Through the Use of Wavelet Transforms. *WSEAS transactions on systems*, *7(3)*, 140-147.

Shupe, T., Lebow, S., Ring, D. (2008). *Causes and control of wood decay, degradation and stain*. Louisiana: LSU Ag Center, 27 pp.

Simoens, T. (2016). *De chaos van het slagveld: Het Belgisch leger in de loopgraven 1914-1918*. Antwerp: Overamstel Uitgevers, 608 pp.

Sittler, B., Hauger, K. (2007). *Les apports du laser aéroporté à la documentation de parcellaires anciens fossilisés par la forêt : l'exemple des champs bombés de Rastatt en Pays de Bade*. In J.-L. Dupouey, E. Dambrine, C. Dardignac & M. Georges-Leroy (Eds.), La mémoire des forêts, 155-161.

Sorensen, K., Christiansen, A., Auken, E. (2009). *The transient electromagnetic method (TEM)*. Retrieved May 17, 2018, from https://www.liag-hannover.de/fileadmin/user_upload/dokumente/grundwassersysteme/burval/buch/065-076.pdf

Starkey, R., Wight, K. (1945). *Anaerobic Corrosion of Iron in Soil: with particular consideration of the soil redox potential as an indicator of corrosiveness*. New York: American Gass Association, 108 pp.

Stichelbaut, B. (2006). The application of First World War aerial photography to archaeology: the Belgian images. *Antiquity*, *80*, 161–172.

Stichelbaut, B. (2009). World War One Aerial Photography: An Archaeological Perspective. Department of Archaeology. *Doctoral dissertation*, Ghent University.

Stichelbaut, B. (2011). The First Thirty Kilometres of the Western Front 1914-1918: an Aerial Archaeoloical Approach with Historical Remote Sensing Data. *Archaeological Prospection*, *18(1)*, 57-66.

Stichelbaut, B. (2015a). *Forgotten and lost? Archival research of aerial photographic collections of the Western Front 1914-1918: A guide to the archives*. Ljubljana: Založba ZRC.

Stichelbaut, B. (2015b). *Heuvelland Kapellerie: Historisch vooronderzoek projectgebied a.d.h.v. historische luchtfoto's en loopgravenkaarten*. Ghent: Centrum voor historische en archeologische luchtfotografie, 28pp.

Stichelbaut, B., Chielens, P. (2013). The Great War seen from the air. Brussels: Mercatorfonds, 352 pp.

Stichelbaut, B., Gheyle, W., Saey, T., Van Eetvelde, V., Van Meirvenne, M., Note, N., Van den Berghe, H., Bourgeois, J. (2016). The First World War from above and below. Historical aerial photographs and mine craters in the Ypres Salient. *Applied Geography*, *66*, 64–72.

Stichelbaut, B., Gheyle, W., Van Eetvelde, V., Van Meirvenne, M., Saey, T., Note, N., Van den Berghe, H., Bourgeois, J. (2017a). The Ypres Salient 1914-1918: historical aerial photography and the landscape of war. *Antiquity*, *91(355)*, 235-249.

Stichelbaut, B., Note, N., Bourgeois, J., Van Meirvenne, M., Van Eetvelde, V., Van den Berghe, H., Gheyle, W. (2018). The archaeology of First World War tanks in the Ypres Salient (Belgium): a non-invasive approach. *Archaeological Prospection*, published online, 28 August 2018.

Stichelbaut, B., Note, N., Saey, T., Hanssens, D., Van den Berghe, H., Bourgeois, J., Van Meirvenne, M., Van Eetvelde, V., Gheyle, W. (2017b). Non-invasive research of tunnelling heritage in the Ypres Salient (1914-1918) – research of the Tor Top tunnel system. *Journal of Cultural Heritage, 26*, 109-117.

Stichelbaut, B., Saey, T., Meeuws, F., Bourgeois, J., Van Meirvenne, M. (2011). *World War One Heritage in Belgium: combining historical aerial photography and EMI*. In D. Cowley (Ed.), Remote Sensing for Archaeological Heritage Management, Volume 3, 265-273. Budapest: Archaeolingua.

Storey, N. (2014). *The Tommy's Handbook*. Gloucestershire: The History Press.

Taborelli, P., Devos, A., Laratte, S., Brenot, J., Bollot, N., Cancès, B., Defossés, Y. (2017). Apport des plans directeurs et de l'outil LiDAR aéroporté pour la caractérisation des impacts morphologiques de la Grande Guerre : exemple de la cote 108 (Berry-au-Bac, France). *Géomorphologie: relief, processus, environnement*, *23(2)*, 26 pp.

Terron, J., Mayoral, V., Salgado, J., Galea, F., Pérez, V., Odriozola, C., Mateos, P., Pizzo, A. (2015). Use of soil apparent electrical resistivity contact sensors for the extensive study of archaeological sites. *Journal of Archaeological Prospection*, *22*, 269-281.

Telford, W., Geldart, L., Sheriff, R. (1990). *Applied Geophysics* (2nd edition). Cambridge: University Press, 770 pp.

*The comfortable German dugouts* (n.d.). Retrieved, August 23, 2018, from http://www.oldmagazinearticles.com/WW1-German_German-Dugouts#.W-BlkdVKiHs

Trachet, J., Deleforstrie, S., Dombrecht, K., Dumolyn, J., Leloup, W., Thoen, E., Van Meirvenne, M., De Clercq, W. (2015). Turning back the tide: The Zwin debate in perspective. A historiographical review of the medieval port system northeast of Bruges. *Archeologie de la Picardie et du Nord de la France, 413(97)*, 305-321.

Trinks, I., Larsson, L., Gabler, M., Nau, E., Neubauer, W., Klimcyk, A., Söderberg, B., Thorén, H. (2013). Large-scale archaeological prospection of the Iron Age settlement site Uppakra – Sweden. *Archaeological Prospection: Proceedings of the 10th international conference – Vienna*.

Tsivouraki, B., Tsokas, N. (2007). Wavelet transform in denoising magnetic archaeological prospecting data. *Archaeological Prospection, 14(2)*, 130 – 141.

Revie, R. (Ed.) (2011). *Uhlig's Corrosion Handbook* (3rd Edition). Electrochemical Society Series. New Jersey: John Wiley & sons, 1253 pp.

Van De Vijver, E. (2017). Proximal soil sensing in the context of urban (re)development: an evaluation of multi-receiver electromagnetic induction and stepped-frequency ground penetrating radar at landfills and industrial sites. *Doctoral dissertation*, Ghent University.

Van den Berghe, H., Gheyle, W., Note, N., Stichelbaut, B., Bourgeois, J, Van Meirvenne, M, Van Eetvelde, V. (2018). Using the past to indicate the possible presence of relics in the present-day landscape: The Western Front of the Great War in Belgium. *Journal of Landscape Research*, published online, 25 January 2018.

Van Outryve d'Ydewalle, P., Viaene, A. (1958). *West-Vlaanderen*. Brugge: Meddens.

Van Grembergen, P. (2003-2004). *Beleidsbrief Monumenten, Landschappen en Archeologie. Beleidsprioriteiten*. Retrieved October 8, 2018, from http://docs.vlaamsparlement.be/pfile?id=1049715

Van Hollebeeke, Y. (2012). Archeologie van het conflict in Vlaanderen: Tien jaar professionele archeologie van de Eerste Wereldoorlog onder de loep. *Master dissertation*, Ghent University.

Van Hollebeeke, Y., Stichelbaut, B., Bourgeois, J. (2014). From landscape of war to archaeological report: ten years of professional World War I archaeology in Flanders (Belgium). *European Journal of Archaeology, 17(4)*, 702-719.

Van Meirvenne, M., Meklit, T., Verstraete, S., De Boever, M., Tack, F. (2008). Could shelling in the First World War have increased copper concentrations in the soil around Ypres? *European Journal of Soil Science*, *59(2)*, 372-379.

Verhoeven, G. (2017). The reflection of two fields – Electromagnetic radiation and its role in aerial imaging. *AARGnews*, *55*, 13-18.

Wait, J. (1962). A note on the electromagnetic response of a stratified earth. *Geophysics, 27*, 382-385.

*World War One Battlefields: Hooge* (n.d.). Retrieved August 27, 2018, from http://www.ww1battlefields.co.uk/flanders/hooge/

Büyüksaraç, Y., Yalçıner, C., Ekinci, Y., Demirci, A., Yücel, M. (2014). Geophysical investigations at Agadere Cemetery, Gallipoli Peninsular, NW Turkey. *Australian Journal of Forensic Sciences*, *46(1)*, 111-123.

Zaksek, K., Ostir, K., Kokalj, Z. (2011). Sky-view factor as a relief visualization technique. *Remote Sensing*, *3(2)*, 398–415.

# Curriculum Vitae

## 1. Personal information


| | |
|---|---|
| Name: | Nicolas Note |
| Date of birth: | 15/11/1990 |
| Address: | Dijk 53, 8670 WULPEN, BELGIUM |
| Email: | Nicolas.Note@UGent.be / nicolasnote@hotmail.com |
| Tel.: | 0032(0)475535897 |


## 2. Education

| | |
|---|---|
| 2015 – 2019 | PhD research |
| 2011 – 2013 | Master of science in geomatics and land surveying |
| 2008 – 2011 | Bachelor of science in geomatics and land surveying |

## 3. Professional experience

| | |
|---|---|
| 2015 – 2019 | doctoral fellow, Ghent University, Belgium |
| 2014-15 | project collaborator, Ghent University, Belgium |
| 2014 | land surveyor, Kortrijk, Belgium |

**Involvement FDEM survey/projects**

- Non-invasive landscape archaeology of the Great War, Ghent University's special research fund Concerted Research Action 2014–2018 [grant number 01G00214].
- Geophysical survey at Waterloo, Project: Waterloo Uncovered
- Geophysical survey at Damme (Oostkerke, Belgium). Project: Medieval Bruges and its outer ports. A landscape archaeological contribution to the Zwin-debate.
- Geophysical research of a moated site in Sint-Baafs-Vijve (2015).

- Geophysical research of the battle of Halen (2016-17), commissioned by the Flanders Agency of Cultural Heritage.
- Archaeological geophysical study for the Bellewaerde aqua park (2017), commissioned by LD-architecten Kortrijk.
- Geophysical prospection domein Raversyde (2018), commissioned by the province of West-Flanders.

## 4. Publications

**(A1)**

**Note, N.**, Saey, T., Gheyle, W., Stichelbaut, B., Van den Berghe, H., Bourgeois, J., Van Eetvelde, V., Van Meirvenne, M. (2018). Evaluation of Fluxgate Magnetometry and Electromagnetic Induction Surveys for Subsurface Characterization of Archaeological Features in World War One Battlefields. *Geoarchaeology*, published online.

Stichelbaut, B., **Note, N.**, Bourgeois, J., Van Meirvenne, M., Van Eetvelde, V., Van den Berghe, H., Gheyle, W. (2018). The archaeology of First World War tanks in the Ypres Salient (Belgium): a non-invasive approach. *Archaeological Prospection*, published online.

Van den Berghe, H., Gheyle, W., **Note, N.**, Stichelbaut, B., Bourgeois, J, Van Meirvenne, M, Van Eetvelde, V. (2018). Using the past to indicate the possible presence of relics in the present-day landscape: The Western Front of the Great War in Belgium. *Journal of Landscape Research*, (published online, 25 January 2018).

**Note, N.**, Gheyle, W., Van den Berghe, H., Saey, T., Bourgeois, J., Van Eetvelde, V., Van Meirvenne, M., Stichelbaut, B. (2018). A new evaluation approach of World War One's devastated front zone: a shell hole density map based on historical aerial photographs and validated by electromagnetic induction field measurements to link the metal shrapnel phenomenon. *Geoderma*, *310(C)*, 257-269.

Gheyle, W., Stichelbaut, B., Saey, T., **Note, N.**, Van den Berghe, H., Van Eetvelde, V., Van Meirvenne, M., Bourgeois, J. (2018) Scratching the surface of war. Airborne laser scans of the Great War conflict landscape in Flanders (Belgium). *Journal of Applied Geography*, *90*, 55-68.

**Note, N.**, De Smedt, P., Saey, T., Gheyle, W., Stichelbaut, B., Van den Berghe, H., Bourgeois, J., Van Eetvelde, V., Van Meirvenne, M. (2017). Removal of sensor tilt noise in fluxgate gradiometer survey data by applying one dimensional wavelet filtering. *Archaeological Prospection*, *24(4)*, 353-360.

Stichelbaut, B., **Note, N.**, Saey, T., Hanssens, D., Van den Berghe, H., Bourgeois, J., Van Meirvenne, M., Van Eetvelde, V., Gheyle, W. (2017). Non-invasive research of tunnelling heritage in the Ypres Salient (1914-1918) – research of the Tor Top tunnel system. *Journal of Cultural Heritage*, *26*, 109-117.

Stichelbaut, B., Gheyle, W., Van Eetvelde, V., Van Meirvenne, M., Saey, T., **Note, N.**, Van den Berghe, H., Bourgeois, J. (2017). The Ypres Salient 1914-1918: historical aerial photography and the landscape of war. *Antiquity*, *91(355)*, 235-249.

Saey, T., Gheyle, W., Stichelbaut, B., Bourgeois, J., Verplaetse, S., Van Eetvelde, V., **Note, N.**, Van Meirvenne M. (2016). The characterization of a former World War I battlefield by integrating multiple signals from multi-receiver EMI soil sensor. *Geoarchaeology*, *31(4)*, 267-281.

Saey, T., **Note, N.**, Gheyle, W., Stichelbaut, B., Bourgeois, J., Van Eetvelde, V., Van Meirvenne, M. (2016). EMI as a non-invasive survey technique to account for the interaction between WW I relicts and the soil environment at the Western front. *Geoderma*, *265*, 39-52.

Gheyle, W., Saey, T., Van Hollebeeke, Y., Verplaetse, S., **Note, N.**, Bourgeois, J., Van Meirvenne, M., Van Eetvelde, V., Stichelbaut, B. (2016). Historical aerial photography and multi-receiver EMI soil sensing, complementing techniques for the study of a Great War conflict landscape. *Archaeological Prospection*, *23(3)*, 149-164.

Stichelbaut, B., Gheyle, W., Saey, T., Van Eetvelde, V., Van Meirvenne, M., **Note, N.**, Van den Berghe, H., Bourgeois, J., (2016). The First World War from above and below. Historical aerial photographs and mine craters in the Ypres Salient. *Applied Geography*, *66*, 64–72.

**(C3)**

Stichelbaut,B., Gheyle, W., **Note, N.**, Van den Berghe, H., Van Eetvelde, V., Van Meirvenne, M., Bourgeois, J. (2018). Non-Invasive Landscape Archaeology of the Great War (Belgium). Colloque Impact 14-18, Reims.

Van den Berghe, H., Gheyle, W., **Note, N.**, Stichelbaut, B., Hanssens, D., Bourgeois, J., Van Meirvenne, M., Van Eetvelde, V. (2017). Discovering the lost Great War heritage in the present-day landscape based on an interdisciplinary landscape change analysis. IALE European congress.

**Note, N.**, Saey, T., Gheyle, W., Stichelbaut., B., Van den Berghe, H., Van Eetvelde, V., Bourgeois, J., Van Meirvenne M. (2017). Insights in the possibilities of an electromagnetic induction sensor to map the military remains, buried in the former World War 1 front zone. Pedometrics, Wageningen.

Van den Berghe, H., Gheyle, W., Stichelbaut, B., **Note, N.**, Saey, T., Bourgeois, J., Van Meirvenne, M., et al. (2016). Identifying relations between the dynamic military landscape and network of linear features throughout the Great War. Permanent European Conference for the Study of the Rural Landscape.

Gheyle, W., Bourgeois, J., Bracke, M., Dalle, S., Deconynck, J., Decorte, J., De Langhe, K., De Mulder, G., Hanssens, D., Heyvaert, B., **Note, N.**, Saey, T., Stichelbaut, B., Van Den Berghe, H., Van Eetvelde, V., Van Hollebeeke, Y., Van Meirvenne, M., Verdegem,

S. (2016a). 'Interdisciplinair onderzoek naar een Brits-Australisch barakkenkamp in het niemandsland te Kemmel (W-VL)'. Conflict in Contact, Gent.

**Note, N.**, Saey, T., Gheyle, W., Stichelbaut., B., Van den Berghe, H., Van Eetvelde, V., Bourgeois, J., Van Meirvenne M. (2016). Belgium's World War 1 front zone today: a sleeping UXO problem characterised by frequency domain EMI. EUROEM, London.